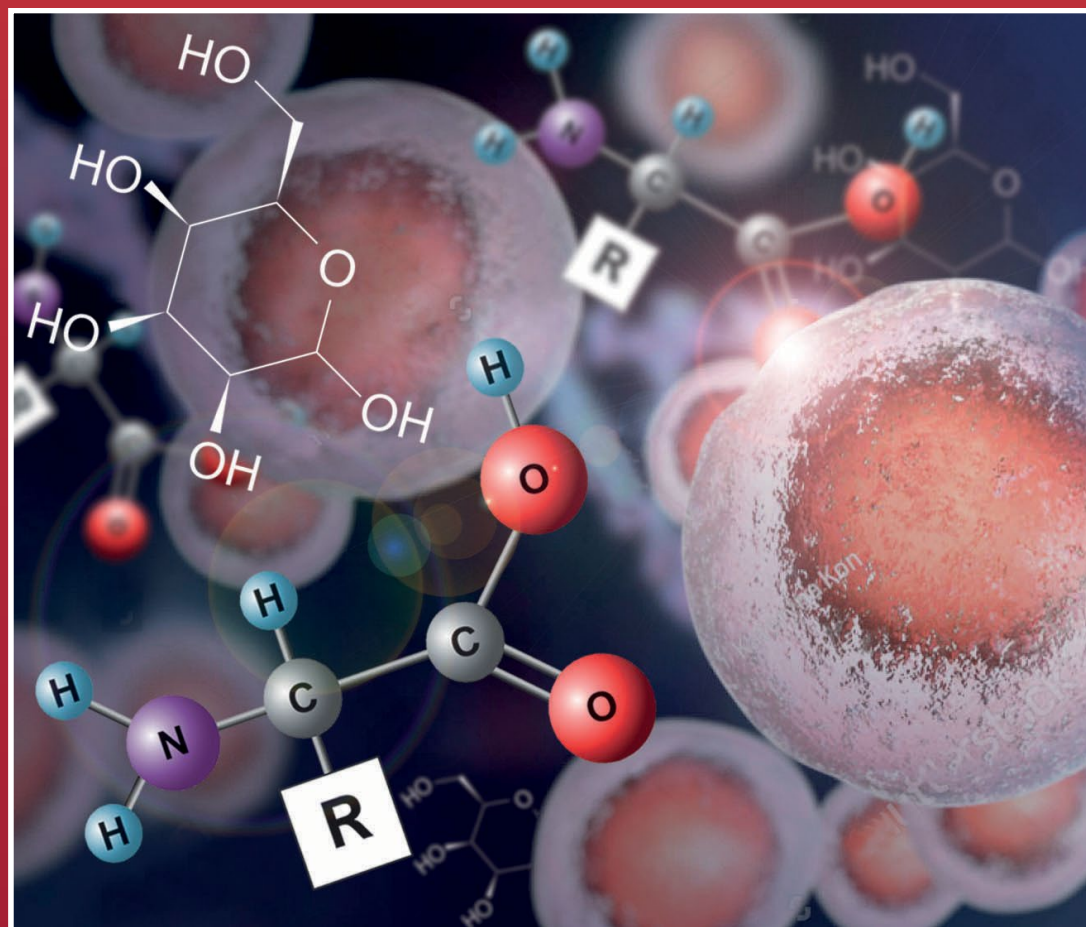




# Acta Chimica Slo Acta Chimica Slo Slovenica Acta C

4

65/2018



---

## EDITOR-IN-CHIEF

**KSENIJA KOGEJ**

Slovenian Chemical Society, Hajdrihova 19, SI-1000 Ljubljana, Slovenija,

E-mail: [ACSi@fkk.uni-lj.si](mailto:ACSi@fkk.uni-lj.si), Telephone: (+386)-1-479-8538

## ASSOCIATE EDITORS

**Janez Cerkovnik**, *University of Ljubljana, Slovenia*  
**Krištof Kranjc**, *University of Ljubljana, Slovenia*  
**Ksenija Kogej**, *University of Ljubljana, Slovenia*  
**Franc Perdih**, *University of Ljubljana, Slovenia*  
**Aleš Podgornik**, *University of Ljubljana, Slovenia*  
**Helena Prosen**, *University of Ljubljana, Slovenia*  
**Damjana Rozman**, *University of Ljubljana, Slovenia*

**Melita Tramšek**, *Jožef Stefan Institute, Slovenia*  
**Irena Vovk**, *National Institute of Chemistry, Slovenia*

## ADMINISTRATIVE ASSISTANT

**Marjana Gantar Albreht**, *National Institute of Chemistry, Slovenia*

---

## EDITORIAL BOARD

**Wolfgang Buchberger**, *Johannes Kepler University, Austria*  
**Alojz Demšar**, *University of Ljubljana, Slovenia*  
**Stanislav Gobec**, *University of Ljubljana, Slovenia*  
**Marko Goličnik**, *University of Ljubljana, Slovenia*  
**Günter Grampp**, *Graz University of Technology, Austria*  
**Wojciech Grochala**, *University of Warsaw, Poland*  
**Danijel Kikelj**, *Faculty of Pharmacy, Slovenia*  
**Janez Košmrlj**, *University of Ljubljana, Slovenia*  
**Blaž Likozar**, *National Institute of Chemistry, Slovenia*  
**Mahesh K. Lakshman**, *The City College and  
The City University of New York, USA*

**Janez Mavri**, *National Institute of Chemistry, Slovenia*  
**Friedrich Sreinc**, *University of Minnesota, USA*  
**Walter Steiner**, *Graz University of Technology, Austria*  
**Jurij Svete**, *University of Ljubljana, Slovenia*  
**Ivan Švancara**, *University of Pardubice, Czech Republic*  
**Jiri Pinkas**, *Masaryk University Brno, Czech Republic*  
**Gašper Tavčar**, *Jožef Stefan Institute, Slovenia*  
**Christine Wandrey**, *EPFL Lausanne, Switzerland*  
**Ennio Zangrando**, *University of Trieste, Italy*

---

## ADVISORY EDITORIAL BOARD

### Chairman

Branko Stanovnik, Slovenia

### Members

Josef Barthel, Germany  
Udo A. Th. Brinkman, The Netherlands  
Attilio Cesaro, Italy  
Dušan Hadži, Slovenia  
Vida Hudnik, Slovenia  
Venčeslav Kaučič, Slovenia

Željko Knez, Slovenia  
Radovan Komel, Slovenia  
Janez Levec, Slovenia  
Stane Pejovnik, Slovenia  
Anton Perdih, Slovenia  
Slavko Pečar, Slovenia  
Andrej Petrič, Slovenia  
Boris Pihlar, Slovenia  
Milan Randić, Des Moines, USA

Jože Škerjanc, Slovenia  
Miha Tišler, Slovenia  
Đurđa Vasić-Rački, Croatia  
Marjan Veber, Slovenia  
Gorazd Vesnaver, Slovenia  
Jure Zupan, Slovenia  
Boris Žemva, Slovenia  
Majda Žigon, Slovenia

---

*Acta Chimica Slovenica* is indexed in: *Chemical Abstracts Plus*, *Current Contents (Physical, Chemical and Earth Sciences)*, *PubMed*, *Science Citation Index Expanded* and *Scopus*. Impact factor for 2017 is IF = 1.104.



Articles in this journal are published under Creative Commons Attribution 3.0 License

<http://creativecommons.org/licenses/by/3.0/>

---

### Izdaja – Published by:

**SLOVENSKO KEMIJSKO DRUŠTVO – SLOVENIAN CHEMICAL SOCIETY**

Naslov redakcije in uprave – Address of the Editorial Board and Administration

Hajdrihova 19, SI-1000 Ljubljana, Slovenija

Tel.: (+386)-1-476-0252; Fax: (+386)-1-476-0300; E-mail: [chem.soc@ki.si](mailto:chem.soc@ki.si)

### Izdajanje sofinancirajo – Financially supported by:

Slovenian Research Agency, Ljubljana, Slovenia

National Institute of Chemistry, Ljubljana, Slovenia

Jožef Stefan Institute, Ljubljana, Slovenia

Faculty of Chemistry and Chemical Technology at University of Ljubljana, Slovenia

Faculty of Chemistry and Chemical Engineering at University of Maribor, Slovenia

Faculty of Pharmacy at University of Ljubljana, Slovenia

University of Nova Gorica, Nova Gorica, Slovenia



*Acta Chimica Slovenica* izhaja štirikrat letno v elektronski obliki na spletni strani <http://acta.chem-soc.si>. V primeru posvečenih števil izhaja revija tudi v tiskani obliki v omejenem številu izvodov.

*Acta Chimica Slovenica* appears quarterly in electronic form on the web site <http://acta.chem-soc.si>. In case of dedicated issues, a limited number of printed copies are issued as well.

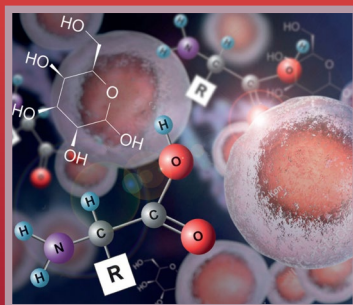
Transakcijski račun: 02053-0013322846 Bank Account No.: SI56020530013322846-Nova Ljubljanska banka d. d., Trg republike 2, SI-1520 Ljubljana, Slovenia, SWIFT Code: LJBA SI 2X

Oblikovanje ovitka – Design cover: KULT, oblikovalski studio, Simon KAJTNA, s. p. Grafična priprava za tisk: Majanafin, d. o. o.

Tisk-Printed by: Tiskarna Stušek, Ljubljana

© Copyright by Slovenian Chemical Society

# Graphical Contents



ActaChimicaSlo  
ActaChimicaSlo  
SlovenicaActaC

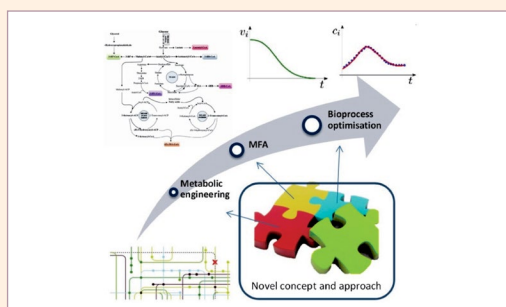
Year 2018, Vol. 65, No. 4

## FEATURE ARTICLE

769–786 Chemical, biochemical and environmental engineering

### Metabolic Network Modelling of Chinese Hamster Ovary (CHO) Culture Bioreactors Operated as Microbial Cell Factories

Jernej Gašperšič, Miha Kastelic, Uroš Novak and Blaž Likozar

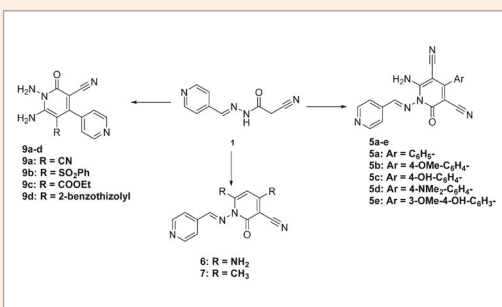


## SCIENTIFIC PAPER

787–794 Organic chemistry

### Synthesis, Characterization and Cytotoxicity Evaluation of Some Novel Pyridine Derivatives

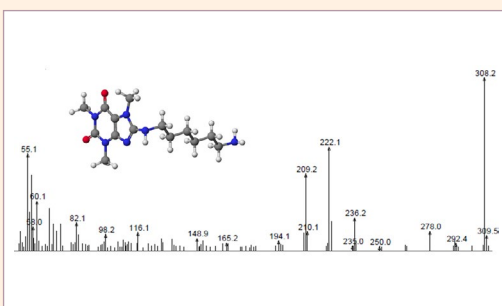
Eman H. Tawfik, Khaled Samir Mohamed, Hemat M. Dardeer and Ahmed Ali Fadda



795–800 Analytical chemistry

### Mass Spectrometry Study of New Polyamine Derivatives of Caffeine

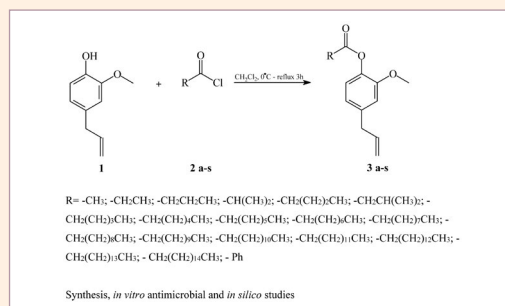
Arleta Sierakowska, Beata Jasiewiczza and Tomasz Pospieszny



801–810 Organic chemistry

## Synthesis, Antimicrobial Activity and *in silico* Studies on Eugenol Ethers

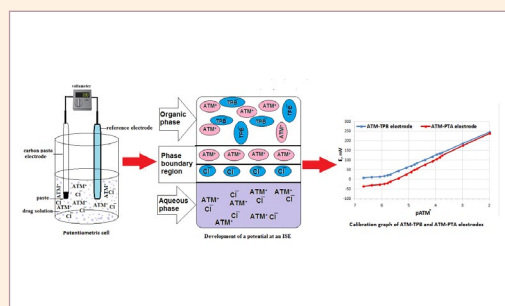
Jelena Lazarević, Ana Kolarević, Gordana Stojanović, Andrija Šmelcerović, Pierangela Ciuffreda and Enzo Santaniello



811–822 Analytical chemistry

## Determination of Atomoxetine Hydrochloride in Biological Fluids Using Potentiometric Carbon Paste Electrode Modified by TiO<sub>2</sub> Nanoparticles

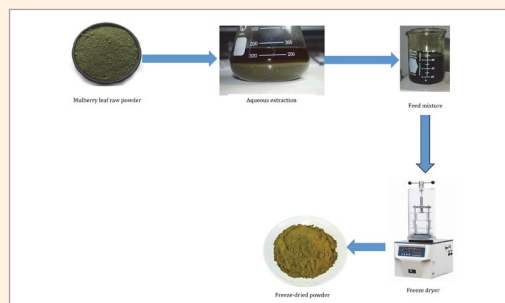
Hazem M. Abu Shawish, Hassan Tamous, Salman M. Saadeh and Ahmad Tbaza



823–835 Applied chemistry

## Carrier Effects on the Chemical and Physical Properties of Freeze-Dried Encapsulated Mulberry Leaf Extract Powder

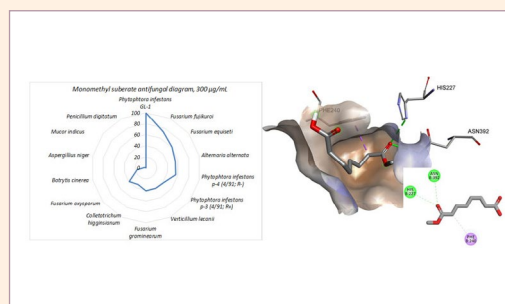
William Tchabo, Yongkun Ma, Giscard Kuate Kaptso, Emmanuel Kwaw, Rosine Wafo Cheno, Meng Wu, Richard Osae, Shengmei Ma and Muhammad Farooq



836–841 Biomedical applications

## Monomethyl Suberate Screening for Antifungal Activity, Molecular Docking and Drug-Like Properties

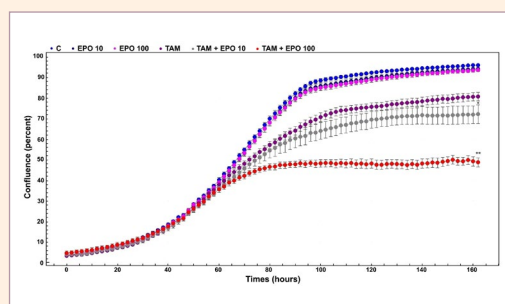
Lyudmyla Antypenko, Fatuma Meyer, Zhanar Sadykova, Leif-Alexander Garbe and Karl Steffens



842–846 Biomedical applications

## Erythropoietin Potentiates the Anti-Proliferative Effect of Tamoxifen in Ovarian Adenocarcinoma A2780 Cells

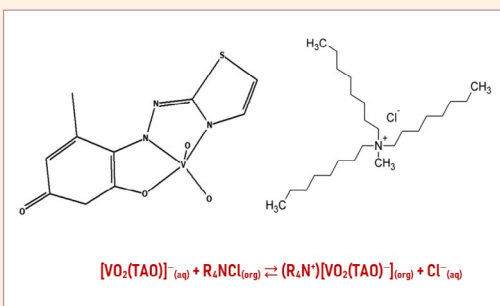
Patřicia Kimáková, Erika Szentpéteriová, Barbora Fecková, Nataša Debeljak and Peter Solár



847–852 Inorganic chemistry

## Liquid-Liquid Extraction-Chromogenic System for Vanadium(V) Based on 4-(2-thiazolylazo)orcinol (TAO) and Aliquat 336

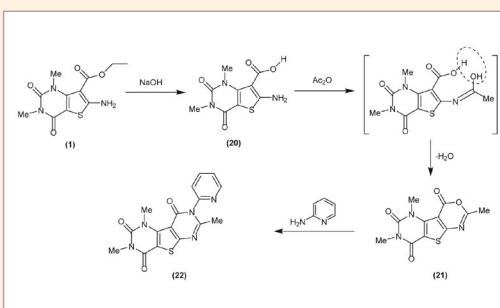
Galya K. Toncheva, Nikolina P. Milcheva, and Kiril Blazhev Gavazov



853–864 Organic chemistry

## Synthesis and Cytotoxic Activity of Some Novel Thieno[2,3-d:4,5-d']Dipyrimidine Derivatives

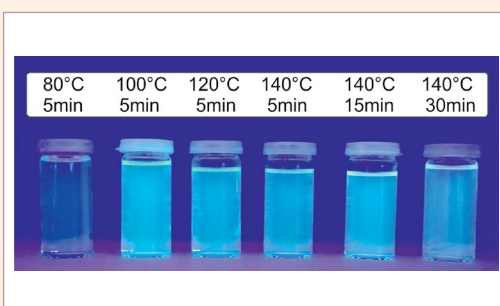
Elsherbiny Hamdy El-Sayed\* and Ahmed Ali Fadda



865–874 Applied chemistry

## Microwave Assisted Conversion of an Amino Acid into a Fluorescent Solution

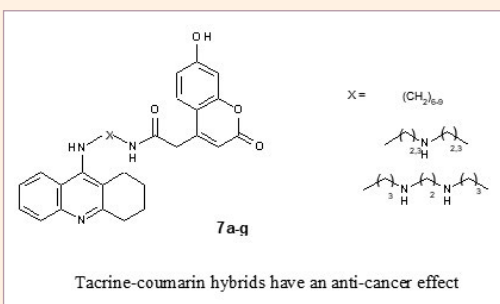
Lena Charlyn Greiler, Hajo Haase and Boris Mahltig



875–881 Biomedical applications

## Anti-Cancer Effect of Tacrine-Coumarin Derivatives on Diverse Human and Mouse Cancer Cell Lines

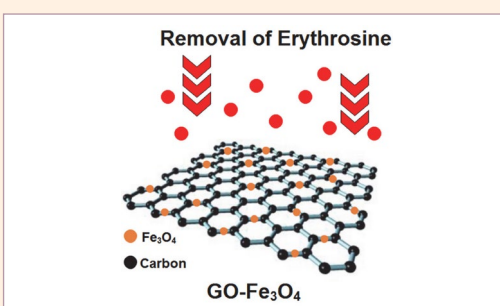
Zuzana Solárová, Martin Kello, Slávka Hamuláková, Ladislav Mirossay and Peter Solár



882–894 Applied chemistry

## Erythrosine Adsorption from Aqueous Solution via Decorated Graphene Oxide with Magnetic Iron Oxide Nano Particles: Kinetic and Equilibrium Studies

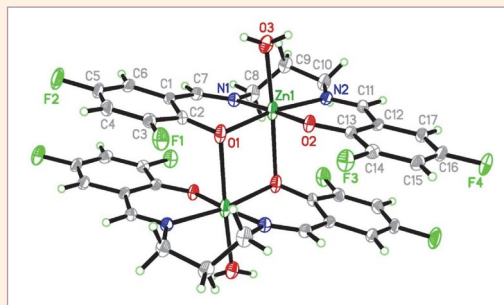
Seyyed Mojtaba Mousavi, Seyyed Alireza Hashemi, Omid Arjmand, Ali Mohammad Amani, Aziz Babapoor, MohammadAli Fateh, Hamed Fateh, Fatemeh Mojoudi, Hossein Esmaeili and Sara Jahandideh



895–901 Organic chemistry

## Syntheses, Characterization and Crystal Structures of Schiff Base Zinc(II) Complexes with Antibacterial Activity

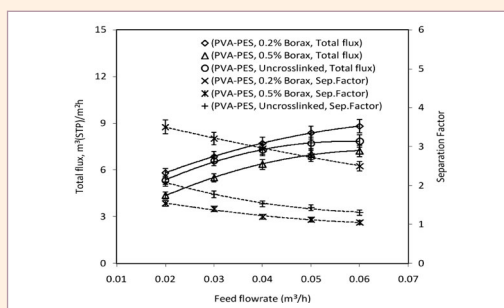
Dong-Lai Peng and Nan Sun



902–918 Chemical, biochemical and environmental engineering

## Synthesis, Characterization and Application of Disodium Tetraborate Cross-Linked Polyvinyl Alcohol Membranes for Pervaporation Dehydration of Ethylene Glycol

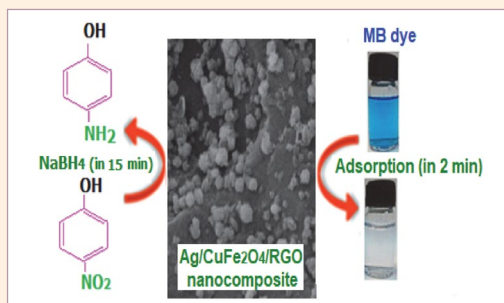
Haresh K. Dave and Kaushik Nath



919–931 Materials science

## Magnetically Separable Ag/CuFe<sub>2</sub>O<sub>4</sub>/Reduced Graphene Oxide Ternary Nanocomposite with High Performance for the Removal of Nitrophenols and Dye Pollutants from Aqueous Media

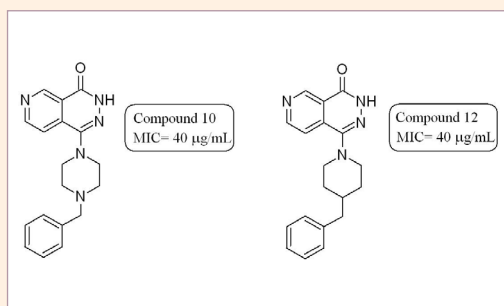
Ladan Nirumand, Saeed Farhadi and Abedin Zabardasti



932–938 Organic chemistry

## Study on Synthesis and Biological Activity of Some Pyridopyridazine Derivatives

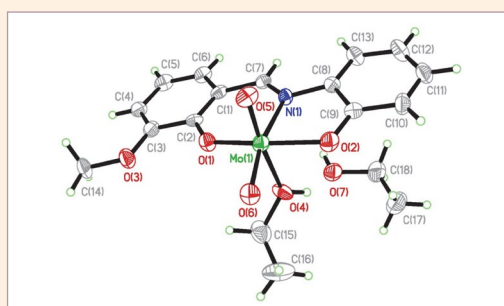
Sevilay Akçay, Mahmut Ülger, Fatma Kaynak Onurdağ and Yasemin Dünder



939–945 Inorganic chemistry

## Synthesis, Crystal Structures and Catalytic Property of Dioxomolybdenum(VI) Complexes Derived from Tridentate Schiff Bases

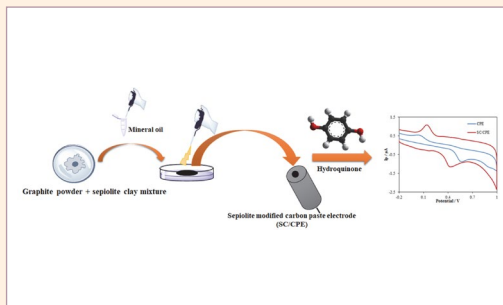
Xue-Wen Zhu



946–954 Analytical chemistry

## A Nano-Sepiolite Clay Electrochemical Sensor for the Rapid Electro-Catalytic Detection of Hydroquinone in Cosmetic Products

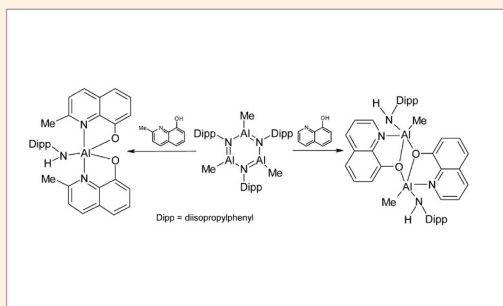
Sevda Aydar, Dilek Eskiköy Bayraktepe and Zehra Yazan



955–963 Inorganic chemistry

## Alumazene Reactivity with Quinolinols – Addition and Substitution Reactions on the $Al_3N_3$ Ring

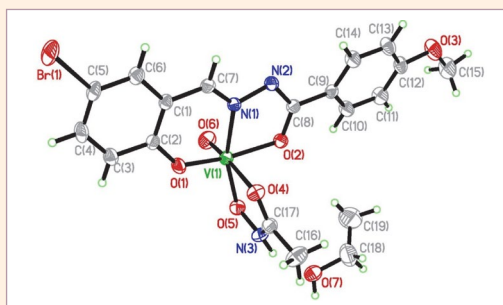
Iva Kollhammerova, Michal Babiak, Marek Necas, Petr Taborsky, Josef Kucera and Jiri Pinkas



964–969 Inorganic chemistry

## Synthesis, Crystal Structures and Catalytic Property of Oxidovanadium(V) Complexes with Similar Aroylhydrazones

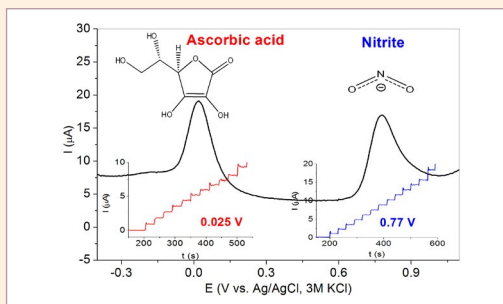
Min Liang, Nan Sun and Dong-Hui Zou



970–979 Materials science

## An Electrochemical Sensing Platform Based on Iridium Oxide for Highly Sensitive and Selective Detection of Nitrite and Ascorbic Acid

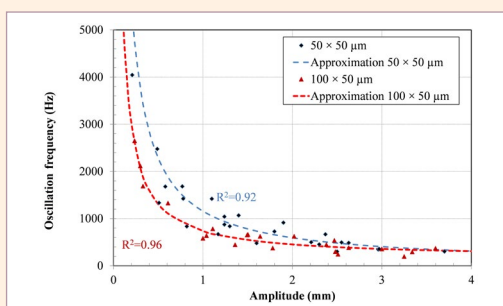
Totka Dodevska, Ivan Shterev and Yanna Lazarova



980–988 Inorganic chemistry

## Oscillations During Flow Boiling in Single Microchannels

Anže Sitar, Andrej Lebar, Michele Crivellari, Alvis Bagolini and Iztok Golobič

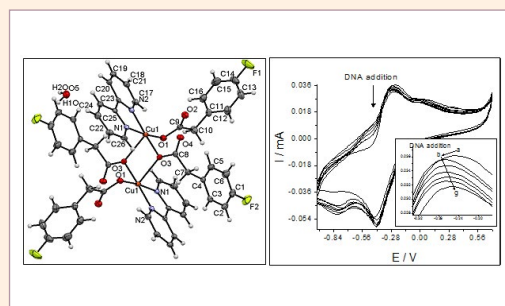


989–997

Inorganic chemistry

## Dinuclear Ternary Copper(II) Complex: Synthesis, Characterization, Structure and DNA-Binding Studies

Muhammad Iqbal, Afifa Mushtaq, Saqib Ali, Manzar Sohail and Paul A. Anderson

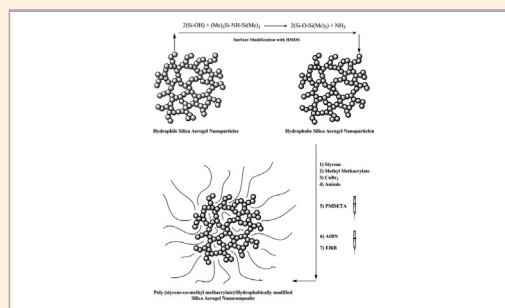


998–1007

Materials science

## A Study on the Properties of Poly (Styrene-co-Methyl Methacrylate)/Silica Aerogel Nanocomposites Prepared via *in situ* SR&NI ATRP

Khezrollah Khezri and Yousef Fazli

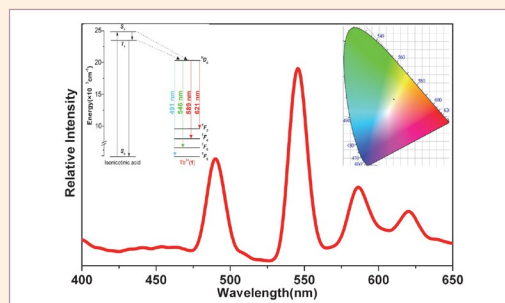


1008–1013

Inorganic chemistry

## Synthesis, Structure, Photoluminescence, Energy Transfer Mechanism and Band Gap of a Terbium-Mercury Complex with a 3-D Framework

Wei-Sheng Lin, Wen-Tong Chen, Han-Mao Kuang and Hui Luo



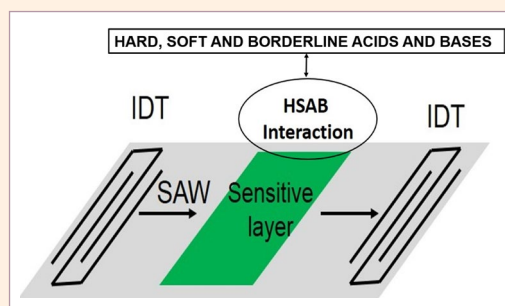
## TECHNICAL PAPERS

1014–1021

Materials science

## Nanostructured Semiconducting Metal Oxides for Ammonia Sensors. A Novel HSAB Sensing Paradigm

Bogdan-Catalin Serban, Octavian Buiu, Cornel Cobianu, Mihai Brezeanu, Marius Bumbac and Cristina Mihaela Nicolescu





Feature article

# Metabolic Network Modelling of Chinese Hamster Ovary (CHO) Culture Bioreactors Operated as Microbial Cell Factories

Jernej Gašperšič,<sup>1,2,\*</sup> Miha Kastelic,<sup>2</sup> Uroš Novak<sup>2</sup> and Blaž Likozar<sup>2</sup><sup>1</sup> Institute of Biochemistry, Medical faculty, University of Ljubljana, Vrazov trg 2, 1000 Ljubljana<sup>2</sup> National Institute of Chemistry, Department of Catalysis and Chemical Reaction Engineering, Hajdrihova 19, 1000 Ljubljana, Slovenia

\* Corresponding author: E-mail: jernej.gaspersic@mf.uni-lj.si

Received: 06-07-2018

## Abstract

Chinese hamster ovary (CHO) epithelial cells are one of the most used therapeutic medical lines for the production of different biopharmaceutical drugs. They have a high consumption rate with a fast duplication cycle that makes them an ideal biological clone. The higher accumulated amounts of toxic intracellular intermediates may lead to lower organism viability, protein productivity and manufactured biosimilar, so a careful optimal balance of medium, bioreactor operational parameters and bioprocess is needed. A precise phenomenological knowledge of metabolism's chemical transformations can predict problems that may arise during batch, semi-continuous fed batch and continuous reactor operation. For a better detailed understanding (and relations), future performance optimization and scaling, mechanistic model systems have been built. In this specific work, the main metabolic pathways in mammalian structured CHO cultures are reviewed. It starts with organic biochemical background, controlling associated phenomena and kinetics, which govern the sustaining conversion routes of biology. Then, individual turnover paths are described, overviewing standard mathematical formulations that are commonly applied in engineering. These are the core of black box modeling, which relates the substrates/products in a simplified relationship manner. Moreover, metabolic flux analysis (MFA)/flux balance analysis (FBA), that are traditionally characterizing mechanisms, are presented to a larger portion extent. Finally, similarities are discussed, illustrating the approaches for their structural design. Stated variables' equations, employed for the description of the growth in the controllable environmental conditions of a vessel, the researched reaction series of proliferating dividing CHO population, joint with the values of maximal enzymatic activity, and solutions are outlined. Processes are listed in a way so that a reader can integrate the state-of-the-art. Our particular contribution is also denoted.

**Keywords:** Microbial cell factory; Chinese hamster ovary (CHO) cell metabolism; Bioreactor operation modeling; Biochemical reaction kinetics; Metabolic flux analysis; Biopharmaceutical and biosimilar

## 1. Introduction

Chinese hamster ovary (CHO) cells are one of the most important cell lines for production of therapeutic biopharmaceuticals.<sup>1,2</sup> CHO cells are characterized by high consumption rates of nutrients and large amount of toxic intermediates, which may lead to lower cell viability and protein production.<sup>1,2,3</sup> Production of recombinant proteins is promoted in growth medium with high content of glucose and glutamine.<sup>4,5</sup> Further optimization of the medium is needed to reduce lactate and ammonia accumulation and to increase antibody yields.<sup>3,6-9</sup> In recent years technology has made a remarkable impact in bioreactor fermentation yields using kinetic models that are commonly used to describe fermentation processes in indus-

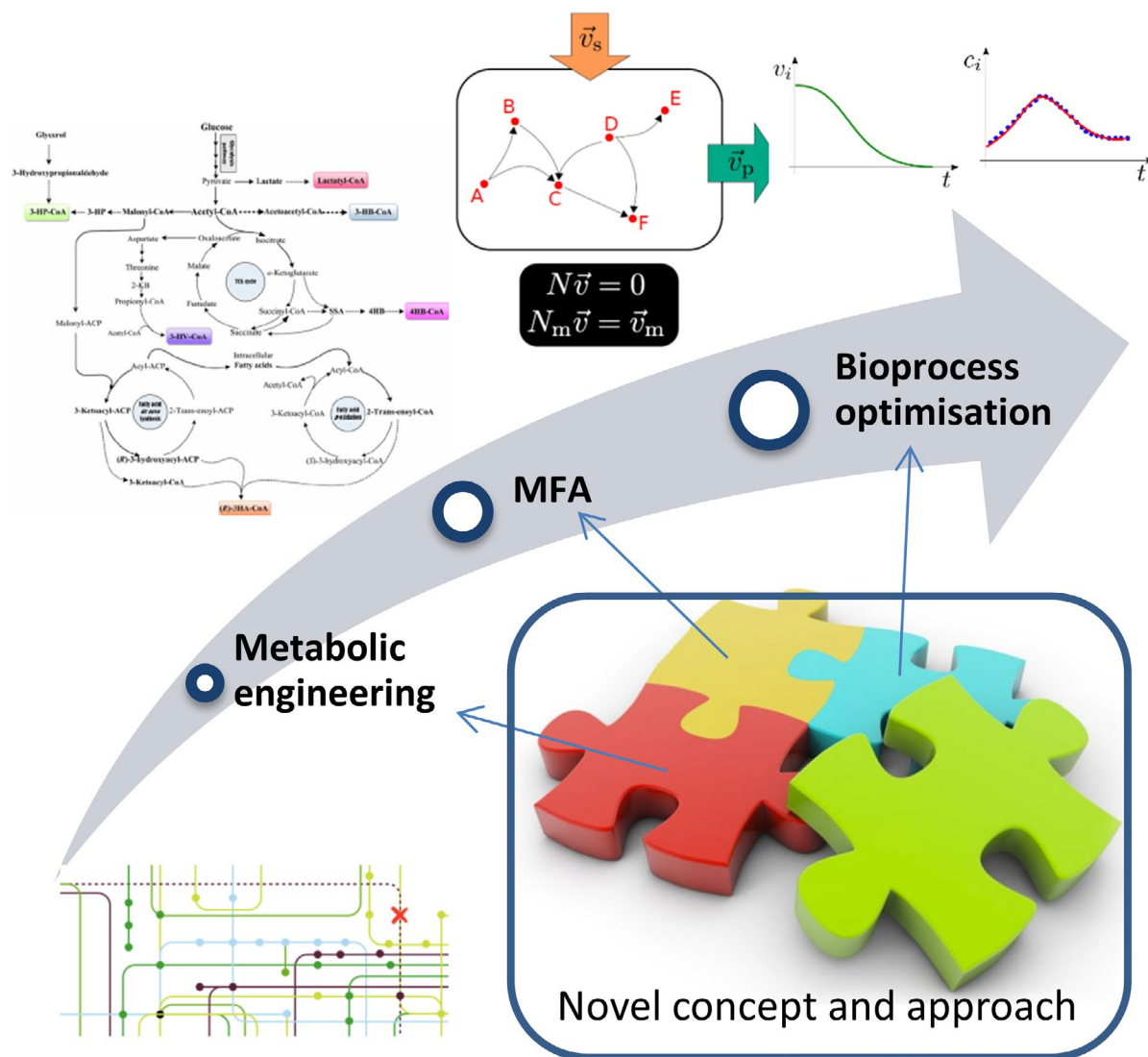
trial fermentors. These models turn out to be useful at process monitoring, acquiring and storing the data, and troubleshooting. In the last three decades databases of CHO cell metabolism have been extended, likewise the tracing of fluxes into biomass and byproducts, which led to major improvements of bioreactor models.<sup>2,5,10-17</sup> This knowledge has guided the researchers to develop several mathematical models, which are able to describe the fluxes within metabolic pathways.<sup>4,18-23</sup>

Analysis of fluxes usually focuses on measuring concentrations of extracellular metabolites.<sup>13</sup> Biocatalysis of substrates into commercially attractive products as well as byproducts is connected through pathways of cell metabolism.<sup>13,24-26</sup> Pathway analysis usually relies on measuring concentration behavior of extracellular metabolites,<sup>13</sup> nev-

ertheless estimates of intracellular fluxes are readily available by using flux balance analysis (FBA) and metabolic flux analysis (MFA).<sup>27</sup> In recent years genotype data have been also included into *in silico* methodologies.<sup>28</sup> The following pathways of the cell metabolism are usually assumed: glycolysis, pentose phosphate (PPP) pathway, tricarboxylic acid (TCA) cycle, amino acid metabolism, protein synthesis, urea cycle, nucleic acid synthesis, membrane lipid synthesis, and biomass production.<sup>1–5,14–19,29–36</sup> Glycogen<sup>5,16</sup> synthesis and glycosylation pathways are part of detailed models.<sup>29,37–41</sup>

Numerous models were developed for the purpose of data analysis and growth optimization in cell cultures. A hybrid simulation framework was proposed to predict the dynamics in bioreactors.<sup>42</sup> A simplified model of central carbon metabolism provides the framework for analyzing measurements of external metabolites.<sup>29</sup> Simulation as-

suming pseudo steady state assumption and extracellular metabolite concentrations accurately predicted the effects of process variables, temperature shift, seeding density, specific productivity and nutrient concentrations.<sup>43</sup> A mathematical model was developed for optimization of batch and fed batch bioreactor.<sup>20</sup> The kinetic model that jointed several phases of cell culture was capable to describe the time evolution of experimental data.<sup>16</sup> Similar model was build and its correctness validated on experimental data from CHO cells grown in spinner flasks.<sup>19</sup> The model was assembled from submodels, where each of them described a separate phase of CHO cell (growth, stationary, and decline phase).<sup>33</sup> The model was then used to explain the experimental data from batch cultivated CHO cells. In another example, the phenotype of mammalian cells was studied by the aims of metabolic flux analysis.<sup>5</sup> Fluxes were measured using <sup>13</sup>C MFA variant and stoichi-



**Figure 1:** Metabolic engineering starts with the metabolic network, which comprises biochemical transformations within living cells (bottom left: unstructured network, top left: structured network). Then we use available experimental data together with theoretical methodologies (paradigm of Metabolic Flux Analysis – MFA) to estimate flux rates of biochemical transformations (top right). These insights help us to perform bioprocess optimization.

ometric modeling.<sup>2,44</sup> MFA was also used to estimate total energy production of growing CHO-320 cells.<sup>24</sup>

New metabolic information was mined from the models and associated simulations. Analysis of experiments showed the existence of multiple steady states.<sup>17</sup> *In silico* modeling of CHO cells allowed the identification of major growth-limiting factors including oxidative stress and depletion of lipid metabolites.<sup>45</sup> These factors may lead to a better development of strategies to enhance CHO culture performance.<sup>45</sup> Continuous cell lines can down-regulate their oxidative metabolism when nutrients get depleted or growth rate slows.<sup>15</sup> Flux analysis shows significant rewiring of intracellular metabolic fluxes in the transition from growth to stationary phase. Changes were noticed in energy metabolism, redox metabolism, oxidative pentose phosphate pathway and anaplerosis.<sup>16</sup> In stationary phase glycolysis is rerouted through PPP pathway – no lactate production is observed.<sup>2</sup> Unusual lipogenic pathway was discovered with modeling. Carbon from glucose supplies mitochondrial production of alpha-ketoglutarate ( $\alpha$ KG), which is trafficked to the cytosol and used to supply reductive carboxylation by isocitrate dehydrogenase.<sup>46</sup> It was suggested that endogenous lactate is not being used for ATP production through TCA cycle when the medium is supplemented with galactose. It was observed that lactate starts to get depleted at the same time as glucose is used up and cell switches to a galactose source.<sup>1</sup> With kinetic model of CHO cell growth Lopez-Meza estimated substrate threshold below which growth is not observed and obtained the  $\alpha$  and  $\beta$  factor from Luedeking-Piret equation.<sup>18</sup> Analysis showed that CTP deficient cells use different central carbon metabolism, suppress pyruvate dehydrogenase, and induce glucose dependent anaplerosis through pyruvate carboxylase.<sup>46</sup>

Composition optimization of limiting amino acids in growth medium increased maximum cell density by 55% and protein titer production by 27%.<sup>3</sup> The medium did not have any influence on sialic acid content. Mannose carbon source also improved recombinant protein productivity.<sup>47</sup> Glucose consumption was 5 times higher than that of glutamine (<sup>13</sup>C labeled glucose, 2D-NMR spectroscopy). Error propagation of Goudar metabolic flux analysis can be routinely used in bioprocess development.<sup>14</sup> Modeled effect of specific rate error on the flux error is a function of both the sensitivity of the flux with respect to the specific rate and relative magnitudes of the flux and the specific rate.<sup>14</sup> 41% of glucose was channeled through PPP, while flux of pyruvate to lactate and to TCA cycle was evenly distributed 55%–45%; anaplerotic conversion to oxaloacetate accounted to 10% of whole pyruvate conversion.<sup>14</sup>

We describe the research done in the area of bioreactor modeling and contribution of our department to the field. Complete literature search and data collection of known metabolic fluxes was made to ease the design of future models. The improvement of models is ongoing with a goal to make a good theoretical framework and to

foresee possible errors in the fermentation process. Schematic illustration of the interplay between metabolic engineering and bioprocess is shown in Figure 1.

## 2. Contribution of the Authors

Modeling brings new insights into existing problems. Great advantage of modeling is to track the problem at molecular, cellular level. Good hypothesis and theories cannot be developed without sufficiently developed model. Development of biotechnology processes is thus easier and cost effective. Models have many disadvantages, because they may be developed on unproven hypothesis or theories that yet need to be confirmed. Theories may have in this case erroneous core.

Complete literature search of published models and metabolism of CHO cells leads to a successful build of model of bioreactor. Review of preferred articles is included with the emphasis on bioreactor operation equations and metabolic pathways of CHO cell lines.

Contribution is divided into three parts:

- Overview of black box models: Evolution of mathematical equations used in CHO mechanistic models
- Overview of CHO cell metabolic pathways and the unique properties of CHO cell lines
- Overview of mechanistic models and our proposed approach toward solution of the problem

### 2. 1. Review of Black Box Models: Formulation of Mathematical Equations

Protein production in a bioreactor requires perfect agitation and aeration to maintain a homogeneous distribution of cells, substrate and oxygen throughout the bioreactor. Extracellular medium composition analysis, coupled with intracellular metabolic pathway analysis give rise to CHO cell bioreactor models.

#### 2. 1. 1. Growth of Biomass

Growth of biomass is described in different ways. Growth is influenced by the specific growth factor ( $\mu$ ) and concentration of cells ( $X$ ) as seen in Eq. (1).<sup>16,19,20</sup>

Standard biomass growth equation:

$$\frac{dX}{dt} = \mu X \quad (1)$$

Specific growth factor ( $\mu$ ) is described in different ways. Commonly used descriptions are Verhulst and Monod equations, which can be adequately modified to account for bioreactor conditions (Eqs. 2 and 6).

One limit substrate Monod<sup>36</sup> kinetics is:

$$\mu = \mu_{\max} \frac{[S]}{[S] + K_s} \quad (2)$$

while two limit substrates Monod<sup>24</sup> kinetics is expressed as:

$$\mu = \mu_{\max} \frac{[S_1]}{[S_1] + K_{S_1}} \frac{[S_2]}{[S_2] + K_{S_2}} \quad (3)$$

and finally  $n$ -limit substrates Monod<sup>24</sup> kinetics as:

$$= \mu_{\max} \frac{[S_1]}{[S_1] + K_{S_1}} \frac{[S_2]}{[S_2] + K_{S_2}} \times \dots \times \frac{[S_n]}{[S_n] + K_{S_n}} \quad (4)$$

By Monod, biomass growth is influenced by limiting substrate (Eq. 2). Here  $X$  represents cell concentration – number of cells per mL;  $S$  represent substrate,  $\mu_{\max}$  is the maximum value of growth rate,  $K_S$  is the substrate saturation constant. Note that specific growth rate ( $\mu$ ) may be influenced by one limiting substrate (Eq. 2),<sup>18</sup> two (Eq. 3)<sup>37</sup> or more limiting substrates from the growth medium (Eq. 4).<sup>48</sup>

del Val<sup>38</sup> proposed modified expression:

$$\mu = \mu_g \left[ \frac{[S]}{K_m + [S]} - \frac{[X_v]}{\alpha_x} \right] \quad (5)$$

By del Val, an upgraded Monod equation for continuous production is utilized, where  $X_v$  is the density of viable cells and  $\alpha_x$  is the specific factor (cellular carrying capacity). Viable cells represent live cell population, while total cells represent a sum of viable and dead cell population. The ratio is changing through cell phases. Each equation is optimized for specific value, so it is necessary to take into account certain value.

Verhulst<sup>49</sup> established the following closure:

$$\mu = \mu_{\max} \left( 1 - \frac{X}{X_{\max}} \right) \quad (6)$$

By Verhulst, maximum cell density of the culture ( $X_{\max}$ ) is a limiting factor to cell growth. In this case substrate is available in large quantities or may be fed additionally to the bioreactor. The equation is commonly used to describe the growth of bacterial cultures.

Equations for biomass growth that are commonly used in bioreactor systems are described below (continuous, fed batch).

Altamirano<sup>17</sup> and Xing<sup>3</sup> suggested to use the following formulation:

$$\mu = D \frac{X_T}{X_V} \quad (7)$$

By Altamirano, the specific growth rate in the continuous bioreactor is described as dilution rate ( $D$ ) multiplied by the ratio of the total cell number ( $X_T$ ) and the viable cell number ( $X_V$ ).

Goudar<sup>4</sup> wrote the growth factor ( $\mu$ ) as:

$$\mu = \frac{F_d}{V} + \frac{F_h X_V^H}{V X_V^B} + \frac{1}{X_V^B} \frac{dX_V^B}{dt} \quad (8)$$

By Goudar, the specific growth rate is designed for perfusion systems, where  $V$  is the reactor volume,  $F_d$  is the discard rate,  $F_h$  is the harvest flow rate,  $X_V^H$  is the harvest

viable cell density, and  $X_V^B$  is the density of viable cells in bioreactor.

Hagrot<sup>21</sup> used the solution of first-order kinetics:

$$\mu = \frac{\ln\left(\frac{X_v}{X_{v,0}}\right)}{t - t_0} \quad (9)$$

By Hagrot, the specific growth rate depends upon viable cell concentration before renewal ( $X_v$ ) and after renewal ( $X_{v,0}$ ). Here  $t$  and  $t_0$  are corresponding times of sampling.

It is essential for the model of bioreactor to select the mathematical formulation that suits type of the bioreactor and the cell culture. To get the best formulation we need to compare numerical simulations with experimental data and choose the best fitting curve. For that we need a set of sensor concentration data of products, substrates, and biomass in bioreactor throughout fermentation process.

## 2. 1. 2. Final Product Formation

Final product formation is described in connection with the cell concentration ( $X$ ) or viable cell concentration ( $X_v$ ) multiplied by product growth factors ( $r$  or  $\alpha$ ) (Eq. 10 and 11).<sup>20,33</sup>

Standard equation to describe product formation:

$$\frac{dP}{dt} = rX \quad (10)$$

Naderi<sup>20</sup> and Provost<sup>19</sup> wrote down the following closure:

$$\frac{dP}{dt} = \alpha_g X_v \quad (11)$$

while Ludeking-Piret<sup>35</sup> suggested additional term:

$$\frac{dP}{dt} = \alpha \frac{dX}{dt} + \beta X \quad (12)$$

By Ludeking-Piret, two coefficients  $\alpha$  and  $\beta$  describe the product formation, both are product specific. Further,  $P$  is the concentration of glycosylated product, and  $dX/dt$  is the slope of biomass increase.

Xing<sup>3</sup> and Berrios<sup>47</sup> suggested two formulations:

$$\frac{dP}{dt} = \frac{D(C_i^{out} - C_i^{in})}{X_V} X \quad (13)$$

$$\frac{dP}{dt} = \frac{C_i(t_2) - C_i(t_1)}{IVCD_i(t_2) - IVCD_i(t_1)} X \quad (14)$$

By Xing, product growth is described by the ratio of concentration difference of product ( $C_i$ ) between two time points.  $X_v$  is the viable cell density, and  $D$  is the dilution factor (Eq. 13). By Berrios concentration difference of the product ( $c_i$ ) was divided by the corresponding difference of integral viable cell density (IVCD) (Eq. 14).

Zamorano<sup>24</sup> proposed linear relationship:

$$\frac{dP}{dt} = N_p v(t) X \quad (15)$$

By Zamorano, the  $r$  factor (Eq. 10) was substituted by multiplication of stoichiometric matrix for final product ( $N_p$ ) and metabolic flux ( $v(t)$ ).

Goudar<sup>4</sup> utilized the extended closure:

$$\frac{dP}{dt} = \frac{1}{X_p^B} \left( \frac{F_m P}{V} + \frac{dP}{dt} \right) X \quad (16)$$

By Goudar, the product growth consists of two terms. Here  $X_p^B$  is viable cell density, and  $F_m$  is the flow rate. The equation is used to describe perfusion systems.

del Val<sup>38</sup> used the following expression:

$$\frac{dP}{dt} = (Y_{P/S}) q_S X \quad (17)$$

By del Val, the expression describes product growth as a yield of product per substrate ( $Y_{P/S}$ ) multiplied by the substrate consumption ( $q_S$ ).

The formula for product growth must be developed for each individual product and is based on the observable physical and biochemical strain characteristics and the type of bioreactor. Reviewed models are optimized to describe formation of secondary metabolites – end products.<sup>1–5,15,17,19,21, 24,29,30,31,37,38,40,43,45,46,50</sup> For production of antibodies post translational glycosylation should be taken into account as well.<sup>37,38,40</sup> Formation of primary metabolites – important for growth and maintenance of cell were most precisely described in Quek's model with thorough description of nucleotide and lipid synthesis.<sup>5</sup>

### 2. 1. 3. Mathematical Description of Substrate Consumption

Substrate consumption is dependent upon cell density ( $X$ ) and specific uptake rate ( $v_S$ ) as follows:<sup>17,24,33</sup>

$$\frac{dS}{dt} = -v_S(t) X(t) \quad (18)$$

Jedrzejewski<sup>37</sup> proposed the formulation with two terms:

$$\frac{dS}{dt} = \left( \frac{\mu}{Y_{glc}} + m_{glc} \right) X \quad (19)$$

By Jedrzejewski substrate consumption is influenced by number of cells, steady state consumption of substrate ( $m_{glc}$ ), and biomass growth coefficient ( $Y_{glc}$ ).

Goudar<sup>4</sup> and Xu<sup>6</sup> suggested another equation:

$$\frac{dS}{dt} = \frac{1}{X_p^B} \left( \frac{F_m (S_m - S)}{V} - \frac{dS}{dt} \right) X \quad (20)$$

By Goudar and Xu specific substrate consumption rate depends upon perfusion rate  $F_m$ , difference of sub-

strate concentration (starting minus current) ( $S_m - S$ ), bioreactor volume ( $V$ ), and viable cell density ( $X_p^B$ ).

del Val<sup>38</sup> extended the Michaelis-Menten kinetics as:

$$\frac{dS}{dt} = \left( \frac{1}{Y_{X/S}} \right) \left( \frac{S}{K_m + S} \right) X \quad (21)$$

By del Val,  $Y_{X/S}$  is the yield coefficient from substrate,  $S$  represents concentration of substrate,  $K_m$  is constant specific for each substrate.

Ahn<sup>16</sup> introduced another expression:

$$\frac{dS}{dt} = -k S - q_S X \quad (22)$$

By Ahn, decomposition of substrate  $k$  is independent of biomass.  $S$  represents substrate concentration,  $X$  represents cell concentration, and  $q_S$  is a substrate consumption per cell concentration unit.

### 2. 1. 4. Oxygen Consumption

Oxygen consumption is traditionally described as follows:<sup>5,17,50</sup>

$$\frac{dDO}{dt} = OTR - OCR \quad (23)$$

$$OTR = K_L a (DO^* - DO) \quad (24)$$

Oxygen concentration is dependent upon oxygen transfer rate (OTR) between gas and liquid phase and oxygen consumption rate (OCR) of biomass.<sup>29,51</sup> OTR is dependent upon  $K_L a$  (bioreactor specific) and dissolved oxygen concentration (DO). Note that saturated oxygen ( $DO^*$ ) is temperature dependent.<sup>29</sup>

Jorjani<sup>52</sup> used the following expression:

$$OCR = q_{O_2} X_v; q_{O_2} = q_{O_2}^0 e^{-E/RT} \quad (25)$$

By Jorjani, OCR is dependent upon  $q_{O_2}^0$  and temperature,<sup>52</sup> while  $q_{O_2}^0$  is cell culture and clone specific. It depends mostly on the number and condition of mitochondria (origin of respiratory chain). It is also dependent upon availability of substrate with which cell and later mitochondria are fed.<sup>53</sup>

Nyberg<sup>29</sup> proposed two terms:

$$OUR = K_L a (C^* - C_R) + D (C_F - C_R) \quad (26)$$

By Nyberg, the formula accounts for the continuous bioreactor, where oxygen uptake rate (OUR) is dependent upon OTR as ( $K_L a (C^* - C_R)$ ), dilution rate ( $D$ ), and the difference between oxygen concentrations (feed minus reactor) as ( $C_F - C_R$ ).  $C^*$  represents saturated oxygen concentration at operating temperature.

Oxygen is consumed in the respiratory chain.  $H_2O$  is the byproduct of the respiratory chain reactions.<sup>54</sup> Oxygen that is incorporated in waste  $CO_2$  comes from glucose or

other substrates. Since metabolism is affected by pH value, O<sub>2</sub> consumption (metabolism) is pH dependent.<sup>55</sup>

### 2. 1. 5. CO<sub>2</sub> and NH<sub>3</sub> Waste Production

CO<sub>2</sub> production is integrated into models to address reactions in TCA cycle.<sup>5,45,50</sup> CO<sub>2</sub> is mostly produced in Krebs cycle, while NH<sub>3</sub> is produced during metabolism of glutamine and other amino acids.<sup>5,17,33,56</sup>

$$\frac{d\text{DCO}_2}{dt} = \text{CO}_2\text{PR} - \text{CO}_2\text{TR} = K_L a (\text{DCO}_2 - \text{DCO}_2^*) + R_{\text{CO}_2} X \quad (27)$$

CO<sub>2</sub> concentration is dependent upon CO<sub>2</sub> transfer rate (CO<sub>2</sub>TR), and CO<sub>2</sub> production from biomass (CO<sub>2</sub>PR). CO<sub>2</sub> importantly influences cell growth and productivity.<sup>57</sup> Free CO<sub>2</sub> can be recycled together with amino group during fixation into carbamoyl phosphate and later integrated into arginine (urea cycle). Dissolved CO<sub>2</sub> (DCO<sub>2</sub>) partially transforms into HCO<sub>3</sub><sup>-</sup> ions, which serve as a regulator of pH in the cell. CO<sub>2</sub> is generated during pyruvate, isocitrate and oxoglutarate degradation (TCA cycle). It is also generated in lysis of lysine and glycine as well as in formation of ribose-6-phosphate from glucose-6-phosphate. R<sub>CO<sub>2</sub></sub> represents rate of CO<sub>2</sub> production.

Nyberg<sup>29</sup> suggested another expression:

$$\text{CER} = \frac{n_g}{V_R} (y_{\text{CO}_2}^R - y_{\text{CO}_2}^F) + D (C_A^R - C_A^F) \quad (28)$$

By Nyberg, expression accounts for carbon dioxide evolution rate. Here  $n_g$  is molar gas flow rate to the reactor,  $V_R$  is liquid volume of the reactor,  $V_R$  is mole fraction of CO<sub>2</sub> in reactor headspace,  $y_{\text{CO}_2}^R$  is mole fraction of CO<sub>2</sub> in the feed gas.  $C_A^R$  is concentration of CO<sub>2</sub> and bicarbonate in the liquid phase,  $C_A^F$  is concentration of CO<sub>2</sub> and bicarbonate in the liquid feed phase.

$$\frac{d\text{DNH}_3}{dt} = \text{NH}_3\text{PR} - \text{NH}_3\text{TR} = K_L a (\text{DNH}_3 - \text{DNH}_3^*) + R_{\text{NH}_3} X \quad (29)$$

In Eq. (29), concentration of NH<sub>3</sub> has similar mathematical dependence as CO<sub>2</sub> in Eq. (27). Note that  $K_L a$  is different for each gas and varies with the reactor and temperature. Ammonia production is highly dependent upon lysis of amino acids that can be biomass dependent and/or independent (catalytic degradation in water medium dependent upon temperature). Ammonia is produced from the amino acids and transferred into gas phase. Then, it is recycled during formation of carbamoyl phosphate.

### 2. 1. 6. Temperature, pH Optimum

Temperature and pH are important process parameters that influence optimal growth of CHO cell lines.<sup>58–64</sup>

Normal operating temperature for the growth of mammalian cells is 37 °C.<sup>65</sup> At 33 °C a remarkable decrease in specific growth rate is observed. At 30 °C, growth of cells starts to stagnate. Mammalian cells grow in the range from 35 to 38 °C.<sup>55,66</sup> On the other hand, production rate of product (unspecified recombinant protein) is increased at 33 and 30 °C. Lower temperatures (below 37 °C) inhibit cell growth, but enhance cellular productivity of the recombinant protein, maintain high cell viability, suppress consumption of nutrients from medium, and suppress release of waste products from the cells.<sup>67,68</sup>

CHO cells have been reported to grow best at pH 7.1.<sup>55</sup> Maximum product concentration (recombinant protein) was achieved at pH 6.8; 1.8-fold higher than at pH 7.1.<sup>55</sup> Regardless of the culture temperature, the highest specific growth rate was observed in the range of pH from 7.0 to 7.4.<sup>34</sup>

### 2. 1. 7. Cell Phases of CHO Cell Lines in Bioreactor

When cells are transferred to a new bioreactor batch, they need time to reach stable operation (lag phase). During lag phase cells adapt to new environment and multiply enzymes that are needed to catalyze biochemical reactions.

Initially, concentrations of glucose and other amino acids are falling, while lactate and glutamate (byproducts) concentrations are rising in the medium. After glucose is depleted, lactate starts to get consumed. When substrates are depleted, biomass stops to grow and uses internal reserves to maintain cell functions. Reserve glycogen and lipids are used to supply the cell with the energy. The nutrients from dead cells can be recycled and reused as the energy source. Most commonly used substrate is glucose. If substrate is switched for example to galactose, specific enzymes must be multiplied to reach optimal concentrations, before cells can re-adapt. In the presence of large concentrations of substrates inside cells, mitochondria divide rapidly and supply the cells with large amounts of energy (ATP). Until mitochondria sufficiently multiply, the excess flux of glucose is diverted to lactate or other metabolites, such as alanine.

In the growth phase cells multiply with ease. The lactate does not accumulate anymore and is used up by cells as a substrate. Cells stop to grow when they reach maximum cell density or when they have used up all substrates. Then, cells start to use nutrients from energy storage: glycogen and lipid molecules. When cells run out of the substrates and nutrients from energy storage they enter an atypical cell death due to starvation.

The viable CHO cells are in G1, S, G2/M (part of the interphase) or apoptotic phase.<sup>69,70</sup> The production of protein is usually phase specific.<sup>69,66</sup> In apoptosis cell enter programmed cell death. After certain number of duplications, cells die off. At that time significant amount of biomass in the bioreactor belongs to dead cells.

Table 1: CHO cell metabolic pathways used in reviewed models.

	Alta- mira- no <sup>17</sup>	Jia- ng <sup>46</sup>	No- lan <sup>43</sup>	Quek <sup>5</sup>	Selva- ra- su <sup>45</sup>	San- der- son <sup>50</sup>	del- Val <sup>38</sup>	Kram- beck <sup>40</sup>	Jedr- zeje- wsk <sup>37</sup>	Zamo- rano <sup>24</sup>	Dean <sup>30</sup>	Yo- ung <sup>15</sup>	Ghor- bani- aghdam <sup>31</sup>	Hag- rot <sup>21</sup>	Nyberg <sup>29</sup>	Sen- gup- ta <sup>2</sup>	Alta- mira- no <sup>1</sup>	Xing <sup>3</sup>	Pro- vost <sup>19</sup>	Gou- dar <sup>4</sup>
Glycolysis	YES	YES	YES	YES	YES	YES	no	no	no	YES	YES	YES	YES	YES	YES	YES	YES	YES	YES	YES
Pentose phosphate pathway	YES	YES	no	YES	YES	YES	no	no	no	YES	YES	YES	no	no	no	YES	no	no	YES	YES
Lactate production	YES	YES	YES	YES	YES	YES	no	no	no	YES	no	YES	no	YES	YES	YES	YES	YES	YES	YES
Glycogen synthesis	no	no	no	YES	no	no	no	no	no	no	no	no	no	no	no	no	no	no	no	no
Nucleotide synthesis	no	no	no	YES	no	no	no	no	no	no	no	no	no	no	no	no	no	no	YES	no
TCA cycle	YES	YES	YES	YES	YES	YES	no	no	no	YES	no	YES	YES	YES	YES	YES	YES	YES	YES	YES
Glutaminolysis	YES	YES	YES	YES	YES	YES	no	no	no	no	YES	YES	YES	YES	YES	no	no	no	YES	YES
Amino acid metabolism	YES	no	YES	YES	YES	YES	no	no	no	no	no	no	no	no	no	no	no	no	no	no
Oxidative phosphorylation	YES	no	YES	YES	no	no	no	no	no	no	no	YES	no	no	no	no	no	no	no	no
Lipid synthesis	no	YES	no	YES	no	no	no	no	no	no	YES	no	no	no	no	no	no	no	no	no
Glycosylation	no	no	no	no	no	no	no	no	YES	no	no	no	no	no	no	no	no	no	no	no

## 2. 2. Overview of Important Metabolic Pathways

In the past two decades much research has been done on CHO cell metabolism. At modeling, cell metabolism is described using kinetic laws, equilibrium equations and associated parameters. Table 1 shows metabolic pathways, which were included in the models published in the literature. The following pathways were reviewed: (i) substrate intake, (ii) glycolysis, (iii) glutaminolysis, (iv) pentose phosphate pathway (PPP), (v) UDP-monosaccharides production, (vi) nucleotide synthesis, (vii) amino acid metabolism, (viii) tricarboxylic acid cycle (TCA), (ix) lipid metabolism, (x) glycogen synthesis, (xi) lipid synthesis, (xii) DNA duplication, (xiii) RNA transcription and protein translation, (xiv) glycosylation, and (xv) feedback loops.

### 2. 2. 1. Substrate Intake (Part of Metabolic Flux Pathway Analysis)

High influxes of substrates contribute to high osmotic pressure.<sup>71</sup> The cell regulates its pressure with fast conversion into more favorable intermediates and products. Other regulatory mechanisms are passive and active transport. One of the major metabolites is glycogen, which serves as energy storage.<sup>72</sup> Glucogenic amino acids may transform into glucose and then into glycogen, while ketogenic amino acids transform into ketone bodies that may be stored through acetyl CoA in fatty acids (Figure 2).<sup>73</sup> Mathematical descriptions (Eqs. 18–22) of substrates' consumption are selected in accordance with phenotype, while associated constants are substrate specific. Majority

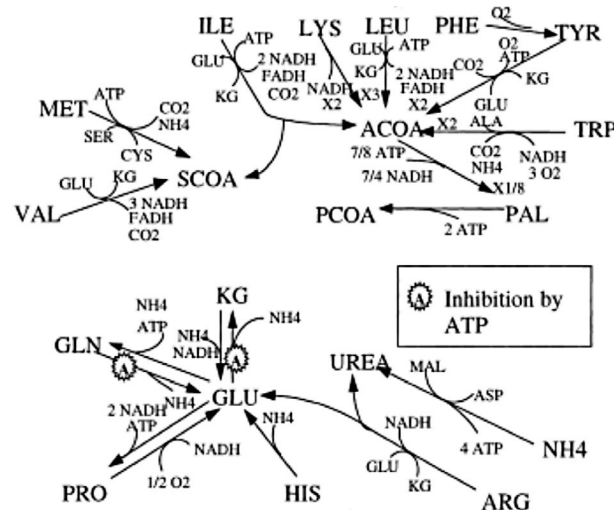
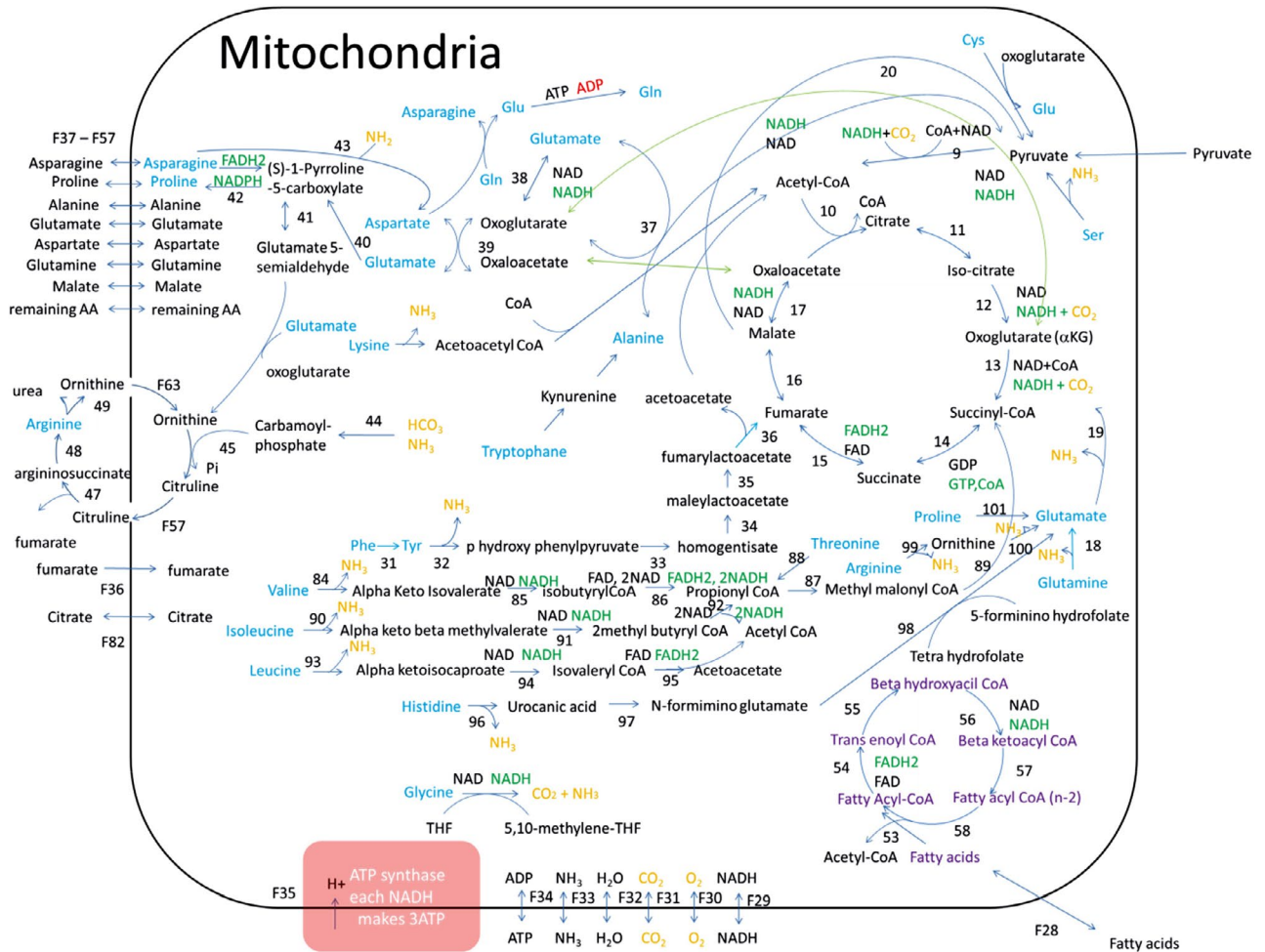


Figure 2: Biochemical reactions associated with mitochondria: degradation pathway of keto- into glucogenic amino acids.<sup>45</sup> Glucogenic amino acids are transformed into acetylCoenzyme A (AcCoA), while keto amino acids are transformed to glutamate that is further transformed into alpha-ketoglutarate (aKG). Three letter amino acid code is standard. From "A structured, dynamic model for animal cell culture systems," by C. S. Sanderson, J. P. Barford, and G. W. Barton, *Biochem. Eng. J.*, 1999, 3, 203–211. Reprinted with permission.







**Figure 4:** Metabolic pathways within mitochondria: TCA cycle is the major metabolic pathway. Fatty acids are pre-metabolized in beta oxidation cycle (purple). Amino acids (blue) enter TCA cycle through oxoglutarate, fumarate, and succinyl CoA. Oligosaccharides enter TCA cycle through PPP and glycolysis pathway. Gases are colored in orange, while phosphate rich energy molecules are colored in green.<sup>1–5,15,17,19,21,24,29–31,43,45,46,50</sup>

tant, short half-life intermediates.<sup>1–4,17,21,29,46</sup> In simplified models, fluxes are diverted directly to stable intermediates. Complete lysis of amino acids shows that amino acids regenerate intermediates of TCA cycle much faster compared to glycolysis due to independent enzyme machinery of each amino acid. Enormous energy comes from branched chain amino acids (BCAA), i.e. valine, isoleucine, and leucine (Figure 4).

### 2. 2. 3. Pentose Phosphate Pathway and UDP-Monosaccharides Stock

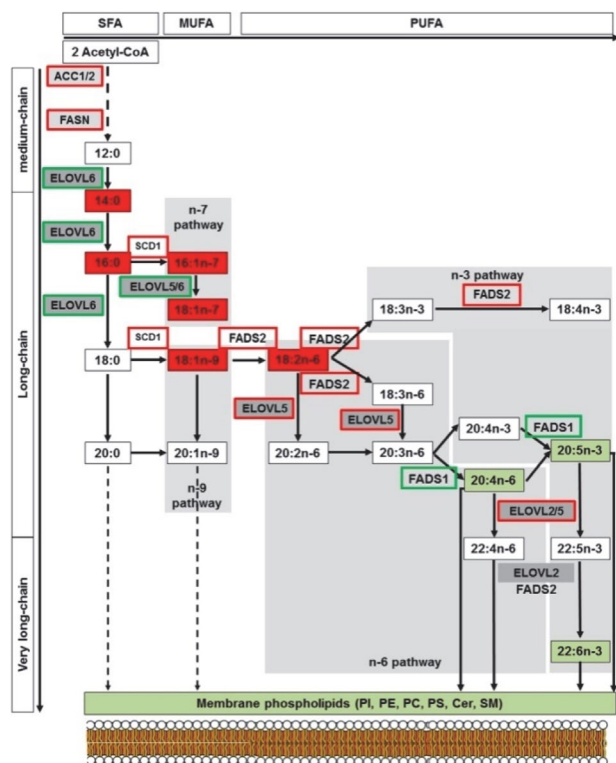
Like glycolysis, pentose phosphate pathway (PPP) is also included in several models (Table 1).<sup>1,2,4,5,15,17,19,30,45,46,50</sup> An alternative route for glucose is generation of different monosaccharides (Figure 3). From glucose-6-phosphate cell produces ribulose-5-phosphate, xylulose-5-phosphate, erythrose-4-phosphate, fructose-6-phosphate sedoheptulose-7-phosphate and ribose-5-phosphate.<sup>33</sup> Ribose-5-phosphate enters synthesis of nucleotides.<sup>5</sup> Monosaccha-

rides from PPP can be transformed into glyceraldehyde-3-phosphate and fructose-6-phosphate, which again enters glycolysis pathway (Figure 3).

Few models also include generation of UDP-mono-saccharides (Figure 3).<sup>37,38,40</sup> In excess of UTP, different nucleotide sugars are generated, including GDP-mannose, UDP-galactose, UDP-glucose, UDP-N-acetyl glucosamine (GlcNAc), and CMP-sialic acid. Nucleotide sugars are included in the models, which describe glycosylation pattern of proteins (Figure 3).<sup>29,37–39</sup> Nucleotide sugars are transported into the endoplasmic reticulum (ER) and the Golgi apparatus (GA), where they get concentrated and ready to be attached to proteins (Figure 3). The attachment is carried out through covalent bond between sugar residue and protein through N-phospho-glycosylation.<sup>37,77</sup>

### 2. 2. 4. Glycogen Synthesis

Glycogen synthesis is included only in a few models (Table 1),<sup>5</sup> despite its important role in glucose homeosta-



**Figure 5:** Synthesis of fatty acids from acetyl-CoA: Complex enzymatic pathway leads to different lipid molecules that assemble into membrane bilayer. The saturated fatty acids and unsaturated fatty acids of the n-3, n-6, n-7 and n-9 series can be synthesized from myristic acid (C14) and palmitic acid (C16), produced from ACC and FASN. Long-chain fatty acids of n-6 and n-3 series can also be synthesized from precursors obtained from dietary precursors to elongation (ELOVL) and desaturation (FADS) steps as indicated in the pathways. Lipids marked red and green are “up” and “down” regulated in our analysis, respectively. Increase in enzyme activities is framed in red whereas a decrease is framed in green. ACC: acetyl-CoA carboxylase; ELOVL: elongase of very long chain fatty acid; FASN: fatty acid synthase; FADS: fatty acid desaturase; SCD: stearyl-CoA desaturase.<sup>78</sup> From “Metabolism dysregulation induces a specific lipid signature of nonalcoholic steatohepatitis in patients,” by F. Chiappini, A. Coilly, H. Kadar, P. Gual, A. Tran, C. Desterke, D. Samuel, J. C. Duclos-Vallée, D. Touboul, J. Bertrand-Michel, A. Brunelle, C. Guettier, and F. Le Naour, *Sci. Rep.*, 2017, 7, 1–17. Reprinted with permission.

sis. In the excess of ATP, cell transfers extra glucose into glycogen that is used as energy source, when glucose is run out from the medium or cytosol. One molecule of glycogen can store up to 30000 molecules of glucose. This contributes to lower osmotic pressure and thus removes harmful effects of high glucose content. Glucose is readily available, if there is a demand on energy or carbon source (Figure 3). The path described above is ATP controlled. Glucose is transformed into glucose-1-phosphate; in this process one molecule of ATP is consumed. UTP molecule binds to glucose-1-phosphate, leading to production of UDP-glucose. UDP-glucose attaches itself to glycogen, leading to release of UDP.

## 2. 2. 5. Lipid Synthesis

Lipid synthesis is included in several models (Table 1). They used simplified pathways<sup>13,15,17,50,76</sup> or very precisely defined pathways.<sup>5</sup>

During cell division, lipid synthesis is enhanced to simulate assembly of membrane. Phosphoglycerides, triglycerides, phosphatidylserine, phosphatidylcholine, cholesterol, sphingomyelin, and geranyl pyrophosphate are synthesized (Figure 3). Successive enzymatic pathway starts with the acetyl-CoA and leads to complex lipid molecules (Figure 5). Different glycerides are synthesized with the addition of fatty acids and other groups to glycerol.

## 2. 2. 6. Amino Acid Synthesis

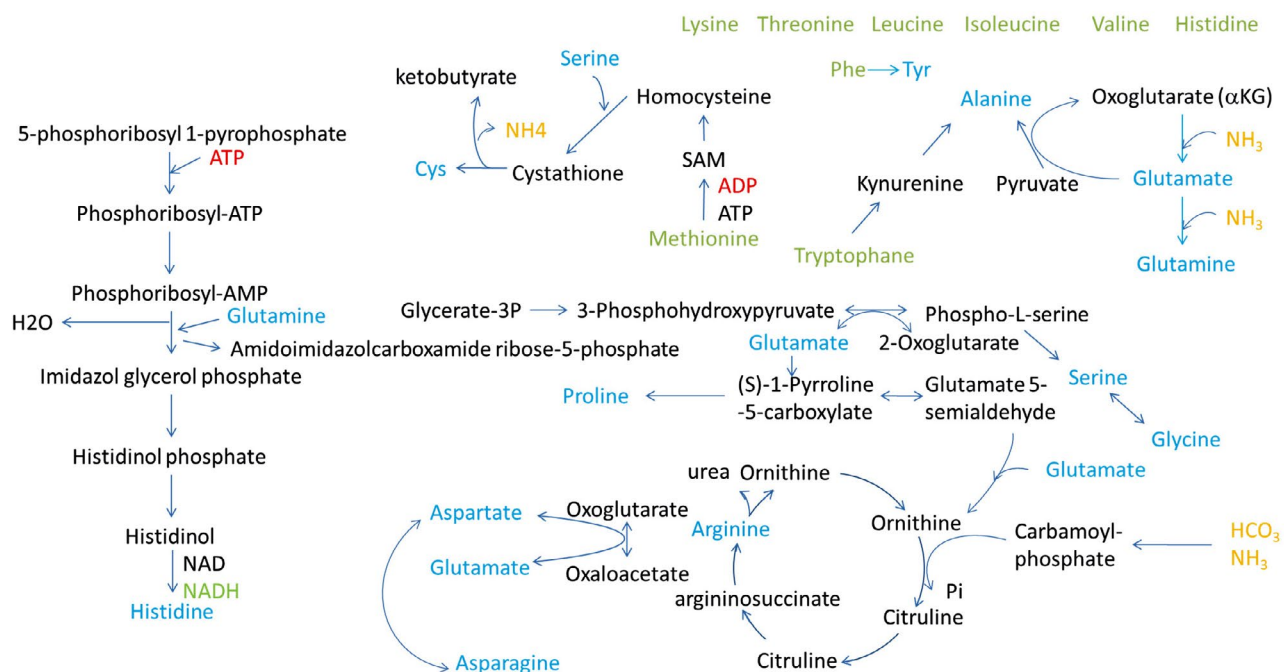
Amino acid degradation is described in most models, but usually only partial set of amino acids is integrated in a model (Table 1).<sup>1–5,15,17,19,21,24,29–31,43,45,46,50</sup> Altamirano et al<sup>17</sup> includes synthesis of alanine, aspartate and glutamine in highly interconnected metabolic network. Quek et al<sup>5</sup> describes precise metabolic network with interconnected synthesis of amino acids: alanine, glutamate, asparagine, proline, serine, glycine, aspartate. Provost et al<sup>19</sup> includes synthesis of alanine into the model.

Essential amino acids cannot be synthesized de novo (from scratch) by the organism, therefore must be supplemented from the medium. There are nine amino acids that humans cannot synthesize: phenylalanine, valine, threonine, tryptophan, methionine, leucine, isoleucine, lysine, and histidine (single letter abbreviations in the order they appear: F, V, T, W, M, L, I, K, and H). Other amino acids are synthesized from essential amino acids and other cell intermediates (Figure 6).

## 2. 2. 7. DNA Duplication, RNA Transcription and Protein Translation

Nucleotides are synthesized through PPP. In a few models nucleotide synthesis is incorporated.<sup>5,19</sup> Provost et al<sup>19</sup> describes highly simplified model. Quek et al<sup>5</sup> describes precise metabolic pathway, where glucose is transformed into ribose, which is further converted to IMP (inosine monophosphate-purine precursor) and UMP (uridine monophosphate-pyrimidine precursor). These precursors are then transformed into ATP, CTP, UTP, GTP, dATP, dCTP, dTTP, and dGTP (Figure 3).

Duplication of DNA and translation of RNAs take place in the cell nucleus. mRNA is transported to the cytosol and rRNA takes position in ribosome, while mRNA is translated into protein by the aid of tRNA. Nucleotide triphosphates (NTPs) are used as an energy source during transcription. For each amino acid, codon is assembled from three NTPs. mRNA is assembled of: 5' cap, 5' and 3' untranslated region (UTR), sequence for signal peptide, coding region, and poly AAA end. mRNA exits the nucleus and enters a ribosome, where the protein is translated



**Figure 6:** AA synthesis of non-essential amino acids.<sup>1, 5, 19</sup> Synthesis of amino acids from essential amino acids, glycolysis intermediates, carbamoyl phosphate and 5-phosphoribosyl 1-phosphate. Essential amino acids are colored in light green, amino acids in blue, and gases in orange. Energy molecules are colored in green (if produced) or in red (if consumed).

by the help of amino acid-bearing tRNA (AA-tRNA). One ATP molecule is used to create AA-tRNA bond (Figure 7). Transcription and translation are usually not integrated into the models, due to unavailability of data of complex interaction between DNA, amino acids and enzymes.

## 2. 2. 8. Glycosylation

Glycosylation is the attachment of a glycan unit to a protein after translation. Commonly, it is modeled separately from the rest of the cell metabolism.<sup>37,38,40</sup> Peptide or protein can enter ER, if signal sequence is in front of protein. Inside ER, specific glycans assembled from monosaccharides are attached to the protein through amino residue of the asparagine. Glycan part of the protein is additionally glycosylated in the ER and at the end of this process consists of two N-acetyl glucosamine and nine mannose residues. Afterwards, the glycosylated protein enters the GA where the glycan part of the protein is additionally modified by the help of specific enzymes. N-acetyl glucosamine, galactose, sialic acid, and fucose might be added to final glycan structures. The final products then leave the GA (Figure 7).<sup>77,79</sup> The destination of the glycosylated protein isoforms is determined by a signal peptide in the protein sequence. Glycosylated proteins can be excreted from the cell, incorporated into membrane or transported to other places inside the cell (Figure 7).<sup>77,79</sup>

Availability of glycosylation machinery relative to cellular secretory capacity plays a crucial role in protein glycosylation.<sup>38</sup> A modeling platform is able to predict the

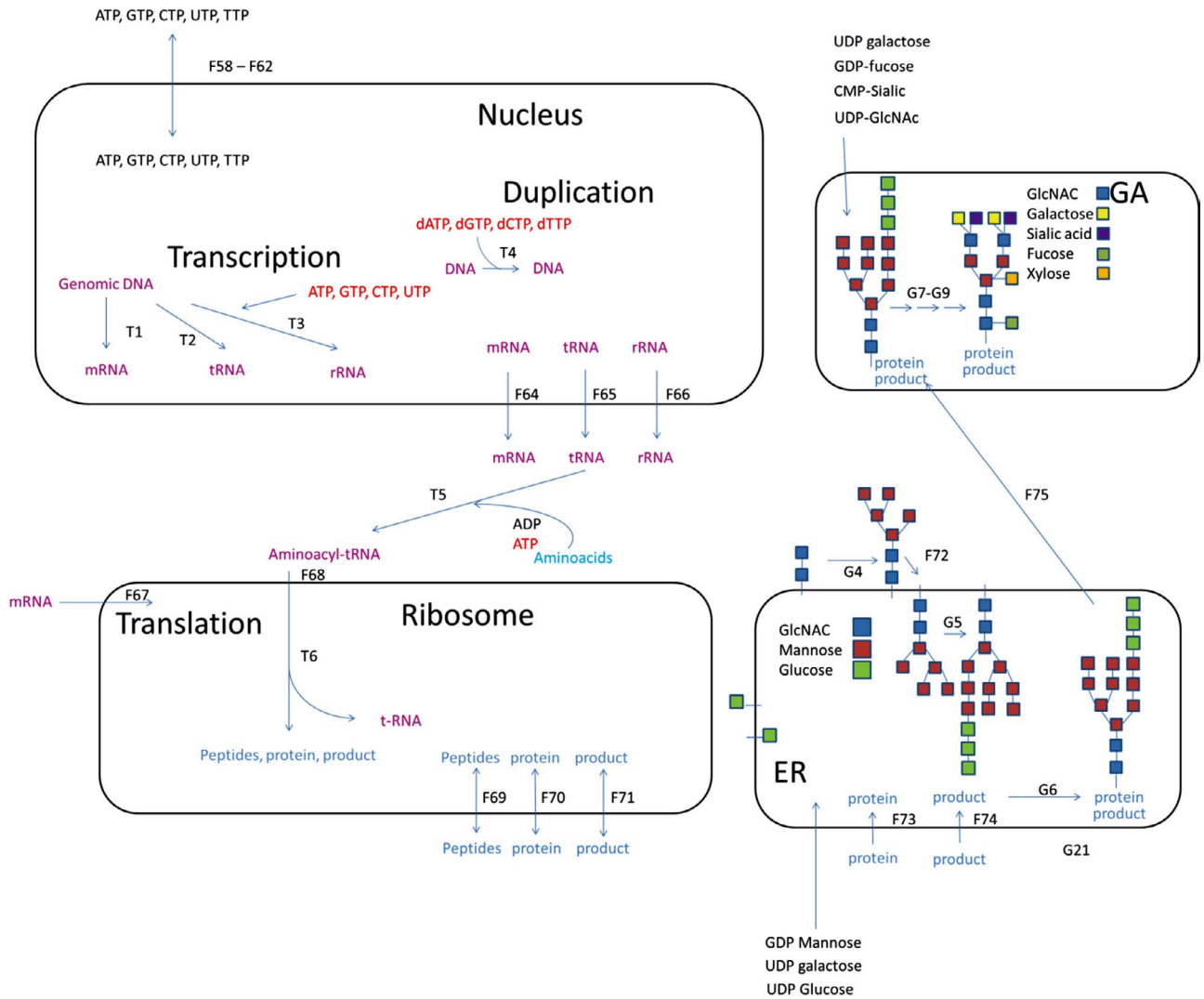
distribution of different glycoforms based on extracellular conditions<sup>37</sup> likewise the form of glycan, when expression of the protein is elevated.<sup>40</sup>

## 2. 2. 9. Feedback Loops

The catabolism is regulated by ATP. High concentration of ATP inhibits conversion of glucose-6-phosphate into ribulose-5-phosphate, fructose-6-phosphate into glyceralate-3-phosphate, phosphoglycerate into phosphoenolpyruvate, pyruvate into acetylCoA (glycolysis), glutamine into glutamate, and glutamate into alpha-ketoglutarate (glutaminolysis).<sup>50</sup> ATP also inhibits Krebs cycle in two places: (i) conversion of alpha-ketoglutarate into succinyl CoA, and (ii) oxaloacetate into citrate.<sup>50</sup>

High concentration of ATP slows down catabolism and transfers excess glucose into glycogen. ATP is used for biomass and production of final product. High ATP concentration stops glutaminolysis; glutamine is converted into other amino acids. Glucose is metabolized into nucleotide monosaccharides that are transported into ER and GA. The pathway of glycolysis is highly regulated to sustain sufficient concentration of ATP (Figure 8). In rapidly dividing cells glucose and glutamine consumptions are major steps for energy supply. Both pathways are ATP regulated by negative feedback loop.

High production of lipids from AcCoA and nucleotides from ribose-5-phosphate and glutamine leads to anabolism in CHO cells. DNA is duplicated by the aid of DNA polymerase. Proteins are synthesized in a more com-

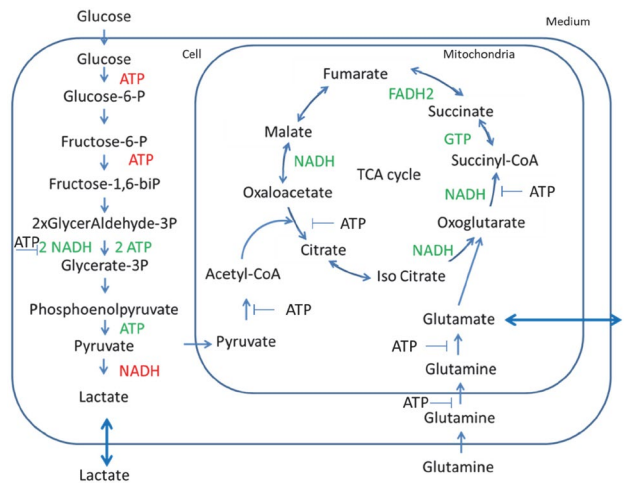


**Figure 7:** Transcription of DNA takes place in the nucleus, while translation of mRNA takes place in the cytosol. Glycan attachments are done in ER, while associated modifications take place in GA.<sup>5, 19, 37, 38, 40, 77, 79</sup> RNA and DNA are colored in purple, polypeptides are colored in blue. Monosaccharides are labeled with colored square, blue square represents N-acetyl glucosamine unit, red square mannose unit, green fucose, yellow galactose, and orange xylose unit (not added to glycan backbone in CHO cells).

plex way; first transcription of mRNA is needed, followed by translation of proteins by the aid of mRNA, tRNAs, and ribosomes.

### 2. 3. Mechanistic Models

In addition to black box models, mechanistic models have gained increasing interest in a detailed description of mammalian cell metabolism. Mechanistic models start with a set of metabolites linked up with biochemical reactions, which organize metabolites in the metabolic network. Metabolic network comprises intracellular transformations of metabolites and the membrane transport,



**Figure 8:** Glycolysis and Glutaminolysis.<sup>5, 50</sup> Molecules colored in green are generated, while molecules in red are used in the transformations. High concentration of ATP stops conversion of pyruvate into acetyl CoA, alpha-ketoglutarate (oxaloacetate) into citrate and oxoglutarate into succinyl CoA.

which couples the cell interior with the cell medium. Metabolic network modeling is commonly associated with the metabolic flux analysis (MFA), flux balance analysis (FBA), and other derived methodologies.<sup>80</sup> MFA considers experimental data to estimate flux rates for biochemical reactions within a metabolic network, while FBA assumes objectives and constraints to tailor the solution space of flux rates. These methods originally provide static insights into metabolic routes, what allows to study cell cultures at a state of particular interest. Even though several extensions were proposed to include extracellular dynamics in the framework of MFA and FBA,<sup>81</sup> precise mathematical representation of reaction kinetics and regulation mechanisms remains a challenge. See the review for a concise overview of metabolic models.<sup>82</sup>

Several attempts have been made to address dynamic behavior of mammalian cell cultures. Nolan et al used the metabolic network with 34 reactions to describe CHO cell metabolism.<sup>43</sup> They used MFA to estimate reactions' flux rates, which were further rationalized by optimization protocols. To imitate the distribution of co-factors they assumed two types: co-factors, which are located within the mitochondria and others within the liquid part of a cytoplasm. They defined the redox variable as the ratio between the rate of generated NADH and the transport rate of NADH from cytosol to mitochondria. The redox variable took place in the kinetic expressions and it was envisaged that governs dynamics of lactate.

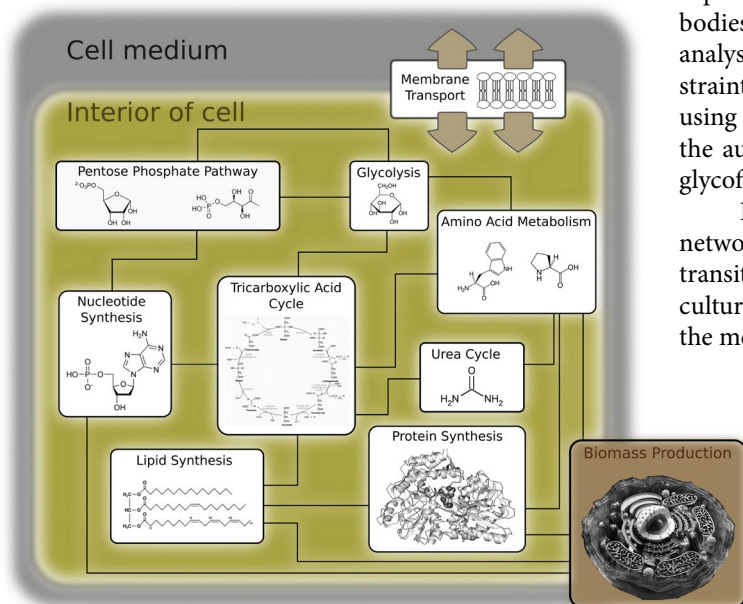
Provost et al<sup>19</sup> and later Zamorano et al<sup>24</sup> used MFA and the associated concept of elementary flux modes (EFMs) to recognize probable metabolic routes (macro reactions). They obtain three sets of macro reactions (three submodels), each for the corresponding phase of the cell culture: growth, stationary, and decline phase. Macro reactions were modeled by the Monod kinetic law (Eq. 4). Fi-

nally, they assume the interplay between submodels to describe transitions through phases of the cell culture.

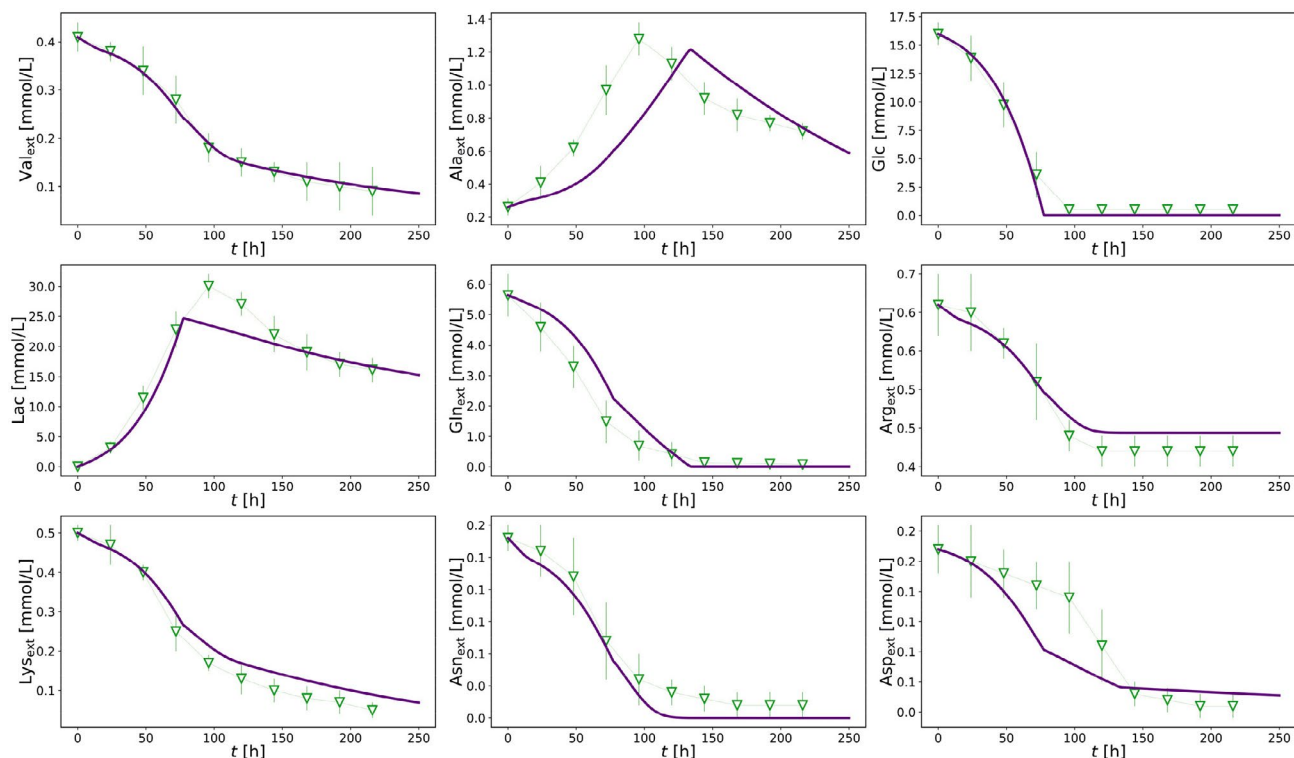
In another approach Hagrot et al<sup>21</sup> used the metabolic network with 30 reactions and enumerate the whole EFM spectrum. Then, they used several experimental sets to estimate maximal flux rates of EFMs. Dynamic behavior of EFMs was induced by additional terms that described substrate saturation, product inhibition, and metabolite inhibition. The so-called Poly-pathway model simulated multiple metabolic stages of CHO cell metabolism and thus addresses the diversity seen from experiments. However, the dissemination of the approach toward metabolic networks of larger extent remains a challenge due to time-consuming of EFM enumeration. An example of such models are the genome-scale metabolic models (GEMs), which treat the metabolic network in a more detail together with enzymatic activity and the genome, which encodes enzymes of biochemical reactions in the metabolic network.<sup>45,83</sup> GEMs are phenotype-specific and requires large amount of data and computer facilities. For further reading, see the excellent review of genome-scale approaches.<sup>84</sup>

Mechanistic models have been applied also to study post-translational modifications (glycosylation) of antibodies within mammalian cell cultures.<sup>34,41,85,86</sup> These processes are modeled by three types of kinetic laws, which describe interplay among enzymes and glycoforms: (i) Michaelis-Menten kinetics with competitive and product inhibitions, (ii) Sequential-order Bi-Bi with competitive and product inhibitions and (iii) Random-order Bi-Bi with competitive and product inhibitions. In a greatly accepted approach, authors assume continuous plug flow reactor (PFR) model to represent maturation of glycoforms along the Golgi apparatus.<sup>85</sup> Coupled with the mass balances for nucleotide sugar donors, byproducts, and transport proteins, the PFR model provides a mechanistic explanation for glycosylation profiles of commercial antibodies. Recently, Hutter et al<sup>41</sup> proposed glycosylation flux analysis (GFA) as an MFA analogue to apply constraint-based modeling of the glycosylation network by using a pseudo steady state assumption. Using the GFA, the authors were able to elucidate dynamical changes of glycoforms, caused by media variations.

In our recent work, we proposed a simple metabolic network with 103 biochemical reactions, to investigate transitions between cell phases in mammalian CHO cell cultures.<sup>87,88</sup> Figure 9 shows schematic representation of the metabolic pathways.



**Figure 9:** Metabolic network comprises Glycolysis, Pentose Phosphate Pathway, Nucleotide Synthesis, Tricarboxylic Acid cycle, Amino Acid Metabolism, Urea Cycle, Lipid Synthesis, Protein Synthesis Biomass Production, and Membrane Transport. Each pathway comprises detailed set of biochemical reactions, which describes transformations among metabolites on the molecular level.



**Figure 10:** Metabolites' concentration profiles as a function of time. Green points label metabolite uptake or secretion in the cell medium during the cultivation of CHO-320 cells.<sup>13</sup> Purple lines apply to macro reactions, which are characterized by kinetic parameters.<sup>88</sup>

In our approach, the biomass (density of viable cells) evolves as dictated by the cell metabolism, and not via the logistic-typed description (Eq. 1), which is traditionally used in mechanistic models for biomass production. Then, we used the interplay between FBA and MFA to impose constraints within the cell interior, and to estimate the reactions' flux rates. We used the random sampling approach to calculate the set of EFMs (macro reactions), without precalculated EFM spectrum. Assigning Monod kinetic law to macro reactions is a common approach to describe individual phases of the cell culture. Unfortunately, the approach is not suitable to describe transitions between growth, stationary, and decline phase. To overcome this issue, we included negative terms (reversible kinetics) in Monod kinetic law to address inhibition phenomena and the possible rewiring of metabolic routes, caused by products in macro reactions. Description of technical details would be beyond the scope of this review, however we shall mention that after performing the model reduction protocol we achieved evident simplification of the kinetic model. Starting from 64 model parameters we finally obtain 17 kinetic parameters, which turned out to be sufficient to describe dynamics of metabolites in the cell medium. Time evolution of the representative metabolites is shown in Figure 10.

Figure 10 shows characteristics of mammalian CHO cell cultures. At the growth phase, cells exhibit very high consumption rates of Glc and Gln, resulting in high secre-

tion of Lac. Amino acids are mostly depleted. The end of growth phase ( $t \approx 90$  h) is characterized by Glc deprivation: to compensate it, the produced Lac is consumed as the carbon source instead of Glc as already mentioned.

As seen in Figure 10, the model is capable to describe transitions between cell phases. The important feature of the model turned out to be reversible nature of kinetic expressions, which allow to describe non-monotonic behavior of metabolites' concentrations by means of flux reversal instead of user-defined switching functions that are in general difficult to obtain.

### 3. Summary

The present review describes how the research should to be done from the start to successfully finish the bioreactor model. In the review we revise recent advances of bioreactor operation and CHO metabolic pathways.

Black box models describe reactor with simple equations that fits curves of growth, substrate consumption and product formation. These are simple formulations that describe working bioreactor with culture at given conditions. Mechanistic models usually describe growth through complex metabolic pathways together with complex operation equations. Black box equations can be also integrated into mechanistic models, a good example is description of biomass growth, where biomass depends on factors inde-

pendent of network metabolic flows. Thorough study of metabolic pathways brings new ideas how to address existing problems that may arise during batch, fed batch and continuous bioreactor operation.

The methodologies we have presented so far are powerful; however there is still an ample room for improvements, which have to be implemented in a consistent way. To improve and extend the current models it is essential to estimate kinetic constants from parallel experiments by measuring response of cell metabolism upon addition of selected nutrients. We expect to gain large benefit by carrying out additional measurements of antibody secretion, which may yield additional flux modes and thus unravel other relevant pathways. Central metabolic pathways should be designed together with glycosylation pathways to form a valuable tool in biotechnology for estimating the quality of product titer. Some of the detailed models we presented have capability to be refined by including the activity of enzymes and their sensitiveness on temperature and pH shifts. Improvements of current methodologies might aid at the development of biotechnology processes and consequentially to facilitate the release of products on the market.

#### 4. Acknowledgements

Special thanks go to partners on the BioPharm.Si project. We are thankful to Dr. Miša Mojca Cajnko for all the help with comments and corrections on the paper.

#### Funding

This work was supported from program BioPharm.Si co-funded by Republic of Slovenia and European Union from European regional development fund.

#### Author biographies

Dr. **Jernej Gašperšič** is a researcher with PhD in the field of biomedicine: biochemistry and molecular biology. He has wide interdisciplinary knowledge of biochemistry, molecular biology, chromatography, bioinformatics, computational modeling that was improved in laboratories of institutes and industry. Past work experience is now upgrading with knowledge and expertise in the field of DNA sequencing.

Dr. **Miha Kastelic** received his PhD in 2017 in Chemical Sciences at the University of Ljubljana. Main research activities during his PhD period include protein aggregation, phase equilibrium, statistical mechanics, and associated thermodynamic properties of protein solutions. After his PhD, he joined to the Department of Catalysis and Chemical Reaction Engineering (National Institute of Chemistry) where he utilizes *in silico* methodologies in or-

der to describe central metabolism and glycosylation pathway of mammalian cell cultures.

Dr. **Uroš Novak** has a Ph.D. from Chemical Sciences at the University of Ljubljana. His current focus is in the field of biopharmaceutical up-stream and downstream process engineering and biotechnology.

Assist. Prof. Dr. **Blaž Likozar** earned his PhD in Chemical Engineering in 2008 at the University of Ljubljana, Faculty of Chemistry and Chemical Technology. He has been a member of NIC since 2011, working as a senior research fellow, assistant professor and department head in the field of chemical engineering (Department of Catalysis and Chemical Reaction Engineering); leading the programme “Chemical Reaction Engineering” as well as several research projects. His expertise lies (among others) in heterogeneous catalyst materials, modelling, simulation and optimization of process fluid mechanics, transport phenomena and chemical kinetics. He worked in 2014–2015 at the University of Delaware (Catalysis Center for Energy Innovation, Newark, Delaware, USA), as a Fulbright Program researcher in the field of chemical engineering.

#### 5. References

1. C. Altamirano, A. Illanes, S. Becerra, J. J. Cairo, F. Godia, *J. Biotechnol.* **2006**, *125*, 547–556. DOI:10.1016/j.jbiotec.2006.03.023
2. N. Sengupta, S. T. Rose, J. A. Morgan, *Biotechnol. Bioeng.* **2011**, *108*, 82–92. DOI:10.1002/bit.22890
3. Z. Xing, B. Kenty, I. Koyrakh, M. Borys, S. H. Pan, Z. J. Li, *Process Biochem.* **2011**, *46*, 1423–1429. DOI:10.1016/j.procbio.2011.03.014
4. C. Goudar, R. Biener, K. B. Konstantinov, J. M. Piret, *American Institute of Chemical Engineers Biotechnol.* **2009**, *25*, 986–998.
5. L. E. Quek, S. Dietmair, J. O. Kromer, L. K. Nielsen, *Metab. Eng.* **2010**, *12*, 161–171. DOI:10.1016/j.ymben.2009.09.002
6. S. Xu, L. Hoshan, H. Chen, *Bioproc. Biosyst. Eng.* **2016**, *39*, 1689–1702. DOI:10.1007/s00449-016-1644-3
7. L. Xie, D. I. Wang, *Biotechnol. Bioeng.* **1994**, *43*, 1175–1189. DOI:10.1002/bit.260431123
8. C. A. Sellick, A. S. Croxford, A. R. Maqsood, G. Stephens, H. V. Westerhoff, R. Goodacre, A. J. Dickson, *Biotechnol. Bioeng.* **2011**, *108*, 3025–3031. DOI:10.1002/bit.23269
9. M. D. Rocha-Pizana, G. Ascencio-Favela, B. M. Soto-Garcia, M. M. Alvarez, M. D. L. Martinez-Fierro, *Protein Expres. Purif.* **2017**, *132*, 108–115. DOI:10.1016/j.pep.2017.01.014
10. H. Hansen, C. Emborg, *Appl. Microbiol. Biotechnol.* **1990**, *41*, 560–564. DOI:10.1007/BF00178489
11. L. Xie, D. I. Wang, *Biotechnol. Bioeng.* **1996**, *52*, 579–590. DOI:10.1002/(SICI)1097-0290(19961205)52:5<579::AID-

- BIT5>3.0.CO;2-G
12. H. P. Bonarius, V. Hatzimanikatis, K. P. Meesters, C. D. de Gooijer, G. Schmid, J. Tramper, *Biotechnol. Bioeng.* **1996**, *50*, 299–318. DOI:10.1002/(SICI)1097-0290(19960505)50:3<299::AID-BIT9>3.0.CO;2-B
  13. F. Zamorano, A. V. Wouwer, G. Bastin, *J. Biotechnol.* **2010**, *150*, 497–508. DOI:10.1016/j.jbiotec.2010.09.944
  14. C. Goudar, R. Biener, C. Boisart, R. Heidemann, J. Piret, A. de Graff, K. Konstantinov, *Metab. Eng.* **2010**, *12*, 138–149. DOI:10.1016/j.ymben.2009.10.007
  15. J. D. Young, *Curr. Opin. Biotech.* **2013**, *24*, 1108–1115. DOI:10.1016/j.copbio.2013.04.016
  16. W. S. Ahn, M. R. Antoniewicz, *Metab. Eng.* **2011**, *13*, 598–609. DOI:10.1016/j.ymben.2011.07.002
  17. C. Altamirano, A. Illanes, A. Casablancas, X. Gamez, J. J. Cairo, C. Godia, *Biotechnol. Progr.* **2001**, *17*, 1032–1041. DOI:10.1021/bp0100981
  18. J. Lopez-Meza, D. Araiz-Hernandez, L. M. Carrillo-Cocom, F. Lopez-Pacheco, M. del Refugio Rocha-Pizan, M. M. Alvarez, *Cytotechnology.* **2016**, *68*, 1287–1300.
  19. A. Provost, G. Bastin, *J. Process Control.* **2004**, *14*, 717–728. DOI:10.1016/j.jprocont.2003.12.004
  20. S. Naderi, M. Meshram, C. Wei, B. McConkey, B. Ingalls, H. Budman, J. Scharer, *Biotechnol. Prog.* **2011**, *27*, 1197–1205. DOI:10.1002/btpr.647
  21. E. Hagrot, H. A. Oddsdottir, J. G. Hosta, E. W. Jacobsen, V. Chotteau, *J. Biotechnol.* **2016**, *228*, 37–49. DOI:10.1016/j.jbiotec.2016.03.015
  22. J. Robitaille, J. K. Chen, M. Jolicoeur, *PLoS ONE.* **2015**, *10*, e0136815. DOI:10.1371/journal.pone.0136815
  23. J. A. Papin, N. D. Stelling, S. Price Klamt; S. Schuster; B. O. Palsson, *Trends Biotechnol.* **2004**, *22*, 400–405. DOI:10.1016/j.tibtech.2004.06.010
  24. F. Zamorano, A. V. Wouwer, R. M. Jungers, G. Bastin, *J. Biotechnol.* **2013**, *164*, 409–422. DOI:10.1016/j.jbiotec.2012.05.005
  25. P. Farzan, B. Mistry, M. G. Ierapetritou, *AIChE J.* **2017**, *63*, 398–408. DOI:10.1002/aic.15442
  26. B. Berry, J. Moretto, T. Matthews, J. Smelko, K. Wiltberger, *Biotechnol. Progr.* **2015**, *31*, 566–577. DOI:10.1002/btpr.2035
  27. X. Chen, A.P. Alonso, D.K. Allen, J. L. Reed, *Metab. Eng.* **2011**, *13*, 38–48. DOI:10.1016/j.ymben.2010.11.004
  28. N. E. Lewis, H. Nagarajan, B. O. Palsson, *Nat. Rev. Microbiol.* **2012**, *10*, 291–305. DOI:10.1038/nrmicro2737
  29. G. B. Nyberg, R. R. Balcarel, B. D. Follstad, G. Stephanopoulos, D. I. C. Wang, *Biotechnol. Bioeng.* **1998**, *62*, 324–335. DOI:10.1002/(SICI)1097-0290(19990205)62:3<324::AID-BIT9>3.0.CO;2-C
  30. J. Dean, P. Reddy, *Biotechnol. Bioeng.* **2013**, *110*, 1735–1747. DOI:10.1002/bit.24826
  31. A. Ghorbaniaghdam, O. Henry, M. Jolicoeur, *Bioproc. Biosyst. Eng.* **2013**, *36*, 469–487. DOI:10.1007/s00449-012-0804-3
  32. B. Ben Yahia, B. Gourevitch, L. Malphettes, E. Heinzle, *Biotechnol. Bioeng.* **2017**, *114*, 785–797. DOI:10.1002/bit.26214
  33. A. Provost, G. Bastin, S. N. Agathos, Y. J. Schneider, *Bioprocess Biosyst. Eng.* **2006**, *29*, 349–366. DOI:10.1007/s00449-006-0083-y
  34. S. N. Galleguillos, D. Ruckerbauer, M. P. Gerstl, N. Borth, M. Hanscho, J. Zanghellini, *Comput. Struct. Biotechnol. J.* **2017**, *15*, 212–221. DOI:10.1016/j.csbj.2017.01.005
  35. Meng Ji, Yelian Miao, Jie Yu Chen, Yebing You, Feilong Liu, and Lin Xu. *Springerplus* **2016**, *5*, 503. DOI:10.1186/s40064-016-2151-3
  36. Monod J. *Annu. Rev. Microbiol.*, **1949**, *3(1)*, 371–394. DOI:10.1146/annurev.mi.03.100149.002103
  37. P. M. Jedrzejewski, I. J. del Val, A. Constantinou, A. Dell, S. M. Haslam, K. M. Polizzi, C. Kontoravdi, *Int. J. Mol. Sci.* **2014**, *15*, 4492–4522. DOI:10.3390/ijms15034492
  38. I. J. del Val, K. M. Polizzi, C. Kontoravdi, *Sci. Rep.* **2016**, *6*, 1–16. DOI:10.1038/srep28547
  39. P. N. Spahn, N. E. Lewis, *Curr. Opin. Biotech.* **2014**, *30*, 218–224. DOI:10.1016/j.copbio.2014.08.004
  40. J. Krambeck, M. J. Betenbaugh, *Biotechnol. Bioeng.* **2005**, *92*, 711–728. DOI:10.1002/bit.20645
  41. S. Hutter, T. K. Villiger, D. Bruhlmann, M. Stettler, H. Broly, M. Soos, R. Gunawan, *Metab. Eng.* **2017**, *43*, 9–20. DOI:10.1016/j.ymben.2017.07.005
  42. E. S. Bayrak, T. Wang, A. Cinar, C. Undey, *IFAC-PapersON-Line.* **2015**, *48*, 1252–1257. DOI:10.1016/j.ifacol.2015.09.140
  43. R. P. Nolan, K. Lee, *Metab. Eng.* **2011**, *13*, 108–124. DOI:10.1016/j.ymben.2010.09.003
  44. N. Templeton, K.D. Smith, A. G. Mcatee-Prereira, H. Dorai, M. J. Betenbaugh, S. E. Lang, J. D. Young, *Metab. Eng.* **2016**, *43*, 218–225. DOI:10.1016/j.ymben.2017.01.008
  45. S. Selvarasu, Y. S. Ho, W. P. K. Chong, N. S. C. Wong, F. N. K. Yusufi, Y. Y. Lee, M. G. S. Yap, D. Y. Lee, *Biotechnol. Bioeng.* **2012**, *109*, 1415–1429. DOI:10.1002/bit.24445
  46. L. Jiang, A. Boufersaoui, C. Yang, B. Ko, D. Rakheja, G. Guevara, Z. Hu, R. J. Debarardinis, *Metab. Eng.* **2017**, *43*, 198–207. DOI:10.1016/j.ymben.2016.11.004
  47. J. Berrios, C. Altmirano, N. Osses, R. Gonzales, *Chem. Eng. Sci.* **2011**, *66*, 2431–2439. DOI:10.1016/j.ces.2011.03.011
  48. E. E. Gonzo, S. Wuertz, V.B. Rajal, *Biotechnol. Bioeng.* **2014**, *111*, 2252–2264. DOI:10.1002/bit.25284
  49. Nishikant Shirsat, Avesh Mohd, Jessica Whelan, Niall J. English, Brian Glennon, and Mohamed Al-Rubeai. *Cytotechnology* **2015**, *67(3)*, 515–530. DOI:10.1007/s10616-014-9712-5
  50. C. S. Sanderson, J. P. Barford, G. W. Barton, *Biochem. Eng. J.* **1999**, *3*, 203–211. DOI:10.1016/S1369-703X(99)00021-2
  51. T. Goudar, R. Biener, B. K. Konstantinov, J. M. Piret, *Biotechnol. Progr.* **2012**, *25*, 986–998. DOI:10.1002/btpr.155
  52. P. Jorjani, S. S. Ozturk, *Biotechnol. Bioeng.* **1999**, *64*, 349–356. DOI:10.1002/(SICI)1097-0290(19990805)64:3<349::AID-BIT11>3.0.CO;2-V
  53. S. R. Chowdhury, J. Djordjevic, B. C. Albensi, P. Fernyhough, *Bioscience Rep.* **2016**, *36*, e00286. DOI:10.1042/BSR20150244
  54. L. P. Zielinski, A. C. Smith, A. G. Smith, A. J. Robinson, *Mito-*



- chondrion*. 2016, 31, 45–55. DOI:10.1016/j.mito.2016.09.003
55. E. Trummer, K. Fauland, S. Seidinger, K. Schriebl, C. Lattenmayer, R. Kunert, K. Vorauer-Uhl, R. Weik, N. Borth, H. Katinger, D. Muller, *Biotechnol. Bioeng.* **2006**, 94, 1033–1044. DOI:10.1002/bit.21013
56. W. S. Ahn, M. R. Antoniewicz, *Biotechnol. J.* **2012**, 7, 61–74. DOI:10.1002/biot.201100052
57. Z. Z. Xing, A. M. Lewis, M. C. Borys, Z. J. Li, *Biotechnol. Bioeng.* **2017**, 114, 1184–1194. DOI:10.1002/bit.26232
58. N. Jenkins and A. Hovey, *Biotechnol. Bioeng.* **1993**, 42, 1029–1036. DOI:10.1002/bit.260420903
59. B. Rossler, H. Lubben, G. Kretzmer, *Enzyme Microb. Tech.* **1996**, 18, 423–427. DOI:10.1016/0141-0229(95)00121-2
60. S. Becerra, J. Berrios, N. Osses, C. Altamirano, *Biochem. Eng. J.* **2012**, 60, 1–8. DOI:10.1016/j.bej.2011.10.003
61. Watanabe and Okada S., *J. Cell Biol.* **1967**, 32, 309–323. DOI:10.1083/jcb.32.2.309
62. P. Ducommun, P. A. Ruffieux, A. Kadouri, U. von Stockar, I. W. Marison, *Biotechnol. Bioeng.* **2002**, 77, 838–42. DOI:10.1002/bit.10185
63. S. K. Yoon, S. L. Choi, J. Y. Song, G. M. Lee, *Biotechnol. Bioeng.* **2005**, 89, 345–56. DOI:10.1002/bit.20353
64. V. Avello, B. Tapia, M. Vergara, C. Acevedo, J. Berrios, J. G. Reyes, C. Altamirano, *Electron. J. Biotechnol.* **2017**, 27, 55–62. DOI:10.1016/j.ejbt.2017.03.008
65. N. Kurano, C. Leist, F. Messi, C. Gandor, S. Kurano, A. Fiechter, *J. Biotechnol.* **1990**, 6, 245–258. DOI:10.1016/0168-1656(90)90040-I
66. J. S. Seo, Y. J. Kim, J. M. Cho, E. Baek, G. M. Lee, *Appl. Microbiol. Biot.* **2013**, 97, 5283–5291. DOI:10.1007/s00253-013-4849-2
67. K. Furukawa, K. Ohsuye, *Cytotechnology*, **1998**, 26, 153–64. DOI:10.1023/A:1007934216507
68. H. Kaufmann, X. Mazur, M. Fussenegger, J. E. Bailey, *Biotechnol. Bioeng.*, **1999**, 63, 573–582. DOI:10.1002/(SICI)1097-0290(19990605)63:5<573::AID-BIT7>3.0.CO;2-Y
69. R. L. Dutton, J. Scharer, M. Moo-Young, *Cytotechnology*, **2006**, 52, 55–69. DOI:10.1007/s10616-006-9041-4
70. V. Hendrick, P. Winnepenninckx, C. Abdelkafi, O. Vandeputte, M. Cherlet, T. Marique, G. Renemann, A. Loa, G. Kretzmer, J. Werenne, *Cytotechnology* **2001**, 36, 71–83. DOI:10.1023/A:1014088919546
71. M. Rasouli, *Clin. Biochem.* **2016**, 49, 936–941. DOI:10.1016/j.clinbiochem.2016.06.001
72. A. Philip, M. Hargreaves, K. Baar, *Am. J. Physiol.* **2012**, 302, 1343–1351.
73. L. Hildebrandt, T. Spennetta, R. Ackerman, C. Elson, E. Shrago, R. T. Ackermann, *Biochem. Biophys. Res. Co.* **1996**, 225, 207–212. DOI:10.1006/bbrc.1996.1171
74. Moncada, S. Higgs, E. A. Colombo, S. L., *Biochem. J.* **2012**, 446, 1–7. DOI:10.1042/BJ20120427
75. O. Feron, *Radiother. Oncol.* **2009**, 92, 329–333. DOI:10.1016/j.radonc.2009.06.025
76. E. J. M. Blondeel, R. Ho, S. Schulze, S. Sokolenko, S. R. Guillemette, I. Sliva, Y. Durocher, J. G. Guillemette, B. J. McConkey, D. Chang, M. G. Aucoin. *J. Biotechnol.* **2016**, 234, 127–138. DOI:10.1016/j.jbiotec.2016.07.027
77. E. Maverakis, K. Kim, M. Shimoda, M. E. Gershwin, F. Patel, R. Wilken, S. Raychaudhuri, L. R. Ruhaak, C. B. Lebrilla, *J. Autoimmun.* **2015**, 57, 1–13. DOI:10.1016/j.jaut.2014.12.002
78. F. Chiappini, A. Coilly, H. Kadar, P. Gual, A. Tran, C. Desterke, D. Samuel, J. C. Duclos-Vallée, D. Touboul, J. Bertrand-Michel, A. Brunelle, C. Guettier, F. Le Naour, *Sci. Rep.* **2017**, 7, 1–17. DOI:10.1038/srep46658
79. B. Imperiali and S.E. O'Connor, *Curr. Opin. Chem. Biol.* **1999**, 3, 643–649. DOI:10.1016/S1367-5931(99)00021-6
80. P. J. D'Huys, I. Lule, D. Vercammen, J. Anné, J. F. Van Impe, K. Bernaerts, *J. Biotechnol.* **2012**, 161, 1–13. DOI:10.1016/j.jbiotec.2012.04.010
81. F. Llaneras, A. Sala, J. Picó, *J. Process Contr.* **2012**, 22, 1946–1955. DOI:10.1016/j.jprocont.2012.09.001
82. E. O. Voit, *WIREs Syst. Biol. Med.* **2017**, 9, e1391.
83. H. Hefzi, K. S. Ang, M. Hanscho, A. Bordbar, D. Ruckerbauer, M. Lakshmanan, C. A. Orellana, D. Baycin-Hizal, Y. Huang, D. Ley, V. S. Martinez, S. Kyriakopoulos, N. E. Jiménez, D.C. Zielinski, L.E. Quek, T. Wulff, J. Arnsdorf, S. Li, J. S. Lee, G. Paglia, N. Loira, P.N. Spahn, L. E. Pedersen, J. M. Gutierrez, Z. A. King, A. M. Lund, H. Nagarajan, A. Thomas, A. M. Abdel-Haleem, J. Zanghellini, H. F. Kildegaard, B. G. Voldborg, Z. P. Gerdtzen, M. J. Betenbaugh, B. O. Palsson, M. R. Andersen, L. K. Nielsen, N. Borth, D. Y. Lee, N. E. Lewis, *Cell Syst.* **2016**, 3, 434–443. DOI:10.1016/j.cels.2016.10.020
84. Ž. Rejc, L. Magdevska, T. Tršelič, T. Osolin, R. Vodopivec, J. Mraz, E. Pavliha, N. Zimic, T. Cvitanović, D. Rozman, M. Moškon, M. Mraz, *Comput. Biol. Med.* **2017**, 88, 150–160.
85. I. J. del VAL, J. M. Nagy, C. A. Kontoravdi, *Biotechnol. Prog.* **2011**, 27, 1730–1743.
86. T. K. Villiger, E. Scibona, M. Stettler, H. Broly, M. Morbidelli, M. Soos. *Biotechnol. Prog.* **2016**, 32, 1135–1148. DOI:10.1002/btpr.2315
87. Kaučič, V. (Ed.), J. Gašperšič, U. Novak, A. Pohar, B. Likozar, *Zbornik referatov in povzetkov, Slovenski kemijski dnevi 2017, Portorož, Slovenia* **2017**, 1–6.
88. M. Kastelic, D. Kopač, U. Novak, B. Likozar, **2018**, *Biochemical Engineering Journal*.  
<https://authors.elsevier.com/tracking/article/details.do?aid=7095&jid=BEJ&surname=Kastelic>

## Povzetek

Epitelijske celice kitajskega hrčka (CHO) so ena izmed najbolj uporabljenih terapevtskih medicinskih linij za proizvodnjo različnih biofarmaceutskih zdravil. Imajo visoko stopnjo porabe s hitrim podvajanjem, kar jih naredi idealen biološki klon. Večja količina akumuliranih toksičnih intracelularnih intermediatov lahko privede do nižje viabilnosti organizma, produktivnosti proteinov in proizvedenih bioloških zdravil, zato je potrebna optimalna izbira sestave medija ter bioreaktorskih operativnih parametrov za vodenje bioprocasa. Natančno fenomenološko znanje o biokemijskih transformacijah v celičnem metabolizmu omogoča zaznavo težav, ki se lahko pojavijo med šaržnim, polkontinuirnim in kontinuirnim obratovanjem bioreaktorja. Za boljše razumevanje (in povezave), so bili izdelani mehanistični modeli, ki se lahko uporabijo za optimiziranje obratovanja in povečevanja skale. V tem delu je narejen pregled glavnih metabolni poti v strukturiranih sesalskih kulturah CHO. Pregled se začne z biokemijskim ozadjem znotraj celica, ki nadzirajo povezane pojave in kinetiko, ki urejajo vzpostavljene biološke poti. Nato sledi opis posamezne pretvorbene poti, preko pregleda standardnih matematičnih formulacij, ki se običajno uporabljajo v inženirstvu. Te formulacije sledijo principu modeliranja t.i. črne škatle (black box), ki povezuje substrate/produkte na poenostavljen način. Poleg tega so predstavljeni modeli, ki vključujejo analizo metabolnih fluksov (MFA) in analizo uteženih fluksov (FBA). Na koncu je pregled podobnosti med različnimi pristopi za njihovo strukturno zasnovu. Izpostavljene so enačbe s spremenljivkami, ki se uporabljajo za opis rasti kontroliranih pogojev v bioreaktorju, raziskane reakcijske serije rasti populacije CHO, povezane z vrednostmi maksimalne encimske aktivnosti. Procesi so naštetni tako, da lahko bralec integrira najsodobnejši pristop. Posebej je izpostavljen tudi prispevek avtorjev.



## 2. 1. 2. Instruments

Melting points were recorded on Gallenkamp electric melting point apparatus (Electronic Melting Point Apparatus, Great Britain, London) and are uncorrected. Infrared spectra were recorded on Pye Unicam SP 1000 IR spectrophotometer (Thermoelectron Co. Egelsbach, Germany) using a KBr wafer technique. The  $^1\text{H}$  NMR spectra were determined by a Bruker 400 MHz spectrometer. DMSO- $d_6$  was used as the solvent, TMS was used as the internal standard and chemical shifts are given on  $\delta$  scale in ppm. Mass spectra were determined on a GC-MS QP-100 EX Shimadzu (Japan). Microwave experiment was carried out using Milestone Start Microwave Lab Station. Elemental analyses were recorded on Perkin-Elmer 2400 Elemental analyzer at the Microanalytical Center at Cairo University, Cairo, Egypt.

## 2. 2. Synthesis

### Synthesis of (*E*)-2-Cyano-*N'*-(pyridin-4-ylmethylene)acetohydrazide (**1**)

*Method A:* A mixture of isonicotinaldehyde (1.07 g, 0.01 mol), 2-cyanoacetohydrazide (9.9 g, 0.01 mol) and TEA (2 drops) in THF or EtOH (15 mL) was refluxed for an appropriate time as shown in Table 1. The reaction progress was monitored by TLC. After completion of the reaction, the mixture was cooled to room temperature, the precipitate formed was collected by filtration and washed with ethyl acetate/petroleum ether (1:3), recrystallized from absolute ethanol to give pure compound **1**.

*Method B:* A mixture of isonicotinaldehyde (1.07 g, 0.01 mol) and 2-cyanoacetohydrazide (9.9 g, 0.01 mol) in a sealed tube was subjected to microwave irradiation at 700 W and microwave oven temperature 120 °C for 20 sec. The reaction mixture was cooled to room temperature and washed by a mixture of ethyl acetate/petroleum ether (1:3). The precipitate formed was recrystallized from absolute ethanol to give the pure product **1** (yield 98%).

Pale yellow crystals; yield: method A: 92% and 39% for THF and EtOH, respectively; method B: 98%; m.p. 169 °C; IR (KBr):  $\nu_{\text{max}}$  3235 (NH), 2259 (CN), 1704 (C=O)  $\text{cm}^{-1}$ ;  $^1\text{H}$  NMR (400 MHz, DMSO- $d_6$ ):  $\delta$  4.26 (s, 2H, CH<sub>2</sub>), 8.02 (d,  $J = 7.2$  Hz, 2H, C<sub>3</sub>-H and C<sub>5</sub>-H pyridine), 8.25 (s, 1H, CH=N), 8.74 (d,  $J = 7.2$  Hz, 2H, C<sub>2</sub>-H and C<sub>6</sub>-H pyridine), 11.86 (s, 1H, NH);  $^{13}\text{C}$  NMR (100 MHz, DMSO- $d_6$ ):  $\delta$  25.02, 119.39, 122.87, 141.01, 145.72, 149.61, 165.35; EI-MS:  $m/z$  188 ( $M^+$ , 10). Anal. Calcd. for C<sub>9</sub>H<sub>8</sub>N<sub>4</sub>O (188.19): C, 57.44; H, 4.29; N, 29.77. Found: C, 57.42; H, 4.33; N, 29.82.

### Synthesis of 2-Amino-cyano-6-oxo-4-aryl-1-((pyridin-4-ylmethylene)amino)-1,6-dihydropyridine-3,5-dicarbonitriles **5a–e**

*General procedure:* To a solution of compound **1** (1.88 g, 0.01 mol) in EtOH (20 mL), arylidene malononitriles **2a–e** (0.01 mol) and a catalytic amount of trimethylamine were added. The reaction mixture was heated under

reflux for 17–20 h (TLC controlled), then, the reaction mixture was left to cool. The precipitate that formed was filtered off, washed with ethyl acetate and recrystallized from ethanol to give the products **5a–e**.

### 2-Amino-6-oxo-4-phenyl-1-((pyridin-4-ylmethylene)amino)-1,6-dihydropyridine-3,5-dicarbonitrile (**5a**)

Brown crystals; yield: 20%; m.p. >300 °C; IR (KBr):  $\nu_{\text{max}}$  3345, 3390 (NH<sub>2</sub>), 2214, 2206 (2×CN), 1673 (C=O)  $\text{cm}^{-1}$ ;  $^1\text{H}$  NMR (400 MHz, DMSO- $d_6$ ):  $\delta$  6.55 (s, 2H, NH<sub>2</sub>), 7.10–7.50 (m, 5H, Ar-H), 7.99 (d,  $J = 7.2$  Hz, 2H, C<sub>3</sub>-H and C<sub>5</sub>-H pyridine), 8.43 (s, 1H, CH=N), 8.73 (d,  $J = 7.2$  Hz, 2H, C<sub>2</sub>-H and C<sub>6</sub>-H pyridine);  $^{13}\text{C}$  NMR (100 MHz, DMSO- $d_6$ ):  $\delta$  77.83, 115.23, 115.81, 116.29, 122.74, 126.90, 128.76, 129.20, 134.88, 145.83, 149.89, 152.66, 158.90, 162.34, 168.88; EI-MS:  $m/z$  340 ( $M^+$ , 50%). Anal. Calcd. for C<sub>19</sub>H<sub>12</sub>N<sub>6</sub>O (340.35): C, 67.05; H, 3.55; N, 24.69. Found: C, 67.12; H, 3.49; N, 24.72.

### 2-Amino-4-(4-methoxyphenyl)-6-oxo-1-((pyridin-4-ylmethylene)amino)-1,6-dihydropyridine-3,5-dicarbonitrile (**5b**)

Dark brown crystals; yield: 31%; m.p. 208 °C. IR (KBr):  $\nu_{\text{max}}$  3320, 3385 (NH<sub>2</sub>), 2212, 2235 (2×CN), 1669 (C=O)  $\text{cm}^{-1}$ ;  $^1\text{H}$  NMR (400 MHz, DMSO- $d_6$ ):  $\delta$  3.85 (s, 3H, CH<sub>3</sub>), 6.58 (s, 2H, NH<sub>2</sub>), 6.95 (d,  $J = 8.0$  Hz, 2H, Ar-H), 7.62 (d,  $J = 8.1$  Hz, 2H, Ar-H), 8.04 (d,  $J = 7.2$  Hz, 2H, C<sub>3</sub>-H and C<sub>5</sub>-H pyridine), 8.43 (s, 1H, CH=N), 8.72 (d,  $J = 7.2$  Hz, 2H, C<sub>2</sub>-H and C<sub>6</sub>-H pyridine);  $^{13}\text{C}$  NMR (100 MHz, DMSO- $d_6$ ):  $\delta$  59.24, 77.64, 115.11, 115.83, 116.22, 116.79, 122.58, 125.69, 131.94, 146.04, 149.91, 152.75, 158.14, 158.99, 161.67, 169.52; EI-MS:  $m/z$  370 ( $M^+$ , 18%). Anal. Calcd. for C<sub>20</sub>H<sub>14</sub>N<sub>6</sub>O<sub>2</sub> (370.37): C, 64.86; H, 3.81; N, 22.69. Found: C, 64.84; H, 3.79; N, 22.63.

### 2-Amino-4-(4-hydroxyphenyl)-6-oxo-1-((pyridin-4-ylmethylene)amino)-1,6-dihydropyridine-3,5-dicarbonitrile (**5c**)

Brown crystals; yield: 33%; m.p. 214 °C; IR (KBr):  $\nu_{\text{max}}$  3425 (OH), 3355, 3314 (NH<sub>2</sub>), 2213, 2229 (2×CN), 1679 (C=O)  $\text{cm}^{-1}$ ;  $^1\text{H}$  NMR (400 MHz, DMSO- $d_6$ ):  $\delta$  6.58 (s, 2H, NH<sub>2</sub>), 6.74 (d,  $J = 7.8$  Hz, 2H, Ar-H), 7.44 (d,  $J = 7.8$  Hz, 2H, Ar-H), 8.00 (d,  $J = 7.2$  Hz, 2H, C<sub>3</sub>-H and C<sub>5</sub>-H pyridine), 8.40 (s, 1H, CH=N), 8.74 (d,  $J = 7.2$  Hz, 2H, C<sub>2</sub>-H and C<sub>6</sub>-H pyridine), 9.77 (s, 1H, OH);  $^{13}\text{C}$  NMR (100 MHz, DMSO- $d_6$ ):  $\delta$  77.37, 115.23, 115.88, 116.17, 116.89, 122.75, 126.73, 130.88, 145.83, 149.93, 152.82, 158.12, 159.18, 161.73, 169.43; EI-MS:  $m/z$  356 ( $M^+$ , 9 %). Anal. Calcd. for C<sub>19</sub>H<sub>12</sub>N<sub>6</sub>O<sub>2</sub> (356.34): C, 64.04; H, 3.39; N, 23.58. Found: C, 63.99; H, 3.42; N, 23.51.

### 2-Amino-4-(4-(dimethylamino)phenyl)-6-oxo-1-((pyridin-4-ylmethylene)amino)-1,6-dihydropyridine-3,5-dicarbonitrile (**5d**)

Brown crystals; yield: 51%; m.p. 220 °C; IR (KBr):  $\nu_{\text{max}}$  3397, 3381 (NH<sub>2</sub>), 2224, 2241 (2×CN), 1670 (C=O)

cm<sup>-1</sup>; <sup>1</sup>H NMR (400 MHz, DMSO-*d*<sub>6</sub>): δ 3.13 (s, 6H, CH<sub>3</sub>), 6.58 (s, 2H, NH<sub>2</sub>), 6.81 (d, *J* = 8.2 Hz, 2H, Ar-H), 7.23 (d, *J* = 8.2 Hz, 2H, Ar-H), 8.00 (d, *J* = 7.2 Hz, 2H, C<sub>3</sub>-H and C<sub>5</sub>-H pyridine), 8.42 (s, 1H, CH=N), 8.72 (d, *J* = 7.3 Hz, 2H, C<sub>2</sub>-H and C<sub>6</sub>-H pyridine); <sup>13</sup>C NMR (100 MHz, DMSO-*d*<sub>6</sub>): δ 40.62, 77.06, 112.89, 115.61, 115.97, 116.22, 122.57, 123.16, 131.11, 146.34, 150.04, 150.96, 153.08, 158.97, 161.82, 169.07; EI-MS: *m/z* 383 (M<sup>+</sup>, 94%). Anal. Calcd. for C<sub>21</sub>H<sub>17</sub>N<sub>7</sub>O (383.42): C, 65.79; H, 4.47; N, 25.57. Found: C, 65.71; H, 4.51; N, 25.60.

## 2-Amino-4-(4-hydroxy-3-methoxyphenyl)-6-oxo-1-((pyridin-4-ylmethylene)amino)-1,6-dihydropyridine-3,5-dicarbonitrile (5e)

Orange red crystals; yield: 22%; m.p. 240 °C. IR (KBr): ν<sub>max</sub> 3418 (OH), 3337, 3308 (NH<sub>2</sub>), 2207, 2225 (2×CN), 1666 (C=O) cm<sup>-1</sup>; <sup>1</sup>H NMR (400 MHz, DMSO-*d*<sub>6</sub>): δ 4.11 (s, 3H, OCH<sub>3</sub>), 6.53 (s, 2H, NH<sub>2</sub>), 6.78–7.12 (m, 3H, Ar-H), 8.01 (d, *J* = 7.2 Hz, 2H, C<sub>3</sub>-H and C<sub>5</sub>-H pyridine), 8.42 (s, 1H, CH=N), 8.75 (d, *J* = 7.2 Hz, 2H, C<sub>2</sub>-H and C<sub>6</sub>-H pyridine), 9.57 (s, 1H, OH); <sup>13</sup>C NMR (100 MHz, DMSO-*d*<sub>6</sub>): δ 58.38, 77.13, 114.92, 115.44, 115.87, 116.89, 117.35, 122.92, 123.79, 127.14, 144.91, 148.49, 149.72, 150.98, 153.42, 158.24, 161.62, 169.38; EI-MS: *m/z* 386 (M<sup>+</sup>, 31%). Anal. Calcd. for C<sub>20</sub>H<sub>14</sub>N<sub>6</sub>O<sub>3</sub> (386.37): C, 62.17; H, 3.65; N, 21.75. Found: C, 62.21; H, 3.58; N, 21.70.

## Synthesis of 4,6-Diamino-2-oxo-1-((pyridin-4-ylmethylene)amino)-1,2-dihydropyridine-3-carbonitrile (6)

A mixture of compound **1** (1.88 g, 0.005 mol) and malononitrile (0.01 mol) in 20 mL of absolute EtOH containing 3 drops of triethylamine was refluxed for 9 h (TLC controlled). Then, the reaction mixture was left to cool and the precipitated solid was filtered off, dried, washed with ethyl acetate and recrystallized from absolute EtOH to afford compound **6**.

Yellow crystals; yield: 65%; m.p. >300 °C; IR (KBr): ν<sub>max</sub> 3399, 3388, 3347, 3321 (2×NH<sub>2</sub>), 2216 (CN), 1683 (C=O) cm<sup>-1</sup>; <sup>1</sup>H NMR (400 MHz, DMSO-*d*<sub>6</sub>): δ 4.62 (s, 1H, CH), 4.65 (s, 2H, NH<sub>2</sub>), 6.68 (s, 2H, NH<sub>2</sub>), 8.03 (d, *J* = 7.2 Hz, 2H, C<sub>3</sub>-H, C<sub>5</sub>-H pyridine), 8.43 (s, 1H, CH=N), 8.71 (d, *J* = 7.2 Hz, 2H, C<sub>2</sub>-H, C<sub>6</sub>-H pyridine); <sup>13</sup>C NMR (100 MHz, DMSO-*d*<sub>6</sub>): δ 72.83, 86.27, 116.17, 123.55, 143.94, 146.25, 151.47, 155.18, 163.48, 178.28; EI-MS: *m/z* 254 (M<sup>+</sup>, 100%). Anal. Calcd. for C<sub>12</sub>H<sub>10</sub>N<sub>6</sub>O (254.25): C, 56.69; H, 3.96; N, 33.05. Found: C, 56.77; H, 4.01; N, 32.96.

## Synthesis of 4,6-Dimethyl-2-oxo-1-((pyridin-4-ylmethylene)amino)-1,2-dihydropyridine-3-carbonitrile (7)

To a solution of **1** (1.88 g, 0.01 mol) and acetylacetone (1.001 g, 0.01 mol) in 20 mL of absolute EtOH containing a few drops of trimethylamine were added. The reaction mixture was heated under reflux for 18 h. After the completion of the reaction, the reaction mixture was cooled and the separated solid product was collected by

filtration, washed with ethanol, dried, and recrystallized from EtOH to give compound **7**.

Buff crystals; yield: 61%; m.p. 190 °C; IR (KBr): ν<sub>max</sub> 2208 (CN), 1674 (C=O) cm<sup>-1</sup>; <sup>1</sup>H NMR (400 MHz, DMSO-*d*<sub>6</sub>): δ 2.13 (s, 3H, CH<sub>3</sub>), 2.22 (s, 3H, CH<sub>3</sub>), 5.66 (s, 1H, CH), 8.01 (d, *J* = 7.2 Hz, 2H, C<sub>3</sub>-H, C<sub>5</sub>-H pyridine), 8.41 (s, 1H, CH=N), 8.70 (d, *J* = 7.2 Hz, 2H, C<sub>2</sub>-H, C<sub>6</sub>-H pyridine); <sup>13</sup>C NMR (100 MHz, DMSO-*d*<sub>6</sub>): δ 18.24, 22.03, 110.94, 116.83, 118.07, 122.44, 135.88, 145.57, 150.21, 153.47, 155.26, 161.47; EI-MS: *m/z* 252 (M<sup>+</sup>, 100%). Anal. Calcd. for C<sub>14</sub>H<sub>12</sub>N<sub>4</sub>O (252.28): C, 66.65; H, 4.79; N, 22.21. Found: C, 66.49; H, 4.81; N, 22.29.

## Synthesis of 1,6-Diamino-2-oxo-5-(alkyl)-1,2-dihydro-[4,4'-bipyridine]-3-carbonitriles 9a–d

*General procedure:* To a mixture of isonicotinaldehyde (1.07 g, 0.01 mol), activated nitriles **8a–d** (0.01 mol) and 2-cyanoacetohydrazide (0.99 g, 0.01 mol) absolute EtOH (20 mL) containing three drops of piperidine was added. The reaction mixture was heated under reflux for 6–8 h (TLC controlled). The reaction mixture was left to cool to the room temperature, then the solid formed was filtered off and recrystallized from absolute EtOH to give compounds **9a–d**

## 1,6-Diamino-2-oxo-1,2-dihydro-[4,4'-bipyridine]-3,5-dicarbonitrile (9a)

Brown crystals; yield: 71%; m.p. > 300 °C; IR (KBr): ν<sub>max</sub> 3428, 3373, 3366, 3345 (2×NH<sub>2</sub>), 2202, 2180 (2CN), 1665 (C=O) cm<sup>-1</sup>; <sup>1</sup>H NMR (400 MHz, DMSO-*d*<sub>6</sub>): δ 5.22 (s, 2H, NH<sub>2</sub>), 6.56 (s, 2H, NH<sub>2</sub>), 7.51 (d, *J* = 7.2 Hz, 2H, C<sub>3</sub>-H, C<sub>5</sub>-H pyridine), 8.63 (d, *J* = 7.2 Hz, 2H, C<sub>2</sub>-H, C<sub>6</sub>-H pyridine); <sup>13</sup>C NMR (100 MHz, DMSO-*d*<sub>6</sub>): δ 77.42, 115.24, 116.27, 122.05, 122.84, 145.14, 150.44, 159.11, 161.57, 171.34; EI-MS: *m/z* 186 (M<sup>+</sup>, 100%). Anal. Calcd. for C<sub>12</sub>H<sub>8</sub>N<sub>6</sub>O (252.24): C, 57.14; H, 3.20; N, 33.32. Found: C, 57.21; H, 3.16; N, 33.33.

## 1,6-Diamino-2-oxo-5-(phenylsulfonyl)-1,2-dihydro-[4,4'-bipyridine]-3-carbonitrile (9b)

Orange crystals; yield: 53%; m.p. 145 °C; IR (KBr): ν<sub>max</sub> 3447, 3403, 3334, 3070 (2×NH<sub>2</sub>), 2202 (CN), 1669 (C=O) cm<sup>-1</sup>; <sup>1</sup>H NMR (400 MHz, DMSO-*d*<sub>6</sub>): δ 5.48 (s, 2H, NH<sub>2</sub>), 6.57 (s, 2H, NH<sub>2</sub>), 7.50–7.80 (m, 7H, Ar-H and C<sub>3</sub>-H, C<sub>5</sub>-H pyridine), 8.59 (d, *J* = 7.2 Hz, 2H, C<sub>2</sub>-H, C<sub>6</sub>-H pyridine); <sup>13</sup>C NMR (100 MHz, DMSO-*d*<sub>6</sub>): δ 102.45, 116.49, 121.69, 122.82, 128.95, 130.14, 133.18, 141.89, 143.15, 143.83, 151.26, 161.77, 170.89; EI-MS: *m/z* 367 (M<sup>+</sup>, 8 %). Anal. Calcd. for C<sub>17</sub>H<sub>13</sub>N<sub>5</sub>O<sub>3</sub>S (367.38): C, 55.58; H, 3.57; N, 19.06; S, 8.73. Found: C, 55.58; H, 3.57; N, 19.06; S, 8.73.

## Ethyl 1,2-Diamino-5-cyano-6-oxo-1,6-dihydro-[4,4'-bipyridine]-3-carboxylate (9c)

Yellow crystals; yield: 48%; m.p. 180–190 °C; IR (KBr): ν<sub>max</sub> 3351, 3339, 3335, 3305 (2×NH<sub>2</sub>), 2215 (CN),

1725, 1674 (2×C=O) cm<sup>-1</sup>; <sup>1</sup>H NMR (400 MHz, DM-SO-*d*<sub>6</sub>): δ 1.01 (t, *J* = 7.2 Hz 3H, CH<sub>3</sub>), 4.03 (q, *J* = 6.8 Hz 2H, CH<sub>2</sub>), 5.39 (s, 2H, NH<sub>2</sub>), 7.08 (s, 2H, NH<sub>2</sub>), 7.56 (d, *J* = 7.4 Hz, 2H, C<sub>3</sub>-H, C<sub>5</sub>-H pyridine), 8.62 (d, *J* = 7.4 Hz, 2H, C<sub>2</sub>-H, C<sub>6</sub>-H pyridine); <sup>13</sup>C NMR (100 MHz, DMSO-*d*<sub>6</sub>): δ 15.37, 64.49, 99.56, 116.47, 121.82, 122.43, 143.73, 150.13, 152.85, 161.04, 167.28, 171.11; EI-MS: *m/z* 299 (M<sup>+</sup>, 100%). Anal. Calcd. for C<sub>14</sub>H<sub>13</sub>N<sub>5</sub>O<sub>3</sub> (299.29): C, 56.18; H, 4.38; N, 23.40. Found: C, 56.21; H, 4.33; N, 23.41.

### 1,6-Diamino-5-(benzo[*d*]thiazol-2-yl)-2-oxo-1,2-dihydro-[4,4'-bipyridine]-3-carbonitrile (9d)

Yellow crystals; yield: 73%; m.p. 315 °C; IR (KBr):  $\nu_{\max}$  3400, 3391, 3255, 3066 (2×NH<sub>2</sub>), 2209 (CN), 1661 (C=O) cm<sup>-1</sup>; <sup>1</sup>H NMR (400 MHz, DMSO-*d*<sub>6</sub>): δ 5.36 (s, 2H, NH<sub>2</sub>), 7.08 (s, 2H, NH<sub>2</sub>), 7.50–8.00 (m, 7H, Ar-H), 8.71 (d, *J* = 7.2 Hz, 2H, C<sub>2</sub>-H, C<sub>6</sub>-H pyridine); <sup>13</sup>C NMR (100 MHz, DMSO-*d*<sub>6</sub>): δ 102.14, 116.40, 121.23, 121.98, 122.73, 124.85, 125.94, 126.48, 138.38, 141.29, 145.34, 150.77, 155.26, 161.14, 161.99, 171.57; EI-MS: *m/z* 360 (M<sup>+</sup>, 83%). Anal. Calcd. for C<sub>18</sub>H<sub>12</sub>N<sub>6</sub>OS (360.40): C, 59.99; H, 3.36; N, 23.32; S, 8.90. Found: C, 59.95; H, 3.41; N, 23.34; S, 8.87.

### Synthesis of 5-Oxo-2-aryl-7-(pyridin-4-yl)-1,2,3,5-tetrahydro-[1,2,4]triazolo[1,5-*a*]pyridine-6,8-dicarbonitriles 11a–c

*General procedure:* A solution of compound **9a** (2.52 g, 0.01 mol), aromatic aldehydes **10a–c** (0.01 mol) in 1,4 dioxane and/or DMF (25 mL) containing a catalytic amount of piperidine (3 drops) was heated under reflux for 12–15 h. The reaction was monitored by TLC. The product that was precipitated on cooling to room temperature was filtered off and recrystallized from absolute EtOH to give the compounds **11a–c**.

### 5-Oxo-2-phenyl-7-(pyridin-4-yl)-1,2,3,5-tetrahydro-[1,2,4]triazolo[1,5-*a*]pyridine-6,8-dicarbonitrile (11a)

Brown crystals; yield: 65%; m.p. > 300 °C; IR (KBr):  $\nu_{\max}$  3245, 3283 (2×NH), 2216, 2195 (2×CN), 1679 (C=O) cm<sup>-1</sup>; <sup>1</sup>H NMR (400 MHz, DMSO-*d*<sub>6</sub>): δ 4.81 (s, 1H, NH), 5.11 (s, 1H, CH), 7.21–7.59 (m, 8H, Ar-H, NH and C<sub>3</sub>-H, C<sub>5</sub>-H pyridine), 8.66 (d, *J* = 7.2 Hz, 2H, C<sub>2</sub>-H, C<sub>6</sub>-H pyridine); <sup>13</sup>C NMR (100 MHz, DMSO-*d*<sub>6</sub>): δ 87.47, 98.79, 116.78, 117.14, 122.16, 123.48, 126.77, 127.14, 130.47, 143.59, 146.41, 150.72, 160.62, 162.34, 170.83; EI-MS: *m/z* 340 (M<sup>+</sup>, 19%). Anal. Calcd. for C<sub>19</sub>H<sub>12</sub>N<sub>6</sub>O (340.35): C, 67.05; H, 3.55; N, 24.69. Found: C, 67.11; H, 3.58; N, 24.60.

### 2-(4-Methoxyphenyl)-5-oxo-7-(pyridin-4-yl)-1,2,3,5-tetrahydro-[1,2,4]triazolo[1,5-*a*]pyridine-6,8-dicarbonitrile (11b)

Brown crystals; yield: 63%; m.p. > 300 °C; IR (KBr):  $\nu_{\max}$  3243, 3291 (2 × NH), 2215, 2195 (2×CN), 1678 (C=O) cm<sup>-1</sup>; <sup>1</sup>H NMR (400 MHz, DMSO-*d*<sub>6</sub>): δ 4.05 (s, 3H,

OCH<sub>3</sub>), 4.77 (s, 1H, NH), 5.08 (s, 1H, CH), 6.95 (d, *J* = 8.4 Hz, 2H, Ar-H), 7.29 (s, 1H, NH), 7.40–7.60 (m, 5H, Ar-H, NH and C<sub>3</sub>-H, C<sub>5</sub>-H pyridine), 8.66 (d, *J* = 7.2 Hz, 2H, C<sub>2</sub>-H, C<sub>6</sub>-H pyridine); <sup>13</sup>C NMR (100 MHz, DMSO-*d*<sub>6</sub>): δ 59.74, 87.51, 98.78, 115.78, 116.78, 117.09, 122.24, 123.50, 129.03, 138.14, 144.10, 150.84, 159.25, 160.81, 162.27, 171.09; EI-MS: *m/z* 370 (M<sup>+</sup>, 30%). Anal. Calcd. for C<sub>20</sub>H<sub>14</sub>N<sub>6</sub>O<sub>2</sub> (370.37): C, 64.86; H, 3.81; N, 22.69. Found: C, 64.91; H, 3.75; N, 22.72.

### 2-(4-Chlorophenyl)-5-oxo-7-(pyridin-4-yl)-1,2,3,5-tetrahydro-[1,2,4]triazolo[1,5-*a*]pyridine-6,8-dicarbonitrile (11c)

Brown crystals; yield: 69%; m.p. > 300 °C; IR (KBr):  $\nu_{\max}$  3239, 3297 (2×NH), 2217, 2199 (2×CN), 1665 (C=O) cm<sup>-1</sup>; <sup>1</sup>H NMR (400 MHz, DMSO-*d*<sub>6</sub>): δ 4.85 (s, 1H, NH), 5.15 (s, 1H, CH), 7.25 (s, 1H, NH), 7.31 (d, *J* = 8.2 Hz, 2H, Ar-H), 7.41 (d, *J* = 8.0 Hz, 2H, Ar-H), 7.58 (d, *J* = 7.1 Hz, 2H, C<sub>3</sub>-H, C<sub>5</sub>-H pyridine), 8.66 (d, *J* = 7.2 Hz, 2H, C<sub>2</sub>-H, C<sub>6</sub>-H pyridine); <sup>13</sup>C NMR (100 MHz, DMSO-*d*<sub>6</sub>): δ 87.63, 100.06, 116.24, 116.88, 122.64, 122.89, 128.64, 129.33, 134.16, 143.08, 144.73, 150.24, 151.24, 162.45, 171.22; EI-MS: *m/z* 376 (M<sup>+</sup> + 2, 0.88), 374 (M<sup>+</sup>, 3%). Anal. Calcd. for C<sub>19</sub>H<sub>11</sub>ClN<sub>6</sub>O (374.79): C, 60.89; H, 2.96; Cl, 9.46; N, 22.42. Found: C, 60.93; H, 2.89; Cl, 9.51; N, 22.43.

### Synthesis of 5-Oxo-7-(pyridin-4-yl)-3,5-dihydro-[1,2,4]triazolo[1,5-*a*]pyridine-6,8-dicarbonitrile (12)

A mixture of **9a** (2.25 g, 0.01 mol) and DMF-DMA (1.19 g, 0.01 mol) was heated under reflux in 50 mL of dry xylene for 8 h. The solid product that precipitated on cooling was filtered off, dried and recrystallized from absolute ethanol to afford compound **12**.

Brown crystals; yield: 70%; m.p. > 300 °C; IR (KBr):  $\nu_{\max}$  3345 (NH), 2217, 2227 (2×CN), 1684 (C=O) cm<sup>-1</sup>; <sup>1</sup>H NMR (400 MHz, DMSO-*d*<sub>6</sub>): δ 5.21 (s, 1H, NH), 8.01 (d, *J* = 7.2 Hz, 2H, C<sub>3</sub>-H, C<sub>5</sub>-H pyridine), 8.79 (s, 1H, CH), 8.98 (d, *J* = 7.2 Hz, 2H, C<sub>2</sub>-H, C<sub>6</sub>-H pyridine); <sup>13</sup>C NMR (100 MHz, DMSO-*d*<sub>6</sub>): δ 115.27, 115.98, 117.54, 122.49, 123.08, 144.37, 149.88, 151.46, 155.21, 161.44, 171.83; EI-MS: *m/z* 262 (M<sup>+</sup>, 10 %). Anal. Calcd. for (C<sub>13</sub>H<sub>6</sub>N<sub>6</sub>O) (262.23): C, 59.54; H, 2.31; N, 32.05. Found: C, 59.56; H, 2.27; N, 32.10.

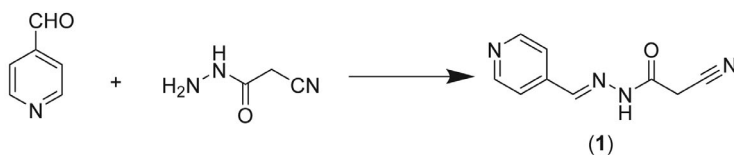
## 2. 3. Determination of the Anticancer Activity

It was carried out according to the previously reported work.<sup>17</sup>

## 3. Results and Discussion

### 3. 1. Chemistry

(*E*)-2-Cyano-*N'*-(pyridin-4-ylmethylene)acetohydrazide (**1**) was synthesized by the reaction of isonicotininaldehyde with 2-cyanoacetohydrazide under various



**Scheme 1.** Synthesis of (*E*)-2-cyano-*N'*-(pyridin-4-ylmethylene)acetohydrazide (**1**)

**Table 1.** Comparison of different conditions for the synthesis of (*E*)-2-cyano-*N'*-(pyridin-4-ylmethylene)acetohydrazide (**1**)

Entry	Catalyst	Condition	Time (h)	Yield (%)
1	No	Solvent free (100 °C)	6	0
2	No	EtOH	24	0
3	No	EtOH (reflux)	9	28
4	TEA	EtOH (rt)	24	0
5	TEA	EtOH (reflux)	6	39
6	TEA	THF (reflux)	4	92
7	No	Solvent free (MW)	20 sec	98

conditions (Scheme 1), and the results are presented in Table 1.

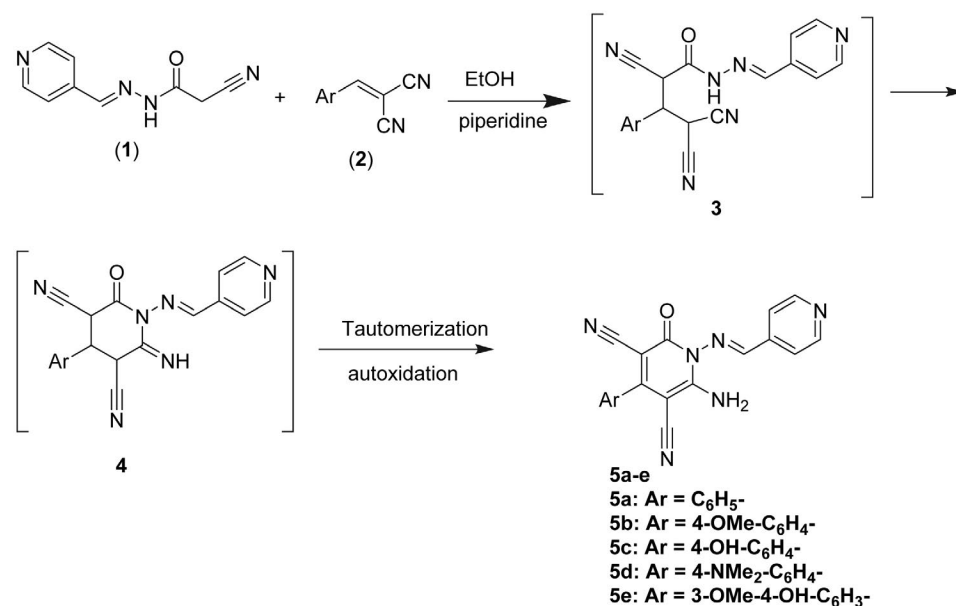
In the absence of any catalyst and under solvent-free conditions or in the presence of triethylamine as the basic catalyst at room temperature the reaction did not proceed even after long reaction time (Table 1, entries 1, 2 and 4). However, in the presence of Et<sub>3</sub>N under reflux with the EtOH or THF as the solvents, the desired product was obtained in 39 or 92% yield, respectively (Table 1, entries 5 and 6). Moreover, when the synthesis of **1** was carried out under microwave irradiation under solvent-free conditions, afforded the desired reaction product in high yield (Table 1, entry 7). The solvent-free conditions are preferable as they avoid the use of toxic, flammable, and expen-

sive organic solvents. The main advantages of microwave irradiation synthesis are thus shorter reaction time, higher yield and better purity of the product.

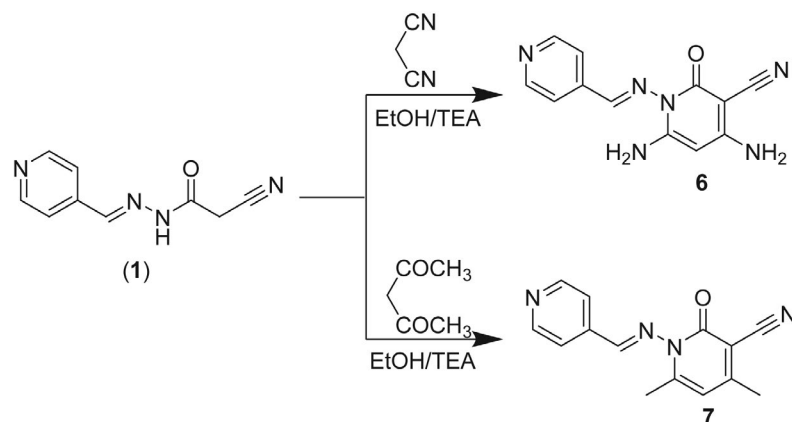
The chemical structure of **1** was confirmed by its spectral and elemental analysis data. The IR spectrum of **1** showed the presence of three stretching frequencies at 3235, 2259 and 1704 cm<sup>-1</sup> attributable to NH, CN and C=O groups, respectively. The <sup>1</sup>H NMR exhibited two singlet signals at δ 4.26 and 8.25 ppm due to CH<sub>2</sub> and CH=N, respectively. In addition, two doublet signals at δ 8.02 and 8.74 ppm due to pyridine protons are observed. The configuration around the double bond of the compound **1** could not be established by <sup>1</sup>H NMR spectroscopy. However, the steric effect enhances that the *E* isomer is more stable than *Z* isomer.

Compound **1** acts as an adaptable material for the synthesis of novel pyridine compounds. Thus, refluxing of **1** and arylidene malononitriles **2a–e** in ethanol catalyzed by piperidine afforded (*E*)-2-amino-4-aryl-5-cyano-6-oxo-1-((pyridin-4-ylmethylene)amino)-1,6-dihydropyridine-3-carbonitriles **5a–e** (Scheme 2).

Formation of compounds **5a–e** could be elucidated by the mechanism presented in Scheme 2. At first, Michael addition of **1** to α,β-unsaturated nitriles **2a–e** gives the intermediates **3**. Then, the intermediates **3** undergo an intermolecular nucleophilic addition of NH group to the cyano function to afford the intermediates **4** and finally an



**Scheme 2.** Synthesis of (*E*)-2-amino-4-aryl-5-cyano-6-oxo-1-((pyridin-4-ylmethylene)amino)-1,6-dihydropyridine-3-carbonitriles **5a–e**



**Scheme 3.** Synthesis of (*E*)-2-oxo-1-((pyridin-4-ylmethylene)amino)-1,2-dihydropyridine-3-carbonitrile derivatives **6** and **7**

autoxidation and tautomerization occur to give isolable products **5a–e**.<sup>18</sup> <sup>1</sup>H NMR spectra of compounds **5a–e** display characteristic signals: singlet signal at  $\delta$  8.40–8.44 ppm and two doublet signals at  $\delta$  7.99–8.04 and 8.72–8.75 ppm due to the CH=N and pyridine protons, respectively. Also, <sup>13</sup>C NMR revealed two signals in the region of  $\delta$  115–118 ppm due to the two cyano groups in addition to the signal in the region of  $\delta$  161–163 ppm attributable to the C=O group. IR spectra of compounds **5a–e** exhibited NH<sub>2</sub> group stretching frequencies in the region of 3308–3397 cm<sup>-1</sup> and the stretching frequency at 2200–2250 cm<sup>-1</sup> that indicated the presence of two nitrile functional groups.

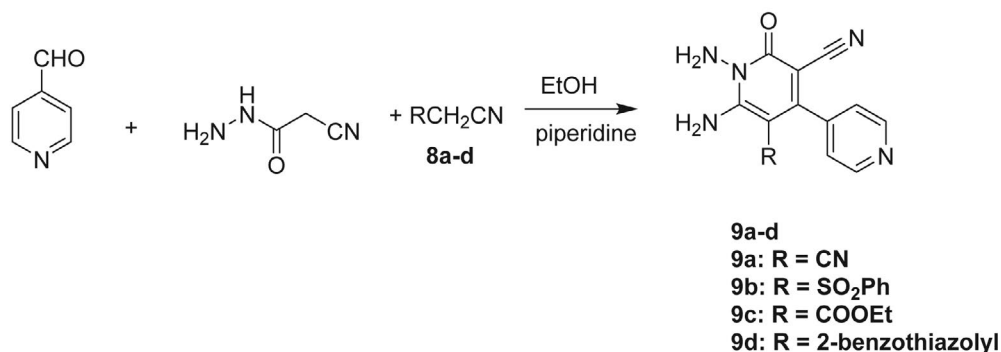
Treatment of **1** with malononitrile or acetylacetone in refluxing ethanol in the presence of trimethylamine as the base catalyst furnished (*E*)-4,6-diamino-2-oxo-1-((pyridin-4-ylmethylene)amino)-1,2-dihydropyridine-3-carbonitrile (**6**) and (*E*)-4,6-dimethyl-2-oxo-1-((pyridin-4-ylmethylene)amino)-1,2-dihydropyridine-3-carbonitrile (**7**), respectively (Scheme 3).

The spectral and analytical data of compounds **6** and **7** were in agreement with their proposed structures. <sup>1</sup>H NMR spectrum of **6** showed two singlet signals at  $\delta$  4.62 and 8.43 ppm owing to the C<sub>5</sub>-H of 2-pyridone ring and CH=N, respectively. Moreover, <sup>1</sup>H NMR of **6** exhibited two singlet signals (D<sub>2</sub>O-exchangable) at  $\delta$  4.65 and 6.68

ppm due to the two NH<sub>2</sub> groups. The IR analysis substantiated the results of <sup>1</sup>H NMR by the presence of four peaks in the region of 3321–4000 cm<sup>-1</sup> for two NH<sub>2</sub> groups.

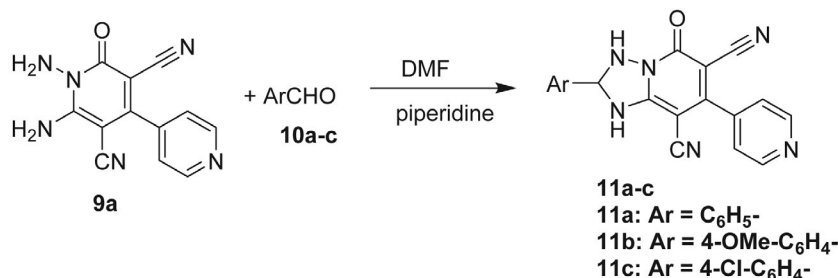
Nowadays, multicomponent reactions are gaining extensive economic and ecological importance as they conform to the fundamental principles of synthetic efficiency and reaction design.<sup>19</sup> We herein provide an efficient and facile procedure for the synthesis of 4,4'-bipyridine derivatives **9a–d** via a one-pot three-components condensation of isonicotinaldehyde, 2-cyanoacetohydrazide and activated nitriles **8a–d**<sup>20,21</sup> (Scheme 4).

The structures of products **9a–d** were assigned according to their IR, <sup>1</sup>H NMR, <sup>13</sup>C NMR and mass spectra. Thus, all compounds **9a–d** gave molecular ion peak which coincides with the proposed structure. <sup>1</sup>H NMR gave an additional evidence for the correct structure of compounds **9a–d**, for example, compound **9c** gave triplet quartet pattern at  $\delta$  1.01 and 4.03 ppm, respectively, which confirm the presence of ethyl ester group in addition to the singlet signal (D<sub>2</sub>O-exchangable) at  $\delta$  7.08 ppm corresponding to the amino group. Compound **9a** was used as a versatile material for the synthesis of 2-aryl-5-oxo-7-(pyridin-4-yl)-1,2,3,5-tetrahydro-[1,2,4]triazolo[1,5-*a*]pyridine-6,8-dicarbonitrile derivatives **11a–c**. Consequently, the reaction of **9a** with aromatic aldehydes **10a–c** afforded compounds **11a–c** (Scheme 5).

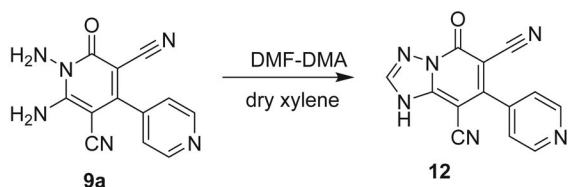


**Scheme 4.** Synthesis of 5-alkyl-1,6-diamino-2-oxo-1,2-dihydro-[4,4'-bipyridine]-3-carbonitriles **9a–d**





**Scheme 5.** Synthesis of 2-aryl-5-oxo-7-(pyridin-4-yl)-1,2,3,5-tetrahydro-[1,2,4]triazolo[1,5-*a*]pyridine-6,8-dicarbonitriles **11a-c**



**Scheme 6.** Synthesis of 5-oxo-7-(pyridin-4-yl)-1,5-dihydro-[1,2,4]triazolo[1,5-*a*]pyridine-6,8-dicarbonitrile (**12**)

Structures **11a-c** were established on the basis of elemental analyses and spectral data. The <sup>1</sup>H NMR spectra of compounds **11a-c**, in general, gave singlet signal at 5.08–5.15 ppm attributable to C<sub>3</sub>-H of [1,2,4]triazole ring in addition to the two singlet signals (D<sub>2</sub>O-exchangable) at δ 4.77–4.85 and 7.25–7.29 ppm due to the two NH groups.

Also, 5-oxo-7-(pyridin-4-yl)-1,5-dihydro-[1,2,4]triazolo[1,5-*a*]pyridine-6,8-dicarbonitrile (**12**) was synthesized *via* cyclocondensation reaction of **9a** with DMF-DMA (Scheme 6).

## 3. 2. Pharmacology

### 3. 2. 1. Cytotoxicity Against Hepatoma Cell Line (HepG-2) and Human Breast Adenocarcinoma Cell Line (MCF-7)

**Cytotoxic activity.** In order to investigate if the chemistry established here has led to possibly interesting nominees in cancer therapy, our primary aim was directed towards checking if the novel synthesized compounds possess any anticancer activities as predicted by this study. *In vitro* cytotoxic study was therefore performed against two mammalian cancer cell lines, HepG-2 (hepatoma cells or human liver hepatocellular carcinoma cell line) and MCF-7 (human breast adenocarcinoma cell line). This study indicated that compounds **9a** and **9b** showed very strong cytotoxic activity against HepG-2 cancer cells with IC<sub>50</sub> values of 8.83±0.30 and 10.08±0.66 µg/mL, respectively. Also, both **9a** and **9b** gave high cytotoxic effects against MCF-7 classifying these compounds as chemotherapeutically significant (Table 2). The rest of other compounds showed a moderate to weak activity against the tested tumor cell lines. IC<sub>50</sub> is the concentration, which can reduce the growth of cancer cells by 50%.

**Table 2.** Cytotoxic activity of the newly synthesized compounds

Compounds	<i>In vitro</i> Cytotoxicity IC <sub>50</sub> (µg/mL)	
	HepG-2	MCF-7
5-FU	7.53 ± 0.22	4.05 ± 0.15
<b>1</b>	45.83 ± 0.28	37.66 ± 0.35
<b>5a</b>	78.53 ± 1.25	84.20 ± 2.23
<b>5b</b>	31.11 ± 0.38	22.27 ± 0.33
<b>5c</b>	18.81 ± 0.14	16.08 ± 0.28
<b>5d</b>	20.23 ± 0.21	31.55 ± 0.34
<b>5e</b>	16.97 ± 0.27	14.99 ± 0.31
<b>6</b>	> 100	>100
<b>7</b>	52.65 ± 0.68	64.37 ± 1.20
<b>9a</b>	8.83 ± 0.30	10.37 ± 0.24
<b>9b</b>	10.08 ± 0.66	8.98 ± 0.61
<b>9c</b>	89.34 ± 1.33	64.38 ± 1.08
<b>9d</b>	71.08 ± 0.98	62.35 ± 0.55
<b>11a</b>	69.35 ± 1.30	58.98 ± 0.84
<b>11b</b>	43.55 ± 0.68	39.63 ± 0.50
<b>11c</b>	>100	>100
<b>12</b>	94.64 ± 1.33	80.37 ± 1.58

IC<sub>50</sub> (µg/mL): 1–10 very strong, 11–20 strong, 21–50 moderate, 51–100 weak and above 100 non-cytotoxic. 5-FU is 5-fluorouracil.

## 4. Conclusion

In conclusion, herein we report a simple and convenient method for the synthesis of novel pyridine derivatives. All synthesized compounds were evaluated against two cancer cell lines (HepG-2 and MCF-7). Among all the synthesized compounds, compounds **9a,b** have high cytotoxic activity against both HepG-2 and MCF-7. The rest of compounds showed a moderate to weak activity against the tested tumor cell lines.

## 5. References

- (a) G. Jones, *Comprehensive Heterocyclic Chemistry II*, Vol. 5 (Eds.: A. R. Katritzky, C. W. Rees, E. F. V. Scriven, A. McKillop), Pergamon, Oxford, 1996, pp. 167–243; DOI:10.1016/B978-008096518-5.00108-8  
 (b) G. D. Henry, *Tetrahedron* **2004**, 60, 6043–6061.; DOI:10.1016/j.tet.2004.04.043

- (c) J. A. Joule, K. Mills, *Heterocyclic Chemistry*, 4<sup>th</sup> ed., Blackwell Science, Cambridge, **2000**; p. 63–120;
- (d) J. P. Michael, *Nat. Prod. Rep.* **2005**, *22*, 627–646.  
DOI:10.1039/b413750g
2. M. T. Cocco, C. Congiu, V. Lilliu, V. Onnis, *Eur. J. Med. Chem.* **2005**, *40*, 1365–1372. DOI:10.1016/j.ejmech.2005.07.005
  3. D. L. Boger, S. Nakahara, *J. Org. Chem.* **1991**, *56*, 880–884.  
DOI:10.1021/jo00002a077
  4. D. L. Boger, A. M. Kasper, *J. Am. Chem. Soc.* **1989**, *111*, 1517–1519. DOI:10.1021/ja00186a067
  5. T. S. Harrison, L. J. Scott, *Drugs* **2005**, *65*, 2309–2336.  
DOI:10.2165/00003495-200565160-00010
  6. M. W. Deininger, B. J. Druker, *Pharmacol. Rev.* **2003**, *55*, 401–423. DOI:10.1124/pr.55.3.4
  7. E. V. Costa, M. L. B. Pinheiro, C. M. Xavier, J. R. Silva, A. C. F. Amaral, A. D. Souza, A. Barison, F. R. Campos, A. G. Ferreira, G. M. A. Machado, *J. Nat. Prod.* **2006**, *69*, 292–294.  
DOI:10.1021/np050422s
  8. R. H. Bahekar, M. R. Jain, P. A. Jadav, V. M. Prajapati, D. N. Patel, A. A. Gupta, A. Sharma, R. Tom, D. Bandyopadhyaya, H. Modi, *Bioorg. Med. Chem.* **2007**, *15*, 6782–6795.  
DOI:10.1016/j.bmc.2007.08.005
  9. F. Shi, C. Li, M. Xia, K. Miao, Y. Zhao, S. Tu, W. Zheng, G. Zhang, N. Ma, *Bioorg. Med. Chem. Lett.* **2009**, *19*, 5565–5568.  
DOI:10.1016/j.bmcl.2009.08.046
  10. K. Nicolaou, R. Scarpelli, B. Bollbuck, B. Werschkun, M. Pereira, M. Wartmann, K. Altmann, D. Zaharevitz, R. Gussio, P. Giannakakou, *Chem. Biol.* **2000**, *7*, 593–599.  
DOI:10.1016/S1074-5521(00)00006-5
  11. J.-P. Liou, K.-S. Hsu, C.-C. Kuo, C.-Y. Chang, J.-Y. Chang, *J. Pharmacol. Exp. Ther.* **2007**, 398–405.  
DOI:10.1124/jpet.107.126680
  12. R. M. Mohareb, N. Y. M. Abdo, F. O. Al-Farouk, *Acta Chim. Slov.* **2017**, *64*, 117–128. DOI:10.17344/acsi.2016.2920
  13. J. M. Chezal, J. Paeshuysse, V. Gaumet, D. Canitrot, A. Maissonial, C. Lartigue, A. Gueiffier, E. Moreau, J. C. Teulade, O. Chavignon, *Eur. J. Med. Chem.* **2010**, *45*, 2044–2047.  
DOI:10.1016/j.ejmech.2010.01.023
  14. W. Xie, Y. Wu, J. Zhang, Q. Mei, Y. Zhang, N. Zhu, R. Liu, H. Zhang, *Eur. J. Med. Chem.* **2018**, *145*, 35–40.  
DOI:10.1016/j.ejmech.2017.12.038
  15. N. K. Binsaleh, C. A. Wigley, K. A. Whitehead, M. van Rensburg, J. Reynisson, L. I. Pilkington, D. Barker, S. Jones, N. C. Dempsey-Hibbert, *Eur. J. Med. Chem.* **2018**, *143*, 1997–2004.  
DOI:10.1016/j.ejmech.2017.11.014
  16. Q. Tang, Y. Duan, L. Wang, M. Wang, Y. Ouyang, C. Wang, H. Mei, S. Tang, Y. Xiong, P. Zheng, P. Gong, *Eur. J. Med. Chem.* **2018**, *143*, 266–275. DOI:10.1016/j.ejmech.2017.11.034
  17. A. A. Fadda, E. Abdel-Latif, R. E. El-Mekawy, *Pharmacol. Pharm.* **2012**, *3*, 148–157. DOI:10.4236/pp.2012.32022
  18. M. R. H. Elmoghayar, A. G. A. El-Agamey, M. Y. A. S. Nasr, M. M. Sallam, *J. Het. Chem.* **1984**, *21*, 1885–1887.
  19. C. C. Cariou, G. J. Clarkson, M. Shipman, *J. Org. Chem.* **2008**, *73*, 9762–9764. DOI:10.1021/jo801664g
  20. A. H. M. Hussein, *Heteroat. Chem.* **1997**, *8*, 1–6.  
DOI:10.1002/(SICI)1098-1071(1997)8:1<1::AID-HC1>3.0.CO;2-J
  21. F. F. A. Latif, R. Mekheimer, E. K. Ahmed, T. B. A. Aleem, *Pharmazie* **1993**, *48*, 736–738.

## Povzetek

Reakcija izonikotinaldehida z 2-cianoacetohidrazidom daje (*E*)-2-ciano-*N*'-(piridin-4-ilmtilen)acetohidrazid (**1**). Spojino **1** smo uporabili kot prekurzor pri sintezi novih piridinskih derivatov, ki smo jih pripravili z reakcijo med različnimi arilidenskimi malononitrili, malononitrilom oz. acetilacetonom, pri čemer so nastali piridinski derivati **5a–e**, **6** in 7. 4,4'-Bipiridinske derivate **9a–d** smo pripravili s trokomponentno reakcijo med izonikotinaldehidom, 2-cianoacetohidrazidom in aktiviranimi nitrili **8a–d**. Obdelava spojine **9a** z različnimi aromatskimi aldehidi je vodila do nastanka [1,2,4]triazolo[1,5-*a*]piridinskih derivatov **11a–c**. Vse reakcijske produkte smo okarakterizirali z analitskimi in spektroskopskimi metodami. Za nove spojine smo raziskali tudi bioaktivnost v vlogi antitumornih učinkovin in *in vitro* testiranju citotoksičnosti proti HepG-2 in MCF-7. Ugotovili smo, da spojini **9a** in **9b** izkazujeta visoko citotoksičnost proti obema, HepG-2 in MCF-7.

Scientific paper

# Mass Spectrometry Study of New Polyamine Derivatives of Caffeine

Arleta Sierakowska\*, Beata Jasiewicz and Tomasz Pospieszny

Faculty of Chemistry, Adam Mickiewicz University in Poznań, Umultowska 89b, 61-614 Poznań, Poland.

\* Corresponding author: E-mail: asierak@amu.edu.pl;

Tel. +48 61 829-1758

Received: 14-03-2018

## Abstract

The mass spectrometric fragmentations of ten new 8-alkylaminocaffeine derivatives were investigated. The fragmentation pathways of new polyamine derivatives of caffeine on the basis of low and high-resolution electron ionization (EI) mass spectra were discussed. In the case of new compounds, classical fragmentation of purine skeleton related to the elimination of a neutral molecule  $\text{CH}_3\text{N}(1)\text{C}(2)\text{O}$  from a molecular ion was not observed. Nevertheless, new interesting fragmentation of described caffeine derivatives was observed. Moreover, heats of formation of odd-electron ions of 8-alkylaminocaffeine derivatives were calculated.

**Keywords:** Caffeine; polyamine; EI-MS; semiempirical calculation.

## 1. Introduction

Alkaloids constitute a large group of naturally occurring chemical compounds with a wide range of pharmacological properties.<sup>1</sup> They are produced by various organisms including bacteria, fungi, plants and animals. Caffeine (1,3,7-trimethylxanthine), the main representative of purine alkaloids, is a bicyclic amine. The most well-known source of this chemical compound are the seeds of coffee (especially Arabica – *Coffea arabica*, and Robusta – *Coffea canephora*) or leaves of tea.<sup>2</sup> This alkaloid is a central nervous system (CNS) stimulant and one of the most addicting psychoactive drugs. This is the result of inhibition of adenosine A2A receptor by caffeine and its derivatives.<sup>3</sup> Caffeine has also the anti-inflammatory capacity and enhances the glucose uptake as well as anticancer capacity and officially modulates drugs against lung, liver, uterine cervix, and breast cancer.<sup>4–7</sup> It enhances the effect of anticancer drugs and the most important is modulation of *cis*-platinum efficacy induced by caffeine.<sup>8</sup> Caffeine is also the lead compound for the development of new drugs. For example, 8-substituted caffeine derivatives are very important chemical compounds that possess pharmacological activity. This kind of derivatives inhibits the monoamine oxidases (MAO) A and B. MAO-A inhibitors can be employed as antidepressant drugs and MAO-B inhibitors can be used in Parkinson's disease therapy.<sup>9,10</sup> 8-aryl- or heteroaryl-substituted xantines are highly potent antago-

nists at human adenosine receptors.<sup>11</sup> 8-[(pyrrolidin-1-yl-carbonothioyl)-sulfanyl]caffeine has exceptionally high antioxidant properties and protects human erythrocytes against AAPH-induced oxidative damage.<sup>12</sup>

According to the literature, the caffeine molecule as well as its derivatives were studied by different analytical methods. Mass spectrometry with electron ionization and chemical ionization in combination with liquid or gas chromatography was found.<sup>13–15</sup> There are a few reports found in the literature describing advanced methods studying the caffeine molecule, e.g. photoion mass spectroscopy (PI-MS),<sup>16</sup> thermal and hyperthermal surface ionization (HSI) mass spectrometry.<sup>17</sup> In this work we propose the fragmentation pathways of new polyamine derivatives of caffeine on the basis of low and high-resolution EI-MS spectra. This is the new report of mass fragmentation of C(8) substituted derivatives of caffeine. The main goal of our study was to establish how far the presence of di- or polyamino group at C-8 position influences the pathways of fragmentation of this important class of compounds.

## 2. Experimental

Low-resolution and high-resolution mass spectra were recorded using a model 432 two-sector mass spectrometer [AMD-Intectra GmbH D-27243 Harpstedt, Ger-

many] at ionizing energy 70 eV, accelerating voltage 8 kV, mass resolution 10 000 at 10 % valley. Samples were introduced by a direct insertion probe at a source temperature of  $\sim 150$  °C. The elemental compositions of the ions were determined by peak matching method relative to perfluorokerosene. The tandem product ion mass spectra in the first field-free region were recorded using linked scans at constant B/E with helium as collision gas at an indicated pressure of  $1.75 \times 10^{-5}$  Pa with an ion source temperature of 180 °C, ionizing energy of 70 eV and an accelerating voltage of 8 KV.

### 3. Results and Discussion

All new di- or polyamine derivatives of caffeine were synthesized according to procedure described in<sup>18</sup> (Scheme 1) with good yields (60–90 %).

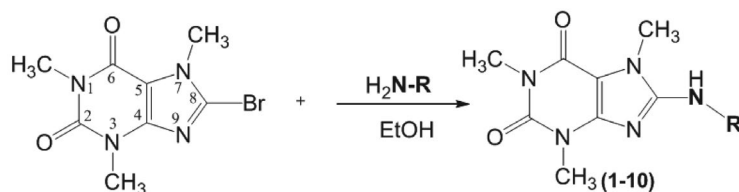
The representative samples of set of EI mass spectra of 8-(6-aminoethylamino)caffeine (5), 8-(4-(3-aminopropylamino)-butylamino)caffeine (8) and 8-(3-(3-(3-aminopropylamino)propylamino)propylamino)caffeine (9) are presented in S1. The EI-MS data of 8-(2-aminoethylamino)caffeine (1), 8-(3-aminopropylamino)caffeine (2), 8-(4-aminobutylamino)caffeine (3), 8-(5-aminopentylamino)caffeine (4) as well as 8-(6-aminoethylamino)caffeine (5) are displayed in Table 1. On the basis of low-resolution EI mass spectra, exact mass measurements and also B/E linked scan spectra, the principal fragmentation routes of 8-(2-aminoalkylamino)caffeines 1-5 are proposed in Scheme 1. The presence of alkylamino chain in position C(8) of caffeine rings caused the absence of classical fragmentation related with the elimination of a neutral molecule  $\text{CH}_3\text{N}(1)\text{C}(2)\text{O}$  from a molecular ion.

In the EI mass spectra of 1-5, molecular ions **a** were observed in all derivatives and for 2, 4 and 5 its relative abundance is 100 % (Scheme 1, Table 1). Furthermore, the even-electron fragment ions **b**<sub>1</sub>, **b**<sub>2</sub>, **b**<sub>3</sub>, **b**<sub>4</sub> and **b**<sub>5</sub> are formed from the molecular ion by the loss of  $\text{CH}_2\text{NH}_2$  radical. The ions **b**<sub>3</sub> and **b**<sub>2</sub> are not created for derivatives

3 and 4. Elimination of alkylaminoradical chain from C(8) of purine ring with migration of two hydrogen atoms leads to even-electron ion **e**. The simultaneous cleavages of  $\text{C}(5)\text{sp}^2\text{-N}(7)\text{sp}^3$  and  $\text{C}(4)\text{sp}^2\text{-N}(9)\text{sp}^2$  bonds of the skeletons of ion **e** of 1-5 lead to the formation of the even-electron ion **i**. Relative abundance for this ion for 8-(5-aminopentylamino)caffeine (4) is 100 %. From this fragment ion, by elimination of the neutral molecules  $\text{CH}_4$  and  $\text{C}_2\text{H}_2$ , ions **j** and **k** are formed, respectively. The decompositions of the 1-5 molecular ions with the cleavages of  $\text{C}(8)\text{sp}^2\text{-Nsp}^3$  bond, and the next elimination of

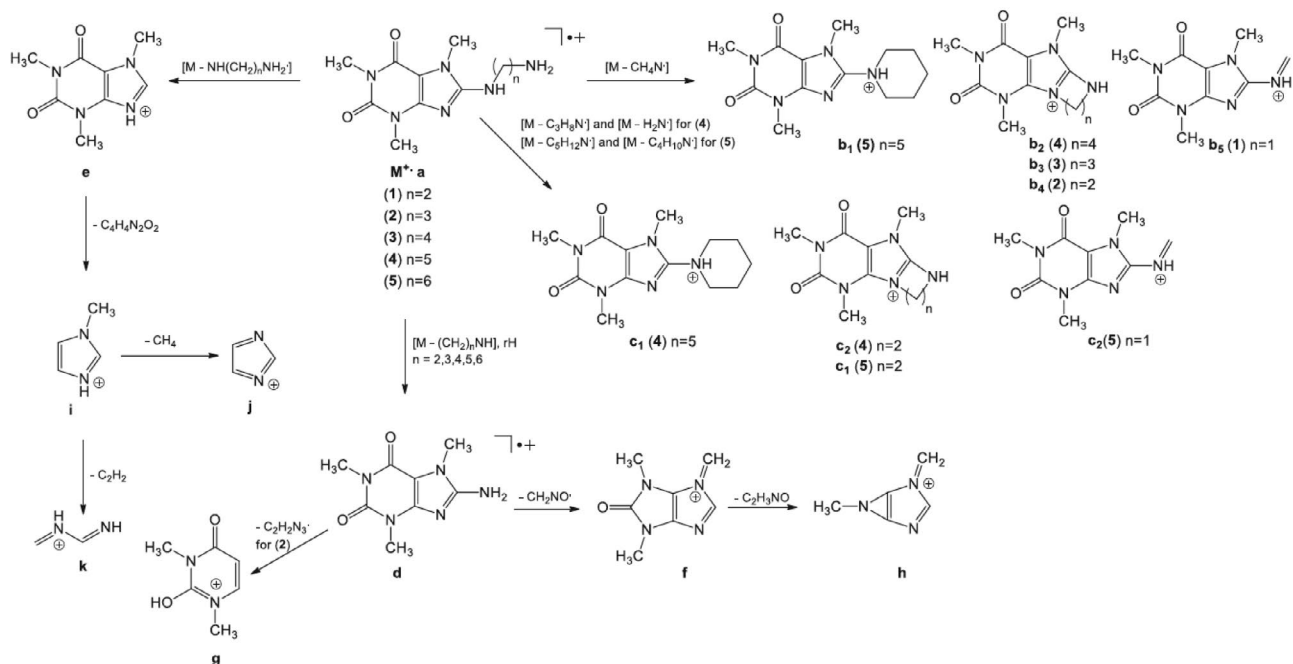
**Table 1.** The EI MS data of 8-(2-aminoethylamino)caffeine (1), 8-(3-aminopropylamino)caffeine (2), 8-(4-aminobutylamino)caffeine (3), 8-(5-aminopentylamino)caffeine (4) and 8-(6-aminoethylamino)caffeine (5).

Ion	<i>m/z</i>	Elemental composition	% Relative abundance				
			1	2	3	4	5
<b>M</b> <sup>+</sup> <b>a</b>	308	$\text{C}_{14}\text{H}_{24}\text{N}_6\text{O}_2$	–	–	–	–	100
	294	$\text{C}_{13}\text{H}_{22}\text{N}_6\text{O}_2$	–	–	–	6	–
	280	$\text{C}_{12}\text{H}_{20}\text{N}_6\text{O}_2$	–	–	100	–	–
	266	$\text{C}_{11}\text{H}_{18}\text{N}_6\text{O}_2$	–	100	–	–	–
	252	$\text{C}_{10}\text{H}_{16}\text{N}_6\text{O}_2$	50	–	–	–	–
<b>b</b> <sub>1</sub>	278	$\text{C}_{13}\text{H}_{20}\text{N}_5\text{O}_2$	–	–	–	–	11
<b>b</b> <sub>2</sub>	264	$\text{C}_{12}\text{H}_{18}\text{N}_5\text{O}_2$	–	–	–	0	–
<b>b</b> <sub>3</sub>	250	$\text{C}_{11}\text{H}_{16}\text{N}_5\text{O}_2$	–	–	0	–	–
<b>b</b> <sub>4</sub>	236	$\text{C}_{10}\text{H}_{14}\text{N}_5\text{O}_2$	–	12	–	–	–
<b>b</b> <sub>5</sub>	222	$\text{C}_9\text{H}_{12}\text{N}_5\text{O}_2$	100	–	–	–	–
<b>c</b> <sub>1</sub>	278	$\text{C}_{13}\text{H}_{20}\text{N}_5\text{O}_2$	–	–	–	2	–
<b>c</b> <sub>2</sub>	236	$\text{C}_{10}\text{H}_{14}\text{N}_5\text{O}_2$	–	–	–	2	–
<b>c</b> <sub>1</sub>	236	$\text{C}_{10}\text{H}_{14}\text{N}_5\text{O}_2$	0	0	0	–	19
<b>c</b> <sub>2</sub>	222	$\text{C}_9\text{H}_{12}\text{N}_5\text{O}_2$	0	0	0	–	60
<b>d</b>	209	$\text{C}_8\text{H}_{11}\text{N}_5\text{O}_2$	35	2	28	4	44
<b>e</b>	195	$\text{C}_8\text{H}_{11}\text{N}_4\text{O}_2$	17	2	26	2	3
<b>f</b>	165	$\text{C}_7\text{H}_9\text{N}_4\text{O}$	20	5	0	3	4
<b>g</b>	141	$\text{C}_6\text{H}_9\text{N}_2\text{O}_2$	–	19	–	–	–
<b>h</b>	108	$\text{C}_5\text{H}_6\text{N}_3$	7	1	17	21	6
<b>i</b>	83	$\text{C}_4\text{H}_7\text{N}_2$	12	2	23	100	9
<b>j</b>	67	$\text{C}_3\text{H}_3\text{N}_2$	40	4	87	63	24
<b>k</b>	57	$\text{C}_2\text{H}_5\text{N}_2$	16	19	65	17	44



- (1) R =  $-(\text{CH}_2)_2\text{NH}_2$   
 (2) R =  $-(\text{CH}_2)_3\text{NH}_2$   
 (3) R =  $-(\text{CH}_2)_4\text{NH}_2$   
 (4) R =  $-(\text{CH}_2)_5\text{NH}_2$   
 (5) R =  $-(\text{CH}_2)_6\text{NH}_2$   
 (6) R =  $-(\text{CH}_2)_2\text{NH}(\text{CH}_2)_2\text{NH}_2$   
 (7) R =  $-(\text{CH}_2)_3\text{NH}(\text{CH}_2)_3\text{NH}_2$   
 (8) R =  $-(\text{CH}_2)_4\text{NH}(\text{CH}_2)_3\text{NH}_2$   
 (9) R =  $-(\text{CH}_2)_3\text{NH}(\text{CH}_2)_3\text{NH}(\text{CH}_2)_3\text{NH}_2$   
 (10) R =  $-(\text{CH}_2)_3\text{NH}(\text{CH}_2)_4\text{NH}(\text{CH}_2)_3\text{NH}_2$

**Figure 1.** The synthesis of di- and polyamine derivatives of caffeine (1–10).

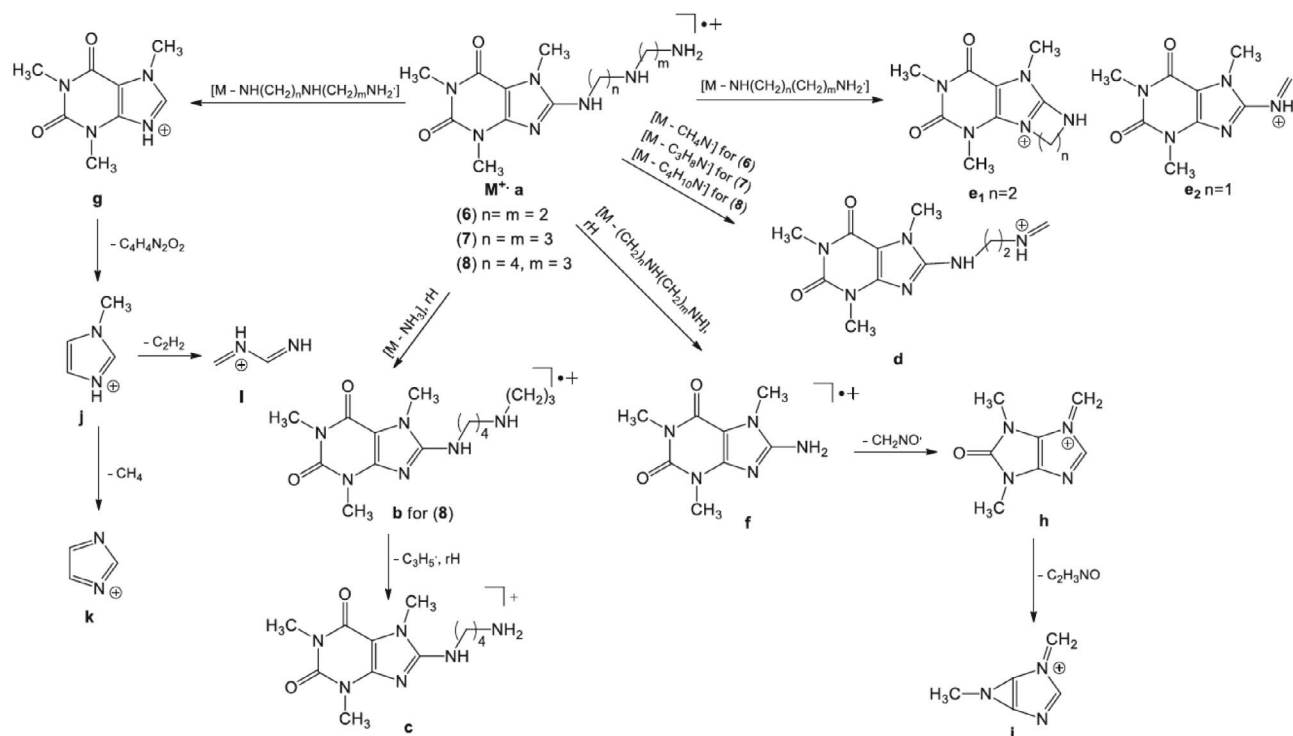


Scheme 1. The EI fragmentation pathways of compounds (1–5).

the  $\text{NH}_2(\text{CH}_2)_m$  radical, where  $m$  is 2, 3, 4, 5, and 6, lead to the formation of the odd-electron ion **d**. Elimination of radicals  $\text{C}_2\text{H}_2\text{N}_3\cdot$  or  $\text{CH}_2\text{NO}\cdot$  from ion **d** leads to even-electron ions **g** (only for **2**) and **f** (for **1-5**), respectively. Elimination of neutral molecule  $\text{C}_2\text{H}_3\text{NO}$  from even-electron ion **f** creates bicyclic even-electron ion **h**. This bicyclic

structure is one of mesomeric and more stable structures of even-electron ion **h**.

The fragmentation process of the molecular ions of **4** and **5** leads to the formation of ions **c**. The accurate mass measurement enables the assignment of peaks to three even-electron ions. They are formed directly from the re-



Scheme 2. The EI fragmentation pathways of compounds (6–8).

spective molecular ions by the loss of two possible radicals  $C_3H_8N^{\cdot}$  or  $H_2N^{\cdot}$  for 8-(5-aminopentylamino)caffeine (4) as well as  $C_5H_{12}N^{\cdot}$  and  $C_4H_{10}N^{\cdot}$  for 8-(6-aminoethylamino)caffeine (5), respectively.

The principal EI-MS fragmentation routes of 8-(3-(3-aminopropylamino)propylamino)propylamino)caf

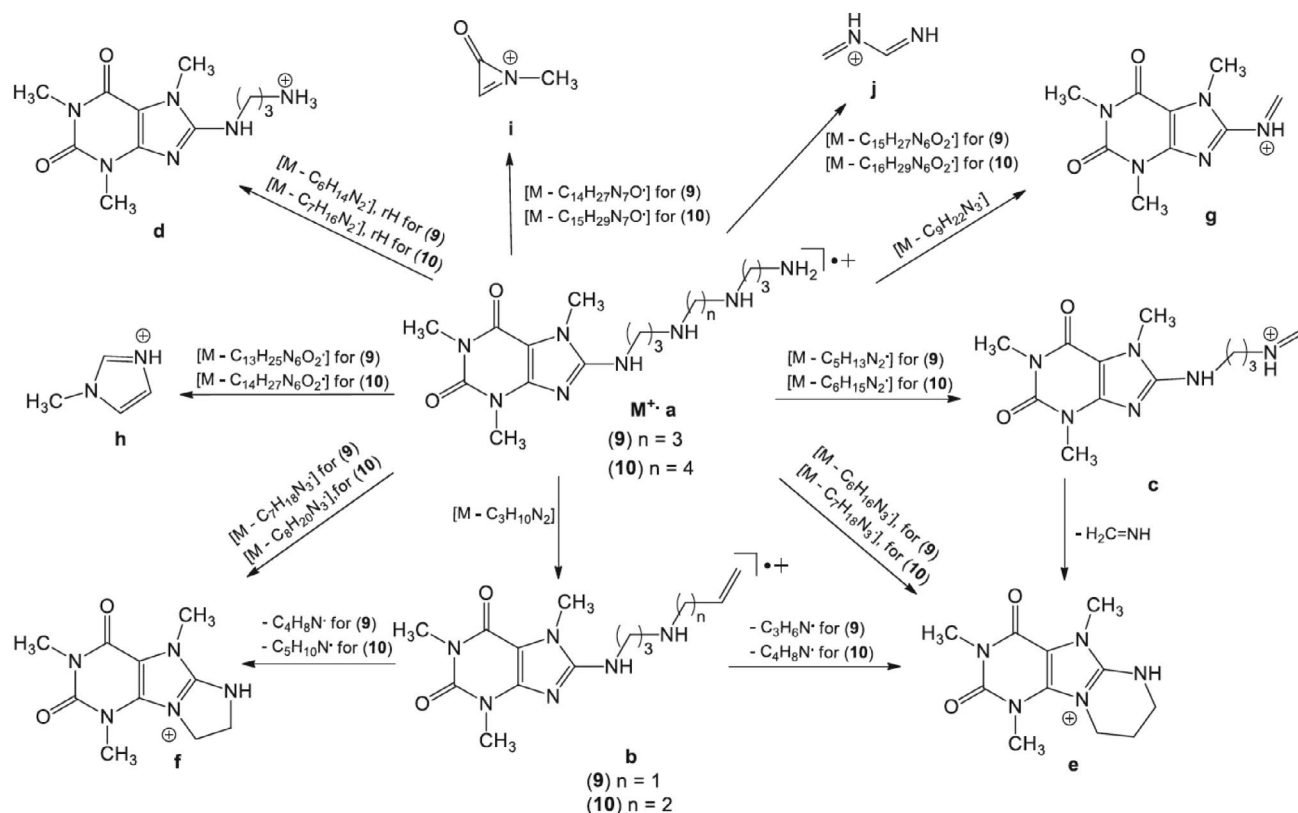
**Table 2.** The EI MS data of 8-(2-(2-aminoethylamino)ethylamino) caffeine (6), 8-(3-(3-aminopropylamino)propylamino)caffeine (7) and 8-(4-(3-aminopropylamino)-butylamino)-caffeine (8).

Ion	<i>m/z</i>	Elemental composition	% Relative abundance		
			6	7	8
$M^+$ a	337	$C_{15}H_{27}N_7O_2$	–	–	100
	323	$C_{14}H_{25}N_7O_2$	–	100	–
	295	$C_{12}H_{21}N_7O_2$	30	–	–
<b>b</b>	321	$C_{15}H_{25}N_6O_2$	–	–	10
<b>c</b>	280	$C_{12}H_{20}N_6O_2$	–	–	22
<b>d</b>	265	$C_{11}H_{17}N_6O_2$	100	2	3
<b>e</b> <sub>1</sub>	236	$C_{10}H_{14}N_5O_2$	12	63	56
<b>e</b> <sub>2</sub>	222	$C_9H_{12}N_5O_2$	43	29	60
<b>f</b>	209	$C_8H_{11}N_5O_2$	43	62	70
<b>g</b>	195	$C_8H_{11}N_4O_2$	10	16	16
<b>h</b>	165	$C_7H_9N_4O$	9	8	17
<b>i</b>	108	$C_5H_6N_3$	3	5	7
<b>j</b>	83	$C_4H_7N_2$	7	11	12
<b>k</b>	67	$C_3H_3N_2$	16	27	24
<b>l</b>	57	$C_2H_3N_2$	42	64	41

fine (9) and 8-(3-(4-(3-aminopropylamino)butylamino)propylamino)caffeine (10) are interpreted as shown in Scheme 3 and Table 3. The molecular ions **a** were observed with 81 % and 100 % relative abundances for **9** and **10**, respectively. The elimination of radicals from the molecular ions **a** leads to the formation of even-electron bicyclic ions: **c**, **g** and tricyclic ions: **e**, **f**. Ions **e** and **f** may be also formed from the odd-electron ion **b**, which is created from the molecular ion **a** by elimination of the 1,3-propanediamine,

**Table 3.** The EI MS data of 8-(3-(3-(3-aminopropylamino)propylamino)propylamino)caffeine (9) and 8-(3-(4-(3-aminopropylamino)butylamino)propylamino)caffeine (10).

Ion	<i>m/z</i>	Elemental composition	% Relative abundance	
			9	10
$M^+$ a	394	$C_{18}H_{34}N_8O_2$	–	81
	380	$C_{17}H_{32}N_8O_2$	100	–
<b>b</b>	321	$C_{15}H_{25}N_6O_2$	–	5
	307	$C_{14}H_{23}N_6O_2$	2	–
<b>c</b>	279	$C_{12}H_{19}N_6O_2$	15	9
	266	$C_{11}H_{18}N_6O_2$	63	3
<b>e</b>	250	$C_{11}H_{16}N_5O_2$	20	22
	236	$C_{10}H_{14}N_5O_2$	52	43
<b>g</b>	222	$C_9H_{12}N_5O_2$	35	23
	83	$C_4H_7N_2$	8	100
<b>i</b>	70	$C_3H_4NO$	40	50
	57	$C_2H_5N_2$	68	78



**Scheme 3.** The EI fragmentation pathways of compounds (9–10).

but can also be generated from the molecular ion by elimination of adequate radicals (Scheme 3). The ion **e** is also formed from the even-electron ion **c** by the elimination of methanimine.

The stability of new caffeine derivatives in gas phase was determined by theoretical method. Heats of formation of odd-electron ions of 8-alkylaminoderivatives were calculated. PM5 semiempirical calculations were performed using the Win-Mopac 2003 program.<sup>19–21</sup> The final heats of formation (HOF) for odd-electron ions of all compounds are presented in Table 4.

**Table 4.** Heats of formation of odd-electron ions of polyamine derivatives of caffeine (1–10) calculated by PM5 semiempirical method.

Ion	Heat of formation [kcal/mol]	$\Delta$ HOF [kcal/mol]
caffeine	–38.7572	–
<b>1</b>	–41.3927	–2.6355
<b>2</b>	–47.3927	–8.6355
<b>3</b>	–53.0808	–14.3236
<b>4</b>	–58.6238	–19.8666
<b>5</b>	–64.3931	–25.6359
<b>6</b>	–39.3269	–0.5697
<b>7</b>	–50.4467	–11.6895
<b>8</b>	–56.4314	–17.6742
<b>9</b>	–51.3852	–12.6280
<b>10</b>	–57.7629	–19.0057

$\Delta$ HOF = HOF (odd-electron ion of **1–10**) – HOF (odd-electron ion of caffeine)

As follows from the results, the odd-electron ions of caffeine derivatives in the gas phase (under the experimental conditions similar to those in EI measurements) are stable. The lowest values of HOF from series **1–5** are observed for odd-electron ion of 8-(6-aminohexylamino) caffeine (**5**). Simultaneously, an increase of the length of an alkyl chain also reduces HOF. A similar relationship can be

observed for odd-electron ions of compounds **6–8** as well as **9** and **10**.

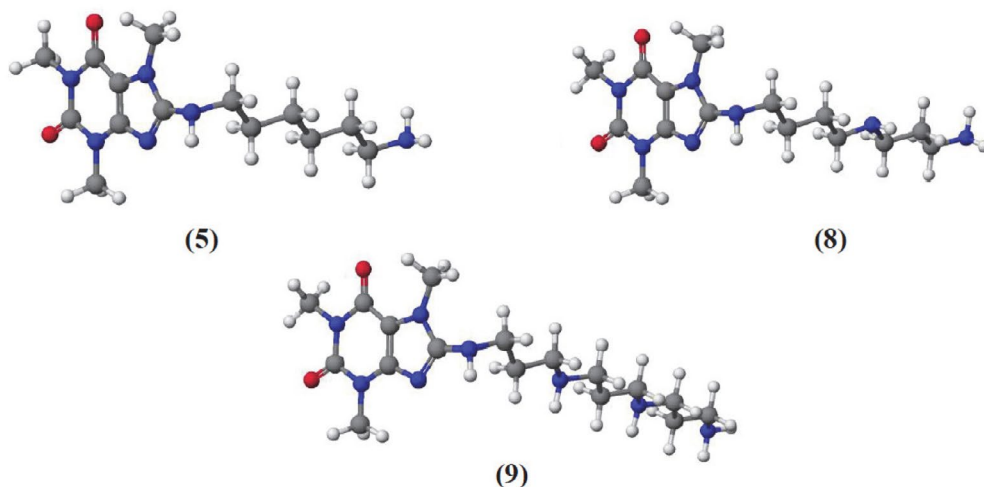
PM5 semiempirical method is a reliable method for visualization of the structures in the gas phase. Calculated structures of odd-electron ions of: 8-(6-aminohexylamino) caffeine (**5**), 8-(4-(3-aminopropylamino)butylamino) caffeine (**8**), and 8-(3-(3-(3-aminopropylamino)propylamino)propylamino) caffeine (**9**) are presented in Figure 2.

## 4. Conclusions

The present study has demonstrated that the best method of mass spectrometric analysis of new polyamine derivatives of caffeine is the analysis of their EI mass spectra. Considering the length of the alkyl chain at C(8) position of caffeine molecule, the EI fragmentation pathways of compounds **1–10** were divided into three groups. The substitution of caffeine ring with alkylamino chain in position C(8) causes that the new pathway becomes more competitive than the primary fragmentation of unsubstituted caffeine with the elimination of a neutral molecule  $\text{CH}_3\text{-N=C=O}$  from purine moiety. Such observation has not been noted previously in the literature in the cases of caffeine derivatives. According to PM5 semiempirical method, the odd-electron ions of caffeine derivatives in gas phase (under the experimental conditions similar to those in EI measurement) are stable. Moreover, an increase in alkyl chain length at C(8) position of caffeine molecule reduces the values of HOF.

## 5. References

1. E. Fattorusso and O. Tagliatela-Scafati (Ed.), “Modern Alkaloids: Structure, Isolation, Synthesis, and Biology”, Wiley-VCH, Weinheim, Germany, 2007, p. 3.  
DOI:10.1002/9783527621071



**Figure 2.** The optimized structures of odd-electron ion of compound **5,8** and **9**.

2. K. Ramalakshmi, L. Jagan Mohan Rao, Y. Takano-Ishikawa and M. Goto, *Food Chem.* **2009**, *115*, 79–85. DOI:10.1016/j.foodchem.2008.11.063
3. S. Rivara, G. Piersanti, F. Bartocchini, G. Diamantini, D. Pala, T. Riccioni, M. A. Stasi, W. Cabri, F. Borsini, M. Mor, G. Tarzia and P. Minetti, *J. Med. Chem.*, **2013**, *56*, 1247–1261 DOI:10.1021/jm301686s
4. S. K. Srivastava and V. B. Singh, *Spectrochim. Acta, Part A*, **2013**, *115*, 45–50. DOI:10.1016/j.saa.2013.06.005
5. Y.-F. Chu, Y. Chen, P. H. Brown, B. J. Lyle, R. M. Black, I. H. Cheng, B. Ou and R. L. Prior, *Food Chem.*, **2012**, *131*, 564–568. DOI:10.1016/j.foodchem.2011.09.024
6. J. Bravo, L. Arbillaga, M. Paz de Pena and C. Cid, *Food Chem. Toxicol.* **2013**, *60*, 397–403. DOI:10.1016/j.fct.2013.08.002
7. I. L. Martins, J. P. Miranda, N. G. Oliveira, A. S. Fernandes, S. Gonçalves and A. M. M. Antunes, *Molecules* **2013**, *18*, 5251–5264. DOI:10.3390/molecules18055251
8. S. Miwa, S. Yano, Y. Tome, N. Sugimoto, Y. Hiroshima, F. Uehara, S. Mii, H. Kimura, K. Hayashi, E. V. Efimova, T. Fujiwara, H. Tsuchiya and R. M. Hoffman, *J. Cell. Biochem.* **2013**, *114*, 2454–2460. DOI:10.1002/jcb.24593
9. H. P. Booyesen, C. Moraal, G. Terre'Blanche, A. Petzer, J. J. Bergh and J. P. Petzer, *Bioorg. Med. Chem.*, **2011**, *19*, 7507–7518. DOI:10.1016/j.bmc.2011.10.036
10. M. Bortolato, K. Chen and J. C. Shih, *Adv. Drug Delivery Rev.*, **2008**, *60*, 1527–1533. DOI:10.1016/j.addr.2008.06.002
11. R. V. Kalla, E. Elzein, T. Perry, X. Li, V. Palle, V. Varkhedkar, A. Gimbel, T. Maa, D. Zeng and J. Zablocki, *J. Med. Chem.*, **2006**, *49*, 3682–3692. DOI:10.1021/jm051268+
12. B. Jasiewicz, A. Sierakowska, N. Wandyszewska, B. Warżajtis, U. Rychlewska, R. Wawrzyniak and L. Mrówczyńska, *Bioorg. Med. Chem. Lett.*, **2016**, *26*, 3994–3998. DOI:10.1016/j.bmcl.2016.06.091
13. C. E. Kientz, A. G. Hulst, A. L. De Jong and E. R. J. Wils, *Anal. Chem.*, **1996**, *68*, 675–681. DOI:10.1021/ac950892z
14. A. Bogo, P. G. Mantle, *Phytochem.* **2000**, *54*, 937–939. DOI:10.1016/S0031-9422(00)00169-2
15. J. L. Venzie, J. Castro, M. V. Balarama Krishna, D. M. Nelson and R. K. Marcus, *Anal. Bioanal. Chem.*, **2007**, *387*, 321–333. DOI:10.1007/s00216-006-0934-z
16. V. Feyrer, O. Plekan, R. Richter, M. Coreno and K. C. Prince, *Chem. Phys.*, **2009**, *358*, 33–39. DOI:10.1016/j.chemphys.2008.12.014
17. S. Dagan, A. Amirav and T. Fujü, *Int. J. Mass. Spectrom. Ion Processes*, **1995**, *15*, 159–165. DOI:10.1016/0168-1176(95)04321-7
18. B. Jasiewicz, A. Sierakowska, W. Jankowski, M. Hoffman, W. Piorońska, A. Górnicka, A. Bielawska, K. Bielawski, L. Mrówczyńska, *Free Radical Res.*, **2018**, *52*(6), 724–738 DOI:10.1080/10715762.2018.1467561
19. CAChe 5.04, UserGuide, Fujitsu. 2003
20. J. J. P. Stewart, *J. Comput. Chem.* **10**, **1989**, 209–220. DOI:10.1002/jcc.540100208
21. J. J. P. Stewart, "Optimization of Parameters for Semiempirical Methods II. Applications", *J. Comput. Chem.* **10**, **1989**, 221–264. DOI:10.1002/jcc.540100209

## Povzetek

Raziskovali smo masno-spektrometrično fragmentacijo desetih novih 8-alkilamino derivatov kofeina. Na osnovi nizko-in visokoločljivostnih EI (elektronska ionizacija) masnih spektrov razpravljamo o poteku fragmentacije novih poliamin-skih derivatov kofeina. Pri novih spojinah nismo opazili klasične fragmentacije purinskega skeleta, povezane z eliminacijo nevtralne molekule  $\text{CH}_3\text{N}(1)\text{C}(2)\text{O}$  iz molekulskega iona. Vendar pa smo opazili nov, zanimiv potek fragmentacije opisanih derivatov kofeina. Izračunali smo tudi entalpijo nastanka ion-radikalov 8-alkilaminokofeinskih derivatov.



Scientific paper

# Synthesis, Antimicrobial Activity and *in silico* Studies on Eugenol Eters

Jelena Lazarević,<sup>1,\*</sup> Ana Kolarević,<sup>2</sup> Gordana Stojanović,<sup>3,\*</sup> Andrija Šmelcerović,<sup>1</sup> Pierangela Ciuffreda<sup>4</sup> and Enzo Santaniello<sup>5</sup>

<sup>1</sup> Department of Chemistry, Faculty of Medicine, University of Niš, Bul. dr Zorana Đinđića 81, 18000 Niš, Serbia

<sup>2</sup> Department of Pharmacy, Faculty of Medicine, University of Niš, Bul. dr Zorana Đinđića 81, 18000 Niš, Serbia

<sup>3</sup> Department of Chemistry, Faculty of Science and Mathematics, University of Niš, Višegradska 33, 18000 Niš, Serbia

<sup>4</sup> Dipartimento di Scienze Biomediche e Cliniche "L. Sacco", Università degli Studi di Milano, Via G.B. Grassi 74, 20157 Milano, Italy

<sup>5</sup> Department of Biomedical Sciences, Humanitas University, Via Manzoni 113, 20089 Rozzano - Milano, Italy

\* Corresponding author: E-mail: E-mail: jelena217@yahoo.com (JL) and gocast@pmf.ni.ac.rs (GS)

Received: 28-03-2018

## Abstract

The results presented herein represent our continued study based on the modification of phenolic functionality in molecules originated from natural sources by acylation. A small focused library of nineteen eugenyl esters, with four of which are new compounds, is reported. All compounds were subjected to *in vitro* antimicrobial testing. *In silico* studies were carried out calculating physico-chemical, pharmacokinetic and toxicological properties, providing more data as additional guidance for further research.

**Keywords:** Chemical synthesis; eugenyl esters; *in vitro* antimicrobial activity; *in silico* calculation

## 1. Introduction

Natural products, especially those derived from plants, represent an excellent source of new bioactive compounds since their structures may be used as natural pharmacophores enabling structural derivatization.<sup>1</sup> Phenylpropenes belong to a vast family of compounds called phenylpropanoids that are biosynthesized in plants from the amino acids phenylalanine and tyrosine *via* shikimate pathway.<sup>2</sup> Phenylpropenes, such as eugenol, isoeugenol, chavicol and anethole are biosynthesized by flowering plants as defense compounds against animals and microorganisms.<sup>3</sup> Because of the antimicrobial properties of phenylpropenes, as well as their pleasant aromas and flavors, since ancient times humans have used plant materials containing such compounds to preserve and flavor their food (cloves, allspice, black pepper, anise, fennel; all of these containing significant amounts of phenylpropenes) and as medicinal agents.<sup>3</sup>

Eugenol (4-allyl-2-methoxyphenol) is naturally occurring in essential oils of variety of plants belonging to

Lamiaceae, Lauraceae, Myrtaceae and Myristicaceae families. It is one of the major constituents of clove (*Syzygium aromaticum* (L.) Merrill & Perry, Myrtaceae) oil and is largely used both in foods and as flavouring agent.<sup>4,5</sup> Eugenol and its close analogues have several proven biological activities<sup>6–16</sup> which make it useful in pharmaceutical production. Additionally, eugenol has been described as an agent with dual effect: antioxidant and pro-oxidant, postulating the existence of beneficial properties in both prevention of cancer formation and in cancer treatment.<sup>17</sup> According to previous *in vitro* and *in vivo* studies eugenol might function as a tumor suppressor in most cancer types inspected.<sup>17–20</sup>

The activity of eugenol against microorganisms is also well known.<sup>21,22</sup> The mechanisms of antimicrobial action have been documented in both bacteria and fungi.<sup>21,23–25</sup> According to a review discussing mechanisms of antimicrobial action of eugenol and essential oils containing eugenol, two main uses of eugenol are particularly indicated: against food-decaying microorganisms and

against bacteria causing oral clinical conditions.<sup>21</sup> In a review published by Freires *et al.*<sup>26</sup> it was concluded that due to its promising antimicrobial activity against streptococci, eugenol should be considered as an anti-cariogenic agent worth of further clinical testing. The mode of action of eugenol against microbials has been thoroughly investigated and reviewed by Marchese *et al.*<sup>21</sup> In this paper a systematic presentation of the mechanisms against bacteria and fungi known so far is given. Compounds obtained by derivatisation of eugenol have also been reported as antimicrobial agents.<sup>1,27–30</sup> So far, the most frequently investigated eugenol derivatives in bioassays are glycosides<sup>27–30</sup> and esters.<sup>31–33</sup> Like eugenol, eugenyl esters can also represent compounds of promising biological properties. Several papers on isolation and/or synthesis and biological activity of eugenyl esters have reported wide range of activities: antioxidant,<sup>9,11,13,34</sup> anticancer,<sup>35</sup> larvicidal,<sup>37</sup> anti-leishmaniasis.<sup>38</sup> On the other hand, little data exists on antimicrobial activity, reporting only few compounds involved with respect to the total number synthesized. Antimicrobial assays evaluated antibacterial activity of eugenyl esters of acetic, 3-methylbutanoic, pentanoic and benzoic acids,<sup>31–33</sup> but no data related to antifungal activity of such derivatives was reported.

The diverse pharmacological activity of eugenol and eugenyl esters, scarce results on antibacterial and no results on antifungal activity of ester derivatives, have determined the aim of our study. By making a modification of a phenolic functionality in eugenol, we have obtained a series of ester compounds (**3a–s**), performed their structural characterization, *in vitro* antimicrobial testing and *in silico* calculation of physico-chemical, pharmacokinetic and toxicological properties. An important contribution of this study is the synthesis of four new compounds (**3l**, **3n**, **3p** and **3r**), followed by the results obtained in antibacterial together with the first results ever obtained in an antifungal assay, and by *in silico* calculations. All together represent an important aspect to guide further research.

## 2. Materials and Methods

### 2.1. Chemicals Used

All the reagents, standards and solvents used were of analytical reagent grade. Unless specified otherwise, all chemicals were purchased from Merck (Darmstadt, Germany).

### 2.2. General Synthetic Procedures

Acetyl, benzoyl and palmitoyl chloride (**2a**, **2r**, **2s**) were purchased from Sigma-Aldrich. For the preparation of acyl chlorides **2b–p**, **2r** and of eugenyl esters (Table 1, entries **3a–s**) methods from the literature<sup>39–42</sup> were utilized and general procedures for the synthesis as reported

in our previously published paper was followed.<sup>43</sup> Scheme 1 represents the synthesis of eugenyl esters.

The obtained esters of eugenol **3a–s** were purified by column chromatography, stationary phase Silica Gel 60 (70–230 mesh), mobile phase (hexane/diethyl ether, gradient 9:1 to 6:4). For yields see Table 1. For solid compounds **3q**, **3r** and **3s** melting points were determined in a Stuart Scientific SMP3 apparatus and are uncorrected.

#### Eugenyl Acetate (3a)

Chromatographic purification gave yellowish oil. C<sub>12</sub>H<sub>14</sub>O<sub>3</sub> (*M* = 206.24); yield 96%; MS (EI): *m/z* (%) 206 (M<sup>+</sup>), 164 (100), 149 (27.23), 133 (15.32), 131 (20.72), 121 (11.81), 104 (16.72), 103 (18.52), 91 (23.22), 77 (17.02), 43 (14.18); RI (HP5-MS): 1538; <sup>1</sup>H NMR (500.13 MHz, CDCl<sub>3</sub>): δ 6.98 (1H, d, *J* = 8 Hz, **H-6**), 6.77 (2H, m, **H-3** and **H-5**), 6.04 (1H, m, **H-9**), 5.13 (2H, m, **H-10**), 3.85 (3H, s, **H-7**), 3.41 (2H, d, *J* = 6 Hz, **H-8**), 2.34 (3H, s, **H-12**); <sup>13</sup>C NMR (125.76 MHz, CDCl<sub>3</sub>): δ 169.28 (**C-11**), 150.88 (**C-2**), 139.05 (**C-1**), 138.00 (**C-4**), 137.06 (**C-9**), 122.53 (**C-6**), 120.69 (**C-5**), 116.19 (**C-10**), 112.73 (**C-3**), 55.84 (**C-7**), 40.12 (**C-8**), 20.71 (**C-12**). Physical and spectroscopic data were in accordance with those reported.<sup>37,38</sup>

#### Eugenyl Propanoate (3b)

Chromatographic purification gave yellowish oil. C<sub>13</sub>H<sub>16</sub>O<sub>3</sub> (*M* = 220.26); yield 89%; MS (EI): *m/z* (%) 220 (M<sup>+</sup>), 165 (16.52), 164 (100), 149 (23.02), 133 (12.01), 132 (9.11), 131 (13.91), 104 (10.11), 103 (10.51), 91 (13.21), 57 (14.01); RI (HP5-MS): 1635; <sup>1</sup>H NMR (500.13 MHz, CDCl<sub>3</sub>): δ 6.98 (1H, d, *J* = 8 Hz, **H-6**), 6.70–6.90 (2H, m, **H-3** and **H-5**), 5.90–6.07 (1H, m, **H-9**), 5.04–5.23 (2H, m, **H-10**), 3.84 (3H, s, **H-7**), 3.41 (2H, d, *J* = 6 Hz, **H-8**), 2.64 (2H, q, *J* = 8 Hz, **H-12**), 1.31 (3H, t, *J* = 7 Hz, **H-13**); <sup>13</sup>C NMR (125.76 MHz, CDCl<sub>3</sub>): δ 172.72 (**C-11**), 150.96 (**C-2**), 138.87 (**C-1**), 138.13 (**C-4**), 137.13 (**C-9**), 122.55 (**C-6**), 120.68 (**C-5**), 116.14 (**C-10**), 112.75 (**C-3**), 55.84 (**C-7**), 40.12 (**C-8**), 27.39 (**C-12**), 9.23 (**C-13**). Physical and spectroscopic data were in accordance with those reported.<sup>37,38</sup>

#### Eugenyl Butanoate (3c)

Chromatographic purification gave colorless oil. C<sub>14</sub>H<sub>18</sub>O<sub>3</sub> (*M* = 234.29); yield 87%; MS (EI): *m/z* (%) 234 (M<sup>+</sup>), 165 (10.91), 164 (100), 149 (19.02), 133 (10.01), 132 (7.91), 131 (11.21), 104 (8.21), 103 (8.41), 91 (10.31), 43 (8.41); RI (HP5-MS): 1729; <sup>1</sup>H NMR (500.13 MHz, CDCl<sub>3</sub>): δ 6.97 (1H, d, *J* = 8 Hz, **H-6**), 6.77–6.84 (2H, m, **H-3** and **H-5**), 5.94–6.04 (1H, m, **H-9**), 5.09–5.17 (2H, m, **H-10**), 3.83 (3H, s, **H-7**), 3.41 (2H, d, *J* = 6 Hz, **H-8**), 2.59 (2H, t, *J* = 7 Hz, **H-12**), 1.83 (2H, spt, *J* = 7 Hz, **H-13**), 1.08 (3H, t, *J* = 7 Hz, **H-14**); <sup>13</sup>C NMR (125.76 MHz, CDCl<sub>3</sub>): δ 171.89 (**C-11**), 150.93 (**C-2**), 138.87 (**C-1**), 138.09 (**C-4**), 137.13 (**C-9**), 122.57 (**C-6**), 120.68 (**C-5**), 116.13 (**C-10**), 112.73 (**C-3**), 55.81 (**C-7**), 40.12 (**C-8**), 35.94 (**C-12**), 18.62 (**C-13**), 13.62 (**C-14**). Physical and spectroscopic data were in accordance with those reported.<sup>11,38</sup>

**Eugenyl 2-Methylpropanoate (3d)**

Chromatographic purification gave colorless oil.  $C_{14}H_{18}O_3$  ( $M = 234.29$ ); yield 76%; MS (EI):  $m/z$  (%) 234 ( $M^+$ ), 165 (11.11), 164 (100), 149 (16.72), 133 (8.71), 131 (10.01), 103 (8.71), 91 (10.61), 77 (7.71), 71 (7.81), 43 (8.41); RI (HP5-MS): 1679;  $^1H$  NMR (500.13 MHz,  $CDCl_3$ ):  $\delta$  6.94–7.03 (1H, m, **H-6**), 6.77–6.82 (2H, m, **H-3** and **H-5**), 5.95–6.03 (1H, m, **H-9**), 5.10–5.16 (2H, m, **H-10**), 3.83 (3H, s, **H-7**), 3.41 (2H, d,  $J = 6.24$  Hz, **H-8**), 2.86 (2H, spt,  $J = 6.9$  Hz, **H-12**), 1.35 (6H, d,  $J = 6.9$  Hz,  $2 \times CH_3$ : **H-13** and **H-14**);  $^{13}C$  NMR (125.76 MHz,  $CDCl_3$ ):  $\delta$  175.40 (**C-11**), 150.97 (**C-2**), 138.76 (**C-1**), 138.25 (**C-4**), 137.16 (**C-9**), 122.49 (**C-6**), 120.68 (**C-5**), 116.08 (**C-10**), 112.80 (**C-3**), 55.87 (**C-7**), 40.11 (**C-8**), 34.00 (**C-12**), 19.08 ( $2 \times CH_3$ : **C-13** and **C-14**). Physical and spectroscopic data were in accordance with those reported.<sup>33,44</sup>

**Eugenyl Pentanoate (3e)**

Chromatographic purification gave colorless oil.  $C_{15}H_{20}O_3$  ( $M = 248.32$ ); yield 85%; MS (EI):  $m/z$  (%) 248 ( $M^+$ ), 165 (11.01), 164 (100), 149 (15.82), 133 (8.81), 131 (9.61), 104 (7.41), 103 (7.51), 91 (9.31), 57 (14.61), 55 (6.71); RI (HP5-MS): 1829;  $^1H$  NMR (500.13 MHz,  $CDCl_3$ ):  $\delta$  6.96 (1H, d,  $J = 8$  Hz, **H-6**), 6.76–6.83 (2H, m, **H-3** and **H-5**), 5.94–6.03 (1H, m, **H-9**), 5.09–5.16 (2H, m, **H-10**), 3.83 (3H, s, **H-7**), 3.40 (2H, d,  $J = 6$  Hz, **H-8**), 2.60 (2H, t,  $J = 8$  Hz, **H-12**), 1.78 (2H, quin,  $J = 7$  Hz, **H-13**), 1.49 (2H, sxt,  $J = 7$  Hz, **H-14**), 1.0 (3H, t,  $J = 7$  Hz, **H-15**);  $^{13}C$  NMR (125.76 MHz,  $CDCl_3$ ):  $\delta$  172.07 (**C-11**), 150.93 (**C-2**), 138.86 (**C-1**), 138.09 (**C-4**), 137.13 (**C-9**), 122.55 (**C-6**), 120.68 (**C-5**), 116.13 (**C-10**), 112.73 (**C-3**), 55.81 (**C-7**), 40.11 (**C-8**), 33.79 (**C-12**), 27.13 (**C-13**), 22.22 (**C-14**), 13.76 (**C-15**). Physical and spectroscopic data were in accordance with those reported.<sup>11,38</sup>

**Eugenyl 3-Methylbutanoate (3f)**

Chromatographic purification gave colorless oil.  $C_{15}H_{20}O_3$  ( $M = 248.32$ ); yield 85%; MS (EI):  $m/z$  (%) 248 ( $M^+$ ) (3.20), 165 (11.41), 164 (100), 149 (15.72), 133 (7.41), 132 (6.81), 121 (2.90); RI (HP5-MS): 1785;  $^1H$  NMR (500.13 MHz,  $CDCl_3$ ):  $\delta$  6.96 (1H, d,  $J = 6.3$  Hz, **H-6**), 6.78–6.82 (2H, m, **H-3** and **H-5**), 5.98 (1H, s, **H-9**), 5.10–5.16 (2H, m, **H-10**), 3.83 (3H, s, **H-7**), 3.41 (2H, d,  $J = 6.24$  Hz, **H-8**), 2.48 (2H, d,  $J = 7.63$  Hz, **H-12**), 2.29 (1H, m, **H-13**), 1.10 (6H, d,  $J = 6.24$  Hz,  $2 \times CH_3$ : **H-14** and **H-15**);  $^{13}C$  NMR (125.76 MHz,  $CDCl_3$ ):  $\delta$  171.26 (**C-11**), 150.94 (**C-2**), 138.87 (**C-1**), 138.08 (**C-4**), 137.13 (**C-9**), 122.57 (**C-6**), 120.68 (**C-5**), 116.11 (**C-10**), 112.75 (**C-3**), 55.75 (**C-7**), 43.14 (**C-12**), 40.11 (**C-8**), 25.97 (**C-13**), 22.39 ( $2 \times CH_3$ : **C-14** and **C-15**). Physical and spectroscopic data were in accordance with those reported.<sup>33</sup>

**Eugenyl Hexanoate (3g)**

Chromatographic purification gave colorless oil.  $C_{16}H_{22}O_3$  ( $M = 262.34$ ); yield 82%; MS (EI):  $m/z$  (%) 262 ( $M^+$ ), 165 (10.71), 164 (100), 149 (13.31), 133 (7.11), 132

(6.11), 103 (6.71), 91 (7.91), 55 (6.81), 43 (8.71); RI (HP5-MS): 1932;  $^1H$  NMR (500.13 MHz,  $CDCl_3$ ):  $\delta$  6.94 (1H, d,  $J = 8$  Hz, **H-6**), 6.72–6.83 (2H, m, **H-3** and **H-5**), 5.90–6.03 (1H, m, **H-9**), 5.05–5.17 (2H, m, **H-10**), 3.82 (3H, s, **H-7**), 3.39 (d,  $J = 6.6$  Hz, 2H, **H-8**), 2.59 (2H, t,  $J = 7.5$  Hz, **H-12**), 1.76 (2H, quin,  $J = 7.5$  Hz, **H-13**), 1.47 (2H, sxt,  $J = 7.5$  Hz, **H-15**), 0.98 (3H, t,  $J = 7.5$  Hz, **H-16**);  $^{13}C$  NMR (125.76 MHz,  $CDCl_3$ ):  $\delta$  172.01 (**C-11**), 150.87 (**C-2**), 138.80 (**C-1**), 138.05 (**C-4**), 137.06 (**C-9**), 122.50 (**C-6**), 120.62 (**C-5**), 116.07 (**C-10**), 112.69 (**C-3**), 55.76 (**C-7**), 40.06 (**C-8**), 33.75 (**C-12**), 27.08 (**C-13**), 22.47 (**C-14**), 22.37 (**C-15**), 13.98 (**C-16**). Physical and spectroscopic data were in accordance with those reported.<sup>38</sup>

**Eugenyl Heptanoate (3h)**

Chromatographic purification gave colorless oil.  $C_{17}H_{24}O_3$  ( $M = 276.37$ ); yield 82%; MS (EI):  $m/z$  (%) 276 ( $M^+$ ), 165 (11.31), 164 (100), 149 (11.71), 133 (6.01), 132 (5.21), 131 (6.61), 103 (4.90), 91 (6.01), 55 (5.91), 43 (6.51); RI (HP5-MS): 2037;  $^1H$  NMR (500.13 MHz,  $CDCl_3$ ):  $\delta$  6.96 (1H, d,  $J = 8$  Hz, **H-6**), 6.76–6.83 (2H, m, **H-3** and **H-5**), 5.94–6.03 (1H, m, **H-9**), 5.09–5.16 (2H, m, **H-10**), 3.83 (3H, s, **C-7**), 3.40 (2H, d,  $J = 7$  Hz, **H-8**), 2.60 (2H, t,  $J = 7$  Hz, **H-12**), 1.78 (2H, quin,  $J = 7$  Hz, **H-13**), 1.46 (2H, bs, **H-14**), 1.31–1.42 (4H, m, **H-15** and **H-16**), 0.94 (3H, bs, **H-17**);  $^{13}C$  NMR (125.76 MHz,  $CDCl_3$ ):  $\delta$  172.08 (**C-11**), 150.93 (**C-2**), 138.86 (**C-1**), 138.09 (**C-4**), 137.13 (**C-9**), 122.55 (**C-6**), 120.68 (**C-5**), 116.13 (**C-10**), 112.73 (**C-3**), 55.81 (**C-7**), 40.12 (**C-8**), 34.10 (**C-12**), 31.49 (**C-15**), 28.75 (**C-14**), 25.05 (**C-13**), 22.55 (**C-16**), 14.06 (**C-17**). Physical and spectroscopic data were in accordance with those reported.<sup>38</sup>

**Eugenyl Octanoate (3i)**

Chromatographic purification gave yellowish oil.  $C_{18}H_{26}O_3$  ( $M = 290.40$ ); yield 86%; MS (EI):  $m/z$  (%) 290 ( $M^+$ ), 165 (16.52), 164 (100), 149 (10.31), 133 (5.41), 132 (4.60), 131 (5.81), 103 (4.60), 91 (5.21), 57 (10.21), 55 (7.71); RI (HP5-MS): 2141;  $^1H$  NMR (500.13 MHz,  $CDCl_3$ ):  $\delta$  6.96 (1H, d,  $J = 8.3$  Hz, **H-6**), 6.76–6.83 (2H, m, **H-3** and **H-5**), 5.94–6.03 (1H, m, **H-9**), 5.09–5.18 (2H, m, **H-10**), 3.83 (3H, s, **C-7**), 3.40 (2H, d,  $J = 6.2$  Hz, **H-8**), 2.59 (2H, t,  $J = 7.3$  Hz, **H-12**), 1.79 (2H, quin,  $J = 7.3$  Hz, **H-13**), 1.28–1.49 (8H, bm, **H-14–H-17**), 0.88–0.97 (3H, m, **H-18**);  $^{13}C$  NMR (125.76 MHz,  $CDCl_3$ ):  $\delta$  172.08 (**C-11**), 150.93 (**C-2**), 138.86 (**C-1**), 138.09 (**C-4**), 137.13 (**C-9**), 122.57 (**C-6**), 120.68 (**C-5**), 116.13 (**C-10**), 112.73 (**C-3**), 55.81 (**C-7**), 40.12 (**C-8**), 34.10 (**C-12**), 31.73 (**C-16**), 29.05 (**C-15**), 28.97 (**C-14**), 25.10 (**C-13**), 22.64 (**C-17**), 14.11 (**C-18**). Physical and spectroscopic data were in accordance with those reported.<sup>38</sup>

**Eugenyl Nonanoate (3j)**

Chromatographic purification gave yellowish oil.  $C_{19}H_{28}O_3$  ( $M = 304.42$ ); yield 76%; MS (EI):  $m/z$  (%) 304 ( $M^+$ ), 165 (11.31), 164 (100), 149 (9.01), 137 (1.90), 133

(4.40), 132 (4.60), 131 (3.10), 121 (1.50), 107 (1.30), 104 (2.00); RI (HP5-MS): 2246;  $^1\text{H}$  NMR (500.13 MHz,  $\text{CDCl}_3$ ):  $\delta$  6.96 (1H, d,  $J = 8.3$  Hz, **H-6**), 6.70–6.84 (2H, m, **H-3** and **H-5**), 5.92–6.04 (1H, m, **H-9**), 5.03–5.18 (2H, m, **H-10**), 3.83 (3H, s, **C-7**), 3.40 (2H, d,  $J = 6.2$  Hz, **H-8**), 2.59 (2H, t,  $J = 7.3$  Hz, **H-12**), 1.78 (2H, quin,  $J = 7.5$  Hz, **H-13**), 1.29–1.49 (10H, bm, **H-14–H-18**), 0.83–1.06 (3H, m, **H-19**);  $^{13}\text{C}$  NMR (125.76 MHz,  $\text{CDCl}_3$ ):  $\delta$  172.08 (**C-11**), 150.93 (**C-2**), 138.86 (**C-1**), 138.09 (**C-4**), 137.13 (**C-9**), 122.57 (**C-6**), 120.68 (**C-5**), 116.13 (**C-10**), 112.73 (**C-3**), 55.81 (**C-7**), 40.11 (**C-8**), 34.10 (**C-12**), 31.84 (**C-17**), 29.27 (**C-16**), 29.19 (**C-15**), 29.10 (**C-14**), 25.09 (**C-13**), 22.68 (**C-18**), 14.13 (**C-19**). Physical and spectroscopic data were in accordance with those reported.<sup>38</sup>

### Eugenyl Decanoate (3k)

Chromatographic purification gave colorless oil.  $\text{C}_{20}\text{H}_{30}\text{O}_3$  ( $M = 318.45$ ); yield 85%; MS (EI):  $m/z$  (%) 318 ( $\text{M}^+$ ), 166 (1.00), 165 (11.31), 164 (100), 149 (7.91), 147 (1.00), 137 (1.70), 133 (4.40), 105 (1.50), 103 (4.00); 85 (1.40); RI (HP5-MS): 2348;  $^1\text{H}$  NMR (500.13 MHz,  $\text{CDCl}_3$ ):  $\delta$  6.96 (1H, d,  $J = 7.6$  Hz, **H-6**), 6.78–6.82 (2H, m, **H-3** and **H-5**), 5.95–6.04 (1H, m, **H-9**), 5.10–5.17 (2H, m, **H-10**), 3.83 (3H, s, **C-7**), 3.40 (2H, d,  $J = 6.2$  Hz, **H-8**), 2.59 (2H, t,  $J = 7.6$  Hz, **H-12**), 1.79 (2H, quin,  $J = 7.6$  Hz, **H-13**), 1.27–1.48 (12H, bm, **H-14–H-19**), 0.92 (3H, t,  $J = 6.9$  Hz, **H-20**);  $^{13}\text{C}$  NMR (125.76 MHz,  $\text{CDCl}_3$ ):  $\delta$  172.08 (**C-11**), 150.93 (**C-2**), 138.86 (**C-1**), 138.09 (**C-4**), 137.13 (**C-9**), 122.57 (**C-6**), 120.68 (**C-5**), 116.13 (**C-10**), 112.73 (**C-3**), 55.81 (**C-7**), 40.12 (**C-8**), 34.10 (**C-12**), 31.91 (**C-18**), 29.5 (**C-16**), 29.32 ( $2 \times \text{CH}_2$ : **C-15** and **C-17**), 29.10 (**C-14**), 25.10 (**C-13**), 22.71 (**C-19**), 14.14 (**C-20**). Physical and spectroscopic data were in accordance with those reported.<sup>38</sup>

### Eugenyl Undecanoate (3l)

Chromatographic purification gave colorless oil.  $\text{C}_{21}\text{H}_{32}\text{O}_3$  ( $M = 332.48$ ); yield 87%; MS (EI):  $m/z$  (%) 332 ( $\text{M}^+$ ), 165 (11.21), 164 (100), 149 (7.31), 133 (3.90), 131 (4.50), 103 (3.70), 91 (4.30), 57 (5.91), 55 (10.01); RI (HP5-MS): 2449;  $^1\text{H}$  NMR (500.13 MHz,  $\text{CDCl}_3$ ):  $\delta$  6.96 (1H, d,  $J = 8.3$  Hz, **H-6**), 6.78–6.82 (2H, m, **H-3** and **H-5**), 5.95–6.03 (1H, m, **H-9**), 5.10–5.16 (2H, m, **H-10**), 3.83 (3H, s, **C-7**), 3.40 (2H, d,  $J = 6.24$  Hz, **H-8**), 2.59 (2H, t,  $J = 7.28$  Hz, **H-12**), 1.78 (2H, quin,  $J = 7.28$  Hz, **H-13**), 1.28–1.45 (14H, bm, **H-14–H-20**), 0.92 (3H, t,  $J = 6.6$  Hz, **H-21**);  $^{13}\text{C}$  NMR (125.76 MHz,  $\text{CDCl}_3$ ):  $\delta$  172.08 (**C-11**), 150.93 (**C-2**), 138.86 (**C-1**), 138.09 (**C-4**), 137.13 (**C-9**), 122.55 (**C-6**), 120.68 (**C-5**), 116.13 (**C-10**), 112.73 (**C-3**), 55.81 (**C-7**), 40.12 (**C-8**), 34.10 (**C-12**), 31.94 (**C-19**), 29.61 (**C-16**), 29.54 (**C-17**), 29.35 (**C-15**), 29.32 (**C-18**), 29.10 (**C-14**), 25.10 (**C-13**), 22.72 (**C-20**), 14.14 (**C-21**).

### Eugenyl Dodecanoate (3m)

Chromatographic purification gave colorless oil.  $\text{C}_{22}\text{H}_{34}\text{O}_3$  ( $M = 346.50$ ); yield 84%; MS (EI):  $m/z$  (%) 346 ( $\text{M}^+$ ), 165 (11.31), 164 (100), 149 (6.41), 133 (3.40), 131

(3.90), 103 (3.10), 91 (3.20), 57 (5.01), 55 (8.51); RI (HP5-MS): 2553;  $^1\text{H}$  NMR (500.13 MHz,  $\text{CDCl}_3$ ):  $\delta$  6.96 (1H, d,  $J = 8.3$  Hz, **H-6**), 6.77–6.82 (2H, m, **H-3** and **H-5**), 5.95–6.03 (1H, m, **H-9**), 5.10–5.16 (2H, m, **H-10**), 3.83 (3H, s, **C-7**), 3.40 (2H, d,  $J = 6.9$  Hz, **H-8**), 2.59 (2H, t,  $J = 7.28$  Hz, **H-12**), 1.78 (2H, quin,  $J = 7.6$  Hz, **H-13**), 1.28–1.51 (16H, bm, **H-14–H-21**), 0.92 (3H, t,  $J = 6.6$  Hz, **H-22**);  $^{13}\text{C}$  NMR (125.76 MHz,  $\text{CDCl}_3$ ):  $\delta$  172.08 (**C-11**), 150.93 (**C-2**), 138.86 (**C-1**), 138.09 (**C-4**), 137.13 (**C-9**), 122.55 (**C-6**), 120.68 (**C-5**), 116.13 (**C-10**), 112.72 (**C-3**), 55.79 (**C-7**), 40.12 (**C-8**), 34.10 (**C-12**), 31.94 (**C-20**), 29.65 ( $2 \times \text{CH}_2$ : **C-16** and **C-18**), 29.54 (**C-17**), 29.37 (**C-15**), 29.32 (**C-19**), 29.10 (**C-14**), 25.10 (**C-13**), 22.72 (**C-21**), 14.14 (**C-22**). Physical and spectroscopic data were in accordance with those reported.<sup>18,38</sup>

### Eugenyl Tridecanoate (3n)

Chromatographic purification gave yellowish oil.  $\text{C}_{23}\text{H}_{36}\text{O}_3$  ( $M = 360.53$ ); yield 87%; MS (EI):  $m/z$  (%) 360 ( $\text{M}^+$ ), 164 (100), 149 (6.51), 131 (3.10), 103 (3.10), 91 (3.11), 57 (5.10), 55 (8.40); RI (HP5-MS): 2655;  $^1\text{H}$  NMR (500.13 MHz,  $\text{CDCl}_3$ ):  $\delta$  6.97 (1H, d,  $J = 8.3$  Hz, **H-6**), 6.78–6.82 (2H, m, **H-3** and **H-5**), 5.95–6.04 (1H, m, **H-9**), 5.10–5.16 (2H, m, **H-10**), 3.83 (3H, s, **C-7**), 3.40 (2H, d,  $J = 6.94$  Hz, **H-8**), 2.60 (2H, t,  $J = 7.28$  Hz, **H-12**), 1.78 (2H, quin,  $J = 7.3$  Hz, **H-13**), 1.27–1.54 (16H, bm, **H-14–H-22**), 0.92 (3H, t,  $J = 6.6$  Hz, **H-23**);  $^{13}\text{C}$  NMR (125.76 MHz,  $\text{CDCl}_3$ ):  $\delta$  172.04 (**C-11**), 150.94 (**C-2**), 138.84 (**C-1**), 138.13 (**C-4**), 137.13 (**C-9**), 122.57 (**C-6**), 120.68 (**C-5**), 116.13 (**C-10**), 112.75 (**C-3**), 55.79 (**C-7**), 40.12 (**C-8**), 34.10 (**C-12**), 31.95 (**C-21**), 29.38–29.70 ( $4 \times \text{CH}_2$ : **C-16–C-19**), 29.32 ( $2 \times \text{CH}_2$ : **C-15** and **C-20**), 29.10 (**C-14**), 25.10 (**C-13**), 22.72 (**C-22**), 14.14 (**C-23**).

### Eugenyl Tetradecanoate (3o)

Chromatographic purification gave yellowish oil.  $\text{C}_{24}\text{H}_{38}\text{O}_3$  ( $M = 374.56$ ); yield 79%; MS (EI):  $m/z$  (%) 374 ( $\text{M}^+$ ), 165 (13.01), 164 (100), 149 (5.81), 133 (3.10), 132 (2.80), 131 (3.50), 69 (2.50), 57 (3.60), 55 (5.51), 43 (2.50); RI (HP5-MS): 2753;  $^1\text{H}$  NMR (500.13 MHz,  $\text{CDCl}_3$ ):  $\delta$  6.97 (1H, d,  $J = 8.32$  Hz, **H-6**), 6.78–6.83 (2H, m, **H-3** and **H-5**), 5.95–6.04 (1H, m, **H-9**), 5.10–5.17 (2H, m, **H-10**), 3.83 (3H, s, **C-7**), 3.41 (2H, d,  $J = 6.24$  Hz, **H-8**), 2.60 (2H, t,  $J = 7.63$  Hz, **H-12**), 1.78 (2H, m, **H-13**), 1.27–1.50 (18H, bm, **H-14–H-23**), 0.97–0.88 (3H, m, **H-24**);  $^{13}\text{C}$  NMR (125.76 MHz,  $\text{CDCl}_3$ ):  $\delta$  171.97 (**C-11**), 150.97 (**C-2**), 138.81 (**C-1**), 138.16 (**C-4**), 137.11 (**C-9**), 122.57 (**C-6**), 120.66 (**C-5**), 116.08 (**C-10**), 112.73 (**C-3**), 55.76 (**C-7**), 40.12 (**C-8**), 34.08 (**C-12**), 31.97 (**C-22**), 29.56–29.72 ( $5 \times \text{CH}_2$ : **C-16–C-20**), 29.71 (**C-18**), 29.67 (**C-20**), 29.62 (**C-17**), 29.56 (**C-19**), 29.42 (**C-22**), 29.34 (**C-15**), 29.11 (**C-14**), 25.12 (**C-13**), 22.74 (**C-23**), 14.14 (**C-24**). Physical and spectroscopic data were in accordance with those reported.<sup>18</sup>

### Eugenyl Pentadecanoate (3p)

Chromatographic purification gave colorless oil.  $\text{C}_{25}\text{H}_{40}\text{O}_3$  ( $M = 388.58$ ); yield 89%; MS (EI):  $m/z$  (%) 388

(M<sup>+</sup>), 165 (10.91), 164 (100), 149 (5.61), 131 (3.70), 69 (5.51), 57 (8.41), 55 (14.11), 43 (9.31), 41 (4.10); RI (HP5-MS): 2858; <sup>1</sup>H NMR (500.13 MHz, CDCl<sub>3</sub>): δ 6.97 (1H, d, *J* = 8.32 Hz, **H-6**), 6.78–6.83 (2H, m, **H-3** and **H-5**), 5.95–6.04 (1H, m, **H-9**), 5.10–5.17 (2H, m, **H-10**), 3.83 (3H, s, **C-7**), 3.41 (2H, d, *J* = 6.24 Hz, **H-8**), 2.60 (2H, t, *J* = 7.63 Hz, **H-12**), 1.78 (2H, m, **H-13**), 1.27–1.50 (18H, bm, **H-14–H-24**), 0.97–0.88 (3H, m, **H-25**); <sup>13</sup>C NMR (125.76 MHz, CDCl<sub>3</sub>): δ 172.02 (**C-11**), 150.96 (**C-2**), 138.82 (**C-1**), 138.16 (**C-4**), 137.11 (**C-9**), 122.57 (**C-6**), 120.68 (**C-5**), 116.11 (**C-10**), 112.75 (**C-3**), 55.78 (**C-7**), 40.12 (**C-8**), 34.10 (**C-12**), 31.97 (**C-23**), 29.56–29.75 (6 × CH<sub>2</sub>: **C-16–C-21**), 29.42 (**C-22**), 29.34 (**C-15**), 29.11 (**C-14**), 25.12 (**C-13**), 22.74 (**C-24**), 14.16 (**C-25**).

### Eugenyl Hexadecanoate (3q)

Chromatographic purification gave white solid. M.p. 39–40 °C. C<sub>26</sub>H<sub>42</sub>O<sub>3</sub> (*M* = 402.61); yield 92%; MS (EI): *m/z* (%) 402 (M<sup>+</sup>), 165 (13.41), 164 (100), 149 (5.31), 133 (2.70), 132 (2.50), 131 (3.10), 69 (2.60), 57 (3.70), 55 (5.40), 43 (2.40); RI (HP5-MS): 2976; <sup>1</sup>H NMR (500.13 MHz, CDCl<sub>3</sub>): δ 6.96 (1H, d, *J* = 7.63 Hz, **H-6**), 6.77–6.82 (2H, m, **H-3** and **H-5**), 5.95–6.04 (1H, m, **H-9**), 5.10–5.16 (2H, m, **H-10**), 3.83 (3H, s, **C-7**), 3.40 (2H, d, *J* = 6.24 Hz, **H-8**), 2.60 (2H, t, *J* = 7.60 Hz, **H-12**), 1.79 (2H, quin, *J* = 7.50 Hz, **H-13**), 1.27–1.48 (20H, bm, **H-14–H-25**), 0.95–0.85 (3H, m, **H-26**); <sup>13</sup>C NMR (125.76 MHz, CDCl<sub>3</sub>): δ 172.07 (**C-11**), 150.94 (**C-2**), 138.84 (**C-1**), 138.11 (**C-4**), 137.11 (**C-9**), 122.55 (**C-6**), 120.68 (**C-5**), 116.11 (**C-10**), 112.73 (**C-3**), 55.81 (**C-7**), 40.11 (**C-8**), 34.10 (**C-12**), 31.95 (**C-24**), 29.54–29.72 (6 × CH<sub>2</sub>: **C-16–C-22**), 29.38 (**C-23**), 29.32 (**C-15**), 29.10 (**C-14**), 25.10 (**C-13**), 22.71 (**C-25**), 14.14 (**C-26**). Physical and spectroscopic data were in accordance with those reported.<sup>18,38</sup>

### Eugenyl Heptadecanoate (3r)

Chromatographic purification gave yellowish solid. M.p. 49–50 °C. C<sub>27</sub>H<sub>44</sub>O<sub>3</sub> (*M* = 416.64); yield 76%; MS (EI): *m/z* (%) 416 (M<sup>+</sup>), 165 (12.11), 164 (100), 149 (4.60), 133 (2.50), 132 (2.10), 131 (2.80), 69 (3.00), 57 (4.20), 55 (6.00), 43 (3.00); RI (HP5-MS): 3096; <sup>1</sup>H NMR (500.13 MHz, CDCl<sub>3</sub>): δ 6.97 (1H, d, *J* = 8 Hz, **H-6**), 6.74–6.88 (2H, m, **H-3** and **H-5**), 5.95–6.05 (1H, m, **H-9**), 5.04–5.22 (2H, m, **H-10**), 3.84 (3H, s, **C-7**), 3.42 (2H, d, *J* = 7.0 Hz, **H-8**), 2.60 (2H, t, *J* = 7.0 Hz, **H-12**), 1.81 (2H, quin, *J* = 7.0 Hz, **H-13**), 1.28–1.51 (22H, bm, **H-14–H-26**), 0.94 (3H, t, *J* = 7.0 Hz, **H-27**); <sup>13</sup>C NMR (125.76 MHz, CDCl<sub>3</sub>): δ 171.97 (**C-11**), 150.97 (**C-2**), 138.81 (**C-1**), 138.16 (**C-4**), 137.11 (**C-9**), 122.57 (**C-6**), 120.66 (**C-5**), 116.10 (**C-10**), 112.73 (**C-3**), 55.76 (**C-7**), 40.12 (**C-8**), 34.10 (**C-12**), 31.99 (**C-25**), 29.57–29.77 (7 × CH<sub>2</sub>: **C-16–C-23**), 29.43 (**C-24**), 29.35 (**C-15**), 29.11 (**C-14**), 25.12 (**C-13**), 22.75 (**C-26**), 14.14 (**C-27**).

### Eugenyl Benzoate (3s)

Chromatographic purification gave white solid. M.p. 70–71 °C. C<sub>17</sub>H<sub>16</sub>O<sub>3</sub> (*M* = 268.31); yield 96%; MS (EI): *m/z*

(%) 268 (M<sup>+</sup>) (20.82), 269 (3.80), 106 (9.61), 105 (100), 91 (5.41), 78 (3.10), 77 (33.93), 65 (1.90), 51 (4.60); RI (HP5-MS): 2170; <sup>1</sup>H NMR (500.13 MHz, CDCl<sub>3</sub>): δ 8.25 (2H, d, *J* = 8.32 Hz, **H-2'** and **H-6'**), 7.66 (1H, t, *J* = 7.28 Hz, **H-4'**), 7.53 (2H, t, *J* = 7.63 Hz, **H-3'** and **H-5'**), 7.10 (1H, d, *J* = 8.32 Hz, **H-6**), 6.87 (1H, s, **H-3**), 6.85 (1H, d, *J* = 8.32 Hz, **H-5**), 5.98–6.06 (1H, m, **H-9**), 5.12–5.18 (2H, m, **H-10**), 3.83 (3H, s, **H-7**), 3.44 (2H, d, *J* = 6.94 Hz, **H-8**); <sup>13</sup>C NMR (125.76 MHz, CDCl<sub>3</sub>): δ 164.91 (**C-11**), 151.13 (**C-2**), 139.08 (**C-4**), 138.22 (**C-9**), 137.14 (**C-1**), 133.42 (**C-4'**), 130.32 (**C-2'** and **C-6'**), 129.55 (**C-1'**), 128.51 (2 × ArC: **C-3'** and **C-5'**), 122.68 (**C-5**), 120.76 (**C-6**), 116.17 (**C-10**), 112.88 (**C-3**), 55.90 (**C-7**), 40.15 (**C-8**). Physical and spectroscopic data were in accordance with those reported.<sup>11,37</sup>

## 2. 3. Identification of Synthetized Compounds

### 2. 3. 1. GC-MS Analysis

MS spectra of samples of the synthesized compounds were recorded on a 7890/7000B GC/MS/MS triple quadrupole system (Agilent Technologies, USA, equipped with a Combi PAL auto sampler). The fused silica capillary column HP-5MS (5% phenylmethylsiloxane, 30 m × 0.25 mm, film thickness 0.25 μm, Agilent Technologies, Palo Alto, CA, USA) was used. The injector, source and interface operated at 250, 230 and 300 °C, respectively. The temperature program: from 60 for 5 min isothermal to 300 °C at a heating rate of 8 °C/min and on 300 °C for 5 min isothermal. The solutions in hexane were injected in split ratio 10:1. The carrier gas was helium with a flow of 1.0 mL/min. Post run: back flash for 1.89 min, at 280 °C, with helium at 50 psi. MS conditions were as follows: ionization voltage of 70 eV, acquisition mass range 50–650, scan time 0.32 s. Semi-quantitative analysis was carried out directly from peak areas in the GC profile.

Linear retention indices (RI) were determined based on the retention times of C<sub>8</sub>–C<sub>40</sub> alkanes run on HP-5MS column using the above mentioned temperature programme.<sup>45</sup>

### 2. 3. 2. NMR Analysis

NMR spectra were registered on a Bruker AVANCE 500 spectrometer equipped with a 5 mm broadband reverse probe with field z-gradient operating at 500.13 and 125.76 MHz for <sup>1</sup>H and <sup>13</sup>C, respectively. All NMR spectra were recorded at 298 K in CDCl<sub>3</sub> (isotopic enrichment 99.95%) solution. Chemical shifts are reported on the δ (ppm) scale and are relative to residual CHCl<sub>3</sub> signals (7.24 for <sup>1</sup>H and 77.0 ppm, central line, for <sup>13</sup>C spectra respectively), and scalar coupling constants are reported in hertz. The experimental error in the measured <sup>1</sup>H–<sup>1</sup>H coupling constants was ± 0.5 Hz.

The signals assignment was given by a combination of 1D and 2D COSY and HSQC experiments, using standard Bruker pulse programs.

Acquisition parameters for 1D were as follows:  $^1\text{H}$  spectral width of 5000 Hz and 32 K data points providing a digital resolution of ca. 0.305 Hz per point, relaxation delay 2 s;  $^{13}\text{C}$  spectral width of 29412 Hz and 64 K data points providing a digital resolution of ca. 0.898 Hz per point, relaxation delay 2.5 s. The experiments were performed through standard pulse sequences. gCOSY-45 experiments were acquired with 512 t1 increments; 2048 t2 points; spectral/spectrum width 10.0 ppm. The acquisition data for gHSQC and gHMBC experiments were obtained with 512 t1 increments; 2048 t2 points; spectral/spectrum width 10.0 ppm for  $^1\text{H}$  and 220 ppm for  $^{13}\text{C}$ . Delay values were optimized for  $^1J_{\text{C,H}}$  140.0 Hz and  $^nJ_{\text{C,H}}$  3.0 Hz. Zero filling in F1 to 1 K, p/2 shifted sine-bell squared (for gHSQC) or sinebell (for gHMBC) apodization functions were used for processing.

## 2. 4. Antimicrobial Activity

### 2. 4. 1. Microbial Strains

The *in vitro* antimicrobial activity of the synthesized compounds was tested against a panel of laboratory control strains belonging to the American Type Culture Collection Maryland, USA: Gram-positive: *Bacillus subtilis* ATCC 6633 and *Staphylococcus aureus* ATCC 6538; Gram-negative: *Escherichia coli* ATCC 8739, fungal organisms: *Aspergillus niger* ATCC 16404 and *Candida albicans* ATCC 10231. The Gram-negative bacteria *Salmonella abony* NCTC 6017 and *Salmonella typhimurium* ATCC 14028 were obtained from the National Collection of Type Cultures. All microorganisms were maintained at  $-20\text{ }^\circ\text{C}$  under appropriate conditions and regenerated twice before use in the manipulations.

### 2. 4. 2. Screening of Antimicrobial Activity

The minimal inhibitory concentration (MIC) of esters was determined based on a broth microdilution method in 96-well microtitre plates.<sup>46</sup> The inocula of the bacterial strains were prepared from overnight broth cultures and suspensions were adjusted to 0.5 McFarland standard turbidity. Dimethyl sulphoxide (10% aqueous solution)

was used to dissolve and to dilute samples to the highest concentration to be tested (stock concentrations 2 mg/mL). A serial doubling dilution of the samples was prepared in a 96-well microtiter plate, using the method of Sarker *et al.*<sup>47</sup> with slight modifications. The minimal bactericidal/fungicidal concentration (MBC/MFC) was evaluated as the lowest concentration of tested samples at which inoculated microorganisms were 99.9% killed. Tests were carried out in triplicate.

## 2. 5. *In silico* Physico-chemical, Pharmacokinetic and Toxicological Properties of the Synthesized Compounds

In order to obtain a complete picture of the synthesized compounds (3a–s) an *in silico* study was performed. Physico-chemical, pharmacokinetic and toxicological properties of compounds were calculated using the Molinspiration,<sup>48</sup> admetSAR,<sup>49</sup> DataWarrior<sup>50</sup> and Toxtree<sup>51</sup> prediction tools.

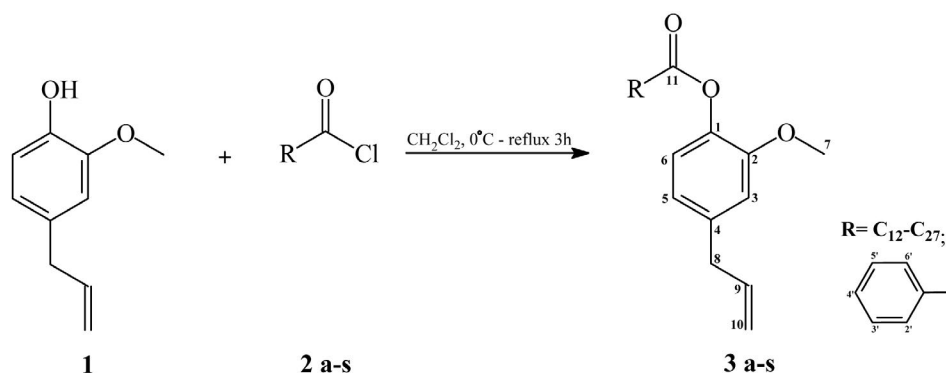
## 3. Results and Discussion

### 3. 1. Chemical Synthesis

A small focused library of nineteen eugenyl esters was synthesized. To the best of our knowledge four out of nineteen compounds are new (3l, 3n, 3p and 3r; Scheme 1). All compounds were synthesized according to previously published standard methodology and with high yields ranging from 76% to 96% (Table 1).

### 3. 2. Antimicrobial Activity

The results obtained in broth microdilution assay are given in Table 2. The assayed samples were less effective than antibiotic/antimycotic used as reference standard and if noted, activity was never greater than the values obtained for the parent compound 1 (MIC/MBC/MFC never exceeded 0.5 mg/mL, Table 2). The results are indicating selective susceptibility of the microorganisms, with *B. subtilis* (3d, 3l, 3n–r), *S. aureus* (3e and 3f), *A. niger* (3f, 3s)



Scheme 1. Synthesis of eugenyl esters

**Table 1.** Eugenyl esters: chemical entity, yields (%) and entry

R	Yield (%)	Entry
CH <sub>3</sub>	96	3a
CH <sub>2</sub> CH <sub>3</sub>	89	3b
CH <sub>2</sub> CH <sub>2</sub> CH <sub>3</sub>	87	3c
CH(CH <sub>3</sub> ) <sub>2</sub>	76	3d
CH <sub>2</sub> (CH <sub>2</sub> ) <sub>2</sub> CH <sub>3</sub>	85	3e
CH <sub>2</sub> CH(CH <sub>3</sub> ) <sub>2</sub>	85	3f
CH <sub>2</sub> (CH <sub>2</sub> ) <sub>3</sub> CH <sub>3</sub>	82	3g
CH <sub>2</sub> (CH <sub>2</sub> ) <sub>4</sub> CH <sub>3</sub>	82	3h
CH <sub>2</sub> (CH <sub>2</sub> ) <sub>5</sub> CH <sub>3</sub>	86	3i
CH <sub>2</sub> (CH <sub>2</sub> ) <sub>6</sub> CH <sub>3</sub>	76	3j
CH <sub>2</sub> (CH <sub>2</sub> ) <sub>7</sub> CH <sub>3</sub>	85	3k
CH <sub>2</sub> (CH <sub>2</sub> ) <sub>8</sub> CH <sub>3</sub>	87	3l
CH <sub>2</sub> (CH <sub>2</sub> ) <sub>9</sub> CH <sub>3</sub>	84	3m
CH <sub>2</sub> (CH <sub>2</sub> ) <sub>10</sub> CH <sub>3</sub>	87	3n
CH <sub>2</sub> (CH <sub>2</sub> ) <sub>11</sub> CH <sub>3</sub>	79	3o
CH <sub>2</sub> (CH <sub>2</sub> ) <sub>12</sub> CH <sub>3</sub>	89	3p
CH <sub>2</sub> (CH <sub>2</sub> ) <sub>13</sub> CH <sub>3</sub>	92	3q
CH <sub>2</sub> (CH <sub>2</sub> ) <sub>14</sub> CH <sub>3</sub>	76	3r
Ph	96	3s

and *C. albicans* (3d, 3f, 3n, 3n and 3s) being the most sensitive strains on the synthesized derivatives. On the other hand, all three Gram-negative microorganisms tested (*E. coli*, *S. abony* and *S. typhimurium*) were completely resistant to synthesized compounds tested (initial concentration 2 mg/mL).

Four of our samples (3a, 3e, 3f, 3s) are matching the samples tested in antibacterial assays so far.<sup>29–31</sup> Eugenyl acetate (3a) was tested in a disc diffusion method on a set of seven Gram-positive and nine Gram-negative bacteria.<sup>30</sup> The results have shown notable antimicrobial effect against all sixteen bacteria tested, with a superior performance when compared to pure eugenol.<sup>30</sup> Even when different methodologies were employed, two crucial and completely opposed observations can be made; our results have shown that derivatives have never exceeded the activity of the parent compound and that all were inactive against Gram-negative bacteria taken into consideration. Eugenyl benzoate (3s) was tested previously in disc diffusion assay against a smaller panel of laboratory controlled bacterial strains (two Gram-positive, two Gram-negative).

**Table 2.** The minimal inhibitory (MIC) and minimal bactericidal/fungicidal (MBC/MFC) concentrations (mg/mL) of the eugenol (1) and the synthesized eugenyl esters 3a–s. MIC and MBC/MFC determinations were carried out in triplicate and consistent values were obtained for each microorganism tested.

Cmpd.	Bacterial strains					Fungal strains	
	Gram-positive		Gram-negative			<i>A. niger</i>	<i>C. albicans</i>
	<i>B. subtilis</i>	<i>S. aureus</i>	<i>E. coli</i>	<i>S. abony</i>	<i>S. typhimurium</i>		
1	MIC = 0.5	MIC = MBC = 0.5	MIC = 0.5 MBC = 1.0	MIC = 0.5 MBC = 1.0	MIC = MBC = 0.5	MIC = MFC = 0.5	MIC = 0.25 MFC = 1.0
3a	na	na	na	na	na	na	MIC = MFC = 0.5
3b	na	na	na	na	na	na	na
3c	na	na	na	na	na	na	na
3d	MIC = 0.5	na	na	na	na	na	MIC = 0.5
3e	na	na	na	na	na	na	na
3f	na	MIC = 0.5	na	na	na	MIC = 0.5	MIC = 0.5
3g	na	na	na	na	na	na	na
3h	na	na	na	na	na	na	na
3i	na	na	na	na	na	na	na
3j	na	na	na	na	na	na	na
3k	na	na	na	na	na	na	na
3l	MIC = 1.0	na	na	na	na	na	na
3m	na	na	na	na	na	na	na
3n	MIC = 0.5	na	na	na	na	na	MIC = 0.5
3o	MIC = 1.0	na	na	na	na	na	na
3p	MIC = 0.5	na	na	na	na	na	na
3q	MIC = 0.5	na	na	na	na	na	na
3r	MIC = 0.5	na	na	na	na	na	MIC = 1.0
3s	na	na	na	na	na	MIC = 1.0	MIC = 1.0
Doxycycline (µg/mL)	MIC = MBC = 1.56	MIC = 6.25 MBC = 0.78	MIC = MBC = 0.78	MIC = MBC = 6.25	MIC = 6.25 MBC > 50	nt	nt
Nystatin (µg/mL)	nt	nt	nt	nt	nt	MIC = MBC = 6.25	MIC = MBC = 0.78
DMSO 10% aqueous solution		na	na	na	na	na	na na

na, not active; nt, not tested

Stronger antibacterial activity of benzoate was observed compared to its unsubstituted analogue, *i.e.* eugenol.<sup>29</sup> Eugenyl pentanoate (**3e**) and 3-methylbutanoate (**3f**) were tested against seventeen different bacterial strains (ATTC, clinical or food isolates) and have shown moderate antibacterial potential, with inhibitory values (MIC) ranging from 0.32 to 6.00 mg/mL.<sup>31</sup> No noticeable difference in the susceptibility of Gram-negative and Gram-positive bacteria was observed.<sup>31</sup> For the rest of the synthesized compounds (**3b–d**, **3g–r**) antibacterial results are reported here for the first time. For all compounds synthesized (**3a–s**) results obtained for antifungal assay are the first ever reported (Table 2).

### 3. 3. *In silico* Study

#### 3. 3. 1. Physico-chemical Properties of the Eugenyl Esters 3a–s

Lipinski's rule of five has been used to evaluate drug likeness and to determine if a pharmacologically or biologically active compound has properties that would make it a likely orally active drug in humans. In our previously published paper we have already summarized factors important for optimal bioavailability of synthesized compounds.<sup>52</sup> According to the physico-chemical properties calculated by Molinspiration software tool,<sup>48</sup> compounds **3a–h** and **3s** fulfilled all requirements for good oral bioavailability, including  $m_i\text{LogP} < 5$ ,  $n_{\text{ON}} < 10$ ,  $n_{\text{OHNH}} < 5$ ,  $\text{MW} < 500$ ,  $\text{TPSA} < 140 \text{ \AA}^2$  ( $< 60 \text{ \AA}^2$ ), and  $n_{\text{rotb}} < 10$  (Supplementary data, Table S1).

#### 3. 3. 2. Pharmacokinetic Properties of the Eugenyl Esters 3a–s

Absorption properties of compounds **3a–s** were predicted by admetSAR<sup>49</sup> (Supplementary data, Table S2). Based on the results, all of the studied compounds were predicted as compounds able to pass through blood-brain barrier and penetrate into the central nervous system, as compounds capable of being absorbed by intestine, as well as compounds permeable across Caco-2 cells. Compounds **3g–r** were predicted as P-glycoprotein substrates, while compound **3s** was predicted as P-glycoprotein inhibitor. None of the studied compounds was predicted as inhibitor of renal organic cation transporter.

Metabolic properties of the eugenyl esters **3a–s** were predicted by admetSAR<sup>49</sup> (Supplementary data, Table S3). None of the studied compounds was predicted as CYP2C9 and/or CYP2D6 substrate, while 15 compounds (**3c**, **3e–r**) were predicted as CYP3A4 substrate. Regarding CYP450 inhibition, enzyme CYP1A2 might be inhibited by compounds **3c**, **3e–s**, CYP2C9 by compound **3s**, CYP2C19 by compounds **3b**, **3c**, **3h–s**. However, none of the compounds was predicted as CYP2D6 inhibitor. Most of the investigated compounds were predicted to have low CYP 450 inhibitory promiscuity, except compounds **3a**, **3d** and **3s**.

#### 3. 3. 3. Toxicological Properties of the Eugenyl Esters 3a–s

Using Toxtree prediction tool based on a decision tree approach,<sup>51</sup> we have predicted structural alerts for DNA and protein binding for the studied compounds. Regarding DNA binding alerts, all of the studied compounds were predicted to have the ability to undergo nucleophilic aliphatic substitution ( $S_{\text{N}}1$  reactions) and Michael addition. Among the protein binding alerts, compounds **3a–s** were predicted as compounds able to undergo Michael addition and  $S_{\text{N}}2$  reactions; **3a–s** were predicted as compounds able to participate in acyl transfer (results given in Supplementary data, Tables S4 and S5).

Based on the toxicological properties predicted by admetSAR<sup>49</sup> compounds **3a–s** have been characterized as weak hERG (human Ether-à-go-go-Related Gene) inhibitors, non-AMES toxic and non-carcinogenic, but highly toxic for fish, *Tetrahymena pyriformis* and honey bee. Five compounds (**3a–c**, **3e** and **3g**) were predicted as ready biodegradable. According to the risk for acute oral toxicity, all of the studied compounds (**3a–s**) were predicted as Category III, or slightly toxic compounds, with  $\text{LD}_{50}$  values between 500 and 5000 mg/kg. Depending on the median toxic dose ( $\text{TD}_{50}$ ), all compounds were predicted as “non-required” or non-carcinogenic chemicals (Supplementary data, Table S6).

Toxicological properties of the studied compounds predicted by DataWarrior<sup>50</sup> indicate that all compounds have high risk for tumorigenic and irritant effects. All compounds were predicted with no risk for mutagenic effects and no risk for reproductive effects (Supplementary data, Table S7).

## 4. Conclusion

We have synthesized nineteen esters of eugenol, of which four represent new compounds (**3l**, **3n**, **3p** and **3r**). All of the compounds were employed in antimicrobial bioassay, with several compounds tested for the first time in antibacterial (**3b–d**, **3g–r**) and all of the compounds (**3a–s**) ever tested in antifungal activity bioassay. The results have indicated microorganisms' selective susceptibility, with *B. subtilis* (**3d**, **3l**, **3n–r**), *S. aureus* (**3e** and **3f**), *C. albicans* (**3d**, **3f**, **3n**, **3r–s**) and *A. niger* (**3f**, **3s**) as the most susceptible ones, with minimal inhibitory or cidal concentrations (MIC/MBC/MFC) never exceeding the range of activity of eugenol as the parent compound. Based on current results and on our previously published ones,<sup>43</sup> having in best case comparable but never greater MIC values than for parent phenolic compound we could not confirm results obtained by previous groups.<sup>29–31</sup> Our results have shown the importance of free phenolic hydroxyl group in terms of activity against microbials, however more detailed research should be conducted involving also a more



complex viewpoint, as for instance, the disclosure of mechanism of action of eugenyl esters on bacteria and fungi.

The results of our *in silico* study have shown that compounds fulfilling Lipinski's rule of five are **3a–h** and **3s** and were predicted to have good oral bioavailability. All of the studied compounds were predicted as to be able to pass through blood-brain barrier capable of being absorbed by intestine and permeable across Caco-2 cells. Metabolic properties differ within the studied compounds, depending on whether they act as substrate and/or inhibitor of various CYP450 enzymes. Compounds **3a–s** were predicted as weak hERG inhibitors, non-AMES toxic and non-carcinogenic, but highly toxic for fish, *T. pyriformis* and honey bee. Further, they were predicted as Category III of risk for acute oral toxicity, as well as compounds with high risk for tumorigenic and irritant effects. Finally, they exhibited at least two structural alerts for both DNA and protein binding, indicating their ability to act as a mutagen or a genotoxic.

Taking in consideration predicted *in silico* properties and estimated drug likeness score, pharmacological and toxicological profile, eugenyl esters might be used as prodrugs of eugenol due to an expected enhanced lipophilicity<sup>53</sup> and passive membrane transport.

## 5. Acknowledgement

The authors acknowledge the Ministry of Science and Technological Development of Serbia for financial support (projects 451-03-821/2012-14, 172044 and 172047) as well as internal project of Faculty of Medicine, University of Niš (project no. 4).

## 6. References

1. T. B. de Souza, M. Orlandi, L. F. L. Coelho, L. C. C. Malaquias, A. L. T. Dias, R. R. de Carvalho, N. C. Silva, D. T. Carvalho, *Med. Chem. Res.* **2014**, *23*, 496–502. DOI:10.1007/s00044-013-0669-2
2. P. M. Dewick, Medicinal natural products: a biosynthetic approach, second edition, John Wiley & Sons Ltd, Baffins Lane, Chichester, West Sussex, PO19 1UD, England, **2002**.
3. T. Koeduka, E. Fridman, D. R. Gang, D. G. Vassão, B. L. Jackson, C. M. Kish, I. Orlova, S. M. Spassova, N. G. Lewis, J. P. Noel, T. J. Baiga, N. Dudareva, E. Pichersky, *Proc. Natl. Acad. Sci. U. S. A.* **2006**, *103*, 10128–10133. DOI:10.1073/pnas.0603732103
4. H. Surburg, J. Panten, Common fragrances and flavor materials: preparation, properties and uses, 5<sup>th</sup> edition, Wiley-VHC Verlag GmbH & Co. KGaA, **2006**. DOI:10.1002/3527608214
5. T. S. Kaufman, *J. Braz. Chem. Soc.* **2015**, *26*, 1055–1085.
6. L. I. Paula-Freire, G. R. Molska, M. L. Andersen, E. L. Carlini, *Planta Med.* **2016**, *82*, 211–216.
7. S. A. Guenette, F. Beaudry, J. F. Marier, P. Vachon, *J. Vet. Pharmacol. Therap.* **2006**, *29*, 265–270. DOI:10.1111/j.1365-2885.2006.00740.x
8. S. Lahloua, A. F. Figueiredo, P. J. C. Magalhaes, J. H. Leal-Cardoso, P. D. Gloria, *Life Sci.* **2004**, *74*, 2401–2412. DOI:10.1016/j.lfs.2003.09.063
9. M. E. Hidalgo, C. de la Rosa, H. Carrasco, W. Cardona, C. Gallardo, L. Espinoza, *Quim. Nova* **2009**, *32*, 1467–1470. DOI:10.1590/S0100-40422009000600020
10. I. Gülçin, *J. Med. Food* **2011**, *14*, 975–985. DOI:10.1089/jmf.2010.0197
11. M. d'Avila Farias, P. S. Oliveira, F. S. Dutra, T. J. Fernandes, C. M. de Pereira, S. Q. de Oliveira, F. M. Stefanello, C. L. Lencina, A. G. Barschak, *J. Pharm. Pharmacol.* **2014**, *66*, 733–746. DOI:10.1111/jphp.12197
12. A. N. Daniel, S. M. Sartoretto, G. Schmidt, S. M. Caparroz-Assef, C. A. Bersani-Amado, R. K. N. Cuman, *Braz. J. Pharmacogn.* **2009**, *19*, 212–217. DOI:10.1590/S0102-695X2009000200006
13. H. Sadeghian, S. M. Seyedi, M. R. Saberi, Z. Arghiania, M. Riazia, *Bioorg. Med. Chem.* **2008**, *16*, 890–901. DOI:10.1016/j.bmc.2007.10.016
14. M. Machado, A. M. Dinis, L. Salgueiro, J. B. A. Custodio, C. Cavaleiro, M. C. Sousa, *Exp. Parasitol.* **2011**, *127*, 732–739. DOI:10.1016/j.exppara.2011.01.011
15. T. Ueda-Nakamura, R. R. Mendonca-Filho, J. M. Morgado-Diaz, P. K. Maza, B. P. Dias Filho, D. A. G. Cortez, D. S. Alviano, M. S. S. Rosa, A. H. C. S. Lopes, C. S. Alviano, C. V. Nakamura, *Parasitol. Int.* **2006**, *55*, 10–99. DOI:10.1016/j.parint.2005.10.006
16. H. Kabuto, M. Tada, M. Kohno, *Biol. Pharm. Bul.* **2007**, *30*, 423–427. DOI:10.1248/bpb.30.423
17. D. P. Bezerra, G. C. G. Militão, M. C. de Moraes, D. P. de Sousa, *Nutrients* **2017**, *9*, 1–15. DOI:10.3390/nu9121367
18. P. K. Awasthi, S. C. Dixit, N. Dixit, A. K. Sinha, *J. Pharm. Res.* **2008**, *1*, 215–220.
19. R. Ghosh, N. Nadiminty, J. E. Fitzpatrick, W. L. Alworth, T. J. Slaga, A. P. Kumar, *J. Biol. Chem.* **2005**, *280*, 5812–5819. DOI:10.1074/jbc.M411429200
20. L. Fangjun, Y. Zhijia, *Thorac. Cancer* **2018**, *9*, 25–29. DOI:10.1111/1759-7714.12508
21. A. Marchese, R. Barbieri, E. Coppo, I. E. Orhan, M. Daglia, S. F. Nabavi, M. Izadi, M. Abdollahi, S. M. Nabavi, M. Ajami, *Crit. Rev. Microbiol.* **2017**, *43*, 668–689. DOI:10.1080/1040841X.2017.1295225
22. D. R. Gang, J. Wang, N. Dudareva, K. H. Nam, J. E. Simon, E. Lewinsohn, E. Pichersky, *Plant Physiol.* **2001**, *125*, 539–555. DOI:10.1104/pp.125.2.539
23. K. Chaieb, T. Zmantar, R. Ksouri, H. Hajlaoui, K. Mahdouani, C. Abdelly, A. Bakhrouf, *Mycoses* **2007**, *50*, 403–406. DOI:10.1111/j.1439-0507.2007.01391.x
24. S. Hemaiswarya, M. Doble, *Phytomedicine* **2009**, *16*, 997–1005. DOI:10.1016/j.phymed.2009.04.006
25. E. Pinto, L. Vale-Silva, C. Cavaleiro, L. Salgueiro, *J. Med. Microbiol.* **2009**, *58*, 1454–1462. DOI:10.1099/jmm.0.010538-0

26. I. A. Freires, C. Denny, B. Benso, S. M. de Alencar, P. L. Rosalen, *Molecules* **2015**, *22*, 7329–7358. DOI:10.3390/molecules20047329
27. H. Carrasco, M. Raimondi, L. Svetaz, M. Di Liberto, M. V. Rodriguez, L. Espinoza, A. Madrid, S. Zacchino, *Molecules* **2012**, *17*, 1002–1024. DOI:10.3390/molecules17011002
28. P. H. O. Abrao, R. B. Pizi, T. B. De Souza, N. C. Silva, A. M. Fregnan, F. N. Silva, L. F. L. Coelho, L. C. C. Malaquias, A. L. T. Dias, D. F. Dias, M. P. Veloso, D. T. Carvalho, *Chem. Biol. Drug Des.* **2015**, *86*, 459–465. DOI:10.1111/cbdd.12504
29. T. B. de Souza, K. M. de Oliveira Brito, N. C. Silva, R. P. Rocha, G. F. de Sousa, L. P. Duarte, L. F. L. Coelho, A. L. T. Dias, M. P. Veloso, D. T. Carvalho, D. F. Dias, *Chem. Biol. Drug Des.* **2016**, *87*, 83–90. DOI:10.1111/cbdd.12625
30. D. B. Resende, H. H. de Abreu Martins, T. B. de Souza, D. T. Carvalho, R. H. Piccoli, R. F. Schwan, D. R. Dias, *Food Chem.* **2017**, *237*, 1025–1029. DOI:10.1016/j.foodchem.2017.06.056
31. G. Zengin, *Chem. Nat. Compd.* **2011**, *47*, 550–555. DOI:10.1007/s10600-011-9994-1
32. V. Chiaradia, N. Paroul, R. L. Cansian, C. V. Júnior, M. R. Detofol, L. A. Lerin, J. Vladimir Oliveira, D. Oliveira, *Appl. Biochem. Biotechnol.* **2012**, *168*, 742–751. DOI:10.1007/s12010-012-9814-5
33. N. S. Radulović, M. Z. Mladenović, P. D. Blagojević, Z. Z. Stojanović-Radić, T. Ilić-Tomić, L. Senerović, J. Nikodinić-Runić, *Food Chem. Toxicol.* **2013**, *62*, 554–565. DOI:10.1016/j.fct.2013.09.017
34. D. P. Bezerra, G. C. Gadelha Militão, M. C. de Moraes, D. P. de Sousa, *Nutrients* **2017**, *9*, pii: nu9121367. DOI:10.3390/nu9121367
35. L. Kamadatu, M. Santoso, Synthesis and Cytotoxicity of 4-Allyl-2 Methoxyphenol Derivatives, <http://iptek.its.ac.id/index.php/jps/article/view/1166/1026>, (Accessed: March 10, 2018).
36. H. A. Carrasco, L. C. Espinoza, V. Cardile, C. Gallardo, W. Cardona, L. Lombardo, K. M. Catalán, M. F. Cuellar, A. Russo, *J. Braz. Chem. Soc.* **2008**, *19*, 543–548. DOI:10.1590/S0103-50532008000300024
37. J. D. F. Barbosa, V. B. Silva, P. B. Alves, G. Gumina, R. L. C. Santos, D. P. Sousae, S. C. H. Cavalcanti, *Pest Manag. Sci.* **2012**, *68*, 1478–1483. DOI:10.1002/ps.3331
38. M. R. C. Raja, A. B. Velappan, D. Chellappan, J. Debnath, S. K. Mahapatra, *Eur. J. Med. Chem.* **2017**, *139*, 503–518. DOI:10.1016/j.ejmech.2017.08.030
39. H. C. Brown, *J. Am. Chem. Soc.* **1938**, *60*, 1325–1328. DOI:10.1021/ja01273a014
40. W. G. Rose, *J. Am. Chem. Soc.* **1947**, *69*, 1384–1387. DOI:10.1021/ja01198a043
41. J. Paolini, A. Muselli, A. F. Bernardini, A. Bighelli, J. Casanova, J. Costa, *Flavour Fragr. J.* **2007**, *22*, 479–487. DOI:10.1002/ffj.1824
42. D. Pavlović, B. Modec, D. Dolenc, *Acta Chim. Slov.* **2015**, *62*, 362–370. DOI:10.17344/acsi.2014.1306
43. J. Lazarević, A. Kolarević, A. Đorđević, G. Stojanović, A. Šmelcerović, P. Ciuffreda, E. Santaniello, *Acta Chim. Slov.* **2017**, *64*, 603–612. DOI:10.17344/acsi.2017.3356
44. A. E. Díaz-Alvarez, P. Crochet, V. Cadierno, *Tetrahedron* **2012**, *68*, 2611–2620. DOI:10.1016/j.tet.2012.01.083
45. H. Van den Dool, P. D. Kratz, *J. Chromatogr. A* **1963**, *11*, 463–471. DOI:10.1016/S0021-9673(01)80947-X
46. NCCLS, Performance Standards for Antimicrobial Susceptibility Testing: Eleventh Informational Supplement, M100-S11. **2003**, National Committee for Clinical Laboratory Standards, Wayne, PA.
47. S. A. Sarker, L. Nahar, Y. Kumarasamy, *Methods* **2007**, *42*, 321–324. DOI:10.1016/j.jymeth.2007.01.006
48. Molinspiration Home Page. <http://www.molinspiration.com/> (Accessed January 2018).
49. admetSAR Home Page. <http://lmmd.ecust.edu.cn:8000/predict/> (Accessed January 2018).
50. DataWarrior Home Page. <http://www.openmolecules.org/datawarrior/> (Accessed January 2018).
51. G. Patlewicz, N. Jeliazkova, R. J. Safford, A. P. Worth, B. Aleksiev, *Environ. Res.* **2008**, *19*, 495–524.
52. C. A. Lipinski, F. Lombardo, B. W. Dominy, P. J. Feeney, *Adv. Drug Deliv. Rev.* **2012**, *64*, 4–17. DOI:10.1016/j.addr.2012.09.019
53. D. Yancheva, E. Cherneva, M. Quick, B. Mikhova, B. Shvachev, R. Nikolova, A. Djordjevic, M. Untergehrer, G. Jürgenliemk, B. Kraus, A. Smelcerovic, *Acta Chim. Slov.* **2015**, *62*, 689–699. DOI:10.17344/acsi.2015.1418

## Povzetek

Rezultati, predstavljeni v tem članku, so nadaljevanje naših študij modifikacij molekul naravnega izvora, s posebnim poudarkom na aciliranju fenolne funkcionalne skupine. Pripravili smo majhno, fokusirano knjižnico devetnajstih estrov evgenola, od katerih so štiri nove spojine. Z vsemi spojinami smo izvedli *in vitro* antimikrobno testiranje. Z *in silico* računskimi študijami smo napovedali fizikalno-kemijske, farmakokinetične in toksikološke lastnosti, kar daje dodatne podatke za boljše usmerjanje raziskav v prihodnosti.

Scientific paper

# Determination of Atomoxetine Hydrochloride in Biological Fluids Using Potentiometric Carbon Paste Electrode Modified by TiO<sub>2</sub> Nanoparticles

Hazem M. Abu Shawish,<sup>1,\*</sup> Hassan Tamous,<sup>2</sup> Salman M. Saadeh<sup>3</sup>  
and Ahmad Tbaza<sup>2,4</sup>

<sup>1</sup> Chemistry Department, College of Sciences, Al-Aqsa University, Gaza, Palestine

<sup>2</sup> Chemistry Department, Al-Azhar University, Gaza, Palestine

<sup>3</sup> Chemistry Department, The Islamic University, Gaza, Palestine

<sup>4</sup> Arab Germany Pharmaceutical Company, Gaza, Palestine

\* Corresponding author: E-mail: hazemona1@yahoo.co.uk

Received: 28-03-2018

## Abstract

Endeavors to improve the limit of detection for atomoxetine-selective electrode were documented. Simple potentiometric carbon paste electrodes (CPEs) based on atomoxetine-derivatized with tetraphenylborate (ATM-TPB) or phosphotungstic acid (ATM-PTA) as ion-pairs decorated with TiO<sub>2</sub> nanoparticles and sodium tetraphenylborate (Na-TPB) as additives were most useful. Parameters affecting the performance of the electrodes were investigated, such as paste composition, type of plasticizers, kind of electroactive materials and interfering species. The electrodes were notable for bringing down the detection limit to  $8.0 \times 10^{-7}$  M and  $9.2 \times 10^{-7}$  M, wide linear ranges  $1.1 \times 10^{-6}$ – $1.0 \times 10^{-2}$  M and  $1.75 \times 10^{-6}$ – $1.00 \times 10^{-2}$  M, slope  $58.7 \pm 0.5$  mV/decade and  $67.2 \pm 0.8$  mV/decade, respectively. Importantly, the potential reading became more stable and rapidly attained in the presence of additives. The selectivity for the drug over other species such as inorganic and organic cations, as well as different excipients that are likely incorporated in pharmaceutical preparations was high making their effect negligible on the response of the electrodes. The sensors, as indicator electrodes, were successfully applied for determination of the drug in pharmaceutical preparation, urine and serum with good accuracy, excellent recovery and efficiency.

**Keywords:** Atomoxetine-ion selective electrodes; carbon paste electrode; nanoparticles; ion-pairs

## 1. Introduction

Determination of drug species in real samples such as biological and pharmaceutical samples is an important branch of analytical chemistry for clinical, quality production control and other applications.<sup>1–4</sup> Atomoxetine hydrochloride (Fig. 1), is designated chemically as (-)-*N*-methyl-3-phenyl-3-(*o*-tolylxy)-propylamine hydrochloride. Atomoxetine is a white solid that exists as a granular powder inside the capsule along with pregelatinized starch and dimethicone.<sup>5–7</sup> Atomoxetine is the first non-stimulant drug approved for the treatment of attention-deficit hyperactivity disorder (ADHD) with no associated side effects. However, cases of chronic overdose and acute and lethal poisoning by atomoxetine were registered.<sup>8,9</sup>

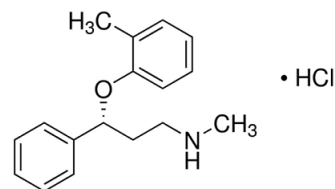


Fig 1. The chemical structure of atomoxetine hydrochloride

Therefore, estimation of trace amounts of atomoxetine in various media is necessary.

Literature survey showed different methods for determination of atomoxetine that are mainly chromato-

graphic utilizing various means of detection such as: UV, colorimetric, fluorometric, mass spectrometric,<sup>10–13</sup> RP-HPLC,<sup>14,15</sup> spectrophotometry,<sup>16,17</sup> and potentiometric method.<sup>18</sup>

Comparatively, most of these methods require sample manipulations giving ways to various interferences. Moreover, they are not applicable for colored and turbid solutions. Even more, they are more expensive for they require large infrastructure backup and qualified personnel. Thus, the development of selective, sensitive, accurate and inexpensive tool for the determination of this drug is of utmost need.

Potentiometric sensors (ion-selective electrodes, ISEs) are taken as one of the simplest and oldest electrochemical techniques being attractive for numerous analyses due to the low cost and ease of implementation.<sup>19–21</sup> They have other interesting properties such as short response times, high selectivity and very low detection limits. In addition, ISEs allow nondestructive, on line monitoring of particular ions in a small volume of sample without any pretreatment. Considering these merits, ISEs are getting more attention as routine tools of chemical analysis in industry, clinical and environmental analyses.<sup>22–26</sup>

Coated-wire ion-selective electrodes that were employed to overcome the problems associated with conventional ISEs<sup>27,28</sup> still suffer some shortcomings such as giving unreliable measurements due to the fluctuation of the electric potential.<sup>29</sup> New measures must be introduced to the working electrodes to alleviate or eliminate these effects and carbon-paste electrodes (CPEs)<sup>30</sup> appear to be suitable alternatives.

Carbon paste electrodes (CPEs), one type of ISEs, combine a carbon powder with a pasting liquid (an organic binder). CPEs are superior to other types of ISEs for their favorable characteristics and advantages such as stable response, easy renewal of surface and no requirement of internal solution, and were utilized in various applications.<sup>31–35</sup> Moreover, CPEs are nontoxic and environmentally friendly making their use soaring. Modification of CPEs with nanoparticles having unique electrochemical properties showed interesting affinity toward various ions and biological molecules. The morphological structure of nanoparticles may improve diffusion of the electroactive species and improve sensitivity thus enhancing a fast response.<sup>36,37</sup>

Careful review of the literature found no reports on potentiometric determination of atomoxetine based on the carbon paste electrode modified with additives such as Na-TPB and the nanoparticles of TiO<sub>2</sub>. In the present work, carbon paste and nano-composite carbon paste electrodes were utilized for determination of atomoxetine drug in pharmaceutical preparations, as well as spiked urine and serum samples with notable selectivity, accuracy and precision. The electrodes exhibit a near-Nernstian slope, wide concentration range, low detection limit and short response time. The lowering of detection limit, wider concentration range and stability of the response are apparently due to the incorporated nanoparticles.

## 2. Materials and Methods

### 2.1. Reagents

All reagents used were of chemically pure grade. Doubly distilled water was used throughout all experiments. Atomoxetine hydrochloride was obtained from (Multi apex pharma, Cairo, Egypt) and its pharmaceutical preparations (capsules 10, 25, 40 mg and tablets 10, 25, 40 mg) were obtained from local drug stores. Silicomolybdc acid (SMA) H<sub>4</sub>[SiMo<sub>12</sub>O<sub>40</sub>] *M* = 1823 Da, silicotungstic acid (STA) H<sub>4</sub>[SiW<sub>12</sub>O<sub>40</sub>] *M* = 2878 Da, phosphomolybdc acid (PMA) H<sub>3</sub>[PMo<sub>12</sub>O<sub>40</sub>] *M* = 1825 Da, phosphotungstic acid (PTA) H<sub>3</sub>[PW<sub>12</sub>O<sub>40</sub>] *M* = 2880 Da, and sodium tetraphenylborate (Na-TPB) Na[C<sub>24</sub>H<sub>20</sub>B] *M* = 342 Da, were purchased from Sigma-Aldrich. Pure graphite powder and the plasticizers: dibutyl phthalate (DBP), dioctyl phthalate (DOP), dioctyl sebacate (DOS), tris(2-ethylhexyl) phosphate (TEPH), and bis(2-ethylhexyl) adipate (DOA) were obtained from Aldrich chemical company. In addition, ranitidine hydrochloride, tramadol hydrochloride, ephedrine hydrochloride, diclofenac potassium, glucose, galactose, fructose, sucrose, ceftriaxone sodium, gentamycin sulfate, lasix, vardenafil hydrochloride, lidocaine hydrochloride, hydralazine hydrochloride, pethidine hydrochloride, dopamine hydrochloride, dexamethasone hydrochloride, midazolam hydrochloride, tranexamic acid, furosemide, amoxicillin, and paracetamol were commercially available. Salts of inorganic cations were used in their soluble forms such as chloride or sulfate.

Titanium(IV) oxide nanopowder, 21 nm primary particle size, was obtained from Aldrich and used as received.

### 2.2. Apparatus

Potentiometric and pH measurements were performed using a Pocket pH/mV meters, (pH315i) from Wissenschaftlich-Technische Werkstätten GmbH (WTW), Weilheim, Germany. A saturated calomel electrode (SCE) was used as reference electrode and was obtained from Sigma-Aldrich Co. (St Louis, MO, USA). Electromotive force measurements with CPE were carried out with the following cell assemblies: Hg, Hg<sub>2</sub>Cl<sub>2(s)</sub>, KCl(sat.) || sample solution || carbon paste electrode.

Solutions having concentrations  $1.0 \times 10^{-7}$ – $10 \times 10^{-2}$  M were made and used to investigate performance of the electrodes with continuous stirring by recording the potential and plotting as a logarithmic function of ATM ion activities.

### 2.3. Preparation of the Ion-Pairs

An ion-pair was made from atomoxetine hydrochloride and one of the following substances: STA, SMA, PTA, PMA and Na-TPB according to a reported method<sup>38</sup> as detailed below. The ion-pairs, (ATM<sub>4</sub>-ST), (ATM<sub>4</sub>-SM), (ATM<sub>3</sub>-PT), (ATM<sub>3</sub>-PM), and (ATM-TPB), were pre-

pared by addition of 20 mL of 0.01 M ATMCl solution to 20 mL of 0.0025 M of STA, 0.0025 M of SMA, 0.0033 M of PTA, 0.0033 M of PMA, and 0.01 M of Na-TPB. The resulting precipitates were left overnight to assure complete coagulation. The products were then filtered and washed thoroughly with copious amounts of distilled water, dried at room temperature and ground to fine powders and applied as the modifiers for constructing the electrodes of atomoxetine hydrochloride.

## 2. 4. Fabrication of the Electrodes

Modified electrodes were made by mixing 0.001–0.03 g ion-exchangers, 0.0005–0.002 g Na-TPB, 0.003–0.009 g TiO<sub>2</sub> nanoparticles, and 0.260–320 g high purity graphite. These components were mixed and 0.260–0.320 g of a plasticizer was added. Thorough homogenization was then assured by careful mixing with a spatula in an agate mortar and pressing with a pestle. The produced paste was then packed in the tip of a polypropylene syringe (3 mm i.d., 0.5 mL). A copper wire conducted the current to the paste. This paste was polished by pressing on a weighing paper to a shining surface before use for potentiometric measurements without pre-soaking. It is best for such sensors to be stored in a dry and cold place until use.

## 2. 5. Effect of Interfering ions

The separate solution method (SSM)<sup>39</sup> and the modified separate solution method (MSSM)<sup>40</sup> were applied to evaluate the potentiometric selectivity factors of the electrode. In the SSM, the potential of a cell constructed from a working electrode containing the drug ions, E<sub>D</sub> and a reference electrode containing the interferent ions (E<sub>J</sub>) is measured one solution at a time. The measured potentials were used to calculate the selectivity coefficient from the following equation:

$$\log K_{D J^{z+}}^{pot} = \frac{E_J - E_D}{S} + \left(1 - \frac{Z_D}{Z_J}\right) \log a_D$$

where E<sub>J</sub> and S is the slope of the calibration graph, Z<sub>D</sub> and Z<sub>J</sub> are the charge of ATM and interfering species, respectively.

In the modified separate solution method (MSSM), the potentiometric calibration curves are measured for the drug ions (D) and interfering ions (J). A plot of the measured potentials at various concentrations of the measured species is made and used to find the potential corresponding to 1.0 M concentration by extrapolation. The selectivity coefficients are calculated from the equation:

$$\log K_{D J}^{pot} = \frac{E_J^o - E_D^o}{S_D}$$

where log K<sub>DJ</sub><sup>pot</sup> is selectivity coefficient; E<sub>J</sub><sup>o</sup> and E<sub>D</sub><sup>o</sup> are values from the extrapolation of calibration curves to log(a) = 0 for various interfering species and drug, for the studied

electrode, respectively; S<sub>D</sub> is the slope of the drug electrode.

## 2. 6. Effect of pH on the Electrode Potential

The effect of pH of the test solution on the potential values of the electrode system in solutions of different concentrations (1.0 × 10<sup>-4</sup> M and 1.0 × 10<sup>-5</sup> M) of the ATM solution was studied. Aliquots of the drug (50 mL) were transferred to a 100-mL titration cell and the tested ISE in conjunction with the SCE, and a combined glass electrode were immersed in the same solution. The pH of the solution was varied over the range of 2.0–9.0 by addition of very small volumes of (0.1 or 1.0 M) HCl and/or NaOH solution. The potential readings were plotted against the pH-values for the different analyte solutions.

## 2. 7. Determination of Atomoxetine Hydrochloride in Miscellaneous Samples

### 2. 7. 1. Potentiometric Titration Method

Real samples containing 1.5–60 mg (5 × 10<sup>-3</sup>–2 × 10<sup>-1</sup> mmol) of atomoxetine hydrochloride were potentiometrically titrated with 0.01 M Na-TPB. The end point was determined from s-shaped plot of potential versus volume of titrant.

### 2. 7. 2. Calibration Graph Method

This method involves addition of the required amounts of drug to the test solution to make 50 mL-solutions with concentrations in the range 2.0 × 10<sup>-7</sup> M–1.0 × 10<sup>-2</sup> M of the drug and the measured potential was recorded using the present sensors. A plot of the potential versus logarithm of the ATM<sup>+</sup> activity was used for determination of unknown drug concentration.

### 2. 7. 3. Analysis of the Drug in Tablets and Capsules

A few tablets were powdered, (20 capsules were emptied and mixed) then an equivalent amount of 10<sup>-4</sup> to 10<sup>-6</sup> M were dissolved and filtered. The measured potential of each solution was used to calculate the concentration of the solution from the calibration plot constructed as detailed above.

### 2. 7. 4. Determination of Atomoxetine in Spiked Human Serum and Urine Samples

Different amounts of atomoxetine and 0.5 mL plasma or 1.0 mL urine were transferred to a 50-mL volumetric flask and diluted to volume. The solution was transferred to a 100-mL beaker and subjected to the calibration curve method for determination of atomoxetine hydrochloride.

### 3. Results and Discussion

Titanium dioxide nanoparticles and sodium tetraperhenylborate as a lipophilic additive were incorporated in the atomoxetine-sensitive electrodes to utilize their electrochemical properties in improving the performance of the present electrode, namely, the detection limit, the linear range and slope of the electrodes which is shown in the results obtained from the present electrodes. These effects add up to those of the other components that exemplify the basic parts in the sensors, namely the ion-pairs, the plasticizers and carbon paste whose properties made the back bone for the response of shown in Table 1.

change kinetics and formation constants in the paste, as well as leaching and interference with existing ions. Each ion-pair is a complex of atomoxetine drug associated with STA, SMA, PMA, PTA, and Na-TPB which are high-molecular weight anions with different lipophilicities and stabilities. A few pastes with different compositions were fabricated and tested, out of which sensors ATM-TPB and ATM-PTA gave the best results. On examination of the results collected in Table 1, it is noticed that the electrodes containing zero percent modifier complexes (electrode #1) have lower sensitivity and selectivity with poor repeatability toward atomoxetine cations. Electrodes comprising various amounts of the ion-pairs, namely 0.2%, 0.5%,

**Table 1.** Response characteristics of ATM-TPB and ATM-PTA electrodes at 0.90 g/p ratio.

No.	Composition% I.P	g	(TEPh)	Slope (mV/decade)	C.R. (M)	LOD (M)	R(s)	
<b>Effect of different ion pair</b>								
<b>ATM-TPB electrode at 0.17% Na-TPB</b>								
1	–	47.50	52.50	27.7 ± 0.6	3.00 × 10 <sup>-5</sup> –1.00 × 10 <sup>-2</sup>	1.50 × 10 <sup>-5</sup>	13	
2	0.20	47.23	52.40	52.1 ± 1.0	8.00 × 10 <sup>-6</sup> –1.00 × 10 <sup>-2</sup>	7.30 × 10 <sup>-6</sup>	10	
3	0.50	47.13	52.20	59.2 ± 0.7	3.00 × 10 <sup>-6</sup> –1.00 × 10 <sup>-2</sup>	2.80 × 10 <sup>-6</sup>	10	
4	1.00	46.90	52.10	44.2 ± 0.4	3.50 × 10 <sup>-6</sup> –1.00 × 10 <sup>-2</sup>	3.10 × 10 <sup>-6</sup>	8	
5	1.00	46.83	52.00	57.9 ± 0.3	2.70 × 10 <sup>-6</sup> –1.00 × 10 <sup>-2</sup>	2.30 × 10 <sup>-6</sup>	5	
6	2.00	46.43	51.40	53.3 ± 0.5	5.40 × 10 <sup>-6</sup> –1.00 × 10 <sup>-2</sup>	4.40 × 10 <sup>-6</sup>	7	
7	3.00	45.83	51.00	52.8 ± 0.6	5.70 × 10 <sup>-6</sup> –1.00 × 10 <sup>-2</sup>	4.60 × 10 <sup>-6</sup>	10	
8	5.00	44.83	50.00	50.7 ± 1.1	4.20 × 10 <sup>-5</sup> –1.00 × 10 <sup>-2</sup>	2.50 × 10 <sup>-5</sup>	10	
<b>ATM-PTA electrode at 0.11% Na-TPB</b>								
9	0.20	47.29	52.40	53.9 ± 0.8	7.70 × 10 <sup>-6</sup> –1.00 × 10 <sup>-2</sup>	6.20 × 10 <sup>-6</sup>	12	
10	0.35	47.20	52.34	55.5 ± 0.7	1.00 × 10 <sup>-5</sup> –1.00 × 10 <sup>-2</sup>	9.20 × 10 <sup>-6</sup>	11	
11	0.50	47.20	52.30	39.7 ± 0.4	5.30 × 10 <sup>-6</sup> –1.00 × 10 <sup>-2</sup>	3.90 × 10 <sup>-6</sup>	9	
12	0.50	47.19	52.20	64.4 ± 0.6	3.60 × 10 <sup>-6</sup> –1.00 × 10 <sup>-2</sup>	2.80 × 10 <sup>-6</sup>	5	
13	1.00	46.89	52.00	73.4 ± 0.5	5.00 × 10 <sup>-5</sup> –1.00 × 10 <sup>-2</sup>	4.20 × 10 <sup>-5</sup>	10	
14	2.00	46.49	51.40	83.2 ± 0.4	8.00 × 10 <sup>-5</sup> –1.00 × 10 <sup>-2</sup>	6.50 × 10 <sup>-5</sup>	11	
15	3.00	45.89	51.00	66.8 ± 0.9	1.50 × 10 <sup>-5</sup> –1.00 × 10 <sup>-2</sup>	9.10 × 10 <sup>-6</sup>	10	
16	5.00	44.89	50.00	66.5 ± 1.2	1.10 × 10 <sup>-5</sup> –1.00 × 10 <sup>-2</sup>	8.20 × 10 <sup>-6</sup>	13	
<b>Effect of amount TiO<sub>2</sub> additive ATM-TPB electrode</b>								
				TiO <sub>2</sub>				
17	1.00	46.33	51.50	1.0	70.0 ± 1.0	3.30 × 10 <sup>-6</sup> –1.00 × 10 <sup>-2</sup>	2.60 × 10 <sup>-6</sup>	05
18*	1.00	45.83	51.00	2.0	58.7 ± 0.5	1.10 × 10 <sup>-6</sup> –1.00 × 10 <sup>-2</sup>	8.00 × 10 <sup>-7</sup>	03
19	1.00	45.33	50.50	3.0	71.1 ± 0.8	8.00 × 10 <sup>-6</sup> –1.00 × 10 <sup>-2</sup>	7.10 × 10 <sup>-6</sup>	06
<b>Effect of amount TiO<sub>2</sub> additive ATM-PTA electrode</b>								
20	0.50	46.69	51.70	1.0	63.0 ± 0.4	8.00 × 10 <sup>-6</sup> –1.00 × 10 <sup>-2</sup>	7.30 × 10 <sup>-6</sup>	09
21*	0.50	45.19	51.20	2.0	67.2 ± 0.8	1.75 × 10 <sup>-6</sup> –1.00 × 10 <sup>-2</sup>	9.20 × 10 <sup>-7</sup>	05
22	0.50	45.69	50.70	3.0	70.1 ± 0.9	6.30 × 10 <sup>-6</sup> –1.00 × 10 <sup>-2</sup>	5.90 × 10 <sup>-6</sup>	08

I.P: ion-pair, g: graphite, p: plasticizer, S: slope (mV/decade), C.R.: concentration range, LOD: limit of detection, R(s): response time(s), \* selected composition.

#### 3. 1. Effect of the Ion-Pair

The ion-pair renders selectivity to the paste by strongly bonding the target ion thus it can transport the ion across the paste of the electrode, an effect which stems from the physico-chemical properties of the composite parts of the ion-pair intentionally incorporated for their properties. More specifically, they affect solubility, ex-

1.0%, 2.0%, 3.0%, and 5.0% (w/w), were made and tested to figure out the composition of the electrode that provides the best results for use in the rest of the study. Two electrodes showed the best characteristics: one composed of 1.0% ATM-TPB, made in the stoichiometry of 1:1 (sensor #5), and the other 0.5% ATM-PTA, made in the stoichiometry of 3:1 (sensor #12). However, increase of the

amount of the modifier complex hampered the sensitivity and the working range as excess modifier changes the ratio of the ionic sites to the ionophore in the paste and possible saturation of the membrane leading to sub-Nernstian slopes.

### 3. 2. Plasticizer Selection

A plasticizer influences the detection limit, selectivity and sensitivity of the electrode. The partition coefficients of chemical species are strongly dependent on the solvation properties of the organic phase<sup>41</sup> which are mainly determined by the polarity of the plasticizer used in the electrode. In addition, the nature of the plasticizer affects both the dielectric constant of the paste and the mobility of the ionophore and its complex.<sup>42</sup> The desirable properties of a plasticizer used in the preparation of the ion-selective electrodes are: compatibility with the polymer, low volatility and low solubility in aqueous solution, low viscosity, low cost and low toxicity.<sup>43,44</sup> The plasticizers viz. DOS, DOP, DBP, TEPH, and DOA with different physical parameters, such as dielectric constant, lipophilicity, viscosity, and molecular weight ( $M$ )<sup>45,46</sup> were employed to study the effect on the electrochemical behavior of the electrodes (Fig. 2) to select the plasticizer that provides the best improvement of the electrode response. Comparatively, tris(2-ethylhexyl) phosphate (TEPh), with relatively high lipophilicity and similarity to that of the ion pair, produced the best improvement to the response, an effect that stems from its direct effect on solubility in the paste which is in line with the rule of the thumb “like dissolve like”. Therefore, it was incorporated in all mixtures utilized in characterization of the present electrode.

### 3. 3. The Graphite/Plasticizer (g/p) Ratio Study

The sensitivity and selectivity of the electrode depend on graphite/plasticizer ratio used.<sup>47</sup> Pastes comprising graphite/plasticizer ratios of 0.75–1.35 were examined. It is interesting to note that the ratio of ca. 0.90 was the best combination as it showed the optimum response as the outcome of the physical properties of the constituents that enabled high mobilities of the inherent constituents.<sup>48</sup> Pastes with g/p ratio >1.35 are crumbly and those with g/p <0.75 are not sticky enough to be workable.

### 3. 4. The Influence of Na-TPB as Anionic Additives

It is intended to improve the sensitivity of the electrode by incorporation of selected components based on their physicochemical properties that show up in the response of the sensor. As for the additives to the ingredients of the paste, it is the hydrophobicity that marks this additive and makes it compatible with other components.<sup>20</sup> Sodium tetraphenyl borate, namely, was found notably effective for this purpose. This behavior is due to tetraphenyl borate anions that repel diffusion of anions from the analyte solution, this diffusion results in a decrease of the number of the cation-anion sites in the bilayer at the membrane-analyte interphase making a smaller difference in the concentrations of this cation-anion combination at the two sides of the membrane, that consequently reduces the measured potential. These additives reduce ohmic resistance and improve response behavior and selectivity. In addition, they may catalyze the exchange kinetics at the sam-

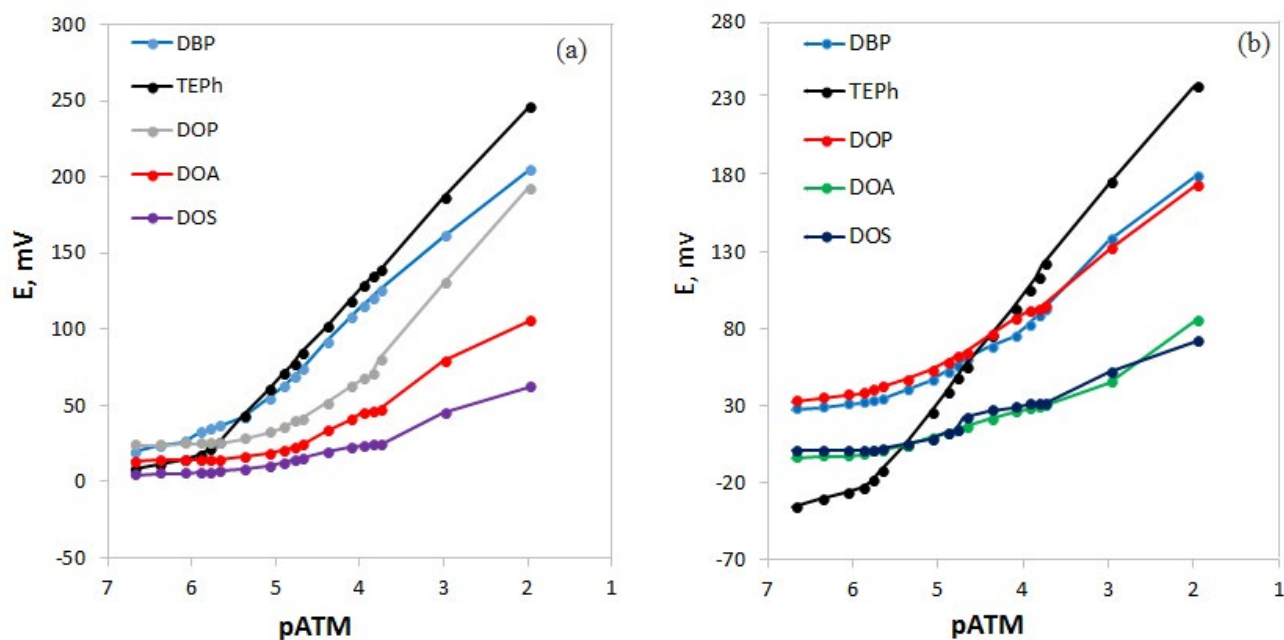


Fig 2. Effect of different plasticizers on the response of (a) ATM-TPB and (b) ATM-PTA electrodes.

ple-electrode interface.<sup>49</sup> The results collected on the present electrodes, as well as reports in the literature<sup>50,51</sup> are in line with this explanation. Electrodes containing various amounts, namely, 0.11, 0.17, and 0.33% (w/w) of Na-TPB were tested among which electrode ATM-TPB and electrode ATM-PTA containing no additive showed slopes of 44.2 and 39.7 mV per decade that were improved to 57.9 and 64.4 mV per decade on incorporation of 0.17 and 0.11% of Na-TPB to these electrodes, respectively.

### 3. 5. The Effect of TiO<sub>2</sub> Nanoparticles

Nanoparticles, as solid matrices, are important for their special properties which are currently utilized in development of the characteristics of ISEs toward stronger signals, increased sensitivity, decreased detection limit, and better reproducibility. For example, TiO<sub>2</sub> nanoparticles are non-toxic, stable, mechanically strong and biocompatible. In addition, they have large surface area and thus can act as an effective electron transfer agent. With these properties, they attracted interest of researchers around the globe for implementation in ISEs in endeavors to develop better electrodes for various purposes.<sup>36,52,53</sup> In the present work, pastes containing different amounts of TiO<sub>2</sub> nanoparticles (as given in Table 1) were incorporated in studying the effect of composition on the performance of the electrode. A lowering of the detection limit and stabilization of the potential reading was observed with the two electrodes containing 2.0% of TiO<sub>2</sub> nanoparticles as shown in Figure 3.<sup>54</sup>

### 3. 6. Effect of Diverse Ions

The selectivity coefficients are the foremost important characteristics of ISEs, informing about the ability of the sensing membrane for discrimination of the primary

ion against other ions of the same charge.<sup>55</sup> The response of the electrode to the analyte must surpass that to other substances in a way that the electrode exhibits Nernstian dependence on concentration of the primary ion over a wide concentration range. The selectivity of the electrode stems from the selectivity of the ion-exchange process at the phase boundary and the mobilities of the relevant ions in the matrix of the sensor. It is desired that an electrode has as low as possible response to all species other than that for which it was fabricated to measure. The selectivity coefficients of these electrodes toward a variety of chemical species and excipients, likely incorporated in pharmaceutical preparations, or found in biological fluids, and some of the tested species are normally taken with the prescribed drug, were evaluated by the separate solution method SSM and the modified separate solution method, MSSM. The results collected for the two methods, listed in Table 2, are clearly different and those obtained by MSSM are much better and are in line with expectations as MSSM is unbiased.<sup>56,57</sup> That entails use of an alternative approach, the modified separate solution method as described by Bakker et al.<sup>40</sup> Consequently, the results (less than 1.0) in Table 2 indicate that the effects of the interfering ions on the response of the electrodes are small which means that the inorganic cations do not interfere for they have different ionic size resulting in different mobility and permeability. Overall, similarity in the composition of the paste to that of drug ion leads to better compatibility and improved response. The results indicate that the constructed sensor displays high selectivity for ATM over common drugs.

### 3. 7. Response Time and Reversibility of the Electrodes

The time between addition of the analyte to the sample solution and the time when a limiting potential was

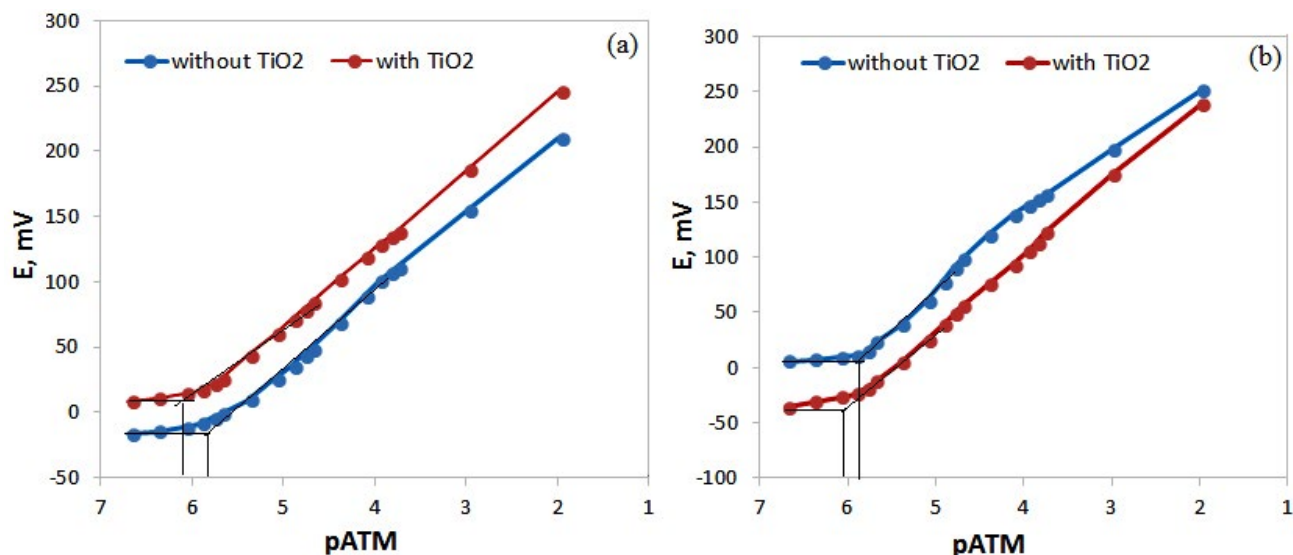


Fig. 3. Calibration graph and limit of detection of (a) ATM-TPB and (b) ATM-PTA electrodes with and without TiO<sub>2</sub> nanoparticles.



**Table 2.** Selectivity coefficients of various interfering ions for sensor ATM-TPB and sensor ATM-PTA.

Interfering species	SSM		MSSM	
	ATM-TPB	ATM-PTA	ATM-TPB	ATM-PTA
Ca(II)	-4.23	-3.45	-5.28	-4.71
Mg(II)	-4.08	-3.89	-4.33	-4.13
Cu(II)	-2.92	-2.13	-5.30	-4.32
Na(I)	-3.99	-3.36	-5.81	-4.83
K(I)	-4.04	-3.38	-5.91	-4.89
maltose	-	-	-6.29	-5.03
L-ascorbic acid	-	-	-6.35	-5.10
galactose	-	-	-6.27	-5.06
glucose	-	-	-6.07	-5.03
sucrose	-	-	-6.10	-5.00
asparagine	-	-	-6.15	-4.91
histidine	-	-	-6.28	-5.07
glycine	-	-	-6.30	-5.05
lactose	-	-	-6.32	-4.98
arginine	-	-	-5.98	-5.06
midazolam hydrochloride	-3.94	-3.48	-5.64	-5.09
dexamethasone hydrochloride	-3.92	-3.45	-5.72	-4.98
tramadol hydrochloride	-1.45	-2.08	-1.64	-2.38
tranexamic acid	-3.97	-3.48	-5.82	-5.03
pethidine hydrochloride	-1.70	-1.93	-2.06	-2.23
ranitidine hydrochloride	-3.15	-3.16	-3.25	-4.46
dopamine hydrochloride	-3.66	-3.12	-5.12	-4.46
furosemide	-4.00	-3.42	-5.88	-5.03
ephedrine hydrochloride	-2.39	-2.23	-2.57	-2.46
hydralazine hydrochloride	-2.47	-1.89	-2.74	-2.01
lidocaine hydrochloride	-1.53	-1.84	-1.90	-1.79
diclofenac potassium	-3.83	-3.31	-5.67	-4.84
vardeafil hydrochloride	-3.66	-3.45	-5.18	-5.06
amoxicillin	-3.83	-3.44	-5.36	-5.03
paracetamol	-3.90	-3.40	-5.81	-4.98
gentamycin sulfate	-2.63	-2.19	-4.04	-3.93
lasix	-2.46	-2.23	-2.66	-2.73
ceftriaxone sodium	-2.05	-1.86	-2.26	-2.31

attained, known as the response time,<sup>58</sup> was measured in accordance with the IUPAC recommendations with all relevant measurements made under the same experimental conditions. As it depends on the membrane type and the interferents, measurements of the response time are related to how quickly the layer of sample adhering to the ISE membrane can be exchanged for a new layer since potentiometric responses require ion movement over nanometers at the phase boundary of the analyte and the ion-selective membrane.<sup>59</sup> In the present contribution,  $1.0 \times 10^{-6}$  M to  $1.0 \times 10^{-2}$  M solutions were used for measurement of the response time of the electrode which reached equilibrium in  $\sim 5$  s as evident in Fig. 4a. The electrode has a long term stability as the response remains practically constant and stable for 35–40 min and starts to drop slightly following this period. The response of each electrode was checked for reversibility. The electrode potentials of  $1.0 \times 10^{-4}$  M and  $1.0 \times 10^{-5}$  M atomoxetine hydrochloride solutions were estimated alternately in the same solution after mak-

ing the proper treatment. The results, shown in Figure 4b, indicate reversibility in potentiometric responses of the sensors.

### 3. 8. Surface-Renewal and Reproducibility of the Electrode

Modified electrodes are attractive for possibility of surface renewal after every use. The slope of the calibration graph constructed for the present electrodes decreased slightly after three consequent uses which may be attributed to memory effect caused by accumulating surface contamination. Fortunately, a fresh surface of the modified electrodes can be exposed by squeezing a little carbon paste out of the tube and smoothing on a piece of weighing paper whenever needed. Accordingly, a paste of optimum composition and suitable mass ( $\sim 2.0$  g) can be used for several months to get dependable response of the electrode. The reproducibility of the new layer of the paste was

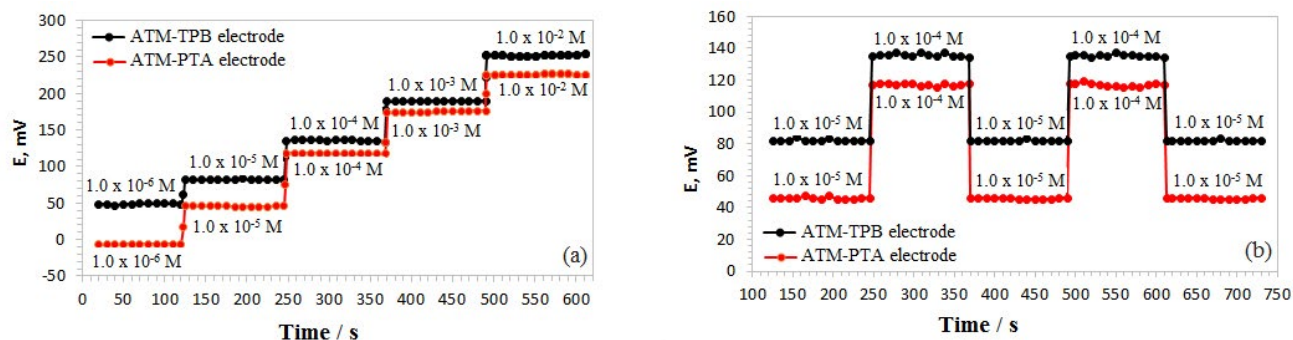


Fig. 4. (a) Typical potential-time plot for response of ATM-TPB and ATM-PTA electrodes (b) Dynamic response of the ATM-TPB and ATM-PTA electrodes for several high-to-low respective measurements.

checked by 10 successive measurements on the same surface giving a lower relative standard deviation. This indicates excellent repeatability of the potential response of the electrodes.

### 3. 9. pH Dependence

It is relevant to state that atomoxetine is a primary amine which is basic and has a pH around 9. The drug is a hydrochloride salt of the primary amine and the pH of the drug in solution lies in the range 4–5. The effect of the acidity of the solution on the response of the ATM-TPB and ATM-PTA electrodes was studied for  $1.0 \times 10^{-4}$  M and  $1.0 \times 10^{-5}$  M atomoxetine hydrochloride in the pH range of 2.0–9.0. The pH was adjusted with 0.2 M solutions of hydrochloric acid or sodium hydroxide. It is noted from Fig. 5a and Fig. 5b that the sensors can be dependently used in the pH range 4.0–7.5 providing acceptable results which clearly shows that they are not affected by slight changes of the pH of the solution in this range. PTA and TPB are components of the electrode which are not normally affected by changes of pH in this range as they are in salt forms and moreover they are components of practically insoluble ingredients of the electrode. Nevertheless, at pH 4.0 a nonlinear response was seen with slight increase in the potential. This is reasonably linked to the effect of the accumulating hydroni-

um ion on the electrode behavior. At high pH the OH<sup>-</sup> ions penetrate the paste and react with counter ions of the drug anions of the polyprotic acid. Therefore, the equilibrium is hampered and shifted to the right by consumption of some drug anions on formation of the insoluble drug in the paste with the effect of slow decrease of the ion-exchanger and a decrease in the concentration of the active species of the sensor, a similar explanation to a few recently reported sensors.<sup>60</sup>

### 3. 10. Effect of Temperature

To study the thermal stability of the electrodes, calibration curves ( $E_{\text{cell}}$  vs.  $\log [\text{drug}]$ ) were constructed at various temperatures covering the range 20–60 °C where it is noticed that the slopes of the calibration graphs remained in the Nernstian range up to 50 °C of the test solution over almost the same linear concentration ranges of the electrodes. These measurements ensure that the present electrodes are usable up to 50 °C without noticeable deviation from the Nernstian behavior, i.e. provide dependable results. However, temperatures higher than 50 °C cause significant deviations from the theoretical values. This effect is likely due to the damage of the electrode surface and probable leaching of the plasticizer due to decreasing viscosity as temperature is raised, a collective effect that shows up in lower response of the electrode.

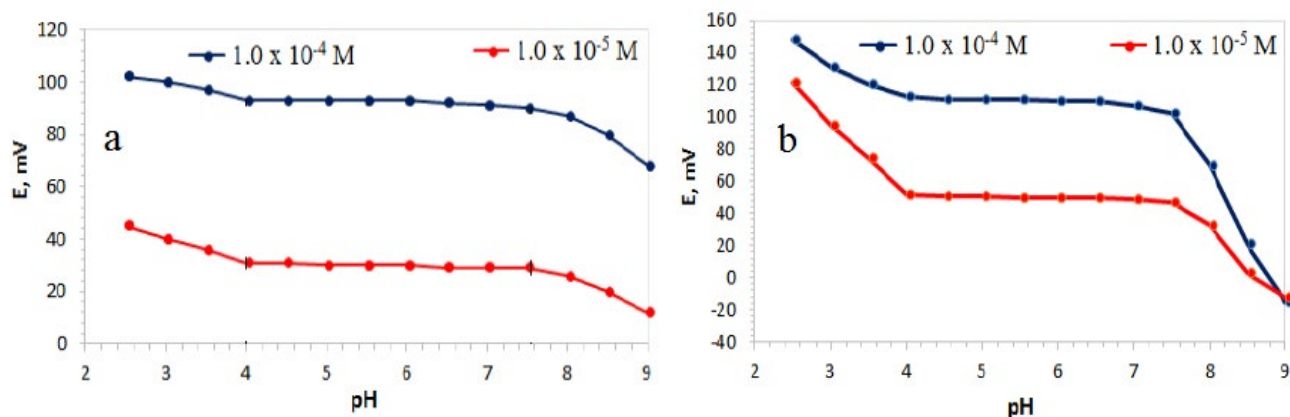


Fig. 5. Effect of pH of the test solution on the potential response of a) ATM-TPB and b) ATM-PTA.

### 3. 11. Analytical Performance

It is important to check the applicability of the present electrode for determination of atomoxetine drug in biological fluids and pharmaceutical preparations. This goal was achieved by using the calibration curve and potentiometric titration methods.

#### 3. 11. 1. Determination of Atomoxetine Drug in Tablets and Capsules

The calibration curve method was employed for determination of the drug in pharmaceutical products (tablets and capsules). The results, collected in Table 3, with the relative standard deviation of the results were calculated and found to range between 0.94% and 1.86% which is an indication of precision of the results. Moreover, percentage recovery of all the experiments was in the range

97.2% to 103% which is an indication of accuracy of the results. These results indicate dependable and successful use of the presently fabricated electrodes for the intended determinations of atomoxetine hydrochloride.

#### 3. 11. 2. Determination of Drug Ions in Urine and Serum

Atomoxetine has high aqueous solubility and biological membrane permeability that facilitates its rapid and complete absorption after oral administration. Absolute oral bioavailability ranges from 63% to 94%, which is governed by the extent of its first-pass metabolism.<sup>61</sup> A small fraction (<3%) of the dose is excreted as unchanged drug in the urine indicating minor role of renal excretion of the drug.<sup>62</sup> Calculation shows that the concentration of the drug in the blood and the urine is within the range covered

**Table 3:** Recovery of atomoxetine hydrochloride from pharmaceutical preparations and spiked biological fluids samples by ATM-TPB and ATM-PTA electrodes.

Samples	Taken (M)	Found (M)	X%	R.S.D %	F-value	t-values
<b>ATM-TPB electrode</b>						
Capsules						
	$1.00 \times 10^{-6}$	$1.01 \times 10^{-6}$	101	1.11	2.51	1.22
	$1.00 \times 10^{-5}$	$9.96 \times 10^{-6}$	99.6	1.05	2.13	1.56
	$1.00 \times 10^{-4}$	$9.79 \times 10^{-5}$	97.9	0.94	1.85	1.40
Tablet						
	$1.00 \times 10^{-6}$	$1.03 \times 10^{-6}$	103	1.41	1.98	1.38
	$1.00 \times 10^{-5}$	$9.89 \times 10^{-6}$	98.9	1.08	1.56	1.87
	$1.00 \times 10^{-4}$	$9.72 \times 10^{-5}$	97.2	1.45	2.18	2.31
Urine						
	$1.00 \times 10^{-6}$	$1.05 \times 10^{-6}$	105	1.76	2.08	2.14
	$1.00 \times 10^{-5}$	$1.02 \times 10^{-5}$	102	1.48	2.39	1.98
	$1.00 \times 10^{-4}$	$9.91 \times 10^{-5}$	99.1	1.64	3.76	2.39
Serum						
	$1.00 \times 10^{-6}$	$1.06 \times 10^{-6}$	106	1.38	4.15	3.17
	$1.00 \times 10^{-5}$	$1.04 \times 10^{-5}$	104	1.67	3.62	2.87
	$1.00 \times 10^{-4}$	$1.01 \times 10^{-4}$	101	1.44	5.98	3.28
<b>ATM-PTA electrode</b>						
Capsules						
	$1.00 \times 10^{-6}$	$9.86 \times 10^{-7}$	98.6	1.28	1.25	1.30
	$1.00 \times 10^{-5}$	$9.91 \times 10^{-6}$	99.1	1.02	1.58	1.52
	$1.00 \times 10^{-4}$	$9.87 \times 10^{-5}$	98.7	1.86	1.98	2.23
Tablet						
	$1.00 \times 10^{-6}$	$1.01 \times 10^{-6}$	101	1.07	1.77	2.45
	$1.00 \times 10^{-5}$	$9.94 \times 10^{-6}$	99.4	1.39	1.23	2.13
	$1.00 \times 10^{-4}$	$9.81 \times 10^{-5}$	98.1	1.26	2.24	1.95
Urine						
	$1.00 \times 10^{-6}$	$1.03 \times 10^{-6}$	103	1.12	3.21	2.58
	$1.00 \times 10^{-5}$	$1.01 \times 10^{-5}$	101	1.18	2.58	2.84
	$1.00 \times 10^{-4}$	$9.97 \times 10^{-5}$	99.7	1.51	3.79	3.11
Serum						
	$1.00 \times 10^{-6}$	$1.07 \times 10^{-6}$	107	1.22	4.52	3.29
	$1.00 \times 10^{-5}$	$9.73 \times 10^{-6}$	97.3	1.42	4.76	3.44
	$1.00 \times 10^{-4}$	$9.91 \times 10^{-5}$	99.1	1.36	3.95	3.08

X: recovery, M: the molar concentration of atomoxetine samples (taken), RSD relative standard deviation, the number of replicate measurements = 3. The critical value of F = 9.28 and the critical value of t = 3.707.

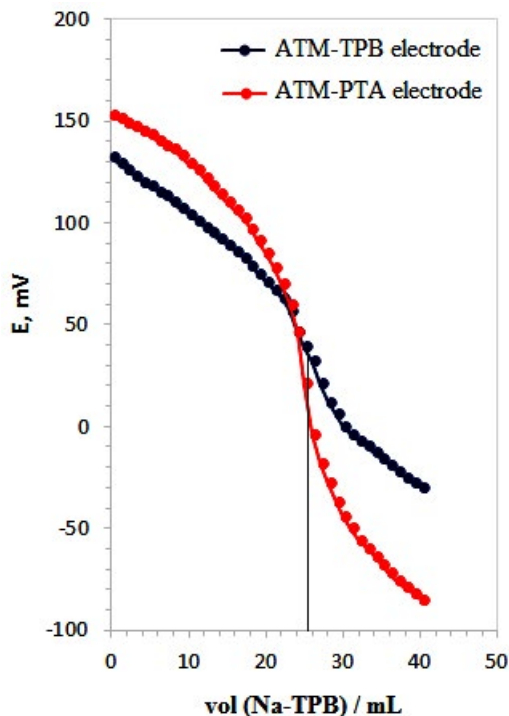


Fig. 6. Potentiometric titration curve of 25.0 mL  $1.0 \times 10^{-3}$  M atomoxetine hydrochloride solution with  $1.0 \times 10^{-3}$  M Na-TPB standard solution using ATM-TPB and ATM-PTA electrodes.

by the present electrodes suggesting that they will be useful tools to assess the drug in biological samples. Experiments were conducted by spiking urine and serum samples with appropriate amounts of ATM ions. Low volume urine (1.0 mL) and serum (0.5 mL) samples gave results with best recovery suitable for low interference. The measured potentials were used to calculate the corresponding concentrations using the calibration curve. As can be seen in Table 3, the results were acceptable and reproducible with quantitative recovery of atomoxetine showing that the proposed sensors can be employed for quantification of the drug in biological fluids.

### 3. 11. 3. Titration of Atomoxetine Hydrochloride Solution with Na-TPB Solution

Potentiometric titrations involve detection of the end-point at a drastic change in the concentrations of the reactants causing a big shift in the electrode potential. 25.0 mL-samples of  $1.0 \times 10^{-3}$  M of atomoxetine hydrochloride solution were titrated successfully against  $1.0 \times 10^{-3}$  M Na-TPB standard solution using the present electrodes ATM-TPB and ATM-PTA. The data, plot in Fig. 6, clearly show a steep potential jump at the end point indicating completeness of the titration. Na-TPB reacts with the drug forming an ion-pair complex and causes its gradual depletion in solution and concomitant drop in the corresponding measured potential. ATM-PTA sensor provided a better response (a steeper titration curve with sharper end point),

a reasonable result for having a higher molar mass and less solubility in the test solution. In brief, the present electrodes can be dependently used as indicators in determination of atomoxetine drug in solutions.

### 3. 11. 4 Statistical Treatment of Results

The results obtained for the above method were compared with the values obtained from the values from the published method.<sup>63</sup> F-test was used for comparing the precision of the two methods and t-test for comparing the accuracy.<sup>64</sup> The estimated F and t-test values in Table 3 were less than the critical (tabulated) ones. Therefore, there is no significant difference between the precisions or the accuracies of the methods at 95% confidence levels and the obtained results indicated a reasonably fair agreement of the present and official methods.

## 4. Conclusions

Two carbon paste atomoxetine-sensitive electrodes were fabricated that employ the various desired characteristics of the composite materials. Their properties comprise lower detection limits  $8.0 \times 10^{-7}$  M and  $9.2 \times 10^{-7}$  M, wider concentration ranges  $1.2 \times 10^{-6}$ – $1.0 \times 10^{-2}$  M and  $2.7 \times 10^{-6}$ – $1.0 \times 10^{-2}$  M, less interferences, and better selectivity. Importantly, these electrodes utilize small particle size, large surface and better conductivity, the favorable characteristics of  $\text{TiO}_2$  nanoparticles to effectively improve the electrode response. These electrodes effectively join the characteristics of the composite materials to fulfil the intended target, fabrication of atomoxetine-sensitive electrodes that were successfully used for determination of atomoxetine in pharmaceutical and biological samples.

## 5. References

1. M. R. Ganjali, B. Larijani and E. Pourbasheer, *Int. J. Electrochem. Sci.*, **2016**, *11*, 2119–2129
2. H. M. Abu Shawish, M. Elhabiby, H. S. Abu Azizb, S. M. Saadeh and A. Tbaza, *Sens. Actuators B*, **2016**, *235*, 18–26  
DOI:10.1016/j.snb.2016.05.058
3. H. M. Abu Shawish, K. I. Abed Almonem, S. M. Saadeh and W. S. Al-Iham, *Measurement*, **2016**, *78*, 180–186  
DOI:10.1016/j.measurement.2015.10.008
4. H. Bagheri, A. Shirzadmehr, M. Rezaei, and H. Khoshsafar, *Ionics*, **2018**, *24*, 833–843 DOI:10.1007/s11581-017-2252-1
5. G. Swathi, A. Srividya, A. Ajitha and V. U. M. Rao, *WJPPS*, **2015**, *4*, 822–890
6. K. Vijetha, A. Ramu, S. Vidyadhara and J. Subbarao, *Der Pharmacia Lettre*, **2015**, *7*, 92–97
7. W. Guo, W. Li, G. Guo, J. Zhang, B. Zhou, Y. Zhai and C. Wang, *J. Chromatogr. B*, **2007**, *854*, 128–134  
DOI:10.1016/j.jchromb.2007.04.007

8. V. A. Reed, J. K. Buitelaar, E. Anand, K. A. Day, T. Treuer, H. P. Upadhyaya, D. R. Coghill, L. A. Kryzhanovskaya and N. C. Savill, *CNS drugs*, **2016**, *30*, 603–628  
DOI:10.1007/s40263-016-0349-0
9. D. Garside, J. D. Roper-Miller and E. C. Riemer, *Journal of Forensic Sciences*, **2006**, *51*, 179–182  
DOI:10.1111/j.1556-4029.2005.00021.x
10. B. M. Ishaq, H. A. Ahad, S. Muneer and B. Praveena, *The Global Journal of Medical Research (GJMR)*, **2013**, *13*, 70–74
11. H. J. Zhu, J. S. Wang, J. L. Donovan, C. L. DeVane and J. S. Markowitz, *J. Chromatogr. B*, **2006**, *846*, 351–354  
DOI:10.1016/j.jchromb.2006.08.019
12. C. Patel, M. Patel, S. Rani, M. Nivsarkar and H. Padh, *J. Chromatogr. B*, **2007**, *850*, 356–360  
DOI:10.1016/j.jchromb.2006.12.011
13. J. H. Mullen, R. L. Shugert, G. D. Ponsler, Q. Li, B. Sundaram, H. L. Coales, J. E. Yakupkovic, R. M. Lelacheur, W. J. Wheeler, F. J. Belas and J. M. Sauer, *J. Pharm. Biomed. Anal.* **2005**, *38*, 720–733 DOI:10.1016/j.jpba.2005.02.007
14. H. R. Prajapati, P. N. Raveshiya and J. M. Prajapati, *E-Journal of Chemistry*, **2011**, *8*, 1958–1964 DOI:10.1155/2011/784807
15. R. Kota, P. Venkateswararao, A. M. S. S. Babu, M. Archana, *International Journal of Biological & Pharmaceutical Research (IJBPR)*, **2012**, *3*, 929–934
16. K. Raghobabu, L. S. Swarup, B. K. Ramu, M. Narayanarao and C. Ramdas, *Rasayan J. Che.* **2011**, *4*, 784–789
17. S. K. Koradia, P. T. Shah, R. R. Rana, S. S. Vaghani, S. Pandey and N. P. Jivani, *Asian J. Research Chem.*, **2009**, *2*, 258
18. R. A. Ammar, *Int. J. Pharm. Sci. Rev. Res.*, **2016**, *36*, 242–246
19. E. Pretsch, The new wave of ion-selective electrodes, *Trends Anal. Chem.* **2007**, *26*, 46–51
20. Y. Tani and Y. Umezawa, Ion-selective electrodes, *Sensor Letters*, **2005**, *3*, 99–107 DOI:10.1166/sl.2005.021
21. R. Yana, S. Qiu, L. Tonga and Y. Qiana, *Chem. Spec. Bioavailab.* **2016**, *28*, 72–77 DOI:10.1080/09542299.2016.1169560
22. Gastón A. Crespo, *Electrochim. Acta*, **2017**, *245*, 1023–1034  
DOI:10.1016/j.electacta.2017.05.159
23. E. M. Hussien, F. M. Abdel-Gawad and Y. M. Issa, *Biochem. Eng. J.*, **2011**, *53*, 210–215 DOI:10.1016/j.bej.2010.10.015
24. H. M. Abu Shawish, S. M. Saadeh, A. R. Al-Dalou, N. Abu Ghalwa and A. A. Abou Assi, *Mater. Sci. Eng., C*, **2011**, *31*, 300–306 DOI:10.1016/j.msec.2010.09.014
25. M. Cuartero, S. Pérez, M. S. García, F. G. Cánovas and J. A. Ortuño, *Talanta*, **2018**, *180*, 316–322  
DOI:10.1016/j.talanta.2017.12.029
26. H. M. Abu Shawish, S. M. Saadeh, H. Tamos, K. I. Abed-Almonem and O. Al khalilie, *Anal. Methods*, **2015**, *7*, 301–308  
DOI:10.1039/C4AY01986E
27. A. Ceresa, A. Radu, S. Peper, E. Bakker and E. Pretsch, *Anal. Chem.* **2002**, *74*, 4027–4036 DOI:10.1021/ac025548y
28. W. Qin, T. Zwickl and E. Pretsch, *Anal. Chem.* **2000**, *72*, 3236–3240 DOI:10.1021/ac000155p
29. N. Rubinova, K. C. Torres and E. Bakker, *Sens. Actuators B*, **2007**, *121*, 135–141 DOI:10.1016/j.snb.2006.09.007
30. B. P. Bator, L. Cabaj, R. Piech, and K. Skupien, *Anal. Chem.* **2013**, *85*, 10255–10261 DOI:10.1021/ac402885y
31. K. Vytrās, I. Švancara and R. Metelka, *J. Serb. Chem. Soc.* **2009**, *74*, 1021–1033
32. I. Švancara, A. Walcarius, K. Kalcher, K. Vytrās, *Cent. Eur. J. Chem.* **2009**, *7*, 598–656
33. H. M. Abu-Shawish, S. M. Saadeh, H. M. Dalloul, B. Najri and H. Al Athamna, *Sens. Actuators B*, **2013**, *182*, 374–381  
DOI:10.1016/j.snb.2013.03.018
34. H. M. Abu-Shawish, *Electroanalysis*, **2008**, *20*, 491–497  
DOI:10.1002/elan.200704078
35. Y. M. Issa, F. M. Abou Attia, O. E. Sherif and A. S. Abo Dena, *Arab J. Chem.*, **2017**, *10*, 751–760
36. N. Wang, F. Wang, Y. Liao, H. Liu, Y. Li and X. He, *Anal. Methods*, **2017**, *9*, 3159–3165 DOI:10.1039/C7AY00358G
37. T. A. Ali, E. M. S. Azzam, M. A. Hegazy, A. F. M. El-Faragy and Ali A. Abd-elaal, *J. Ind. Eng. Chem.*, **2014**, *20*, 3320–3328  
DOI:10.1016/j.jiec.2013.12.015
38. I. Svancara, K. Vytrās, K. Kalcher, A. Walcarius and J. Wang, *Electroanalysis*, **2009**, *21*, 7–28 DOI:10.1002/elan.200804340
39. Y. Umezawa, P. Buhlmann, K. Umezawa and K. Tohda, *Pure Appl. Chem.* **2000**, *72*, 1851–2082  
DOI:10.1351/pac200072101851
40. E. Bakker, E. Pretsch and P. Buhlmann, *Anal. Chem.* **2000**, *72*, 1127–1133 DOI:10.1021/ac991146n
41. M. A. A. Perez, L. P. Marin, J. C. Quintana and M. Y. Pedram, *Sens. Actuators B*, **2003**, *89*, 262–268  
DOI:10.1016/S0925-4005(02)00475-6
42. R. Eugster, T. Rosatzin, B. Rusterholz, B. Aebersold, U. Pedrazza, D. Riiegg, A. Schmid, U. E. Spichiger and W. Simon, *Anal. Chim. Acta.*, **1994**, *289*, 1–13  
DOI:10.1016/0003-2670(94)80001-4
43. M. O'Rourke, N. Duffy, R. D. Marco and I. Potter, *Membranes*, **2016**, *1*, 132–148 DOI:10.3390/membranes1020132
44. M. O'Rourke, R. W. Cattrall, S. D. Kolev and I. D. Potter, *Solvent Extr. Res. Dev. Jpn.*, **2009**, *16*, 1–12
45. J. K. Sears and J. R. Darby (Eds.), *The Technology of Plasticizers*, Wiley, New York, **1982**.
46. H. M. Abu-Shawish, *J. Hazard. Mater.* **2009**, *167*, 602–608  
DOI:10.1016/j.jhazmat.2009.01.018
47. A. Ensafi, S. Meghdadi, A. R. Allafchian, *IEEE Sens. J.* **2008**, *8*, 248–254 DOI:10.1109/JSEN.2007.913146
48. M. Shamsipur, M. Yousefi, M. Hosseini, M.R. Ganjali, *Anal. Chem.* **2002**, *74*, 5538–5543 DOI:10.1021/ac0110451
49. U. Schaller, E. Bakker, U. E. Spichiger and E. Pretsch, *Anal. Chem.*, **1994**, *66*, 391–398 DOI:10.1021/ac00075a013
50. Z. Yan, H. Wang, C. Xu, X. Wen, B. Gu, *J. Mol. Liq.*, **2014**, *190*, 185–189 DOI:10.1016/j.molliq.2013.11.014
51. H. M. Abu-Shawish, N. Abu Ghalwa, F. R. Zaggout, S. M. Saadeh, A. R. Al-Dalou, A. A. Abou Assi, *Biochem. Eng. J.*, **2010**, *48*, 237–245 DOI:10.1016/j.bej.2009.10.019
52. R. M. Kakhki, *Russ. J. Electrochem.* **2013**, *49*, 458–465  
DOI:10.1134/S1023193513050078
53. L. H. Ching, H. H. Yi, W. C. Yeh, L. J. Ling, C. Y. Lung, S. T. Ping, *Sens. Lett.*, **2011**, *9*, 41–45 DOI:10.1166/sl.2011.1415
54. H. Bagheri, A. Afkhami, A. Shirzadmehr and H. Khoshsafar, *J. Mol. Liq.*, **2014**, *197*, 52–57  
DOI:10.1016/j.molliq.2014.04.023

55. E. Lindner and Y. Umezawa, *Pure Appl. Chem.*, **2008**, *80*, 85–104 DOI:10.1351/pac200880010085
56. A. Radu, S. Peper, E. Bakker and D. Diamond, *Electroanalysis*, **2007**, *19*, 144–154 DOI:10.1002/elan.200603741
57. E. Bakker, *Anal. Chem.* **1997**, *69*, 1061–1069 DOI:10.1021/ac960891m
58. P. R. Buck and E. Lindner, *Pure Appl. Chem.* **1994**, *66*, 2527–2536 DOI:10.1351/pac199466122527
59. P. A. Gale and J. W. Steed, *Supramolecular Chemistry: From Molecules to Nanomaterials*, John Wiley & Sons, Ltd, 2012, ISBN: 978-0-470-74640-0. DOI:10.1002/97804706661345
60. M. Gaber, H. M. Abu Shawish, A. M. Khedr and K. I. Abed Almonem, *Mat. Sci. Eng. C*, **2012**, *32*, 2299–2305 DOI:10.1016/j.msec.2012.06.018
61. J. Sauer, B. J. Ring and J. W. Witcher, *Clinical Pharmacokinetics*, **2005**, *44*, 571–590 DOI:10.2165/00003088-200544060-00002
62. G. Yu, G. Li, and J. S. Markowitz, *Atomoxetine: J. Child Adolesc. Psychopharmacol.* **2016**, *26*, 314–326 DOI:10.1089/cap.2015.0137
63. Z. S. Abdulraheman, M. R. Patel and K. R. Patel, *IJUPBS*, **2014**, *3*, 207–242
64. J. C. Miller, J. N. Miller, *Statistics for Analytical Chemistry*, Ellis Horwood: Chichester, UK, **1984**

## Povzetek

Opisujemo raziskavo za izboljšanje mej zaznave pri elektrodi, selektivni za atomoksetin. Najbolje sta se izkazali preprosti potenciometrični elektrodi z ogljikovo pasto (CPE), osnovani na atomoksetinu, derivatiziranem z tetrafenilboratom (ATM-TPB) ali s fosfovolframovo kislino (ATM-PTA) kot ionskima paroma, z dodanimi nanodelci  $\text{TiO}_2$  in z natrijevim tetrafenilboratom (Na-TPB) kot aditivom. Raziskali smo parametre, ki vplivajo na odgovor elektrod, kot so: sestava paste, vrsta plastifikatorja, vrsta elektroaktivnega materiala in moteče zvrsti. Elektrodi sta imeli dobre karakteristike, saj so se meje zaznave spustile do  $8,0 \times 10^{-7}$  M in  $9,2 \times 10^{-7}$  M, imeli sta široko linearno območje  $1,1 \times 10^{-6}$ – $1,0 \times 10^{-2}$  M in  $1,75 \times 10^{-6}$ – $1,00 \times 10^{-2}$  M, naklon  $58,7 \pm 0,5$  mV/dekado in  $67,2 \pm 0,8$  mV/dekado. Pomembno je tudi, da je odčitek potenciala postal bolj stabilen in je bil hitreje dosežen v prisotnosti aditivov. Selektivnost za učinkovino nasproti drugim zvrstem, kot so anorganski in organski kationi, pa tudi različne pomožne snovi, ki so lahko prisotne v farmacevtskih pripravkih, je bila visoka in njihov učinek na odgovor elektrod je bil zanemarljiv. Senzorja smo kot indikatorski elektrodi uspešno uporabili za določitev učinkovine v farmacevtskih pripravkih, urinu in serumu z dobro točnostjo, izvrstnim izkoristkom in učinkovitostjo.

*Scientific paper*

# Carrier Effects on the Chemical and Physical Properties of Freeze-Dried Encapsulated Mulberry Leaf Extract Powder

William Tchabo,<sup>1</sup> Yongkun Ma,<sup>\*,1</sup> Giscard Kuate Kaptso,<sup>2</sup> Emmanuel Kwaw,<sup>1</sup> Rosine Wafo Cheno,<sup>3</sup> Meng Wu,<sup>1</sup> Richard Osae,<sup>1</sup> Shengmei Ma<sup>1</sup> and Muhammad Farooq<sup>1</sup>

<sup>1</sup> School of Food and Biological Engineering, Jiangsu University, 301 Xuefu Road, Zhenjiang 212013, P.R. China.

<sup>2</sup> Department of Social Economy and Family Management, Higher Technical Teacher's Training College (HTTTC), University of Buea, P.O Box 249 Buea Road, Kumba, Cameroon

<sup>3</sup> Department of Health Policy and Management, Jiangsu University, 301 Xuefu Road, Zhenjiang 212013, P.R. China.

\* Corresponding author: E-mail: mayongkun@ujs.edu.cn

Received: 20-04-2018

## Abstract

In this study mulberry leaf extract biocompounds were encapsulated with sodium carboxymethyl cellulose (0.55%, 0.70%, and 0.75% w/v) or maltodextrin (8%, 10%, and 12% w/v). The outcome of this work demonstrated that maltodextrin showed the highest encapsulation efficiency towards the phenolic acids and 1-deoxyojirimycin whereas the flavonols and gamma-aminobutyric acid were best encapsulated by sodium carboxymethyl cellulose. Moreover, the antioxidant properties of the encapsulated powders were found to be associated with their nutraceutical constituents. In addition, the powders produced with sodium carboxymethyl cellulose were typified by suitable hygroscopicity, wettability time, glass transition temperature, and bulk properties than those obtained with maltodextrin which was characterized by desirable porosity, water solubility, moisture content, water activity, color, particle, and flowability properties.

**Keywords:** Freeze drying, mulberry leaf; encapsulation; sodium carboxymethyl cellulose; maltodextrin

## 1. Introduction

Morus plant species possess enormous importance in economic, industrial, and domestic fields.<sup>1</sup> In Asia the plant is grown chiefly for their leaves as food for silkworms (*Bombyx mori* L.).<sup>2</sup> With the development of sericulture production and advancement in biotechnology, new mulberry varieties are increasingly in demand. However, a huge amount of the leaves are wasted by the end of the silk production cycle.<sup>2</sup> Recent studies have highlighted the health benefits of the leaf in the treatment of human ailments.<sup>3,4</sup> Nevertheless, the leaf is mostly harvested seasonally, thus making it hard to be utilized by the food and nutraceutical industries, because of their delicate structure, susceptibility to spoilage and low stability in storage. Hence, considering, the fragile nature of the leaves and the large quantities lost during postharvest handling, mulber-

ry leaf could be processed into powder to increase its economic value.

The potential industrial application of mulberry leaf powder as a functional ingredient for the food and pharmaceutical industries as an alternative solution for its post-harvest conservation of mulberry leaf is limited due to its high perishability and postharvest handling costs (storage, packing, and transport). Moreover, the high content of nutraceuticals in mulberry leaf makes its powder less soluble in water and unstable during processing, therefore leading to technical hitches in its industrial utilization,<sup>5</sup> In addition, bioactive compounds are highly susceptible to degradation when exposed to environmental conditions thus, reducing their bioavailability.<sup>6</sup> In this sense, production of an encapsulated powder from mulberry leaf extract might be an alternative to reduce the technical difficulties in its industrial application and ensure product availability.

From a food engineering perspective, encapsulation is an effectual process frequently employed in the pharmaceutical and food industries to preserve the functionality of biomolecules by entrapping the active agents in wall materials.<sup>7</sup> Encapsulation of plant extract enhance the final product quality and process capability, low-cost delivery, easy maintenance, and protect active compounds against physical and chemical stress.<sup>8</sup>

Encapsulation using freeze drying is a suitable process employed to improve the stability of thermosensitive biocompounds while preserving their biological activities.<sup>9</sup> Several encapsulating agents such as carbohydrates, cellulose derivatives, and gums have been applied in freeze drying owing to their low viscosity and high solubility.<sup>10</sup> However, each wall material has advantages and drawbacks in terms of their characteristics, which influence the properties of the encapsulated powder.<sup>11</sup>

In the last decade, encapsulation of herbal extract has been investigated by numerous scientists and it has been established that entrapment efficiency of biocompounds depends on the encapsulation conditions, such as the type and concentration of the wall material.<sup>12</sup> As reported by Da Rosa et al.,<sup>13</sup> the type of encapsulating agent is a key determinant of the functional properties of an encapsulated microparticle. Moreover, the polarity, molar mass, and functionality of the carrier significantly influence the chemical stability, solubility, physical state, and entrapment of nutraceutical compounds.<sup>14</sup> Individual nutraceutical components from different groups differ in structure, properties and may have different encapsulation trends during freeze-drying.<sup>15</sup> However, most research conducted in literature focus on the entrapment efficiency of the total polyphenol content. Howbeit, these scientific contributions are pertinent but, none of them utterly covers the encapsulation efficiency of individual nutraceuticals of the herbal extracts. Despite, numerous scientific reports on encapsulation of herbal extracts, there is still scarcity of knowledge on the impact of carrier materials on entrapment efficiency of individual nutraceutical compounds in the herbal extracts and the physical characteristics of encapsulated extract powder.

To the best of our knowledge, there are limited studies on mulberry leaf extract encapsulation. Hence, the present investigation sought to assess the effects of encapsulating materials (sodium carboxymethyl cellulose and maltodextrin) and fractions of carrier materials to core ratio on the chemical (individual nutraceuticals retention, encapsulation efficiency, and antioxidant) and physical (particle, packing, reconstitution, shelf-life, and chromatographic) characteristics of encapsulated mulberry leaf extract powder. The scientific contribution of this investigation was to valorize mulberry leaf by the development of a powder with nutraceutical value, while the technological application of encapsulating mulberry leaf extract was to preserve the physical characteristics of the powder that define its behavior during processing, storage, and handling to ensure its industrial utilization.

## 2. Materials and Methods

### 2. 1. Materials

Mulberry leaf (*Morus alba*) was acquired from Zhenjiang mulberry variety nursery base (Jiangsu, China). Maltodextrin 13-17DE (MD, ~1200 DA), sodium carboxymethyl cellulose (CMC, ~90000 DA), nutraceutical standards, and other reagents of AnalaR grade were obtained from Sigma-Aldrich (St. Louis, USA).

### 2. 2. Experimental Methodology

#### 2. 2. 1. Nutraceuticals Extraction

The extraction of nutraceutical compounds was conducted following the methodology described by Tchabo et al.<sup>16</sup> using a two-step extraction. Concisely, the fresh leaf was lyophilized (48 h, -60 °C, 0.02 mbar, FD-1A-50, Boyikang Laboratory Instruments, Beijing, China) and powdered using a jet miller (0101S Jet-O-Mizer Milling, Fluid Energy Processing and Equipment Company, Telford, USA). Subsequently, 10 g of the powder (500 mesh) was added to warm distilled water (70 °C, 400 ml) and stirred for 40 min at 300 rpm using a rotary water bath (isothermal shaker DK-600B, Jianqiao Testing Equipment, Guangdong, China). Afterward, the mixture was centrifuged (15 min/6000 g/4 °C, Beckman Avanti J-26 XP Coulter, Fullerton, California, USA), and filtered (whatman #1 paper). Then, the nutraceutical extract (NE) was kept at 4 °C in an amber flask prior to encapsulation.

#### 2. 2. 2. Nutraceutical Extract Encapsulation

The addition rate of encapsulating agents was chosen based on trials with respect to the feed mixture stability, processing cost, and encapsulated powders quality (unpublished data). Concisely, the NE and different ratio of CMC (0.55%, 0.70%, and 0.75% w/v) or MD (8%, 10%, and 12% w/v) were homogenized (Ika-Ultra-Turrax T25, China) at 25 °C for 5 min at 12000 g. The feed mixtures were then poured into a petri dish (1 cm depth), frozen at -29 °C for 24 h, and lyophilized (FD-1A-50, Boyikang Laboratory Instruments, Beijing, China) for 72 h (0.02 mbar, -60 °C). Afterwards, the freeze-dried cake was powdered (50 g/10 s/40 rpm) with a laboratory blender Mixomat mini (Fuchs Maschinen AG, Switzerland) and the encapsulated nutraceuticals powder (ENP) was stored (at 25 °C) in a vacuum sealed aluminum bag and kept in a desiccator containing silica gel prior to assay (within 2 weeks).

### 2. 3. Nutraceuticals Assay

The free nutraceuticals supernatant (non-encapsulated) and the total supernatant (within and outside the microparticles) were obtained as reported by Akbas et al.<sup>17</sup> Briefly, for the free nutraceuticals supernatant, the ENP



(500 mg) was dissolved in an ethanol and methanol mixture (1:10, 50 ml). For the total supernatant, the ENP (500 mg) was added to an ethanol, acetic acid and distilled water mixture (50:8:42, v/v, 50 ml). The mixtures were stirred (10 s) and centrifuged (9056 g/5 min/4 °C). The supernatants were used to assay the contents of nutraceutical compounds. The contents were expressed as milligram per gram of sample on a dry basis.

Nutraceutical assays were carried out according to Tchabo et al.<sup>16</sup> using an HPLC system (Shimadzu Corporation, Kyoto, Japan) constituted of a SCL-10A system controller, LC-20AB pump, DGU-20A5R degasser, SIL 20AC autosampler, CTO-20AC column oven, SPD-M20A photodiode array detector coupled with a ZORBAX-SB C18 (250 mm × 4.6mm, 5- $\mu$ m) column (Agilent, Santa Clara, USA).

### 2. 3. 1. Phenolics

Chlorogenic acid (CHA), caffeic acid (CA), kaempferol-7-O-glucoside (K7G), quercetin-3-rutinoside (Q3R), quercetin-3-O-glucoside (Q3G), kaempferol 3-(6-rhamnosylglucoside) (K3R), quercetin 3-(6-malonylglucoside) (Q3M), kaempferol-3-glucoside (K3G) and kaempferol 3-(6-malonylglucoside) (K3M) were measured as described by Tchabo et al.<sup>16</sup> Concisely, the supernatant (10  $\mu$ l) was eluted (60 min, 1 ml/min, 40 °C) with a mobile phase of acetonitrile and 0.1% formic acid (20:80). The data was recorded at 280 nm for phenolic acids and 370 nm for flavonols.

### 2. 3. 2. 1-deoxyojirimycin

1-deoxyojirimycin (DNJ) was measured as described by Tchabo et al.<sup>16</sup> Concisely, the supernatant (500  $\mu$ l) was mixed with potassium borate buffer (0.4 M, pH 8.5, 50  $\mu$ l) and 9-fluorenylmethyl chloroformate (5 mM in acetonitrile, 100  $\mu$ l). The mixture was held at 20 °C for 20 min after which glycine (50  $\mu$ l) and acetic acid (17.5 mM, 4.3 ml) were added. Then, 10  $\mu$ l of the mixture was eluted (30 min, 1 ml/min, 25 °C) with a mobile phase of acetonitrile and 0.1% acetic acid (50:50). The data was recorded at 254 nm.

### 2. 3. 3. Gamma-aminobutyric Acid

Gamma-aminobutyric acid (GABA) was measured as described by Tchabo et al.<sup>16</sup> Concisely, the supernatant (400  $\mu$ l) was mixed with potassium borate buffer (0.5 M, pH 8.5, 100  $\mu$ l) and 9-fluorenylmethyl chloroformate (3 mM in acetonitrile, 500  $\mu$ l). The mixture was held at 25 °C for 10 min after which acetic acid (1 M, 100  $\mu$ l) was added. Then, 20  $\mu$ l of the mixture was eluted (0.5 ml/min, 40 °C) with a mobile phase constituted of eluent (A) sodium acetate buffer (0.1 M, pH 5.8, 0.05% triethylamine) and eluent (B) acetonitrile (80%). The gradient was as follows: 20–

50% B (0–5 min), 50–100% B (5–10 min), 100% B (10–20 min), 100–20% B (20–25 min) and 20% B (25–35 min). The data was recorded at 262 nm.

### 2. 3. 4. Nutraceutical Retention

Nutraceutical retention (NR) was assessed according to Du et al.<sup>18</sup> as the ratio between the total content of each nutraceutical compound present in the ENP to that present in the NE. The NR was calculated as follows:

$$\%NR = \frac{((total\ content\ of\ ENP * 100))}{(total\ content)\ of\ NE}$$

### 2. 3. 5. Encapsulation Efficiency

Encapsulation efficiency (EE) was determined according to Akbas et al.<sup>17</sup> as the difference between the total content and the free content of each nutraceutical compound. The EE was calculated as follows:

$$\%EE = \frac{((total\ content - free\ content))}{(total\ content)} \times 100$$

## 2. 4. Antioxidants Assay

The antioxidant assays were performed according to Tchabo et al.<sup>16</sup> using the total supernatant. The cupric ion reducing capacity (CUPRAC), 2,2-azino-bis-(3-ethylbenzothiazoline-6-sulfonic acid) (ABTS), 1,1-diphenyl-2-picrylhydrazyl (DPPH) and ferric reducing antioxidant power capacity (FRAP) were expressed as mM of Trolox equivalent per gram of sample on dry basis.

### 2. 4. 1. ABTS

The supernatant (125  $\mu$ l) was mixed with 5 ml of ABTS solution which was constituted of 2.45 mM ABTS in ammonium persulfate (incubated in darkness for 16 hours). The mixture was held for 15 min at 25 °C and the absorbance read at 734 nm.

### 2. 4. 2. CUPRAC

The supernatant (100  $\mu$ l) was mixed with 4 ml of a solution which was constituted of neocuproine (7.5 mM), copper(II) chloride (10 mM), ammonium acetate (1M) and distilled water (1:1:1:1). The mixture was held for 60 min at 25 °C and the absorbance read at 450 nm.

### 2. 4. 3. DPPH

The supernatant (1 ml) was mixed with 6 ml of DPPH solution (60 mM in methanol). The mixture was held for 30 min at 25 °C (in darkness) and the absorbance read at 517 nm.

#### 2. 4. 4. FRAP

The supernatant (200  $\mu$ l) was mixed with 6 ml of a solution which was constituted of acetate buffer (300 mM, pH 3.6), iron(III) chloride (20 mM), TPTZ (10 mM in 40 mM HCl) (1:10:1) and distilled water (600  $\mu$ l). The mixture was held for 30 min at 37 °C and the absorbance read at 593 nm.

#### 2. 5. Particle Properties

Particle size (PS) and particle density (PD) were measured according to Santhalakshmy et al.<sup>19</sup>

PS of the ENP was measured using a Master-Sizer 3000 (Malvern Instrument Ltd, Worcestershire, UK) and expressed as geometric mean ( $d_{50}$ ). For the determination of the PD, the ENP (1 g) was added to petroleum ether (5 ml) in a graduated cylinder and stirred (5min). The cylinder was washed with petroleum ether (1 ml) and the total volume (suspended particle and petroleum ether) recorded. The PD of the ENP was calculated as follows:

$$PD = \text{powder weight/total volume of suspended particle and petroleum ether-6}$$

#### 2. 6. Packing Properties

Bulk density (BD), tapped density (TD), Hausner ratio (HR), Carr index (CI), and porosity (PO) were measured as described by Santhalakshmy et al.<sup>19</sup> Briefly, the ENP (2 g) was loaded into a graduated cylinder (10 ml) and the ratio of the mass of the ENP and the volume occupied was determined as the BD. The TD was determined, by vortexing the cylinder for 1 min and the volume occupied was used to calculate the TD. The HR, CI, and PO of the ENP were calculated as follows:

$$HR = \text{tapped density/bulk density} \quad (4)$$

$$CI = (\text{tapped density-bulk density/ tapped density}) \times 100 \quad (5)$$

$$PO = (\text{particle density-tapped density/ particle density}) \times 100 \quad (6)$$

#### 2. 7. Reconstitution Properties

Water solubility index (WSI) and wettability time (WET) were measured according to Santhalakshmy et al.<sup>19</sup> Briefly, the ENP (2.5 g) was added to distilled water (30 ml, 30 °C), vortex (15 min), and then centrifuged (9056 g, 10 min). The supernatant was collected in a petri dish and oven dried (105 °C, 8 h). The WSI of the ENP was expressed as a percentage according to the following equation:

$$WSI = (\text{dry weight of supernatant/dry weight of ENP}) \times 100 \quad (7)$$

WET was determined by recording the time for complete wetting of the ENP (1 g) deposited on the surface of the distilled water (400 ml, 25 °C).

#### 2. 8. Shelf-life Properties

Moisture content (MC), hygroscopicity (HG), glass transition temperature (GT), and water activity (WA) were measured according to Santhalakshmy et al.<sup>19</sup>

MC of the ENP was measured gravimetrically (105 °C, 24 h) and expressed as a percentage of dry basis. For the determination of the HG, the ENP (1 g) was stored (at 25 °C) for 7 days in a container containing a saturated solution of NaCl (75% relative humidity). The HG of the ENP was expressed as a percentage of 1 g of adsorbed moisture per 100 g of the sample on dry basis. The GT of the ENP was measured using a Differential Scanning Calorimeter (DSC S-650, Scinco, Seoul, Korea) calibrated with indium (156.6 °C) and purge with dry nitrogen (50 ml/min). The test was conducted from -20 °C to 200 °C (heating rate of 10 °C/min) using an empty aluminum pan as a reference. The glass transition midpoint was reported as the GT. The WA of the ENP was measured at 25 °C using a water activity meter Aqualab 4TE (Decagon Devices, Washington, USA).

#### 2. 9. Chromatic Properties

The chromatic properties of the ENP were measured using a Hunterlab colorimeter (Color Quest XE, Reston, USA) and expressed as  $L^*$  (lightness/darkness),  $a^*$  (redness/greenness), and  $b^*$  (yellowness/blueness). The chroma ( $C^*$ ) and hue ( $H^\circ$ ) were calculated as follows:

$$C^* = (a^{*2} + b^{*2})^{(1/2)} \quad (8)$$

$$H^\circ = \tan^{-1} (b^*/a^*) \quad (9)$$

#### 2. 10. Statistical Analysis

All experiment and assays were done thrice. Tukey test for statistical difference and Pearson correlation were assessed at 5% level using OriginPro 2017 (OriginLab, Northampton, USA).

### 3. Results and Discussion

#### 3. 1. Influence of Carrier Materials on Chemical Properties

##### 3. 1. 1. Influence of Carrier Materials on Nutraceuticals Retention

In order to assess the effect of the encapsulating agents on the level of NR, a comparative analysis was done between the biocompounds content of the NE and the

ENP. The ENP had similar nutraceuticals profile (phenolic acids, flavonols, DNJ and GABA) to that of the NE (Table 1). All the ENP assessed in this work presented high NR (ranging from 66.09 to 97.86%) of the targeted bioactive compounds (Fig. 1). Similar retention of phenolic compounds through freeze drying have been reported in literature.<sup>20–22</sup>

With respect to the wall material, the type of carrier was noted to have significantly ( $p < 0.0001$ ) altered the nutraceutical content. As graphically illustrated in Fig. 1, encapsulation using MD provided the highest NR of phenolic acids (96.16 to 97.86% for CHA; 88.89 to 90.45% for CA) and DNJ (95.57 to 97.80%) as compared to the CMC which resulted in the highest NR of flavonols (83.87 to 88.35% for K3M; 75.93 to 82.75% for K3R; 84.39 to 85.75% for K3G; 80.27 to 83.85% for K7G; 87.97 to 90.88% for Q3R; 91.67 to 92.89% for Q3M; 95.03 to 97.75% for Q3G, and GABA 86.67 to 92.45%). Stoll et al.<sup>23</sup> also observed differences in the retention of individual anthocyanins with different wall materials during freeze-drying of grape pomace extract. This discrepancy in NR could be attributed to the formation of complexes between the biomolecule and polysaccharides. As stated by Laine et al.,<sup>24</sup> biocompounds may form complexes with polysaccharides depending on the nature of the core compounds (hydrophil-

ic/hydrophobic character, and positive/negative charge), and the chemical structure of the carrier agent (conformational mobility and molecular size). Hence, the hydrophobic properties of CMC<sup>25</sup> could explain its better retention of flavonols and GABA, while the hydrophilic properties of MD<sup>26</sup> could account for its better retention of DNJ and phenolic acids. A similar observation has been reported by Stănciuc et al.<sup>27</sup>

Regarding the effect of addition rate of the encapsulating agent, the carrier concentration was found to have a significant effect ( $p < 0.0001$ ) on the nutraceutical content. In line with Oberoi et al.<sup>28</sup> an increase in carrier concentration resulted in a decrease in NR (Fig. 1). This might have resulted from the dilution of the nutraceutical content, due to the addition rate of wall material since the amount of NE was kept constant.

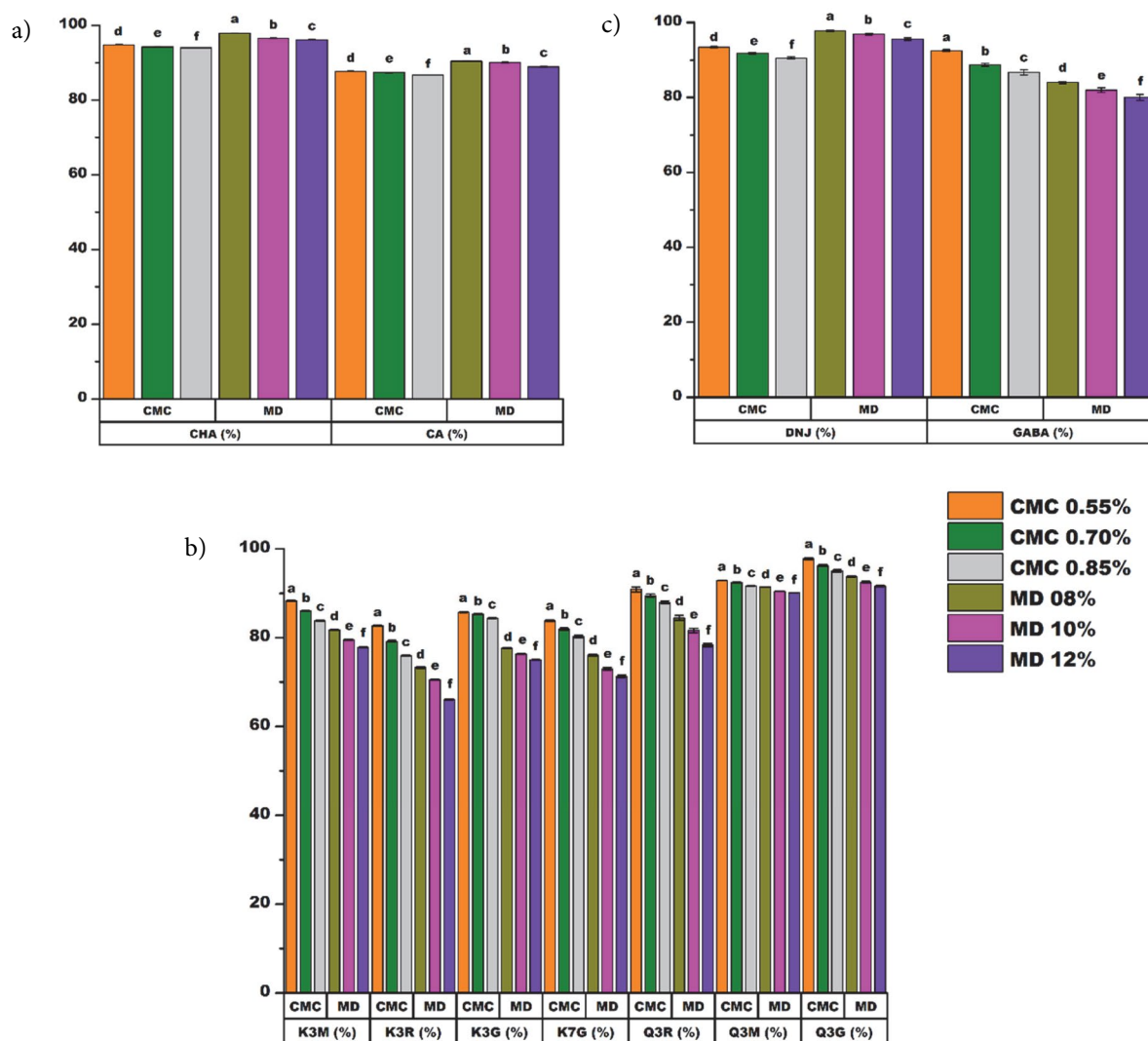
Moreover, the two-way ANOVA analysis highlighted a significant interactive effect between the type of wall material and the carrier concentration ( $p < 0.0001$  CHA and K3G;  $p < 0.001$  CA, K3R, Q3R, and Q3M;  $p < 0.05$  K3M, K7G, and GABA) on the NR. This implies that significant quantity of the nutraceuticals remained at the surface of the capsules and were probably degraded during the freeze drying. As stated by Rajabi et al.<sup>8</sup> and Garofulić et al.,<sup>15</sup> the interaction between wall material and carrier concentra-

**Table 1.** Nutraceuticals and antioxidant properties of encapsulated freeze-dried mulberry leaf extract powders

Parameters	CMC (%)			MD (%)			NE
	0.55	0.70	0.85	08	10	12	
<i>Phenolic acids (mg/g db)</i>							
CHA	58.86 ± 0.03 <sup>e</sup>	58.52 ± 0.04 <sup>f</sup>	58.37 ± 0.02 <sup>g</sup>	60.77 ± 0.03 <sup>b</sup>	59.96 ± 0.04 <sup>c</sup>	59.72 ± 0.02 <sup>d</sup>	62.10 ± 0.06 <sup>a</sup>
CA	28.25 ± 0.01 <sup>e</sup>	28.14 ± 0.03 <sup>f</sup>	27.93 ± 0.01 <sup>g</sup>	29.13 ± 0.02 <sup>b</sup>	29.00 ± 0.04 <sup>c</sup>	28.63 ± 0.04 <sup>d</sup>	32.21 ± 0.06 <sup>a</sup>
<i>Flavonols (mg/g db)</i>							
K3M	44.33 ± 0.07 <sup>b</sup>	43.18 ± 0.04 <sup>c</sup>	42.09 ± 0.06 <sup>d</sup>	41.04 ± 0.04 <sup>e</sup>	39.92 ± 0.05 <sup>f</sup>	39.06 ± 0.06 <sup>g</sup>	50.18 ± 0.12 <sup>a</sup>
K3R	35.19 ± 0.06 <sup>b</sup>	33.69 ± 0.07 <sup>c</sup>	32.29 ± 0.05 <sup>d</sup>	31.16 ± 0.09 <sup>e</sup>	29.98 ± 0.05 <sup>f</sup>	28.10 ± 0.06 <sup>g</sup>	42.52 ± 0.09 <sup>a</sup>
K3G	56.83 ± 0.05 <sup>b</sup>	56.55 ± 0.07 <sup>c</sup>	55.93 ± 0.07 <sup>d</sup>	51.47 ± 0.05 <sup>e</sup>	50.64 ± 0.07 <sup>f</sup>	49.73 ± 0.03 <sup>g</sup>	66.27 ± 0.06 <sup>a</sup>
K7G	16.18 ± 0.04 <sup>b</sup>	15.81 ± 0.05 <sup>c</sup>	15.49 ± 0.06 <sup>d</sup>	14.68 ± 0.04 <sup>e</sup>	14.09 ± 0.06 <sup>f</sup>	13.77 ± 0.05 <sup>g</sup>	19.30 ± 0.04 <sup>a</sup>
Q3R	14.26 ± 0.09 <sup>b</sup>	14.04 ± 0.05 <sup>c</sup>	13.80 ± 0.05 <sup>d</sup>	13.26 ± 0.09 <sup>e</sup>	12.81 ± 0.08 <sup>f</sup>	12.29 ± 0.06 <sup>g</sup>	15.69 ± 0.07 <sup>a</sup>
Q3M	60.55 ± 0.04 <sup>b</sup>	60.23 ± 0.06 <sup>c</sup>	59.76 ± 0.05 <sup>d</sup>	59.61 ± 0.04 <sup>e</sup>	58.99 ± 0.05 <sup>f</sup>	58.76 ± 0.04 <sup>g</sup>	65.19 ± 0.06 <sup>a</sup>
Q3G	31.65 ± 0.07 <sup>b</sup>	31.17 ± 0.07 <sup>c</sup>	30.77 ± 0.08 <sup>d</sup>	30.36 ± 0.06 <sup>e</sup>	29.96 ± 0.05 <sup>f</sup>	29.67 ± 0.05 <sup>g</sup>	32.38 ± 0.11 <sup>a</sup>
<i>Other nutraceutical compounds (mg/g db)</i>							
DNJ	14.56 ± 0.03 <sup>e</sup>	14.30 ± 0.04 <sup>f</sup>	14.10 ± 0.05 <sup>g</sup>	15.24 ± 0.03 <sup>b</sup>	15.09 ± 0.04 <sup>c</sup>	14.89 ± 0.05 <sup>d</sup>	15.58 ± 0.07 <sup>a</sup>
GABA	4.67 ± 0.01 <sup>b</sup>	4.48 ± 0.02 <sup>c</sup>	4.38 ± 0.04 <sup>d</sup>	4.24 ± 0.01 <sup>e</sup>	4.14 ± 0.03 <sup>f</sup>	4.04 ± 0.04 <sup>g</sup>	5.05 ± 0.04 <sup>a</sup>
<i>Antioxidant activities (mM/g db)</i>							
ABTS	31.58 ± 0.09 <sup>e</sup>	30.05 ± 0.20 <sup>f</sup>	29.18 ± 0.17 <sup>g</sup>	37.56 ± 0.08 <sup>b</sup>	37.04 ± 0.12 <sup>c</sup>	35.16 ± 0.12 <sup>d</sup>	39.98 ± 0.14 <sup>a</sup>
CUPRAC	53.44 ± 0.22 <sup>b</sup>	51.98 ± 0.24 <sup>c</sup>	50.95 ± 0.12 <sup>d</sup>	48.38 ± 0.18 <sup>e</sup>	47.80 ± 0.18 <sup>f</sup>	46.07 ± 0.12 <sup>g</sup>	58.93 ± 0.21 <sup>a</sup>
DPPH	89.25 ± 0.03 <sup>e</sup>	85.23 ± 0.03 <sup>f</sup>	83.27 ± 0.06 <sup>g</sup>	95.02 ± 0.06 <sup>b</sup>	94.74 ± 0.07 <sup>c</sup>	92.56 ± 0.08 <sup>d</sup>	101.33 ± 0.10 <sup>a</sup>
FRAP	219.46 ± 0.28 <sup>b</sup>	211.69 ± 0.33 <sup>c</sup>	205.26 ± 0.16 <sup>d</sup>	201.67 ± 0.13 <sup>e</sup>	200.07 ± 0.15 <sup>f</sup>	193.63 ± 0.17 <sup>g</sup>	233.77 ± 0.23 <sup>a</sup>

Values with different letters in the same row are significantly different at  $p < 0.05$  (Anova, Tukey's test)

CHA-chlorogenic acid, CA-caffeic acid, K3M-kaempferol-3-(6-malonylglucoside), K3R-kaempferol-3-(6-rhamnosylglucoside), K3G-kaempferol-3-glucoside, K7G-kaempferol-7-O-glucoside, Q3R-quercetin-3-rutinoside, Q3M-quercetin-3-(6-malonylglucoside), Q3G-quercetin-3-O-glucoside, DNJ-1-deoxynojirimycin, GABA-gamma-aminobutyric acid, ABTS-2,2-azino-bis-(3-ethylbenzothiazoline-6-sulfonic acid), CUPRAC-cupric ion reducing capacity, DPPH-1,1-diphenyl-2-picrylhydrazyl, FRAP-ferric reducing antioxidant power capacity, CMC-sodium carboxymethyl cellulose, MD-maltodextrin, and NE-nutraceutical-dried extract



**Figure 1.** Phenolic acids (a), flavonols (b), and other nutraceutical compounds (c) retention of encapsulated freeze-dried mulberry leaf extract powders

CHA-chlorogenic acid, CA-caffeic acid, K3G-kaempferol-3-glucoside, K3M-kaempferol-3-(6-malonylglucoside), K3R-kaempferol-3-(6-rhamnonylglucoside), K7G-kaempferol-7-O-glucoside, Q3G-quercetin-3-O-glucoside, Q3M-quercetin-3-(6-malonylglucoside), Q3R-quercetin-3-rutinoside, DNJ-1-deoxynojirimycin, GABA-gamma-aminobutyric acid, CMC- sodium carboxymethyl cellulose, and MD-maltodextrin

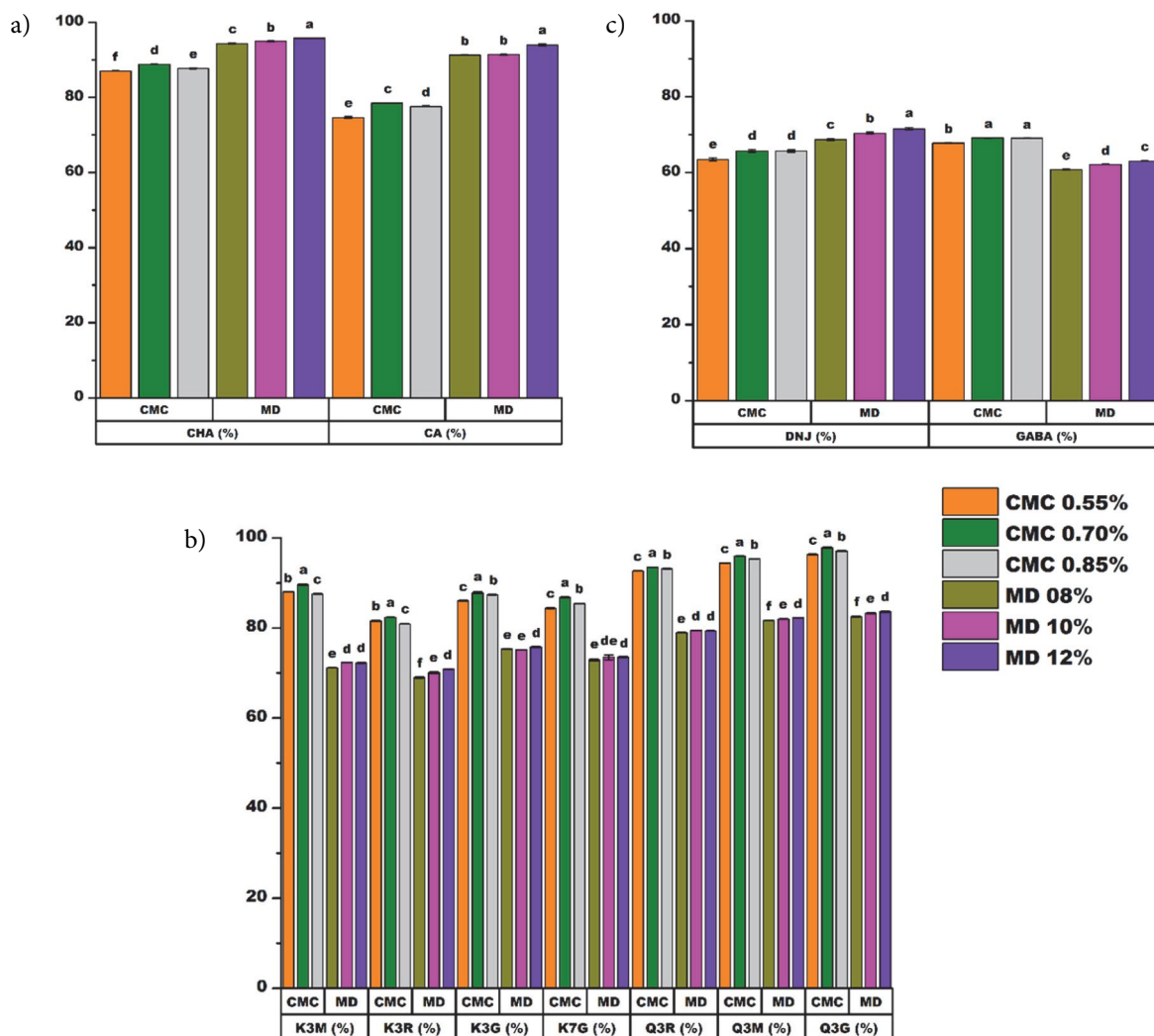
tion significantly influence the layer formation around the particles during encapsulation.

### 3. 1. 2. Influence of Carrier Materials on Encapsulation Retention

The encapsulation data (Fig. 2) shows that the entrapment of the nutraceuticals inside the matrix was significantly ( $p < 0.05$ ) dependent on the type of encapsulating agent and carrier concentration.

In terms of the carrier type, MD was more capable in encapsulating phenolic acids (94.37 to 95.79% for CHA; 91.35 to 94.00% for CA) and DNJ (68.70 to 71.54%) as compared to the CMC which had a greater ability to entrap the flavonols (87.58 to 89.64% for K3M; 80.82 to 82.36% for K3R; 86.06 to 87.87% for K3G; 84.41 to 86.82%

for K7G; 92.68 to 93.51% for Q3R; 94.45 to 95.99% for Q3M; 96.32 to 97.83% for Q3G) and GABA (67.82 to 69.15%). As reported in literature<sup>29,30</sup> the EE of biocompounds depends on the class of biocompounds and the type of coating material. Hence, this dissimilarity in EE could be ascribed to the chemical morphology of each wall material. The presence of several hydrophilic groups and shorter chains of MD makes it more appropriate for the encapsulation of the hydrophilic biocompounds (phenolic acids and DNJ) owing to the formation of solid network through electrostatic interaction.<sup>15,24</sup> Besides, the affinity of the CMC towards the flavanols and GABA might be ascribed to the formation of hydrophobic interactions which might have resulted in an increase in their solubility due to the disruption of their crystal structure.<sup>31</sup> This behavior was more evident in the entrapment of quercetin glyco-



**Figure 2.** Phenolic acids (a), flavonols (b), and other nutraceutical compounds (c) encapsulation efficiency of encapsulated freeze-dried mulberry leaf extract powders

CHA-chlorogenic acid, CA-caffeic acid, K3G-kaempferol-3-glucoside, K3M-kaempferol-3-(6-malonylglucoside), K3R-kaempferol-3-(6-rhamnonylglucoside), K7G- kaempferol-7-O-glucoside, Q3G-quercetin-3-O-glucoside, Q3M-quercetin-3-(6-malonylglucoside), Q3R-quercetin-3-rutinoside, DNJ-1-deoxyojirimycin, GABA-gamma-aminobutyric acid, CMC- sodium carboxymethyl cellulose, and MD-maltodextrin

sides (91.68 to 97.83%) than kaempferol glycosides (80.92 to 89.64%) because of the quercetin planar three-dimensional structure.<sup>15</sup>

Furthermore, the addition rate of the carriers ( $p < 0.0001$ ) and the interactive effect of the carrier concentration and the carrier type ( $p < 0.0001$  for CHA, CA, K3M, K3R, K3G, Q3M, Q3G, and GABA;  $p < 0.001$  for K7G and Q3R;  $p < 0.05$  for DNJ) significantly impact on the EE. According to Peanparkdee et al.,<sup>12</sup> an increase in carrier concentration results in an increase in EE due to the addition of more functional groups (hydrophobic/hydrophilic) which leads to more interactions (electrostatic/hydrogen bonding) between the polymer and the active compounds. Furthermore, the sublimation of water during freeze drying results in pore formation in the particles, thus resulting in a premature release of en-

trapped nutraceuticals hence their degradation.<sup>22,29</sup> As reported by some researchers,<sup>11,32,33</sup> the type of carrier affects the viscosity of the feed mixture, thus impacting on the freezing rate which is related to ice crystals formation. The larger the ice crystals, the bigger the pore diameters of the freeze-dried particles.<sup>34</sup> Therefore, as portrayed in Fig. 2, an increase in MD concentration resulted in a higher EE of the nutraceutical compounds. On the contrary, increasing the CMC concentration more than a threshold of 0.70% w/v led to a decrease in the EE of the biocompounds (Fig. 2). This behavior could be ascribed to the long-term aeration of the sample due to the high molar mass of CMC, which might have modified the viscosity of the feed mixture, thereby elongating the formation of ice crystals. Similar behavior was reported by Ogradowska et al.<sup>35</sup>

### 3. 1. 3. Influence of Carrier Materials on Antioxidant Properties

The antioxidant activities (AA) of the ENP are shown in Table 1. The type of wall material ( $p < 0.0001$ ), the core to wall ratio ( $p < 0.0001$ ), and their interaction significantly ( $p < 0.0001$  for ABTS, DPPH and FRAP;  $p < 0.05$  for CUPRAC) altered the AA of the ENP. This might be attributed to the direct correlation between the retained nutraceuticals and AA as reported by others authors.<sup>21,29</sup> This assertion was buttressed by the strong significant correlation noted between the AA and CHA (ABTS:  $r = 0.971$  and DPPH:  $r = 0.940$ ); CA (ABTS:  $r = 0.990$  and DPPH:  $r = 0.964$ ); K3M (CUPRAC:  $r = 0.990$  and FRAP:  $r = 0.981$ ); K3R (CUPRAC:  $r = 0.987$  and FRAP:  $r = 0.984$ ); K3G (CUPRAC:  $r = 0.972$  and FRAP:  $r = 0.894$ ); K7G (CUPRAC:  $r = 0.990$  and FRAP:  $r = 0.947$ ); Q3R (CUPRAC:  $r = 0.984$  and FRAP:  $r = 0.940$ ); Q3M (CUPRAC:  $r = 0.967$  and FRAP:  $r = 0.964$ ); Q3G (CUPRAC:  $r = 0.989$  and FRAP:  $r = 0.983$ ); DNJ (ABTS:  $r = 0.991$  and DPPH:  $r = 0.992$ ) and GABA (CUPRAC:  $r = 0.988$  and FRAP:  $r = 0.988$ ). Similar correlations have been reported for freeze-dried powder.<sup>29,30</sup>

## 3. 2. Influence of Carrier Materials on Physical Properties

### 3. 2. 1. Effect of Carrier Materials on Particle Properties

According to Kuck et al.,<sup>22</sup> PS of encapsulated powders depends on the concentration and the type of wall material. In agreement with this, the type of carrier agent ( $p < 0.0001$ ) and the addition rate of carrier ( $p < 0.0001$ ) significantly impacted on the PS of the ENP. As depicted in Fig. 3a, an increase in carrier concentration led to larger particle size. This could be as a result of the enhancement of the aggregation of the particles resulting from the formation of bridges between molecules due to the increase in total solid content.<sup>11,17,22</sup> The effect of the carrier type on PS may be attributed to their molecular weights which could have altered the freezing point, thereby impacting on the ice crystal size and sublimation rate hence the difference in the PS.<sup>11,32,33</sup>

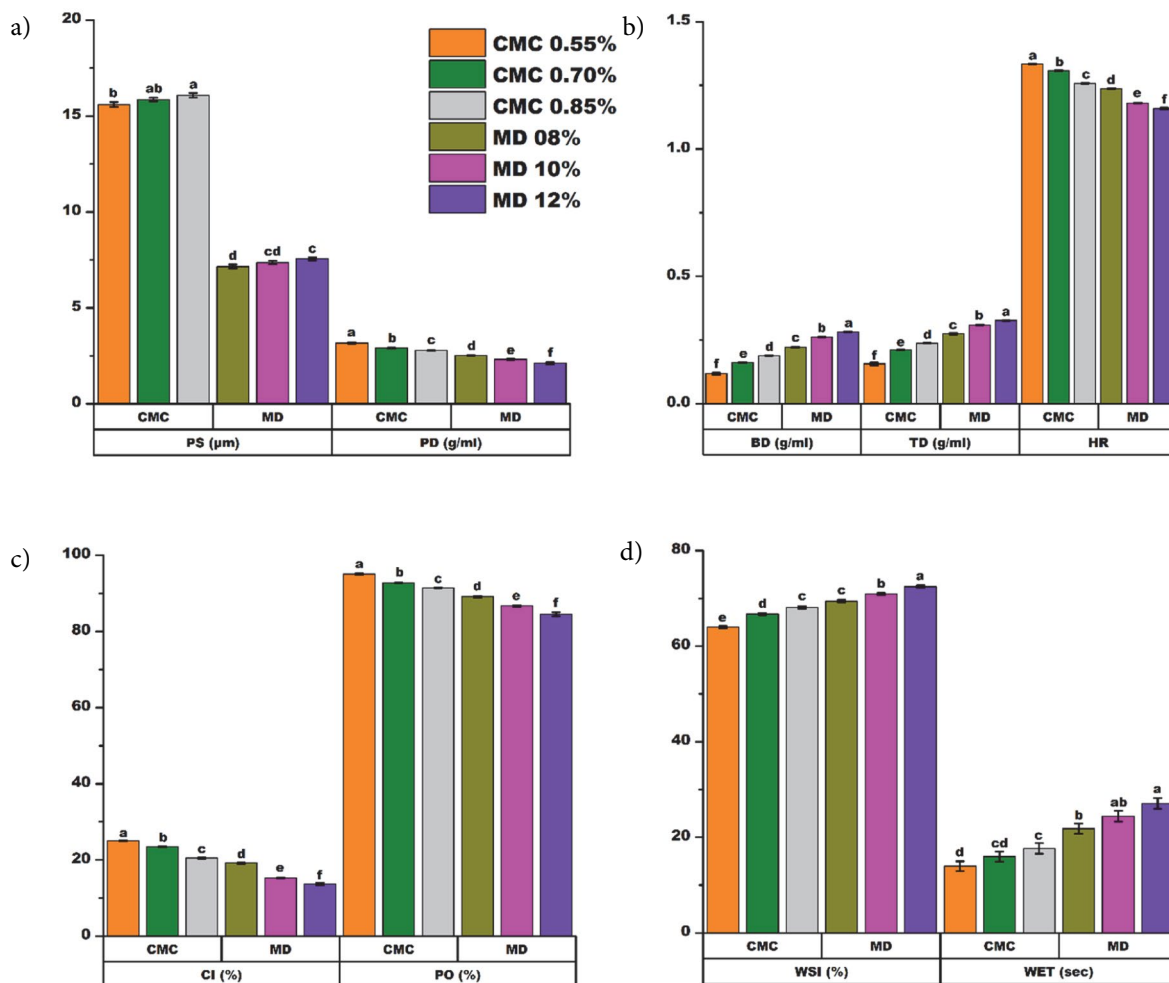
PD has been reported to be related to the viscosity and occluded air density.<sup>36</sup> Therefore, the significant effect of the carrier type ( $p < 0.0001$ ) on PD of the ENP could be attributed to the differences in their molar mass, which might have modified the viscosity of the feed mixture.<sup>37</sup> In this study, the PD was significantly influenced ( $p < 0.0001$ ) by the addition rate of the carrier. In line with Seerangurayar et al.,<sup>11</sup> increasing the concentration of the wall material resulted in lower PD (Fig. 3a). This might have resulted from the increment in occluded air in the particle, due to the increase in feed viscosity which could have resulted in particulate inflation-ballooning.<sup>38,39</sup> This statement was buttressed by the significant positive correlation between PS and PD ( $r = 0.868$ ).

### 3. 2. 2. Effect of Carrier Materials on Packing Properties

The type of encapsulating agent ( $p < 0.0001$ ), addition rate of the carrier ( $p < 0.0001$ ), and their interaction ( $p < 0.001$  for BD;  $p < 0.0001$  for TD) showed significant effect on the BD and TD of the ENP. According to Celli et al.,<sup>40</sup> the effect of encapsulating agents on BD may be ascribed to their impact on crystals formation during lyophilization. As illustrated in Fig. 3b, the BD and the TD increased with increasing proportion of the encapsulating agents. Caliskan et al.,<sup>41</sup> reported that, the residual MC of freeze-dried powder influences the BD, as particulates with higher MC might lead to incomplete dry agglomerate with bigger particles, thus resulting in a lower BD. Furthermore, the increase in TD with an increase in carrier concentration may be accredited to size enlargement of powder particles, as smaller particles could easily occupy inter-particle voids during tapping.<sup>11</sup> These assertions were buttressed by the significant negative correlations found between MC and BD ( $r = -0.989$ ) as well as PS and TD ( $r = -0.853$ ).

The wall materials ( $p < 0.0001$ ), carrier concentration ( $p < 0.0001$ ), and their interactive ( $p < 0.0001$ ) effects were found to have significantly impacted on the HR and the CI of the ENP. In line with earlier reports,<sup>11,41</sup> the HR and the CI decreased with increasing addition rate of the wall material (Fig. 3b & c). Based on the classification of powder flowability expressed as CI (very bad:  $>45\%$ , bad:  $35-45\%$ , passable:  $20-35\%$ , good:  $15-20\%$ , and excellent:  $<15\%$ ) and powder cohesiveness expressed as HR (high:  $>1.4$ , intermediated:  $1.2-1.4$ , and low:  $<1.2$ ),<sup>11,41</sup> the ENP were found to be highly cohesive with fair flowability. According to Caliskan et al.,<sup>41</sup> increase in flowability properties of lyophilized powder could be ascribed to the impact of the encapsulating agents on the MC. Moreover, the increase in PS which is related to molar mass of carrier tends to reduce the cohesion due to the reduction in particle surface area per unit mass, thus inducing lower surface area for inter-particle interactions and bonding, thereby lessening HR and resulting in an upsurge in CI.<sup>38</sup> These statements were supported by the significant positive correlation between MC ( $r = 0.975$ ;  $0.972$ ) and PS ( $r = 0.834$ ;  $0.833$ ) with HR and CI, respectively.

The type of wall material ( $p < 0.0001$ ), addition rate of the carrier ( $p < 0.0001$ ), and their interaction ( $p < 0.05$ ) significantly impacted on the PO of the ENP. PO is associated with BD since it assesses the fraction of total volume which is occupied by air.<sup>11,42</sup> According, to Seerangurayar et al.,<sup>11</sup> a negative relationship between PO and BD indicates that the amount of air incorporated into the feed mixture promoted air accumulation within the dried particles, thereby making them more porous.<sup>11</sup> Therefore, the effect of the carrier type on the PO may be credited to their skin-forming abilities. This statement was supported by the significant negative correlation between PO and BD ( $r = -0.994$ ). Moreover, as mentioned above, the ice crystal



**Figure 3.** Effect of carriers on particle, packing and reconstitution properties of encapsulated freeze-dried mulberry leaf extract powders

PS-particle size, PD-particle density, BD-bulk density, TD-tapped density, HR-Hausner ratio, CI-Carr index, PO-porosity, WSI-water solubility index, WET-wettability time, CMC-sodium carboxymethyl cellulose, and MD-maltodextrin

size which is related to the type of carrier has been reported to be associated with PO.<sup>40</sup> Hence, as shown in Fig. 3c, increasing carrier concentration led to a decrease in PO. According to Seerangurayar et al.,<sup>11</sup> high levels of carrier can cause substantial size enlargement and heavier particles, thereby filling the void spaces between agglomerates.

### 3. 2. 3. Effect of Carrier Materials on Reconstitution Properties

The encapsulating materials ( $p < 0.0001$ ), proportion of the carriers ( $p < 0.0001$ ), and their interaction ( $p < 0.05$ ) significantly alter the WSI of the ENP. According to Kuck et al.,<sup>22</sup> high WSI is related to small PS owing to the large surface area available for moisturizing. MC has been reported to be among the main factors that impacts on powder solubility, thus a lower MC results in high WSI.<sup>39</sup> Therefore, the increase in WSI with an increase in the carrier concentration (Fig. 3d) may be ascribed to the effect of

the addition rate of the encapsulating agent on PS and MC of the ENP. This was supported by the negative significant correlations between WSI and PS ( $r = -0.820$ ) as well as MC ( $r = -0.998$ ). Besides, the WSI of plant extract powder in an aqueous phase depends on the structure of the wall material.<sup>41</sup> Therefore, as depicted in Fig. 3d, the effect of the carrier type on the WSI may be due to their inherent aqueous solubility and ability to withstand hydrophobic/hydrophilic conditions.<sup>43</sup> Moreover, increase in molar mass reduces diffusivity, hence materials with low diffusivity usually have low solubility.<sup>44</sup>

Large particles form wide pores, high porosity, and small contact angles between penetrating solvent and powder surface, which swift wetting by boosting solvent penetration into agglomerate.<sup>42,45</sup> Selomulya et al.<sup>36</sup> reported that granulation positively impacts on WET. Therefore, reduction in PD that occurred at high carrier concentration leads to reduction in powder compactness which accelerated infiltration of solvent in agglomerate, thus

causing an increase in WET.<sup>46</sup> Furthermore, caking which usually happens in powders with high MC may contribute to WET since it eases the passage of water through the pores.<sup>47</sup> Hence, the significant effect of the type ( $p < 0.0001$ ) and addition rate of the wall material ( $p < 0.0001$ ) on WET of the ENP could be attributed to their effect on PS, PO, PD, and MC of the ENP. This was supported by the negative significant correlations between WET and PS ( $r = -0.899$ ), PO ( $r = -0.996$ ), PD ( $r = -0.995$ ), as well as MC ( $r = -0.973$ ). In line with Caliskan et al.,<sup>41</sup> increasing in the carrier concentration resulted in an increment in WET of the ENP (Fig. 3d).

### 3. 2. 4. Effect of Carrier Materials on Shelf-life Properties

The encapsulating agents ( $p < 0.0001$ ), addition rate of wall material ( $p < 0.0001$ ), and their interaction ( $p < 0.05$ ) had a significant effect on the MC of the ENP. A sim-

ilar observation has been reported.<sup>11, 48</sup> An increase in the addition rate of wall material resulted in a decrease in MC (Fig. 4a). This could be ascribed to the higher level of carrier concentration, which led to an increment in total solids of the feed mixture, thereby decreasing the amount of free water available for sublimation.<sup>38</sup> This finding is consistent with earlier reports on freeze dry powders.<sup>11,28,48</sup>

The HG of freeze dry powder has been reported to be related to PS. The smaller the PS, the larger the surface area exposed to the ambient air, thus leading to more water absorption.<sup>22</sup> Furthermore, carrier materials have been proven to be less hygroscopic due to their high GT.<sup>45</sup> Moreover, reduction in HG is linked to the carrier's molecular weight.<sup>11,38</sup> Hence, the significant effect of the type ( $p < 0.0001$ ), the addition rate of wall material ( $p < 0.0001$ ), and their interaction ( $p < 0.0001$ ) on the HG may be related to their effect on PS and GT of the ENP. This was supported by the negative significant correlations between HG and PS ( $r = -0.939$ ) as well as GT ( $r = -0.997$ ). Further, in ac-

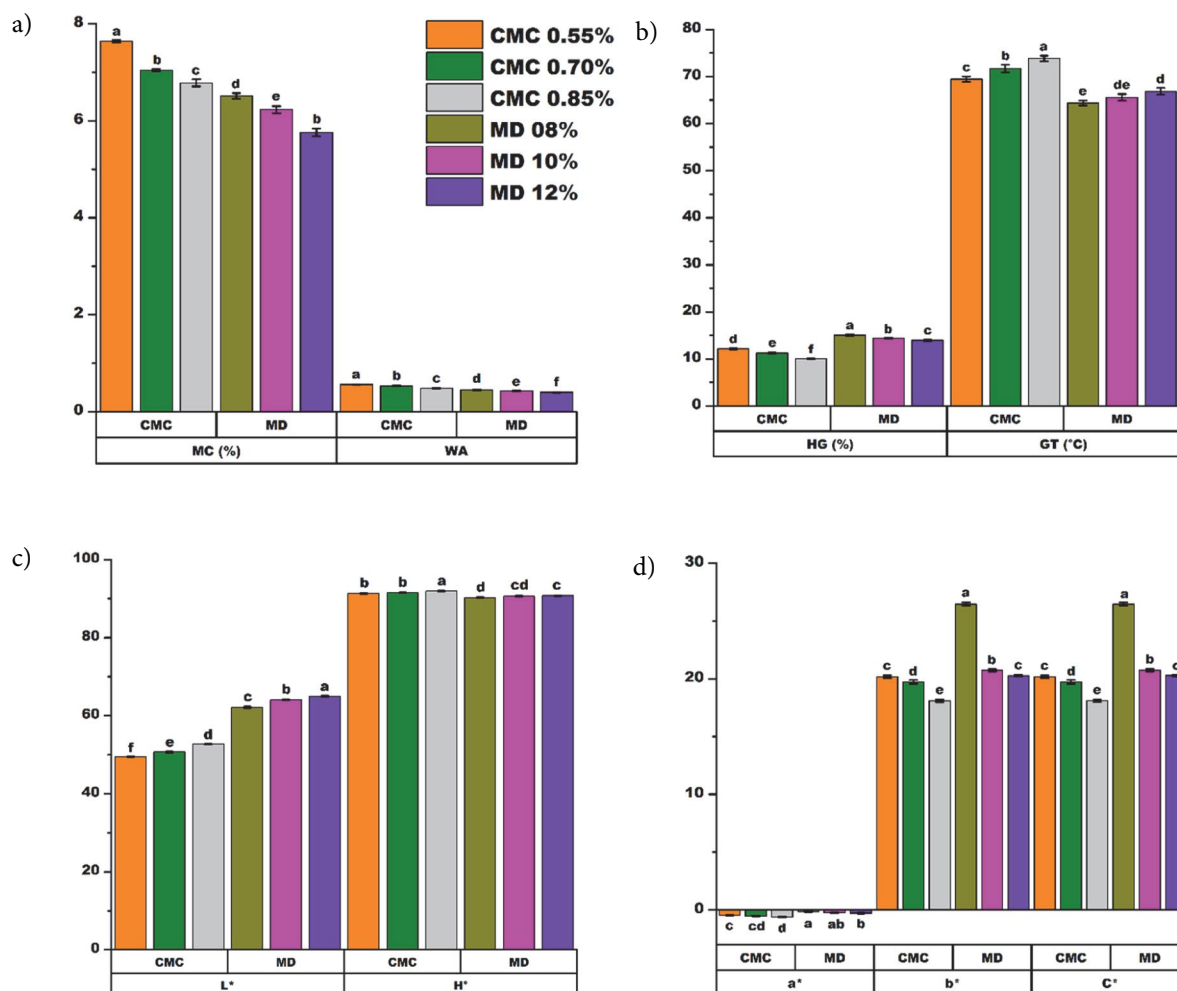


Figure 4: Effect of carriers on shelf-life and chromatic properties of encapsulated freeze-dried mulberry leaf extract powders

MC-moisture content, WA-water activity, HG-hygroscopicity, GT-glass transition temperature,  $L^*$ -lightness/darkness,  $a^*$ -redness/greenness,  $b^*$ -yellowness/blueness,  $C^*$ -chroma,  $H^*$ -Hue, CMC-sodium carboxymethyl cellulose, and MD-maltodextrin



cordance with others authors,<sup>38,45</sup> a decrease in HG was observed with an increase in the type and concentration of encapsulated agent used (Fig. 4b).

The type ( $p < 0.0001$ ) and addition ( $p < 0.0001$ ) of carrier significantly alter the GT of the ENP. According to Kuck et al.,<sup>22</sup> GT is affected by molecular weight of encapsulating agent. Consequently, the addition rate of the carrier led to an increase in the GT.<sup>49</sup> Therefore, in agreement with previous authors,<sup>38,49</sup> an increase in the ratio of encapsulating agents resulted in a higher GT (Fig. 4b). However, MC depresses GT by acting as a plasticizer,<sup>20</sup> thus a decrease in GT resulted from an increase in the MC (Fig. 4a & b). Similar behavior was reported for freeze-dried mango pulp using maltodextrin as wall material.<sup>50</sup> Furthermore, the decrease in GT may also be attributed to the high content of nutraceutical component in encapsulated powders.<sup>40</sup>

The type of wall material ( $p < 0.0001$ ), addition rate of carrier ( $p < 0.0001$ ), and their interaction ( $p < 0.05$ ) significantly affected the WA of the ENP. WA has been linked to MC, through sorption isotherms.<sup>49</sup> According to Bitar et al.,<sup>51</sup> the moisture sorption isotherm highlights that initial absorbed water molecules could interact with binding sites of wall materials. Therefore, the impact of the carrier type on the WA may be due to their differences in water-binding capacity which is related to their chemical structure.<sup>11</sup> This assertion was supported by the significant positive correlation between MC ( $r = 0.982$ ) and WA. Furthermore, in line with previous reports,<sup>11,41</sup> a decrease in WA was observed with an increase in carrier concentration (Fig. 4a).

### 3. 2. 5. Effect of Carrier Materials on Chromatic Properties

The type of encapsulating agent ( $p < 0.0001$ ), carrier concentration ( $p < 0.0001$  for  $L^*$ ,  $b^*$ ,  $C^*$ , and  $H^{\circ}$ ;  $p < 0.001$  for  $a^*$ ), and their interaction ( $p < 0.001$  for  $L^*$ ;  $p < 0.0001$  for  $b^*$  and  $C^*$ ) showed significant effect on the chromatic indices of the ENP. An increase in addition rate of encapsulating agent resulted in an increase in  $L^*$  and  $H^{\circ}$  (Fig. 4c) conversely to  $a^*$ ,  $b^*$ , and  $C^*$  (Fig. 4d). This behavior may be ascribed to the inherent white color and dilution effect induced by the higher addition rate of the coating material.<sup>45,52</sup> Similar results have been reported by other researchers.<sup>28,38,45,52,53</sup>

## 4. Conclusion

Encapsulation of nutraceutical compounds from mulberry leaf extract with sodium carboxymethyl cellulose or maltodextrin as encapsulating agents efficiently reduced the loss of nutraceuticals. The results from this study demonstrated that the use of sodium carboxymethyl cellulose was more suitable for the retention of flavonols and gamma-aminobutyric acid, resulting in highest en-

trapment efficiency of these bioactive components inside the matrix as compared to the maltodextrin which had a greater retention ability for the phenolic acids and 1-deoxyojirimycinin. Moreover, due to the effect of carriers on ice crystal formation, the core to wall ratio was found to be crucial with regards to the physical properties of the ENP. Regardless of the type of wall material, increasing the carrier concentration resulted in an increase in particle size, bulk density, tapped density, water solubility index, wettability time, and glass transition temperature conversely to the particle density, Hausner ratio, Carr index, porosity, moisture content, water activity, and hygroscopicity. The chromatic indexes of the ENP were mainly affected by the type of carrier material which led to the formation of a lighter and more greenish powder with an increase in addition rate of the carrier.

The current study demonstrated that sodium carboxymethyl cellulose and maltodextrin could be used as wall material for the production of a nutraceutical mulberry leaf powder with adequate characteristic to be utilized as a bioactive additive for the development of functional products in the food and nutraceutical industries. From an economic aspect and industrial level, the proposed encapsulation process was found to improve the physical properties of the powder which significantly influence the processing, storage, handling, packing, shipping, and commercialization cost.

## 5. Conflict of Interest

This manuscript has no conflict of interest.

## 6. Acknowledgement

This research did not receive any specific grant from funding agencies in the public, commercial, or not-for-profit sectors.

## 7. References

1. A. A. Memon, N. Memon, D. L. Luthria, M. I. Bhangar and A. A. Pitafi, *Polish Journal of Food and Nutrition Sciences* **2010**, *60*.
2. Y. Huo, *Mulberry for Animal Production, FAO Animal Production, and Health Paper* **2002**, *147*, 11–43.
3. A. Gryn-Rynko, G. Bazylak and D. Olszewska-Slonina, *Bio-medicine & Pharmacotherapy* **2016**, *84*, 628–636. DOI:10.1016/j.biopha.2016.09.081
4. K. Nagalakshamma, *Journal of Pharmacy* **2012**, *2*, 2250–3013.
5. S. Struck, M. Plaza, C. Turner and H. Rohm, *Int. J. Food Sci. Tech.* **2016**, *51*, 1305–1318. DOI:10.1111/ijfs.13112
6. L. Medina-Torres, R. Santiago-Adame, F. Calderas, J. Gal-

- legos-Infante, R. González-Laredo, N. Rocha-Guzmán, D. Núñez-Ramírez, M. Bernad-Bernad and O. Manero, *Industrial Crops and Products* **2016**, *90*, 1–8.  
DOI:10.1016/j.indcrop.2016.06.009
7. F. Sansone, T. Mencherini, P. Picerno, M. d'Amore, R. P. Aquino and M. R. Lauro, *Journal of Food Engineering* **2011**, *105*, 468–476. DOI:10.1016/j.jfoodeng.2011.03.004
8. H. Rajabi, M. Ghorbani, S. M. Jafari, A. S. Mahoonak and G. Rajabzadeh, *Food hydrocolloids* **2015**, *51*, 327–337.  
DOI:10.1016/j.foodhyd.2015.05.033
9. S. Ray, U. Raychaudhuri and R. Chakraborty, *Food Bioscience* **2016**, *13*, 76–83. DOI:10.1016/j.fbio.2015.12.009
10. A. C. P. Souza, P. D. Gurak and L. D. F. Marczak, *Food Bioprod. Process.* **2017**, *102*, 186–194.  
DOI:10.1016/j.fbp.2016.12.012
11. T. Seerangurayar, A. Manickavasagan, A. M. Al-Ismaili and Y. A. Al-Mulla, *J. Food Eng.* **2017**, *215*, 33–43.  
DOI:10.1016/j.jfoodeng.2017.07.016
12. M. Peanparkdee, S. Iwamoto, C. Borompichaichartkul, K. Duangmal and R. Yamauchi, *Int. J. Food Sci. Tech.* **2016**, *51*, 649–655. DOI:10.1111/ijfs.13032
13. C. G. Da Rosa, C. D. Borges, R. C. Zambiasi, M. R. Nunes, E. V. Benvenuti, S. R. da Luz, R. F. D'Avila and J. K. Rutz, *Industrial crops and products* **2013**, *46*, 138–146.  
DOI:10.1016/j.indcrop.2012.12.053
14. M. I. Dias, I. C. Ferreira and M. F. Barreiro, *Food & function* **2015**, *6*, 1035–1052. DOI:10.1039/C4FO01175A
15. I. E. Garofulić, Z. Zorić, S. Pedisić and V. Dragović-Uzelac, *LWT-Food Science and Technology* **2017**, *83*, 110–117.  
DOI:10.1016/j.lwt.2017.05.017
16. W. Tchabo, Y. Ma, E. Kwaw, L. Xiao, M. Wu and A. T. Maurice, *Int. J. Food Prop.* **2018**, *21*, 717–732.  
DOI:10.1080/10942912.2018.1446025
17. E. Akbas, M. Kilercioglu, O. N. Onder, A. Koker, B. Soyler and M. H. Oztop, *Journal of Functional Foods* **2017**, *28*, 19–27.  
DOI:10.1016/j.jff.2016.11.010
18. J. Du, Z.-Z. Ge, Z. Xu, B. Zou, Y. Zhang and C.-M. Li, *Drying Technol.* **2014**, *32*, 1157–1166.  
DOI:10.1080/07373937.2014.886259
19. S. Santhalakshmy, S. J. D. Bosco, S. Francis and M. Sabeena, *Powder Technol.* **2015**, *274*, 37–43.  
DOI:10.1016/j.powtec.2015.01.016
20. V. Sanchez, R. Baeza, M. V. Galmarini, M. C. Zamora and J. Chirife, *Food and Bioprocess Technology* **2013**, *6*, 1350–1354.  
DOI:10.1007/s11947-011-0654-z
21. L. F. Ballesteros, M. J. Ramirez, C. E. Orrego, J. A. Teixeira and S. I. Mussatto, *Food Chem.* **2017**, *237*, 623–631.  
DOI:10.1016/j.foodchem.2017.05.142
22. L. S. Kuck and C. P. Z. Noreña, *Food Chem.* **2016**, *194*, 569–576. DOI:10.1016/j.foodchem.2015.08.066
23. L. Stoll, T. M. H. Costa, A. Jablonski, S. H. Flôres and A. de Oliveira Rios, *Food and bioprocess technology* **2016**, *9*, 172–181. DOI:10.1007/s11947-015-1610-0
24. P. Laine, P. Kylli, M. Heinonen and K. Jouppila, *J. Agric. Food Chem.* **2008**, *56*, 11251–11261. DOI:10.1021/jf801868h
25. C. G. Lopez, S. E. Rogers, R. H. Colby, P. Graham and J. T. Cabral, *J. Polym. Sci., Part B: Polym. Phys.* **2015**, *53*, 492–501.  
DOI:10.1002/polb.23657
26. A. N. Negrão-Murakami, G. L. Nunes, S. S. Pinto, F. S. Murakami, E. R. Amante, J. C. C. Petrus, E. S. Prudêncio and R. D. M. C. Amboni, *LWT – Food Science and Technology* **2017**, *79*, 561–567. DOI:10.1016/j.lwt.2016.11.002
27. N. Stănciuc, M. Turturică, A. M. Oancea, V. Barbu, E. Ioniță, I. Aprodu and G. Răpeanu, *Food and Bioprocess Technology* **2017**, *10*, 1715–1726. DOI:10.1007/s11947-017-1938-8
28. D. P. S. Oberoi and D. S. Sogi, *J. Food Eng.* **2015**, *165*, 172–178.  
DOI:10.1016/j.jfoodeng.2015.06.024
29. Y. R. R. S. Rezende, J. P. Nogueira and N. Narain, *Food Chem.* **2018**, *254*, 281–291. DOI:10.1016/j.foodchem.2018.02.026
30. C. G. Da Rosa, C. D. Borges, R. C. Zambiasi, J. K. Rutz, S. R. da Luz, F. D. Krumreich, E. V. Benvenuti and M. R. Nunes, *LWT-Food Science and Technology* **2014**, *58*, 527–533.  
DOI:10.1016/j.lwt.2014.03.042
31. B. Li, S. Konecke, K. Harich, L. Wegiel, L. S. Taylor and K. J. Edgar, *Carbohydr. Polym.* **2013**, *92*, 2033–2040.  
DOI:10.1016/j.carbpol.2012.11.073
32. N. Harnkarnsujarit, S. Charoenrein and Y. H. Roos, *Carbohydr. Polym.* **2012**, *88*, 734–742.  
DOI:10.1016/j.carbpol.2012.01.028
33. A. M. Ceballos, G. I. Giraldo and C. E. Orrego, *J. Food Eng.* **2012**, *111*, 360–365.  
DOI:10.1016/j.jfoodeng.2012.02.010
34. M. J. Ramirez, G. I. Giraldo and C. E. Orrego, *Powder Technol.* **2015**, *277*, 89–96. DOI:10.1016/j.powtec.2015.02.060
35. D. Ogrodowska, M. Tańska and W. Brandt, *Food and Bioprocess Technology* **2017**, *10*, 1265–1280.  
DOI:10.1007/s11947-017-1898-z
36. C. Selomulya and Y. Fang: *Handbook of Food Powders*, Woodhead Publishing, Philadelphia, **2013**, pp. 379–408.  
DOI:10.1533/9780857098672.2.379
37. K. Samborska, P. Gajek and A. Kamińska-Dwórznička, *Polish Journal of Food and Nutrition Sciences* **2015**, *65*, 109–118.  
DOI:10.2478/pjfn-2013-0012
38. S. Bhusari, K. Muzaffar and P. Kumar, *Powder Technol.* **2014**, *266*, 354–364. DOI:10.1016/j.powtec.2014.06.038
39. A. M. Goula and K. G. Adamopoulos, *Drying Technol.* **2008**, *26*, 726–737. DOI:10.1080/07373930802046377
40. G. B. Celli, R. Dibazar, A. Ghanem and M. S.-L. Brooks, *Drying Technol.* **2016**, *34*, 1175–1184.  
DOI:10.1080/07373937.2015.1099546
41. G. Caliskan and S. N. Dirim, *Powder Technol.* **2016**, *287*, 308–314. DOI:10.1016/j.powtec.2015.10.019
42. C. C. Ferrari, S. P. M. Germer, I. D. Alvim, F. Z. Vissotto and J. M. de Aguirre, *Int. J. Food Sci. Tech.* **2012**, *47*, 1237–1245.  
DOI:10.1111/j.1365-2621.2012.02964.x
43. S. Murali, A. Kar, D. Mohapatra and P. Kalia, *Food Sci. Technol. Int.* **2015**, *21*, 604–612.  
DOI:10.1177/1082013214557843
44. Q. Shi, Z. Fang and B. Bhandari, *Drying Technol.* **2013**, *31*, 1681–1692. DOI:10.1080/07373937.2013.783593
45. T. Seerangurayar, A. Manickavasagan, A. M. Al-Ismaili and Y. A. Al-Mulla, *Drying Technol.* **2017**, *1*–12.

46. R. V. d. B. Fernandes, D. A. Botrel, E. K. Silva, C. G. Pereira, E. L. d. Carmo, A. L. d. A. Dessimoni and S. V. Borges, *Drying Technol.* **2017**, *35*, 1098–1107. DOI:10.1080/07373937.2016.1231690
47. R. V. d. B. Fernandes, S. V. Borges, D. A. Botrel and C. R. d. Oliveira, *Int. J. Food Sci. Tech.* **2014**, *49*, 1522–1529. DOI:10.1111/ijfs.12449
48. S. Saikia, N. K. Mahnot and C. L. Mahanta, *Food Chem.* **2015**, *171*, 144–152. DOI:10.1016/j.foodchem.2014.08.064
49. L. E. Kurozawa, K. J. Park and M. D. Hubinger, *J. Food Eng.* **2009**, *91*, 287–296. DOI:10.1016/j.jfoodeng.2008.09.006
50. S. Fongin, K. Kawai, N. Harnkarnsujarit and Y. Hagura, *J. Food Eng.* **2017**, *210*, 91–97. DOI:10.1016/j.jfoodeng.2017.04.025
51. M. Bitar, G. Roudaut, J. Maalouly, S. Brandès, R. D. Gougeon, P. Cayot and E. Bou-Maroun, *React. Funct. Polym.* **2017**, *114*, 1–7. DOI:10.1016/j.reactfunctpolym.2017.02.012
52. L. D. Daza, A. Fujita, C. S. Fávaro-Trindade, J. N. Rodrigues-Ract, D. Granato and M. I. Genovese, *Food Bioprod. Process.* **2016**, *97*, 20–29. DOI:10.1016/j.fbp.2015.10.001
53. V. T. Šaponjac, G. Četković, J. Čanadanović-Brunet, S. Djilas, B. Pajin, J. Petrović, S. Stajčić and J. Vulić, *Acta Chimica Slovenica* **2017**, *64*, 283–289. DOI:10.17344/acsi.2016.2789

## Povzetek

Ekstrakt iz listov murve smo inkapsulirali z natrijkarboksimetil celulozo (0.55 %, 0.70 % in 0.75 % w/v) ali maltodekstrinom (8 %, 10 % in 12 % w/v). Izsledki raziskav so pokazali, da je inkapsulacija z maltodekstrinom bolj učinkovita za fenolne kisline in 1-deksinojirimicin medtem ko so flavonoli in gama-aminobutanojska kislina bolje inkapsulirani z natrijkarboksimetil celulozo. Pokazali smo tudi, da so antioksidativne lastnosti uprašenih inkapsulatov povezane z njihovimi hranilnimi sestavinami. Prah pridobljen iz natrijkarboksimetil celuloznega inkapsulata je izkazoval primerno higroskopnost, čas omakanja, temperaturo steklastega prehoda in snovne lastnosti, medtem ko je prah pridobljen iz maltodekstrina izkazoval željeno poroznost, vodotopnost, vsebnost vlage, vodno aktivnost, barvo, delčnost in pretočne lastnosti.

Scientific paper

# Monomethyl Suberate Screening for Antifungal Activity, Molecular Docking and Drug-Like Properties

Lyudmyla Antypenko,\* Fatuma Meyer, Zhanar Sadykova, Leif-Alexander Garbe and Karl Steffens

Faculty of Agriculture and Food Science, Neubrandenburg University Brodaer Str. 2, 17033, Neubrandenburg, Germany

\* Corresponding author: E-mail: antypenkol@gmail.com

Received: 03-05-2018

## Abstract

Antifungal activity of suberic acid monomethyl ester (monomethyl suberate) was investigated in a growth inhibition assay comprising of 11 different fungi and 3 *Phytophthora* oomycetes strains relevant in agriculture. In comparison to standard antifungal hymexazol, monomethyl suberate showed moderate antifungal effects at a concentration range of 100–300 µg/mL. *Alternaria alternata*, *Fusarium equiseti*, *Fusarium fujikuroi* and *Phytophthora infestans* GL-1 were the most sensitive fungi showing inhibition rates up to 100%. Physico-chemical descriptors of monomethyl suberate revealed its low toxicity profile. Molecular docking analysis comprising several known antifungal targets points to the *N*-myristoyltransferase as the most probable site of interaction.

**Keywords:** Monomethyl suberate; antifungal activity; molecular docking; drug-like descriptors

## 1. Introduction

In continuation of our search for highly effective natural antifungal agents among trihydroxy fatty acids with low toxicity, the starting reagent in synthesis of pinnelic acid (9,12,13-trihydroxy-10-octadecenoic acid),<sup>1</sup> namely, suberic acid (octanedioic acid) (Figure 1) attracted our interest.

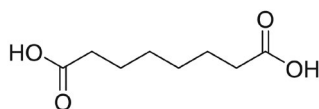


Figure 1. Chemical structure of suberic acid.

Suberic acid is known to be obtained along with azelaic acid through oxidation of ricinoleic acid<sup>2</sup> or as a component isolated from oil extracted from *Vernonia galamensis*.<sup>3</sup> Antonova *et al.* described its synthesis by oxidation of cyclooctane-1,2-diol.<sup>4</sup> Suberic acid (4.13%) and its monomethyl ester (2.38%) were also detected by gas chromatography-mass spectrometry (GC-MS) in methanolic extracts of *Hibiscus micranthus* stem along with 56 other compounds.<sup>5</sup> Furthermore, monomethyl suberate was found by GC-MS in an ethylacetate/hexane extract of *Pestalotiopsis* JCM2A4, an endophyte growing on Chinese mangrove plant *Rhizophora mucronata*.<sup>6</sup>

To our knowledge, reports on physiological role(s) and potential biotechnological application(s) of suberic acid or its derivatives are scarce. *Staphylococcus aureus* and *Candida albicans* were shown to be sensitive to a chloroform extract of *Polysiphonia denudate* f. *fragilis* (Rhodophyceae), which contained suberic acid dimethyl ester (0.2%) among other biologically active substances.<sup>7</sup> The latter was also detected by GC-MS in the larval and pupal internal lipids of medically important flies *Calliphora vicina* (0.15–0.20 µg/g) and *Sarcophaga carnaria* (0.14–0.21 µg/g).<sup>8</sup> In the same study it was shown, that the substance itself slightly inhibited the growth of entomopathogenic fungi of *Beauveria bassiana* (Dv-1/07), *B. bassiana* (Tve-N39), *Lecanicillium lecanii*, *Metarhizium anisopliae*, *Paecilomyces fumosoroseus* and *Paecilomyces lilacinus* with a minimal inhibitory concentration (MIC) of 512 µg/mL. Antimicrobial tests carried out with diverse gram-positive and gram-negative bacterial strains, as well as with the fungi *Candida albicans* and *Candida tropicalis*, were without any positive results.<sup>8</sup>

Recently, Iornumbe *et al.*<sup>9</sup> investigated the antifungal activity of suberic acid organotin derivatives against *Microsporium gypseum*, *M. audouinii*, *M. distortum*, *M. gallinae* and *Trichoephyton*: *mentagrophytes* and *T. equinum*. They found a decreasing average activity according to diverse octandioate rests: potassium triphenyltin(IV) oc-

tanedioate > potassium tributyltin(IV) octanedioate > potassium dibutyltin(IV) octanedioate > potassium diphenyltin(IV) octanedioate. The activities were comparable to standard antifungals fulcin and fluconazole. The leading compounds MICs were found to be 25 µg/mL. The free suberic acid or its monopotassium salt exhibited a weaker antifungal activity than synthesized organotin compounds, inhibiting growth of only *M. distortum* and *T. equinum*. This fits to the observation that many biologically compounds enhance their activity upon complexation.<sup>10</sup>

Only few suberic acid derivatives were reported to have non-pharmacological applications: octacalcium phosphate carboxylates as bone reconstructors for biomedical applications;<sup>11</sup> suberate as thermotropic liquid crystalline polymers;<sup>12</sup> poly(propylene suberate)s<sup>13</sup> and poly(butylene suberate)s<sup>14,15</sup> as biodegradable polyesters for sutures, implant materials for tissue engineering, and biologically active controlled drug-release devices; anhydrous copper suberates as polymers with extended bridged structures, which are interesting materials to study spin exchange and charge transfer between metal ions.<sup>16</sup> Interestingly, in a very different context suberic bishydroxamate was found to be a potent agent in overcoming resistance of melanoma to “TNF-related apoptosis-inducing ligand”, which induces apoptosis by acting as a histone deacetylase inhibitor.<sup>17</sup>

Here we present an investigation of antifungal activity of monomethyl suberate.

## 2. Results and Discussion

### 2.1. Antifungal Activity

We decided to work on monomethyl suberate, because dimethyl ester was already described having only a moderate antifungal activity (512 µg/mL MIC).<sup>8</sup> Furthermore, the monoethyl ester of azelaic acid, which bears a molecular scaffold structure very similar to suberate, showed a pronounced antifungal activity against *Pyricularia oryzae* with an MIC<sub>50</sub> of 50 µg/mL (free acid: MIC<sub>50</sub> at 95 µg/mL).<sup>18,19</sup> This observation is probably due to higher lipophilicity of the monoethyl ester form.<sup>20</sup> Thus, antifungal studies of shorter in one carbon dicarboxylic acid, namely, suberic, seemed promising with enhancing its lipophilicity in monomethyl ester form.

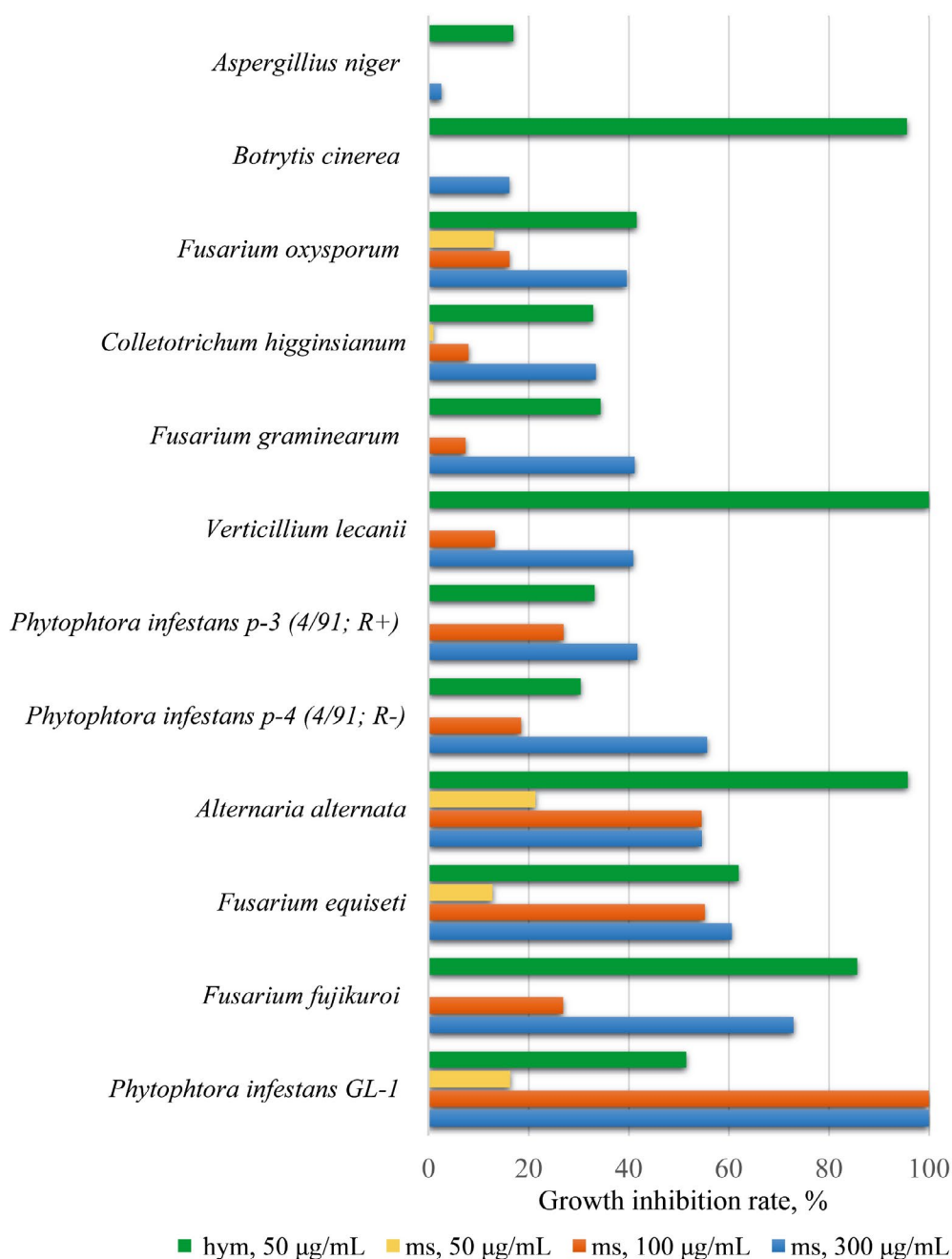
Eleven fungi and three *Phytophthora* strains were probed with methyl suberate at 50, 100 and 300 µg/mL. Hymexazol (50 µg/mL) was included used as standard antifungal. The findings are summarized in Figure 2. At the lowest concentration (50 µg/mL) four strains showed a moderate sensitivity to monomethyl suberate: *Alternaria alternata* (21.3%), *Phytophthora infestans* GL-1 (16.3%), *Fusarium oxysporum* (13.1%) and *F. equiseti* (12.8%). At this concentration hymexazol was effective against each strain with a higher inhibition activity (17–100%) than monomethyl suberate.

At 100 µg/mL *P. infestans* GL-1 was the most sensitive strain showing 100% of inhibition. A nearly 50% inhibition was observed to *Alternaria alternata* and *F. equiseti*. Only moderate effects were detected against *P. infestans* p-3 (4/91; R+) and *F. fujikuroi*, with approximately 27% of inhibition. Antifungal activities were even lower against *P. infestans* p-4 (4/91; R-) (18.5%), *F. oxysporum* (16.2%), *Verticillium lecanii* (13.3%), *Colletotrichum higginsianum* (8.0%) and *F. graminearum* (7.4%). *Aspergillus niger*, *Botrytis cinerea*, *Mucor indicus* and *Penicillium digitatum* were completely insensitive to the monomethyl suberate at the studied concentration. At a concentration of 300 µg/mL only two fungi remained resistant: *M. indicus* and *P. digitatum*. Interestingly, against *A. alternata* and *F. equiseti* the antifungal effect remained practically unchanged (54–60% of growth inhibition). Antifungal activity against all other fungi became stronger with elevated concentrations. The most sensitive strain was *F. fujikuroi* (72.9%). Fungi *F. oxysporum*, *F. graminearum*, *Verticillium lecanii*, and strains p-3 (4/91; R+) and p-4 (4/91; R-) of *P. infestans* were only moderately inhibited (40–56%). Lower inhibition effects were found against *C. higginsianum* (33.5%), *Botrytis cinerea* (16.2%), and *Aspergillus niger* (16.2%).

### 2.2. Drug-Likeness Physico-Chemical Parameters and Promiscuity Score

Considering the found moderate antifungal activity of monomethyl suberate at 300 µg/mL, its physico-chemical parameters were calculated by Molinspiration engine<sup>21</sup> (Table 1) in order to predict the level of drug-likeness, toxicity<sup>22–24</sup> and substance promiscuity.<sup>25</sup> These properties may be of value if monomethyl suberate will be considered as a compound in human medical care, food processing or as an antifungal in agriculture. For comparison, corresponding data for the standard antifungal hymexazol are also shown (ChEMBL244877).<sup>26</sup>

As it is seen from the Table 1, monomethyl suberate complies to all presented criteria for molecular properties, that influence the oral bioavailability of drug candidates,<sup>22–24</sup> except of molecular polar surface area (TPSA). Its surface is larger (63.30 Å<sup>2</sup>) than that of hymexazol (42.26 Å<sup>2</sup>), which implies its penetration of the blood brain barrier is less likely. Calculating the promiscuity of biological activity of monomethyl suberate with “bioactivity data associative promiscuity pattern learning engine” (Badapple),<sup>25</sup> no data were found in the database, which means a neutral result with respect to toxicity prediction. At least the predicted promiscuity was not found to be high. For hymexazol the pScore was shown with a moderate true value (238) based on reported biological activity data of drugs with isoxazole scaffold. So, the reference antifungal hymexazol demonstrated higher level of potentially binding to a variety of bimolecular targets, and thereby may have higher level of toxicity than tested natural monomethyl suberate.<sup>27</sup>



**Figure 2.** Growth inhibition of studied fungal strains by hymexazol (hym) in 50 µg/mL and monomethyl suberate (ms) in 50, 100 and 300 µg/mL. *Mucor indicus* and *Penicillium digitatum* were insensitive in all tests.

**Table 1.** Calculated parameters of lead-like & structure optimization and promiscuity scores

Substance / SMILES	MW*	log P	TPSA	nrotb	HBA	HBD	pScore
<b>Monomethyl suberate</b> COC(=O)CCCCCCC(O)=O	188.2	1.67	63.30	8	4	1	no data
<b>Hymexazol</b> CC1=CC(=NO1)O	99.1	0.73	42.26	0	2	1	238
Drug lead-like criteria	≤ 500	≥ -0.5 ≤ 5	≥ 75 ≤ 140	≤ 10	≤ 10	≤ 5	-

\*MW – molecular weight; log P – octanol/water partition coefficient; TPSA – molecular polar surface area; nrotb – number of rotatable bonds; HBA – hydrogen bonds acceptors; HBD – hydrogen bonds donors; pScore – promiscuity score.

## 2. 3. Molecular Docking

A literature survey did not give us any indication with respect to a biological target, to which monomethyl suberate may bind and thereby reveal a mode of action of growth inhibition. Only PubChem BioAssays (CHEM-BL1162491)<sup>26</sup> reported suberic acid to be an antagonist of the retinoid-related orphan receptor gamma, farnesoid-X-receptor, thyroid hormone receptor beta and NFkB signaling pathways. All these reports are related to human health studies. So, investigations to elucidate antifungal mechanism(s) of suberate's with respect to fungi of agricultural importance are worth to study.

Analysis of *in silico* molecular docking predicted affinity scores<sup>28</sup> to six common fungal targets (enzymes)<sup>29</sup> and showed, that monomethyl suberate may interact with them with higher probability, than hymexazol (Table 2).

The highest affinity score (−6.0) of monomethyl suberate was calculated to *N*-myristoyltransferase (NMT). In

Figure 3 it is shown how it fits into the active site of this enzyme.

Two conventional hydrogen bonds are formed with HIS B:227 (3.05 Å) and ASN B:392 (3.04 Å) due to carbonyl oxygen in methyl ester residue of suberate. A further hydrophobic Pi-sigma bond build up between PHE B:240 (3.76 Å) and MeC(O)CH<sub>2</sub> fragment. Thus, *N*-myristoyltransferase (NMT) should be among priority antifungal targets for further *in vitro* enzymatic studies.

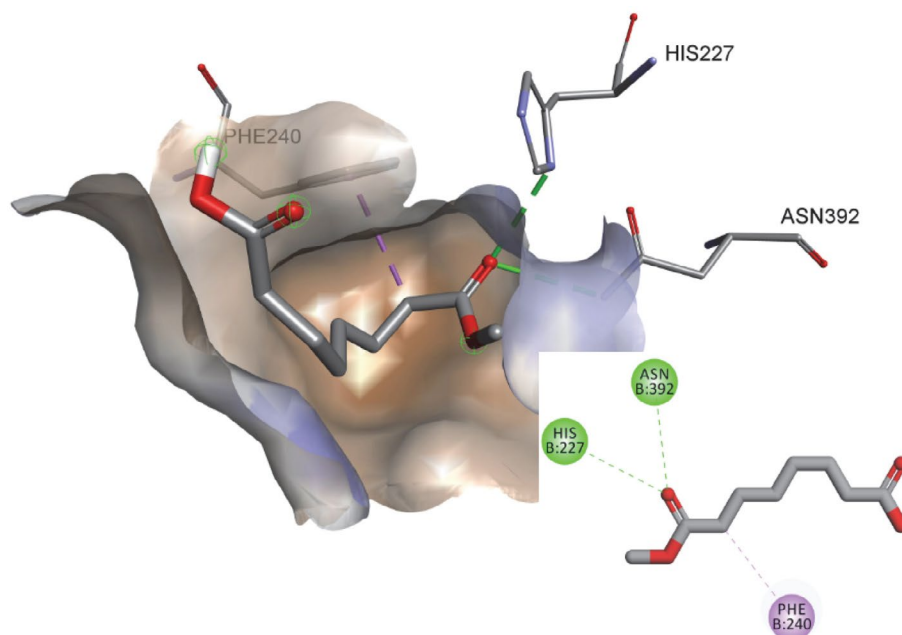
## 3. Experimental

### 3. 1. Antifungal Studies

The mycelial growth rate assay was used for antifungal studies.<sup>30</sup> Strains of filamentous fungi were obtained from the following sources: *Asperillus niger* DSM 246, *Alternaria alternata* DSM 1102, *Fusarium equiseti* DSM 21725,

**Table 2.** Calculated affinities of monomethyl suberate and reference hymexazol to common antifungal enzymatic targets, Kcal/Mol

Target enzyme	PDB code	Affinity for monomethyl suberate	Affinity for hymexazol
<i>N</i> -Myristoyltransferase (NMT)	1IYL	−6.0	−4.9
Topoisomerase II (Topo II)	1Q1D	−5.5	−4.7
Sterol 14 $\alpha$ -demethylase (CYP51)	5TZ1	−5.3	−4.3
UDP- <i>N</i> -acetyl-muramoyl- <i>L</i> -alanine: <i>D</i> -glutamate ligase (MurD)	1UAG	−5.1	−4.4
Secreted aspartic proteinase (SAP2)	1EAG	−4.8	−3.9
<i>L</i> -Glutamine: <i>D</i> -fructose-6-phosphate aminotransferase (GlcN-6-P)	1XFF	−4.7	−4.8



**Figure 3.** Visual representation (3D and 2D) of the monomethyl suberate showing bonds formation and position in the active site of *N*-myristoyltransferase (NMT) of *Candida albicans*.<sup>29</sup>

*F. graminearum* DSM 1095, *F. fujikuroi* DSM 893, *Verticillium lecanii*, *Mucor indicus* DSM 2185, *Penicillium digitatum* DSM 2731 from DSMZ (Braunschweig, Germany); *Fusarium oxysporum* 39/1201 St. 9336 and *Botrytis cinerea* from the Technische Universität Berlin (Germany); *Colletotrichum higginsianum* MAFF 305635, originally isolated in Japan, via the Department of Biology, Friedrich-Alexander-Universität (Erlangen, Germany); oomycetes *Phytophthora infestans* GL-1 01/14 wild strain, p-3 (4/91; R+) and p-4 (4/91; R-) strains were kindly donated by Julius Kühn-Institut (Quedlinburg, Germany). Potato Dextrose Agar (PDA) were purchased from C. Roth (Karlsruhe, Germany). Hymexazol (98%) was obtained from Prosperity World Store (Hebei, China). Monomethyl suberate (97%) was purchased from Jinan Yudong Trading Co., Ltd. (Jinan, China). Strains were cultivated on PDA for 6 d at 25°C. Spores from each strain were gently harvested with a sterile glass rod from plate surfaces with deionized water. Spore concentration numbers in suspension were determined microscopically and adjusted to  $7.5 \times 10^6$  spores/mL. A clear stock solution of 5 mg/mL was made of 0.050 g of reference substance hymexazol in 10 mL of deionized sterile water as solvent. 1 ml of each stock solution was mixed *in situ* into 99 ml of PDA prior to solidification to obtain a final concentration of 50 µg/mL. In the same way mixtures of PDA with monomethyl suberate were prepared with final concentrations of 50, 100 and 300 µg/mL. 9 mL of each mixture were poured into 6 cm diameter petri dishes. After solidification central hole (diameter: 2.5 mm) was cut out and inoculated with 6.5 µL spore suspension. Plates were incubated at 25 °C (+/- 1 °C) for 6 d. Control plates containing only PDA and water were prepared in the same way. Inhibitory effects (I %) were determined by analyzing growth zone diameters and calculated as described by Tang *et al.*:

$$I \% = [(C-T) / (C - 2.5 \text{ mm})] * 100, \quad (1)$$

where C (mm) represents the growth zone of control PDA, and T (mm) the average growth zone in presence of methyl suberate.<sup>30</sup> All growth experiments were carried out in triplicate. Means and standard deviations were calculated with software "Excel 2016" (Microsoft, USA).

### 3. 2. Molecular Docking

Macromolecular data was downloaded from the Protein Data Bank (PDB),<sup>31</sup> namely, the crystal structures of sterol 14 $\alpha$ -demethylase (CYP51) 5TZ1, topoisomerase II (Topo II) 1Q1D, L-glutamine: D-fructose-6-phosphate amidotransferase (GlcN-6-P) 1XFF, secreted aspartic proteinase (SAP2) 1EAG, N-myristoyltransferase (NMT) 1IYL, and UDP-N-acetylmuramoyl-L-alanine: D-glutamate ligase (MurD) 1UAG. As reference hymexazol (3-hydroxy-5-methylisoxazole) was chosen according to reported antifungal analysis.<sup>30</sup>

**Ligand preparation.** Substances were drawn using MarvinSketch 6.3.0 and were saved in mol format.<sup>32</sup> Afterwards they were optimized by program Chem3D using molecular dynamics MM2 algorithm and saved as pdb-files. Molecular mechanics was used to produce more realistic geometry values for the majority of organic molecules owing to the fact of being highly parameterized. By using AutoDockTools-1.5.6 pdb-files were converted to PDBQT, and number of active torsions was set as default.<sup>28</sup>

**Protein preparation.** PDB files were downloaded from the protein data bank.<sup>31</sup> Discovery Studio 4.0 was used to delete water molecules and ligand from the crystal. The proteins were saved as pdb-files. In AutoDockTools-1.5.6 polar hydrogens were added and saved as PDBQT. Grid box was set as following: center\_x = 70.728, center\_y = 65.553, center\_z = 3.865, size\_x = 20, size\_y = 20, size\_z = 20. Vina was used to carry out docking. For visualization Discovery Studio Visualizer v17.2.0.16349 was applied.<sup>33</sup>

## 4. Conclusion

The antifungal spectrum of monomethyl suberate was investigated against 11 different fungi and 3 *Phytophthora* oomycetes strains of agricultural importance. The monomethyl ester derivative revealed a significantly higher activity than the dimethyl ester<sup>8</sup>, but an average lower activity than reference antifungal hymexazol. Nevertheless, an extraordinary activity was observed against strain GL-1 of the devastating oomycete *P. infestans*. Furthermore, monomethyl suberate as a naturally occurring substance has a more environmentally friendly structure with less promiscuity score than conventional antifungals with heterocyclic ring systems. Therefore, we expect to have at hand an antifungal drug with an attractive profile with respect to potential toxicity and mutagenicity.

## 5. Acknowledgements

Authors gratefully acknowledge German Federal Ministry of Education and Research (Grant: FKZ 03FH025IX4) for financial support of this work; Federal Research Centre for Cultivated Plants (Quedlinburg, Germany) for presenting the strain *Phytophthora infestans*; Department of Biology, Friedrich Alexander University, Erlangen, Nürnberg, Germany for the strain *Colletotrichum higginsianum*, and Dr. Oleksii Antypenko (Zaporizhzhya State Medical University, Ukraine) for conducting molecular docking.

## 6. References

1. T. Shirahata, T. Sunazuka T, K. Yoshida, S. Omura, *Tetraedron Org. Chem. Ser.* **2006**, 62, 9483–9496.  
DOI:10.1016/j.tet.2006.06.088



2. P. E. Verkade, *Recueil des Travaux Chimiques des PaBas* **1927**, 46, 137–143. DOI:10.1002/recl.19270460209
3. F. O. Ayorinde, G. Osman, R. L. Shepard, F. T. Powers, *J. Am. Oil Chem. Soc.* **1988**, 65, 1774–1777. DOI:10.1007/BF02542380
4. T. N. Antonova, S. A. Mashina, A. A. Kunitskii, N. V. Artemèva, *Khim. Khim. Tekhnol.* **2003**, 46, 114–116.
5. K. Ashok, S. R. Setty, L. Narsu, *Pharmacogn. J.* **2010**, 2, 21–30. DOI:10.1016/S0975-3575(10)80074-4
6. L. Liu, X. Lu, *Plast. Rubber Compos.* **2002**, 31, 283–288. DOI:10.1179/146580102225005009
7. S. De Rosa, Z. Kamenarska, V. Bankova, K. Stefanov, S. Dimitrova-konaklieva, H. Najdenski, I. Trevtkova, S. Popov, *Zeitschrift fur Naturforsch – Sect. C. J. Biosci.* **2001**, 56, 1008–1014. DOI:10.1515/znc-2001-11-1218
8. M. Golebiowski, M. Cerkowniak, A. Urbanek, M. Dawgul, W. Kamysz, M. Bogus, P. Stepnowski, *Microbiol Res.* **2015**, 170, 213–222. DOI:10.1016/j.micres.2014.06.004
9. E. N. Iornumbe, S. G. Yiase, R. Sha 'ato, T. A. Tor-Anyiin, *IOSR J. Appl. Chem.* **2015**, 8, 7–15. DOI:10.9790/5736-08610715
10. S. Hadi, R. Mita, Nurhasanah, *Modern Applied Science Journal* **2009**, 3, 12–17.
11. T. Yokoi, H. Kato, I. Y. Kim, K. Kikuta, M. Kawashita, C. Ohtsuki, *Ceram. Int.* **2012**, 38, 3815–3820. DOI:10.1016/j.ceramint.2012.01.030
12. A. Djeghri, F. Balegroune, A. Guehria-Laidoudi, T. Roisnel, *J. Chem. Crystallogr.* **2007**, 37, 97–101. DOI:10.1007/s10870-006-9154-9
13. D. Li, S. Yan, P. Proksch, Z. Liang, Q. Li, J. Xu, *Afr. J. Biotechnol.* **2013**, 12, 3802–3806. DOI:10.5897/AJB2013.12417
14. G. Z. Papageorgiou, C. Panayiotou, *Thermochim. Acta* **2011**, 523, 187–190. DOI:10.1016/j.tca.2011.05.023
15. Z. Cui, Z. Qiu, *Polym. (United Kingdom)*. **2015**, 67, 12–19. DOI:10.1016/j.polymer.2015.04.069
16. X. Shi, Z. Qiu, *RSC Adv.* **2015**, 5, 79691–79698. DOI:10.1039/C5RA16801E
17. X. D. Zhang, S. K. Gillespie, J. M. Borrow, P. Hersey, *Biochem. Pharmacol.* **2003**, 66, 1537–1545. DOI:10.1016/S0006-2952(03)00509-4
18. K. Hiroyuki, T. Yoshihara, S. Sakamura, T. Shimanuki, T. Sato, A. Tajimi, *Agric. Biol. Chem.* **1989**, 53, 2527–2528. DOI:10.1080/00021369.1989.10869341
19. M. Watanabe, Y. Sakai, T. Teraoka, H. Abe, Y. Kono, J. Uzawa, K. Kobayashi, Y. Suzuki, A. Sakurai, *Agric. Biol. Chem.* **1990**, 54, 1103–1104. DOI:10.1080/00021369.1990.10870045
20. Y. Suzuki, O. Kurita, Y. Kono, H. Hyakutake, A. Sakurai, *Bio-sci. Biotechnol. Biochem.* **1995**, 59, 2049–2051. DOI:10.1271/bbb.59.2049
21. Molinspiration Cheminformatics Software, <http://www.molinspiration.com/cgi-bin/properties>, (assessed: April 14, 2018).
22. C. A. Lipinski, F. Lombardo, B. W. Dominy, P. J. Feeney, *Adv. Drug. Delivery Rev.* **1997**, 23, 4–25. DOI:10.1016/S0169-409X(96)00423-1
23. D. F. Veber, S. R. Johnson, H. Y. Cheng, B. R. Smith, K. W. Ward, K. D. Kopple, *J. Med. Chem.* **2002**, 45, 2615–2623. DOI:10.1021/jm020017n
24. P. Ertl, B. Rohde, P. Selzer, *J. Med. Chem.* **2000**, 43, 3714–3717. DOI:10.1021/jm000942e
25. Bioactivity data associative promiscuity pattern learning engine, <http://pasilla.health.unm.edu/tomcat/badapple/badapple>, (assessed: April 14, 2018).
26. ChEMBL. Compound Report card. The European Bioinformatics Institute (EMBL-EBI), <https://www.ebi.ac.uk/chembl/compound/inspect>, (assessed: April 10, 2018).
27. B. A. Fowler (Ed.): Computational toxicology methods and applications for risk assessment. ICF International, Fairfax, VA, USA, **2013**, p. 176.
28. O. Trott, A. J. Olson, *J. Comput. Chem.* **2010**, 31, 455–461.
29. A. Siwek, P. Staczek, A. Strzelczyk, J. Stefanska, *Lett. Drug Des. Discovery* **2013**, 10, 2–10. DOI:10.2174/157018013804142393
30. R. Tang, L. Jin, C. Mou, J. Yin, S. Bai, D. Hu, J. Wu, S. Yang, B. Song, *Chem. Cent. J.* **2013**, 7, 1–8. DOI:10.1186/1752-153x-7-30
31. Protein Data Bank. Worldwide pdb, <http://www.pdb.org>, (assessed: April 12, 2018).
32. MarvinSketch version: 6.3.0, 2015, ChemAxon, <http://www.chemaxon.com>. (accessed: April 12, 2018).
33. J. Alvarez, B. Shoichet, PART V: Docking Strategies and Algorithms, Virtual Screening in Drug Discovery. CRC Press, Taylor & Francis: Boca Raton, FL, **2005**, pp. 301–348. DOI:10.1201/9781420028775

## Povzetek

Protiglavno aktivnost monometil estra suberne kisline (monometil suberata) smo preučevali preko inhibicije rasti 11 različnih gliv in 3 oomicetnih sevov *Phytophthora* pomembnih v kmetijstvu. V primerjavi z referenčnim fungicidom himeksazolom, je monometil suberat izkazoval zmerno protiglavno aktivnost v koncentracijskem območju 100–300 µg/mL. Vrste *Alternaria alternata*, *Fusarium equiseti*, *Fusarium fujikuroi* in *Phytophthora infestans* *GL-1* so bile najbolj občutljive, saj je povzročil tudi 100 % inhibicijo rasti. Fizikalno-kemijski deskriptorji monometil suberata kažejo nizko toksičnost. Analiza molekularne umestitve, ki je vključevala sedem znanih protiglavnih tarčnih pozicij, je nakazala N-miristoil transferazo kot najverjetnejše mesto interakcije.

Scientific paper

# Erythropoietin Potentiates the Anti-Proliferative Effect of Tamoxifen in Ovarian Adenocarcinoma A2780 Cells

Patrícia Kimáková,<sup>1</sup> Erika Szentpéteriová,<sup>1</sup> Barbora Fecková,<sup>1</sup>  
Nataša Debeljak<sup>2</sup> and Peter Solár<sup>1,3,\*</sup>

<sup>1</sup> Department of Cell Biology, Institute of Biology and Ecology, Faculty of Science, Pavol Jozef Šafárik University in Košice, SK-04154 Košice, Slovak Republic

<sup>2</sup> Institute of Biochemistry, Faculty of Medicine, University of Ljubljana, SI-1000 Ljubljana, Slovenia

<sup>3</sup> Department of Medical Biology, Faculty of Medicine, Pavol Jozef Šafárik University in Košice, SK-04154 Košice, Slovak Republic

\* Corresponding author: E-mail: peter.solar@upjs.sk

Received: 07-05-2018

## Abstract

We have recently shown that erythropoietin receptor (EPOR) protects cancer cells from tamoxifen (TAM)-induced cell death in the absence of erythropoietin (EPO). In this study, we analyzed the effect of EPOR silencing and EPO treatment on the response to TAM in human ovarian adenocarcinoma cells A2780. We demonstrated that the EPOR siRNA silencing decreases cell proliferation and sensitizes and/or potentiates the anti-proliferative effect of TAM on A2780 cells. Similarly, the combined effect of EPO and TAM treatment significantly reduced cell proliferation compared to TAM alone. Our *in vitro* results indicated the need for further investigation of EPO effects on a similar *in vivo* model.

**Keywords:** Erythropoietin receptor; erythropoietin; tamoxifen; A2780; cancer cell line

## 1. Introduction

Erythropoietin (EPO) is a glycoprotein, the biological effects of which are mediated through the binding to the EPO receptor (EPOR). EPOR is expressed not only in erythroid cells, but also in many non-hematopoietic cells including vascular endothelial and cancer cells.<sup>1</sup> Several scientists have proved the presence of EPOR expression in ovarian cancer cells,<sup>2–4</sup> with contrasting results regarding its localization and functionality. Solár et al.<sup>5</sup> uncovered only a poor EPOR signal in A2780 cells, where EPOR protein was found in the cytoplasm as an intracellular membrane-associated rather than a soluble protein. Silencing of EPOR expression resulted in reduced A2780 proliferation as well as a reduction of EPO-induced ERK1/2 phosphorylation.<sup>5</sup> Indeed, the formation of EPO-EPOR complex resulted in the activation of many proteins,<sup>6</sup> such as Janus kinase (JAK), Signal transducer and activator of transcription (STAT),<sup>7</sup> as well as other signal pathways involved in cell proliferation, survival and/or gene expression control.<sup>8</sup> The presence of EPOR in tumor cells question its possible negative effects on both tumor cell proliferation and the in-

hibition of apoptosis. In fact, these effects might be induced by recombinant human EPO or its analogs (e.g., erythropoiesis-stimulating agents, ESA) in cancer patients who suffer from chemotherapy-induced anemia.<sup>9</sup>

Tamoxifen (TAM) is classified as a selective estrogen receptor modulator (SERM)<sup>10</sup> that exerts its anti-proliferative action by binding to the estrogen receptor (ER) and blocking the mitogenic effect of estradiol.<sup>11</sup> Although it has been used extensively in the treatment of ER positive breast cancer,<sup>12</sup> its effectiveness was also shown in the treatment of estradiol-independent neoplasia, such as ER-negative breast cancer<sup>13</sup> and ovarian cancer.<sup>14</sup> However, the mechanism underlying the anti-proliferative action of TAM in tumor cells has not been completely clarified, as the induction of apoptosis could also mediate its cytotoxic effect.<sup>15</sup> Moreover, many studies have demonstrated that TAM acts in both cytostatic (arrest of G0/G1 phase) and cytotoxic (inducing apoptosis) manners.<sup>16,17</sup> It was shown that 1  $\mu\text{M}$  of TAM induced cell cycle arrest in G1 phase,<sup>18</sup> whereas concentration between 5 and 50  $\mu\text{M}$  TAM induced apoptosis.<sup>17</sup> This dual effect suggests that TAM can be used as a checkpoint between the cell cycle arrest and apoptosis.

Based on our previous results which showed that EPOR protects cancer cells against TAM-induced cell death even in the absence of EPO.<sup>19</sup> In this study, we aimed to analyze the effect of EPOR silencing as well as the effect of EPO treatment on the anti-proliferative potential of TAM therapy in human ovarian adenocarcinoma cells A2780.

## 2. Experimental

### 2. 1. Cell lines and Cell Culture

Human ovarian adenocarcinoma cell line A2780 was obtained from the American Tissue Culture Collection and grown in RPMI-1640 medium (Life Technologies, Carlsbad, CA, USA) supplemented with 10% fetal calf serum (FCS) (Life Technologies) and the antibiotic/antimycotic solution (100 U/ml penicillin, 100 µg/ml streptomycin, and 25 µg/ml amphotericin B, Life Technologies). The cells were maintained in the incubator under standard tissue culture conditions at 37 °C, 95 % air/5 % CO<sub>2</sub>.

### 2. 2. IncuCyte ZOOM System

We performed the experiments using an IncuCyte ZOOM system (Essen BioScience, Ann Arbor, MI, USA), which consists of a microscope with a 20 × objective (Nikon) placed inside the incubator and a networked external controller hard drive that gathers and processes image data. The A2780 cells were seeded in the antibiotic free medium in tetraplicates in 96-well plates at 5000 cells/well (as 100 µl cell suspension/well) and placed in the IncuCyte ZOOM system. After the initial 24 h of incubation, medium was removed, the siRNA prepared by DharmaFECT general transfection protocol (<http://www.molecularinfo.com/MTM/K/K1/K1-1/K1-1-16.pdf>) at the concentration of 2 µM (in the total volume of 100 µl antibiotic free medium) was added and followed by the incubation of cells for 48 h. After this period, cells were treated with 12.5 µM TAM and/or EPO (10 IU/ml and 100 IU/ml) in the antibiotic free medium (200 µl medium/well) and incubated for 72 h. The IncuCyte ZOOM system automatically monitored the cell confluence in each well every 2 h up to 72 h of TAM treatment. The experiment was performed three times. The data from three independent experiments are presented as the mean normalized Cell Index curves ± SD.

### 2. 3. Western Blotting

The A2780 cells were seeded in antibiotic free medium (3 ml/well) in 6-well plates at 4.5 × 10<sup>5</sup> cells/well. After 24 h, siRNA prepared by DharmaFECT general transfection protocol was added and cells were incubated for additional 96 hours at 37 °C in 5 % CO<sub>2</sub>. The medium was replaced with new antibiotic free medium and cells were incubated with TAM, EPO, and TAM+EPO for 15 min, fol-

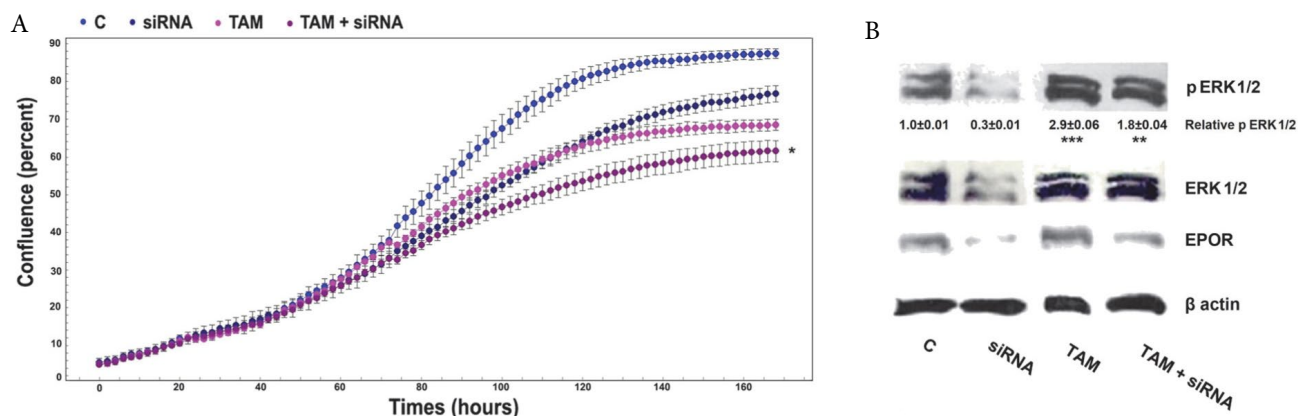
lowed by cell lysis and protein isolation. The cells were lysed for 10 min in lysis buffer on ice and the soluble proteins were recovered in the supernatant followed by centrifugation at 12,000 × g for 10 min. The protein samples were separated on 12% SDS-PAGE gels, electroblotted onto Immobilon-P transfer membrane (Millipore Co., Billerica, MA, USA), and incubated overnight with primary antibodies: anti-p44/42 MAP kinase (#9102, 1:1000, Cell Signaling Technology, Danvers, MA, USA), anti-phospho-p44/42 MAP kinase (#9102, 1:1000, Cell Signaling Technology), anti-EPOR A82 (1:1250; Amgen, Inc., CA, USA, donated from Amgen), and anti-β-actin (clone AC-74, 1:10000, Sigma). The membranes were then incubated with secondary horseradish peroxidase-conjugated antibodies, Goat anti-Rabbit IgG F(AB')<sub>2</sub> (1:10000, PI-31461, Thermo Fisher Scientific, Loughborough, UK) and Goat anti-Mouse IgG F(AB')<sub>2</sub> (1:10000, PI-31436, Thermo Fisher Scientific), for 1 h and subsequently visualized with ECL Western blotting substrate (PI-32106, Pierce) using Kodak Biomax films (#1788207, Sigma-Aldrich). Protein bands were quantified using ELLIPSE software version 2.0.7.1 (ViDiTo, SR).

## 3. Results and Discussion

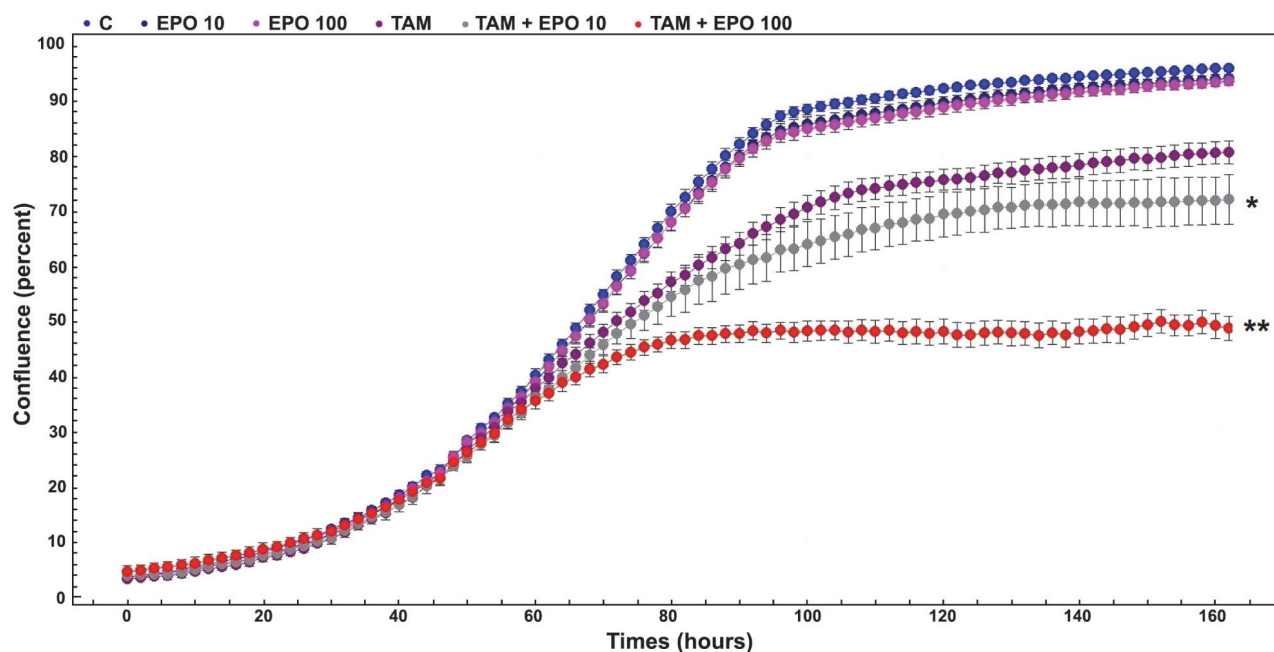
Both downregulation of EPOR as well as TAM therapy reduced cell proliferation of A2780 cells compared to controls. Moreover, their mutual combination reduced cell proliferation in greater extent compared to TAM treatment alone (Fig.1A). On the other hand, while siRNA against EPOR decreased the phosphorylation of ERK1/2 proteins, conversely TAM increased the phosphorylation. Interestingly, the combination of siRNA against EPOR and TAM therapy reduced the phosphorylation of ERK1/2 proteins compared to TAM treatment alone (Fig.1B).

We therein confirmed our previous results, indicating that EPOR plays a significant role in the proliferation of A2780 cells. Many other studies have also indicated that EPO/EPOR plays a role in tumor progression<sup>20</sup> mainly through the stimulation of cell proliferation and/or inhibition of apoptosis. On the other hand, some studies have claimed that despite of EPOR presence in cancer cells, its biological activity is weak<sup>4</sup> and does not lead to increased tumor cell proliferation after EPO stimulation.<sup>21</sup>

Our results correlate with *in vivo* study of the Paragh et al.<sup>4</sup> in which inhibition of EPOR expression led to abrogated A2780 tumor xenograft growth with reduced EPOR signaling. Our current and previous EPOR silencing study,<sup>5</sup> together with Paragh et al.,<sup>4</sup> yielded identical results, showing reduced cell proliferation of A2780 cells. On the other hand, Swift et al.<sup>2</sup> found no effect of EPOR knockdown on the viability of A2780. Application of different cell lines and different culturing (inactivated or regular serum) and/or experimental conditions could also account for inconsistent EPOR results.



**Figure 1.** The effect of siRNA against EPOR and/or TAM exposure on the proliferation and signaling of A2780 cells. Four groups of A2780 cells were set: control cells (C), cells incubated with siRNA against EPOR (siRNA), cells incubated with tamoxifen (TAM, 12.5  $\mu$ M), and cells incubated with EPOR siRNA in combination with TAM (TAM+siRNA). **A.** Cell proliferation data were normalized through the cell index curves  $\pm$  standard deviations of three independent experiments. Asterisk (\*) designates statistically significant difference in cell proliferation between TAM+siRNA versus TAM at  $p < 0.05$ . **B.** Western blot analysis of EPOR, ERK1/2, and phosphorylated ERK1/2 (p ERK1/2). Ratios  $\pm$  standard deviations from quantitative densitometric analysis of p ERK1/2 were normalized to ERK1/2. Equal loading was confirmed by detection of  $\beta$ -actin. Ratio of C was arbitrarily set to 1. \*\* $p < 0.01$ ; \*\*\* $p < 0.001$  versus C (three independent experiments; one-way ANOVA tests).



**Figure 2.** The effect of EPO and/or TAM on the proliferation of A2780 cells. The A2780 cells were incubated with erythropoietin (EPO) at concentrations of 10 IU/ml (EPO 10) or 100 IU/ml (EPO 100), with tamoxifen (TAM, 12.5  $\mu$ M), or with their combinations TAM+EPO 10 or TAM+EPO 100. Data are normalized through the cell index curves  $\pm$  standard deviations of three independent experiments. Asterisk (\*) designates statistically significant difference in cell proliferation between TAM+EPO 10 versus TAM at  $p < 0.05$  and two asterisk (\*\*) indicates significant difference in cell proliferation between TAM+EPO100 versus TAM at  $p < 0.01$ .

The incubation of A2780 cells with pharmacological concentrations of EPO (10 IU/ml or 100 IU/mL) resulted in proliferation comparable to that of the control; however, EPO did potentiate the anti-proliferative effect on TAM exposed cells (Fig. 2).

Our study showed for the first time that EPOR siRNA silencing sensitizes and/or potentiates the anti-proliferative effect of TAM on A2780 cells (Fig. 1A). This finding is

consistent with our recent study in which EPOR overexpression showed a protective effect on rat mammary adenocarcinoma cells RAMA 37-28 against TAM without the addition of EPO. In this regard, although the proliferation potential of parental RAMA 37 (low/no EPOR expression) was higher under the control conditions, the treatment with TAM affected RAMA 37 cells more and resulted in a greater inhibition of proliferation and more significant cell

death than in EPOR overexpressed RAMA 37-28 cells.<sup>19</sup> Moreover, the same study demonstrated early (5 min after TAM addition) response of RAMA 37 and RAMA 37-28 to TAM treatment with the activation of RAS/MAPK signaling pathway and ERK1/2 phosphorylation. In this regard, TAM-activated phosphorylation of ERK1/2 was slightly faster and more powerful in parental RAMA 37 than in RAMA 37-28 cells.<sup>19</sup> Similarly, ERK1/2 signalization together with other cascades were also involved in ER-positive and -negative as well as cisplatin-resistant and -sensitive ovarian cancer cells' response to TAM therapy, which led to the cell-cycle arrest in the G1 phase.<sup>20</sup> On the other hand, TAM activated ERK2 and JNK1 in HeLa cells<sup>21</sup> as well as in ER-negative MDA-MB-231 breast cancer cells in which the expression of dominant-negative JNK prevented TAM-induced apoptosis.<sup>22</sup> Similarly, the combination of TAM with inhibitors of PKC $\alpha$  and ERK could promote TAM-induced apoptosis in breast cancer cells.<sup>23</sup> Interestingly, EPOR down-regulation potentiated the anti-proliferative effect of TAM therapy and reduced TAM activated ERK1/2 phosphorylation in A2780 cells (Fig. 1B). Based on mentioned above results it seems that ERK1/2 proteins may have a dual function in TAM induced tumor cells, as both anti-proliferative as well as cell-protective effects are observed. Indeed, further studies are needed to explain when a particular effect of Erk1/2 is manifested.

Furthermore, our current study revealed also that pharmacological concentrations of EPO 10 IU/ml and 100 IU/ml increase the effect of TAM, so the combination of EPO and TAM significantly reduces the proliferation of ER-negative A2780 cells compared to TAM therapy alone (Fig. 2). Rasedee et al.,<sup>24</sup> demonstrated the synergistic effect of EPO and TAM combination which was capable of reducing the clonogenicity of the cancerous cells and cell viability significantly more than TAM alone. Moreover, the combination of EPO and TAM resulted in a 90% tumor regression in mammary tumor-induced Sprague Dawley rats, which was 20% more than that obtained with TAM alone.<sup>25</sup> Recently, EPO-conjugated TAM-loaded lipid nanoparticles enhanced the *in vitro* cytotoxicity of TAM to MCF-7 cells and showed that EPOR expressed on cancer cells is a potential receptor for drug-targeted therapy.<sup>26</sup> Although EPOR has been detected with specific A82 antibody in A2780 cells (Fig. 1B), neither the effect of 10 IU/ml nor the effect of 100 IU/ml of EPO on the proliferation of these cells was observed. On the contrary, 100 IU/ml of EPO suppressed cell proliferation of A2780 cells by 30% more than TAM alone (Fig. 2).

What underlies such potentiating effect of EPO on TAM therapy? In theory, it might be ERK1/2 and/or PKC signalization induced by both EPO and TAM exposure<sup>5,23</sup> but also EPO activated JAK2/STAT5 or PI3K.<sup>9</sup> Future study should identify specific signal pathway(s) which is (are) responsible for the potentiating effect of EPO on TAM therapy of A2780 cells.

## 4. Conclusions

Finally, siRNA against EPOR confirmed our previous results, which supported the role of EPOR protein in the proliferation of human ovarian adenocarcinoma cells A2780. In addition, we outlined the potentiating effect of EPO on TAM therapy in A2780 cells *in vitro*, which could benefit future investigations on the EPO effects in similar *in vivo* model and to indicate a possible relationship to the clinic.

## 5. Conflict of Interest

There is no conflict of interest

## 6. Acknowledgements

The present study was supported by the Scientific Grant Agency of the Ministry of Education, Science, Research, and Sport of the Slovak Republic (Bratislava, Slovak Republic, grant no. VEGA 1/0394/15).

## 7. References

1. M. E. Hardee, M. O. Arcasoy, K. L. Blackwell, J. P. Kirkpatrick and M. W. Dewhirst, *Clin Cancer Res* **2006**, *12*, 332–9. DOI:10.1158/1078-0432.CCR-05-1771
2. S. Swift, A. R. Ellison, P. Kassner, I. McCaffery, J. Rossi, A. M. Sinclair, C. G. Begley and S. Elliott, *Blood* **2010**, *115*, 4254–63. DOI:10.1182/blood-2009-10-248674
3. J. Y. Jeong, L. Feldman, P. Solar, J. Szenajch and A. J. Sytkowski, *Int J Cancer* **2008**, *122*, 274–80. DOI:10.1002/ijc.23068
4. G. Paragh, S. M. Kumar, Z. Rakosy, S. C. Choi, X. Xu and G. Acs, *Am J Pathol* **2009**, *174*, 1504–14. DOI:10.2353/ajpath.2009.080592
5. P. Solar, G. Hrcakova, L. Varinska, Z. Solarova, J. Kriska, I. Uhrinova, M. Kello, J. Mojzis, P. Fedorocko and A. J. Sytkowski, *Oncol Rep* **2012**, *28*, 141–6.
6. S. S. Watowich, D. J. Hilton and H. F. Lodish, *Mol Cell Biol* **1994**, *14*, 3535–49. DOI:10.1128/MCB.14.6.3535
7. V. Pelekanou, M. Kampa, M. Kafousi, K. Dambaki, K. Darivianaki, T. Vrekoussis, E. Sanidas, D. D. Tsiptsis, E. N. Stathopoulos and E. Castanas, *Cancer Epidemiol Biomarkers Prev* **2007**, *16*, 2016–23. DOI:10.1158/1055-9965.EPI-06-1023
8. J. E. Darnell, Jr., I. M. Kerr and G. R. Stark, *Science* **1994**, *264*, 1415–21. DOI:10.1126/science.8197455
9. N. Debeljak, P. Solar and A. J. Sytkowski, *Front Immunol* **2014**, *5*, 563. DOI:10.3389/fimmu.2014.00563
10. B. Fisher, J. P. Costantino, C. K. Redmond, E. R. Fisher, D. L. Wickerham and W. M. Cronin, *J Natl Cancer Inst* **1994**, *86*, 527–37. DOI:10.1093/jnci/86.7.527

11. V. C. Jordan, *Breast Cancer Res Treat* **1990**, *15*, 125–36.  
DOI:10.1007/BF01806350
12. R. R. Love, *J Clin Oncol* **1989**, *7*, 803–15.  
DOI:10.1200/JCO.1989.7.6.803
13. I. A. Jaiyesimi, A. U. Buzdar, D. A. Decker and G. N. Hortobagyi, *J Clin Oncol* **1995**, *13*, 513–29.  
DOI:10.1200/JCO.1995.13.2.513
14. M. Markman, K. A. Iseminger, K. D. Hatch, W. T. Creasman, W. Barnes and B. Dubeshter, *Gynecol Oncol* **1996**, *62*, 4–6.  
DOI:10.1006/gyno.1996.0181
15. E. P. Gelmann, *J Natl Cancer Inst* **1996**, *88*, 224–6.  
DOI:10.1093/jnci/88.5.224
16. C. K. Osborne, D. H. Boldt, G. M. Clark and J. M. Trent, *Cancer Res* **1983**, *43*, 3583–5.
17. R. R. Perry, Y. Kang and B. Greaves, *Ann Surg Oncol* **1995**, *2*, 238–45. DOI:10.1007/BF02307030
18. A. M. Otto, R. Paddenberg, S. Schubert and H. G. Mannherz, *J Cancer Res Clin Oncol* **1996**, *122*, 603–12.  
DOI:10.1007/BF01221192
19. L. Ilkovicova, N. Trost, E. Szentpeteriova, P. Solar, R. Komel and N. Debeljak, *Int J Oncol* **2017**, *51*, 737–746.  
DOI:10.3892/ijo.2017.4061
20. S. Mabuchi, M. Ohmichi, A. Kimura, Y. Ikebuchi, K. Hisamoto, E. Arimoto-Ishida, Y. Nishio, K. Takahashi, K. Tasaka and Y. Murata, *Endocrinology* **2004**, *145*, 1302–13.  
DOI:10.1210/en.2003-0709
21. J. L. Duh, R. Yu, J. J. Jiao, G. A. Matwysyn, W. Li, T. H. Tan and A. N. Kong, *Pharm Res* **1997**, *14*, 186–9.  
DOI:10.1023/A:1012048626963
22. S. Mandlekar, V. Hebbar, K. Christov and A. N. Kong, *Cancer Res* **2000**, *60*, 6601–6.
23. Z. Li, N. Wang, J. Fang, J. Huang, F. Tian, Ch. Li, and F. Xie, *Oncol Rep* **2012**, *27*, 1879–86. DOI:10.3892/or.2012.1635
24. A. Rasedee, R. Rozita, B. M. A. Noorjahan and G. Y. Teo, Paper presented at: International Exposition of Research and Innovations of Institutions of Higher Learning (PECIPTA). Organized by Ministry of Higher Education and University of Science Malaysia; August 10–12, **2007**; Kuala Lumpur.
25. A. K. Sairah, A. Rasedee, O. Sheikh, R. Rozita and N. Al-Haj, *Am J Pharmacol Toxicol* **2009**, *4*, 12–6.  
DOI:10.3844/ajtp.2009.12.16
26. Ch. Y. Beh, Ch. W. How, J. B. Foo, J. N. Foong, G. T. Selvarajah and A. Rasedee, *Drug Des Devel Ther* **2017**, *11*, 771–82.  
DOI:10.2147/DDDT.S123939

## Povzetek

Pred kratkim smo pokazali, da receptor za eritropoetin (EPOR), tudi v odsotnosti eritropoetina (EPO), ščiti rakave celice pred s tamoksifenom (TAM) povzročeno celično smrtjo. V trenutnem članku smo analizirali odzivnost človeških ovarijskih adenokarcinomskih celic A2780 na TAM ob utišanju EPOR in izpostavitvi EPO. Pokazali smo, da utišanje EPOR s siRNA zmanjša celično proliferacijo in senzibilizira in / ali poveča antiproliferativni učinek TAM na celice A2780. Sočasen učinek zdravljenja z EPO in TAM bistveno zmanjša proliferacijo celic v primerjavi s samim TAM. Naši rezultati *in vitro* nakazujejo potrebo po nadaljnji raziskavi učinkov EPO na modelu *in vivo* ter predstavljajo izziv za prihodnje klinične raziskave.

Scientific paper

# Liquid-Liquid Extraction-Chromogenic System for Vanadium(V) Based on 4-(2-thiazolylazo)orcinol (TAO) and Aliquat 336

Galya K. Toncheva,<sup>1</sup> Nikolina P. Milcheva,<sup>2</sup> and Kiril Blazhev Gavazov<sup>2,\*</sup>

<sup>1</sup> Department of General and Inorganic Chemistry with Methodology of Chemical Education, University of Plovdiv Paisii Hilendarski, 24 Tsar Assen St., Plovdiv 4000, Bulgaria

<sup>2</sup> Department of Chemical Sciences, Medical University of Plovdiv, 120 Buxton Brothers St., Plovdiv 4004, Bulgaria

\* Corresponding author: E-mail: kgavazov@abv.bg

Received: 24-05-2018

## Abstract

The quaternary ammonium salt Aliquat 336 (A336;  $R_4N^+Cl^-$ ) and the azo dye 4-(2-thiazolylazo)orcinol (TAO) were examined as constituents of a water-isobutanol extraction-chromogenic system for vanadium(V). Under the optimum conditions ( $c_{TAO} = 1.6 \times 10^{-3} \text{ mol dm}^{-3}$ ,  $c_{A336} = 1.3 \times 10^{-2} \text{ mol dm}^{-3}$  and pH 5.0), vanadium(V) is extracted as a ternary complex which can be represented by the formula  $(R_4N^+)[VO_2(TAO^2-)]$ . The key extraction-spectrophotometric characteristics were determined. The interfering effect of foreign ions was studied as well. The wavelength of maximum absorption ( $\lambda_{max}$ ), molar absorptivity ( $\epsilon_{max}$ ), constant of extraction ( $K_{ex}$ ) and fraction extracted ( $E$ ) were found to be  $\lambda = 547 \text{ nm}$ ,  $\epsilon = 3.1 \times 10^4 \text{ dm}^3 \text{ mol}^{-1} \text{ cm}^{-1}$ ,  $\text{Log } K_{ex} = 2.8$  and  $E = 90.2\%$ , respectively. Beer's law was obeyed in the range of  $0.084\text{--}2.0 \text{ } \mu\text{g cm}^{-3}$  and the limit of detection was  $25 \text{ ng cm}^{-3}$  of vanadium(V).

**Keywords:** Vanadium(V); 5-methyl-4-(2-thiazolylazo)resorcinol; ternary complex; solvent extraction; spectrophotometric determination; room temperature ionic liquid

## 1. Introduction

Ionic liquids (ILs) possess fascinating properties that are rather different from those of conventional molecular solvents. This makes ILs of fundamental interest to specialists in various areas of chemistry and physics.<sup>1,2</sup> The IL Aliquat 336 (A336;  $R_4N^+Cl^-$ ) finds applications as a surfactant, phase-transfer catalyst and ion-association reagent.<sup>3</sup> The methyltrialkyl( $C_8\text{--}C_{10}$ )ammonium cations it contains can form hydrophobic ion-associates with various anions and the obtained compounds can be separated by extraction methods, such as liquid-liquid extraction (LLE) and cloud-point extraction. In LLE procedures, A336 is dissolved in organic solvents, which improve its physical properties, such as viscosity and surface tension. The following solvents have been used: carbon tetrachloride,<sup>4,5</sup> benzene,<sup>6,7</sup> toluene,<sup>8</sup> xylene,<sup>9</sup> chloroform,<sup>5</sup> cyclohexane,<sup>5</sup> 1-octanol<sup>10</sup> and kerosene + higher alcohols.<sup>11–15</sup> Unfortunately, many of them are highly toxic which limits the application of the developed methods.

The present paper aims at to study the LLE of  $V^V$  in a chromogenic system containing 5-methyl-4-(2-thiazolylazo)resorcinol {4-(2-thiazolylazo)orcinol, TAO} and A336, dissolved in isobutanol (2-methylpropan-1-ol). This solvent is among the least toxic butanols.<sup>16</sup> It is not as volatile or corrosive as lower alcohols,<sup>16</sup> can be produced from renewable resources<sup>17</sup> and is either added as a flavoring agent or present naturally in food and drink systems, such as cognac, whiskey, wine, brandy, arrack, Chinese quince fruit, nectarine, hog plum, etc.<sup>18</sup>

It should be mentioned that the LLE of TAO-containing complexes is an almost unexplored area.<sup>19,20</sup> Chloroform-extracted  $V^V$ -TAO ternary complexes with tetrazolium cations were recently investigated in our laboratory.<sup>20,21</sup> It was found that their structures differs from the structures of the ternary complexes of  $V^V$  with similar ligands, such as 4-(2-thiazolylazo)resorcinol (TAR) and 4-(2-pyridylazo)resorcinol (PAR), due to the influence of the  $-CH_3$  group of TAO, which is capable to form a H-bond with an oxygen atom of the  $-VO_2$  group.<sup>21</sup>

The list of related studies can be extended by the chloroform extraction of  $V^V$  as a ternary complex with PAR and methyltriocylammonium chloride,<sup>22</sup> which is one of the main components of A336.<sup>23</sup> Ligandless LLE of  $V^V$  with A336 in acidic<sup>11,12,14</sup> and alkaline<sup>12</sup> medium was studied as well. However, in the absence of a chelating reagent, the extraction equilibrium is established slowly and there are practical problems with the formation of a third phase.<sup>24</sup>

## 2. Experimental

### 2.1. Reagents and Apparatus

Vanadium(V) solution ( $2 \times 10^{-4}$  mol dm<sup>-3</sup>) was prepared by dissolving  $NH_4VO_3$  (puriss. p.a., VEB Laborchemie Apolda, Germany) in water. TAO (95%, Sigma-Aldrich Chemie GmbH) was dissolved in the presence of KOH (1–2 pellets per 100 cm<sup>3</sup>); the obtained slightly alkaline aqueous solution (pH 8–9) was at concentration of  $5.3 \times 10^{-3}$  mol dm<sup>-3</sup>. Aliquat 336 was purchased from Sigma-Aldrich Chemie and dissolved in isobutanol (p. a. Merck). Solutions with concentrations of  $1.6 \times 10^{-2}$  and  $1.3 \times 10^{-2}$  mol dm<sup>-3</sup> were used; the calculations were based on the average molar mass of A336, 432 g mol<sup>-1</sup>.<sup>3</sup> The acidity of the aqueous medium was set by the addition of buffer solution, prepared by mixing 2.0 mol dm<sup>-3</sup> aqueous solutions of  $CH_3COOH$  and ammonia. pH was checked by a Hanna HI-83141 (Romania) and a WTW InoLab 7110 (Germany) instruments. Absorbance measurements were performed by using a Camspec M508 and a Ultrospec3300 pro UV-Vis spectrophotometers (UK), equipped with 1 cm path-length glass cells. Distilled water was used throughout the work.

### 2.2. Determination of the Optimum LLE-Spectrophotometric Conditions

Solutions of  $V^V$ , TAO and buffer were placed into separatory funnels. The aqueous phase volume was made up to 10 cm<sup>3</sup> with water. Then A336 solution was added and the organic phase was made up to 5 cm<sup>3</sup> or 10 cm<sup>3</sup> with isobutanol. The funnel was shaken for a fixed time interval. After separation of the phases, the aqueous phase was discarded, the organic phase was transferred into a beaker and dried with a pinch of anhydrous  $Na_2SO_4$ . Finally, the dried extract was poured into the spectrophotometer cell and the absorbance was measured against isobutanol or simultaneously prepared blank solution.

### 2.3. Determination of the Coefficient of Distribution

The coefficient of distribution  $D$  was calculated by the formula  $D = A_1/(A_3 - A_1)$ , where  $A_1$  is the absorbance obtained after a single extraction (under the optimal ex-

traction conditions, Table 1), and  $A_3$  is the absorbance obtained after a triple extraction under the same conditions. The final volume of the solutions in both cases was 25 cm<sup>3</sup>.<sup>21,25,26</sup>

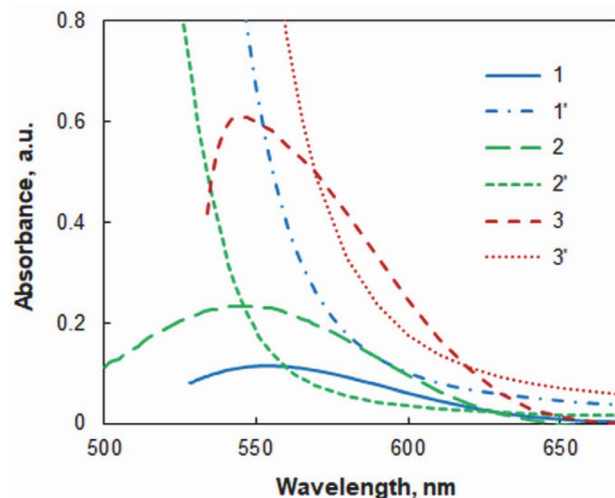
### 2.4. Investigation of the Influence of Foreign Ions

Solutions of  $V^V$  ( $1 \text{ cm}^3, 2 \times 10^{-4}$  mol dm<sup>-3</sup>), foreign ion, TAO ( $3 \text{ cm}^3, 5.3 \times 10^{-3}$  mol dm<sup>-3</sup>) and buffer ( $1 \text{ cm}^3$ , pH 5) were successively placed into a separatory funnel. The aqueous phase volume was made up to 10 cm<sup>3</sup> with water. Then A336 solution ( $5 \text{ cm}^3, 1.3 \times 10^{-2}$  mol dm<sup>-3</sup>) was added and the funnel was shaken for 30 sec. After separation of the phases, the organic phase was transferred into a beaker, dried with a pinch of anhydrous  $Na_2SO_4$  and poured into the spectrophotometer cell. The absorbance was measured at 547 nm against isobutanol. For control, samples prepared in the absence of the foreign ion or  $V^V$  were also run.

## 3. Results and Discussion

### 3.1. LLE-Spectrophotometric Optimization

It is known that  $V^V$  forms a red complex with TAO in aqueous ethanolic medium.<sup>21,27</sup> It has a composition of 1:1 and cannot be extracted in chloroform, due to its anionic nature.<sup>21</sup> Our preliminary studies on the  $V^V$ -TAO-water-isobutanol system showed that the red complex can partially pass into the organic phase (Fig. 1, spectrum 1). This can be explained by the existing equilibrium between anionic and neutral (protonated) complex species.<sup>28,29</sup>



**Figure 1.** Absorption spectra in isobutanol of complexes against blanks (1–3;  $c_V = 2 \times 10^{-5}$  mol dm<sup>-3</sup>) and blanks against isobutanol (1'–3'). (1, 1')  $c_{TAO} = 1.6 \times 10^{-3}$  mol dm<sup>-3</sup>, pH 5.0, extraction time  $t = 120$  sec; (2, 2')  $c_{TAO} = 2.0 \times 10^{-4}$  mol dm<sup>-3</sup>, pH 5.0,  $c_{A336} = 1.3 \times 10^{-2}$  mol dm<sup>-3</sup>, extraction time  $t = 30$  sec; (3, 3')  $c_{TAO} = 1.6 \times 10^{-3}$  mol dm<sup>-3</sup>, pH 5.0,  $c_{A336} = 1.3 \times 10^{-2}$  mol dm<sup>-3</sup>, extraction time  $t = 30$  sec.



Upon addition of A336, the rate of extraction increases sharply due to the formation of a ternary complex (Fig. 1, spectra 2 and 3). At that, the absorption maximum shifts hypsochromically by several nanometers. The profile of the absorption band of the ternary complex and the exact position of the maximum depend on the concentration of the reagents. At high concentrations, ensuring  $V^V$  fraction extracted close to 90%, the profile of the absorption band is asymmetric (Fig. 1, spectrum 3) and the absorption maximum lies at 547 nm.

The effect of pH on the absorbance of the extract is shown in Fig. 2. The results were obtained in the presence of ammonia-acetate solutions ( $1 \text{ cm}^3$ ), which provide buffering around pH 4.75 (the  $pK_a$  of acetic acid) and pH 9.25 (the  $pK_a$  of ammonium).<sup>30</sup> In the absence of the buffer, a stable emulsion is formed and the phase separation is slow.

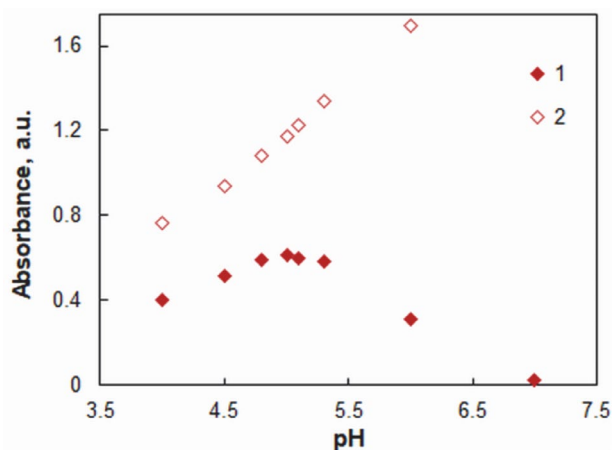
Fig. 2 shows that the absorbance of the complex is maximal in the pH range of 4.9–5.2. This range is close to the  $pK_a$  value of acetic acid, indicating that the buffer used is suitable. The decrease in absorbance at pH-values less than *ca.* 4.9 can be attributed to incomplete complex formation due to the prevalence of protonated TAO species in the solution.<sup>31</sup> The decrease in absorbance at pH-values higher than *ca.* 5.2 can be explained by the formation of non-extractable negatively charged vanadium-containing species of the type  $[V(O)_x(TAO)_y]^{n-}$  (where  $n > 1$  and vanadium oxidation state is +5). Another reason can be the simultaneous extraction of the TAO-A336 ion-pair, which reduces the effective reagents concentrations with increasing pH (see Fig. 2, series 2). A change in the oxidation state of vanadium under the reaction conditions is not expected.<sup>20,21</sup>

Further optimization experiments were directed to the selection of working concentrations of the reagents, TAO and A336 (Fig. 3), and the time of extraction. The optimization ranges and the set of optimal values are summarized in Table 1.

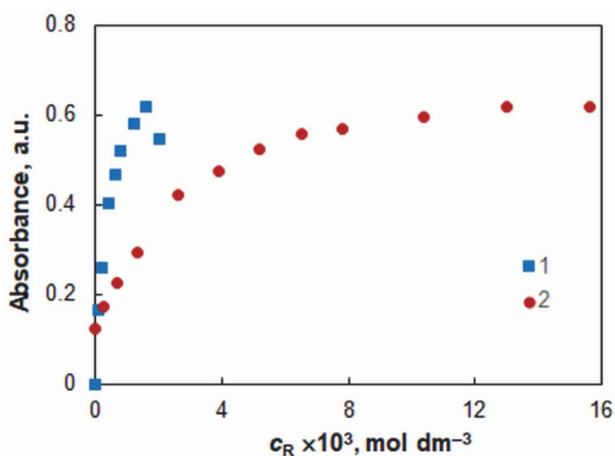
When comparing the optimal TAO concentrations in this work and in our previous studies with tetrazolium salts,<sup>20,21</sup> it is clear that the TAO concentration in the present system should be higher  $\{1.6 \times 10^{-3} \text{ mol dm}^{-3} \text{ vs. } (3.0\text{--}4.5) \times 10^{-4} \text{ mol dm}^{-3}\}$ . The same is valid for the concentration of the cationic ion-association reagent  $\{1.3 \times 10^{-2} \text{ mol dm}^{-3} \text{ vs. } (3.9\text{--}9.4) \times 10^{-4} \text{ mol dm}^{-3}\}$ . This disadvantage can be attributed to the lower stability of the ternary

complex, provoked by the shape of the cation used and localized charge in it.<sup>32,33</sup>

It is important to be mentioned that the extraction time in the present work does not affect the absorbance in the entire investigated range (5–240 sec). No decrease in absorption was observed by increasing the extraction time



**Figure 2.** Absorbance of the  $V^V$  – TAO – A336 complex (1) and the blank (2) vs. pH of the aqueous phase.  $c_V = 2 \times 10^{-5} \text{ mol dm}^{-3}$ ,  $c_{TAO} = 1.6 \times 10^{-3} \text{ mol dm}^{-4}$ , pH 5.0,  $c_{A336} = 1.3 \times 10^{-2} \text{ mol dm}^{-3}$ , extraction time  $t = 120 \text{ sec}$ .



**Figure 3.** Effect of TAO (1) and A336 (2) concentration on the absorbance. (1)  $c_V = 2 \times 10^{-5} \text{ mol dm}^{-3}$ , pH 5.0,  $c_{A336} = 1.3 \times 10^{-2} \text{ mol dm}^{-3}$ , extraction time  $t = 120 \text{ sec}$ .; (2)  $c_V = 2 \times 10^{-5} \text{ mol dm}^{-3}$ ,  $c_{TAO} = 1.6 \times 10^{-3} \text{ mol dm}^{-4}$ , pH 5.0, extraction time  $t = 120 \text{ sec}$ .

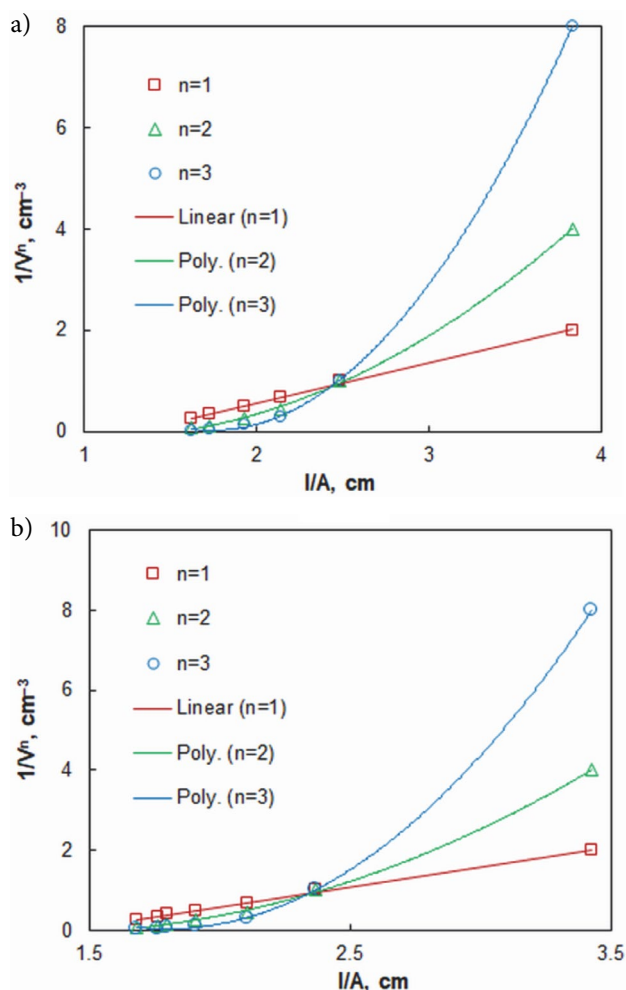
**Table 1.** LLE-spectrophotometric optimization of the  $V^V$  – TAO – Aliquat 336 – water – isobutanol system.

Parameter	Optimization range	Optimal value
Wavelength, nm	Visible range	547
pH	4.0–7.0	5.0
Concentration of TAO, $\text{mol dm}^{-3}$	$(0.08\text{--}2) \times 10^{-3}$	$1.6 \times 10^{-3}$
Concentration of Aliquat 336, $\text{mol dm}^{-3}$	$(0\text{--}1.56) \times 10^{-2}$	$1.3 \times 10^{-2}$
Extraction time, seconds	5–240	30

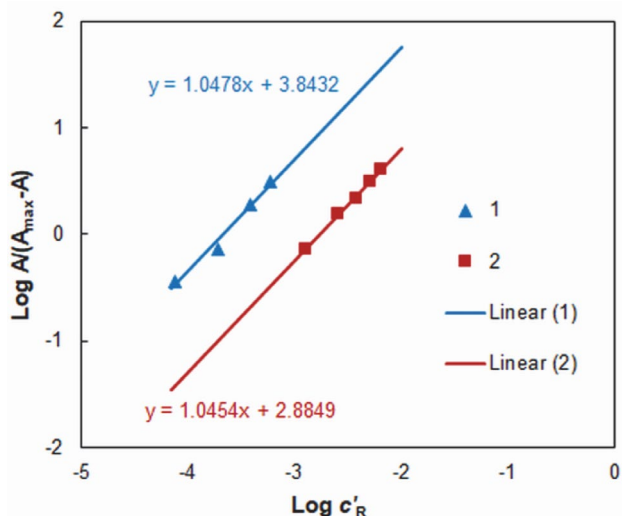
as reported in the literature<sup>34</sup> on the extraction of  $V^V$  with PAR into similar solvents, such as n-pentanol and n-butanol. We extracted for 30 seconds in our further investigations. This contact time is slightly shorter than the times for  $V^V$  extraction by TAO and tetrazolium salts (several minutes)<sup>20,21</sup> and much shorter than the times for  $V^V$  extraction by Aliquat 336 in the absence of chelate reagents.<sup>11,12,14</sup>

### 3. 2. Molar Ratios, Complex Composition and Extraction Characteristics

The molar TAO-to- $V^V$  ratio was determined by the method of Asmus<sup>35</sup> (Fig. 4a) and the mobile equilibrium method<sup>36</sup> (Fig. 5, line 1). The molar Aliquat 336-to- $V^V$  ratio was determined by the same methods (Fig. 4b and Fig. 5, line 2). The results show that the composition of the ternary complex is 1:1:1. Such a composition was reported for the chloroform extracted  $V^V$ -PAR-methyltriocetylammmonium complex.<sup>22</sup> There are no signs of dimerization in the



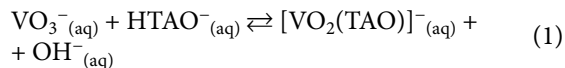
**Figure 4.** Determination of the TAO/ $V^V$  (a) and A336/ $V^V$  (b) molar ratios by the straight-line method of Asmus. The experimental conditions are given in Fig. 3.



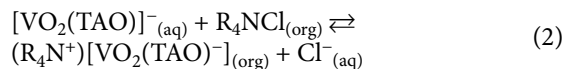
**Figure 5.** Determination of the TAO/ $V^V$  (1) and A336/ $V^V$  (2) molar ratios by the mobile equilibrium method. The experimental conditions are given in Fig. 3.

organic phase, as in the extraction of the  $V^V$ -TAO anionic complex  $[\text{VO}_2(\text{TAO})]^-$  with tetrazolium salts.<sup>20,21</sup>

The formation of the binary complex in the aqueous phase can be represented by equation 1. It is based on information concerning the state of  $V^V$ <sup>37</sup> and TAO<sup>29</sup> at the reaction conditions.



The next steps, ion-association and extraction, are represented by equation 2.



In it, A336 and its cation are denoted as  $\text{R}_4\text{NCl}$  and  $\text{R}_4\text{N}^+$ , respectively. The conditional equilibrium constant characterizing equation 2 was calculated by the mobile equilibrium method<sup>36</sup> (Fig. 5, straight line 2). The obtained value was  $\text{Log } K_{\text{ex}} = 2.8 \pm 0.1$ . The coefficient of distribution  $D$  was found by comparison of the absorbance values obtained after single and triple extractions as described above:  $\text{Log } D = 0.97 \pm 0.04$  (three replicate measurements). The fraction extracted,  $E = (90.2 \pm 0.8)\%$ , was calculated by the formula  $E\% = 100 \times D / (D + 1)$ .

### 3. 3. Beer's Law and Analytical Characteristics

The dependence between the concentration of  $V^V$  in the aqueous phase and the absorbance of the extracted complex was studied under the optimum conditions (Table 1). The volumes of the aqueous and organic phase were set to 10 and 5  $\text{cm}^3$ , respectively. A good linearity was obtained in the range of  $0.084\text{--}2.0 \mu\text{g cm}^{-3}$  ( $r^2 = 0.9994$ ,  $N =$

9). The linear regression equation was  $A = 0.615\gamma - 0.0067$ , where  $A$  is the absorbance and  $\gamma$  is the concentration of  $V^V$  ( $\mu\text{g cm}^{-3}$ ). The standard deviations of the slope and intercept were both equal to 0.005. The limits of detection (LOD) and quantitation (LOQ), calculated as 3 and 10 times standard deviation of the intercept divided by the slope, were  $\text{LOD} = 25 \text{ ng cm}^{-3}$  and  $\text{LOQ} = 84 \text{ ng cm}^{-3}$ . The molar absorptivity ( $\epsilon$ ) and Sandell's sensitivity ( $S$ ) at  $\lambda_{\text{max}} = 547 \text{ nm}$  were  $\epsilon = 3.1 \times 10^4 \text{ dm}^3 \text{ mol}^{-1} \text{ cm}^{-1}$  and  $S = 1.6 \times 10^{-3} \mu\text{g cm}^{-2}$ , respectively.

### 3. 4. Effect of Foreign Ions

Various ions which are often found together with vanadium in environmental and industrial samples were used to test the selectivity of the developed procedure. Their effect at  $\lambda = 547 \text{ nm}$  is presented in Table 2.  $\text{Co}^{\text{II}}$ ,  $\text{Cu}^{\text{II}}$ ,  $\text{Ni}^{\text{II}}$  and  $\text{Fe}^{\text{III}}$  form intensively colored extractable complexes with TAO. They cause serious positive errors in the spectrophotometric determination of  $V^V$ .  $\text{Mo}^{\text{VI}}$ ,  $\text{Al}^{\text{III}}$ ,  $\text{Cr}^{\text{III}}$ ,  $\text{Re}^{\text{VII}}$  and  $\text{W}^{\text{VI}}$  can cause negative errors, however their interfering effect is smaller. When present in moderate amounts, alkaline and alkaline earth cations and the most of the anions studied do not significantly affect the absorbance.  $V^{\text{IV}}$  causes an increase in absorption as if it were  $V^V$ . Most likely, it is oxidized to  $V^V$  by the air oxygen<sup>38,39</sup> in the initial step of the procedure when the slightly alkaline TAO solution is added to the vanadium.

## 4. Conclusions

The ternary complex formed in the liquid-liquid extraction-chromogenic system  $V^V$ -TAO-A336 has a composition of 1:1:1 and can be represented by the formula  $(\text{R}_4\text{N}^+)[\text{VO}_2(\text{TAO})]$ . Its anionic part  $[\text{VO}_2(\text{TAO})]^-$  has an intense red coloration, while the bulky cationic part  $\text{R}_4\text{N}^+$  is responsible for the easy extraction of the target metal ion ( $V^V$ ) into organic phase. The organic solvent, isobutanol, is less toxic than the solvents commonly applied is methods involving Aliquat 336. Additional advantages of the proposed procedure are its simplicity and rapidity. Disadvantages in comparison to similar extraction systems, containing tetrazolium salts (instead of Aliquat 336), are the need for higher concentration of the reagents and smaller fraction extracted. These disadvantages can be attributed to the lower stability of the ion-associate, provoked by the shape of the cation and localized charge in it.

## 5. References

1. M. Koel, *Ionic liquids in chemical analysis*, CRC press, Boca Raton-London-New York, **2009**.
2. P. Sun, D. W. Armstrong, *Anal. Chim. Acta* **2010**, *661*, 1–16. DOI: 10.1016/j.aca.2009.12.007.
3. J.-P. Mikkola, P. Virtanen, R. Sjöholm, *Green Chem.* **2006**, *8*, 250–255. DOI: 10.1039/B512819F.

Table 2. Effect of foreign ions in determination of 10.2  $\mu\text{g}$  of  $V^V$ .

Foreign ion (FI) added	Added salt	FI : $V^V$ mass ratio	Amount of $V^V$ found ( $\mu\text{g}$ )	(%)
$\text{Al}^{\text{III}}$	$\text{Al}_2(\text{SO}_4)_3 \cdot 18\text{H}_2\text{O}$	10	9.8	96.2
$\text{Br}^-$	$\text{NaBr}$	100	10.2	100
$\text{Cd}^{\text{II}}$	$\text{CdCl}_2$	5	10.7	105
$\text{Cl}^-$	$\text{NH}_4\text{Cl}$	200	10.0	98.3
$\text{Co}^{\text{II}}$	$\text{CoSO}_4 \cdot 7\text{H}_2\text{O}$	1	17.5	172
$\text{Cr}^{\text{III}}$	$\text{Cr}_2(\text{SO}_4)_3$	2	9.8	96.1
$\text{Cr}^{\text{VI}}$	$\text{K}_2\text{CrO}_4$	1	11.2	110
$\text{Cu}^{\text{II}}$	$\text{CuSO}_4 \cdot 5\text{H}_2\text{O}$	2	19.9	195
$\text{F}^-$	$\text{NH}_4\text{F}$	300	10.2	100
$\text{Fe}^{\text{III}}$	$\text{Fe}_2(\text{SO}_4)_3$	1	14.8	145
$\text{HPO}_4^{2-}$	$\text{Na}_2\text{HPO}_4$	200	10.4	102
$\text{I}^-$	$\text{KI}$	100	9.69	95.0
$\text{Mg}^{\text{II}}$	$\text{MgSO}_4$	300	10.2	100
$\text{Mn}^{\text{II}}$	$\text{MnSO}_4 \cdot 5\text{H}_2\text{O}$	2	10.6	104
$\text{Mo}^{\text{VI}}$	$(\text{NH}_4)_6\text{Mo}_7\text{O}_{24} \cdot 4\text{H}_2\text{O}$	100	10.2	100
$\text{Ni}^{\text{II}}$	$\text{NiSO}_4 \cdot 7\text{H}_2\text{O}$	1	14.9	146
$\text{NO}_3^-$	$\text{NH}_4\text{NO}_3$	200	10.2	100
$\text{Re}^{\text{VII}}$	$\text{NH}_4\text{ReO}_4$	20	10.0	98.0
Tartrate	$\text{KNaC}_4\text{H}_4\text{O}_6 \cdot 4\text{H}_2\text{O}$	100	9.75	95.9
$\text{U}^{\text{VI}}$	$\text{UO}_2(\text{CH}_3\text{COO})_2 \cdot \text{H}_2\text{O}$	2	10.6	104
$V^{\text{IV}}$	$\text{VO}_2 \cdot 5\text{H}_2\text{O}$	1	20.3	199
		0.5	15.3	150
$\text{W}^{\text{VI}}$	$\text{Na}_2\text{WO}_4 \cdot 2\text{H}_2\text{O}$	5	10.2	100
$\text{Zn}^{\text{II}}$	$\text{ZnSO}_4 \cdot 7\text{H}_2\text{O}$	30	10.2	100

4. K. Grudpan, C.G. Taylor, *Analyst* **1984**, *109*, 585–588.  
DOI: 10.1039/AN9840900585.
5. M. Atanassova, I. L. Dukov, *Sep. purify. Technol.* **2004**, *40*, 171–176. DOI: 10.1016/j.seppur.2004.02.007.
6. I. Dukov, M. Atanassova, S. Zhivkova, A. Lirkov, *J. Univ. Chem. Technol. Met.* **2006**, *41*, 75–80.
7. W. Wei, C.-W. Cho, S. Kim, M.-H. Song, J. K. Bediako, Y.-S. Yun, *J. Mol. Liq.* **2016**, *216*, 18–24.  
DOI: 10.1016/j.molliq.2016.01.016.
8. V. Gardoňová, M. Labaška, I. Antalík, J. Kuruc, *J. Radioanal. Nucl. Chem.* **2013**, *295*, 1353–1360.  
DOI: 10.1007/s10967-012-1955-z.
9. A. G. Gaikwad, A. D. Damodaran, *J. Radioanal. Nucl. Chem.* **1992**, *163*, 277–288. DOI: 10.1007/BF02034801.
10. A. Keshav, K. L. Wasewar, S. Chand, *Ind. Eng. Chem. Res.* **2008**, *47*, 6192–6196. DOI: 10.1021/ie800006r.
11. A. Nayl, H. Aly, *Trans. Nonferrous Met. Soc. China* **2015**, *25*, 4183–4191. DOI: 10.1016/S1003-6326(15)64021-3.
12. Y. El-Nadi, N. Awwad, A. Nayl, *Int. J. Miner. Process.* **2009**, *92*, 115–120. DOI: 10.1016/j.minpro.2009.03.005.
13. F. M. Fábrega, M. B. Mansur, *Hydrometallurgy* **2007**, *87*, 83–90. DOI: 10.1016/j.hydromet.2007.02.004.
14. R. Navarro, J. Guzman, I. Saucedo, J. Revilla, E. Guibal, *Waste Manag.* **2007**, *27*, 425–438.  
DOI: 10.1016/j.wasman.2006.02.002.
15. J. A. López-López, B. Herce-Sesa, C. Moreno, *Talanta* **2016**, *159*, 117–121. DOI: 10.1016/j.talanta.2016.06.018.
16. A. Pal, V. Manish, S. Gupta, N. Kumar, *SAE Technical Paper 2013-24-0151*. DOI: 10.4271/2013-24-0151.
17. S. Atsumi, T. Hanai, J. C. Liao, *Nature* **2008**, *451*, 86–90.  
DOI: 10.1038/nature06450.
18. G. A. Burdock, *Encyclopedia of food & color additives*. Vol. I., CRC Press, Boca Raton-New York-London-Tokyo, **1996**, pp. 1443–1444.
19. V. A. Lemos, E. S. Santos, M. S. Santos, R. T. Yamaki, *Microchim. Acta* **2007**, *158*, 189–204.  
DOI: 10.1007/s00604-006-0704-9
20. K. B. Gavazov, T. S. Stefanova, *Croat. Chem. Acta* **2014**, *87*, 233–240. DOI: 10.5562/cca2436.
21. K. B. Gavazov, V. B. Delchev, K. T. Mileva, T. S. Stefanova, G. K. Toncheva, *Acta Chim. Slov.* **2016**, *63*, 392–398.  
DOI: 10.17344/acsi.2016.2431.
22. E. Papp, J. Inczédy, *Talanta* **1980**, *27*, 49–51.  
DOI: 10.1016/0039-9140(80)80011-7.
23. G. L. Lee, R. W. Cattrall, H. Daud, J. F. Smith, I. C. Hamilton, *Anal. Chim. Acta* **1981**, *123*, 213–220.  
DOI: 10.1016/S0003-2670(01)83173-1.
24. Y. Bal, K. E. Bal, G. Cote, A. Lallam, *Hydrometallurgy* **2004**, *75*, 123–134. DOI: 10.1016/j.hydromet.2004.07.004.
25. K. T. Stojnova, K. B. Gavazov, V. D. Lekova, *Acta Chim. Slov.* **2013**, *60*, 390–396.
26. K. B. Gavazov, G. K. Toncheva, V. B. Delchev, *Open Chem.* **2016**, *14*, 197–205. DOI: 10.1515/chem-2016-0022.
27. G. G. Shalamova, *Tr. Perm. Med. Inst.* **1972**, *108*, 48–53.
28. O. I. Karpova, V. V. Lukachina, A. T. Pilipenko, *Ukr. Khim. Zh.* **1973**, 39 194–195.
29. J. J. Arias, F. Jlmenez, F. Garcia Montelongo, *An. Qulfh., Ser. B* **1980**, *76*, 452–459.
30. L. Konermann, *J. Am. Soc. Mass Spectrom.* **2017**, *28*, 1827–1835. DOI: 10.1007/s13361-017-1739-3.
31. N. Menek, E. Eren, S. Topçu, *Dyes Pigment.* **2006**, *68*, 205–210.  
DOI: 10.1016/j.dyepig.2005.01.010.
32. K. Tōei, *Anal. Sci.* **1987**, *3*, 479–488.  
DOI: 10.2116/analsci.3.479.
33. K. B. Gavazov, *Chemistry* **2013**, *22*, 222–253.
34. R. M. Pogranichnaya, V. V. Nerubashchenko, A. V. Tsevina, *Zh. Anal. Khim.* **1972**, *27*, 1845–1847.
35. E. Asmus, *Fresenius' J. Anal. Chem.* **1960**, *178*, 104–116.  
DOI: 10.1007/bf00467200.
36. Z. Zhiming, M. Dongsten, Y. Cunxiao, *J. Rare Earths* **1997**, *15*, 216–219.
37. L. D. Kurbatova, O. V. Koryakova, M. A. Valova, M. Yu. Yanchenko, *Z. Anorg. Allg. Chem.* **2015**, *641*, 617–621.  
DOI: 10.1002/zaac.201400426.
38. F. Genç, K. B. Gavazov, M. Türkyilmaz, *Cent. Eur. J. Chem.* **2010**, *8*, 461–467. DOI: 10.2478/s11532-009-0119-7.
39. N. K. Temel, R. Gürkan, *Acta Chim. Slov.* **2018**, *65*, 138–149.  
DOI: 10.17344/acsi.2017.3724.

## Povzetek

Proučevali smo možnost uporabe kvarterne amonijeve soli Aliquat 336 ( $A_{336}$ ;  $R_4N^+Cl^-$ ) in azo barvila 4-(2-tiazolilazo) orcinol (TAO) kot komponenti ekstrakcijsko-kromogenega sistema za vanadij(V) v zmesi voda-izobutanol. Pod optimalnimi pogoji ( $c_{TAO} = 1,6 \times 10^{-3} \text{ mol dm}^{-3}$ ,  $c_{A_{336}} = 1,3 \times 10^{-2} \text{ mol dm}^{-3}$  in pH 5,0) smo ekstrahirali vanadij(V) kot ternarni kompleks s formulo  $(R_4N^+)[VO_2(TAO^{2-})]$ . Določili smo ključne ekstrakcijsko-spektrofotometrične karakteristike. Proučili smo tudi interferenco nekaterih ionov. Valovna dolžina maksimalne absorpcije ( $\lambda_{max}$ ), molska absorptivnost ( $\epsilon_{max}$ ), konstanta ekstrakcije ( $K_{ex}$ ) in delež ekstrakcije ( $E$ ) so  $\lambda = 547 \text{ nm}$ ,  $\epsilon = 3.1 \times 10^4 \text{ dm}^3 \text{ mol}^{-1} \text{ cm}^{-1}$ ,  $\log K_{ex} = 2.8$  in  $E = 90.2 \%$ . Beerov zakon velja v območju 0,084–2,0  $\mu\text{g cm}^{-3}$ , meja detekcije za vanadij(V) je 25  $\text{ng cm}^{-3}$ .

Scientific paper

# Synthesis and Cytotoxic Activity of Some Novel Thieno[2,3-*d*:4,5-*d'*]Dipyrimidine Derivatives

Elsherbiny Hamdy El-Sayed<sup>1,\*</sup> and Ahmed Ali Fadda<sup>2</sup><sup>1</sup> Department of Chemistry, Faculty of Science, Port Said University, 42526 Port Said, Egypt,<sup>2</sup> Department of Chemistry, Faculty of Science, Mansoura University, Mansoura, Egypt

\* Corresponding author: E-mail: Saeed201691@yahoo.com

Tel.: +201024689767

Received: 29-05-2018

## Abstract

Synthesis of some novel tricyclic compounds bearing thienodipyrimidine moiety by the reaction of ethyl 6-amino-1,3-dimethyl-2,4-dioxo-1,2,3,4-tetrahydrothieno[3,2-*d*]pyrimidine-7-carboxylate (**1**) with different types of aromatic amines to give the corresponding carboxamide derivatives **2–11**, which cyclized with triethyl orthoformate in acetic anhydride to afford thieno[2,3-*d*:4,5-*d'*]dipyrimidine derivatives **12–15** is described. Similarly, thieno[2,3-*d*:4,5-*d'*]dipyrimidine derivative **17** was also prepared *via* the reaction of carboxamide derivative **2** with chloroacetyl chloride in chloroform to give thieno[3,2-*d*]pyrimidine-7-carboxamide derivative **16**, followed by a cyclization in boiling acetic anhydride. The structure of these compounds was confirmed on the basis of their spectral and analytical data such as IR, <sup>1</sup>H-NMR, <sup>13</sup>C-NMR spectroscopy and mass spectral data. The synthesized compounds were screened for their cytotoxic activity.

**Keywords:** Thienopyrimidine; thienodipyrimidine; cytotoxic activity

## 1. Introduction

Thienopyrimidines represent structural analogues for biogenic purines and potential nucleic acid antimetabolites.<sup>1</sup> In particular, they are currently an important group of compounds that display anticancer activity, especially against solid tumors (*e.g.*, breast and ovarian).<sup>2–4</sup> On the other hand, the classes of tricyclic compounds bearing thienopyrimidine scaffolds have been the focus of great interest because of their pharmacological activities, such as antitumor,<sup>5–9</sup> anti-allergic, anti-inflammatory, analgesic, antifungal and antibacterial activities.<sup>10–20</sup> Consequently, thienopyrimidines have become an important class of compounds in drug discovery programs and the medicinal chemistry.<sup>21–25</sup>

In continuation of our previous work on biologically active nitrogen and sulfur heterocycles,<sup>26–29</sup> it was of interest to synthesize some novel thieno[2,3-*d*:4,5-*d'*]dipyrimidine derivatives and evaluate these compounds for their cytotoxic activity.

## 2. Experimental

All melting points are uncorrected and were determined on Gallenkamp electric melting point device. Pre-

coated Merck silica gel 60F-254 plates were utilized for thin-layer chromatography (TLC) and the spots were visualized under UV light (254 nm). The infrared (IR) spectra were recorded (KBr disk) on Pye Unicam SP 1000 IR spectrophotometer (Thermoelectron Co. Egelsbach, Germany). The <sup>1</sup>H-NMR spectra were obtained on Varian Gemini 400 MHz (Varian Co., Cairo university, Egypt), and <sup>13</sup>C-NMR on the same instrument at 100 MHz. Deuterated DMSO-*d*<sub>6</sub> was used as the solvent, tetramethylsilane (TMS) was used as the internal standard and chemical shifts were measured in δ ppm. Mass spectra were determined on a GC-MS.QP-100 EX Shimadzu (Japan). Elemental analyses were recorded on Perkin-Elmer 2400 Elemental analyzer at the Micro-analytical Center at Cairo University, Cairo, Egypt.

### General Procedure for the Reaction of Compound **1** with Different Aromatic Amines

An equimolar amount of compound **1** (2.83 g, 0.01 mol) and different aromatic amines namely, 2-aminopyridine (0.94 g, 0.01 mol), 4-aminobenzenesulfonamide (1.72 g, 0.01 mol), 2-aminothiazole (1.00 g, 0.01 mol), 4-amino-*N*-(thiazol-2-yl)benzenesulfonamide (2.55 g, 0.01 mol), 4-aminoantipyrene (2.03 g, 0.01 mol), creatinine (1.13 g,

0.01 mol), 6-amino-2-thioxo-4-(*p*-tolyl)-1,2,3,4-tetrahydropyrimidine-5-carbonitrile (2.44 g, 0.01 mol), ethyl 5-acetyl-4-amino-2-(phenylamino)thiophene-3-carboxylate (3.04 g, 0.01 mol), 2-amino-4-hydroxyquinoline-3-carbonitrile (1.85 g, 0.01 mol), or 2,6-diaminopyridine (1.09 g, 0.01 mol), in the presence of freshly fused AcONa were heated on an oil bath for 1 h, then dil. HCl was added to the mixture, the formed solids were collected by filtration, washed with water, dried and crystallized from EtOH/DMF to give compounds 2–11, respectively.

**6-Amino-1,3-dimethyl-2,4-dioxo-N-(pyridin-2-yl)-1,2,3,4-tetrahydrothieno[3,2-d]pyrimidine-7-carboxamide (2)**

Deep brown crystals; yield (68%); mp > 300 °C (DMF-EtOH (1:2)); IR (KBr):  $\nu/\text{cm}^{-1}$  = 3435–3415 (NH<sub>2</sub>), 3385 (NH), 1671 (3C=O); <sup>1</sup>H-NMR (400 MHz, DMSO-*d*<sub>6</sub>)  $\delta$  (ppm): 3.20 (s, 6H, 2N-CH<sub>3</sub>), 7.34 (s, 2H, NH<sub>2</sub>), 7.22–8.36 (m, 4H, Ar-H), 10.67 (s, 1H, CONH, D<sub>2</sub>O exchangeable); <sup>13</sup>C-NMR (100 MHz, DMSO-*d*<sub>6</sub>)  $\delta$  (ppm): 27.5, 30.3, 114.5, 116.8, 118.5, 121.2, 136.4, 143.2, 145.7, 146.6, 151.4, 155.6, 166.8, 171.6; MS (EI, 70 eV)  $m/z$  = 331 (M<sup>+</sup>). *Anal. Calcd for* C<sub>14</sub>H<sub>13</sub>N<sub>5</sub>O<sub>3</sub>S (331.35): C, 50.75; H, 3.95; N, 21.14; S, 9.68. Found: C, 50.71; H, 3.89; N, 21.09; S, 9.64.

**6-Amino-1,3-dimethyl-2,4-dioxo-N-(4-sulfamoylphenyl)-1,2,3,4-tetrahydrothieno[3,2-d]pyrimidine-7-carboxamide (3)**

Brown powder; yield (78%); mp > 300 °C (DMF-EtOH (1:2)); IR (KBr):  $\nu/\text{cm}^{-1}$  = 3476–3453 (2NH<sub>2</sub>), 3343 (NH), 1653 (3C=O); <sup>1</sup>H-NMR (400 MHz, DMSO-*d*<sub>6</sub>)  $\delta$  (ppm): 3.24 (s, 6H, 2N-CH<sub>3</sub>), 6.84 (s, 2H, NH<sub>2</sub>), 7.33 (s, 2H, NH<sub>2</sub>), 7.61 (d, 2H, *J* = 7.50 Hz, Ar-H), 8.25 (d, 2H, *J* = 7.50 Hz, Ar-H), 10.67 (s, 1H, CONH, D<sub>2</sub>O exchangeable); <sup>13</sup>C-NMR (100 MHz, DMSO-*d*<sub>6</sub>)  $\delta$  (ppm): 27.6, 30.5, 114.3, 117.5, 121.4, 131.4, 136.3, 143.5, 145.2, 151.8, 155.2, 166.7, 171.5; MS (EI, 70 eV)  $m/z$  = 410 (M<sup>+</sup>+1). *Anal. Calcd for* C<sub>15</sub>H<sub>15</sub>N<sub>5</sub>O<sub>5</sub>S<sub>2</sub> (409.44): C, 44.00; H, 3.69; N, 17.11; S, 15.66. Found: C, 44.68; H, 3.64; N, 17.15; S, 15.61.

**6-Amino-1,3-dimethyl-2,4-dioxo-N-(thiazol-2-yl)-1,2,3,4-tetrahydrothieno[3,2-d]pyrimidine-7-carboxamide (4)**

Brown powder; yield (67%); mp > 300 °C (DMF-EtOH (1:2)); IR (KBr):  $\nu/\text{cm}^{-1}$  = 3446–3422 (NH<sub>2</sub>), 3381 (NH), 1681 (3C=O); <sup>1</sup>H-NMR (400 MHz, DMSO-*d*<sub>6</sub>)  $\delta$  (ppm): 3.25 (s, 6H, 2N-CH<sub>3</sub>), 7.35 (s, 2H, NH<sub>2</sub>), 7.42 (d, 1H, *J* = 7.10 Hz, Ar-H), 7.58 (d, 1H, *J* = 7.10 Hz, Ar-H), 10.67 (s, 1H, CONH, D<sub>2</sub>O exchangeable); <sup>13</sup>C-NMR (100 MHz, DMSO-*d*<sub>6</sub>)  $\delta$  (ppm): 27.5, 30.4, 114.7, 118.9, 121.2, 138.4, 143.3, 151.7, 155.5, 160.8, 166.5, 171.3; MS (EI, 70 eV)  $m/z$  = 337 (M<sup>+</sup>). *Anal. Calcd for* C<sub>12</sub>H<sub>11</sub>N<sub>5</sub>O<sub>3</sub>S<sub>2</sub> (337.37): C, 42.72; H, 3.29; N, 20.76; S, 19.01. Found: C, 42.67; H, 3.23; N, 20.72; S, 18.94.

**6-Amino-1,3-dimethyl-2,4-dioxo-N-(4-(N-(thiazol-2-yl)sulfamoyl)phenyl)-1,2,3,4-tetrahydrothieno[3,2-d]pyrimidine-7-carboxamide (5)**

Brown powder; yield (62%); mp 283–284 °C (DMF-EtOH (1:2)); IR (KBr):  $\nu/\text{cm}^{-1}$  = 3456–3475 (NH<sub>2</sub>), 3234 (2NH), 1627 (3C=O); <sup>1</sup>H-NMR (400 MHz, DMSO-*d*<sub>6</sub>)  $\delta$  (ppm): 3.21 (s, 6H, 2N-CH<sub>3</sub>), 7.36 (s, 2H, NH<sub>2</sub>), 7.40 (d, 1H, *J* = 7.10 Hz, thiazole H<sub>4</sub>), 7.55 (d, 1H, *J* = 7.10 Hz, thiazole H<sub>5</sub>), 7.72 (d, 2H, *J* = 7.50 Hz, Ar-H), 8.28 (d, 2H, *J* = 7.50 Hz, Ar-H), 10.66, 11.84 (s, 2H, 2NH, D<sub>2</sub>O exchangeable); <sup>13</sup>C-NMR (100 MHz, DMSO-*d*<sub>6</sub>)  $\delta$  (ppm): 27.7, 30.6, 114.7, 117.3, 118.6, 121.5, 131.5, 136.4, 138.9, 143.6, 146.2, 151.6, 155.7, 166.4, 168.6, 171.6; MS (EI, 70 eV)  $m/z$  = 492 (M<sup>+</sup>). *Anal. Calcd for* C<sub>18</sub>H<sub>16</sub>N<sub>6</sub>O<sub>5</sub>S<sub>3</sub> (492.54): C, 43.89; H, 3.27; N, 17.06; S, 19.53. Found: C, 43.81; H, 3.23; N, 16.98; S, 19.44.

**6-Amino-N-(1,5-dimethyl-3-oxo-2-phenyl-2,3-dihydro-1H-pyrazol-4-yl)-1,3-dimethyl-2,4-dioxo-1,2,3,4-tetrahydrothieno[3,2-d]pyrimidine-7-carboxamide (6)**

Brown powder; yield (78%); mp > 300 °C (DMF-EtOH (1:2)); IR (KBr):  $\nu/\text{cm}^{-1}$  = 3447–3423 (NH<sub>2</sub>), 3384 (NH), 1680, 1650 (4C=O); <sup>1</sup>H-NMR (400 MHz, DMSO-*d*<sub>6</sub>)  $\delta$  (ppm): 2.34 (s, 3H, CH<sub>3</sub>), 3.21 (s, 6H, 2N-CH<sub>3</sub>), 3.26 (s, 3H, N-CH<sub>3</sub>), 7.43 (s, 2H, NH<sub>2</sub>), 7.27–7.70 (m, 5H, Ar-H), 10.64 (s, 1H, NH, D<sub>2</sub>O exchangeable); <sup>13</sup>C-NMR (100 MHz, DMSO-*d*<sub>6</sub>)  $\delta$  (ppm): 14.6, 27.4, 30.3, 32.8, 108.4, 114.5, 121.6, 122.8, 124.9, 127.7, 130.2, 137.3, 143.4, 151.8, 155.7, 163.7, 166.8, 171.5; MS (EI, 70 eV)  $m/z$  = 441 (M<sup>+</sup>+1). *Anal. Calcd for* C<sub>20</sub>H<sub>20</sub>N<sub>6</sub>O<sub>4</sub>S (440.48): C, 54.54; H, 4.58; N, 19.08; S, 7.28. Found: C, 54.49; H, 4.60; N, 18.99; S, 7.25.

**6-Amino-1,3-dimethyl-N-(1-methyl-4-oxo-4,5-dihydro-1H-imidazol-2-yl)-2,4-dioxo-1,2,3,4-tetrahydrothieno[3,2-d]pyrimidine-7-carboxamide (7)**

Brown powder; yield (60%); mp > 300 °C (DMF-EtOH (1:2)); IR (KBr):  $\nu/\text{cm}^{-1}$  = 3447–3422 (NH<sub>2</sub>), 3249 (NH), 1637 (4C=O); <sup>1</sup>H-NMR (400 MHz, DMSO-*d*<sub>6</sub>)  $\delta$  (ppm): 3.16 (s, 3H, N-CH<sub>3</sub>), 3.19 (s, 3H, N-CH<sub>3</sub>), 3.22 (s, 3H, N-CH<sub>3</sub>), 3.60 (s, 2H, imidazole H<sub>5</sub>), 7.31 (s, 2H, NH<sub>2</sub>), 9.51 (s, 1H, NH, D<sub>2</sub>O exchangeable); <sup>13</sup>C-NMR (100 MHz, DMSO-*d*<sub>6</sub>)  $\delta$  (ppm): 27.6, 30.3, 38.3, 61.6, 114.6, 121.5, 143.4, 151.8, 153.2, 155.6, 163.8, 166.7, 171.4; MS (EI, 70 eV)  $m/z$  = 351 (M<sup>+</sup>+1). *Anal. Calcd for* C<sub>13</sub>H<sub>14</sub>N<sub>6</sub>O<sub>4</sub>S (350.35): C, 44.57; H, 4.03; N, 23.99; S, 9.15. Found: C, 44.56; H, 4.03; N, 23.97; S, 9.13.

**6-Amino-N-(5-cyano-2-thioxo-6-(*p*-tolyl)hexahydropyrimidin-4-yl)-1,3-dimethyl-2,4-dioxo-1,2,3,4-tetrahydrothieno[3,2-d]pyrimidine-7-carboxamide (8)**

Brown powder; yield (69%); mp > 300 °C (DMF-EtOH (1:2)); IR (KBr):  $\nu/\text{cm}^{-1}$  = 3447–3422 (NH<sub>2</sub>), 3380, 3249 (3NH), 2218 (CN), 1641 (3C=O) 1383 (C=S); <sup>1</sup>H-NMR (400 MHz, DMSO-*d*<sub>6</sub>)  $\delta$  (ppm): 2.18 (s, 3H, CH<sub>3</sub>), 3.13 (m, 1H, pyrimidine H<sub>5</sub>), 3.21 (s, 6H, 2N-CH<sub>3</sub>), 3.67 (d,

1H,  $J = 7.50$  Hz, pyrimidine H<sub>6</sub>), 3.77 (d, 1H,  $J = 7.50$  Hz, pyrimidine H<sub>4</sub>), 7.68 (s, 2H, NH<sub>2</sub>), 7.50 (d, 2H,  $J = 6.90$  Hz, Ar-H), 7.89 (d, 2H,  $J = 6.90$  Hz, Ar-H), 8.96, 10.15, 10.36 (s, 3H, 3NH, D<sub>2</sub>O exchangeable); <sup>13</sup>C-NMR (100 MHz, DMSO-*d*<sub>6</sub>)  $\delta$  (ppm): 18.3, 27.4, 30.5, 45.6, 58.8, 78.4, 114.8, 117.6, 121.5, 126.4, 130.3, 134.2, 140.3, 143.4, 151.6, 155.3, 166.7, 171.5, 176.8; MS (EI, 70 eV)  $m/z = 483$  (M<sup>+</sup>). *Anal. Calcd for* C<sub>21</sub>H<sub>21</sub>N<sub>7</sub>O<sub>3</sub>S<sub>2</sub> (483.57): C, 52.16; H, 4.38; N, 20.28; S, 13.26. Found: C, 52.08; H, 4.32; N, 20.21; S, 13.18.

**Ethyl 5-Acetyl-4-(6-amino-1,3-dimethyl-2,4-dioxo-1,2,3,4-tetrahydrothieno[3,2-d]pyrimidine-7-carboxamido)-2-(phenylamino)thiophene-3-carboxylate (9)**

Brown powder; yield (71%); mp > 300 °C (DMF-EtOH (1:2)); IR (KBr):  $\nu/\text{cm}^{-1} = 3446\text{--}3418$  (NH<sub>2</sub>), 3221 (2NH), 1703, 1683, 1641 (5C=O); <sup>1</sup>H-NMR (400 MHz, DMSO-*d*<sub>6</sub>)  $\delta$  (ppm): 1.33 (t, 3H,  $J = 7.10$  Hz, CH<sub>3</sub>), 3.14 (s, 6H, 2N-CH<sub>3</sub>), 3.77 (s, 3H, COCH<sub>3</sub>), 4.43 (q, 2H,  $J = 7.10$  Hz, CH<sub>2</sub>), 7.47 (s, 2H, NH<sub>2</sub>), 7.27–7.58 (m, 5H, Ar-H), 9.31, 10.25 (s, 2H, 2NH, D<sub>2</sub>O exchangeable); <sup>13</sup>C-NMR (100 MHz, DMSO-*d*<sub>6</sub>)  $\delta$  (ppm): 14.6, 26.2, 27.8, 30.6, 61.3, 114.3, 118.6, 121.4, 124.3, 126.6, 128.4, 139.5, 140.6, 143.5, 145.3, 151.6, 155.7, 160.2, 162.3, 166.3, 171.4, 186.3; MS (EI, 70 eV)  $m/z = 541$  (M<sup>+</sup>). *Anal. Calcd for* C<sub>24</sub>H<sub>23</sub>N<sub>5</sub>O<sub>6</sub>S<sub>2</sub> (541.60): C, 53.22; H, 4.28; N, 12.93; S, 11.84. Found: C, 53.18; H, 4.25; N, 12.88; S, 11.77.

**6-Amino-N-(3-cyano-4-hydroxyquinolin-2-yl)-1,3-dimethyl-2,4-dioxo-1,2,3,4-tetrahydrothieno[3,2-d]pyrimidine-7-carboxamide (10)**

Brown powder; yield (64%); mp > 300 °C (DMF-EtOH (1:2)); IR (KBr):  $\nu/\text{cm}^{-1} = 3417\text{--}3331$  (NH<sub>2</sub>, OH), 3222 (NH), 2219 (CN), 1676 (3C=O); <sup>1</sup>H-NMR (400 MHz, DMSO-*d*<sub>6</sub>)  $\delta$  (ppm): 3.21 (s, 6H, 2N-CH<sub>3</sub>), 7.37 (s, 2H, NH<sub>2</sub>), 7.68–8.46 (m, 4H, Ar-H), 10.21 (s, 1H, OH), 10.67 (s, 1H, NH, D<sub>2</sub>O exchangeable); <sup>13</sup>C-NMR (100 MHz, DMSO-*d*<sub>6</sub>)  $\delta$  (ppm): 27.6, 30.4, 79.8, 110.6, 114.5, 117.3, 120.0, 121.6, 124.6, 126.4, 134.3, 143.8, 148.6, 150.2, 151.7, 155.9, 161.4, 166.2, 171.3; MS (EI, 70 eV)  $m/z = 422$  (M<sup>+</sup>). *Anal. Calcd for* C<sub>19</sub>H<sub>14</sub>N<sub>6</sub>O<sub>4</sub>S (422.42): C, 54.02; H, 3.34; N, 19.90; S, 7.59. Found: C, 53.96; H, 3.38; N, 19.84; S, 7.51.

**N,N'-(Pyridine-2,6-diyl)bis(6-amino-1,3-dimethyl-2,4-dioxo-1,2,3,4-tetrahydrothieno[3,2-d]pyrimidine-7-carboxamide) (11)**

Reddish brown powder; yield (61%); mp > 300 °C (DMF-EtOH (1:2)); IR (KBr):  $\nu/\text{cm}^{-1} = 3574\text{--}3475$  (2NH<sub>2</sub>), 3368 (2NH), 1687 (6C=O); <sup>1</sup>H-NMR (400 MHz, DMSO-*d*<sub>6</sub>)  $\delta$  (ppm): 3.21 (s, 6H, 2N-CH<sub>3</sub>), 3.25 (s, 6H, 2N-CH<sub>3</sub>), 7.46 (s, 4H, 2NH<sub>2</sub>), 7.21–7.64 (m, 3H, Ar-H), 10.74 (s, 2H, 2CONH, D<sub>2</sub>O exchangeable); <sup>13</sup>C-NMR (100 MHz, DMSO-*d*<sub>6</sub>)  $\delta$  (ppm): 27.8, 30.5, 114.2, 116.8, 121.3, 136.6, 143.5, 145.4, 151.6, 155.7, 166.5, 171.3; MS (EI, 70 eV)  $m/z = 585$  (M<sup>+</sup>+2). *Anal. Calcd for* C<sub>23</sub>H<sub>21</sub>N<sub>9</sub>O<sub>6</sub>S<sub>2</sub> (583.60): C, 47.34; H, 3.63; N, 21.60; S, 10.99. Found: C, 47.28; H, 3.59; N, 21.55; S, 10.92.

**General Procedure for the Reaction of Compounds 2, 4, 5, 7 and 1 with Triethyl Orthoformate**

To a solution of compound 2 (3.31 g, 0.01 mol), compound 4 (4.09 g, 0.01 mol), compound 5 (3.37 g, 0.01 mol), compound 7 (4.40 g, 0.01 mol) or compound 1 (2.83 g, 0.01 mol) in acetic anhydride (20 mL) triethyl orthoformate (1.48 g, 0.01 mol) was added. The reaction mixture was heated on water bath for 8–10 hours, then poured onto iced water and the formed solid product was collected by filtration, and crystallized from EtOH/DMF to give compounds 12–15 and 23, respectively.

**1,3-Dimethyl-8-(pyridin-2-yl)thieno[2,3-d:4,5-d']dipyrimidine-2,4,9(1H,3H,8H)-trione (12)**

Brownish blue powder; yield (67%); mp > 300 °C (DMF-EtOH (1:2)); IR (KBr):  $\nu/\text{cm}^{-1} = 1667$  (3C=O); <sup>1</sup>H-NMR (400 MHz, DMSO-*d*<sub>6</sub>)  $\delta$  (ppm): 3.01 (s, 3H, N-CH<sub>3</sub>), 3.09 (s, 3H, N-CH<sub>3</sub>), 7.26–8.46 (m, 4H, Ar-H), 8.56 (s, 1H, pyrimidine-H<sub>7</sub>); <sup>13</sup>C-NMR (100 MHz, DMSO-*d*<sub>6</sub>)  $\delta$  (ppm): 28.2, 30.3, 114.4, 118.3, 122.6, 130.3, 136.5, 143.2, 145.3, 146.6, 148.5, 151.6, 155.5, 166.4, 168.6; MS (EI, 70 eV)  $m/z = 341$  (M<sup>+</sup>). *Anal. Calcd for* C<sub>15</sub>H<sub>11</sub>N<sub>5</sub>O<sub>3</sub>S (341.35): C, 52.78; H, 3.25; N, 20.52; S, 9.39. Found: C, 52.74; H, 3.22; N, 20.46; S, 9.41.

**4-(1,3-Dimethyl-2,4,9-trioxo-1,2,3,4-tetrahydrothieno[2,3-d:4,5-d']dipyrimidin-8(9H)-yl)benzenesulfonamide (13)**

Yellowish brown powder; yield (70%); mp > 300 °C (DMF-EtOH (1:2)); IR (KBr):  $\nu/\text{cm}^{-1} = 3476\text{--}3445$  (NH<sub>2</sub>), 1668 (3C=O); <sup>1</sup>H-NMR (400 MHz, DMSO-*d*<sub>6</sub>)  $\delta$  (ppm): 3.01 (s, 3H, N-CH<sub>3</sub>), 3.09 (s, 3H, N-CH<sub>3</sub>), 6.82 (s, 2H, NH<sub>2</sub>), 7.63 (d, 2H,  $J = 7.10$  Hz, Ar-H), 8.16 (d, 2H,  $J = 7.10$  Hz, Ar-H), 8.54 (s, 1H, pyrimidine-H<sub>7</sub>); <sup>13</sup>C-NMR (100 MHz, DMSO-*d*<sub>6</sub>)  $\delta$  (ppm): 27.5, 30.6, 114.5, 117.3, 130.8, 131.9, 136.8, 143.7, 145.2, 148.3, 151.7, 155.4, 166.5, 168.8; MS (EI, 70 eV)  $m/z = 419$  (M<sup>+</sup>). *Anal. Calcd for* C<sub>16</sub>H<sub>13</sub>N<sub>5</sub>O<sub>5</sub>S<sub>2</sub> (419.43): C, 45.82; H, 3.12; N, 16.70; S, 15.29. Found: C, 45.73; H, 3.06; N, 16.63; S, 15.22.

**4-(1,3-Dimethyl-2,4,9-trioxo-1,2,3,4-tetrahydrothieno[2,3-d:4,5-d']dipyrimidin-8(9H)-yl)-N-(thiazol-2-yl)benzenesulfonamide (14)**

Gray crystals; yield (68%); mp > 300 °C (DMF-EtOH (1:2)); IR (KBr):  $\nu/\text{cm}^{-1} = 3245$  (NH), 1667 (3C=O); <sup>1</sup>H-NMR (400 MHz, DMSO-*d*<sub>6</sub>)  $\delta$  (ppm): 3.01 (s, 3H, N-CH<sub>3</sub>), 3.09 (s, 3H, N-CH<sub>3</sub>), 7.45 (d, 1H,  $J = 7.10$  Hz, thiazole H<sub>4</sub>), 7.62 (d, 1H,  $J = 7.10$  Hz, thiazole H<sub>5</sub>), 7.74 (d, 2H,  $J = 7.50$  Hz, Ar-H), 8.24 (d, 2H,  $J = 7.50$  Hz, Ar-H), 8.52 (s, 1H, pyrimidine-H<sub>7</sub>), 11.68 (s, 1H, NH, D<sub>2</sub>O exchangeable); <sup>13</sup>C-NMR (100 MHz, DMSO-*d*<sub>6</sub>)  $\delta$  (ppm): 27.8, 30.4, 114.8, 116.5, 118.8, 130.6, 131.7, 136.4, 138.3, 143.8, 145.2, 148.1, 151.5, 155.3, 166.7, 168.5, 170.2; MS (EI, 70 eV)  $m/z = 502$  (M<sup>+</sup>). *Anal. Calcd for* C<sub>19</sub>H<sub>14</sub>N<sub>6</sub>O<sub>5</sub>S<sub>3</sub> (502.54): C, 45.41; H, 2.81; N, 16.72; S, 19.14. Found: C, 45.32; H, 2.73; N, 16.66; S, 19.06.

**8-(1,5-Dimethyl-3-oxo-2-phenyl-2,3-dihydro-1H-pyrazol-4-yl)-1,3-dimethylthieno[2,3-d:4,5-d']dipyrimidine-2,4,9-(1H,3H,8H)-trione (15)**

Red powder; yield (72%); mp > 300 °C (DMF-EtOH (1:2)); IR (KBr):  $\nu/\text{cm}^{-1}$  = 1667, 1655 (4C=O);  $^1\text{H-NMR}$  (400 MHz, DMSO- $d_6$ )  $\delta$  (ppm): 2.26 (s, 3H, CH<sub>3</sub>), 3.01 (s, 3H, N-CH<sub>3</sub>), 3.09 (s, 3H, N-CH<sub>3</sub>), 3.23 (s, 3H, N-CH<sub>3</sub>), 7.38–7.78 (m, 5H, Ar-H), 8.51 (s, 1H, pyrimidine-H<sub>7</sub>);  $^{13}\text{C-NMR}$  (100 MHz, DMSO- $d_6$ )  $\delta$  (ppm): 14.6, 27.6, 30.5, 35.8, 105.6, 114.3, 118.1, 122.8, 128.6, 130.5, 131.7, 136.5, 143.3, 148.4, 151.6, 155.8, 163.7, 166.8, 168.6; MS (EI, 70 eV)  $m/z$  = 450 (M<sup>+</sup>). *Anal. Calcd for* C<sub>21</sub>H<sub>18</sub>N<sub>6</sub>O<sub>4</sub>S (450.47): C, 55.99; H, 4.03; N, 18.66; S, 7.12. Found: C, 55.97; H, 3.97; N, 18.59; S, 7.06.

**Ethyl 6-((Ethoxymethylene)amino)-1,3-dimethyl-2,4-dioxo-1,2,3,4-tetrahydrothieno[3,2-d]pyrimidine-7-carboxylate (23)**

Yellowish brown crystals; yield (63%); mp 123–125 °C (DMF-EtOH (1:2)); IR (KBr):  $\nu/\text{cm}^{-1}$  = 1708, 1659 (3C=O);  $^1\text{H-NMR}$  (400 MHz, DMSO- $d_6$ )  $\delta$  (ppm): 1.22 (t, 3H,  $J$  = 7.50 Hz, CH<sub>2</sub>CH<sub>3</sub>), 2.93 (t, 3H,  $J$  = 7.10 Hz, CH<sub>2</sub>CH<sub>3</sub>), 3.01 (s, 3H, N-CH<sub>3</sub>), 3.09 (s, 3H, N-CH<sub>3</sub>), 3.71 (q, 2H,  $J$  = 7.10 Hz, CH<sub>2</sub>CH<sub>3</sub>), 4.15 (q, 2H,  $J$  = 7.50 Hz, CH<sub>2</sub>CH<sub>3</sub>), 8.45 (s, 1H, N=CH);  $^{13}\text{C-NMR}$  (100 MHz, DMSO- $d_6$ )  $\delta$  (ppm): 18.5, 18.9, 27.5, 30.4, 67.6, 68.7, 115.4, 123.4, 143.5, 151.8, 155.6, 158.5, 163.4, 169.5; MS (EI, 70 eV)  $m/z$  = 340 (M<sup>+</sup>+1). *Anal. Calcd for* C<sub>14</sub>H<sub>17</sub>N<sub>3</sub>O<sub>5</sub>S (339.37): C, 49.55; H, 5.05; N, 12.38; S, 9.45. Found: C, 49.48; H, 4.97; N, 12.31; S, 9.37.

**Synthesis of 6-(2-Chloroacetamido)-1,3-dimethyl-2,4-dioxo-N-(pyridin-2-yl)-1,2,3,4-tetrahydrothieno[3,2-d]pyrimidine-7-carboxamide (16)**

To a solution of compound **2** (3.31 g, 0.01 mol) in chloroform (25 mL) chloroacetyl chloride (1.12 g, 0.01 mol) was added at room temperature overnight. The reaction mixture was concentrated under reduced pressure and cooled. The obtained solid product was collected by filtration, dried and crystallized from EtOH/DMF to give compound **16**. Purple powder; yield (88%); mp > 300 °C (DMF-EtOH (1:2)); IR (KBr):  $\nu/\text{cm}^{-1}$  = 3421 (2NH), 1698, 1671 (4C=O), 756 (C-Cl);  $^1\text{H-NMR}$  (400 MHz, DMSO- $d_6$ )  $\delta$  (ppm): 3.01 (s, 3H, N-CH<sub>3</sub>), 3.09 (s, 3H, N-CH<sub>3</sub>), 3.65 (s, 2H, CH<sub>2</sub>), 7.24–8.44 (m, 4H, Ar-H), 10.67, 11.54 (s, 2H, 2NH);  $^{13}\text{C-NMR}$  (100 MHz, DMSO- $d_6$ )  $\delta$  (ppm): 27.4, 30.5, 51.6, 114.3, 116.8, 118.6, 121.3, 136.5, 143.2, 145.7, 146.5, 151.6, 155.3, 166.9, 168.4, 178.8; MS (EI, 70 eV)  $m/z$  = 407 (M<sup>+</sup>). *Anal. Calcd for* C<sub>16</sub>H<sub>14</sub>ClN<sub>5</sub>O<sub>4</sub>S (407.83): C, 47.12; H, 3.46; N, 17.17; S, 7.86. Found: C, 47.11; H, 3.40; N, 17.09; S, 7.82.

**Synthesis of 7-(Chloromethyl)-1,3-dimethyl-8-(pyridin-2-yl)thieno[2,3-d:4,5-d']dipyrimidine-2,4,9-(1H,3H,8H)-trione (17)**

A solution of compound **16** (4.07 g, 0.01 mol) in acetic anhydride (20 mL) was refluxed for 6 h (TLC, mob.

phase petroleum ether/ethyl acetate (8:2)). The reaction mixture was poured onto crushed ice water and the solid separated was collected by filtration, dried and crystallized from EtOH/DMF to give compound **17**. Pink powder; yield (78%); mp > 300 °C (DMF-EtOH (1:2)); IR (KBr):  $\nu/\text{cm}^{-1}$  = 1657, 1645 (3C=O), 760 (C-Cl);  $^1\text{H-NMR}$  (400 MHz, DMSO- $d_6$ )  $\delta$  (ppm): 3.01 (s, 3H, N-CH<sub>3</sub>), 3.09 (s, 3H, N-CH<sub>3</sub>), 4.45 (s, 2H, CH<sub>2</sub>), 7.32–8.45 (m, 4H, Ar-H);  $^{13}\text{C-NMR}$  (100 MHz, DMSO- $d_6$ )  $\delta$  (ppm): 27.8, 30.6, 48.5, 114.5, 118.3, 122.2, 130.4, 136.5, 143.2, 145.3, 146.7, 151.4, 155.8, 158.5, 164.8, 168.3; MS (EI, 70 eV)  $m/z$  = 389 (M<sup>+</sup>). *Anal. Calcd for* C<sub>16</sub>H<sub>12</sub>ClN<sub>5</sub>O<sub>3</sub>S (389.81): C, 49.30; H, 3.10; N, 17.97; S, 8.22. Found: C, 49.24; H, 3.06; N, 17.92; S, 8.17.

**General Procedure for the Reaction of Compound 16 with Piperidine and Morpholine**

To an equimolar amount of **16** (4.07 g, 0.01 mol) and piperidine (0.85 g, 0.01 mol) or morpholine (0.87 g, 0.01 mol) in dry xylene (20 mL) DMF (5 drops) was added. The reaction mixture was refluxed for 3 h, then poured onto iced water and the formed solid products, in each case, were collected by filtration and crystallized from EtOH/DMF to give compounds **18** and **19**, respectively.

**1,3-Dimethyl-2,4-dioxo-6-(2-(piperidin-1-yl)acetamido)-N-(pyridin-2-yl)-1,2,3,4-tetrahydrothieno[3,2-d]pyrimidine-7-carboxamide (18)**

Greenish brown crystals; yield (64%); mp 270–272 °C (DMF-EtOH (1:2)); IR (KBr):  $\nu/\text{cm}^{-1}$  = 3435 (2NH), 1665 (4C=O);  $^1\text{H-NMR}$  (400 MHz, DMSO- $d_6$ )  $\delta$  (ppm): 1.13–1.45 (m, 6H, 3CH<sub>2</sub>), 2.27 (t, 4H, 2NCH<sub>2</sub>), 3.01 (s, 3H, N-CH<sub>3</sub>), 3.09 (s, 3H, N-CH<sub>3</sub>), 3.46 (s, 2H, COCH<sub>2</sub>N), 7.29–8.56 (m, 4H, Ar-H), 10.86, 11.46 (s, 2H, 2NH, D<sub>2</sub>O exchangeable);  $^{13}\text{C-NMR}$  (100 MHz, DMSO- $d_6$ )  $\delta$  (ppm): 22.3, 25.5, 27.8, 30.7, 54.3, 67.6, 114.5, 116.2, 118.6, 121.4, 136.3, 143.3, 145.3, 146.5, 151.8, 155.6, 166.7, 168.5, 178.6; MS (EI, 70 eV)  $m/z$  = 456 (M<sup>+</sup>). *Anal. Calcd for* C<sub>21</sub>H<sub>24</sub>N<sub>6</sub>O<sub>4</sub>S (456.52): C, 55.25; H, 5.30; N, 18.41; S, 7.02. Found: C, 55.19; H, 5.27; N, 18.33; S, 6.96.

**1,3-Dimethyl-6-(2-morpholinoacetamido)-2,4-dioxo-N-(pyridin-2-yl)-1,2,3,4-tetrahydrothieno[3,2-d]pyrimidine-7-carboxamide (19)**

Brown crystals; yield (61%); mp 258–260 °C (DMF-EtOH (1:2)); IR (KBr):  $\nu/\text{cm}^{-1}$  = 3433 (2NH), 1656 (4C=O);  $^1\text{H-NMR}$  (400 MHz, DMSO- $d_6$ )  $\delta$  (ppm): 2.29 (t, 4H,  $J$  = 6.88 Hz, 2NCH<sub>2</sub>), 3.01 (s, 3H, N-CH<sub>3</sub>), 3.09 (s, 3H, N-CH<sub>3</sub>), 3.47 (s, 2H, COCH<sub>2</sub>N), 3.78 (t, 4H,  $J$  = 6.88 Hz, 2OCH<sub>2</sub>), 7.31–8.44 (m, 4H, Ar-H), 10.87, 11.42 (s, 2H, 2NH, D<sub>2</sub>O exchangeable);  $^{13}\text{C-NMR}$  (100 MHz, DMSO- $d_6$ )  $\delta$  (ppm): 27.4, 30.6, 54.6, 65.3, 67.8, 114.3, 116.7, 118.8, 121.5, 136.5, 143.4, 145.5, 146.7, 151.3, 155.5, 166.5, 168.6, 177.2; MS (EI, 70 eV)  $m/z$  = 458 (M<sup>+</sup>). *Anal. Calcd for* C<sub>20</sub>H<sub>22</sub>N<sub>6</sub>O<sub>5</sub>S (458.49): C, 52.39; H, 4.84; N, 18.33; S, 6.99. Found: C, 52.36; H, 4.86; N, 18.25; S, 6.94.



**Synthesis of 6-Amino-1,3-dimethyl-2,4-dioxo-1,2,3,4-tetrahydrothieno[3,2-d]pyrimidine-7-carboxylic Acid (20)**

A solution of compound **1** (2.83 g, 0.01 mol) in DMF (15 mL) and NaOH (25 mL, 0.5%) was refluxed for 3 h. The reaction mixture was allowed to cool. The obtained solid product was collected by filtration, washed by water, dried and crystallized from EtOH/DMF to give compound **20**. Brown powder; yield (81%); mp 251–253 °C (DMF-EtOH (1:2)); IR (KBr):  $\nu/\text{cm}^{-1}$  = 3435–3417 (NH<sub>2</sub>), 3387 (OH), 1698, 1671 (3C=O); <sup>1</sup>H-NMR (400 MHz, DMSO-*d*<sub>6</sub>)  $\delta$  (ppm): 3.01 (s, 3H, N-CH<sub>3</sub>), 3.09 (s, 3H, N-CH<sub>3</sub>), 7.34 (s, 2H, NH<sub>2</sub>), 11.85 (s, 1H, OH); <sup>13</sup>C-NMR (100 MHz, DMSO-*d*<sub>6</sub>)  $\delta$  (ppm): 27.3, 30.2, 114.6, 123.7, 143.8, 151.7, 155.4, 163.5, 169.6; MS (EI, 70 eV)  $m/z$  = 255 (M<sup>+</sup>). *Anal. Calcd for* C<sub>9</sub>H<sub>9</sub>N<sub>3</sub>O<sub>4</sub>S (255.25): C, 42.35; H, 3.55; N, 16.46; S, 12.56. Found: C, 42.30; H, 3.49; N, 16.38; S, 12.48.

**Synthesis of 1,3,7-Trimethyl-9H-pyrimido[4',5':4,5]thieno[2,3-d][1,3]oxazine-2,4,9(1H,3H)-trione (21)**

A solution of compound **20** (1.4 g, 0.005 mol) in Ac<sub>2</sub>O (10 mL) was refluxed for 5 h. The reaction mixture was allowed to cool. The obtained solid product was collected by filtration, dried and crystallized from EtOH/DMF to give compound **21**. Gray crystals; yield (68%); mp > 300 °C (DMF-EtOH (1:2)); IR (KBr):  $\nu/\text{cm}^{-1}$  = 1732, 1657 (3C=O); <sup>1</sup>H-NMR (400 MHz, DMSO-*d*<sub>6</sub>)  $\delta$  (ppm): 2.12 (s, 3H, CH<sub>3</sub>), 3.01 (s, 3H, N-CH<sub>3</sub>), 3.09 (s, 3H, N-CH<sub>3</sub>); <sup>13</sup>C-NMR (100 MHz, DMSO-*d*<sub>6</sub>)  $\delta$  (ppm): 21.4, 28.5, 30.6, 114.2, 130.3, 143.6, 151.6, 155.5, 158.3, 164.5, 168.1; MS (EI, 70 eV)  $m/z$  = 279 (M<sup>+</sup>). *Anal. Calcd for* C<sub>11</sub>H<sub>9</sub>N<sub>3</sub>O<sub>4</sub>S (279.27): C, 47.31; H, 3.25; N, 15.05; S, 11.48. Found: C, 47.25; H, 3.31; N, 14.96; S, 11.38.

**Synthesis of 1,3,7-Trimethyl-8-(pyridin-2-yl)thieno[2,3-d:4,5-d']dipyrimidine-2,4,9(1H,3H,8H)-trione (22)**

A solution of compound **21** (2.79 g, 0.01 mol) in acetic acid (15 mL) and 2-aminopyridine (0.94 g, 0.01 mol) was refluxed for 4 h. The reaction mixture was allowed to cool. The obtained solid product was collected by filtration, dried and crystallized from EtOH/DMF to give compound **22**. Brown powder; yield (66%); mp > 300 °C (DMF-EtOH (1:2)); IR (KBr):  $\nu/\text{cm}^{-1}$  = 1671 (3C=O); <sup>1</sup>H-NMR (400 MHz, DMSO-*d*<sub>6</sub>)  $\delta$  (ppm): 2.30 (s, 3H, CH<sub>3</sub>), 3.01 (s, 3H, N-CH<sub>3</sub>), 3.09 (s, 3H, N-CH<sub>3</sub>), 7.45–8.37 (m, 4H, Ar-H); <sup>13</sup>C-NMR (100 MHz, DMSO-*d*<sub>6</sub>)  $\delta$  (ppm): 21.8, 28.6, 30.7, 114.3, 118.4, 122.5, 130.5, 136.3, 143.8, 145.6, 146.8, 151.9, 155.6, 158.4, 166.8, 168.5; MS (EI, 70 eV)  $m/z$  = 355 (M<sup>+</sup>). *Anal. Calcd for* C<sub>16</sub>H<sub>13</sub>N<sub>5</sub>O<sub>3</sub>S (355.37): C, 54.08; H, 3.69; N, 19.71; S, 9.02. Found: C, 54.00; H, 3.61; N, 19.63; S, 8.98.

**General Procedure for the Reaction of Compound 23 with Aniline, Phenylhydrazine and Hydrazine Hydrate**

To a solution of compound **23** (3.39 g, 0.01 mol) in dry xylene (20 mL), aniline (0.93 g, 0.01 mol) or phenylhydrazine (1.08 g, 0.01 mol) or hydrazine hydrate (0.50 g,

0.01 mol) was added. The reaction mixture was refluxed for 3 h, then poured onto iced water and the formed solid products, in each case, were collected by filtration and crystallized from EtOH/DMF to give compounds **24**, **26** and **27**, respectively.

**Ethyl 1,3-Dimethyl-2,4-dioxo-6-(((phenylamino)methylene)amino)-1,2,3,4-tetrahydrothieno[3,2-d]pyrimidine-7-carboxylate (24)**

Gray fine powder; yield (61%); mp 180–182 °C (DMF-EtOH (1:2)); IR (KBr):  $\nu/\text{cm}^{-1}$  = 3285 (NH), 1701, 1653 (3C=O); <sup>1</sup>H-NMR (400 MHz, DMSO-*d*<sub>6</sub>)  $\delta$  (ppm): 3.00 (t, 3H,  $J$  = 7.10 Hz, CH<sub>3</sub>), 3.01 (s, 3H, N-CH<sub>3</sub>), 3.09 (s, 3H, N-CH<sub>3</sub>), 3.71 (q, 2H,  $J$  = 7.10 Hz, CH<sub>2</sub>), 6.80–7.48 (m, 5H, Ar-H), 8.44 (s, 1H, N=CH), 10.47 (s, 1H, NH, D<sub>2</sub>O exchangeable); <sup>13</sup>C-NMR (100 MHz, DMSO-*d*<sub>6</sub>)  $\delta$  (ppm): 18.3, 27.6, 30.2, 67.5, 115.3, 116.5, 121.5, 123.1, 130.1, 143.4, 145.8, 151.5, 155.4, 158.6, 163.2, 169.4; MS (EI, 70 eV)  $m/z$  = 386 (M<sup>+</sup>). *Anal. Calcd for* C<sub>18</sub>H<sub>18</sub>N<sub>4</sub>O<sub>4</sub>S (386.43): C, 55.95; H, 4.70; N, 14.50; S, 8.30. Found: C, 55.89; H, 4.62; N, 14.44; S, 8.25.

**1,3-Dimethyl-8-(phenylamino)thieno[2,3-d:4,5-d']dipyrimidine-2,4,9(1H,3H,8H)-trione (26)**

Orange crystals; yield (77%); mp > 300 °C (DMF-EtOH (1:2)); IR (KBr):  $\nu/\text{cm}^{-1}$  = 3283 (NH), 1652 (3C=O); <sup>1</sup>H-NMR (400 MHz, DMSO-*d*<sub>6</sub>)  $\delta$  (ppm): 3.01 (s, 3H, N-CH<sub>3</sub>), 3.09 (s, 3H, N-CH<sub>3</sub>), 6.82–7.74 (m, 5H, Ar-H), 8.45 (s, 1H, pyrimidine H<sub>7</sub>) and 10.24 (s, 1H, NH, D<sub>2</sub>O exchangeable); <sup>13</sup>C-NMR (100 MHz, DMSO-*d*<sub>6</sub>)  $\delta$  (ppm): 28.7, 30.1, 114.5, 116.3, 122.4, 128.5, 131.2, 143.2, 145.4, 148.6, 151.3, 155.8, 166.7, 168.5; MS (EI, 70 eV)  $m/z$  = 355 (M<sup>+</sup>). *Anal. Calcd for* C<sub>16</sub>H<sub>13</sub>N<sub>5</sub>O<sub>3</sub>S (355.37): C, 54.08; H, 3.69; N, 19.71; S, 9.02. Found: C, 54.00; H, 3.62; N, 19.68; S, 9.05.

**Ethyl 6-((Hydrazinylmethylene)amino)-1,3-dimethyl-2,4-dioxo-1,2,3,4-tetrahydrothieno[3,2-d]pyrimidine-7-carboxylate (27)**

Yellowish red crystals; yield (71%); mp > 300 °C (DMF-EtOH (1:2)); IR (KBr):  $\nu/\text{cm}^{-1}$  = 3448–3419 (NH<sub>2</sub>), 3285 (NH), 1701, 1649 (3C=O); <sup>1</sup>H-NMR (400 MHz, DMSO-*d*<sub>6</sub>)  $\delta$  (ppm): 3.00 (t, 3H,  $J$  = 7.10 Hz, CH<sub>3</sub>), 3.01 (s, 3H, N-CH<sub>3</sub>), 3.09 (s, 3H, N-CH<sub>3</sub>), 3.71 (q, 2H,  $J$  = 7.10 Hz, CH<sub>2</sub>), 4.45 (s, 2H, NH<sub>2</sub>), 5.63 (s, 1H, NH), 8.49 (s, 1H, N=CH); <sup>13</sup>C-NMR (100 MHz, DMSO-*d*<sub>6</sub>)  $\delta$  (ppm): 18.5, 27.4, 30.5, 67.4, 115.2, 123.4, 143.2, 151.7, 155.6, 158.4, 163.5, 169.3; MS (EI, 70 eV)  $m/z$  = 325 (M<sup>+</sup>). *Anal. Calcd for* C<sub>12</sub>H<sub>15</sub>N<sub>5</sub>O<sub>4</sub>S (325.34): C, 44.30; H, 4.65; N, 21.53; S, 9.85. Found: C, 44.24; H, 4.59; N, 21.46; S, 9.76.

**Synthesis of 8-Amino-1,3-dimethylthieno[2,3-d:4,5-d']dipyrimidine-2,4,9(1H,3H,8H)-trione (28)**

To a solution of compound **27** (2.79 g, 0.01 mol) in DMF (20 mL) TEA (5 drops) was added. The reaction mixture was heated for 5 hours then poured into iced wa-

ter and the formed solid product was collected by filtration, and crystallized from EtOH/DMF to give compound **28**. Greenish brown powder; yield (78%); mp > 300 °C (DMF-EtOH (1:2)); IR (KBr):  $\nu/\text{cm}^{-1}$  = 3443–3385 (NH<sub>2</sub>), 1649 (C=O); <sup>1</sup>H-NMR (400 MHz, DMSO-*d*<sub>6</sub>)  $\delta$  (ppm): 3.01 (s, 3H, *N*-CH<sub>3</sub>), 3.09 (s, 3H, *N*-CH<sub>3</sub>), 5.45 (s, 2H, NH<sub>2</sub>), 8.43 (s, 1H, pyrimidine H<sub>7</sub>); <sup>13</sup>C-NMR (100 MHz, DMSO-*d*<sub>6</sub>)  $\delta$  (ppm): 28.1, 30.8, 114.3, 131.4, 143.7, 148.8, 151.4, 155.6, 166.8, 168.3; MS (EI, 70 eV)  $m/z$  = 279 (M<sup>+</sup>). *Anal. Calcd for* C<sub>10</sub>H<sub>9</sub>N<sub>5</sub>O<sub>3</sub>S (279.27): C, 43.01; H, 3.25; N, 25.08; S, 11.48. Found: C, 43.05; H, 3.20; N, 25.00; S, 11.47.

## 2. 1. Cytotoxic Activity

The potential cytotoxicity of the tested compounds was evaluated using the MTT assay. The cell lines were plated in 96-multiwell plate (10<sup>4</sup> cells/well) for 24 h before treatment with the prepared compounds to allow the attachment of cells to the wall of the plate. The tested compounds were dissolved in dimethylsulfoxide (DMSO) and diluted 1000-fold in the assay. Different concentrations of the tested compounds ranging from 1 to 50  $\mu\text{g}/\text{mL}$ , were added to the cell monolayer. The monolayer cells were incubated with the compounds for 48 h at 37 °C, in atmosphere of 5% CO<sub>2</sub>. After 48 h, cells were fixed, washed and stained for 30 min with 0.4% (wt/vol) sulforhodamine B (SRB). The excess stain was washed with 1% acetic acid and attached stain was recovered with base tris-(hydroxymethyl)aminomethane (tris-EDTA) buffer, color intensity was measured in a plate reader at 570 nm, the relation between surviving fraction and drug concentration was plotted to get the survival curve of tumor cell line and the IC<sub>50</sub> was calculated. The obtained IC<sub>50</sub> values are illustrated in Table 1.

## 3. Results and Discussion

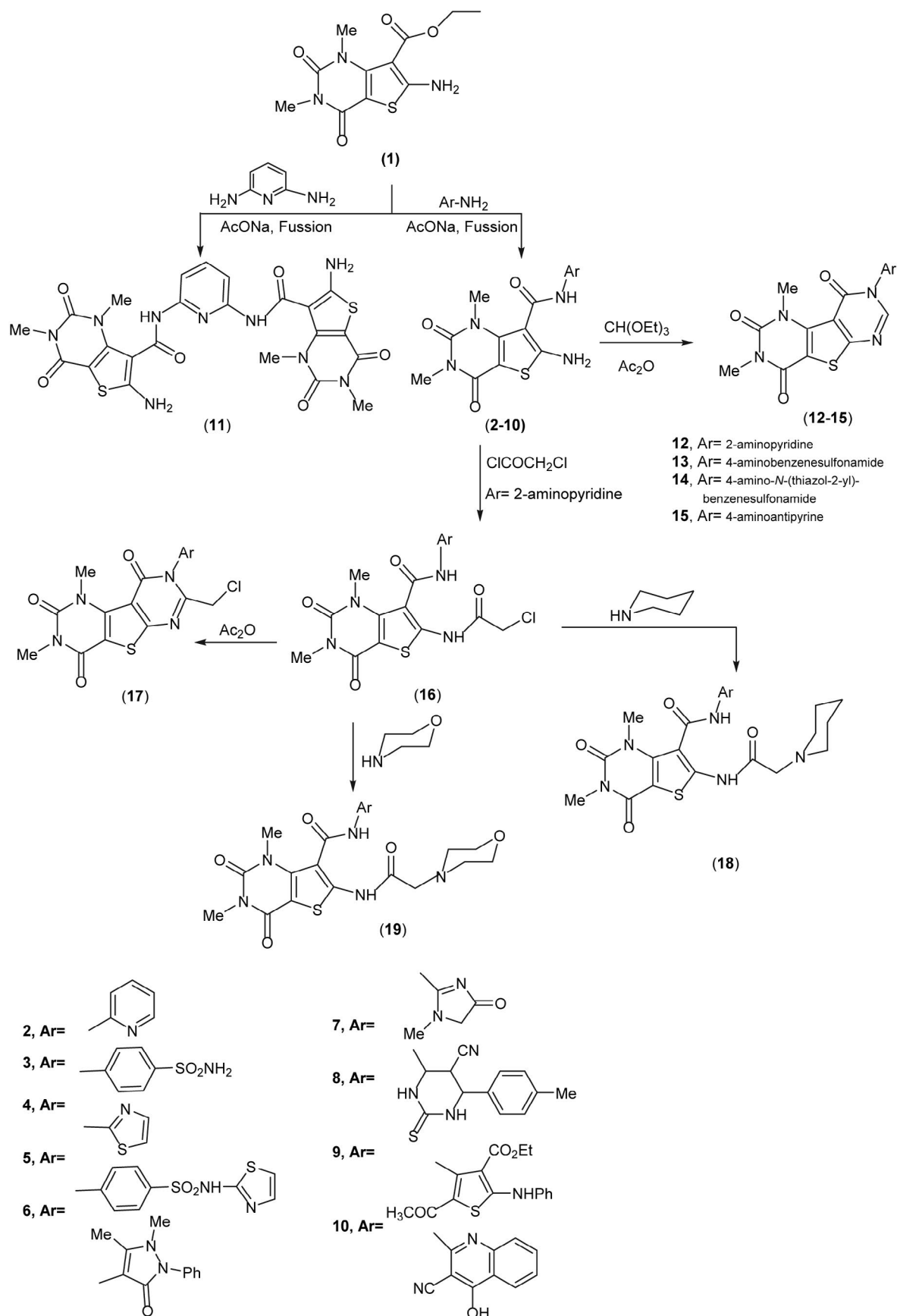
The synthetic procedures adopted to obtain the target compounds are depicted in Schemes 1–3. The reaction of ethyl 6-amino-1,3-dimethyl-2,4-dioxo-1,2,3,4-tetrahydrothieno[3,2-*d*]pyrimidine-7-carboxylate (**1**),<sup>29</sup> with equimolar ratio of different types of aromatic amines, namely 2-aminopyridine, 4-aminobenzenesulfonamide, 2-aminothiazole, 4-amino-*N*-(thiazol-2-yl)benzenesulfonamide, 4-aminoantipyrine, creatinine, 6-amino-2-thioxo-4-(*p*-tolyl)-1,2,3,4-tetrahydropyrimidine-5-carbonitrile, ethyl 5-acetyl-4-amino-2-(phenylamino)thiophene-3-carboxylate and 2-amino-4-hydroxyquinoline-3-carbonitrile in the presence of a catalytic amount of freshly fused sodium acetate furnished the corresponding carboxamide derivatives **2–10**. Analytical and spectral data for compounds **2–10** were in agreement with the proposed structures. In general, the IR spectra of these derivatives showed the absorption bands at 1687–1641 cm<sup>-1</sup> for C=O amide groups instead of C=O ester groups.

Also, compounds **8** and **10** showed the absorption bands at 2218–2219 cm<sup>-1</sup> due to CN groups. Whereas <sup>1</sup>H-NMR spectra revealed singlet signals at 3.21, 7.68 and 10.67 ppm assignable to two *N*-CH<sub>3</sub>, NH<sub>2</sub> and NH protons. In addition, the <sup>1</sup>H-NMR spectrum of **9** exhibited a triplet signal at  $\delta$  1.33 ppm due to CH<sub>3</sub> and a quartet signal at 4.43 ppm due to CH<sub>2</sub> of ester group. Also, the mass spectra of these compounds **2–10** showed the molecular ion peaks at  $m/z$  = 331 (M<sup>+</sup>), 410 (M<sup>+</sup>+1), 337 (M<sup>+</sup>), 492 (M<sup>+</sup>), 441 (M<sup>+</sup>+1), 351 (M<sup>+</sup>+1), 483 (M<sup>+</sup>), 541 (M<sup>+</sup>) and 422 (M<sup>+</sup>), respectively, which are in agreement with their molecular formula.

Compound **1** reacted with 2,6-diaminopyridine to give *N,N'*-(pyridine-2,6-diyl)bis(6-amino-1,3-dimethyl-2,4-dioxo-1,2,3,4-tetrahydrothieno[3,2-*d*]pyrimidine-7-carboxamide) (**11**). The assignment of structure **11** was supported by elemental analysis and spectral data. The IR spectrum showed absorption bands at 3574–3475, 3368, 1687 cm<sup>-1</sup> due to two NH<sub>2</sub>, two NH and six CO groups. Its <sup>1</sup>H-NMR spectrum revealed singlet signals at 3.21, 3.25, 7.46 and 10.74 ppm assignable to two *N*-CH<sub>3</sub>, two NH<sub>2</sub> and two NH protons. The mass spectrum showed the molecular ion peak at  $m/z$  = 585 (M<sup>+</sup>+2), corresponding to the molecular formula C<sub>23</sub>H<sub>21</sub>N<sub>9</sub>O<sub>6</sub>S<sub>2</sub>.

Next, we aimed to prepare the tricyclic compounds bearing thienopyrimidine scaffolds, being the focus of great interest because of their pharmacological activities. Thus, treatment of carboxamide derivatives **2**, **3**, **5** and **6** with triethyl orthoformate in acetic anhydride afforded thieno[2,3-*d*:4,5-*d'*]dipyrimidine derivatives **12–15**. Structures **12–15** were established on the basis of elemental and spectral analyses. In general, the IR spectra showed absorption bands at 1667–1655 cm<sup>-1</sup> due to carbonyl groups. Its <sup>1</sup>H-NMR spectra revealed singlet signals at 3.01 and 3.09 assignable to two *N*-CH<sub>3</sub> protons, in addition to a singlet signal at 8.51–8.56 ppm assignable to pyrimidine-H<sub>7</sub>. The mass spectra of these compounds showed the molecular ion peaks at  $m/z$  = 341 (M<sup>+</sup>), 419 (M<sup>+</sup>), 502 (M<sup>+</sup>) and 450 (M<sup>+</sup>) respectively, which are in agreement with their molecular formulas.

Also, the reaction of carboxamide derivative **2** with chloroacetyl chloride in chloroform at room temperature gave 6-(2-chloroacetamido)-1,3-dimethyl-2,4-dioxo-*N*-(pyridin-2-yl)-1,2,3,4-tetrahydro-thieno[3,2-*d*]pyrimidine-7-carboxamide (**16**). The assignment of structure **16** was supported by elemental analysis and spectral data. The IR spectrum showed absorption band at 3421 cm<sup>-1</sup> due to two NH groups, in addition to the stretching vibration of four carbonyl groups at 1698 and 1671 cm<sup>-1</sup> and showed a band at 756 cm<sup>-1</sup> due to C–Cl group. Its <sup>1</sup>H-NMR spectrum revealed singlet signals at 3.01, 3.09, 3.65, 10.67 and 11.54 ppm assignable to two *N*-CH<sub>3</sub>, CH<sub>2</sub> and two NH protons. Also, <sup>13</sup>C-NMR spectra showed a signal at 51.6 ppm due to CH<sub>2</sub>Cl. The mass spectrum showed the molecular ion peak at  $m/z$  = 407 (M<sup>+</sup>), corresponding to the molecular formula C<sub>16</sub>H<sub>14</sub>ClN<sub>5</sub>O<sub>4</sub>S.



Scheme 1

Cyclization of compound **16** in acetic anhydride afforded the corresponding 7-(chloromethyl)-1,3-dimethyl-8-(pyridin-2-yl)thieno[2,3-*d*:4,5-*d'*]dipyrimidine-2,4,9-(1*H*,3*H*,8*H*)-trione (**17**). The assignment of structure **17** was supported by elemental analysis and spectral data. The IR spectrum showed bands at 1657 and 1645  $\text{cm}^{-1}$  due to three carbonyl groups. In addition a band at 760  $\text{cm}^{-1}$  due to C–Cl group was observed.  $^1\text{H-NMR}$  spectrum of **17** revealed singlet signals at 3.01, 3.09 and 4.45 ppm assignable to two *N*-CH<sub>3</sub> and  $\text{CH}_2\text{-Cl}$  protons. The mass spectrum showed the molecular ion peak at  $m/z = 389$  ( $\text{M}^+$ ), corresponding to the molecular formula  $\text{C}_{16}\text{H}_{12}\text{ClN}_5\text{O}_3\text{S}$ .

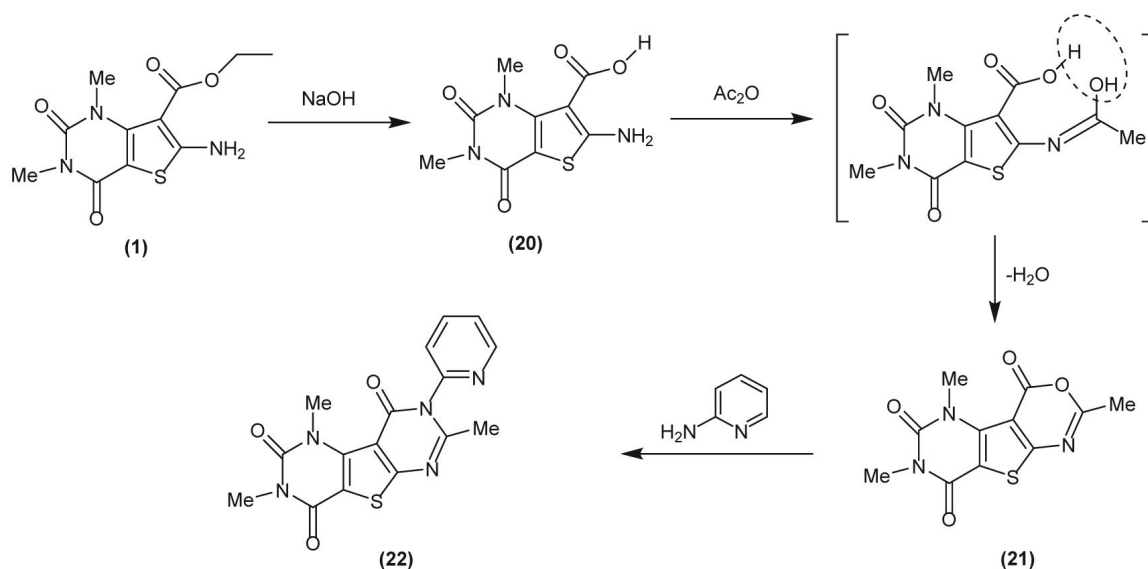
In contrast to the behaviour of compound **16** toward heterocyclic secondary amines, piperidine or morpholine in DMF reacted with **16** to furnish ethyl 1,3-dimethyl-2,4-dioxo-6-(2-(piperidin-1-yl)acetamido)-1,2,3,4-tetrahydrothieno[3,2-*d*]pyrimidine-7-carboxylate (**18**) and ethyl 1,3-dimethyl-6-(2-morpholino-acetamido)-2,4-dioxo-1,2,3,4-tetrahydrothieno[3,2-*d*]pyrimidine-7-carboxylate (**19**), respectively. The assignment of structures **18** and **19** was supported by elemental analysis and spectral data. The IR spectra showed absorption bands at 3433–3435 and 1656–1665  $\text{cm}^{-1}$  due to two NH and four CO groups. Their  $^1\text{H-NMR}$  spectra revealed singlet signals at 3.46, 10.86 and 11.46 ppm assignable to  $\text{COCH}_2\text{N}$  and two NH protons. Also,  $^{13}\text{C-NMR}$  spectra showed signals in the region 22.3–65.3 ppm due to the cyclic  $\text{CH}_2$  groups and in addition a signal at 67.6 due to  $\text{NHCOCH}_2$ . The mass spectra of compounds **18** and **19** showed their molecular ion peaks at  $m/z = 456$  ( $\text{M}^+$ ) and 458 ( $\text{M}^+$ ), respectively, which are in agreement with their molecular formula.

Thieno[2,3-*d*][1,3]oxazine heterocyclic frameworks have been found to be associated with diverse biological activities. Therefore, hydrolysis of *o*-aminoester derivative **1** in aqueous sodium hydroxide afforded the correspond-

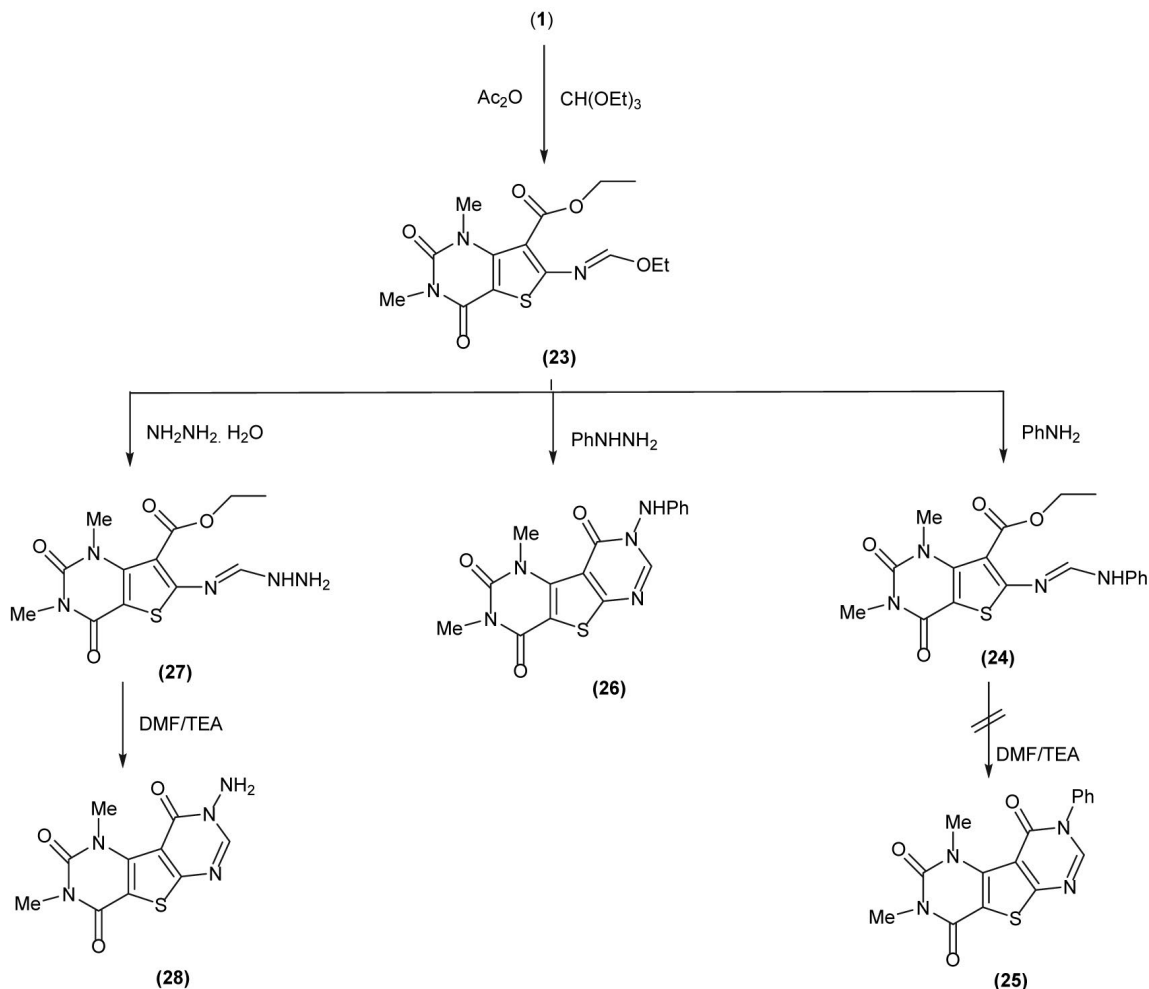
ing 6-amino-1,3-dimethyl-2,4-dioxo-1,2,3,4-tetrahydrothieno[3,2-*d*]pyrimidine-7-carboxylic acid (**20**). The assignment of structure **20** was supported by elemental analysis and spectral data. The IR spectrum showed bands at 3435, 3417 and 3387  $\text{cm}^{-1}$  due to  $\text{NH}_2$  and OH groups, in addition to the stretching vibration of three carbonyl groups at 1698 and 1671  $\text{cm}^{-1}$ . Its  $^1\text{H-NMR}$  spectrum revealed singlet signals at 3.01, 3.09, 7.34 and 11.85 ppm assignable to two *N*-CH<sub>3</sub>,  $\text{NH}_2$  and OH protons. The mass spectrum showed the molecular ion peak at  $m/z = 255$  ( $\text{M}^+$ ), corresponding to the molecular formula  $\text{C}_9\text{H}_9\text{N}_3\text{O}_4\text{S}$ .

Refluxing of the amino acid derivative **20** with acetic anhydride seemed to be a logical method for the preparation of the corresponding 1,3,7-trimethyl-9*H*-pyrimido[4,5':4,5]thieno[2,3-*d*][1,3]oxazine-2,4,9-(1*H*,3*H*)trione (**21**). The assignment of structure **21** was supported by elemental analysis and spectral data. The IR spectrum showed the disappearance of  $\text{NH}_2$  group and presence of the three carbonyl groups at 1732 and 1657  $\text{cm}^{-1}$ . Its  $^1\text{H-NMR}$  spectrum revealed singlet signals at 2.12, 3.01 and 3.09 ppm assignable to three  $\text{CH}_3$  protons. Also,  $^{13}\text{C-NMR}$  spectra showed signals at 21.4, 28.5 and 30.6 ppm due to three  $\text{CH}_3$ . The mass spectrum showed the molecular ion peak at  $m/z = 279$  ( $\text{M}^+$ ), corresponding to the molecular formula  $\text{C}_{11}\text{H}_9\text{N}_3\text{O}_4\text{S}$ .

1,3,7-Trimethyl-8-(pyridin-2-yl)thieno[2,3-*d*:4,5-*d'*]dipyrimidine-2,4,9-(1*H*,3*H*,8*H*)-trione (**22**) was obtained through the reaction of **21** with 2-aminopyridine in acetic acid. The assignment of structure **22** was supported by elemental analysis and spectral data. The IR spectrum showed the three carbonyl groups at 1671  $\text{cm}^{-1}$ . Its  $^1\text{H-NMR}$  spectrum revealed singlet signals at 2.30, 3.01 and 3.09 ppm assignable to three  $\text{CH}_3$  protons. In addition, the mass spectrum showed the molecular ion peak at  $m/z = 355$  ( $\text{M}^+$ ), corresponding to the molecular formula  $\text{C}_{16}\text{H}_{13}\text{N}_5\text{O}_3\text{S}$ .



Scheme 2



Scheme 3

Refluxing of compound **1** in acetic anhydride and triethyl orthoformate formed ethyl 6-((ethoxymethylene)amino)-1,3-dimethyl-2,4-dioxo-1,2,3,4-tetrahydrothieno[3,2-*d*]pyrimidine-7-carboxylate (**23**). The assignment of structure **23** was supported by elemental analysis and spectral data. The IR spectrum showed absorption bands at 1708 and  $1659\text{ cm}^{-1}$  due to the three carbonyl groups. Its  $^1\text{H-NMR}$  spectrum revealed triplet signals at 1.22, 2.93 ppm assignable to two  $\text{CH}_3$  protons, quartet signals at 3.71, 4.15 ppm assignable to two  $\text{CH}_2$ , two singlet signals at 3.01 and 3.09 ppm assignable to two  $N\text{-CH}_3$  and a singlet signal at 8.45 ppm assignable to  $\text{N}=\text{CH}$  proton. The mass spectrum showed the molecular ion peak at  $m/z = 340$  ( $\text{M}^+ + 1$ ), corresponding to the molecular formula  $\text{C}_{14}\text{H}_{17}\text{N}_3\text{O}_5\text{S}$ .

We studied the reactivity of *N*-ethoxymethino group with different types of amines. Thus, treatment of compound **23** with aniline gave ethyl 1,3-dimethyl-2,4-dioxo-6-(((phenylamino)methylene)amino)-1,2,3,4-tetrahydrothieno[3,2-*d*]pyrimidine-7-carboxylate (**24**). The assignment of structure **24** was supported by elemental analysis and spectral data. The IR spectrum showed an absorption band at  $3285\text{ cm}^{-1}$  due to NH group, in addition to the

stretching vibration of three carbonyl groups at 1701 and  $1653\text{ cm}^{-1}$ . Its  $^1\text{H-NMR}$  spectrum revealed a triplet signal at 3.00 ppm assignable to  $\text{CH}_3$  protons, a quartet signal at 3.71 ppm assignable to  $\text{CH}_2$ , two singlet signals at 3.01 and 3.09 ppm assignable to two  $N\text{-CH}_3$ , a singlet signal at 8.44 ppm assignable to  $\text{N}=\text{CH}$  and a singlet signal at 10.47 ppm assignable to NH proton. Also,  $^{13}\text{C-NMR}$  spectra showed signals at 18.3, 67.5 and 158 ppm due to  $\text{OCH}_2\text{CH}_3$  and  $\text{N}=\text{CH}$ . The mass spectrum showed the molecular ion peak at  $m/z = 386$  ( $\text{M}^+$ ), corresponding to the molecular formula  $\text{C}_{18}\text{H}_{18}\text{N}_4\text{O}_4\text{S}$ . We tried to obtain the cyclic compound **25** by refluxing the compound **24** in DMF and TEA but failed.

On the other hand, the compound **23** was treated with phenylhydrazine to give 1,3-dimethyl-8-(phenylamino)thieno[2,3-*d*:4,5-*d'*]dipyrimidine-2,4,9(1*H*, 3*H*,8*H*)-trione (**26**). The assignment of structure **26** was supported by elemental analysis and spectral data. The IR spectrum showed absorption bands at 3283 and  $1652\text{ cm}^{-1}$  due to NH group and carbonyl group. Its  $^1\text{H-NMR}$  spectrum revealed two singlet signals at 3.01 and 3.09 ppm assignable to two  $N\text{-CH}_3$ , a singlet signal at 8.45 ppm assign-

able to pyrimidine-H<sub>7</sub> and a singlet signal at 10.24 ppm assignable to NH proton. Also, <sup>13</sup>C-NMR spectra showed a signal at 148.6 ppm due to C7 of pyrimidine ring. The mass spectrum showed the molecular ion peak at *m/z* = 355 (M<sup>+</sup>), corresponding to the molecular formula C<sub>16</sub>H<sub>13</sub>N<sub>5</sub>O<sub>3</sub>S.

Moreover, compound **23** reacted with hydrazine hydrate to afford ethyl 6-((hydrazinylmethylene)amino)-1,3-dimethyl-2,4-dioxo-1,2,3,4-tetrahydrothieno[3,2-*d*]pyrimidine-7-carboxylate (**27**). The assignment of structure **27** was supported by elemental analysis and spectral data. The IR spectrum showed absorption bands at 3448, 3419 and 3285 cm<sup>-1</sup> due to NH<sub>2</sub> and NH groups, in addition to the stretching vibration of three carbonyl groups at 1701 and 1649 cm<sup>-1</sup>. Its <sup>1</sup>H-NMR spectrum revealed a triplet signal at 3.00 ppm assignable to CH<sub>3</sub> protons, a quartet signal at 3.71 ppm assignable to CH<sub>2</sub>, two singlet signals at 3.01 and 3.09 ppm assignable to two *N*-CH<sub>3</sub>, a singlet signal at 4.45 ppm assignable to NH<sub>2</sub>, a singlet signal at 5.63 ppm assignable to NH and a singlet signal at 8.49 ppm assignable to N=CH proton. The mass spectrum showed the molecular ion peak at *m/z* = 325 (M<sup>+</sup>), corresponding to the molecular formula C<sub>12</sub>H<sub>15</sub>N<sub>5</sub>O<sub>4</sub>S.

Finally, cyclization of compound **27** in DMF and TEA to afford the corresponding 8-amino-1,3-dimethylthieno[2,3-*d*:4,5-*d'*]dipyrimidine-2,4,9(1*H*,3*H*, 8*H*)-trione (**28**) succeeded. The assignment of structure **28** was supported by elemental analysis and spectral data. The IR spectrum showed absorption bands at 3443, 3385 cm<sup>-1</sup> due to NH<sub>2</sub> groups, in addition to the stretching vibration of three carbonyl groups at 1649 cm<sup>-1</sup>. Its <sup>1</sup>H-NMR spectrum revealed two singlet signals at 3.01 and 3.09 ppm assignable to two *N*-CH<sub>3</sub>, a singlet signal at 5.45 ppm assignable to NH<sub>2</sub> and a singlet signal at 8.43 ppm assignable to

pyrimidine-H<sub>7</sub>. Also, <sup>13</sup>C-NMR spectra showed a signal at 148.8 ppm due to C7 of pyrimidine ring. The mass spectrum showed the molecular ion peak at *m/z* = 279 (M<sup>+</sup>), corresponding to the molecular formula C<sub>10</sub>H<sub>9</sub>N<sub>5</sub>O<sub>3</sub>S.

### 3. 1. Cytotoxic Activity

The newly synthesized target compounds were evaluated for their *in vitro* anticancer effects *via* the standard MTT method,<sup>30–32</sup> against a panel of four human tumor cell lines namely; Hepatocellular carcinoma (HePG-2), Colorectal carcinoma (HCT-116), Mammary gland (MCF-7) and Epithelioid Carcinoma (Hela). The cell lines were obtained from ATCC *via* the Holding company for biological products and vaccines (VACSERA), Cairo, Egypt. 5-Fluorouracil (5-FU) was used as the standard anticancer drug for comparison. The data of cytotoxic activity are reported in Table 1.

The results are expressed as IC<sub>50</sub> (inhibitory concentration 50%), the concentration of compounds which inhibits the tumor cell growth by 50%. The obtained results revealed that eight of the tested compounds namely; **2**, **3**, **5**, **7**, **9**, **10**, **26** and **27** exhibited variable degrees of inhibitory activity towards the four tested human tumor cell lines. The compounds **2**, **3** and **26** showed the highest cytotoxic activity against all four cell lines. In addition, compounds **5**, **9**, **10** and **27** exhibited a strong cytotoxic activity against the four cell lines, whereas, compound **7** had a moderate activity against HePG-2 cell line and a strong cytotoxic activity against remaining three cell lines. Finally, the rest of compounds showed the lowest activity against all four cell lines. On the other hand, compound **2** showed activity better than that of the standard drug against HePG-2 (IC<sub>50</sub> = 6.9 ± 0.69), and the most potent activity

Table 1. *In vitro* cytotoxic activity of some new compounds against four cell lines

Compounds	<i>In vitro</i> Cytotoxicity IC <sub>50</sub> (μg/ml)*			
	HePG2	HCT-116	MCF-7	Hela
5-FU	7.9 ± 0.41	5.5 ± 0.28	5.3 ± 0.38	4.8 ± 0.31
<b>1</b>	70.0 ± 4.78	32.7 ± 2.54	30.1 ± 2.79	48.9 ± 3.75
<b>2</b>	6.9 ± 0.69	9.5 ± 0.99	8.2 ± 0.87	8.7 ± 0.73
<b>3</b>	7.8 ± 0.80	5.6 ± 0.47	5.6 ± 0.59	9.7 ± 1.10
<b>4</b>	46.2 ± 3.64	34.9 ± 3.05	37.5 ± 3.12	27.6 ± 2.54
<b>5</b>	20.7 ± 1.86	20.1 ± 1.85	17.7 ± 1.58	18.8 ± 1.66
<b>6</b>	49.9 ± 3.21	40.3 ± 3.67	47.8 ± 4.15	30.3 ± 3.80
<b>7</b>	31.1 ± 2.57	13.2 ± 1.18	12.3 ± 1.03	19.8 ± 1.58
<b>8</b>	59.3 ± 4.31	49.2 ± 3.60	51.2 ± 4.35	39.9 ± 3.14
<b>9</b>	20.0 ± 1.52	22.8 ± 2.06	15.8 ± 1.24	16.1 ± 1.28
<b>10</b>	16.0 ± 1.35	15.8 ± 1.23	10.7 ± 1.37	14.9 ± 1.34
<b>11</b>	89.4 ± 5.10	62.9 ± 4.70	62.2 ± 5.30	87.1 ± 5.47
<b>19</b>	>100	94.1 ± 6.34	94.3 ± 5.89	>100
<b>24</b>	93.0 ± 5.12	79.9 ± 5.16	80.1 ± 5.45	94.3 ± 6.34
<b>26</b>	9.8 ± 0.84	7.7 ± 0.56	8.9 ± 0.57	10.8 ± 0.97
<b>27</b>	13.1 ± 1.04	11.4 ± 1.10	9.1 ± 0.98	12.2 ± 1.53

\*IC<sub>50</sub> (μg/ml): 1–10 (very strong), 11–20 (strong), 21–50 (moderate), 51–100 (weak) and above 100 (non-cytotoxic), 5-FU = 5-Fluorouracil

against Hela ( $IC_{50} = 8.7 \pm 0.73$ ), whereas compound **3** had the most potent activity against HCT-116 and MCF-7 ( $IC_{50} = 5.6 \pm 0.47$ ) and ( $IC_{50} = 5.6 \pm 0.59$ ), respectively.

Regarding the structure–activity relationship we can reveal that compounds, such as **2**, containing a pyridine ring besides a thienopyrimidine ring and as the number of heterocyclic rings increases, especially when a six membered ring which contains one heteroatom is present, possess a high potency and their activity increases in comparison with the other compounds. In addition, compound **3** showed a more potent activity due to the presence of a sulfonamide moiety that was shown to be able to selectively concentrate in tumor tissues in addition to playing a unique role in carbonic anhydrase inhibition.<sup>33,34</sup>

Also, compound **26** has a strong activity due to the presence of phenylhydrazinyl moiety and compound **27** has a very good activity due to the hydrazenyl group. Moreover, compounds **5**, **9** and **10** showed very good activities due to the presence of sulfathiazole, thiophene and hydroxyquinoline rings, respectively; as a heterocyclic ring increases the activity otherwise, not very strong like compound **2** due to steric hindrance. Finally, compound **7** has a moderate activity due to the introduction of dihydroimidazol-4-one ring beside the thienopyrimidine reducing the activity towards the four cell lines.

## 4. Conclusion

The present study describes the synthesis of a series of novel tricyclic compounds bearing thienopyrimidine scaffolds having been the focus of great interest because of their promising pharmacological activities. This work has advantages of cheap starting materials, excellent yields, mild reaction conditions and simple experimental procedures. The compounds **2**, **3** and **26** showed the most potent antitumor activity against HepG2, HCT-116, MCF-7 and Hela cell lines.

## 5. Acknowledgements

The authors are thankful for Pharmacology Department, Faculty of Pharmacy, Mansoura University, for biological activity screening of the tested compounds. The authors declare no conflict of interest.

## 6. References

- V. P. Litvinov, *Russ. Chem. Bull.* **2004**, *53*, 487–516. DOI:10.1023/B:RUCB.0000035630.75564.2b
- J. D. Oslob, M. J. Romanowski, D. A. Allen, S. Baskaran, M. Minna Bui, R. E. Elling, W. M. Flanagan, A. M. Fung, E. J. Hanan, S. Harris, S. A. Heumann, U. Hoch, J. W. Jacobs, J. Lam, C. E. Lawrence, R. S. McDowell, M. A. Nannini, W. Shen, J. A. Silverman, M. M. Sopko, B. T. Tangonan, J. Teague, J. C. Yoburn, C. H. Yu, M. Zhong, K. M. Zimmerman, T. O'Brien, W. Lew, *Bioorg. Med. Chem. Lett.* **2008**, *18*, 4880–4884. DOI:10.1016/j.bmcl.2008.07.073
- J. Kaplan, J. C. Verheijen, N. Brooijmans, L. Toral-Barza, I. Hollander, K. Yu, A. Zask, *Bioorg. Med. Chem. Lett.* **2010**, *20*, 640–643. DOI:10.1016/j.bmcl.2009.11.050
- E. R. Wood, L. M. Shewchuk, B. E. Ellis, P. Brignola, R. L. Brashear, T. R. Caferro, S. H. Dickerson, H. D. Dickson, K. H. Donaldson, M. Gaule, R. J. Griffin, A. M. Hassell, B. Keith, R. Mullin, K. G. Petrove, M. J. Reno, D. W. Rusnak, S. M. Tadepalli, J. C. Ulrich, C. D. Wagner, D. E. Vanderwall, A. G. Waterson, J. D. Williams, W. L. White, D. E. Uehlingeh, *Proc. Natl. Acad. Sci. U. S. A.* **2008**, *105*, 2773–2778. DOI:10.1073/pnas.0708281105
- M. Lindvall, C. McBride, M. McKenna, T. G. Gesner, A. Yabannavar, K. Wong, S. Lin, A. Walter, C. M. Shafer, *ACS Med. Chem. Lett.* **2011**, *2*, 720–723. DOI:10.1021/ml200029w
- A. J. Folkes, K. Ahmadi, W. K. Alderton, S. Alix, S. J. Baker, G. Box, I. S. Chuckowree, P. A. Clarke, P. Depledge, S. A. Eccles, L. S. Friedman, A. Hayes, T. C. Hancox, A. Kugendradas, L. Lensun, P. Moore, A. G. Olivero, J. Pang, S. Patel, G. H. Pergl-Wilson, F. I. Raynaud, A. Robson, N. Saghir, L. Salphati, S. Sohal, M. H. Ultsch, M. Valenti, H. J. A. Wallweber, N. C. Wan, C. Wiesmann, P. Workman, A. Zhyvoloup, M. J. Zvelebil, S. J. Shuttleworth, *J. Med. Chem.* **2008**, *51*, 5522–5532. DOI:10.1021/jm800295d
- T. P. Heffron, M. Berry, G. Castanedo, C. Chang, I. Chuckowree, J. Dotson, A. Folkes, J. Gunzner, J. D. Lesnick, C. Lewis, S. Mathieu, J. Nonomiya, A. Olivero, J. Pang, D. Peterson, L. Salphati, D. Sampath, S. Sideris, D. P. Sutherlin, V. Tsui, N. C. Wan, S. Wang, S. Wong, B. Zhu, *Bioorg. Med. Chem. Lett.* **2010**, *20*, 2408–2411. DOI:10.1016/j.bmcl.2010.03.046
- T. T. Junttila, R. W. Akita, K. Parsons, C. Fields, G. D. L. Phillops, L. S. Friedman, D. Sampath, M. X. Sliwowski, *Cancer Cell* **2009**, *15*, 429–440. DOI:10.1016/j.ccr.2009.03.020
- W. F. Zhu, X. Zhai, S. Li, Y. Y. Cao, P. Gong, Y. J. Liu, *Chin. Chem. Lett.* **2012**, *23*, 703–706. DOI:10.1016/j.ccl.2012.04.012
- W. W. Wardakhan, H. M. Gaber, S. A. Ouf, S. M. Sherif, *Phosphorus, Sulfur Silicon Relat. Elem.* **2005**, *180*, 601–618. DOI:10.1080/104265090517406
- R. M. Mohareb, S. M. Sherif, H. E. Moustafa, *Phosphorus, Sulfur Silicon Relat. Elem.* **2009**, *184*, 2078–2096. DOI:10.1080/10426500802421127
- I. M. I. Fakhr, M. A. A. Radwan, S. El-Batran, O. M. E. Abd El-Aalam, S. M. El-Shenawy, *Eur. J. Med. Chem.* **2009**, *44*, 1718–1725. DOI:10.1016/j.ejmech.2008.02.034
- B. Abdel-Fattah, M. M. Kandeel, M. Abdel-Hakeem, Z. M. Fahmy, *J. Chin. Chem. Soc.* **2006**, *53*, 403–412. DOI:10.1002/jccs.200600051
- N. S. Shetty, R. S. Lamani, I. A. M. Khaz, *J. Chem. Sci.* **2009**, *121*, 301–307. DOI:10.1007/s12039-009-0034-7
- S. Nag, S. Batra, *Tetrahedron* **2011**, *67*, 8959–9061. DOI:10.1016/j.tet.2011.07.087
- S. Dadiboyena, A. Nefzi, *Eur. J. Med. Chem.* **2011**, *46*, 5258–5275. DOI:10.1016/j.ejmech.2011.09.016

17. S. I. Panchamukhi, J. A. S. Mulla, N. S. Shetty, M. I. A. Khazil, A. Y. Khan, M. B. Kalashetti, I. A. M. Khazi, *Arch. Pharm. Chem. Life Sci.* **2011**, *344*, 358–365. DOI:10.1002/ardp.201000227
18. S. I. Panchamukhi, A. K. M. Iqbal, M. B. Kalashetti, I. M. Khazi, *Pharm. Chem. J.* **2011**, *44*, 694–696. DOI:10.1007/s11094-011-0545-7
19. C. J. Shishoo, V. S. Shirsath, I. S. Rathod, V. D. Yande, *Eur. J. Med. Chem.* **2000**, *35*, 351–358. DOI:10.1016/S0223-5234(00)00128-8
20. B. V. Ashalatha, B. Narayana, K. K. Vijaya Raj, N. S. Kumari, *Eur. J. Med. Chem.* **2007**, *42*, 719–728. DOI:10.1016/j.ejmech.2006.11.007
21. M. N. Nasr, M. M. Gineinah, *Arch. Pharm.* **2002**, *335*, 289–295. DOI:10.1002/1521-4184(200208)335:6<289::AID-ARDP289>3.0.CO;2-Z
22. P. G. Baraldi, M. G. Pavani, M. C. Nunez, P. Brigidi, B. Vitali, R. Gambari, R. Romagnoli, *Bioorg. Med. Chem.* **2002**, *10*, 449–456. DOI:10.1016/S0968-0896(01)00294-2
23. R. Mohareb, F. Al-Omran, M. Abdelaziz, R. Ibrahim, *Acta Chim. Slov.* **2017**, *64*, 349–364. DOI:10.17344/acsi.2017.3200
24. S. Botros, O. M. Khalil, M. M. Kamel, Y. S. El-Dash, *Acta Chim. Slov.* **2017**, *64*, 102–116. DOI:10.17344/acsi.2016.2901
25. R. M. Mohareb, N. Y. Abdo, F. O. Al-Farouk, *Acta Chim. Slov.* **2017**, *64*, 117–128. DOI:10.17344/acsi.2016.2920
26. A. Fadda, H. Refat, S. Kamal, *Eur. J. Chem.* **2014**, *5*, 296–304. DOI:10.5155/eurjchem.5.2.296-304.1001
27. H. M. Refat, Khaled S. Mohamed, *Heterocycl. Commun.* **2015**, *21*, 219–224.
28. A. A. Fadda, A. M. El-badrawy, H. M. Refat, E. Abdel-Latif, *Phosphorus, Sulfur Silicon Relat. Elem.* **2016**, *191*, 778–785. DOI:10.1080/10426507.2015.1100183
29. H. M. Refat, A. A. Fadda, R. E. El-Mekawy, A. M. Sleat, *Heterocycles* **2015**, *91*, 2271–2284. DOI:10.3987/COM-15-13321
30. T. Mosmann, *J. Immunol. Methods* **1983**, *65*, 55–63. DOI:10.1016/0022-1759(83)90303-4
31. F. Denizot, R. Lang, *J. Immunol. Methods* **1986**, *89*, 271–277. DOI:10.1016/0022-1759(86)90368-6
32. M. I. Thabrew, R. D. Hughes, I. G. McFarlane, *J. Pharm. Pharmacol.* **1997**, *49*, 1132–1135. DOI:10.1111/j.2042-7158.1997.tb06055.x
33. Z. Huang, Z. Lin, J. Huang, *Eur. J. Med. Chem.* **2001**, *36*, 863–872. DOI:10.1016/S0223-5234(01)01285-5
34. E. E. Knaus, A. Innocenti, A. Scozzafava, C. T. Supuran, *Bioorg. Med. Chem. Lett.* **2011**, *21*, 5892–5896. DOI:10.1016/j.bmcl.2011.07.090

## Povzetek

Opisujemo sintezo nekaterih novih tricikličnih spojin, ki vsebujejo tienodipirimidinski fragment. Sinteza temelji na reakciji etil 6-amino-1,3-dimetil-2,4-dioksa-1,2,3,4-tetrahidrotieno[3,2-*d*]pirimidin-7-karboksilata (**1**) z različnimi vrstami aromatskih aminov **2–11**, ki daje ustrezne karboksamide, ki ob prisotnosti trietil ortoformata in acetanhidrida ciklizirajo v tieno[2,3-*d*:4,5-*d'*]dipirimidinske derivate **12–15**. Podobno smo pripravili tudi tieno[2,3-*d*:4,5-*d'*]dipirimidinski derivat **17**, ki je nastal s ciklizacijo v vrelem acetanhidridu iz tieno[3,2-*d*]pirimidin-7-karboksamidnega derivata **16**, ki smo ga pripravili iz karboksamida **2** z obdelavo s kloroacetyl kloridom v kloroformu. Strukture pripravljenih spojin smo potrdili na osnovi njihovih spektroskopskih in analitskih podatkov, kot so IR, <sup>1</sup>H-NMR, <sup>13</sup>C-NMR spektroskopija in masna spektrometrija. Pripravljenim spojinam smo določili tudi njihove citotoksične aktivnosti.



Scientific paper

# Microwave Assisted Conversion of an Amino Acid into a Fluorescent Solution

Lena Charlyn Greiler,<sup>1</sup> Hajo Haase<sup>2</sup> and Boris Mahltig<sup>1,\*</sup><sup>1</sup> Niederrhein University of Applied Sciences, Faculty of Textile and Clothing Technology, Webschulstr. 31, 41065 Mönchengladbach, Germany<sup>2</sup> Technische Universität Berlin, Institut für Lebensmitteltechnologie und Lebensmittelchemie, Gustav-Meyer Allee 25, 13355 Berlin, Germany

\* Corresponding author: E-mail: boris.mahltig@hs-niederrhein.de

Received: 31-05-2018

## Abstract

Microwave assisted synthesis is a well established method in organic and inorganic chemistry. It is also used in material science to realize novel carbon nanoparticles exhibiting fluorescence properties. The results presented here are related to a microwave driven solvothermal process used for the conversion of amino acid and 1,2-diaminoethane into fluorescent solutions. Arginine, lysine and glycine are used as amino acids. The process temperatures are set in the range of 80° to 140 °C and the maximum process pressure is 4.5 bar. The process duration is set from 5 to 30 minutes. The fluorescence effect is increased with increasing temperature. The prepared aqueous fluorescent solutions can be used as media to introduce fluorescence in textile substrates. The current study can be understood as a first proof-of-concept of a very simple microwave-assisted solvothermal synthesis of fluorescent compounds useful for the modification of different substrates.

**Keywords:** Microwave synthesis; solvothermal process; fluorescence; carbon nanoparticles

## 1. Introduction

Nanoparticles made from metals or semi-metals are well known and intensively investigated during the last decades.<sup>1–8</sup> In comparison, the investigations of nanoparticles made from carbon started only recently. The fluorescence properties of carbon nanoparticles are discovered in 2004 during the investigation of carbon nanotubes.<sup>9</sup> Carbon nanoparticles with diameters below 10 nm are named carbon quantum dots or more simply C-dots.<sup>10</sup> These C-dots are counted together with the other carbon modification of the fullerene type to the zero-dimensional carbon nanomaterials.<sup>11,12</sup> Various different applications are suggested for C-dots, as e.g. biosensing, photocatalytic or fluorescent materials.<sup>13</sup> The combination of C-dots into mesoporous materials is reported to be an innovative and interactive platform for new functional applications.<sup>14</sup>

It is suggested that the fluorescence properties of carbon nanoparticles are caused by defects of the particle surface.<sup>12,15</sup> An important influence on the fluorescence is caused by presence of amino groups onto the carbon particle surface.<sup>16</sup> It is reported that the nitrogen content influences the intensity and duration of luminescence of car-

bon nanoparticles. Especially the preparation of carbon nanoparticles starting from nitrogen containing educts is expected to lead to high fluorescence components.<sup>11</sup> Conventional fluorescence dyes often have the disadvantage of low light stability. With this background, the development of new fluorescent carbon particles is of high interest, especially to realize long-term stable fluorescent components.<sup>17,18</sup>

The preparation of carbon nanoparticles can be achieved by several methods and especially the use of bio-material precursors is prominently reported in literature. Carbon dots can be prepared e.g. by treatment of chicken egg substrate with a plasma beam or by hydrothermal treatment of tomato extract.<sup>12,19</sup> Microwave assisted preparations are well known in organic chemistry and are also applied for the preparation of carbon dots.<sup>15,20</sup> The use of microwave assisted devices is very well known in organic chemistry to prepare new compounds with higher yield and high purity.<sup>21–25</sup> For the synthesis of inorganic materials, microwave assisted procedures are also developed. Platinum nanoparticles are prepared by using a microwave assisted solvothermal technique.<sup>26</sup> Metal particles of copper, silver and gold are available from microwave assisted

solvothermal processes.<sup>27,28</sup> Compounds such as titanium dioxide or calcium hydroxyapatite can be obtained with microwave processes.<sup>28,29</sup>

A very simple experiment shows the formation of carbon dots by the treatment of yogurt in a household microwave oven at 800 W for 30 min. The carbon dots obtained by this method are reported to have a size of 2 nm and a significant content of nitrogen and oxygen.<sup>30</sup> Biomaterials like the mentioned chicken egg, tomatoes or yogurt are attractive examples to show how simple the preparation of carbon dots is. However, the reproducibility of such preparations is limited, because of the possible variation in material composition of substances from natural resources.

Other scientists report the preparation of carbon nanodots using the precursors citric acid and tetraoctylammonium ions or several types of carbohydrates treated in a domestic microwave.<sup>31,32</sup> Further, carbon quantum dots can be prepared by microwave treatment of very simple organic molecules such as the amino acid arginine and ethylenediamine in water.<sup>15,33,34</sup> This preparation has been reported to be done in a domestic microwave oven with 700 W and duration of 3 min. As result of this procedure a brown solid is obtained, which has to be cleaned by centrifugation, dialysis and freeze drying.<sup>15</sup>

With this background, the aim of the present investigation is to support a synthesis of fluorescent carbon nanoparticles under defined and controlled microwave assisted conditions. To reach this aim, an aqueous solution of an amino acid is treated in a synthesis microwave originally developed for organic synthesis. This microwave device is a closed system, so the preparation can be carried out under solvothermal conditions, which is one main difference to a conventional domestic microwave. Also the process temperature and pressure can be controlled during the preparation. By this microwave assisted process it is possible to prepare stable and transparent solutions with fluorescence properties. The correlation between process parameters and the gained fluorescence properties is clearly determined.

To give an example for a first application of these fluorescent solutions in a first proof-of-concept study, they are applied in a simple padding process onto textile substrates made from cotton.

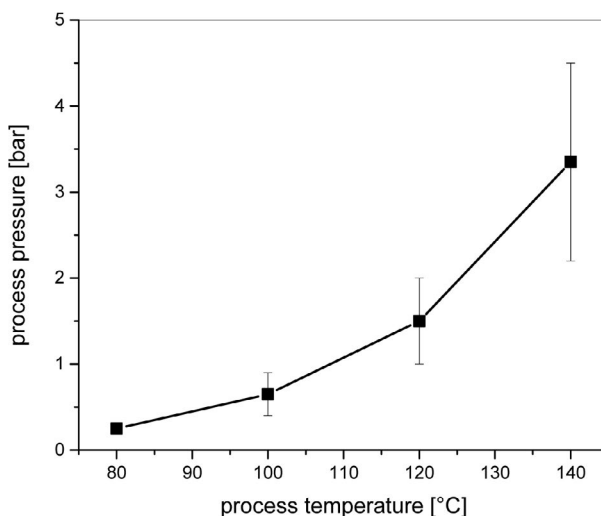
## 2. Experimental Section

### 2.1. Preparation

For the preparation, two types of chemicals are used: 1,2-diaminoethane (ethylenediamine)  $C_2H_8N_2$  and L-arginine monohydrochloride (arginine HCl)  $C_6H_{14}N_4O_2$  HCl both from Carl Roth GmbH (Karlsruhe, Germany). First, 21.4 mL ethylenediamine is mixed into 160 mL distilled water. Second, 67.4 g L-arginine monohydrochloride is dissolved in this solution. After stirring for 5 minutes, a colorless clear solution results. This solution is treated in a

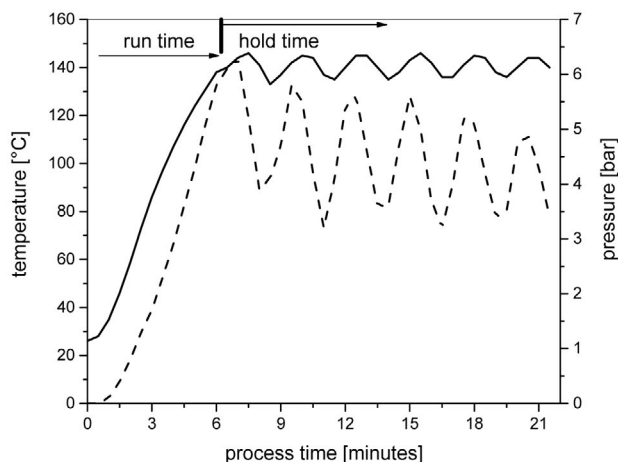
microwave synthesis device (Discover LabMate, CEM GmbH, Kamp-Lintfort, Germany). Detailed information concerning this device are available in the literature.<sup>35,36</sup>

Each preparation is performed with heating power of 250 W. The process temperatures are set in the range from 80° to 140 °C. The process vessel is a closed system, so the preparation is done under solvothermal conditions. Process pressures are determined by the chosen process temperatures. The relation of process pressure to process temperature is depicted in Figure 1.



**Figure 1.** Process pressure as function of the set process temperature in the used solvothermal arrangement. The error bars indicate the range of process pressures observed during the whole process time of 5 minutes.

A typical temperature / pressure diagram as a function of time for a process temperature of 140 °C is presented in Figure 2. After the set process temperature is reached,



**Figure 2.** Process temperature and process pressure as a function of the process time. In this example the set temperature is 140 °C and the process duration is 15 min. This set temperature is reached after a run time of around 6 min.

the process duration starts. Process temperatures of higher than 140 °C are not tested, because of the pressure limits of the used device. For all process temperatures, the process duration is set to 5 min. For the highest process temperature of 140 °C, also longer process durations of 15 and 30 min are evaluated.

After microwave treatment the gained solutions appear clear and transparent. With treatment for 5 min duration, the solutions exhibit a light yellow color. Both samples prepared with heating to 140 °C and longer process duration, exhibit deeper yellow color and also a significant smell. The received solutions are subjected to dialysis against distilled water. For dialysis a tube with an average pore size of 2.5 to 3 nm is used (Nadir-Dialyses Schlauch, Carl Roth GmbH, Karlsruhe, Germany). After dialysis solutions are colorless and their smell disappeared.

Further, the described microwave process is used to evaluate, if also other kind of amino acids beside L-arginine HCl are suitable precursors for the preparation of the fluorescent solutions. For this, the amino acids glycine  $C_2H_5NO_2$  and L-lysine monohydrochloride  $C_6H_{14}N_2O_2$  HCl are used as precursors. The amino acids are supplied by Carl Roth GmbH (Karlsruhe, Germany). For preparation of the starting solutions the amino acids are solved in mixtures of 21.4 mL ethylenediamine and 160 mL distilled water. 18 g glycine or 44 g L-lysine are used. For these preparations the process temperature is set to 140 °C and the process duration is set to 15 minutes. Also the use of L-histidine and L-tryptophan is evaluated. However, here unstable solutions with strong precipitation occur which are not further used in solvothermal microwave synthesis.

Solutions obtained after cleaning with dialysis are used for textile treatment. For this, cotton substrates with a size of 6 cm X 3 cm and a weight per area of 388 g/m<sup>2</sup> are used. Cotton fabrics are chosen for the investigations due to the hydrophilic properties of cotton fibers. The up-take of the water based fluorescent solution is expected to be higher compared to hydrophobic synthetic fibers. Of course, also the application onto other textile fiber materials is possible. The textile treatment is done by dipping of the textile samples into the solutions. A subsequent drying is performed at room temperature or at 120 °C in an oven.

## 2. 2. Analytics

The first evaluation of the prepared solutions is done visually by illumination with a UV-lamp with a maximum intensity around 365 to 370 nm (Philips Lighting Holding B.V.). Further, the optical properties of the solutions are investigated using UV/Vis spectroscopy in transmission arrangement. For this, a UV-2600 spectrometer of Shimadzu is used.

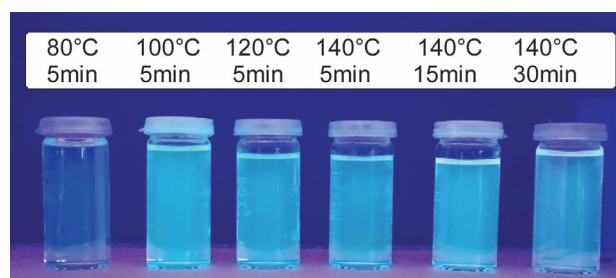
Fluorescence properties are examined with a SPARK fluorescence well plate reader equipped with monochromators (Tecan Deutschland GmbH, Crailsheim, Germany). All measurements are performed by placing the sam-

ples in 96-multiwell cell culture plates from TPP (Techno Plastic Products AG, Trasadingen, Switzerland), using 30 flashes per wavelength, an integration time of 40 μs and a lag time of 0 μs. For the investigation of liquids, 100 μL per well are applied, measuring excitation spectra from 280 to 400 nm (in steps of 2 nm) at an emission wavelength of 440 nm. Emission spectra are recorded from 380 to 600 nm (4 nm steps) at an excitation wavelength of 360 nm. In each case, measurements are performed as top reading with a Z-position of 15,500 μm, excitation and emission band widths of 5 nm, and a manual gain of 100. For the investigation of textile samples, 5 mm diameter disks are prepared by a conventional hole puncher, and analyzed in bottom reading mode with the Z-position manually set to 31,000 μm and a manual gain of 50. Excitation spectra are obtained from 280 to 400 nm (steps of 10 nm, excitation and emission band widths of 5 nm) measuring the emission at 440 nm. Emission spectra are recorded from 410 to 600 nm (10 nm steps, excitation and emission band widths of 10 nm) at an excitation wavelength of 360 nm.

## 3. Results and Discussion

### 3. 1. Properties of Prepared Solutions

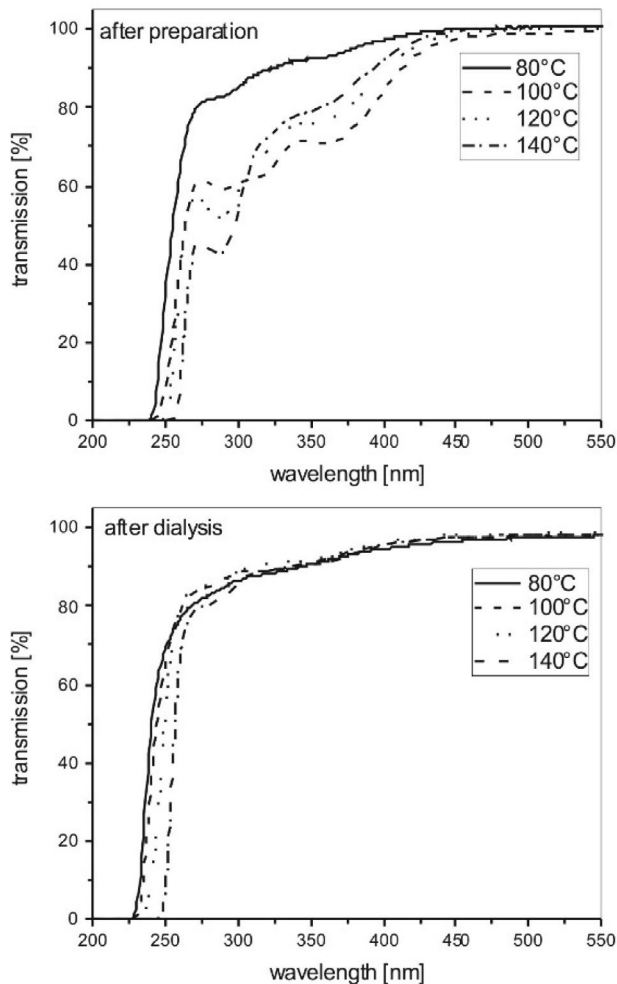
The prepared solutions are at first investigated simply by illumination with a UV-lamp emitting UV-A light. For all prepared samples, the fluorescence is obvious upon illumination with UV-A light (Figure 3). Even for the solution prepared with the lowest process temperature of 80 °C and a short process duration of 5 min, a fluorescence effect is observed. However, only the low fluorescence effect of the sample prepared at 80 °C is clearly indicated (Figure 3).



**Figure 3.** Solutions after preparation under illumination with a UV lamp. The process temperature and process duration is indicated for each solution.

The optical transmission of the prepared liquid samples is different for the UV-range from 230 to 400 nm (Figure 4), especially for the samples prepared with higher process temperature exhibiting a light yellow color, which is related to a lower optical transmission of these solutions for visible light in the range of 400 to 450 nm. The sample prepared at 100 °C exhibits two minima in the transmis-

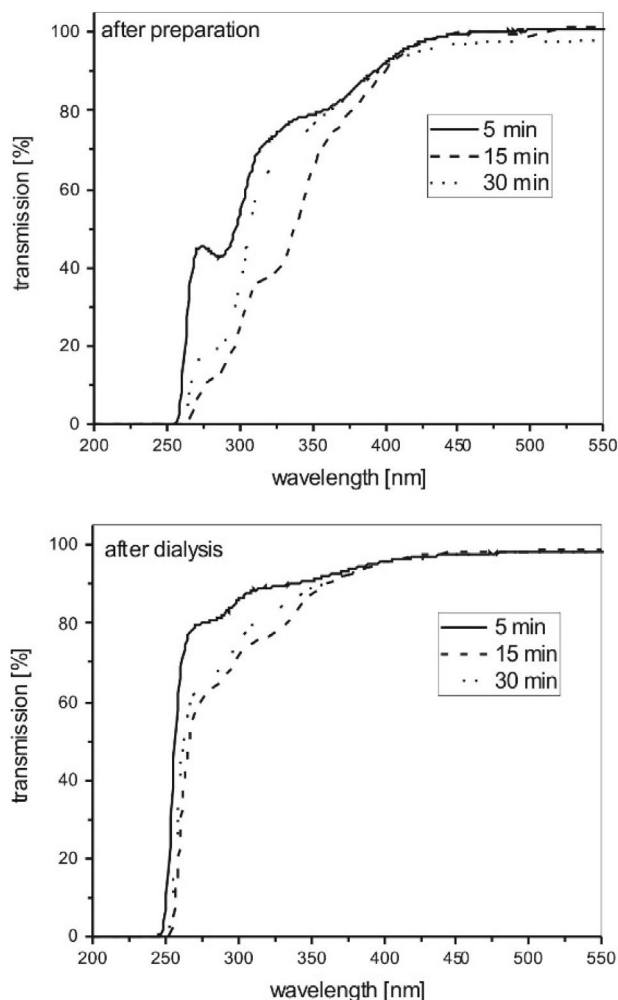
sion spectrum at 290 and at 358 nm. For the samples prepared at 120° or 140 °C, around 370 nm only a shoulder is detected in the transmission. However, the second minimum around 290 nm is more significant for these two samples. For UV-light below 240 nm, all samples exhibit no transmission. The samples are cleaned by dialysis with a tube containing a pore size of 2.5 to 3 nm. After the dial-



**Figure 4.** UV/Vis-transmission spectra of the prepared solution recorded directly after preparation (image above) and after treatment by dialysis (image below). Presented are spectra from solutions prepared at different process temperatures with a process duration of 5 min.

ysis, the samples are non-smelling and the yellow color is disappeared, which is also confirmed by the optical transmission spectra shown in Figure 4.

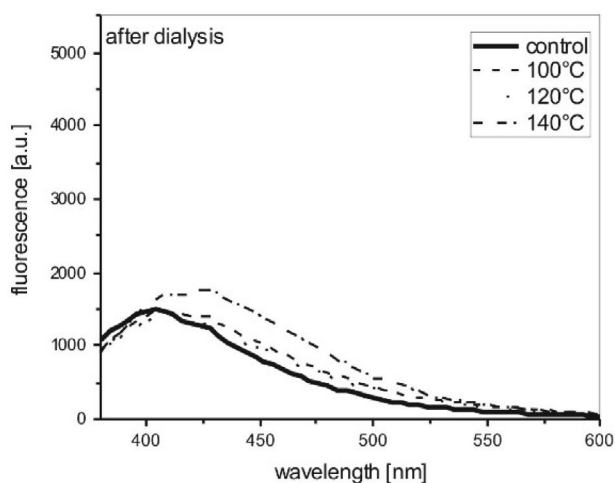
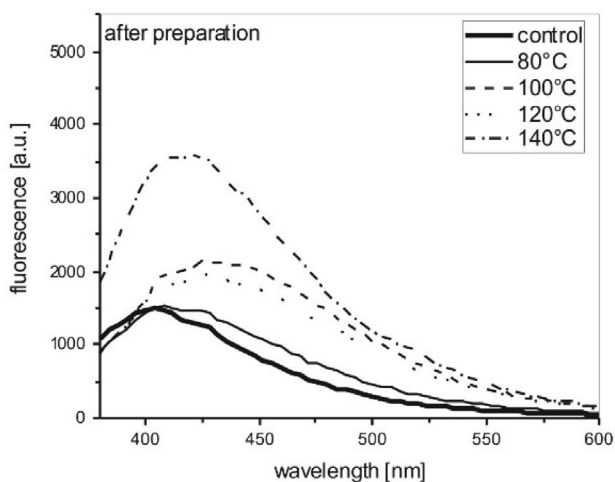
The optical transmission spectra of the solutions prepared at 140 °C at different process durations are compared in Figure 5. Compared to the sample obtained after 5 min, a longer process duration leads to lower transmission values in the range of 250 to 400 nm. The lowest values are determined for the sample with 15 min process duration. Even after dialysis, the transmission



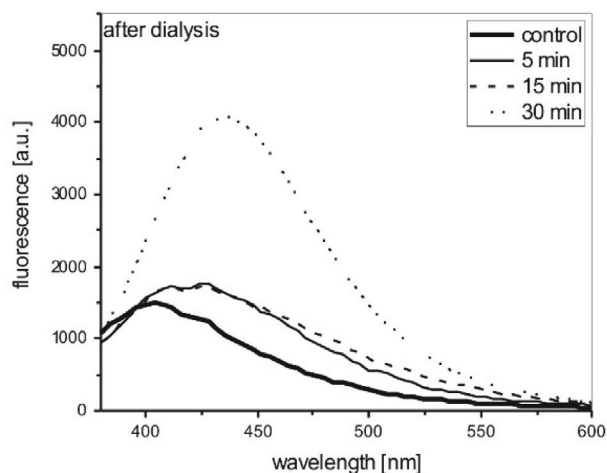
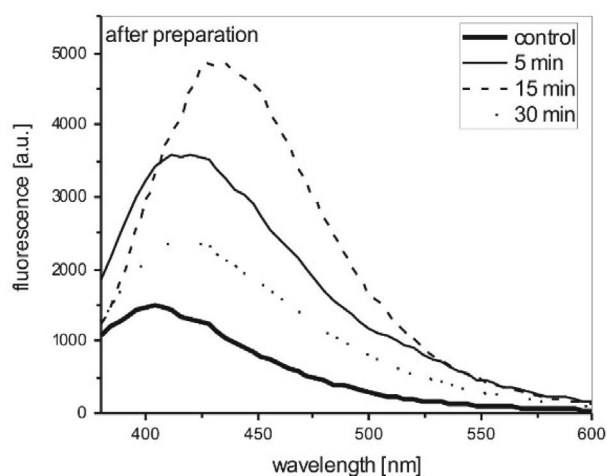
**Figure 5.** UV/Vis-transmission spectra of the prepared solution recorded directly after preparation (image above) and after treatment by dialysis (image below). Presented are spectra from solutions prepared with different process duration under a process temperature of 140 °C.

values are still low (compare Figures 4 and 5). This observation indicates that during microwave synthesis UV-absorbing particles with diameters larger than 3 nm are formed.

The fluorescence spectra of the prepared solutions are presented in Figure 6. The activation of fluorescence is done with UV-light of 360 nm. The fluorescence is correlated to the used process temperature for sample preparation. The lowest fluorescence is found for samples prepared at 80 °C (Figure 6). The strongest fluorescence is reached after preparation at 140 °C. Using a process temperature of 100° or 120 °C leads to solutions with similar mean fluorescence values. After cleaning by dialysis, the fluorescence is strongly decreased but for samples prepared at 140 °C it is still significant (Figure 6). It can be assumed that fluorescent compounds are formed by the used microwave synthesis. These components have different particle sizes higher and lower than 3 nm. The larger



**Figure 6.** Fluorescence emission spectra of the prepared solutions. For activation, light with 360 nm is used. Presented are spectra from solutions prepared at different process temperatures with a process duration of 5 minutes.



**Figure 7.** Fluorescence emission spectra of the prepared solutions. For activation light with 360 nm is used. Presented are spectra from solutions prepared with different process duration under a process temperature of 140 °C.

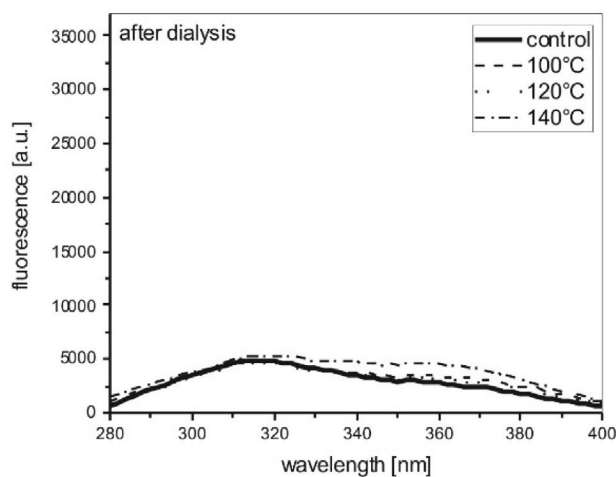
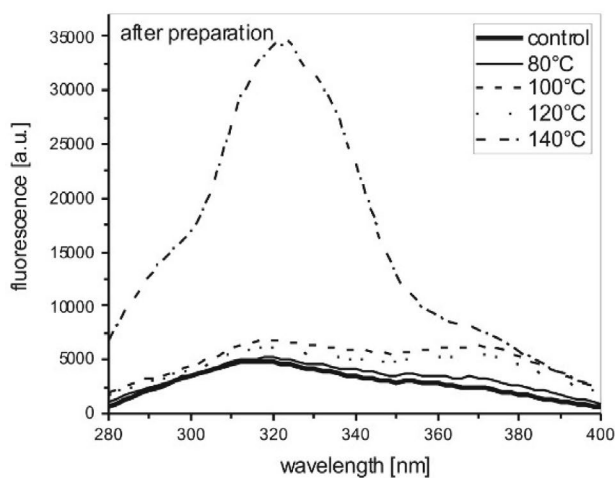
fluorescence particles are still present in the solution after the dialysis.

The fluorescence emission spectra of samples prepared at 140 °C and with increasing process duration are compared in Figure 7. It is clearly seen that the process duration has a significant influence on the gained fluorescence. Highest fluorescence values are received for the sample prepared at 140 °C with 15 minutes process duration in the microwave. For fluorescence activation with light of 360 nm, the maximum fluorescence emission is found to be at 428 nm. After performing the dialysis, the intensity of the fluorescence decreases but is still significant. The strongest fluorescence is gained for the sample prepared at 140 °C with a process duration of 30 min. For these preparation conditions the fluorescence emission maximum is observed at 436 nm for an activation with light of 360 nm.

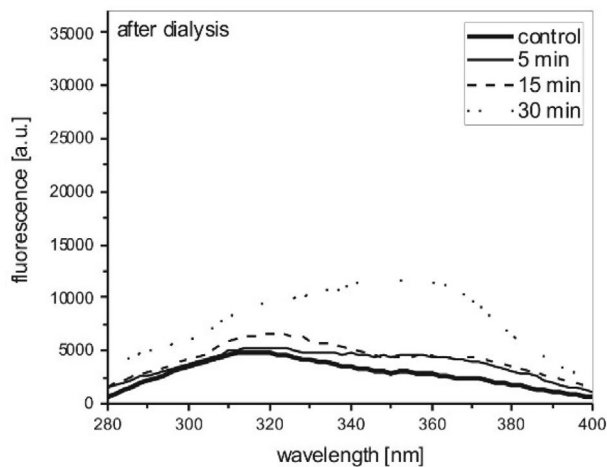
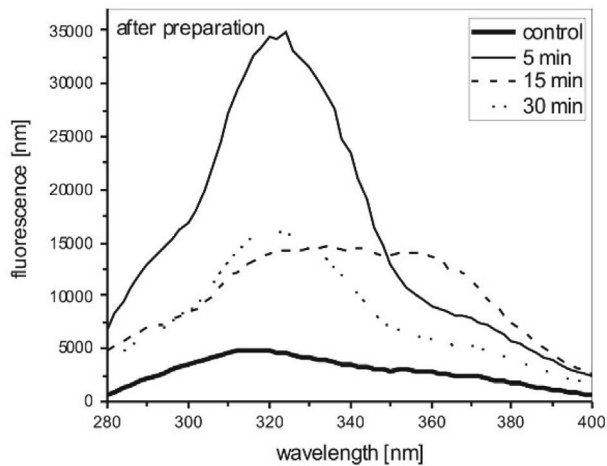
The activation spectra for an emission at 440 nm are recorded in Figures 8 and 9. For samples prepared at 80°, 100° or 120 °C, the activation of fluorescence is mainly

supported by UV-light in the range of 360 to 380 nm (Figure 8). In contrast, the activation spectrum for the sample prepared at 140 °C is totally different. In addition to the activation in the area of 360° to 380 °C, for this sample the activation spectrum exhibits a strong maximum at 324 nm (Figure 8). After dialysis, no fluorescence activation around 320 nm or below is recorded. The fluorescence for that spectral area is obviously related to lower molecular mass compounds or small particles with diameters smaller than 3 nm. However, the fluorescence in the range of 340 to 380 nm is still present after dialysis, so this fluorescence is probably related to particles with diameters larger than 3 nm.

For many practical applications, as e.g. on textile substrates, a fluorescence activation in the range of 360 to 380 nm is required, while an activation at lower wavelengths of around 320 nm is of lower relevance. An optical brightener transfers UV-light into visible blue light and gives the treated textile a whitened appearance.<sup>37,38</sup> For this application a fluorescence activation in the range of 360 to 380 nm is important, because the UV-content in



**Figure 8.** Fluorescence activation spectra of the prepared solutions. The activation is recorded for fluorescence light emitted at 440 nm. Presented are spectra from solutions prepared at different process temperatures with a process duration of 5 min.



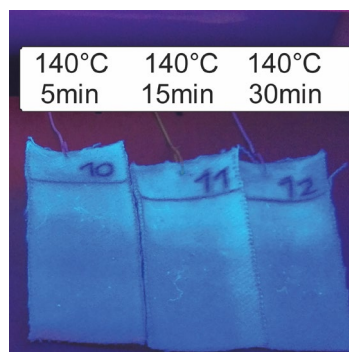
**Figure 9.** Fluorescence activation spectra of the prepared solutions. The activation is recorded for fluorescence light emitted at 440 nm. Presented are spectra from solutions prepared with different process duration under a process temperature of 140 °C.

sunlight filtered by glass is mainly present in this range and not at lower wavelength of 320 nm.<sup>39,40</sup>

The fluorescence activation spectra for an emission of 440 nm of samples prepared at 140 °C and different process durations are presented in Figure 9. The fluorescence activation is strong over the whole range from 280 to 400 nm. For a process duration of 5 or 30 min a prominent activation maximum around 320 nm is recorded. For the intermediate duration of 15 min a broad activation plateau from 320 to 360 nm is observed. After dialysis, the activation is decreased, especially for wavelengths smaller than 340 nm. The sample prepared after 30 min exhibits after dialysis a significant fluorescence activation with UV-light around 360 nm.

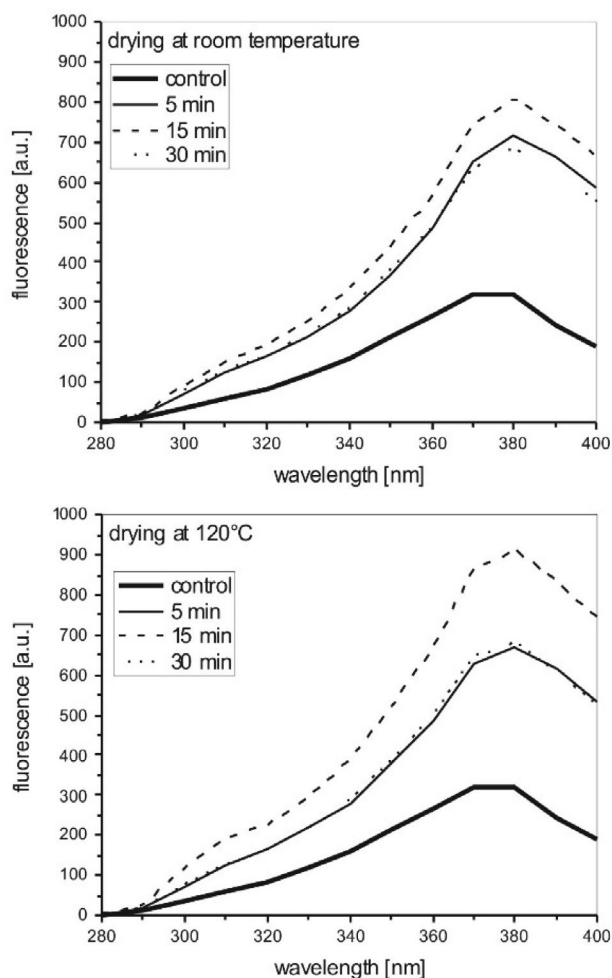
### 3. 2. Properties of Prepared Textile Samples

Cotton samples treated with the solutions prepared at 140 °C and cleaned by dialysis are presented in Figure 10. Under illumination with UV-A light, these samples exhibit the emission of a blue fluorescence.



**Figure 10.** Textile samples treated with the different solutions under illumination with a UV-lamp. The process temperature of 140 °C and process duration for solution preparation is indicated for each sample. After application of the solution, the textile samples are dried at 120 °C.

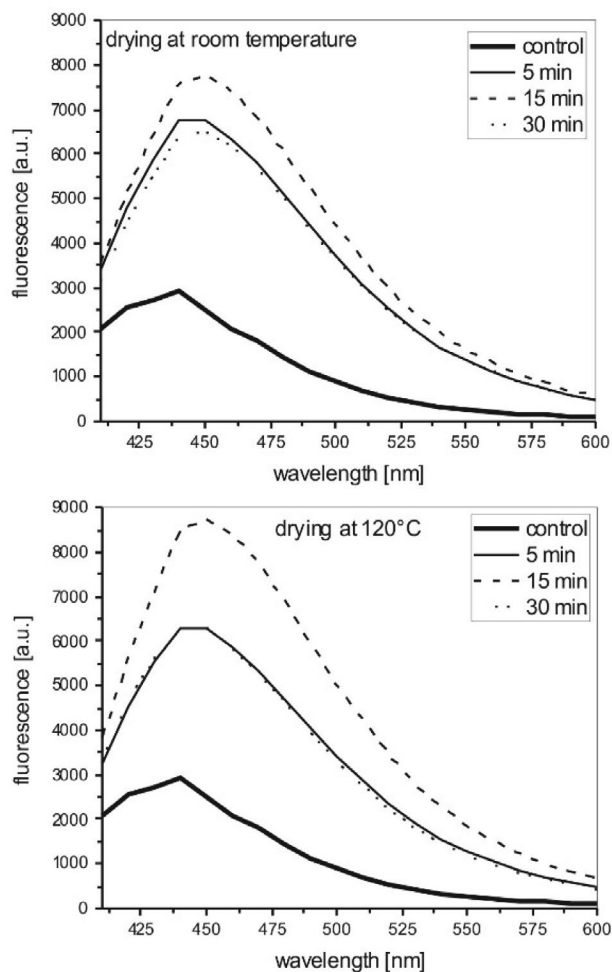
The fluorescence activation spectra of the textiles are given in Figure 11. These activation spectra are recorded for fluorescence light emitted at 440 nm. In Figure 11, sam-



**Figure 11.** Fluorescence activation spectra of the prepared textiles. The activation is recorded for fluorescence light emitted at 440 nm. Presented are textiles prepared with solutions realized with different process duration under a process temperature of 140 °C. After solution application the textile samples are dried at room temperature or at 120 °C.

ples with different process duration for solution preparation and different drying procedures of the treated textiles are compared. All samples exhibit a significant activation maximum for UV-light with 380 nm. A slightly stronger activation is determined for the sample with process duration of 15 min. The drying of textile samples at 120 °C does not lead to a decrease of the fluorescence, so the fluorescent components are obviously stable under these thermal conditions. As mentioned above, from the point of view of practical applications, both the activation maximum around 380 nm and the thermal stability are important.

The fluorescence emission spectra of the treated textiles (380 nm activation) are summarized in Figure 12. The maximum of the fluorescence emission is around 450 nm. Samples prepared from solutions with process durations of 5 or 30 min exhibit nearly the same intensity of fluorescence. In comparison with the intermediate process duration of 15 min a higher fluorescence emission is observed.

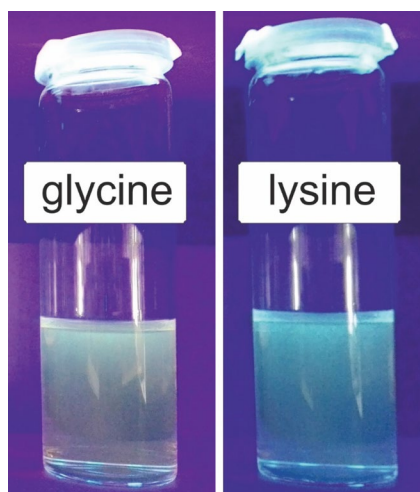


**Figure 12.** Fluorescence emission spectra of the prepared textiles. For activation light with 380 nm is used. Presented are textiles prepared with solutions realized with different process duration under a process temperature of 140 °C. After solution application the textile samples are dried at room temperature or at 120 °C.

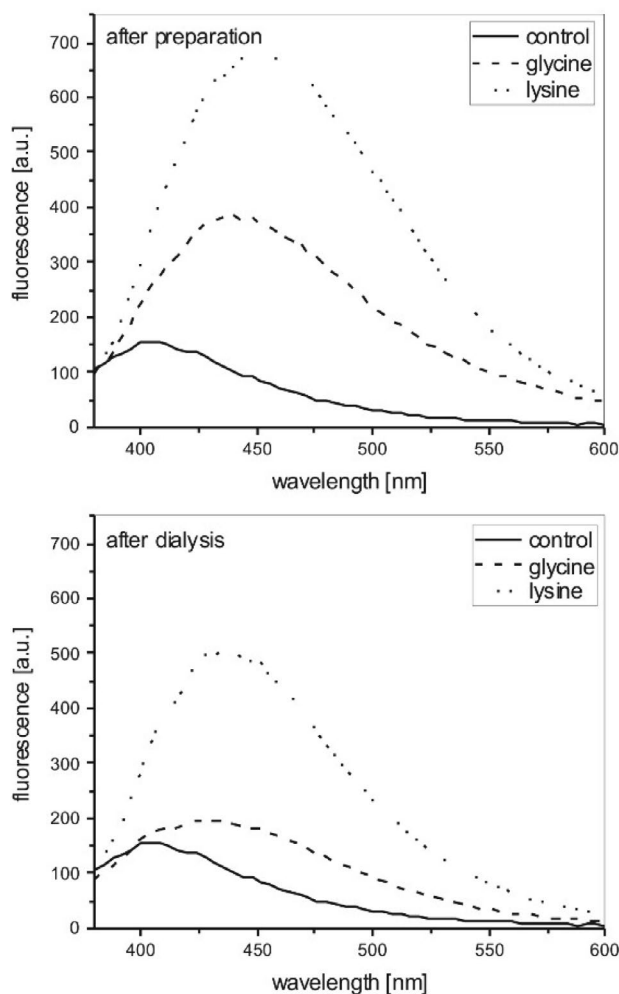
For both drying procedures of the treated textiles (at room temperature or at 120 °C) the same high fluorescence values are determined.

### 3. 3. Modification of Recipe with Different Amino Acids

Taking the both amino acids glycine and lysine as precursors, fluorescent solutions can be prepared by the used microwave assisted process using a process temperature of 140 °C with a duration of 15 minutes (see Figure 13). Under the chosen conditions, different fluorescent coloration results depending on the type of amino acid used as precursor. By using lysine, blue fluorescent coloration results, which is similar to the result gained with the precursor L-arginine (compare Figures 3 and 13). In comparison, the use of glycine leads to a fluorescent coloration that can be described as yellow to white (Figure 13).

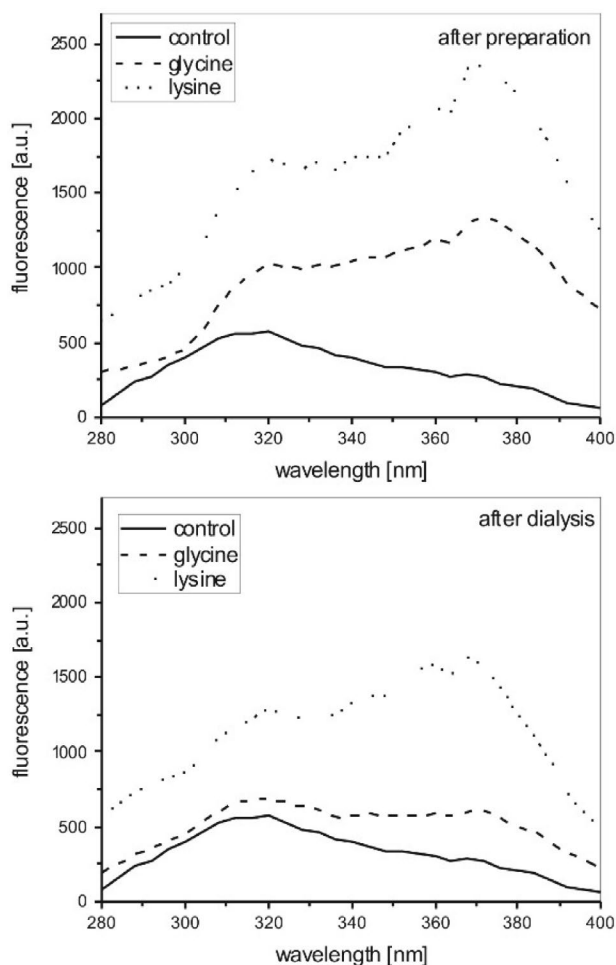


**Figure 13.** Solutions after preparation with the precursors glycine or lysine under illumination with a UV lamp. The process temperature is 140 °C and the process duration is 15 minutes.



**Figure 14.** Fluorescence emission spectra of solutions prepared with the amino acids glycine or lysine. For activation, light with 360 nm is used. Presented are spectra from solutions prepared with a process temperature of 140 °C and a process duration of 15 minutes.

The fluorescence emission spectra of solutions prepared with the amino acids glycine or lysine are shown in Figure 14. With lysine as precursor a stronger fluorescence can be reached compared to lower values gained with glycine. The maximum of fluorescence for preparations with lysine can be determined at 452 nm after preparation and at 436 nm after dialysis of the solutions. This spectroscopic result corresponds well to the observed blue coloration (Figure 13). The preparation with glycine leads to fluorescent maxima at lower wavelength – 440 nm after preparation and 424 nm after dialysis of the solutions. Compared to the emission intensity at the fluorescence maximum for solutions from lysine as precursor, the fluorescence decreased stronger at higher wavelength. At 600 nm only around 9 % of the emission intensity of the fluorescent maximum is determined, for solutions from lysine as precursor. For glycine prepared solutions, at 600 nm a higher ratio of around 13 % emission intensity of the fluorescent maximum is observed (Figure 14). This more intensive flu-



**Figure 15.** Fluorescence activation spectra of the solutions prepared with the amino acids glycine and lysine. The activation is recorded for fluorescence light emitted at 440 nm. Presented are spectra from solutions prepared with a process temperature of 140 °C and a process duration of 15 minutes.



orescence emission at higher wavelength is in relation with the yellow coloration of this solution, as seen in Figure 13.

The fluorescence activation spectra of solutions prepared with the amino acids glycine or lysine are shown in Figure 15. The activation spectra of both solutions exhibit different activation intensity but a similar shape of the spectra with two dominating maxima at 320 nm and 372 nm. After dialysis, especially the glycine based solution exhibits a strong decrease in fluorescence activation. This decrease could be explained by the formation of fluorescent molecules and particles smaller 3 nm, which are removed by dialysis from the prepared solution.

## 4. Conclusions

A microwave process driven under solvothermal conditions can be used for the preparation of fluorescent solutions based on the thermal conversion of simple amino acids, which are arginine, lysine and glycine. The effectivity of conversion is determined by the process temperature used in the solvothermal process. Best results are gained for a process temperature of 140 °C. The fluorescent components can be distinguished into components with different particle sizes smaller and larger than 3 nm in diameter. The solutions are suitable for application onto textiles, e.g. as optical brighteners or as fluorescence marker. The fluorescence activation is driven mainly with UV-light in the range of 360 to 380 nm which fits to the UV-light present in sunlight. Also the thermal stability necessary for drying and fixation processes is given. A first proof-of-concept is provided that by microwave synthesis the conversion of amino acids into fluorescent particles is possible. These particles present in homogeneous, transparent and aqueous solutions can be used as finishing agent for textiles.

## 5. Acknowledgements

All product and company names mentioned in this chapter may be trademarks of their respective owners, also without labeling. For many helpful discussions and technical help in the lab many thanks have to be acknowledged to Dr. Thomas Grethe from Niederrhein University of Applied Sciences.

## 6. References

1. P. K. Jain, X. Huang, I. H. El-Sayed, M. A. El-Sayed, *Plasmonics* **2007**, *2*, 107–118. DOI:10.1007/s11468-007-9031-1
2. F. E. Kruis, H. Fissan, A. Peled, *J. Aerosol Sci.* **1998**, *29*, 511–535. DOI:10.1016/S0021-8502(97)10032-5
3. S. Farhadi, B. Ajerloo, A. Mohammadi, *Acta Chim. Slov.* **2017**, *64*, 129–143. DOI:10.17344/acsi.2016.2956
4. E. Soleimani, N. Zamani, *Acta Chim. Slov.* **2017**, *64*, 644–653. DOI:10.17344/acsi.2017.3459
5. S. Abdolmohammadi, M. Afsharpour, *Z. Naturforsch.* **2015**, *70b*, 171–176.
6. B. Mahltig, H. Haufe, K. Muschter, A. Fischer, Y. H. Kim, E. Gutmann, M. Reibold, D. C. Meyer, T. Textor, C. W. Kim, Y. S. Kang, *Acta Chim. Slov.* **2010**, *57*, 451–457.
7. B. Mahltig, M. Reibold, E. Gutmann, T. Textor, J. Gutmann, H. Haufe, H. Haase, *Z. Naturforsch.* **2011**, *66b*, 905–916.
8. D. Salz, B. Mahltig, A. Baalmann, M. Wark, N. Jaeger, *Phys. Chem. Chem. Phys.* **2000**, *2*, 3105–3110. DOI:10.1039/b002327m
9. X. Xu, R. Ray, Y. Gu, H. J. Ploehn, L. Gearheart, K. Raker, W. A. Scrivens, *J. Am. Chem. Soc.* **2004**, *126*, 12736–12737. DOI:10.1021/ja040082h
10. Y. Wang, A. Hu, *J. Mater. Chem. C* **2014**, *2*, 6921–6939. DOI:10.1039/C4TC00988F
11. X. T. Zheng, A. Ananthanarayanan, K. Q. Luo, P. Chen, *Small* **2015**, *11*, 1620–1635. DOI:10.1002/sml.201402648
12. J. Wang, C. F. Wang, S. Chen, *Angew. Chem. Int. Ed.* **2012**, *51*, 9297–9301. DOI:10.1002/anie.201204381
13. S. Y. Lim, W. Shen, Z. Gao, *Chem. Soc. Rev.* **2015**, *44*, 362–381. DOI:10.1039/C4CS00269E
14. P. Innocenzi, L. Malfatti, D. Carboni, *Nanoscale* **2015**, *7*, 12759–12772. DOI:10.1039/C5NR03773E
15. K. Suzuki, L. Malfatti, D. Carboni, D. Loche, M. Casula, A. Moretto, M. Maggini, M. Takahashi, P. Innocenzi, *J. Phys. Chem. C* **2015**, *119*, 2837–2843. DOI:10.1021/jp510661d
16. X. Zhai, P. Zhang, C. Liu, T. Bai, W. Li, L. Dai, W. Liu., *Chem. Commun.* **2012**, *48*, 7955–7957. DOI:10.1021/jp510661d
17. J. Baker, 50 Schlüsselideen Quantenphysik, Springer Spektrum Verlag, Berlin, **2015**. DOI:10.1007/978-3-662-45033-8
18. K. A. S. Fernando, S. Sahu, Y. Liu, W. K. Lewis, E. A. Gulians, A. Jafariyan, P. Wang, C. E. Bunker, Y. P. Sun, *ACS Appl. Mater. Interfaces* **2015**, *7*, 8363–8376. DOI:10.1021/acsami.5b00448
19. P. Wang, R. B. Zhong, M. Yuan, P. Gong, X. Zhao, F. Zhang, *Nucl. Sci. Techn.* **2016**, *27*, 35. DOI:10.1007/s41365-016-0038-1
20. M. Gupta, S. Paul, R. Gupta, *Acta Chim. Slov.* **2009**, *56*, 749–764.
21. C. O. Kappe, *Ange. Chem. Int. Ed.* **2004**, *43*, 6250–6284.
22. N. Kuhnert, *Ange. Chem. Int. Ed.* **2002**, *41*, 1863–1866.
23. M. Larhed, A. Hallberg, *Drug Discovery Today* **2001**, *6*, 406–416. DOI:10.1016/S1359-6446(01)01735-4
24. P. Lidström, J. Tierney, B. Wathey, J. Westman, *Tetrahedron* **2001**, *57*, 9225–9283. DOI:10.1016/S0040-4020(01)00906-1
25. R. M. Shaker, M. A. Elrady, *Z. Naturforsch.* **2008**, *63b*, 1431–1437.
26. D. Li, S. Komarneni, *Z. Naturforsch.* **2006**, *61b*, 1566–1572.
27. S. Komarneni, Y. D. Noh, J. Y. Kim, S. H. Kim, H. Katsuki, *Z. Naturforsch.* **2010**, *65b*, 1033–1037.
28. B. Mahltig, E. Gutmann, M. Reibold, D. C. Meyer, H. Böttcher, *J. Sol-Gel Sci. Technol.* **2009**, *51*, 204–214. DOI:10.1007/s10971-009-1972-8
29. B. Mahltig, H. Miao, *J. Coat. Technol. Res.* **2017**, *14*, 721–733. DOI:10.1007/s11998-016-9891-4

30. S. Dinc, M. Kara, M. D. Kars, F. Aykül, H. Cicekci, M. Akkus, *Appl. Phys. A* **2017**, *123*, 572–579. DOI:10.1007/s00339-017-1184-y
31. M. L. Bhaisare, A. Talib, M. S. Khan, S. Pandey, H. F. Wu, *Microchim. Acta* **2015**, *182*, 2173–2181. DOI:10.1007/s00604-015-1541-5
32. X. Wang, K. Qu, B. Xu, J. Ren, X. Qu, *J. Mater. Chem.* **2011**, *21*, 2445–2450. DOI:10.1039/c0jm02963g
33. D. Mazzier, M. Favaro, S. Agnoli, S. Silvestrini, G. Granozzi, M. Maggini, A. Moretto, *Chem. Commun.* **2014**, *50*, 6592–6595. DOI:10.1039/C4CC02496F
34. D. Mosconi, D. Mazzier, S. Silvestrini, A. Privitera, C. Marega, L. Franco, A. Moretto, *ACS Nano* **2015**, *9*, 4156–4164. DOI:10.1021/acsnano.5b00319
35. U. Sengutta, H. P. Meier, *GIT Labor-Fachzeitschrift* **2002**, *46*, 1038–1043.
36. H. Ritter, J. Theis, *GIT Labor-Fachzeitschrift* **2011**, *55*, 170–173.
37. R. A. Mustalish, *Studies in Conservation* **2000**, *45*, 133–136. DOI:10.1179/sic.2000.45.Supplement-1.133
38. I. H. Leaver, B. Milligan, *Dyes and Pigments* **1984**, *5*, 109–144. DOI:10.1016/0143-7208(84)80008-X
39. P. Brennan, C. Fedor, G. Pausch, *Paint and Resin* **1988**, *58*, 17.
40. C. Tuchinda, S. Srivannaboon, H. W. Lim, *J. Am. Acad. Dermatol.* **2006**, *54*, 845–854. DOI:10.1016/j.jaad.2005.11.1082

## Povzetek

Sinteza z uporabo mikrovalov je že dobro uveljavljena metoda v organski in anorganski sintezni kemiji. Prav tako se uporablja na področju materialov za pripravo novih ogljikovih nanodelcev, ki izražajo fluorescenčne lastnosti. V tej raziskavi je predstavljena z mikrovalovi spodbujena solvatotermna sinteza, ki je bila uporabljena za pretvorbo amino kislin in 1,2-diaminoetana v različne fluorescenčne raztopine. V študiji so kot modelne amino kisline uporabili arginin, lizin in glicin, v temperaturnem območju reakcije od 80° do 140 °C in pri tlaku 4.5 bar. Reakcije so potekale od 5 do 30 minut. Fluorescenčni efekt se povečuje s višanjem temperature. Pripravljene vodne fluorescenčne raztopine lahko uporabimo kot medij za indukcijo fluorescence na tekstilnih substratih. Študija je prvi primer potrditve koncepta preproste, z mikrovalovi asistiranje solvatotermne sinteze fluorescenčnih raztopin, ki je uporaben za modifikacijo različnih substratov.

Scientific paper

# Anti-Cancer Effect of Tacrine-Coumarin Derivatives on Diverse Human and Mouse Cancer Cell Lines

Zuzana Solárová,<sup>1</sup> Martin Kello,<sup>1</sup> Slávka Hamuláková,<sup>2</sup>  
Ladislav Mirossay<sup>1</sup> and Peter Solár<sup>3,\*</sup>

<sup>1</sup> Institute of Pharmacology, Faculty of Medicine, P. J. Šafárik University in Košice, SK-04154 Košice, Slovak Republic

<sup>2</sup> Department of Organic Chemistry, Institute of Chemistry, Faculty of Science, P. J. Šafárik University in Košice, SK-04154 Košice, Slovak Republic

<sup>3</sup> Institute of Medical Biology, Faculty of Medicine, P. J. Šafárik University in Košice, SK-04154 Košice, Slovak Republic

\* Corresponding author: E-mail: peter.solar@upjs.sk

Received: 04-06-2018

## Abstract

Acridine derivatives were first used as antibacterial and antiparasitic agents, later as antimalarial and anti-HIV drugs, and now as potentially anticancer agents due to their high cytotoxic activity. Due to their serious adverse effects, new synthetic derivatives were introduced and tested based on modified naturally occurring substances, such as acridone derivatives, which also exhibit potential anti-tumor activity. Most of them are DNA-damaging substances, causing relatively strong and selective destruction of tumor cells. We have tested *in vitro* anti-proliferative effects of newly-synthesized tetrahydroacrid derivatives, namely tacrine-coumarin hybrid molecules, on various human and mouse cancer cell lines. Our results showed that tacrine-coumarin hybrids with seven, eight, and nine methylene groups in spacer reduce proliferation of cancer cells. A hybrid with nine methylene groups had the most significant anti-cancer effect.

**Keywords:** Tacrine-coumarin hybrid molecules; cancer cells; antiproliferative effects

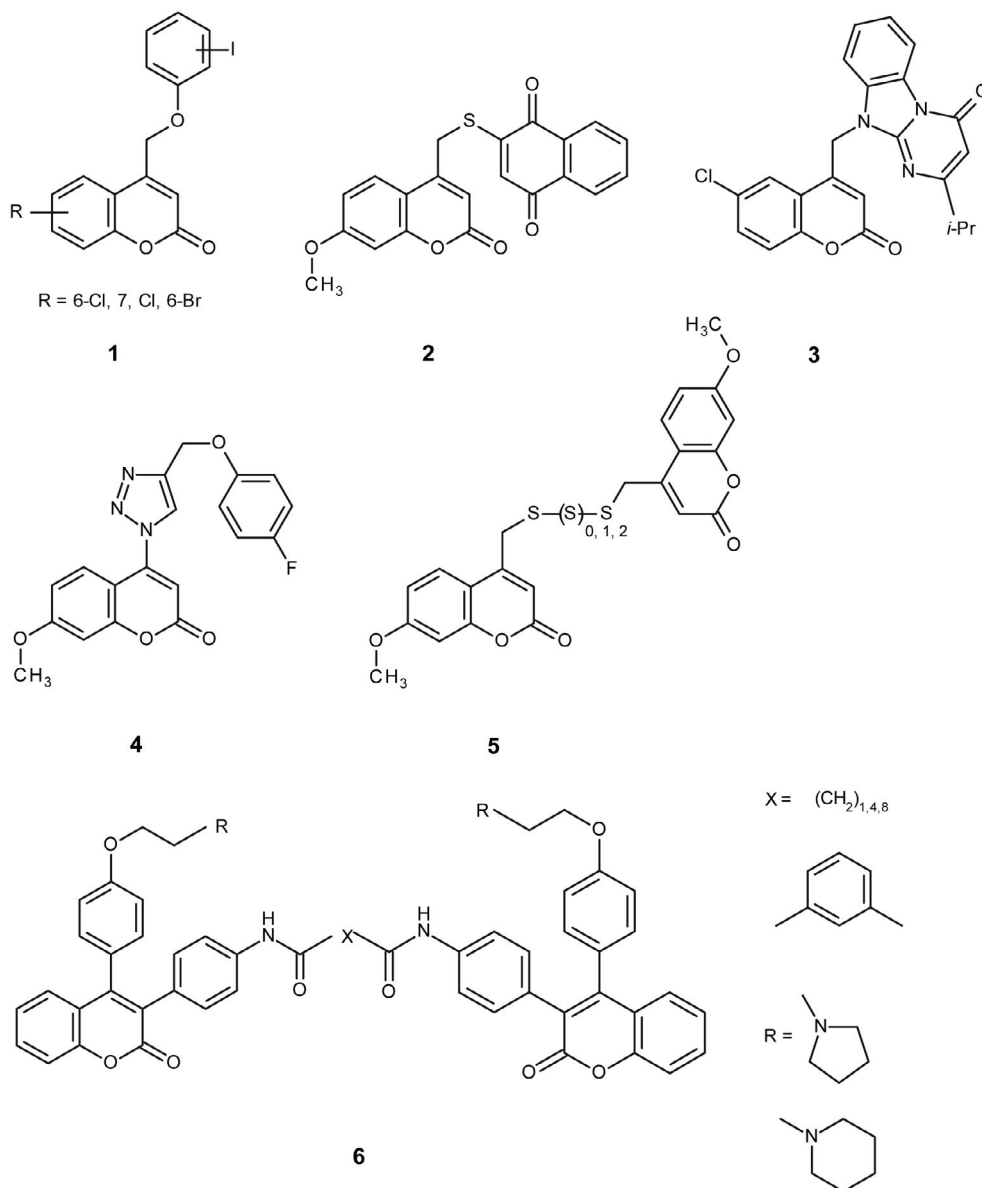
## 1. Introduction

Coumarin and coumarin derivatives are well known anticancer agents. The anticancer activity of coumarin derivatives, 3-, 4-, 7-, 8- substituted biscoumarins and fused coumarins, has been described according to the type and position of the side chain of the coumarin core structure.<sup>1</sup> The number, location, and length of the side chain have important effects on anti-tumor activities.<sup>2</sup> Fig. 1 shows the chemical structure of 4-substituted coumarins that reveal interesting anti-cancer activity.

Basanagouda et al.<sup>3</sup> synthesized a new series of iodinated-4-aryloxymethyl coumarin derivatives **1** (Fig. 1). These compounds were screened for their *in vitro* anti-cancer activity against two cancer cell lines, MDA-MB human adenocarcinoma mammary gland and A-549 human lung carcinoma. The compounds in which the chlorine was in C-6 and C-7 position on coumarin ring and iodine was in C-4 position on phenoxy moiety exhibited significant anti-cancer activity (MIC = 1.56 µg/mL).<sup>3</sup> Bana et al.<sup>4</sup> designed and synthesized a novel couma-

rin-quinone inhibitor **2** (SV37, Fig. 1), the structure of which is based on both coumarin and quinone moieties as a potent CDC25 inhibitor. An analytical *in vitro* approach shows that this compound efficiently inhibits all three purified human CDC25 isoforms, CDC25A, B, and C, with IC<sub>50</sub> between 1 and 9 µM. Moreover, **2** isoforms had superior antiproliferative activity against MCF-7 and MDA-MB-231 cells (IC<sub>50</sub> = 1–11 µM) versus hTERT-HME1 (IC<sub>50</sub> = 18 µM).<sup>4</sup> Puttaraju et al.<sup>5</sup> designed and synthesized a new series of coumarin substituted dihydrobenzo[4,5]imidazo[1,2-a]pyrimidin-4-ones derivatives **3**. The coumarin derivative with *i*-Pr in C-3 position on dihydrobenzo[4,5]imidazo[1,2-a]pyrimidin-4-one and chlorine in C-6 position on coumarin ring was found to be the most potent cytotoxic compound (88%) against Dalton's Ascitic Lymphoma cell line.<sup>5</sup>

Sequences of 4-(1,2,3-triazol-1-yl)coumarin derivatives **4** were synthesized and their anti-cancer activities against human cancer cell lines, including human breast carcinoma MCF-7 cell, colon carcinoma SW480 cell, and lung carcinoma A549 cell, were subsequently studied *in*



**Figure 1.** Structures of 4-substituted coumarin derivatives 1-4 and bis-coumarines 5, 6 revealing anticancer activities

*vitro*. Among them, 4-(4-(4-fluorophenoxy) methyl)-1,2,3-triazol-1-yl)-7-methoxycoumarin **4** exhibited excellent broad spectrum anti-cancer *in vitro* activity against MCF-7, SW480, and A549 ( $IC_{50}$  = 5.89, 1.99, and 0.52  $\mu$ M, respectively).<sup>6</sup>

In general, the dimeric coumarin tends to show greater efficacy against cancer cells compared to the monomeric one.<sup>2</sup> Some bis-coumarin polymers with the anti-cancer activity are shown in Fig. 1. Novel bis-coumarin polysulfides as di-, tri-, and tetrasulfides **5** were synthesized and tested in the HCT116 colorectal cancer cell line to assess their ability to induce cell growth inhibition and apoptosis. The coumarin polysulfides effectively reduced cell viability (around 50%) in a concentration and time dependent manner and reduced cell viability more efficiently compared to the corresponding diallyldisulfide.<sup>7</sup>

Tan et al.<sup>2</sup> designed and synthesized novel dimers of triphenylethylene-coumarin hybrid **6** containing one amino side chain. These dimeric substances were subjected to anti-proliferative tests against four tumor cell lines, MCF-7, A549, K562, and HeLa, and exhibited significant anti-proliferative activity at  $IC_{50}$  concentrations approaching 10  $\mu$ M.

Since the anti-cancer activity of hybrids in which the coumarin ring is connected with tacrine has not yet been reported, based on the knowledge that coumarin functional groups as well as tetrahydroacridine derivatives have anti-tumor effects, we decided to test such effects using newly synthesized tacrine-coumarin hybrids **7a-g** (Fig. 2). Both the synthesis and the biological activity of relevant tacrine-coumarin hybrids, except for anti-cancer ones, have already been published.<sup>8</sup>

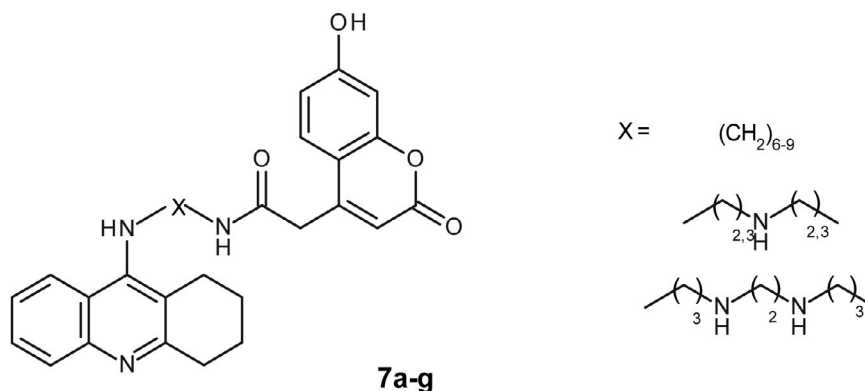


Figure 2. Structures of tacrine-coumarin hybrids 7a-g

Little work has been done on the anti-tumor effects of tacrine. However, published results clearly demonstrated that only high concentration of tacrine can induce apoptosis via lysosome- and mitochondrial-dependent pathway in HepG2 cells.<sup>9,10</sup> On the other hand, despite high concentration, tacrine did not show any cytotoxic effect on the promyelocytic leukemia HL-60 cell line.<sup>11</sup> In this study, we decided to test the anti-cancer effects of tacrine-coumarin hybrids on highly invasive (4T1), less invasive (A549, HCT) and non-invasive (MCF-7) cell lines. To reinforce the hypothesis of different effects of tacrine-coumarin hybrids on cancer cells compared to normal ones, we compared human cancer cell lines (MCF-7, A549, HCT) with normal HUVEC cells and mouse tumor cell line 4T1 with the normal mouse cells NMuMG.

## 2. Experimental

### 2. 1. Cell lines and Cell Culture

Human colorectal carcinoma HCT116 (HCT), human breast adenocarcinoma MCF-7, human A549 lung carcinoma, and mouse mammary carcinoma 4T1, as well as non-cancer mouse mammary gland cells NMuMG and human endothelial cells isolated from umbilical vein HUVEC, were used in our experiments. The HCT, MCF-7, and 4T1 cell lines were cultured in RPMI medium (Sigma-Aldrich, St. Louis, MO, USA), A549 and NMuMG in DMEM medium with high glucose (4.5 g/l), and L-glutamine (GE Healthcare, Little Chalfont, UK) and HUVEC cells in HMEC medium (Sigma-Aldrich) with added vascular endothelial growth factor and bovine fibroblast growth factor. All media contained 10% fetal bovine serum (Thermo Fisher Scientific, Inc., Waltham, MA, USA) and antibiotics (Sigma-Aldrich), except 4T1 and NMuMG cells, which did not contain antibiotics. The cells were incubated at 37 °C in a humidified 5% CO<sub>2</sub> (v/v) atmosphere. Dr. Hamuláková of the Institute of Chemistry, Faculty of Science, Pavol Jozef Šafárik University in Košice, synthesized Tacrine-coumarin derivatives.

### 2. 2. MTT Assay

HCT, MCF-7, A549, 4T1, NMuMG, and HUVEC cells were seeded into 96-well cell culture plates at a density of  $5 \times 10^3$  per well. MTT (3-(4,5-dimethylthiazol-2-yl)-2,5-diphenyl tetrazolium bromide; Sigma-Aldrich Co.) was added at the final concentration of 0.2 mg/ml after 72 h incubation at the concentration ranging from 0.001 to 10  $\mu$ M of tacrine-coumarin hybrid molecules [Fig. 1; synthesized and characterized by Hamuláková et al.,<sup>8</sup> followed by 4 h incubation at 37 °C and solubilization of MTT-formazan product using 3.3% sodium dodecyl sulphate (Sigma-Aldrich Co.)]. The absorbance was measured using a universal microplate reader (FLUOstar Optima, BMG Labtechnologies GmbH, Offenburg, Germany) and expressed as a percentage of the dye extracted from untreated control cells [(OD value of treated cells/mean OD value of control cells)  $\times$  100%].

### 2. 3. Cell cycle Analysis

Flow cytometric DNA analysis was used to estimate the distribution of monitored cancer and normal cells at different stages of the cell cycle. All the cell lines were harvested after 72 h incubation at 10  $\mu$ M concentration of 1b/sh\_7, 1c/sh\_8 or 1d/sh\_9, washed with phosphate-buffered saline (PBS), fixed in 70% ice cold ethanol, and stored at 4 °C for 24 h. Fixed cells were centrifuged, washed with PBS, stained with staining solution [20  $\mu$ g/mL propidium iodide, 137  $\mu$ g/mL RNase A, and 0.1% Triton X-100 (Sigma-Aldrich Co.) in PBS] in the dark for 30 min, and measured with a flow cytometer (FACSCalibur, Becton Dickinson, San Diego, CA, USA). For each sample, a minimum of  $15 \times 10^3$  cells was evaluated and analysed using FlowJo software (FLOWJO, LLC; Ashland, OR, USA). Cells characterized by DNA content lower than diploid (subG<sub>0</sub>/G<sub>1</sub> population) were considered as apoptotic cells.

### 2. 4. IncuCyte ZOOM System

Experiments were performed using an IncuCyte ZOOM system (Essen BioScience, Ann Arbor, MI, USA),

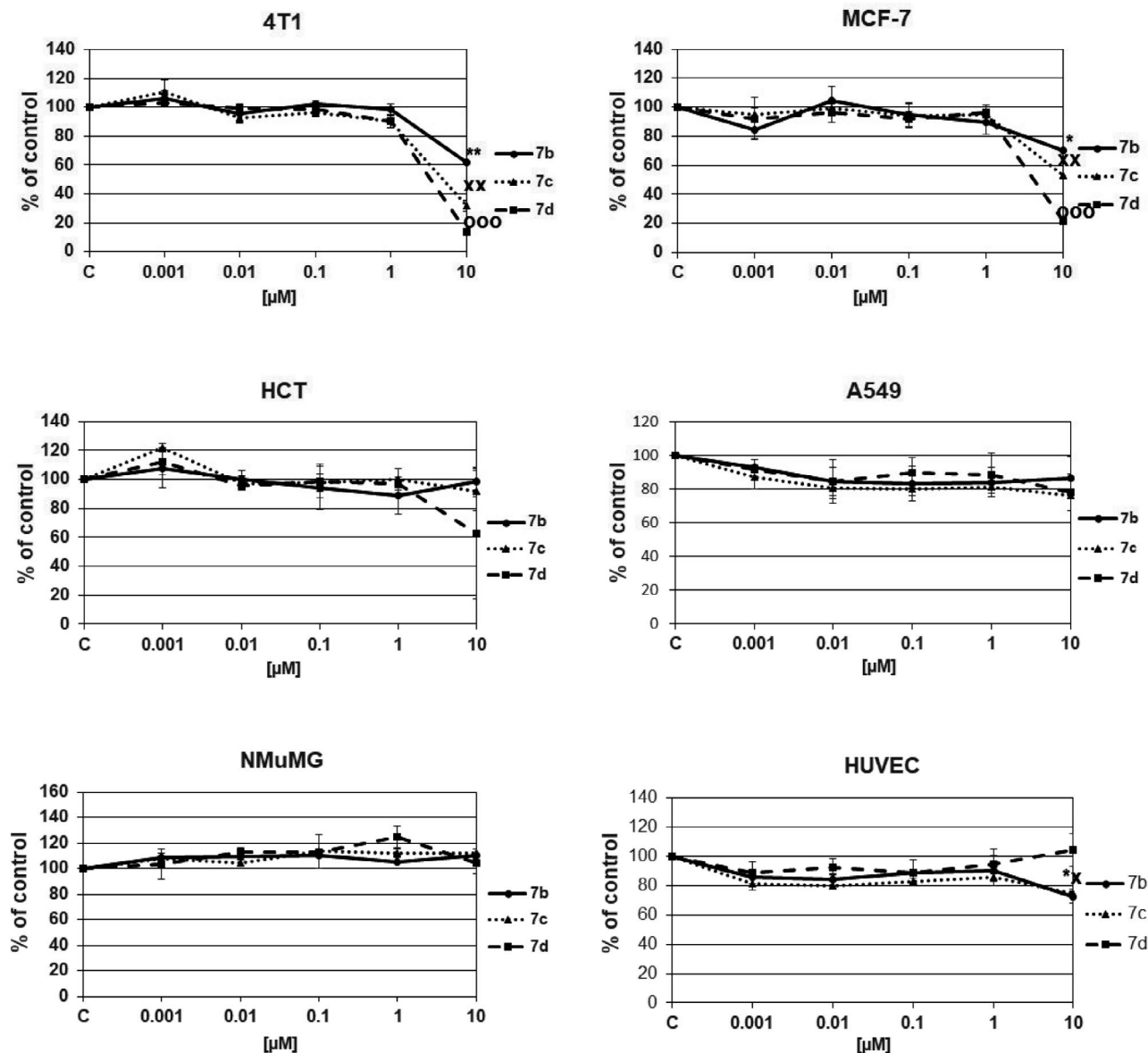
which consists of a microscope gantry that resides in a humidified incubator at 37 °C and 5% CO<sub>2</sub>, and a networked external controller hard drive that gathers and processes image data. The cells were seeded in 96-well plates in sextuplicates at 5000 cells/well (as 100 µl cell suspension/well) and placed in the IncuCyte ZOOM system. After attachment (24 h), the cells were treated with 1b/sh\_7, 1c/sh\_8 a 1d/sh\_9 test substances (dissolved in media). The cells growing in media without tested substances were used as controls. The IncuCyte zoom system automatically monitored the cell confluence in each well through a 4X objective (Nikon) every 2 h up to 130 h of the substance treatment. The experiment was performed two times.

## 2. 5. Statistical Analysis

Data were analyzed using one-way ANOVA followed by Tukey's multiple comparison tests in ORIGIN analysis software (OriginLab Co., Northampton, MA, USA).

## 3. Results and Discussion

In the view of biological significance of tacrine and coumarin derivatives, potential cytotoxic and/or anti-cancer activities of tacrine-coumarin heterodimers **7a-g** were tested using tumor as well as normal cell lines. In this re-

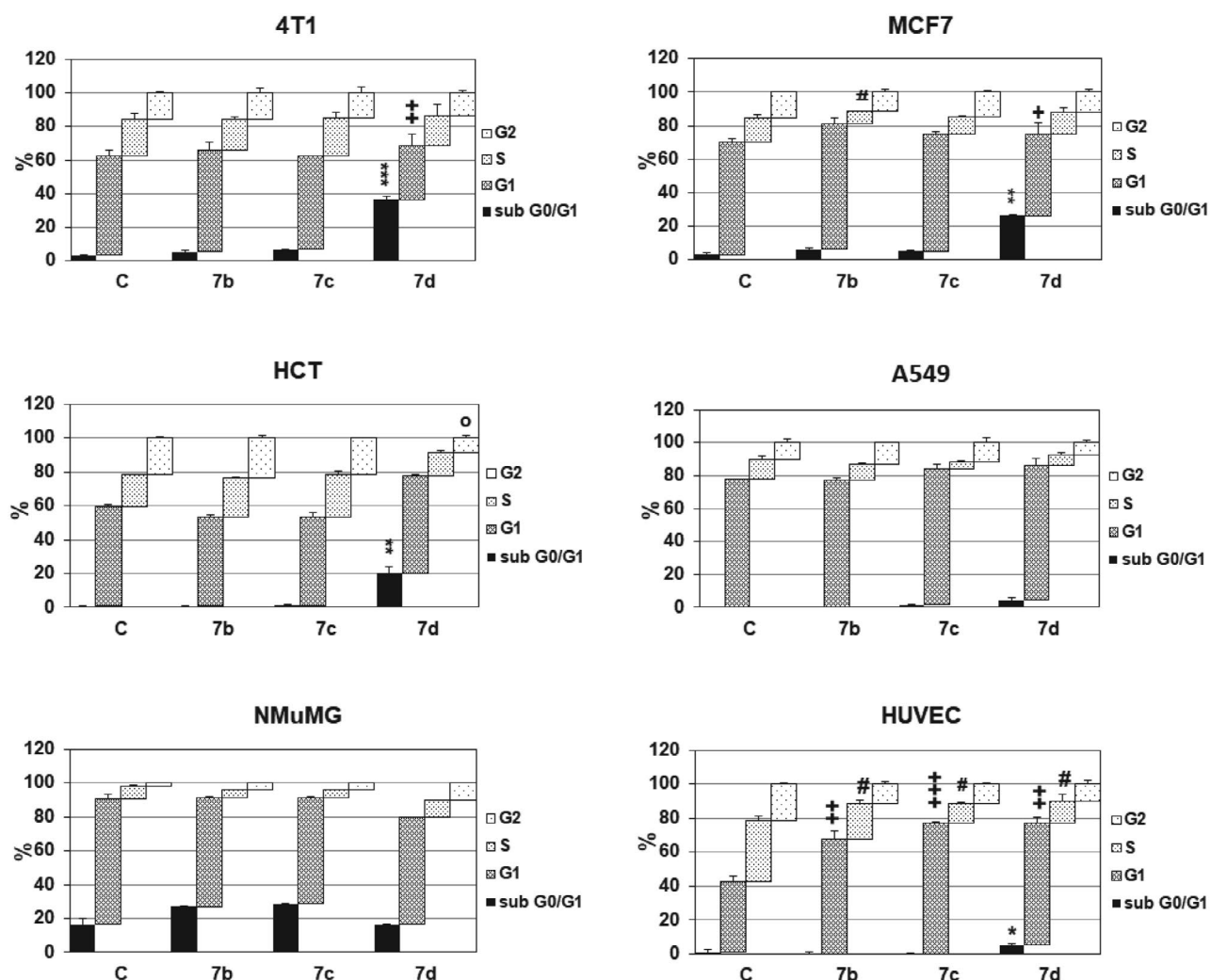


**Figure 3.** The effect of 7b-d tacrine-coumarine derivatives on the metabolic activity of 4T1, MCF-7, HCT, A549, NMuMG, and HUVEC cells. The metabolic activity of 4T1, MCF-7, HCT, A549, NmuMG, and HUVEC cells was analyzed by MTT assay after their treatment with 7b-d derivatives for 72 h. Data are expressed as mean  $\pm$  SEM (% of control) across three independent experiments. The statistical significance is designated as follows: \* p < 0.05 and \*\* p < 0.01 for 7b derivative vs. control (C); x p < 0.05 and xx p < 0.01 for 7c derivative vs. C; and ooo p < 0.001 for 7d derivative vs. C.

gard, the responses of 4T1 (mouse mammary carcinoma), MCF-7 (human breast adenocarcinoma), HCT116 (human colorectal carcinoma), A549 (human lung carcinoma), NMuMG (normal mouse mammary gland cells), and HUVEC (human endothelial cells isolated from umbilical vein) were compared. Application of compounds **7a** and **7e-g** did not show toxic effects on either cancer or normal cells (not shown). Thus, only **7b-d** compounds were included in further analysis. The concentrations of **7b-d** hybrids used in both cell cycle as well as cell proliferation assays were derived based on the extensive screening of the cell metabolism and/or cell growth response (MTT). The concentrations of **7b-d** derivatives inhibiting 50% (IC<sub>50</sub>) of the metabolic activity and/or the cell growth are shown in supplementary data (Table S01). Based on IC<sub>50</sub> values, the synthesized compounds showed moderate to significant activity in the  $\mu\text{M}$  range from 5.7 to > 100  $\mu\text{M}$ . The effect

of chain lengths linking tacrine and coumarin skeleton was examined. Compounds **7d** and **7c** showed significant anti-metabolic activity against 4T1 cell lines, with IC<sub>50</sub> values of 5.7  $\mu\text{M}$  and 7.0  $\mu\text{M}$ , respectively (Fig. 3). The compound **7d** also showed promising activity against MCF-7 cell line, with IC<sub>50</sub> value of 6.0  $\mu\text{M}$  (Fig. 3). Furthermore, derivatives **7b** and **7c** showed stronger effect compared to **7d** in the reduction of HUVEC cells metabolism (Fig. 3). Interestingly, based on MTT results, HCT, A549, and NMuMG cells did not respond to the effect of **7b-d** compounds (Fig. 3). These results demonstrate that the length of the alkyl spacer influences, at least to some degree, the metabolic activity and/or the cell growth of breast cancer cell lines 4T1 and MCF-7.

Flow cytometric analysis was performed to evaluate the cell cycle progression in all monitored cell lines after their incubation with **7b-d** derivatives at the concentration



**Figure 4.** The cell cycle distribution of 4T1, MCF-7, HCT, A549, NmuMG, and HUVEC cells after treatment with 7b-d tacrine-coumarine derivatives. 4T1, MCF-7, HCT, A549, NmuMG, and HUVEC cells were treated with 7b-d derivatives at the concentration of 10  $\mu\text{M}$  for 72 h. Data from the three independent experiments are expressed as mean  $\pm$  SEM. The statistical significance is expressed as follows: \*  $p < 0.05$ , \*\*  $p < 0.01$ , \*\*\*  $p < 0.001$  for sub G0/G1 fraction of 7b-d vs. control cells (C); +  $p < 0.05$ , ++  $p < 0.01$ , +++  $p < 0.001$  for G1 fraction of 7b-d vs. C; #  $p < 0.05$  for S fraction of 7b-d vs. C and °  $p < 0.05$  for G2 fraction of 7b-d vs. C.

of 10  $\mu\text{M}$ . Data showed that **7d** hybrid had the most significant effect on the cell cycle progression (Fig. 4). This compound increased apoptotic sub G0/G1 population in 4T1, MCF-7, HCT, and HUVEC cells and reduced G1 population in 4T1 and MCF-7. On the other hand, all derivatives **7b-d** increased G1 and decreased S population of HUVEC cells (Fig. 4). Without the change in the cell cycle progression stayed cancer A549 and normal NMuMG cells (Fig. 4).

The synthesized compounds **7b-d** were also evaluated for their *in vitro* anti-proliferative activity monitored by InCuCyte system. The most sensitive tumor cell line was the MCF-7 (Supplementary data, Fig. S01), for which the decrease of proliferative activity depended on the increase of carbon number in the tested compounds **7b-d**. HCT (Supplementary data, Fig. S02) and 4T1 (Supplementary data, Fig. S03) tumor cell lines showed lower sensitivity to the tested hybrids **7b-d** with similar responses. On the other hand, A549 tumor cells (Supplementary data, Fig. S04) proved to be the most resistant, with proliferation not significantly different from other cell lines after the administration of the above-mentioned three tacrine-coumarin derivatives. In addition, HUVEC cells (Supplementary data, Fig. S05) responded only to the **7d** derivative while the normal mouse mammary gland cells of NMuMG (Supplementary data, Fig. S06) did not demonstrate a decrease in proliferation after the application of the tested substances.

Among the synthesized compounds, the tacrine-coumarin heterodimer **7d** with nine methylene groups between the two amino groups in the side chain exhibited the greatest efficiency. According to the results, in the case of tacrine-coumarin heterodimers **7e-g** with longer side chains, replacing some methylene groups with amine moiety dramatically decreased the anti-cancer activity.

Emami et al.<sup>1</sup> have also confirmed that the anti-proliferative activity depends on the presence of the quinone skeleton. The structure-activity relationship of compound 4-(4-((4-fluorophenoxy)methyl)-1,2,3-triazol-1-yl)-7-methoxycoumarin **4** (Fig. 1) suggested that - C-4 position of 1,2,3-triazole core is the optimal position for  $\text{CH}_2\text{-O}$ -bridge because of its bioactivity. A hydrogen bond acceptor at C-4 position of phenyl is indispensable for the improvement of the potency while a hydrogen bond acceptor at C-7 position of coumarin can positively contribute to the activity.<sup>6</sup>

For bis-coumarin derivatives possessing one amino side chain **6** (Fig. 1), the length of the linker (dicarboxylic acid) had profound effects on their anti-proliferative activities. Compounds linked by the malonic amide (three carbons) showed the best anti-proliferative activities against MCF-7, A549, K562, and Hela cell lines; however, as the linker increased to five, six, or ten carbons, their anti-proliferative activities clearly decreased. In this regard, the incorporation of the aromatic or heterocyclic ring into the chain also decreased anti-proliferative activity.<sup>2</sup>

## 4. Conclusions

In conclusion, structural modification of natural substances can yield new analogues, the biological efficacy of which can be higher compared to that of the parent compounds. In our experimental study, we found that tacrine-coumarin hybrids with seven, eight, and nine methylene groups in spacer have significant anti-cancer activity in all cancer cell lines tested, with the exception of A549 cells. Indeed, hybrid with nine methylene groups had the most significant anti-cancer effect. Interestingly, the sensitivity of tumor cells was greater compared to the sensitivity of normal cells, which points to the importance of further research on the anti-tumor effects of tacrine-coumarin hybrid molecules.

## 5. Conflict of Interest

The authors declare no conflict of interest.

## 6. Acknowledgment

This study was supported (50%) by the project Medicínsky univerzitný park v Košiciach (MediPark, Košice) ITMS: 26220220185 (95%) funded by Operational Programme Research and Development (OP VaV-2012/2.2/08-RO) (Contract No. OPVaV/12/2013).

## 7. References

1. S. Emami and S. Dadashpour, *Eur J Med Chem* **2015**, *102*, 611–30. DOI:10.1016/j.ejmech.2015.08.033
2. G. Tan, Y. Yao, Y. Gu, S. Li, M. Lv, K. Wang, H. Chen and X. Li, *Bioorg Med Chem Lett* **2014**, *24*, 2825–30. DOI:10.1016/j.bmcl.2014.04.106
3. M. Basanagouda, V. B. Jambagi, N. N. Barigidad, S. S. Laxmeshwar, V. Devaru and Narayanachar, *Eur J Med Chem* **2014**, *74*, 225–33. DOI:10.1016/j.ejmech.2013.12.061
4. E. Bana, E. Sibille, S. Valente, C. Cerella, P. Chaimbault, G. Kirsch, M. Dicato, M. Diederich and D. Bagrel, *Mol Carcinog* **2015**, *54*, 229–41. DOI:10.1002/mc.22094
5. K. B. Puttaraju, K. Shivashankar, Chandra, M. Mahendra, V. P. Rasal, P. N. Venkata Vivek, K. Rai and M. B. Chanu, *Eur J Med Chem* **2013**, *69*, 316–22. DOI:10.1016/j.ejmech.2013.07.015
6. W. Zhang, Z. Li, M. Zhou, F. Wu, X. Hou, H. Luo, H. Liu, X. Han, G. Yan, Z. Ding and R. Li, *Bioorg Med Chem Lett* **2014**, *24*, 799–807. DOI:10.1016/j.bmcl.2013.12.095
7. N. E. Saidu, S. Valente, E. Bana, G. Kirsch, D. Bagrel and M. Montenarh, *Bioorg Med Chem* **2012**, *20*, 1584–93. DOI:10.1016/j.bmc.2011.12.032
8. S. Hamulakova, P. Poprac, K. Jomova, V. Brezova, P. Lauro, L. Drostinova, D. Jun, V. Sepsova, M. Hrabínova, O. Soukup, P. Kristian, Z. Gazova, Z. Bednarikova, K. Kuca and M. Valko, *J Inorg Biochem* **2016**, *161*, 52–62.



DOI:10.1016/j.jinorgbio.2016.05.001

9. C. Gao, Y. Ding, L. Zhong, L. Jiang, C. Geng, X. Yao and J. Cao, *Toxicol In Vitro* **2014**, 28, 667–74.

DOI:10.1016/j.tiv.2014.02.001

10. M. J. Ezoulin, C. Z. Dong, Z. Liu, J. Li, H. Z. Chen, F. Hey-

mans, L. Lelievre, J. E. Ombetta and F. Massicot, *Toxicol In Vitro* **2006**, 20, 824–31. DOI:10.1016/j.tiv.2006.01.002

11. J. Janockova, J. Plsikova, J. Koval, R. Jendzelovsky, J. Mikes, J. Kasparkova, V. Brabec, S. Hamulakova, P. Fedorocko and M. Kozurkova, *Bioorg Chem* **2015**, 59, 168–76.

DOI:10.1016/j.bioorg.2015.03.002

## Povzetek

Derivati akridina so bili prvič uporabljeni kot antibakterijsko sredstvo in sredstvo proti parazitom, kasneje pa tudi kot zdravila proti malariji in HIV. Zaradi njihove visoke citotoksične dejavnosti jih uporabljajo tudi kot potencialna zdravila proti raku. Zaradi njihovih resnih škodljivih učinkov so bili uvedeni in testirani novi sintetični derivati, ki temeljijo na spreminjanju naravno prisotnih snovi, kot so derivati akridona, ki kažejo tudi potencialno aktivnost proti tumorjem. Večina od teh spojin lahko poškoduje DNA, kar povzroča razmeroma močno in selektivno uničenje tumorskih celic. Testirali smo *in vitro* antiproliferativne učinke na novo sintetiziranih tetrahidroakridinskih derivatov, in sicer takrin-kumarinskih hibridnih molekul. Naši rezultati so pokazali zmanjšano deljenje rakavih celic ob izpostavitvi takrin-kumari hibridom s sedem, osem in devet metilenskimi skupinami v distančniku. Najmočnejši učinek proti raku je pokazal hibrid z devetimi metilenskimi skupinami.

Scientific paper

# Erythrosine Adsorption from Aqueous Solution via Decorated Graphene Oxide with Magnetic Iron Oxide Nano Particles: Kinetic and Equilibrium Studies

Seyyed Mojtaba Mousavi,<sup>1,2,\*</sup> Seyyed Alireza Hashemi,<sup>1,2,\*</sup> Omid Arjmand,<sup>3</sup> Ali Mohammad Amani,<sup>1,2</sup> Aziz Babapoor,<sup>4</sup> MohammadAli Fateh,<sup>5</sup> Hamed Fateh,<sup>6</sup> Fatemeh Mojoudi,<sup>7</sup> Hossein Esmaeili<sup>8</sup> and Sara Jahandideh<sup>9</sup>

<sup>1</sup> Department of Medical Nanotechnology, School of Advanced Medical Sciences and Technologies, Shiraz University of Medical Sciences, Shiraz, Iran.

<sup>2</sup> Pharmaceutical Sciences Research Center, Shiraz University of Medical Sciences, Shiraz, Iran. 71348-14336.

<sup>3</sup> Department of Chemical Engineering, South Tehran Branch, Islamic Azad University, Tehran, Iran.

<sup>4</sup> Department of Chemical Engineering, University of Mohaghegh Ardabili, Ardabil, Iran.

<sup>5</sup> Department of Civil Engineering, Estahban Branch, Islamic Azad University, Estahban, Iran

<sup>6</sup> Department of Chemical Engineering, School of Chemical and Petroleum Engineering, Shiraz University, Shiraz, Iran

<sup>7</sup> Department of Environment, Faculty of Natural Resources, College of Agriculture & Natural Resources, University of Tehran, Karaj, Iran.

<sup>8</sup> Department of Chemical Engineering, Bushehr Branch, Islamic Azad University, Bushehr, Iran.

<sup>9</sup> Department of Chemical and Polymer Engineering, Faculty of Engineering, Yazd University, Yazd, Iran.

\* Corresponding author: E-mail: [mousavi.nano@gmail.com](mailto:mousavi.nano@gmail.com)) and [s.a.hashemi0@gmail.com](mailto:s.a.hashemi0@gmail.com) or [sa\\_hashemi@sums.ac.ir](mailto:sa_hashemi@sums.ac.ir)

Received: 14-06-2018

## Abstract

In this research, first graphene oxide (GO) was synthesized using modified Hummers method and thence via a multi-step procedure, surface of GO was decorated with Fe<sub>3</sub>O<sub>4</sub> nanoparticles (GO-Fe<sub>3</sub>O<sub>4</sub>). Thereafter, developed nanoparticles were characterized using FTIR, XRD and SEM analyses and their magnetic properties confirmed using VSM analysis. Moreover, performance of the GO-Fe<sub>3</sub>O<sub>4</sub> for the removal and adsorption of Erythrosine dye from the aqueous solution under variable conditions including pH, phosphate buffer solution (PBS), adsorbent content, stirring time, electrolyte concentration, solution content and temperature were examined. In this regard, for obtained solutions from the chicken slaughterhouse and hospital sewage disposal system containing 20, 50 and 70 mg mL<sup>-1</sup> Erythrosine dye, GO-Fe<sub>3</sub>O<sub>4</sub> nanoparticles adsorbed from approximately 94% to 97% of the total dye, respectively. What is more, the highest adsorption capacity was obtained at 149.25 mg/g by means of Langmuir model. The obtained results clearly showed that GO-Fe<sub>3</sub>O<sub>4</sub> nanoparticles present a fabulous performance for the absorption and removal of dyes from disposal systems.

**Keywords:** Adsorption; dye removal rate; erythrosine; graphene oxide; iron oxide

## 1. Introduction

Erythrosine or Acid Red 51 (C.I. 45430, E127) is a xanthene class and water soluble synthetic dye that frequently use as a food colorant.<sup>1</sup> Erythrosine is a common dye in various industries and has wide range of applications in numerous fields including cosmetics, drugs, food

industry especially for biscuits, chocolate, luncheon meat, sweets and chewing gums.<sup>2</sup> Several biodegradability evaluations on dyes revealed that azo dyes are not likely to be biodegradable under aerobic condition.<sup>2,3</sup> In this matter, more and more studies were performed to determine the adsorption capacity and capability of natural and treated vegetal materials including peat,<sup>4</sup> sugar cane bagasse,<sup>5</sup> bio-

mass,<sup>6</sup> eucalyptus bark<sup>7,8</sup> and other biological materials with animal sources such as chitin and chitosan.<sup>8</sup>

Erythrosine ( $C_{20}H_{14}Na_2O_5$ ) or 2-(6-Hydroxy-2,4,5,7-tetraido-3-oxo-xanthen-9-yl) benzoic acid mixture with industrial or civil wastewater can highly affect the nature and cause severe damages to the public health,<sup>9</sup> thereby it is very essential to detect and remove these kinds of impurities from the sewage disposal systems. However, application of multivariate analyses in adsorption studies is rather limited.<sup>10</sup> What is more, high toxicity of Erythrosine is one of the basic reasons for many environmental studies to remove this harmful dye from wastewaters. In this case, various materials and techniques were used to minimize these kinds of impurities from wastewaters including photochemical degradation using  $TiO_2$  nanoparticles,<sup>11</sup> biochemical degradation<sup>12</sup> and adsorption process.<sup>11,13–16</sup>

In addition, the adsorption isotherms indicated that phenol and methylene blue presenting a better adsorption rate compared with the erythrosine dye which is attributed to the large structure and the negative charge of dye molecules.<sup>13</sup> Generally speaking, adsorption of erythrosine by activated carbon is acceptable with a maximum capacity of 89.3 mg/g at 40 °C and pH = 7. The reported adsorption capacity is modest when compared to adsorption capacity of positively charged methylene blue (C.I. 52015).<sup>17</sup>

Magnetic nanoparticles proved to be an effective removal agent for various kinds of wastes.<sup>18,19</sup> Herein, graphene oxide (GO) was first synthesized using modified Hummers method and then fabricated GO was enhanced via  $Fe_3O_4$  nanoparticles to improve their magnetic permeability and absorption rate. Afterward, fabricated GO- $Fe_3O_4$  nanoparticles were used to remove erythrosine dye from the treated deionized water, hospital and chicken slaughterhouse sewer output under variable conditions.

## 2. Materials and Methods

### 2.1. Materials

Natural graphite flakes with average particle size of 150  $\mu m$  and purity of >98% were supplied from Merck. Moreover, all of required materials including concentrated sulfuric acid ( $H_2SO_4$ ) (A.R., 98%), hydrochloric acid (HCl) (A.R., 36%), hydrogen peroxide ( $H_2O_2$ ) (A.R., 30%), potassium permanganate ( $KMnO_4$ ) (A.R.), phosphoric acid ( $H_3PO_4$ ),  $FeCl_3 \cdot 6H_2O$ ,  $FeSO_4 \cdot 7H_2O$ , phosphate buffer solution (PBS), ammonia ( $NH_3$ ), sodium hydroxide (NaOH) and erythrosine dye were supplied by Merck.

### 2.2. Preparation of Erythrosine Solution

For preparation of erythrosine solution, first 0.1 g of erythrosine dye poured into a 1000 mL volumetric flask along with deionized water (100  $\mu g mL^{-1}$ ) and then dissolved to reach homogenous solution. This solution was used to prepare other solutions with different concentrations.

### 2.3. Preparation of Phosphate Buffer Solution (PBS)

For preparation of (PBS), 100 mL phosphoric acid (0.1 molar) poured in a beaker and then the pH of the suspension was set on 7 using pH meter and 1 mL solution of sodium hydroxide and hydrochloric acid.

### 2.4. Preparation of Graphene Oxide (GO)

In this study, GO nanoparticles were fabricated using modified Hummers method.<sup>20,21</sup> In this case, first 10 g graphite poured into a round-bottom flask and then 2 L  $H_2SO_4$  was added to the vessel and stirred for 30 min (500 rpm) at room temperature (RT). Thence 110 mL  $H_3PO_4$  was added to the suspension, stirred for further 30 min (500 rpm at RT) and thereafter the temperature of the suspension was decreased to less than 5 °C using ice bath. Next, 50 g  $KMnO_4$  was slowly added to the suspension and stirred (500 rpm) for 30 min. In the next step, the temperature of the suspension was smoothly increased to about 50 °C and then stirred for (500 rpm) 72 h. Afterward, the suspension was poured in a vacuum Erlenmeyer flask and some pieces of ice cubes (made from deionized water) were poured into the flask. Thereupon, 10 mL  $H_2O_2$  was poured in the suspension very slowly and then the vacuum Erlenmeyer flask was filled with deionized water. The resulting suspension was kept without stirring for 48 h for further fillers sedimentation. Afterward, the suspension was filtered and washed with HCl for removal of metal ions, and then remained fillers on the filter paper were washed with deionized water in order to set their pH at 7. Filtered and washed nanoparticles were dried for 1 h at 80 °C in a heating oven and thence placed in a humidity absorbing chamber for 48 h.

### 2.5. Preparation of Decorated Graphene Oxide with Iron Oxide Nanoparticles (GO- $Fe_3O_4$ )

For the production of GO- $Fe_3O_4$  nanoparticles, first, 3.89 g  $FeCl_3$  and 4.55  $FeSO_4$  poured into 320 mL deionized water and stirred for 1 h at 80 °C. Thence, 0.0844 g ultrasonicated GO in 100 mL deionized water (at 300 W for 10 min) were added to the previous suspension and stirred for further 1 h at 80 °C. Thereafter, 40 mL  $NH_3$  was slowly added to the resulting suspension and thereafter stirred for 24 h at 80 °C. Next, finalized suspension was vacuum filtered and washed with deionized water to neutralize the fabricated GO- $Fe_3O_4$  nanoparticles.

### 2.6. Nanoparticles Evaluation Methods

For evaluation of developed fillers performance for removal of erythrosine dye from aqueous solutions, first 15 mL erythrosine dye (100  $\mu g mL^{-1}$ ) and 2 mL PBS (with

pH = 7) poured into a 50 mL volumetric flask and then filled with deionized water. Thereafter, 0.2 g of GO-Fe<sub>3</sub>O<sub>4</sub> poured into the resulting suspension and then stirred for 2 min at 500 rpm. Afterward, the beaker containing the resulting suspension was put on a strong magnet for 1 min for sediment of GO-Fe<sub>3</sub>O<sub>4</sub> nanoparticles. Experimental evaluation showed that erythrosine dye has a peak at 523 nm in visible light region (can be seen in section.3.1). In this case, for determination of erythrosine removal rate, the adsorption rate by fillers were examined at 523 nm wavelength. In the final stage, the dye removal rate (%) was calculated using the following equation:<sup>22</sup>

$$\text{Removal (\%)} = ((C_i - C_f)/C_i) \times 100 \quad (1)$$

Where the  $C_i$  and  $C_f$  are the initial dye concentration (before reaction with GO-Fe<sub>3</sub>O<sub>4</sub>) and the final dye concentration (after reaction with GO-Fe<sub>3</sub>O<sub>4</sub>), respectively.

## 2. 7. Choosing the Maximum Wavelength

( $\lambda_{\text{max}}$ )

Maximum wavelength peak related to the erythrosine dye was determined via UV-vis spectroscopy in the visible-light region ranging from 400 to 700 nm. In this matter, the maximum wavelength for the erythrosine dye was saw at 523 nm. Therefore, the final adsorption rate by developed fillers was measured at the fixed wavelength of 523 nm during all processes.

## 2. 8. Characterization

In order to examine developed fillers, various instruments were used including Fourier-transform infrared spectroscopy (FTIR) (Bruker model VECTOR22), X-ray diffraction (XRD) (Bruker model D8-ADVANCE), vibrating sample magnetometer (VSM), scanning electron microscope (SEM) (Tescan model VEGA3) and UV-vis Spectrophotometer (Shimadzu model UV-1800).

# 3. Results and Discussions

## 3. 1. Examination of Fabricated GO-Fe<sub>3</sub>O<sub>4</sub> Nanoparticles

In this section, specifications of fabricated GO-Fe<sub>3</sub>O<sub>4</sub> nanoparticles were evaluated using FTIR, XRD, VSM and SEM analyses. In Fig. 1 (a), FTIR results of Fe<sub>3</sub>O<sub>4</sub>, GO and GO-Fe<sub>3</sub>O<sub>4</sub> can be seen, respectively. As can be seen in the spectrum of Fe<sub>3</sub>O<sub>4</sub> (red color), peaks in region between 530–630 cm<sup>-1</sup> are correspond to the stretching vibration mode of Fe-O. In this case, broad and strong peak at 575 cm<sup>-1</sup> is correspond to the Fe<sub>3</sub>O<sub>4</sub> and indicate the successful synthesize of Fe<sub>3</sub>O<sub>4</sub> nanoparticles.<sup>23–25</sup> Moreover, peaks at 923 and 1108 cm<sup>-1</sup> are related to the sp<sup>2</sup> alkene C-H

band (disubstituted-E) and stretching vibration of in-plane C-H, respectively. Besides, peak with wavenumber 1616 cm<sup>-1</sup> is belong to the FeOO<sup>-</sup>,<sup>24</sup> while peaks in region between 2838–2921 cm<sup>-1</sup> are belong to the C-H stretching vibration (sp<sup>3</sup> stretching of hexyl aliphatic side). Weak peaks in the region between 3500–3700 cm<sup>-1</sup> are belong to the amine N-H. Furthermore, broad and strong peak at 3424 cm<sup>-1</sup> is correspond to the hydroxyl functional group (-OH).<sup>24</sup> In addition, as shown in the GO spectrum (Figure 1 (a) green color), GO was successfully synthesized with compatible functional groups including carboxyl (1715 cm<sup>-1</sup>), hydroxyl (3398 cm<sup>-1</sup>) and epoxide (1057 cm<sup>-1</sup>) which provide the possibility of molecular attachment between GO and Fe<sub>3</sub>O<sub>4</sub> nanoparticles. In GO spectrum, peaks with wavenumbers 584, 854, 891, 1006, 1165 and 1632 are correspond to the C=O in amides, C-H sp<sup>2</sup>, geminal disubstituted, vibration of a p-disubstituted phenyl group  $\nu_{C-H}$  in plane bending), C-OH in alcohols and C=C bonds (sp<sup>2</sup> C-X double bonds) in aromatic ring, respectively.<sup>18</sup>

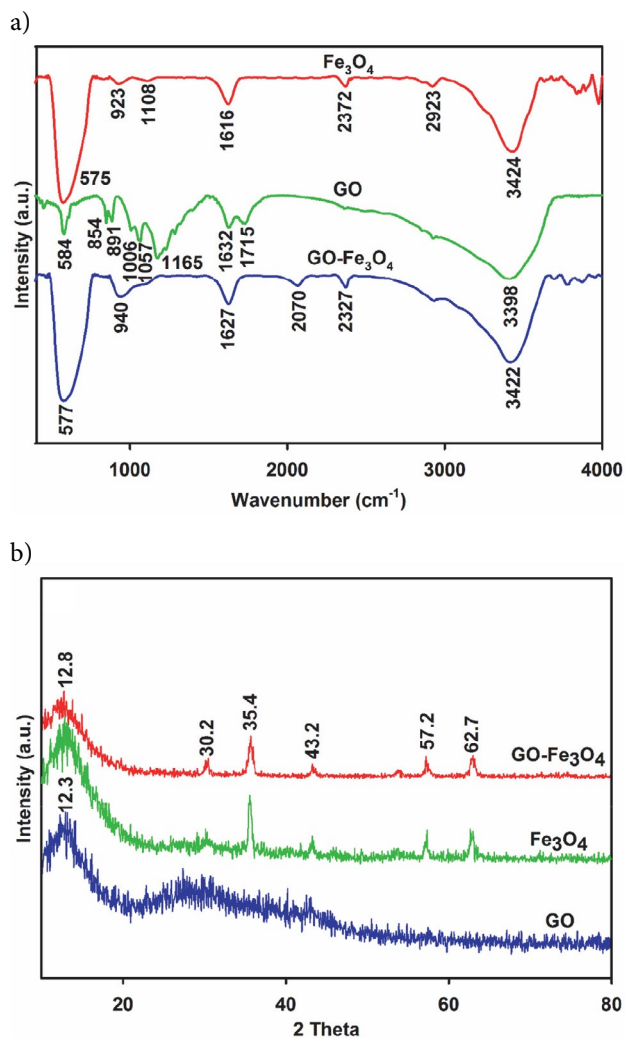


Figure 1. (a) FTIR and (b) XRD results of Fe<sub>3</sub>O<sub>4</sub>, GO and GO-Fe<sub>3</sub>O<sub>4</sub>.

In Fig. 1 (a) (blue color), it can be seen that GO-Fe<sub>3</sub>O<sub>4</sub> was successfully synthesized. In this case, strong peak at 577 cm<sup>-1</sup>, which known as the fingerprint of Fe<sub>3</sub>O<sub>4</sub>,<sup>23–25</sup> along with peak at 1627 cm<sup>-1</sup> that correspond to the FeOO<sup>-</sup>,<sup>24</sup> clarify the molecular attachment of Fe<sub>3</sub>O<sub>4</sub> nanoparticles on the surface of GO. Furthermore, peaks with wavenumbers 940 and 3422 cm<sup>-1</sup> are correspond to the sp<sup>2</sup> alkene C-H bond and hydroxyl functional group, respectively. Appearance of peaks at 577 and 1627 cm<sup>-1</sup> along with disappearance of carboxyl and epoxide functional groups related peaks and decrease in the intensity of hydroxyl functional group in the GO-Fe<sub>3</sub>O<sub>4</sub> spectrum compared with GO and Fe<sub>3</sub>O<sub>4</sub> spectrums, confirm whether the successful decoration of GO with Fe<sub>3</sub>O<sub>4</sub> or molecular attachment of Fe<sub>3</sub>O<sub>4</sub> on the surface of GO. In fact, decrease in the intensity of hydroxyl functional group and disappearance of carboxyl and epoxide functional groups clarify the interaction between functional groups of GO and Fe<sub>3</sub>O<sub>4</sub>.

In addition, in Fig. 1 (b), XRD results for GO, Fe<sub>3</sub>O<sub>4</sub> and GO-Fe<sub>3</sub>O<sub>4</sub> can be seen, respectively. As can be seen in this figure, XRD results shows that GO nanoparticles were successfully synthesized, while they show a peak (2 $\theta$ ) around 12.3 which is correspond to the inter planer spacing of 0.84 nm.<sup>26</sup> On the other hand, in Fig. 1 (b) it can be seen that related XRD peaks for Fe<sub>3</sub>O<sub>4</sub> and GO-Fe<sub>3</sub>O<sub>4</sub> are the same as each other, which are in accord of previous studies outcomes.<sup>26–28</sup>

In this regard, the diffraction peaks (2 $\theta$ ) at 30.2, 35.4, 43.2, 57.2 and 62.7 are correspond to the (111), (220), (311), (222), (400) and (422) planes of the Fe<sub>3</sub>O<sub>4</sub> which have appeared in the spectrum of GO-Fe<sub>3</sub>O<sub>4</sub> and it is correspond with pure spinel Fe<sub>3</sub>O<sub>4</sub> (no. 89–3854) (Xie *et al.* 2012; Hur *et al.* 2015; Ai *et al.* 2011). Moreover, decoration of GO with Fe<sub>3</sub>O<sub>4</sub> nanoparticles did not cause any shifts in diffraction peaks. Achieved data from FTIR and XRD analyses clearly confirmed the successful modification of GO flakes with Fe<sub>3</sub>O<sub>4</sub> nanoparticles.

What is more, In Fig. 2 (a), VSM magnetization of GO-Fe<sub>3</sub>O<sub>4</sub> nanoparticles can be seen. As can be seen in this figure, hysteresis loop of developed GO-Fe<sub>3</sub>O<sub>4</sub> is S-like curve, while its specific saturation magnetization (M<sub>s</sub>), remanence (M<sub>r</sub>), coercivity (H<sub>c</sub>), squareness ratio (SQR=M<sub>r</sub>/M<sub>s</sub>) and switching field distribution (SDF=ΔH/H<sub>c</sub>) are 51.84 emu g<sup>-1</sup>, 14.81 emu g<sup>-1</sup>, 176.4 Oe, 0.285 and 1.945, respectively. Additionally, GO-Fe<sub>3</sub>O<sub>4</sub> is an intermediate magnetic material with anisotropic behavior, which has presented fantastic magnetic performance. In fact, GO-Fe<sub>3</sub>O<sub>4</sub> can improve the removal rate of the erythrosine dye from any kind of wastewater due to its intermediate magnetic properties. Furthermore, In Fig. 2 (b), (c) and (d), SEM images of GO, GO-Fe<sub>3</sub>O<sub>4</sub> and Fe<sub>3</sub>O<sub>4</sub> can be seen, respectively. As can be seen in these figures, GO nanoparticles were successfully decorated and modified with magnetic Fe<sub>3</sub>O<sub>4</sub> nanoparticles which is in accord with obtained data from FTIR and XRD analyses.

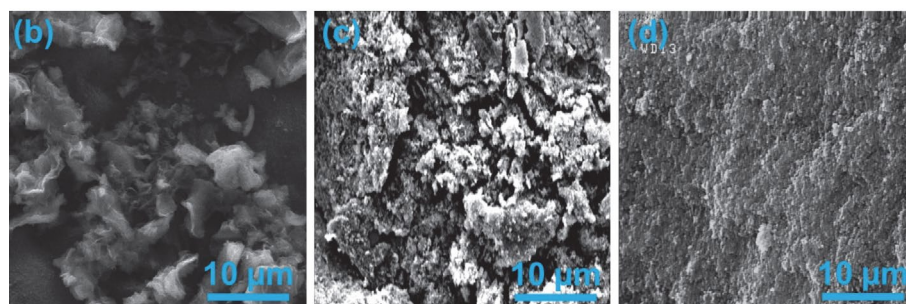
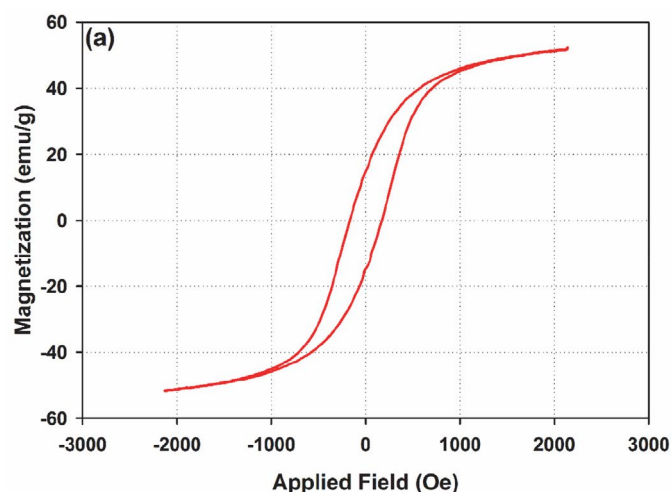


Figure 2. (a) VSM results for GO-Fe<sub>3</sub>O<sub>4</sub> nanoparticles and SEM images of (b) GO, (c) GO-Fe<sub>3</sub>O<sub>4</sub> and (d) Fe<sub>3</sub>O<sub>4</sub>.

## 3. 2. Examination of Erythrosine Dye Removal Rate

### 3. 2. 1. Effect of pH on the Erythrosine Removal Rate

Solution pH is one of the most important factors on the adsorption of pollutants. In this section, the effect of variable pH (ranging from 3–9) on the dye removal rate and final adsorption rate of Erythrosine dye from aqueous solution were examined. In this case, the final pH of the solution containing Erythrosine dye was fixed and regulated via addition of hydrochloric acid and sodium hydroxide. Moreover, in order to achieve the optimal pH, 15 mL of Erythrosine dye ( $100 \mu\text{g mL}^{-1}$ ) was poured into a 50 mL volumetric flasks and thence variable volumes of a solution containing hydrochloric acid and sodium hydroxide was added to the primary solution to regulate the pH on the

desirable value. Afterward, 0.2 g of  $\text{GO-Fe}_3\text{O}_4$  was poured into the dye solution and stirred for 2 min (500 rpm) and then placed on a strong magnet for further sediment of fillers and adsorption of the dye by magnetic fillers. Thereafter, the level of dye adsorption rate was measured at wavelength of 523 nm. In Fig. 3 (a) and (c) the effect of variable pH on the dye removal rate and final adsorption of Erythrosine dye can be seen, respectively. As can be seen in this figure, increase in the pH of the suspension and neutralization of the suspension can enhance the dye removal rate, thus pH = 7 was selected as the optimal pH for the solution.

### 3. 2. 2. Effect of PBS Content on the Erythrosine Removal Rate

In this section, effect of variable buffer content on the removal rate and final adsorption of the dye was eval-

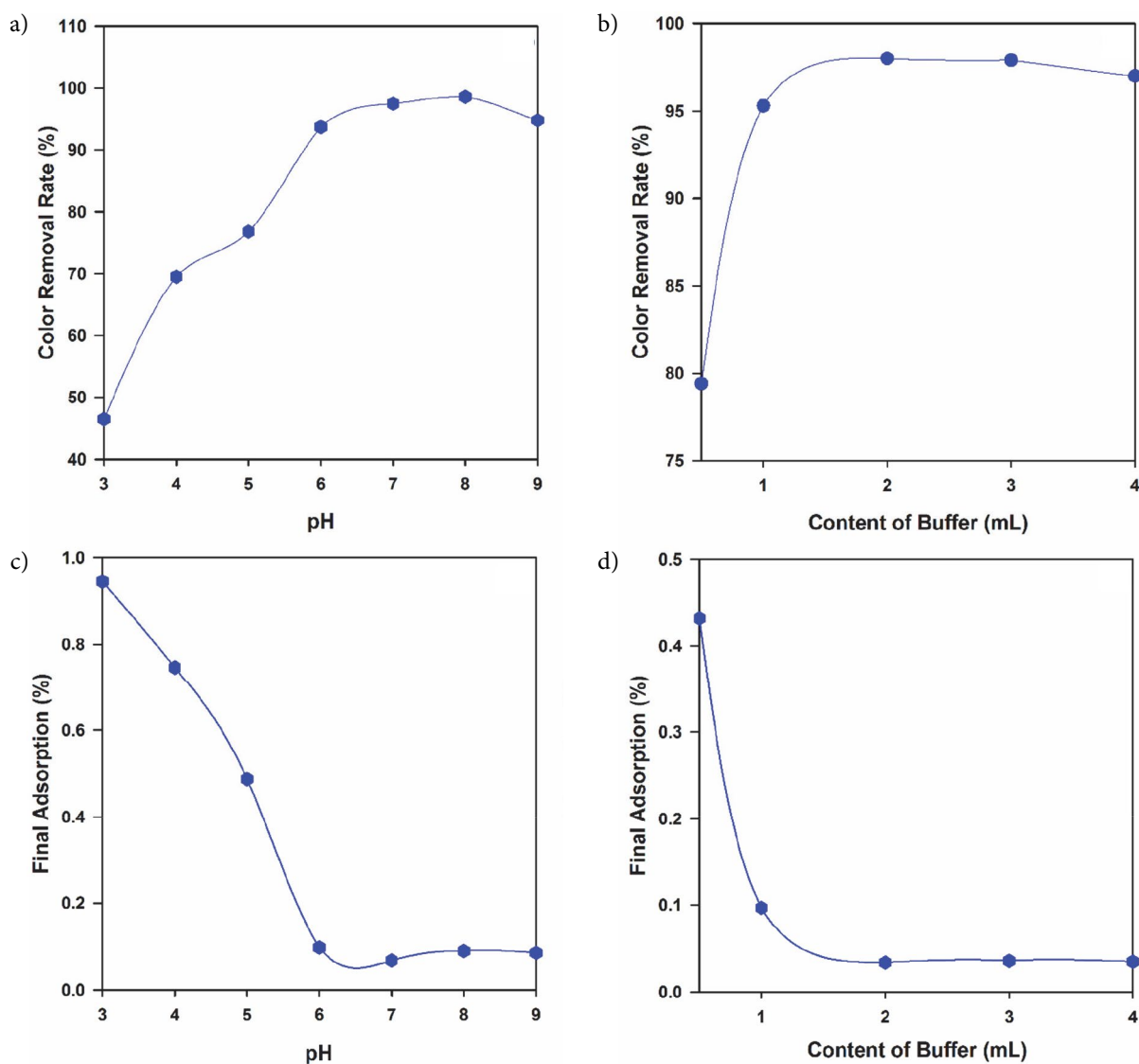


Figure 3. (a) The effect of variable pH and (b) PBS volume on the dye removal rate; and (c) the effect of variable pH and (d) PBS volume on the final adsorption rate of Erythrosine dye.

uated. In this regard, various volumes of PBS were added to the solution containing Erythrosine dye (at pH = 7), while the dye removal rate and final adsorption were recorded at 523 nm wavelength. Figure 3 (b) and (d), show the dye removal rate and final adsorption of the dye at various contents of PBS. Obtained results revealed that increase in the content of PBS up to 2 mL can lead to significant improvement in the dye removal rate, while the dye removal rate was levelled off at contents more than 2 mL. Therefore, 2 mL PBS was considered as the optimal buffer volume.

### 3. 2. 3. Effect of GO-Fe<sub>3</sub>O<sub>4</sub> Content on the Erythrosine Removal Rate

In this section, effect of adsorbent content on the dye removal rate and final adsorption rate of dye was ex-

amined. In this regard, 15 mL of Erythrosine dye (100 µg mL<sup>-1</sup>) along with 2 mL PBS (with pH = 7) were poured into a 50 mL volumetric flask and then the flask was filled with deionized water. Afterward, same amount of the resulting suspension was poured into six different beakers and various amount of GO-Fe<sub>3</sub>O<sub>4</sub> ranging from 0.05 to 0.3 g was added to the suspension and sonicated for 2 min (500 rpm). Then, the resulting suspension was placed on a strong magnet for further 1 min and after fillers sediment, the dye removal rate and final adsorption rate of Erythrosine dye were measured at wavelength of 523 nm. In Fig. 4 (a) and (c), the effect of filler content on the dye removal rate and final adsorption can be seen, respectively. Obtained results showed that increase in the content of fillers up to 0.2 g can lead to significant improvement in the dye removal rate, while the level of removal rate was levelled off in contents more than 0.2 g, thereby 0.2 g GO-

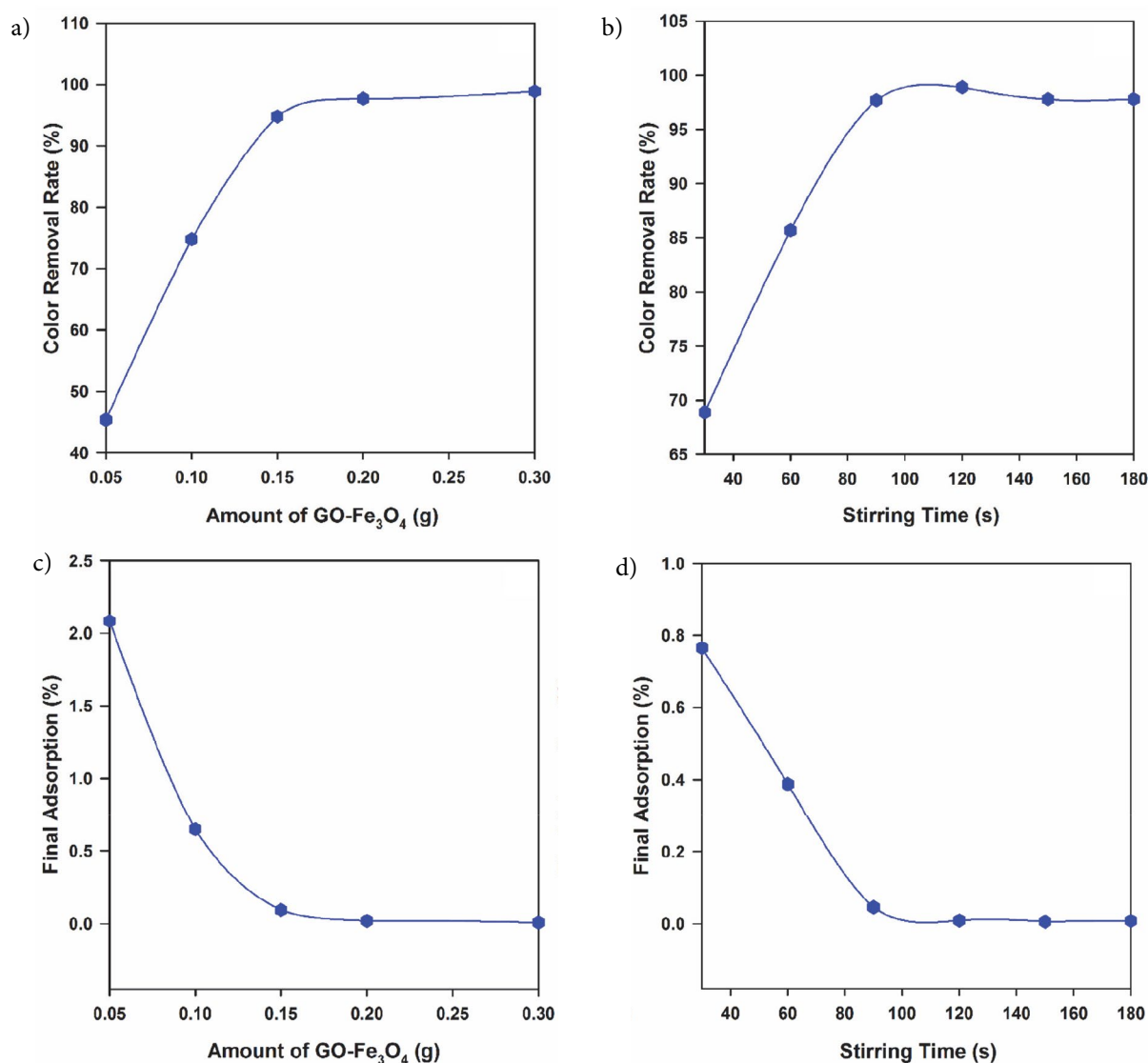


Figure 4. The effect of (a) magnetite filler content and (b) stirring time on the color removal rate; and the effect of (c) magnetite filler content and (d) stirring time on the final adsorption of Erythrosine dye.

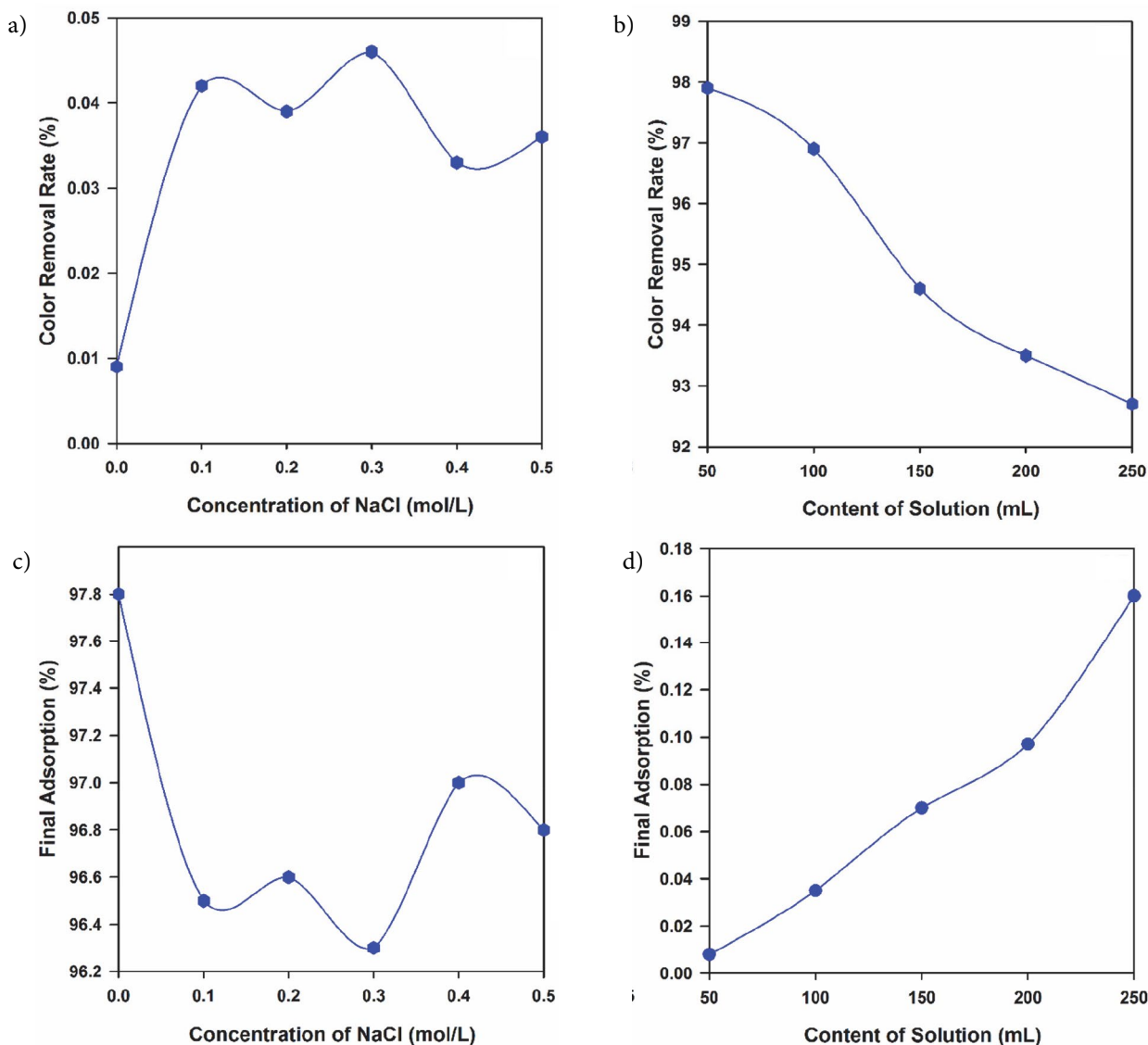
$\text{Fe}_3\text{O}_4$  was considered as the optimal amount of adsorbent.

### 3. 2. 4. Effect of Stirring Time on the Erythrosine Removal Rate

In this section, effect of diverse mixing times (40–180 s) on the dye removal rate and final adsorption of dye at wavelength of 523 nm were examined. In this case, produced solution containing 2 mL PBS (pH = 7) along with 0.2 g GO- $\text{Fe}_3\text{O}_4$  was stirred at different selected times. In Fig. 4, obtained results can be seen, which parts (b) and (d) showing the dye removal rate and final adsorption of dye from aqueous solution. Achieved results showed that by increase in the stirring time up to 2 min, the final dye removal rate remains at balanced amount. Therefore, 2 min stirring was considered as the optimal mixing time.

### 3. 2. 5. Effect of Electrolyte Concentration on the Erythrosine Removal Rate

In this section, the effect of the electrolyte concentration on the dye removal rate and final adsorption of dye at wavelength of 523 nm was evaluated. For this matter, 15 mL of Erythrosine solution ( $100 \mu\text{g mL}^{-1}$ ) along with 2 mL PBS (pH = 7) and variable amount of 1 molar sodium chloride were poured into a 50 mL volumetric flask and afterward the flask was filled with deionized water. Thence, 0.2 g GO- $\text{Fe}_3\text{O}_4$  was added to the suspensions containing various concentrations of electrolyte. Then, each beaker was placed on a strong magnet for 1 min and after sediment of fillers, the dye removal rate and final adsorption were calculated at wavelength of 523 nm, which can be seen in Figure 5 (a) and (c), respectively. Achieved results revealed that increase in the concentration of electrolyte has negligible effects on the dye removal rate and final ad-



**Figure 5.** The effect of variable (a) electrolyte concentration and (b) solution content on the dye removal rate; and the effect of (c) electrolyte concentration and (d) solution content on the final adsorption rate of Erythrosine dye.



sorption rate. Moreover, addition of electrolyte to the suspension containing adsorbent and dye neutralizing the surface of the adsorbent that can further decrease the absorption of dye molecules by the adsorbent's surface. On the other hand, electrolyte can lead to decrease in the ionization of dye molecules. This process eases the extraction of non-ionic compositions and leads to higher absorption of neutral dye molecules compared with ionic molecules with whether positive or negative charges.

### 3. 2. 6. Effect of Solution Content on the Erythrosine Removal Rate

In this section, various volumes of solution (ranging from 50–250 mL) containing 1500 µg Erythrosine dye were examined to evaluate the effect of solution content on the dye removal rate and final adsorption of Erythrosine dye, which can be seen in Fig. 5 (b) and (d), respectively. Achieved results showed that increase in the solution content to more than 100 mL can lead to significant decrease in the percentage of dye removal rate and final adsorption. Furthermore, the maximum dye removal rate was observed at 50 mL solution volume.

### 3. 2. 7. Effect of Temperature on the Erythrosine Removal Rate

In this section, effect of variable temperature (ranging from 5 to 60 °C) on the dye removal rate and the final adsorption of Erythrosine dye from aqueous solution was examined. A view of these results can be seen in Fig. 6 (a) and (b), respectively. Obtained results showed that increase in the temperature to more than 15 °C can highly enhance and improve the final dye removal rate.

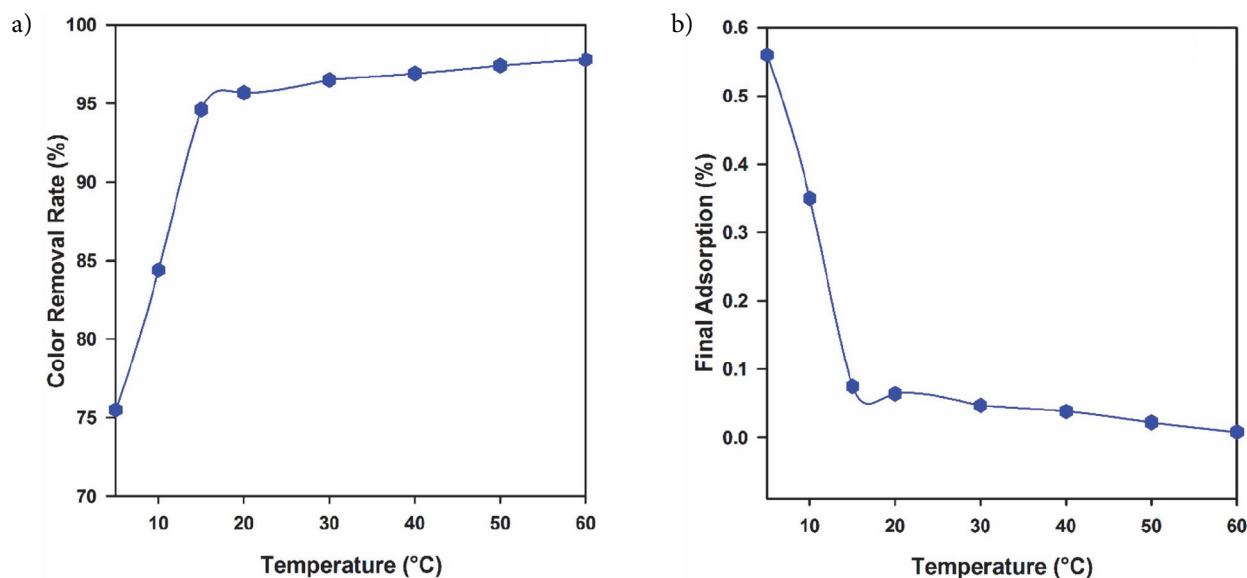


Figure 6. The effect of variable temperature on the (a) dye removal rate and (b) final adsorption of the Erythrosine dye.

### 3. 3. Isotherm of Adsorption Process

In this section, adsorption performance of developed GO-Fe<sub>3</sub>O<sub>4</sub> nanoparticles was described through isotherm. In this case, distribution of metal ions between both liquid and solid phases were examined using Langmuir and Freundlich isotherm models via obtained results from experimental data.

In this regard, for examination of adsorption process isotherm by developed adsorbents, different solutions containing various amount of Erythrosine dye (30, 35 and 40 µg mL<sup>-1</sup>) were poured into a 50 mL volumetric flask along with 2 mL PBS (pH = 7). Afterward, each prepared solution was added to several beakers and then 0.2 g GO-Fe<sub>3</sub>O<sub>4</sub> was added to each beaker. Thence, the resulting suspension was stirred for 150 s and placed on a strong magnet for further sediment of fillers. Thereafter, adsorption rate of each prepared sample was evaluated at wavelength of 523 nm. Obtained data from experimental evaluation can be seen in Fig. 7 (a).

What is more, the Langmuir isotherm consider monolayer adsorption for a surface which containing a finite number of adsorption sites of uniform strategies without transmigration of adsorbate in the plane surface,<sup>29–31</sup> which is defined as follow:

$$\frac{C_e}{q_e} = \frac{1}{bq_{max}} + \frac{C_e}{q_{max}} \quad (2)$$

Where  $C_e/q_e$ ,  $C_e$ , constant  $b$  and  $q_{max}$  are the specification of adsorption, equilibrium concentration, maximum adsorption capacity and energy of adsorption, respectively. The liner plot of the adsorption specification ( $C_e/q_e$ ) versus the equilibrium concentration ( $C_e$ ) can be

seen in Fig. 7 (b). Obtained results show that Langmuir isotherm model is perfectly compatible with experimental data. On the other hand, the Freundlich isotherm is an empirical model which can be defined as follows.<sup>32</sup>

$$q_e = K_f C_e^{1/n} \quad (3)$$

Where  $q_e$ ,  $C_e$ ,  $K_f$  and  $n$  are the amount of adsorbed per amount of adsorbent at the equilibrium (mg/g), equilibrium concentration (mg/L), parameters that depend on the adsorbate and parameters that depend on the adsorbent, respectively. Mentioned equation can be linearized and temperature dependence parameters such as  $K_f$  and  $1/n$  can be transformed into the linear form as follows.<sup>33</sup>

$$\ln q_e = \ln K_f + \frac{1}{n} \ln C_e \quad (4)$$

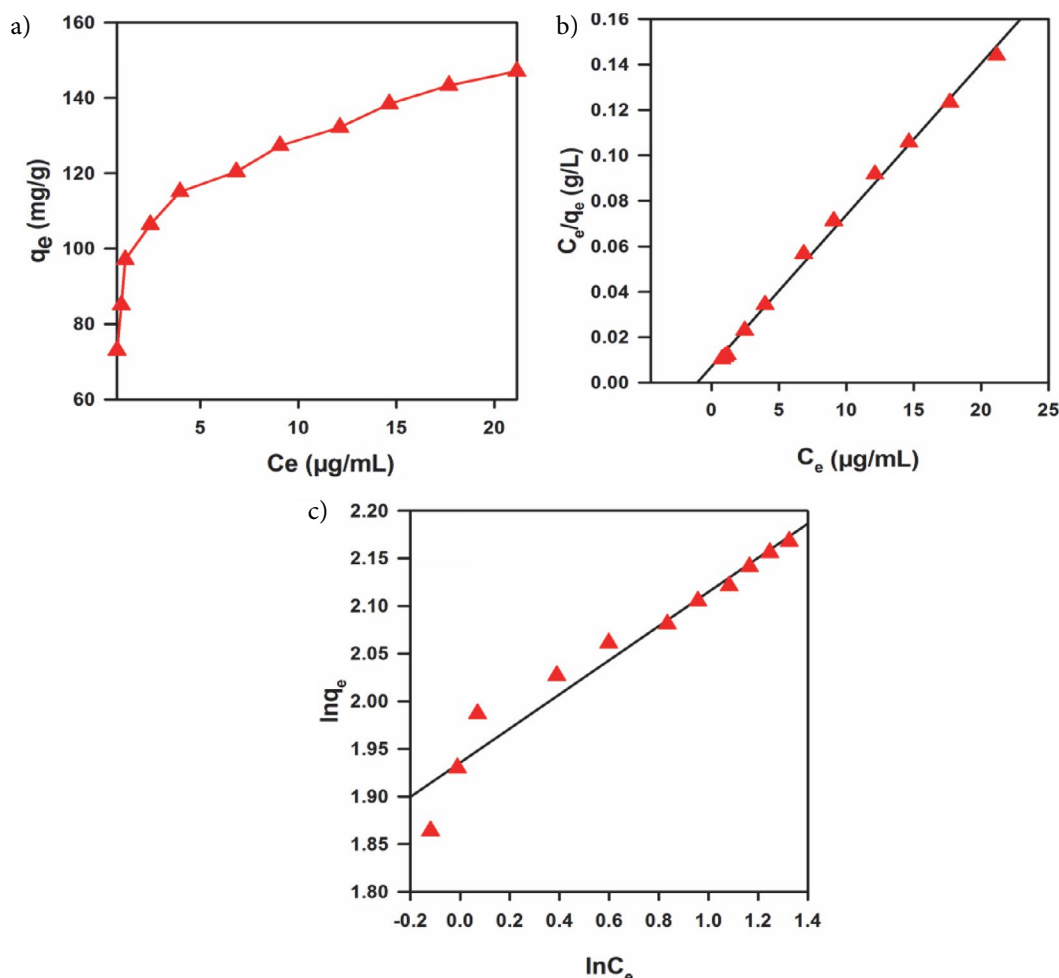
Where  $K_f$  and  $n$  are the Freundlich constants based on the adsorption capacity and intensity, respectively. Freundlich equilibrium constants can be determined from plot of  $\ln q_e$  against  $\ln C_e$ , which can be seen in Fig. 7 (c). Achieved

results from both Langmuir and Freundlich isotherm models shows that the experimental data are more compatible with Langmuir model than Freundlich model. Moreover, the related equations for Langmuir and Freundlich are as follow:

$$Y = 0.0067 X + 0.0072 \text{ and } R^2 = 0.9982 \quad (5)$$

$$Y = 0.1791 X + 1.9355 \text{ and } R^2 = 0.9734 \quad (6)$$

In addition, obtained results from both experimental evaluation and simulation via Langmuir and Freundlich isotherm models indicated that increase in the concentration of adsorbent can lead to significant improvement in the final adsorption rate. Additionally, smaller correlation coefficient ( $R^2$ ) of Freundlich isotherm than Langmuir isotherm shows that the Langmuir isotherm model is proper to predict the behavior of adsorption process. It also shows that the adsorption of dye on the adsorbent is monolayer. Additionally, the maximum adsorption capacity obtained by Langmuir isotherm model was obtained at 149.25 mg/g which is a considerable amount.



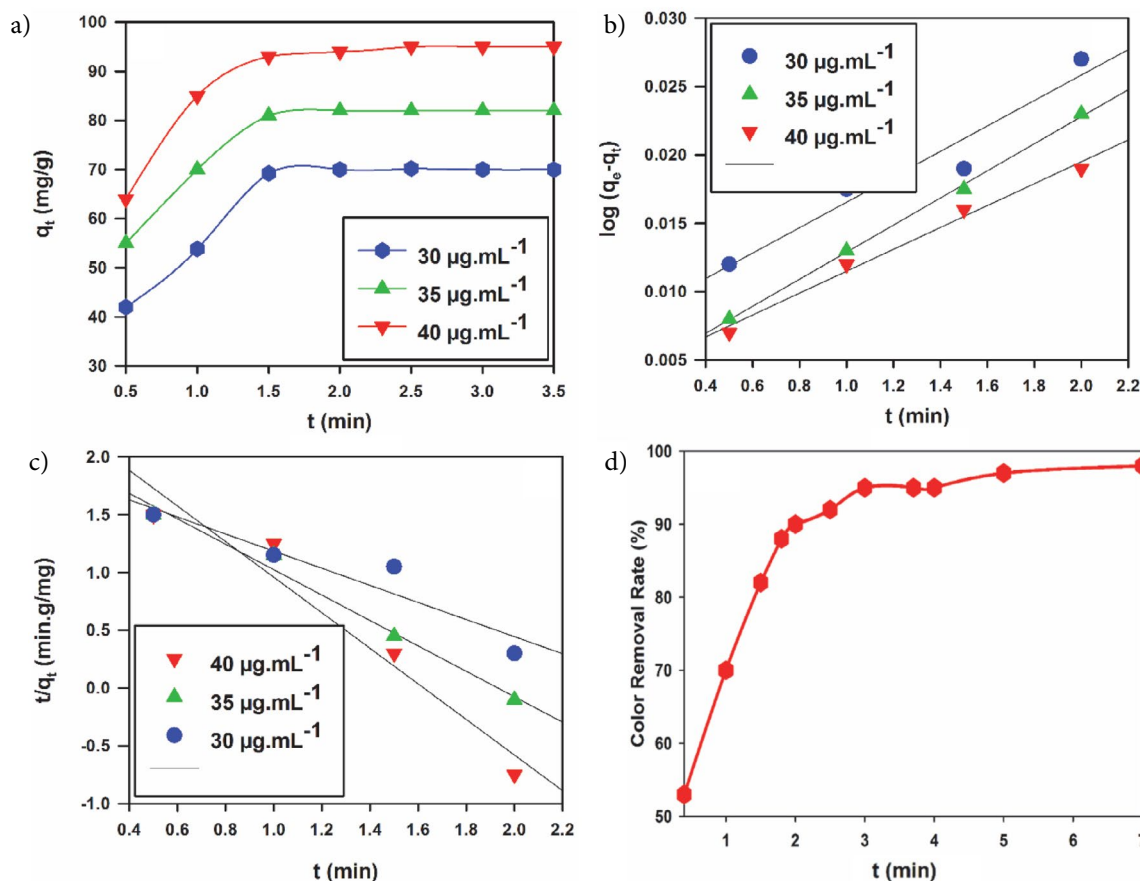
**Figure 7.** Adsorption isotherm of Erythrosine dye from aqueous solution obtained from (a) experimental evaluation, (b) Langmuir isotherm model and (c) Freundlich isotherm model.

### 3. 3. 1. Kinetic Study of the Adsorption Process

In this section, the kinetic of GO-Fe<sub>3</sub>O<sub>4</sub> adsorption process was examined at variable time ranging from 0.5 to 3.5 min. Figure 8 (a), indicating that the adsorption process reached the balanced situation after 2.5 min, while increase in the concentration of adsorbent can highly improve the adsorption rate. Furthermore, adsorption process of Erythrosine dye via GO-Fe<sub>3</sub>O<sub>4</sub> was also examined using the pseudo-first order equation (Figure 8 (b)) and pseudo-second order equation (Figure 8 (c)).<sup>34,35</sup> According to the correlation coefficient of these two models, the dye adsorption process follows both pseudo-first order model and pseudo-second order equations; however, the pseudo-second order model is much more compatible with the experimental outcomes than the pseudo-first order model, which indicate the mechanism of chemical adsorption. The obtained line equations and the correlation coefficients are as follow:

$$30 \mu\text{g mL}^{-1} \rightarrow \log (q_e - q_t) = -1.5614t + 2.4655, \quad (7) \\ r = 0.9753$$

$$35 \mu\text{g mL}^{-1} \rightarrow \log (q_e - q_t) = -1.1282t + 2.134, \quad (8) \\ r = 0.9941$$



**Figure 8.** (a) The effect of the contact time and the concentration of Erythrosine dye solutions on the adsorption rate of the Erythrosine by the adsorbent, (b) The examination of the kinetic based on the pseudo-first order model and (c) The examination of the kinetic based on the pseudo-second order model (d) Average dye removal rate of Erythrosine dye from real samples obtained from chicken slaughterhouse and hospital.

$$40 \mu\text{g mL}^{-1} \rightarrow \log (q_e - q_t) = -0.8352t + 2.002, \quad (9) \\ r = 0.9602$$

In addition, in order to examine the kinetic based on the pseudo-second order model, the diagram of  $t/q_t$  changes was illustrated based on  $t$ , which can be seen in Fig. 8 (c). The obtained line equations and the correlation coefficients are as follow:

$$30 \mu\text{g mL}^{-1} \rightarrow t/q_t = 0.01t + 0.0067, R^2 = 0.9918 \quad (10)$$

$$35 \mu\text{g mL}^{-1} \rightarrow t/q_t = 0.0092t + 0.0045, \quad (11) \\ R^2 = 0.9990$$

$$40 \mu\text{g mL}^{-1} \rightarrow t/q_t = 0.0086t + 0.003, \quad (12) \\ R^2 = 0.9984$$

### 3. 4. Performance of Fillers for Removal of Erythrosine dye From Real Samples

In this section, performance of developed GO-Fe<sub>3</sub>O<sub>4</sub> nanoparticles for removal of Erythrosine dye from real samples obtained from chicken slaughterhouse and hospital sewage disposal system was evaluated. In this

**Table 1.** Adsorption of Erythrosine dye from chicken slaughterhouse and hospital wastewaters.

Sample	Added dye (mg mL <sup>-1</sup> )	Adsorbed dye (mg mL <sup>-1</sup> )	Adsorption (%)
Chicken slaughterhouse wastewater	20	16	94
	50	47.75	95.5
	70	67	96
Hospital wastewater	20	18	96
	50	49	97
	70	67	98

case, various concentrations of Erythrosine dye (20, 50 and 70 mg mL<sup>-1</sup>) were added to two real samples that were obtained from chicken slaughterhouse and hospital, respectively, and thence the adsorption rate of dye via magnetic fillers was investigated. For this matter, in two turns, 0.2, 0.5 and 0.7 mL of Erythrosine dye (10 µg mL<sup>-1</sup>) was added to two different volumetric flasks, respectively, which were filled with wastewater obtained from chicken slaughterhouse and hospital, respectively. Then, prepared solutions were passed through an adsorbent pillar, while the washing action was performed with 2 mL of 2 molar ammonia (NH<sub>3</sub>) buffer (pH = 7). Afterward, the adsorption rate was measured at wavelength of 523 nm using UV-vis spectrophotometer. Achieved results can be seen in Table 1 and Fig. 8 (d). Calculated data within the Table 1 was measured based on the method that explained in the section 2.6.

Furthermore, one of the most important parts of an adsorption study is to investigate the possible disturbance role of each ion during the adsorption process, which could be used to develop the research for real samples. By evaluation of possible disturbance factors, we can figured out whether a method is practical or not. In this regard, possible disturbance effect of various kinds of cations and anions were investigated. If a considered ion create more than 5% systematic error during the calculation, we consider that ion as the annoying ion which should be removed from the system. In order to examine the current adsorption process, 1 mL of Erythrosine dye (5 µg mL<sup>-1</sup>) was added to a volumetric flask, while the pH was set on 7. Thereafter, various amount of annoying ions were poured into a 100 mL beaker and then the beaker was filled with

**Table 2.** Disturbance effect of various kinds of ions during the adsorption process.

Concentration of Ion or dye (mg/mL)	Annoying kind
1500	S <sub>2</sub> O <sub>3</sub> <sup>2-</sup> , C <sub>2</sub> O <sub>4</sub> <sup>2-</sup> , F <sup>-</sup> , Cl <sup>-</sup> , Br <sup>-</sup> , I <sup>-</sup> , Pb <sup>2+</sup> , Zn <sup>2+</sup> , Hg <sup>2+</sup> , Na <sup>+</sup>
500	Cu <sup>2+</sup> , K <sup>+</sup> , Mn <sup>2+</sup> , Mg <sup>2+</sup> , NO <sub>3</sub> <sup>-</sup> , Cr <sup>3+</sup> , CO <sub>3</sub> <sup>2-</sup> , HCO <sub>3</sub> <sup>-</sup> , Ni <sup>2+</sup> , Ca <sup>2+</sup> , Fe <sup>3+</sup> , Fe <sup>2+</sup>

deionized water. Thence, via vacuum pump, each solution was passed through a pillar containing 0.1 g of adsorbent. List of annoying kinds during the process can be seen in the Table 2.

Besides, in order to evaluate the standard deviation and repeatability of current method, the limit of detection (LOD) and relative standard deviations (RSD) were measured, respectively. The standard deviation can be calculated via the following equation:

$$S_b = \sqrt{\sum_{i=1}^n \frac{(x_i - \bar{x})^2}{n-1}} \quad (13)$$

Where the calculated  $S_b$  and  $\bar{x}$  are 5.67 and 0.0071, respectively. On the other hand, LOD can be measured via the following formula:

$$LOD = \frac{KS_b}{m} \quad (14)$$

Where K, m and  $S_b$  are constant factor with value 3, standard curve slop and standard deviation, respectively. The measured value of LOD was determined to be 1.82 mg mL<sup>-1</sup>. In addition, in order to evaluate the repeatability of the adsorption procedure, the final adsorption of solutions containing 100 and 250 mg mL<sup>-1</sup> Erythrosine dye were re-

**Table 3.** Results of repeatability at concentration 100 mg mL<sup>-1</sup>.

Number	Adsorption (%)	Concentration (mg mL <sup>-1</sup> )
1	0.048	45.28
2	0.048	45.28
3	0.050	47.43
4	0.050	47.43
5	0.050	47.43
6	0.048	45.28
7	0.048	45.28
8	0.050	47.43
9	0.049	46.35
10	0.048	45.28

**Table 4.** Results of repeatability at concentration 250 mg mL<sup>-1</sup>.

Number	Adsorption (%)	Concentration (mg mL <sup>-1</sup> )
1	0.242	252.99
2	0.277	232.78
3	0.262	274.44
4	0.258	270.12
5	0.255	266.91
6	0.250	261.56
7	0.244	255.13
8	0.239	249.78
9	0.240	250.85
10	0.250	261.56

peated for ten times and then measured with respect to the line equation of various concentrations. Obtained results for 100 and 250 mg mL<sup>-1</sup> concentrations can be seen in the Tables 3 and 4, respectively, while the RSD for concentrations 100 and 250 mg mL<sup>-1</sup> was determined to be 2.3 and 4.79%, respectively. In this case, all of absorption rates were calculated based on the procedure that mentioned in section 2.6.

## 4. Conclusions

In this study, GO was fabricated via modified Hummers method and thence decorated with magnetite nanoparticles (Fe<sub>3</sub>O<sub>4</sub>) through a multi-step manufacturing procedure. Thence, fabricated GO-Fe<sub>3</sub>O<sub>4</sub> nanoparticles were evaluated using FTIR, XRD, VSM and SEM analyses, and these analyses confirmed the successful synthesis of GO-Fe<sub>3</sub>O<sub>4</sub> and their fantastic magnetic properties. Thereafter, performance of developed fillers for the removal of Erythrosine dye from aqueous solutions under variable conditions and at variety of concentrations were examined and studied. Afterward, obtained experimental outcomes were used to evaluate the adsorption isotherm and kinetic of GO-Fe<sub>3</sub>O<sub>4</sub> nanoparticles. Finally, performance of developed magnetic nanoparticles for the removal of Erythrosine dye from real samples obtained from chicken slaughterhouse and hospital sewerage disposal system were investigated. Achieved results revealed the fantastic performance of GO-Fe<sub>3</sub>O<sub>4</sub> nanoparticles for removal of Erythrosine dye from various kinds of aqueous solutions under variety of conditions.

## 5. Funding

This research did not receive any specific grant from funding agencies in the public, commercial, or not-for-profit sectors

## 6. Conflicts of Interest

The authors declare that they have no conflicts of interest.

## 7. References

1. R. Bernstein, H. Haugen and H. Frey, *Scandinavian journal of clinical and laboratory investigation* **1975**, 35, 49–52. DOI:10.3109/00365517509068004
2. S. Bonan, G. Fedrizzi, S. Menotta and C. Elisabetta, *Dyes and Pigments* **2013**, 99, 36–40. DOI:10.1016/j.dyepig.2013.03.029
3. E. V. Hess, *Toxicology* **2002**, 181, 65–70.
4. I. Poullos, D. Makri and X. Prohaska, *Global Nest: Int. J* **1999**, 1, 55–62.
5. Y. Ho and G. McKay, *Process safety and environmental protection* **1998**, 76, 313–318. DOI:10.1205/095758298529678
6. I. El-Thalouth, M. Kamel, K. Haggag and M. El-Zawahry, *American Dyestuff Reporter* **1993**, 82, 36–36.
7. J. A. Laszlo, *American Dyestuff Reporter* **1994**, 83, 5.
8. L. Morais, O. Freitas, E. Goncalves, L. Vasconcelos and C. G. Beca, *Water Research* **1999**, 33, 979–988. DOI:10.1016/S0043-1354(98)00294-2
9. M. Hasnat, I. Siddiquey and I. S. Saiful, **2003**.
10. J. I. Álvarez-Uriarte, U. Iriarte-Velasco, N. Chimeno-Alanís and J. R. González-Velasco, *Separation Science and Technology* **2011**, 46, 2239–2249. DOI:10.1080/01496395.2011.594847
11. R. Jain and S. Sikarwar, *Journal of hazardous materials* **2009**, 164, 627–633. DOI:10.1016/j.jhazmat.2008.08.043
12. Y. TONOGAI, M. IWAIDA, M. TATI, Y. OSE and T. SATO, *The Journal of toxicological sciences* **1978**, 3, 205–214.
13. Z. Hu and M. Srinivasan, *Microporous and Mesoporous Materials* **2001**, 43, 267–275. DOI:10.1016/S1387-1811(00)00355-3
14. Z. Jin, X. Wang, Y. Sun, Y. Ai and X. Wang, *Environmental science & technology* **2015**, 49, 9168–9175. DOI:10.1021/acs.est.5b02022
15. S. Yu, X. Wang, Y. Ai, X. Tan, T. Hayat, W. Hu and X. Wang, *Journal of Materials Chemistry A* **2016**, 4, 5654–5662. DOI:10.1039/C6TA00890A
16. G. Zhao, L. Jiang, Y. He, J. Li, H. Dong, X. Wang and W. Hu, *Advanced materials* **2011**, 23, 3959–3963. DOI:10.1002/adma.201101007
17. Y. S. Al-Degs, R. Abu-El-Halawa and S. S. Abu-Alrub, *Chemical engineering journal* **2012**, 191, 185–194. DOI:10.1016/j.ccej.2012.03.002
18. S. M. Mousavi, S. A. Hashemi, A. M. Amani, H. Esmaeili, Y. Ghasemi, A. Babapoor, F. Mojoudi and O. Arjomand, *Physical Chemistry Research* **2018**, 6, 759–771.
19. S. M. Mousavi, S. A. Hashemi, H. Esmaeili, A. M. Amani and F. Mojoudi, *Acta Chimica Slovenica* **2018**.
20. S. A. Hashemi, S. M. Mousavi, R. Faghihi, M. Arjmand, S. Sina and A. M. Amani, *Radiation Physics and Chemistry* **2018**, 146, 77–85. DOI:10.1016/j.radphyschem.2018.01.008
21. S. M. Mousavi, S. A. Hashemi, M. Arjmand, A. M. Amani, F. Sharif and S. Jahandideh, *ChemistrySelect* **2018**, 3, 7200–7207. DOI:10.1002/slct.201800996
22. F. S. Khoo and H. Esmaeili, *J. Serb. Chem. Soc.* **2018**, 83, 237–249.
23. F. Entezari Juybari, A. Kamran-Pirzaman and M. Ghorbani, *Inorganic and Nano-Metal Chemistry* **2017**, 47, 121–126. DOI:10.1080/15533174.2016.1149733
24. Y. Wei, B. Han, X. Hu, Y. Lin, X. Wang and X. Deng, *Procedia Engineering* **2012**, 27, 632–637. DOI:10.1016/j.proeng.2011.12.498
25. S. Baharin, N. Muhamad Sarih and S. Mohamad, *Polymers* **2016**, 8, 117. DOI:10.3390/polym8050117
26. G. Xie, P. Xi, H. Liu, F. Chen, L. Huang, Y. Shi, F. Hou, Z. Zeng, C. Shao and J. Wang, *Journal of Materials Chemistry* **2012**, 22, 1033–1039. DOI:10.1039/C1JM13433G

27. J. Hur, J. Shin, J. Yoo and Y.-S. Seo, *The Scientific World Journal* **2015**, 2015.
28. L. Ai, C. Zhang and Z. Chen, *Journal of hazardous materials* **2011**, 192, 1515–1524. DOI:10.1016/j.jhazmat.2011.06.068
29. M. B. Desta, *Journal of thermodynamics* **2013**, 2013.
30. B. Hameed, A. M. Din and A. Ahmad, *Journal of hazardous materials* **2007**, 141, 819–825. DOI:10.1016/j.jhazmat.2006.07.049
31. S. Mohammad Beigi, A. Babapoor, V. Maghsoodi, S. M. Mousavi and N. Rajabi, *Iranian Journal of Chemistry and Chemical Engineering (IJCCE)* **2009**, 28, 81–89.
32. A. Teimouri, H. Esmaeili, R. Foroutan and B. Ramavandi, *Korean Journal of Chemical Engineering* **2018**, 35, 479–488. DOI:10.1007/s11814-017-0311-y
33. B. S. Zadeh, H. Esmaeili and R. Foroutan, *Indonesian Journal of Chemistry*, **18**, 265–271.
34. W. Rudzinski and W. Plazinski, *Adsorption* **2009**, 15, 181. DOI:10.1007/s10450-009-9167-8
35. X. Li, Y. Liu, C. Zhang, T. Wen, L. Zhuang, X. Wang, G. Song, D. Chen, Y. Ai and T. Hayat, *Chemical Engineering Journal* **2018**, 336, 241–252. DOI:10.1016/j.cej.2017.11.188

## Povzetek

V tej raziskavi smo s pomočjo modificirane Hummersove metode sintetizirali grafen oksid (GO), ki smo mu nato v večstopenjskem postopku površino modificirali z nanodelci  $\text{Fe}_3\text{O}_4$  (GO- $\text{Fe}_3\text{O}_4$ ). Material smo karakterizirali z naslednjimi metodami: infrardečo spektroskopijo (FTIR), rentgensko praškovno difrakcijo (XRD) in vrstično elektronsko mikroskopijo (SEM). Magnetne lastnosti materiala smo preučili z merilnikom namagnetnosti s tresočim se vzorcem (VSM). Preučevali smo tudi učinkovitost GO- $\text{Fe}_3\text{O}_4$  za odstranjevanje in adsorpcijo barvila eritrozina iz vodne raztopine pod različnimi pogoji kot so: pH, dodatek fosfatnega pufru (PBS), vsebnost adsorbenta, čas mešanja, koncentracija elektrolita in temperatura. Za ta del raziskav smo uporabili vzorce iz sistema za odstranjevanje odpadka v obratu piščančje klavnice in bolnišnice, ki so vsebovali 20, 50 in 70 mg/ml barvila eritrozina. Od 94 % do 97 % celotnega barvila smo uspeli adsorbirati z uporabo nanodelcev GO- $\text{Fe}_3\text{O}_4$ . Najvišjo adsorpcijsko zmogljivost smo določili s pomočjo Langmuirjevega modela in je znašala 149,25 mg/g. Dobljeni rezultati so jasno pokazali, da so nanodelci GO- $\text{Fe}_3\text{O}_4$  primerni za adsorpcijo in odstranjevanje barvil iz odpadka.

Scientific paper

# Syntheses, Characterization and Crystal Structures of Schiff Base Zinc(II) Complexes with Antibacterial Activity

Dong-Lai Peng<sup>1,\*</sup> and Nan Sun<sup>2</sup>

<sup>1</sup> Key Laboratory of Surface and Interface Science of Henan Province, School of Material & Chemical Engineering, Zhengzhou University of Light Industry, Zhengzhou 450001, P.R. China

<sup>2</sup> College of Chemistry, Chemical Engineering and Material Science, Shandong Normal University, Jinan 250014, P.R. China

\* Corresponding author: E-mail: pengdonglai2015@sina.com

Received: 17-06-2018

## Abstract

Two polynuclear zinc(II) complexes,  $[\text{Zn}_2(\text{L}^1)_2(\text{OH}_2)_2]$  (**1**) and  $[\text{ZnL}^2(\mu_{1,1}\text{-N}_3)]_n$  (**2**), where  $\text{L}^1$  is the dianionic form of *N,N'*-bis(3,5-difluoro-2-hydroxybenzylidene)-1,3-diaminopropane, and  $\text{L}^2$  is the monoanionic form of 2-[(2-dimethylaminoethylimino)methyl]-4,6-difluorophenol, have been prepared and structurally characterized by elemental analyses, IR and UV-Vis spectroscopy, as well as single-crystal X-ray diffraction. In complex **1**, the Zn atom is in octahedral coordination, with the donor atoms of the Schiff base ligands  $\text{L}^1$  and one water O atom. In complex **2**, the Zn atom is in trigonal-bipyramidal coordination, with the three donor atoms of the Schiff base ligand  $\text{L}^2$  and two azido N atoms. The complexes have strong antibacterial activity against *B. subtilis* and *S. aureus*.

**Keywords:** Schiff base; zinc complex; hydrogen bonds; crystal structure; antibacterial activity

## 1. Introduction

The rational design and preparation of new coordination compounds have attracted remarkable attention in coordination chemistry.<sup>1</sup> Azide anion is an interesting ligand in the self-assembly of new structures of complexes. A variety of azido complexes with discrete or one-, two-, and three-dimensional polymeric structures have been reported.<sup>2</sup> Schiff bases derived from salicylaldehyde and its derivatives usually possess two or more donor atoms, which can chelate to transition metal atoms, to form a variety of complexes.<sup>3</sup> Metal complexes with Schiff base ligands have attracted much attention in the fields of magnetic, catalytic, as well as biological materials.<sup>4</sup> Zinc complexes with Schiff base ligands are reported to have interesting antibacterial activities.<sup>5</sup> As a continuation of the work on Schiff base complexes, and to explore new and effective antibacterial materials, we report here the synthesis, characterization, and self-assembly of two new zinc(II)

complexes,  $[\text{Zn}_2(\text{L}^1)_2(\text{OH}_2)_2]$  (**1**) and  $[\text{ZnL}^2(\mu_{1,1}\text{-N}_3)]_n$  (**2**), where  $\text{L}^1$  is the dianionic form of *N,N'*-bis(3,5-difluoro-2-hydroxybenzylidene)-1,3-diaminopropane, and  $\text{L}^2$  is the monoanionic form of 2-[(2-dimethylaminoethylimino)methyl]-4,6-difluorophenol. The antibacterial activities of the complexes were investigated.

## 2. Experimental

### 2.1. Materials and Physical Measurements

3,5-Difluorosalicylaldehyde, propane-1,3-diamine and *N,N*-dimethylethane-1,2-diamine were purchased from Aldrich. All other reagents and solvents used in the synthesis were procured commercially and used without subsequent purification. The Schiff bases were synthesized according to the literature method.<sup>6</sup> Microanalyses (C,H,N) were performed using a Perkin-Elmer 2400 elemental analyzer. Infrared spectra were measured on KBr

disks with a Hitachi I-5040 FT-IR spectrophotometer. Electronic spectra were measured with a Lambda 35 spectrophotometer. Single crystal X-ray data were collected on a Bruker SMART APEX II diffractometer.

**Caution!** Azide complexes of metal ions are potentially explosive. Only a small amount of material should be prepared, and they should be handled with caution.

## 2. 2. Synthesis of Complex 1

A methanol solution (10 mL) of zinc(II) bromide (0.10 mmol, 22.5 mg) was added to the methanol solution (10 mL) of  $H_2L^1$  (0.10 mmol, 35.4 mg) and  $NaN_3$  (0.10 mmol, 6.5 mg). The reaction mixture was magnetic stirred for 1 h at ambient temperature to give colorless solution. Single-crystals suitable for X-ray diffraction were obtained from the filtrate by slow evaporation in a refrigerator. Yield: 205 mg, 47%.  $\lambda_{max}$  (nm) [ $\epsilon_{max}$  (L mol<sup>-1</sup> cm<sup>-1</sup>)] in methanol: 270 (16,550), 365 (12,070). IR data (KBr, cm<sup>-1</sup>): 3454 (OH), 1638 (CH=N), 1461, 1362, 1259, 1155, 952, 853, 532. Anal. calcd. for  $C_{34}H_{28}F_8N_4O_6Zn_2$  (%): C, 46.86; H, 3.24; N, 6.43. Found (%): C, 46.67; H, 3.33; N, 6.54.

## 2. 3. Synthesis of Complex 2

A methanol solution (10 mL) of zinc(II) bromide (0.10 mmol, 22.5 mg) was added to the methanol solution (10 mL) of  $HL^2$  (0.10 mmol, 22.8 mg) and  $NaN_3$  (0.10 mmol, 6.5 mg). The reaction mixture was magnetic stirred for 1 h at ambient temperature to give colorless solution. Single-crystals suitable for X-ray diffraction were obtained from the filtrate by slow evaporation in a refrigerator. Yield: 173 mg, 52%.  $\lambda_{max}$  (nm) [ $\epsilon_{max}$  (L mol<sup>-1</sup> cm<sup>-1</sup>)] in methanol: 270 (17,380), 377 (11,025). IR data (KBr, cm<sup>-1</sup>): 2052 (N<sub>3</sub>), 1642 (CH=N), 1556, 1469, 1353, 1289, 1254, 1123, 989, 820, 781, 753, 578. Anal. calcd. for  $C_{11}H_{13}F_2N_5OZn$  (%): C, 39.48; H, 3.92; N, 20.93. Found (%): C, 39.27; H, 4.03; N, 20.72.

## 2. 4. X-ray Crystallography

Data collection for the complexes was performed with a Bruker Apex II CCD diffractometer at 298 K using Mo K $\alpha$  ( $\lambda = 0.71073$  Å) radiation. The structures were solved by direct methods with SHELXS-97 and refined by full-matrix least squares (SHELXL-97) on  $F^2$ .<sup>7</sup> All non-hydrogen atoms were refined anisotropically. The water H atoms of complex **1** were located from an electronic density map and refined isotropically, with O-H and H...H distances restrained to 0.85(1) and 1.37(2) Å, respectively. The remaining hydrogen atoms were placed geometrically and refined with a riding model, with isotropic displacement coefficients  $U(H) = 1.2 U(C)$  or  $1.5 U(C_{methyl})$ . Crystallographic data for the complexes are summarized in Table 1. Selected bond lengths and angles are listed in Table 2.

**Table 1.** Crystallographic data for the complexes

	<b>1</b>	<b>2</b>
Empirical formula	$C_{34}H_{28}F_8N_4O_6Zn_2$	$C_{11}H_{13}F_2N_5OZn$
Formula weight	871.34	334.63
Crystal system	Triclinic	Monoclinic
Space group	$P-1$	$P2_1/c$
$a$ / Å	6.9736(8)	20.034(2)
$b$ / Å	10.8352(12)	10.1610(17)
$c$ / Å	11.3007(13)	6.7339(12)
$\alpha$ / °	75.958(2)	90
$\beta$ / °	89.667(2)	92.477(2)
$\gamma$ / °	79.652(2)	90
$V$ / Å <sup>3</sup>	814.26(16)	1369.5(4)
$Z$	1	4
$D_{calc}$ / g cm <sup>-3</sup>	1.777	1.623
Crystal size / mm	0.33 × 0.30 × 0.28	0.16 × 0.15 × 0.15
$\mu$ (Mo K $\alpha$ ) / mm <sup>-1</sup>	1.574	1.819
$F(000)$	440	680
Number of reflections	4324	4580
Unique reflections	3004	1946
Observed reflections ( $I > 2\sigma(I)$ )	2527	1055
Parameters	250	183
Restraints	3	0
$R_{int}$	0.0125	0.1137
Goodness of fit on $F^2$	1.047	0.971
$R_1, wR_2$ ( $I > 2\sigma(I)$ )	0.0345, 0.0739	0.0863, 0.1668
$R_1, wR_2$ (all data)	0.0455, 0.0792	0.1553, 0.2087

**Table 2.** Selected bond lengths (Å) and angles (°) for the complexes with estimated standard deviations (e.s.d.s) in parentheses

<b>1</b>			
Zn1–O1	2.0519(18)	Zn1–O2	2.0073(17)
Zn1–N1	2.091(2)	Zn1–N2	2.126(2)
Zn1–O3	2.201(2)	Zn1–O1A	2.560(2)
O2–Zn1–O1	89.14(7)	O2–Zn1–N1	176.20(8)
O1–Zn1–N1	87.05(8)	O2–Zn1–N2	88.87(8)
O1–Zn1–N2	170.55(9)	N1–Zn1–N2	94.91(8)
O2–Zn1–O3	90.32(8)	O1–Zn1–O3	96.92(9)
N1–Zn1–O3	90.00(9)	N2–Zn1–O3	92.33(8)
N1–Zn1–O1A	86.31(9)	N2–Zn1–O1A	88.72(9)
O1–Zn1–O1A	82.17(9)	O2–Zn1–O1A	93.31(9)
O3–Zn1–O1A	176.24(9)		
<b>2</b>			
Zn1–O1	2.024(8)	Zn1–N1	2.055(8)
Zn1–N2	2.280(9)	Zn1–N3	2.053(8)
Zn1–N3B	2.097(8)		
O1–Zn1–N3	94.2(4)	O1–Zn1–N1	88.7(3)
N3–Zn1–N1	127.6(3)	O1–Zn1–N3B	92.5(3)
N3–Zn1–N3B	108.5(3)	N1–Zn1–N3B	123.6(3)
O1–Zn1–N2	169.8(3)	N3–Zn1–N2	93.1(4)
N1–Zn1–N2	81.2(3)	N3A–Zn1–N2	91.8(3)

Symmetry codes: A:  $-x, 1 - y, 1 - z$ ; B:  $x, \frac{1}{2} - y, \frac{1}{2} + z$ .



## 2. 5. Antibacterial Activity

The antibacterial activities were tested against *B. subtilis* ATCC 6633, *E. coli* ATCC 35218, *P. putida* TS 1138 and *S. aureus* ATCC 25923 using MH medium (Mueller–Hinton medium: casein hydrolysate 17.5 g, soluble starch 1.5 g, beef extract 1000 mL). The MICs (minimum inhibitory concentrations) of the test compounds were determined by a colorimetric method using the dye MTT [3-(4,5-dimethylthiazol-2-yl)-2,5-diphenyl tetrazolium bromide]. A stock solution of the synthesized compound ( $50 \mu\text{g mL}^{-1}$ ) in DMSO was prepared and quantities of the test compounds were incorporated in specified quantity of sterilized liquid MH medium. A specified quantity of the medium containing the compound was poured into microtitration plates. A suspension of the microorganism was prepared to contain approximately  $10^5 \text{ cfu mL}^{-1}$  and applied to micro-titration plates with serially diluted compounds in DMSO to be tested and incubated at  $37^\circ\text{C}$  for 24 h. After the MICs were visually determined on each of the micro-titration plates,  $50 \mu\text{L}$  of PBS (phosphate buffered saline  $0.01 \text{ mol L}^{-1}$ , pH 7.4:  $\text{Na}_2\text{HPO}_4$  2.9 g,  $\text{KH}_2\text{PO}_4$  0.2 g, NaCl 8.0 g, KCl 0.2 g, distilled water 1000 mL) containing 2 mg of MTT per  $\text{mL}^{-1}$  was added to each well. Incubation was continued at room temperature for 4–5 h. The content of each well was removed and  $100 \mu\text{L}$  of isopropanol containing 5% HCl ( $1 \text{ mol L}^{-1}$ ) was added to extract the dye. After 12 h of incubation at room temperature, the optical density (OD) was measured with a microplate reader at 550 nm.

## 3. Results and Discussion

### 3. 1. Synthesis

The complexes were prepared by reaction of equimolar quantities of the Schiff base ligands with zinc bromide and sodium azide in methanol. It is interesting that the azide anion did not coordinate to the Zn atom in complex

1, and the bromide anion did not coordinate to the Zn atom in complex 2. Crystals of the complexes are stable in air, and soluble in methanol, ethanol, DMF and DMSO, insoluble in water. The molar conductance of the complexes is  $27 \Omega^{-1} \text{ cm}^2 \text{ mol}^{-1}$  for 1 and  $19 \Omega^{-1} \text{ cm}^2 \text{ mol}^{-1}$  for 2, indicating that the complexes are non-electrolytes.

### 3. 2. Description of the Structure of Complex 1

Complex 1 is a phenolate oxygen bridged dinuclear zinc(II) compound, with the Zn...Zn distance of  $3.492(2) \text{ \AA}$  (Figure 1). The molecule of the complex possesses crystallographic inversion center symmetry, with the inversion center located at the midpoint of the two Zn atoms. The Zn atom is in octahedral coordination, with the phenolate oxygen and imino nitrogen of one Schiff base ligand defining the equatorial plane, and with the phenolate oxygen of the other Schiff base ligand and one water O atom occupying the axial positions. The Zn–O and Zn–N bond lengths in the equatorial plane involving donor atoms from the Schiff base ligand are Zn1–O1  $2.0519(18) \text{ \AA}$ , Zn1–O2  $2.0073(17) \text{ \AA}$ , Zn1–N1  $2.091(2) \text{ \AA}$ , and Zn1–N2  $2.126(2) \text{ \AA}$ . The Zn–O bond lengths in the axial positions are Zn1–O3  $2.201(2) \text{ \AA}$  and Zn1–O1A  $2.560(2) \text{ \AA}$ , which are much longer than those in the equatorial plane. The Zn–O and Zn–N bond lengths in the complex are comparable to those reported for Schiff

Table 3. Hydrogen bond distances ( $\text{\AA}$ ) and bond angles ( $^\circ$ ) for complex 1

D–H...A	$d(\text{D–H})$	$d(\text{H...A})$	$d(\text{D...A})$	Angle (D–H...A)
O3–H3A...F1 <sup>#</sup>	0.85(1)	2.27(2)	3.057(3)	155(3)
O3–H3A...O1 <sup>#</sup>	0.85(1)	2.44(3)	3.099(3)	135(3)
O3–H3B...O2 <sup>#</sup>	0.85(1)	1.96(2)	2.746(3)	155(3)
O3–H3B...F3 <sup>#</sup>	0.85(1)	2.52(3)	3.119(3)	128(3)

Symmetry code for #:  $1 - x, 1 - y, 1 - z$ .

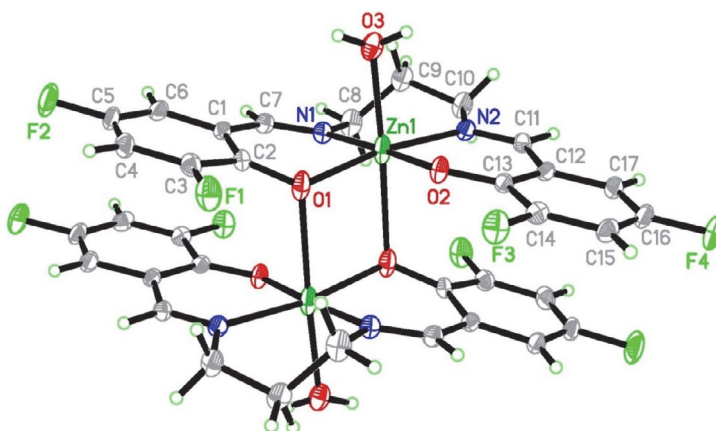


Figure 1. Molecular structure of complex 1, with 30% thermal probability. Unlabeled atoms are at the symmetry position  $-x, 1 - y, 1 - z$ .

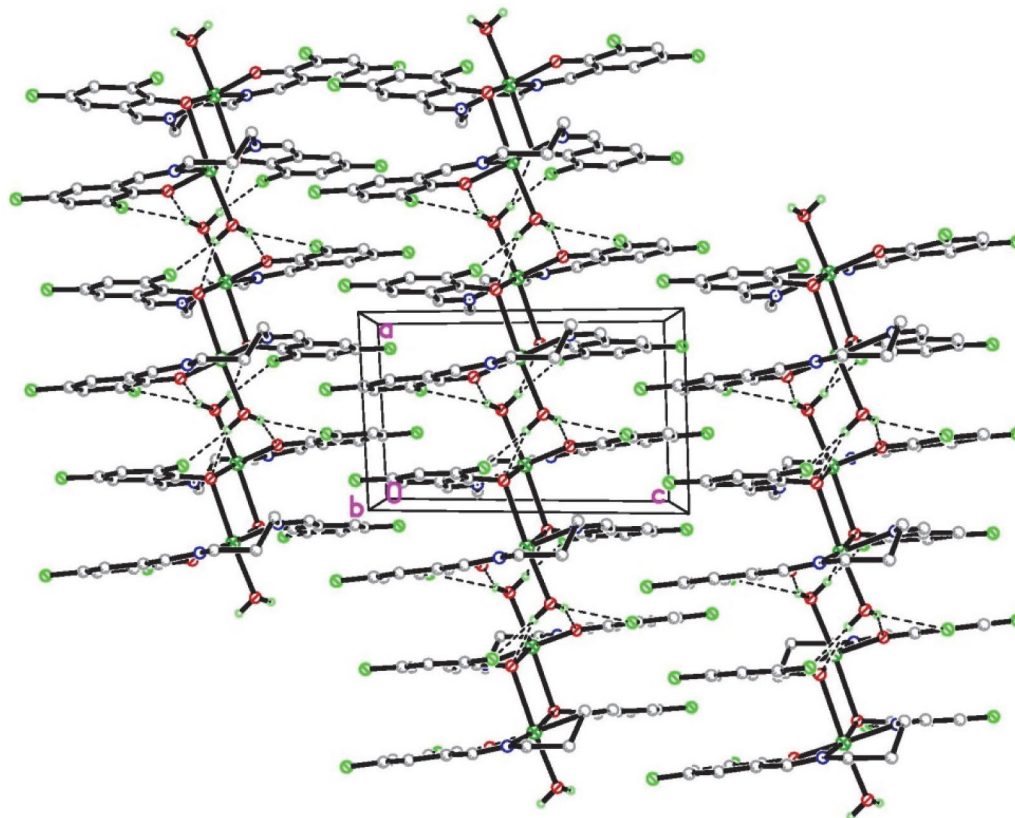


Figure 2. The hydrogen linked structure of complex 1, viewed along the axis-*b* direction. Hydrogen bonds are shown as dashed lines.

base zinc(II) complexes.<sup>8</sup> As is apparent from Table 2, there are only slight deviation from an ideal octahedral geometry, with all *cis* angles within 7° of 90°, with the exception of the chelating O1–Zn1–O1A angle of 82.17(9)°. The four atoms in the equatorial plane, O1, O2, N1 and N2, are approximately in a plane, with mean deviation of 0.082(3) Å, and with the Zn atom being 0.086(2) Å from the plane in the direction of O3.

In the crystal structure of the complex, the water ligands participate in the hydrogen bonds with the phenolate oxygen and fluorine groups of the Schiff base ligands. The molecules are linked through O–H...O and O–H...F hydrogen bonds (Table 3), to form chains running along the *a* axis (Figure 2).

### 3. 3. Description of the Structure of Complex 2

Complex 2 is an end-on azido-bridged polynuclear zinc(II) compound, with the Zn...Zn distance of 3.533(2) Å (Figure 3). The Zn atom is in a trigonal bipyramidal coordination, with the imino nitrogen of the Schiff base ligand and two azido nitrogen defining the basal plane, and with the phenolate oxygen and amino nitrogen occupying the axial positions. The Zn–N bond lengths in the basal plane involving donor atoms from the Schiff base and azide ligands are Zn1–N1 2.055(8) Å, Zn1–N3 2.053(8) Å,

and Zn1–N3B 2.097(8) Å. The Zn–O and Zn–N bond lengths in the axial positions are Zn1–O1 2.024(8) Å and Zn1–N2 2.280(9) Å. The Zn–O and Zn–N bond lengths in the complex are similar to those of complex 1, and also comparable to those reported for Schiff base zinc(II) com-

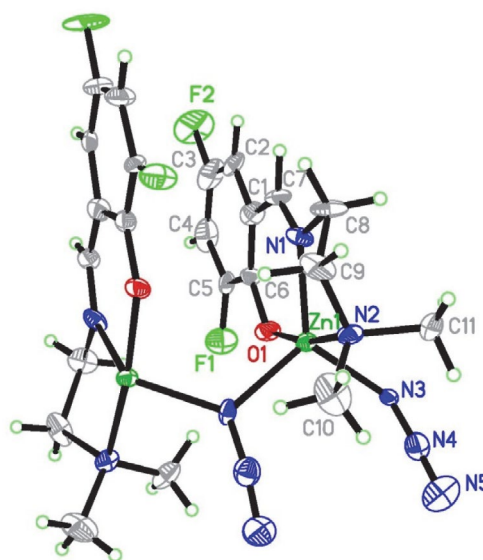


Figure 3. Molecular structure of complex 2, with 30% thermal probability. Unlabeled atoms are at the symmetry position  $x, \frac{1}{2} - y, \frac{1}{2} + z$ .

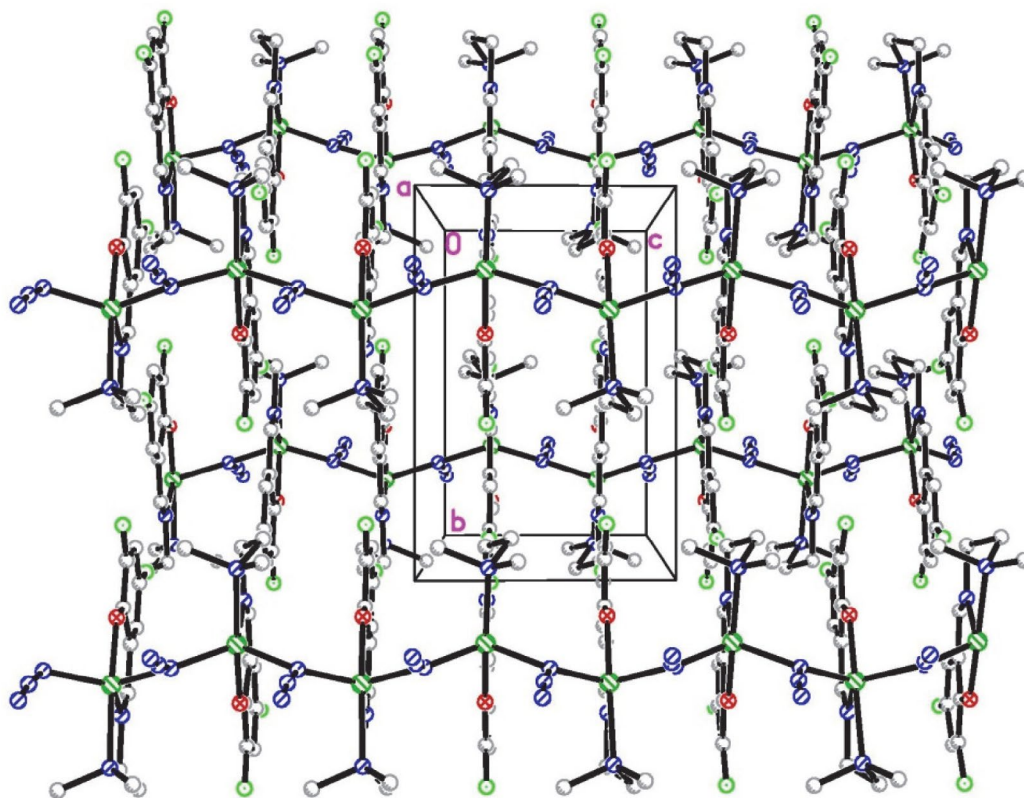


Figure 4. The end-on azido bridged polynuclear structure of complex 2, viewed along the axis-*a* direction.

plexes.<sup>9</sup> As is apparent from Table 2, there are only slight deviation from an ideal trigonal bipyramidal geometry, with the angles at the basal plane within 12° of 120°. The three atoms in the basal plane, N1, N3 and N3B, are coplanar, and with the Zn atom being 0.060(2) Å from the plane in the direction of O1. The [ZnL<sup>2</sup>] moieties are linked through end-on azido bridges, to form chains running along the *c* axis (Figure 4).

The question arises as to whether the coordination polyhedron around the five-coordinated zinc atom can be described as a distorted square pyramid or a distorted trigonal bipyramid. Further information can be obtained by determining the structural index  $\tau$  which represents the relative amount of trigonality (square pyramid,  $\tau = 0$ ; trigonal bipyramid,  $\tau = 1$ );  $\tau = (\beta - \alpha)/60^\circ$ ,  $\alpha$  and  $\beta$  being the two largest angles around the central atom.<sup>10</sup> The values of  $\tau$  is 0.70. The coordination geometry of the zinc atom in this complex is therefore approximately described as a trigonal bipyramid.

### 3. 4. Spectral Characterization

In the infrared spectra of the complexes, the bands corresponding to the azomethine (CH=N) groups are observed at 1638 cm<sup>-1</sup> for **1** and 1642 cm<sup>-1</sup> for **2**.<sup>11</sup> The typical absorptions for the azide ligand in **2** is located at 2052 cm<sup>-1</sup>.<sup>12</sup> The appearance of the band at 1353 cm<sup>-1</sup> indicates

the asymmetric nature of the azide groups in complex **2**. The weak and broad band centered at 3512 cm<sup>-1</sup> for **1** is ascribed to the O–H vibrations of the water ligands. The weak bands in the region of 420–570 cm<sup>-1</sup> for the complexes can be assigned to  $\nu(\text{Zn–N})$  and  $\nu(\text{Zn–O})$ . The electronic spectra of the complexes were recorded using the methanol as solvent. The absorptions appear in the range 270–380 nm are most likely due to the  $\pi \rightarrow \pi^*$  transitions and ligand-to-metal charge transfer.

### 3. 5. Antibacterial Activity

The complexes were screened for antibacterial activity against *B. subtilis* ATCC 6633, *E. coli* ATCC 35218, *P. putida* TS 1138 and *S. aureus* ATCC 25923 by the MTT method. The MIC values of the complexes against these bacteria are presented in Table 4. The antibiotic Penicillin was included as a reference. In general, the two zinc complexes have effective activities against the bacteria *B. subtilis* and *S. aureus*, medium activity against *E. coli*, and weak activity against *P. putida*. It is interesting that for *B. subtilis*, complex **1** has the most activity with MIC value of 0.39  $\mu\text{g mL}^{-1}$ , and for *S. aureus*, complexes **1** and **2** have effective activity with MIC values of 0.39 and 0.78  $\mu\text{g mL}^{-1}$ , respectively. So, the complexes showed a wide range of bactericidal activities against the bacteria, more potent than, or similar with, commercial antibiotic Penicillin.

**Table 4.** MIC ( $\mu\text{g mL}^{-1}$ ) values of the antibacterial activity of the complexes

Compound	<i>B. subtilis</i>	<i>E. coli</i>	<i>P. putida</i>	<i>S. aureus</i>
1	0.39	12.5	25.0	0.39
2	1.56	25.0	50.0	0.78
Penicillin	0.78	>100	12.5	3.13

## 4. Conclusion

A new phenolate oxygen bridged dinuclear zinc(II) complex and a new end-on azido-bridged polynuclear zinc(II) complex have been prepared and structurally characterized in this article. The dianionic Schiff base ligand in the phenolate oxygen bridged complex coordinates to the Zn atom through the phenolate oxygen and imino nitrogen. The monoanionic Schiff base ligand in the end-on azido bridged complex coordinates to the Zn atom through the phenolate oxygen, imino nitrogen and amino nitrogen. During the self-assembly of the complexes, the bis-Schiff base zinc complex choose the neutral water molecule as co-ligand, while the mono-Schiff base zinc complex choose the azide as co-ligand. The complexes have strong antibacterial activity against *B. subtilis* and *S. aureus*.

## 5. Supplementary Data

Crystallographic data for the analysis have been deposited with the Cambridge Crystallographic Data Centre, CCDC Nos. 1848822 (1) and 1848823 (2). Copies of this information may be obtained free of charge from CCDC, 12 Union Road, Cambridge CB2 1EZ, UK (fax: +44 1223 336 033; e-mail: deposit@ccdc.cam.ac.uk or www: http://www.ccdc.cam.ac.uk).

## 6. Acknowledgments

This work was supported by Zhengzhou University of Light Industry.

## 7. References

- (a) R. A. Baglia, J. P. T. Zaragoza, D. P. Goldberg, *Chem. Rev.* **2017**, *117*, 13320–13352; DOI:10.1021/acs.chemrev.7b00180  
(b) S. E. Sherman, Q. Xiao, V. Percec, *Chem. Rev.* **2017**, *117*, 6538–6631; DOI:10.1021/acs.chemrev.7b00097  
(c) A. J. Jasniewski, L. Que, *Chem. Rev.* **2018**, *118*, 2554–2592. DOI:10.1021/acs.chemrev.7b00457
- (a) A. Hazari, C. Diaz, A. Ghosh, *Polyhedron* **2018**, *142*, 16–24; DOI:10.1016/j.poly.2017.12.022  
(b) D. Bandyopadhyay, M. Layek, M. Fleck, R. Saha, C. Rizzoli, *Inorg. Chim. Acta* **2017**, *461*, 174–182; DOI:10.1016/j.ica.2017.02.018  
(c) M. Zhang, D.-M. Xian, N. Zhang, Z.-L. You, *J. Coord. Chem.* **2012**, *65*, 1837–1846. DOI:10.1080/00958972.2012.684383
- (a) A. B. Deilami, M. Salehi, A. Arab, A. Amiri, *Inorg. Chim. Acta* **2018**, *476*, 93–100; DOI:10.1016/j.ica.2018.02.013  
(b) T. Basak, K. Ghosh, C. J. Gomez-Garcia, S. Chattopadhyay, *Polyhedron* **2018**, *146*, 42–54; DOI:10.1016/j.poly.2017.12.040  
(c) J. Wang, D. Qu, J.-X. Lei, Z. You, *J. Coord. Chem.* **2017**, *70*, 544–555; DOI:10.1080/00958972.2016.1262538  
(d) L.-X. Li, Y. Sun, Q. Xie, Y.-B. Sun, K.-H. Li, Z.-L. You, *Chinese J. Inorg. Chem.* **2016**, *32*, 369–376.
- (a) G. Kumaravel, P. P. Utthra, N. Raman, *Bioorg. Chem.* **2018**, *77*, 269–279; DOI:10.1016/j.bioorg.2018.01.024  
(b) S. M. Daskalova, X. H. Bai, S. M. Hecht, *Biochem.* **2018**, *57*, 2711–2722. DOI:10.1021/acs.biochem.8b00308
- (a) Z. H. Chohan, M. Arif, A. Rashid, *J. Enzyme Inhib. Med. Chem.* **2008**, *23*, 785–796; DOI:10.1080/14756360701450145  
(b) H. T. Y. L. K. Wah, S. Bangarigadu-Sanasy, *Asian J. Chem.* **2013**, *25*, 9221–9225;  
(c) H. Keypour, A. Shooshtari, M. Rezaeivala, F. Mohsenzadeh, H. A. Rudbari, *Transition Met. Chem.* **2015**, *40*, 715–722;  
(d) W. G. Zhang, J. H. Liang, *Russ. J. Coord. Chem.* **2017**, *43*, 540–546.
- (a) G. G. Mohamed, E. M. Zayed, A. M. M. Hindy, *Spectrochim. Acta A-Mol. Biomol. Spectrosc.* **2015**, *145*, 76–84; DOI:10.1016/j.saa.2015.01.129  
(b) M. Salehi, A. Amoozadeh, A. Salamatmanesh, M. Kubicki, G. Dutkiewicz, S. Samiee, A. Khaleghian, *J. Mol. Struct.* **2015**, *1091*, 81–87; DOI:10.1016/j.molstruc.2015.02.060  
(c) A. Goszczynska, H. Kwiecien, K. Fijalkowski, *Med. Chem. Res.* **2015**, *24*, 3561–3577; DOI:10.1007/s00044-015-1397-6  
(d) A. E. Amr, M. A. Al-Omar, *Russ. J. Gen. Chem.* **2016**, *86*, 161–166. DOI:10.1134/S1070328417080085 DOI:10.1134/S1070363216010254
- G. M. Sheldrick, *Acta Crystallogr.* **2008**, *A64*, 112–122. DOI:10.1107/S0108767307043930
- (a) H. Keypour, A. Shooshtari, M. Rezaeivala, F. Mhosenzadeh, H. A. Rudbari, *Transition Met. Chem.* **2015**, *40*, 715–722;  
(b) M. Montazerzohori, S. Farokhiyani, A. Masoudiasl, J. M. White, *RSC Adv.* **2016**, *6*, 23866–23878;  
(c) S. Shit, M. Nandy, D. Saha, L. Zhang, W. Schmitt, C. Rizzoli, T. N. G. Row, *J. Coord. Chem.* **2016**, *69*, 2403–2414; DOI:10.1080/00958972.2016.1197390  
(d) J. Qin, Z. N. Xia, Y. Zhang, F. Niu, Z. L. You, H. L. Zhu, *Synth. React. Inorg. Met.-Org. Nano-Met. Chem.* **2016**, *46*, 1805–1809; DOI:10.1080/15533174.2015.1137065  
(e) J. Qin, Y. Sun, Z. N. Xia, Y. Zhang, X. L. Zhao, Z. L. You, H. L. Zhu, *Russ. J. Coord. Chem.* **2016**, *42*, 330–337. DOI:10.1134/S1070328416050055
- (a) S. Saeednia, P. Iranmanesh, M. H. Ardakani, M. Mohammedi, G. Norouzi, *Mater. Res. Bull.* **2016**, *78*, 1–10; DOI:10.1016/j.materresbull.2016.02.010  
(b) M. A. Aldamen, N. Charef, H. K. Juwhari, K. Sweidan,

- M. S. Mubarak, D. G. Peters, *J. Chem. Crystallogr.* **2016**, *46*, 411–420; DOI:10.1007/s10870-016-0670-y
- (c) M. Jafari, M. Salehi, M. Kubicki, A. Arab, A. Khaleghian, *Inorg. Chim. Acta* **2017**, *462*, 329–335; DOI:10.1016/j.ica.2017.04.007
- (d) D. Majumdar, J. K. Biswas, M. Mondal, M. S. S. Babu, R. K. Metre, S. Das, K. Bankura, D. Mishra, *J. Mol. Struct.* **2018**, *1155*, 745–757. DOI:10.1016/j.molstruc.2017.11.052
10. A. W. Addison, T. N. Rao, J. Reedijk, J. van Rijn, G. C. Verschoor, *J. Chem. Soc. Dalton Trans.* **1984**, 1349–1356. DOI:10.1039/DT9840001349
11. S. A. Patil, V. H. Naik, A. D. Kulkarni, P. S. Badami, *Spectrochim. Acta A*, **2010**, *75*, 347–354. DOI:10.1016/j.saa.2009.10.039
12. S. Jana, P. Bhowmik, M. Das, P. P. Jana, K. Harms, S. Chattopadhyay, *Polyhedron* **2012**, *37*, 21–26. DOI:10.1016/j.poly.2012.01.031

## Povzetek

Sintetizirali smo dva cinkova(II) kompleksa,  $[\text{Zn}_2(\text{L}^1)_2(\text{OH})_2]$  (**1**) in  $[\text{ZnL}^2(\mu_{1,1}\text{-N}_3)]_n$  (**2**), kjer je  $\text{L}^1$  dianionska oblika  $N,N'$ -bis(3,5-difluoro-2-hidroksibenziliden)-1,3-diaminopropana, in  $\text{L}^2$  monoanionska oblika 2-[(2-dimetilaminoetil-imino)metil]-4,6-difluorofenola, ter ju okarakterizirali z elementno analizo, IR in UV-Vis spektroskopijo ter rentgensko difrakcijo. V kompleksu **1** je Zn atom oktaedrično koordiniran z donorskimi atomi liganda Schiffove baze  $\text{L}^1$  in enim kisikovim atomom molekule vode. V kompleksu **2** je Zn atom trikotno-bipiramidalno koordiniran s tremi donorskimi atomi Schiffove baze  $\text{L}^2$  in dveh atomov dušika z azidnih ionov. Kompleksa izkazujeta močno protibakterijsko aktivnost proti *B. subtilis* in *S. aureus*.

Scientific paper

# Synthesis, Characterization and Application of Disodium Tetraborate Cross-Linked Polyvinyl Alcohol Membranes for Pervaporation Dehydration of Ethylene Glycol

Haresh K. Dave and Kaushik Nath

New Separation Laboratory, Department of Chemical Engineering G H Patel College of Engineering & Technology (Gujarat Technological University) Vallabh Vidyanagar-388120

\* Corresponding author: E-mail: kaushiknath@gcet.ac.in (K Nath)

Received: 01-07-2018

## Abstract

Dehydration of ethylene glycol-water mixture was carried out in a laboratory pervaporation unit using a flat sheet membrane test cell. Polyvinyl alcohol-polyether sulfone (PVA-PES) composite membranes were synthesized and cross linked with two different concentrations, viz 0.2 and 0.5% of disodium tetraborate (borax). The derived membranes were extensively characterized for their morphology, intermolecular interactions, thermo-mechanical stability, and physicochemical properties using field emission scanning electron microscopy (FESEM), atomic force microscopy (AFM), Fourier transform infrared spectroscopy (FTIR), X-ray diffraction (XRD), thermogravimetric analysis (TGA), differential scanning calorimetry (DSC) and water uptake studies. The membrane performance was evaluated in terms of pervaporation flux, separation factor, selectivity, permeability and solute diffusion coefficients of EG-water mixture at varying feed flow rate. Both in terms of flux and separation factor PVA-PES-0.2% borax composite membrane was found superior to PVA-PES-0.5% borax crosslinked and its uncrosslinked counterpart. Cross-linking the composite with borax produced a membrane with lower crystallinity and a smaller swelling degree, but having improved thermostability and mechanical properties.

**Keywords:** Pervaporation; membrane; swelling, flux; selectivity; separation factor, diffusion coefficient

## 1. Introduction

Pervaporation is much touted as an efficient and environmentally benign separation process both as a stand-alone unit and a supplementary to the distillation. It has been the focus of basic and applied research encompassing the membrane modification, process performance evaluation and exploration of newer areas of applications for more than three decennia. Herein we report the dehydration of ethylene glycol (EG) – a widely used precursor in organic chemical industries for the manufacturing of unsaturated polyester resins, polyacetate fibers, plasticizers antifreezing agents, lubricants, non-ionic surfactants, brake fluid, solvent and so on. Currently, direct hydration of ethylene oxide, i.e. the pressurized hydration process is the preferred route for the commercial production of EG.<sup>1</sup> The process entails the addition of excess amount of water (about 10–25 times the molar quantity of ethylene oxide) to raise the selectivity of ethylene oxide to the EG. There-

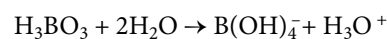
fore, the concentration of the EG obtained after completion of the reaction is at most around 10–20% by weight. EG (boiling point: 198 °C) dehydration by traditional multistage evaporation and distillation is highly energy intensive, requiring high pressure steam for reboiler. Here comes the importance of an alternative dehydration protocol for EG-water mixture. Several recent studies have evaluated a number of pervaporative dehydration processes of EG using an assortment of polymeric or ceramic membranes. Some of these recently used membranes include polyvinyl alcohol/hyper-branched polyester,<sup>2</sup> polyvinyl alcohol/polypropylene,<sup>3</sup> polyamide/polydopamine,<sup>4</sup> polybenzimidazole/polyetherimide,<sup>5</sup> polyvinyl alcohol-Na-zeolite mixed matrix membrane,<sup>6</sup>  $\gamma$ -alumina-Na-zeolite,<sup>7</sup> Na-A zeolite,<sup>8</sup> polyvinylamine/polyvinyl alcohol-carbon nanotube<sup>9</sup> and so on. Wu et al. (2015) reported a novel polymer of intrinsic microporosity for the separation of EG – water with separation factor of 24.2.<sup>4</sup> Rao et al. (2007)

prepared a cross-linked chitosan membrane with a very high separation factor of 234 in the pervaporation of EG-water mixture at 30 °C.<sup>10</sup> In essence, most of these works underscore the need for the optimization of the membrane formation conditions for solute transport which is largely a function of the binding interface between active and support layers.

Modification of the support layer surface of a thin film composite membrane towards a more facile permeation of the solute poses a technical challenge in the pervaporation membrane fabrication. Typically water permselective composite membranes consist of a hydrophilic active layer imparting permeability and selectivity on a hydrophobic support layer having swelling resistance propensity.<sup>11</sup> Alleviating the surface tension and improving the interfacial interactions between these two layers have become a standard approach of the tailor-made membrane fabrication. Imparting hydrophilicity on the surface of the support layer as well as on to the bulk,<sup>12,13</sup> incorporation of a coupling agents or surfactants<sup>14</sup> are some of the ways in order to reap the benefit of trans-layer interfacial interaction. Additionally a strong adhesive strength between active and support layers is another prerequisite of an efficient composite membrane failing which the support layer may get peeled off and dissolve into aqueous solution. For polyvinyl alcohol (PVA) based pervaporation membranes incorporation of an interfacial cross linking agent can not only counter the inherent swelling susceptibility of PVA to ensure that the contaminants in water can be retained, but also minimize compaction under pressure while used in other pressure driven processes.<sup>15</sup> There is a challenge for any membrane to achieve high permeate flux but not at expense of its stability and mechanical properties.

Although a growing body of literature in recent years has investigated the structural, mechanical, and thermal properties of different polymeric hydrogels, disodium tetraborate (borax) cross-linked polyvinyl alcohol composite membrane for pervaporative separation of

EG-water solution has not been extensively focused so far to the best of our knowledge. The impetus for the present work was stimulated firstly by the potential advantage of pervaporation for efficient concentration of EG from wastewater, and secondly to obtain a further insight into the permeation properties of a novel type cross linked composite membrane. The rationale of incorporating borax as a cross linking agent for PVA stems from the premise of its di-diol complexation reaction with PVA resulting in significant enhancement of its malleability. Disodium tetraborate acts as cross linking agent to bind PVA chain together. This results in the solidification of polyvinyl alcohol and trapping of water molecules, forming a slimy mass. Sodium borate dissolve in water to form boric acid, which then accepts a hydroxide from water to become  $B(OH)_4^-$ .



$B(OH)_4^-$  then reacts in a condensation reaction with polyvinyl alcohol as indicated in Fig. 1 Water from this condensation reaction as well as the excess water from the two solution gets trapped in the cross linked polymer which produces slimy, flexible properties. Polyvinyl alcohol- polyether sulfone (PVA-PES) composite membranes were synthesized using two different concentrations of borax as cross linking agents. The as-prepared membranes were characterized by X-ray diffraction (XRD), Fourier transform infrared spectroscopy (FTIR), scanning electron microscopy (SEM), Atomic force microscopy (AFM), mechanical testing, moisture absorption, thermogravimetric analysis (TGA) and differential scanning calorimetry. The membrane performance was evaluated in terms of pervaporation flux, separation factor, selectivity, permeability and solute diffusion coefficients of EG-water mixture at varying feed flow rate. An attempt has been made to establish their structure-property correlation. The results obtained in the present study could provide additional in-

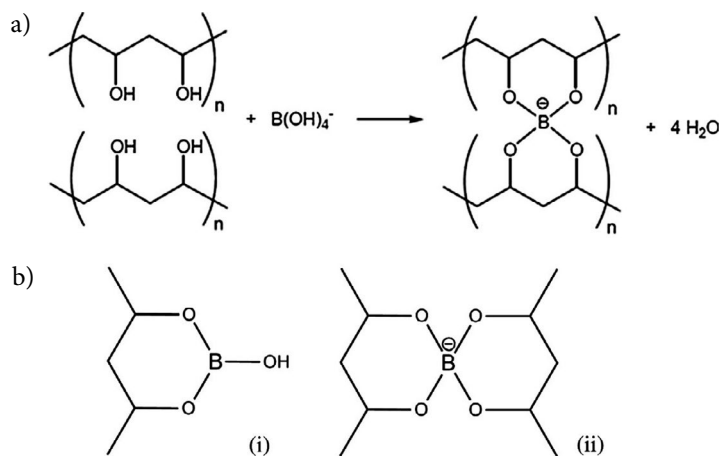


Fig. 1. Cross linking condensation reaction of polyvinyl alcohol with borax

put to the fundamental aspects of PVA-PES composites doped with borax for dehydration of EG on a commercial scale.

## 2. Experimental

### 2. 1. Chemicals

Polyvinyl alcohol (Average molecular mass 125,000 g/mol and degree of hydrolysis 99%) granules, ethylene glycol and disodium tetraborate (borax) (AR grade) was purchased from S D. Fine-Chem, Mumbai, India and were used as received without additional processing. Stock solutions were prepared with deionized water obtained from a reverse osmosis system, having conductivity of 20  $\mu\text{S}/\text{cm}$ . Poly ether sulfone (PES) support membrane swatch was kindly provided by M/s Permionics Membrane Pvt. Ltd, Baroda, India. The PES ultrafiltration membrane (molecular weight cutoff of 25,000) was of asymmetric structure supported by nonwoven polyester fabric.

### 2. 2. Preparation and Cross Linking of Membrane

The 4% by weight PVA solution was prepared by slowly stirring 4 g of polyvinyl alcohol powder into 96 mL of hot distilled water at approximately 80 °C using magnetic stirrer. The solution was then allowed to stand in a covered container. At the same time 0.2% and 0.5% by weight sodium borate solutions were prepared by dissolving requisite amount of sodium borate decahydrate (borax) in distilled water. The as-prepared PVA solution was poured into a styrofoam cup and stirred in the sodium borate solution. The PES ultrafiltration support membranes were soaked in double distilled water for 24 h to remove any adherent solvent and then fully dried. The dried PES support layer was then dipped into PVA-Borax slime for 15 min to enhance the hydrophilicity and was subsequently pressed through a heated roller to give the uniform thickness. Dip-coating was repeated twice to ensure a complete coverage of the support layer and to minimize morphological defects. The as-prepared composite membrane was finally dried for around 24 h at ambient temperature.

### 2. 3. Pervaporation Experiment

Pervaporation experiments were conducted in a small laboratory set-up the schematic representation of which is described elsewhere.<sup>16</sup> The model feed solution was prepared by making four different (50, 60, 70 and 80% by volume) concentrations of EG in deionized water. The as-prepared feed was allowed to circulate continuously in contact with the membrane using a peristaltic pump from a feed tank provided with a thermostat to maintain the constant temperature of 60 °C.

Effect of flow rate on permeation flux, separation factor and diffusion coefficient were investigated by varying feed flow rate but at constant initial feed concentration and temperature. Prior to the pervaporation experiment, the membrane was allowed to equilibrate for 3 h. The sample was collected after 2 h and the pervaporate compositions were analyzed by measuring its water content using an automated Karl Fisher Apparatus. Each of the pervaporation experiments was repeated two times and the results were averaged to minimize error. The experimental data points were reproducible with errors less than 5%.

### 2. 4. Contact Angle Measurement

The wettability of the prepared membranes used in the present study was analyzed by measuring contact angle using the sessile drop method with an optical Tensiometer. Water droplet of about 2  $\mu\text{L}$  of distilled water with a tight syringe was placed on the clean and dry membrane samples and the droplet was imaged. Each equilibrium contact angle was the average of the left and right contact angles, and the reported values are the average of three equilibrium contact angles.

### 2. 5. Thermogravimetric Analysis (TGA) and Differential Scanning Calorimetry

The thermal degradation propensity of the as-prepared membranes were assessed as a function of increasing temperature with a TGA 2050 'Thermogravimetric Analyzer (TA Instruments)', with a ramp of 5 °C/min at the temperature ranging from 40 to 900 °C, under nitrogen atmosphere. The weight of the samples taken was around 10 mg. The glass transition temperature  $T_g$  was measured by means of the extrapolated onset temperature using an in-built data analysis software.

### 2. 6. Fourier Transform Infrared Spectroscopy (FTIR)

The presence of organic functional groups on the membrane surface was analyzed by the Fourier transform infrared spectroscopy (Perkin Elmer Spectrum GX) using a wave number range of 400–4000  $\text{cm}^{-1}$  at a resolution of 4.0  $\text{cm}^{-1}$  with an acquisition time of 1 min. The test chamber was nitrogen purged at a flow rate of 10  $\text{mL min}^{-1}$  to avoid signal interference from the surrounding moisture and  $\text{CO}_2$ . At least 2 replicates were obtained for each sample type without applying any baseline corrections.

### 2. 7. AFM Analysis

Atomic force microscopy (AFM) was carried out using a NT-MDT NTEGRA Aura Autoprobe CP atomic force microscope. Measurements were performed on dry membrane samples under ambient atmospheric condi-



tions. Silicon cantilevers with integrated pyramidal tips were used to image membrane surface topography. The membrane surfaces with a scan size of  $5\ \mu\text{m} \times 5\ \mu\text{m}$  were imaged in tapping mode. After image acquisition the surface roughness parameter in terms of root mean square (RMS) roughness was calculated from the AFM images using an AFM image processing toolbox.

## 2. 8. FESEM Analysis

The topology of the top surface and the cross section of the prepared membranes were investigated via field emission scanning electron microscopy (FE-SEM) using JEOLFE-SEM (JSM-6701F) at 5kV under different magnifications. For cross sectional analysis, cryogenically fractured membrane samples under liquid  $\text{N}_2$  were freeze-dried overnight and sputtered with a thin layer of platinum using JEOL JFC-1600 auto fine coater.

## 2. 9. XRD Analysis

The crystallinity of the composite polymer membranes were examined using X-Pert-MPD (Philips, Holland) X-ray diffractometer (XRD) with Cu K radiation of wavelength  $\lambda = 1.54056\ \text{\AA}$  in the range  $5^\circ \leq 2\theta \leq 50^\circ$ . The X-ray generator was operated at an excitation voltage of 45 kV and a current of 40 mA.

## 2. 10. Mechanical Properties

Tensile strength, elongation at break and modulus of elasticity of the membranes used in the present work were measured using Universal Testing Machine (UTM) (Simadzu AG 100 KNG, Japan) tested at room temperature. Rectangular strips of 6 mm width were cut out from the polymer membrane. The strips were well gripped using thick paper during the measurement of tensile strength. The length of the specimens was 250 mm, the thickness of the specimens was around 0.1 mm and the thickness was uniform to within 5% of the thickness between the grips. The load was set to maximum with a constant cross head speed of 1 mm/min.

## 2. 11. Degree of Swelling Measurement

Percent degree of swelling of the prepared membranes were determined by dipping the membrane specimens into the feed solution having different concentration of EG at ambient temperature kept overnight to ensure equilibrium. The membrane specimens were then taken out and the residual surface water was wiped out smoothly by a tissue paper. The degree of swelling (DS) was estimated using Eq (1)

$$\%DS = \frac{W_2 - W_1}{W_1} \times 100 \quad (1)$$

where  $W_1$  and  $W_2$  are the weight of swollen and dry membranes respectively.

## 2. 12. Flux and Separation Factor

The performance of pervaporation process can be determined by mainly two parameters, namely, the separation factor and the permeant flux. Using a general approach of mass transport through membranes, the flux for the compound  $i$  ( $J_i$ ) is expressed as compound  $i$  in volume or mass divided by the permeating time and the membrane area. In gas separation, flux is normally given as a molar flux ( $j_i$ ) with units  $\text{cm}^3$  (STP)/ $\text{cm}^2$  s or  $\text{m}^3$ (STP)/ $\text{m}^2$  s. Ignoring simple numerical conversion terms ( $\text{m}^2$  to  $\text{cm}^2$ , h to s), it is expressed as Eq (2)

$$J_i = j_i \frac{M_i}{v_i} \quad (2)$$

Where  $v_i$  is the molar volume of component  $i$  (22.4 l (STP)/mol) and  $M_i$  is the molecular weight of component  $i$ . The separation factor ( $\beta$ ) can be defined as the ratio of the molar component concentrations in the fluids on either side of the membrane. Hence:

$$\beta = \frac{y_i(1-x_i)}{x_i(1-y_i)} \quad (3)$$

Where ' $x_i$ ' and ' $y_i$ ' represent the feed and permeate concentrations of the faster permeating component  $i$  which is water in the present case.

## 2. 13. Permeability and Membrane Selectivity

The volumetric permeability ( $P_{m,i}$ ), (or permeability coefficient) and selectivity ( $\alpha$ ) (or ideal membrane separation factor) are the intrinsic properties of membranes under study and are independent from operating conditions (feed composition, feed stream, fluid dynamics, and permeate pressure). Following the solution-diffusion mechanism, it is defined as the transport flux of material through the membrane per unit driving force per unit membrane thickness, given as Eq. (4)<sup>17</sup>

$$P_{m,i} = J_i \frac{\delta}{(y_i x_i P_s - y_i P_p)} \quad (4)$$

Where  $P_{m,i}$  is the membrane permeability,  $\delta$  is the membrane thickness and  $g$  is the activity coefficient, which may be calculated using Van Laar equation. The mole fraction in the feed solution is denoted as  $x$ ,  $P_s$  is the saturated vapor pressure calculated with Antoine's equation,  $y$  is the mole fraction in the permeate and  $P_p$  is the permeate pressure obtained for the component during the PV experiment. It is generally denoted as Barrers (1 Barrer =  $1 \times 10^{-10}$   $\text{cm}^3$ (STP) $\text{cm}/\text{cm}^2$  s cm Hg) for the gas

separation. Alternatively, when the membrane thickness is not known, membrane permeance ( $P_{m,i}/\delta$ ), ratio of membrane permeability to membrane thickness can be used. Permeance is most commonly reported as gas permeation unit (gpu) ( $1 \text{ gpu} = 1 \times 10^{-6} \text{ cm}^3(\text{STP})\text{cm}/\text{cm}^2 \text{ s cm Hg}$ ).

The membrane selectivity is defined as the ratio of the permeabilities or permeances of components  $i$  and  $j$  through the membrane is given by Eq. (5)

$$\beta = \frac{P_{m,i}}{P_{m,j}} \quad (5)$$

Both selectivity and separation factor parameters quantify how compound  $i$  is preferably permeated through a certain membrane material when compared to the permeation of compound  $j$ .

## 2. 14. Diffusion Coefficient

In a binary mixture, Fick's law is often used to describe the binary diffusion, which can be expressed as

$$J_i = -D_i \frac{dC}{d\delta} \quad (6)$$

where  $J_i$  is the permeation flux of component  $i$  per unit area ( $\text{kg}/\text{m}^2\text{h}$ ),  $D_i$  is the diffusion coefficient of component  $i$  ( $\text{m}^2/\text{s}$ ),  $C$  is the concentration of permeant ( $\text{kg}/\text{m}^3$ ) and  $\delta$  (m) is the diffusion length or the thickness of the PVA active layer only, as diffusion is assumed to take place through this layer only. The concentration profile in this study is as-

sumed to be linear along the diffusion length. As a result, transport Eq (6) can be rewritten as<sup>16</sup>

$$D_i = \frac{J_i \delta}{C} \quad (7)$$

## 3. Results and Discussion

### 3. 1. FTIR Analysis

The systematic interpretation of the FTIR spectrum can be of great help in determining the presence of functional groups in the test samples. FTIR spectra of the cross linked composite membranes with two different concentration of borax over wave numbers of  $4000\text{--}400 \text{ cm}^{-1}$  are presented in Fig. 2. In the indicated wave number range, both the PES support-layer and PVA skin layers of the composite membranes could be sampled due to the relatively deep penetration depth ( $> 300 \text{ nm}$ ). Principal band assignments of FTIR spectra are presented in Table 1. Formation of PVA-PES composite membranes is modulated by the addition of a cross-linking agent, borax in the present study, which leads to the formation of esters with hydroxyl groups on the polymer network.<sup>18</sup> A close inspection of the FTIR spectra as presented in Figure 2 indicates the presence of a number of sharp, medium and broad peaks in the entire range of  $400\text{--}4000 \text{ cm}^{-1}$ . The sharp peaks at  $3438.52$  and  $3452.92 \text{ cm}^{-1}$  were observed due to O–H stretching vibration – an indicative of the presence of unreacted OH group, but this was partly broadened as a result of H-bonding interaction. The characteristic bands between  $2925$  and  $2934 \text{ cm}^{-1}$  are due to symmetric and

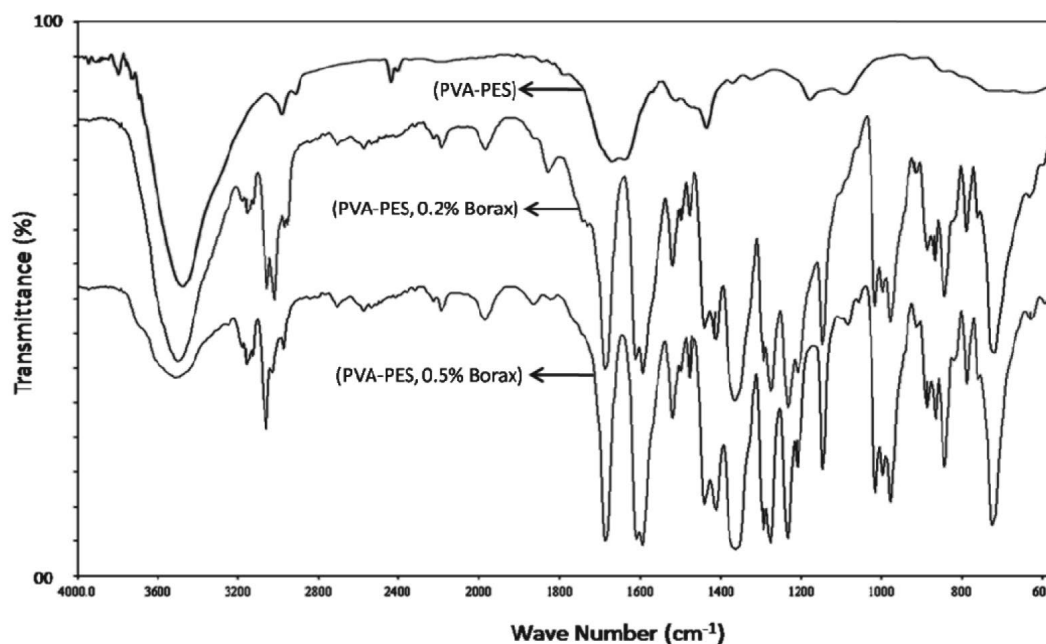


Fig. 2. FTIR spectra of PVA-PES composite membrane specimens cross linked with 0.2% and 0.5% borax as cross-linking agent used in the present study

**Table 1.** Principal band assignments of FTIR spectra over wave number 4000–400  $\text{cm}^{-1}$ 

Wave numbers ( $\text{cm}^{-1}$ )		Band Assignments
Crosslinked with 0.2% borax	Crosslinked with 0.5% borax	
3438	3452	O – H stretching vibration
2925	2968	C-H Stretching vibration
1738	1776	H–O–H bending (lattice, interstitial water)
1409.19	1409.06	Asymmetric stretching relaxation of B–O–C (Trigonal $\text{BO}_3$ group)
1364.24	1324	Asymmetric stretching relaxation of B–O–C (Tetrahedral $\text{BO}_4$ group)
1103.86, 1013.01	1106.07, 1073.52	Asymmetric stretching vibration of $\text{B}_4\text{--O}$
873.47	873.96	Symmetric stretching of $\text{B}_3\text{--O}$
854	853	Symmetric stretching of $\text{B}_4\text{--O}$
832	834	B–O stretching from residual $\text{B}(\text{OH})_4$
688.61	691.18	Bending of B–O–B linkages within borate network
834.33	877.92	In-phase out-of-plane hydrogen deformation of para-substituted phenyl groups
735	716	Out of plane bending of B–O–H
688	691	Symmetric pulse vibration of triborate and hexaborate anion.
558	565	Bending of $\text{B}_3\text{--O}$ and $\text{B}_4\text{--O}$

asymmetric C–H stretching vibrations. There was no major visible influence on peak intensity of C–H stretching bands in any of the composites. The spectra of the 0.2% and 0.5% borax cross-linked PVA-PES composites show a number of additional bands between 400–1400  $\text{cm}^{-1}$ . Two types of complexes can be formed between PVA and borate; trigonal and tetrahedral.<sup>19</sup> The band near 1409.19  $\text{cm}^{-1}$  is presumably due to the asymmetric stretching relaxation of B–O–C linkage in trigonal  $\text{BO}_3$  group, whereas that near 1324–1364  $\text{cm}^{-1}$  is due to asymmetric stretching relaxation of B–O–C in tetrahedral  $\text{BO}_4$  group. A rough comparison of peak of the two B–O–C stretching indicates that that trigonal complex have sharper and larger peaks and are more prominent within the membrane than their tetrahedral counterparts. The free hydroxyl groups on trigonal complexes for potential hydrogen bonding with PVA-PES composite leading to a dominant interaction system within the hydrogels. The bands in the vicinity of 1073–1103  $\text{cm}^{-1}$  are due to asymmetric stretching vibration of  $\text{B}_4\text{--O}$  bonds. The bands near 873.47–873.96  $\text{cm}^{-1}$  and 854–853  $\text{cm}^{-1}$  are due to symmetric stretching of  $\text{B}_3\text{--O}$  and  $\text{B}_4\text{--O}$  bonds respectively.<sup>20</sup> This band correlates to hydroxyl groups that have complexed (formed crosslinks) with borate ions and those involved in intermolecular hydrogen bonding. The peak at 2924  $\text{cm}^{-1}$  was attributed to CH stretching of the  $\text{CH}_2$  group.<sup>18</sup> A perusal of the spectra indicates the presence of certain principal bands in the cross-linked membranes, although some of them were diluted significantly or shifted to relatively to lower wave numbers as a result of cross linking complexation reaction. Although borax crosslinked PVA-PES composite membrane with two different proportion of borax exhibited peaks in the range of 1324–1409  $\text{cm}^{-1}$ , confirming cross-link formation, a considerable amount of the borate within these hydrogels appeared to preferentially form networks amongst themselves.

### 3. 2. Thermogravimetric Analysis

Heat resistance and thermal stability of the polymeric membranes as a function of increasing temperature (with constant heating rate) were studied using thermogravimetric analysis.

TGA characterizations of the cross-linked composite membranes having 0.2% and 0.5% borax cross linking are shown in Fig. 3. A perusal of TGA thermograms show that the weight loss for both the composite membranes started at about 380 °C. There were two consecutive stages of weight loss. The first weight loss starting at about 380 °C was mainly due to desorption of the adsorbed water molecules while the 2nd stage of weight loss from 400 °C to 450 °C was plausibly contributed by the elimination of the side groups or the thermal desulfonation. The first stage of weight loss was very small about 1.07% but the weight loss at second stage was significant (about 42.15%). A further weight loss of about 33.97% took place at the 3<sup>rd</sup> stage in the vicinity of 500 °C. This was corresponding to the degradation of the polymeric backbone.<sup>21,22</sup> At this temperature range, the degradation of PVA occurs, leading to the formation of water, acetaldehyde, acetone, ethanol, etc. In general the primary structural decomposition of PVA membranes occurs in the vicinity of 275 °C temperature but it shifted to nearly 380 °C for cross-linked PVA sample, suggesting considerable stability enhancement due to the formation of homogeneous cross linked layer. Clearly, cross linked PVA membrane used in the study imparted sufficient thermal stability. This was due the restriction of the amount of water inside the membrane network as a result of cross linking. Additionally, we notice that the difference in weight loss of the used PVA membrane after a repeated cycle of operation was not much different from the original membrane. Taken together, these findings implicate that that both the membranes possess considerable thermal stability over a wide temperature range.

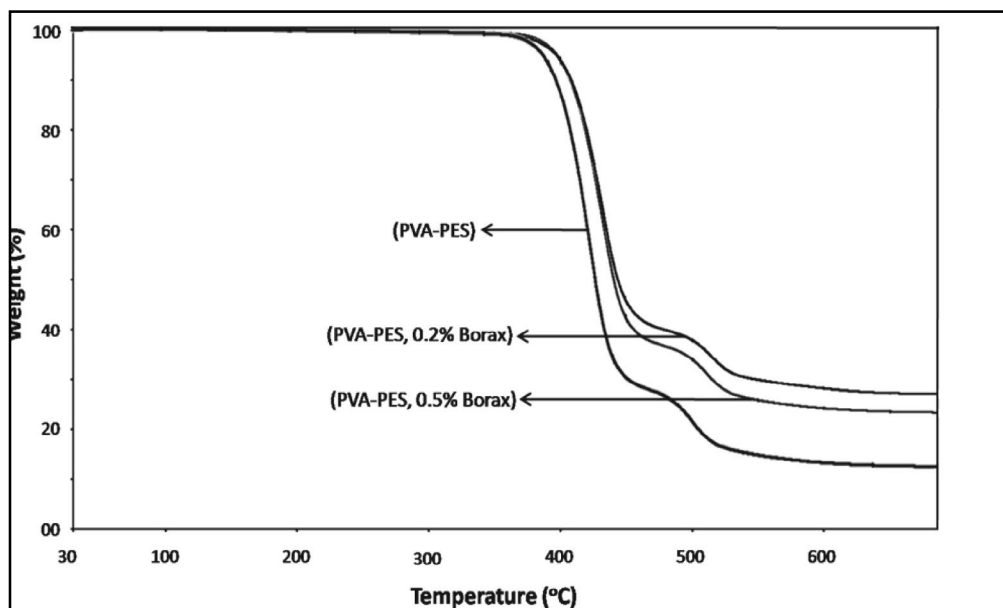


Fig. 3. TGA thermograms of PVA-PES composite membrane specimens cross linked with 0.2% and 0.5% borax as cross-linking agent used in the present study.

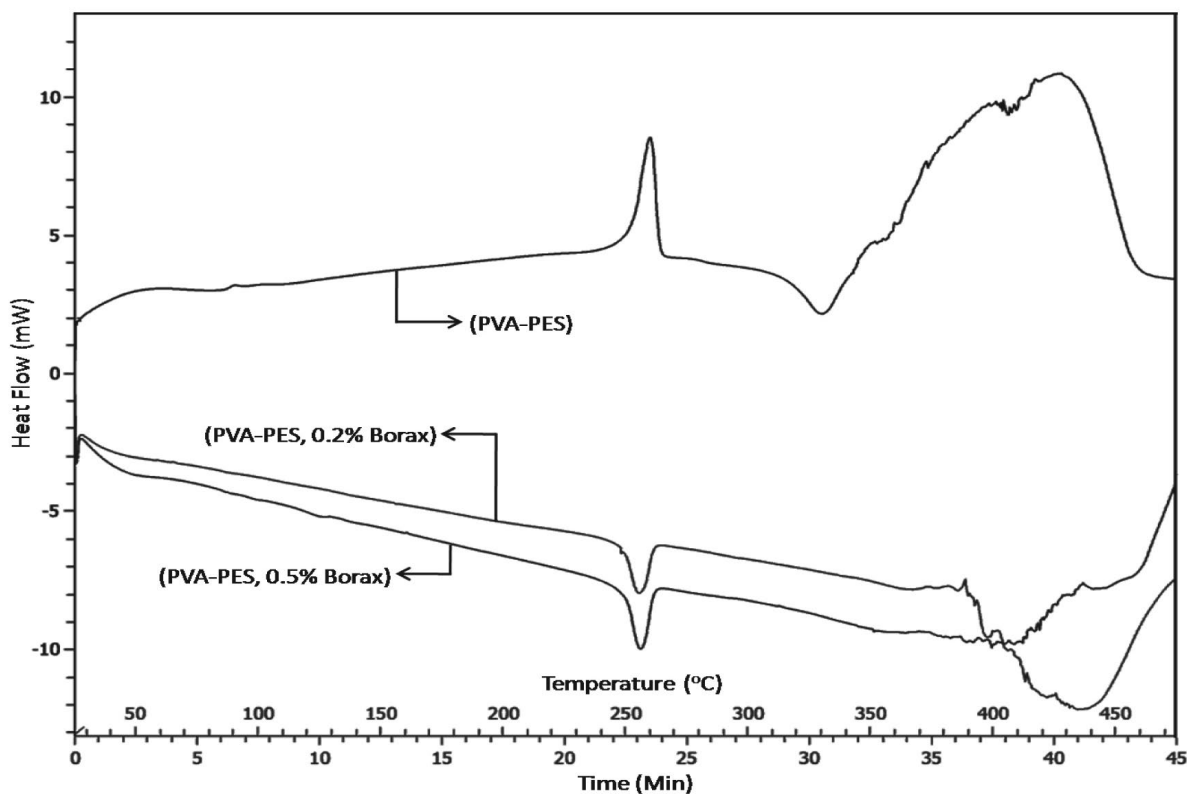


Fig. 4. Differential Scanning Calorimetry thermograms of the prepared composite membranes used in the present study.

### 3. 3. Differential Scanning Calorimetry

Differential scanning calorimetry (DSC) was used to investigate the response of polymers to heating. The analogue differential scanning calorimetry study can be used

to predict the miscibility behavior for the blending of polymer by measuring their heat of mixing.<sup>23,24</sup> In the present study it was applied to determine the melting temperature, glass transition temperature and latent heat of melting of the prepared composite membranes. In semi-crystalline

polymer of any type the glass transition is the best indicator of material properties. As the glass transition changes due to either different degrees of polymerization or modification by additives, the physical properties of the material change. DSC thermograms of the prepared composite membranes are presented in Fig. 4. There were two exothermic up-peaks and one down-peak found in the thermogram of uncrosslinked membrane specimen, while in the borax cross-linked membranes one endothermic up and two down peaks were observed. The endothermic peaks indicate that the heat of mixing of polymer is positive.<sup>25</sup> The first, second and third peaks were the indications of  $T_g$  (glass transition temperature),  $T_c$  (crystalline temperature) and  $T_m$  (melting temperature) respectively. The glass transition temperature of the uncrosslinked PVA-PES membrane was found out to be 87.86 °C, while the same for 0.2% and 0.5% borax cross-linked membranes were 100 °C and 110 °C respectively. Increase in the  $T_g$  value confirms the cross-linking of borax with polyvinyl alcohol (PVA) as the polymers can not be blended below their glass transition temperatures.<sup>26</sup> Crosslinking the membrane with borax restricts the segmental motion of its chain resulting in enhancement of glass transition temperature.<sup>27</sup> It was also observed from the thermogram that after around 480 °C, the behavior of the peaks became random. The crystallinity temperature of the three membranes were found out to be 251.1 (uncrosslinked), 248.49 (0.2% borax crosslinked) and 261.89 °C (0.5% borax cross-linked) respectively. On the other hand the melting temperatures of the same were 315, 435.29, and 477.99 °C respectively. The melting temperature ( $T_m$ ) in a DSC indicates not only the onset of melting but also the peak temperature, which corresponds to complete melting in or-

ganics and the energy that the melting transition needs in order to occur. This is the enthalpy of the transitions, and it is associated with the crystallinity of materials.

### 3. 4. XRD Analysis

The X-ray diffraction measurement was carried out to observe the crystallinity of the composite polymer membrane. The sharp diffraction maxima in the X-ray diffractogram indicate the presence of crystalline region of the polymer while the broad maxima are the representative of semi-crystalline to amorphous phases. Fig. 5 represents the wide angle

X ray diffraction pattern of the borax cross-linked PVA-PES composites membranes used in the present study with two different borax concentrations viz 0.2% and 0.5%. The X-ray diffractogram reveals the presence of a sharp peak at  $2\theta = 15^\circ$  and a minor peak at  $2\theta = 25^\circ$  corresponding to the borate ions, originated from the borax in aqueous solution.  $\text{Na}_2\text{B}_4\text{O}_7$  hydrolyzes in solution to produce  $\text{B}(\text{OH})_4^-$ . This reacts with the  $-\text{OH}$  groups on PVA to generate a cross linked structure. XRD pattern of uncross-linked PVA membrane is also given in Figure 5 for comparison. The un-crosslinked pristine PVA membrane shows diffraction peak at  $2\theta = 20^\circ$  due to the mixture of  $\{1\ 0\ 1\}$  and  $\{2\ 0\ 0\}$  crystalline plane Bragg reflections, typical for an orthorhombic lattice.<sup>28</sup> For pure PVA, the crystallinity was high due to the hydroxyl groups in its side-chain. When borax content was lower (0.2%) the steric effect and hydrogen bonding between PVA and borax in the cross-linking network interfered the ordered packing of PVA polymer chains, which resulted in a compression of amorphous region and thereby prevented from the forma-

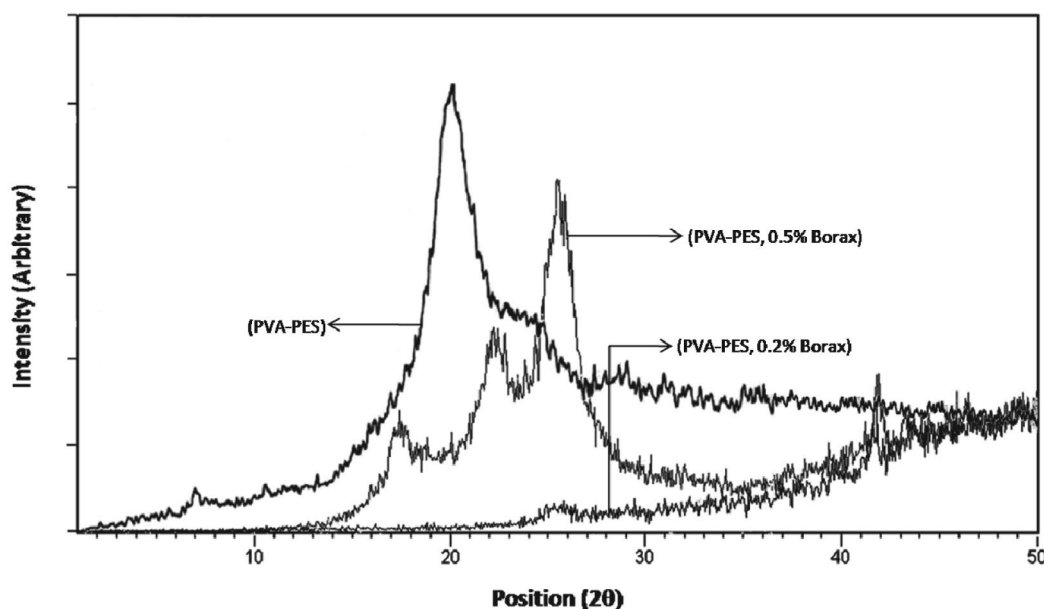
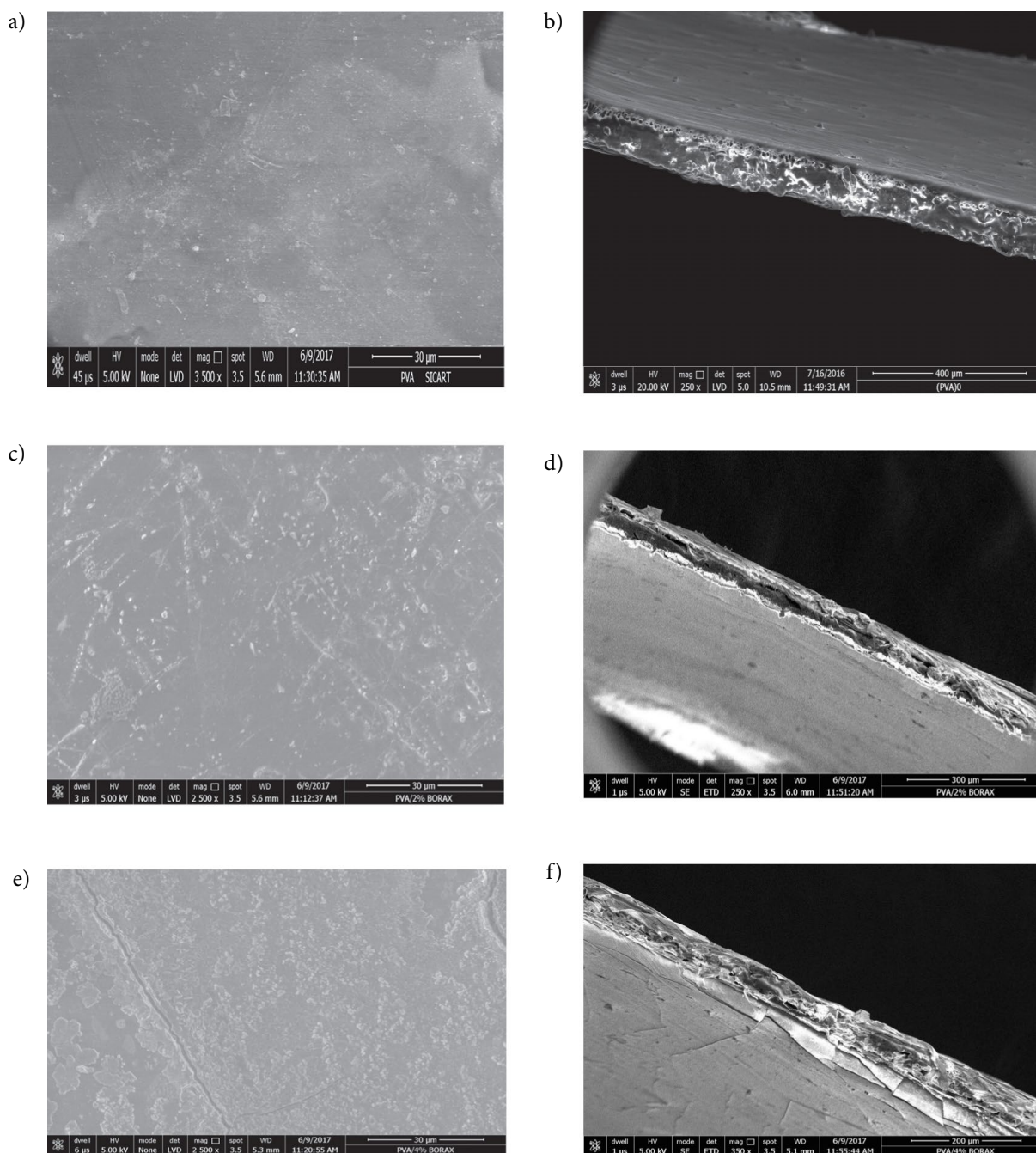


Fig. 5. Wide angle X ray diffraction pattern of the borax cross-linked PVA-PES composites membranes used in the present study with two different borax concentrations viz 0.2% and 0.5%.



**Fig. 6.** Scanning electron micrographs of the top surface and cross sections of the uncrosslinked PVA-PES composite, and PVA-PES composite membrane specimens doped with 0.2% and 0.5% of borax crosslink (a: uncrosslinked PVA -PES top surface, magnification: 3500; b: uncrosslinked PVA-PES cross section, magnification: 250; c: PVA-PES-0.2% borax top surface, magnification: 2500; d: PVA-PES-0.2% borax cross section, magnification 250; e: PVA-PES-0.5% borax top surface, magnification: 2500; f: PVA-PES-0.5% borax cross section, magnification: 350)

tion of crystalline region. Crystallinity of polymeric membranes is closely linked with the solute transport properties.

The permeability in a semi crystalline polymer membrane is substantially lower than that in an amorphous due to reduction of spaces available for diffusion and the tortuous path around the crystallites.<sup>29</sup> Thus, an overall decrease in the relative crystallinity was observed in PVA-PES com-

posite membrane crosslinked with 0.2% borax as compared to that crosslinked with 0.5% borax.

### 3.5 Surface Morphology by SEM Analysis

Scanning electron micrographs of the top surface as well as cross sections of the uncrosslinked PVA-PES composite, and PVA-PES composite membrane specimens

doped with 0.2% and 0.5% of borax crosslinker respectively are presented in Fig. 6. A perusal of the SEM micrographs reveals that the surface topography of the un-crosslinked PVA-PES membrane appears smooth and dense having continuous matrix without much visibility of pores or fissures and with good structural integrity. SEM images of the high and low molecular weights poly(vinylidene fluoride) blend membranes revealed asymmetric structures with finger-like macro-voids and sponge-like layer.<sup>30</sup> The granules shape of PVA indicates some crystalline behavior occurring in the uncrosslinked PVA-PES composite polymer (Fig.6-a). On the other hand the surface morphology of the cross linked composite polymer sample shows many different sizes of aggregates or chunks that are randomly distributed on the top surface. The cross-section of the SEM image shows some more void space in the borax crosslinked membrane. The presence of this void space might have contributed to the high flux of the membrane.<sup>31</sup> With increasing the amount of crosslinker, the surface of the PVA-PES composite membranes tends to become less gritty compared to their uncrosslinked counterparts (Fig. 6-b). Apparently, the crosslinker gradually densifies the membrane surface. Nevertheless, small defects were visible in the structures of the cross linked membranes. The cross sections of the composite membranes showed a compaction and densification with increasing amount of crosslinker. From the SEM micrographs the total thickness of the PVA-PES membranes was estimated to be approximately  $105 \pm 10$  mm and that of the active layer thickness was 34.60 mm. Both the membranes exhibited a porous cross-section at higher magnification. The support materials successfully helped the coating layer maintain the pore channel structure.<sup>32</sup> By increasing the amount of crosslinker up to 0.5 wt%, the structure became denser and uniform (Figure 6-c). This confirms the result obtained for the surface analysis of the membrane. It is flat and compact with very sparsely distributed small particles without any phase separation.

### 3. 6. Surface Topography by AFM Analysis

Atomic force microscopy (AFM) was used to analyze the surface topography and roughness of the prepared composite membranes. Roughness is one of the most important surface properties having strong influence on ad-

hesion as well as membrane transport. Adhesive force becomes larger for membranes with high roughness compared to the smoother ones. AFM images of the uncrosslinked and cross linked PVA-PES membranes are presented in Fig. 7. A close inspection of the images recorded for PVA/PES composite membranes confirm that borax cross linking has imparted rougher surfaces. The virgin PVA/PES membrane has smoother structure than the modified membranes with borax. Root-mean-square (RMS) height is a key physical parameter obtained from the AFM analysis, and defines as the mean of the root for the deviation from the standard surface to the indicated surface. The high RMS means high surface roughness. RMS roughness, average roughness and the contact angles of the membrane specimens from the present study are presented in Table 2. It indicates that RMS roughness of the uncrosslinked PVA-PES composite was 44.63 nm which increased to 52.24 and 53.17 nm in the specimens cross linked with 0.2% and 0.5% borax respectively.

Data presented in Table 2 reflect higher standard deviation for borax crosslinked membrane. Higher standard deviation represents higher surface roughness of composite membranes.<sup>33</sup> Similar observations were reported by Rana et al (2012)<sup>34</sup> for the cellulose membrane by the addition of 3 wt% additives of charged surface modifying macromolecule and poly(ethylene glycol). The membrane thus prepared was reported to decrease the surface contact angle and increase the roughness of membrane.<sup>34</sup> Contact angle, which is an indication of hydrophilicity of the membrane, was also high for the un-crosslinked PVA-PES composite membranes. Hydroxyl-terminated polybutadiene (HTPB) blended poly(ether sulfone) (PES) membranes also showed the decreasing trend of contact angles by adding solvents such as N-methyl-2-pyrrolidone (NMP) and N,N-dimethylacetamide (DMAc).<sup>31</sup> On the other hand, the increase in RMS and average roughness parameters was accompanied by the decrease in contact angles. This implies that unmodified PES-PES composites had less hydrophilicity compared to their cross-linked counterparts.

### 3. 7. Mechanical Properties

The mechanical properties of the PVA-PES composite membranes cross linked with borax are presented in Table 3. The values indicate that the tensile stress and the

**Table 2.** Roughness parameters and contact angles of the membrane specimens in AFM image analysis (Sampling area  $5 \mu\text{m} \times 5 \mu\text{m}$ ) (The figures in the bracket in column 4 indicate standard deviation.)

Membrane specimens	RMS roughness (nm)	Average roughness (nm)	Contact angle (°)
PVA-PES	44.63	41.69	52.5 ( $\pm 0.43$ )
PVA-PES-Borax 0.2%	52.24	38.25	49.4 ( $\pm 0.58$ )
PVA-PES-Borax 0.5%	53.17	43.16	45.6 ( $\pm 0.76$ )

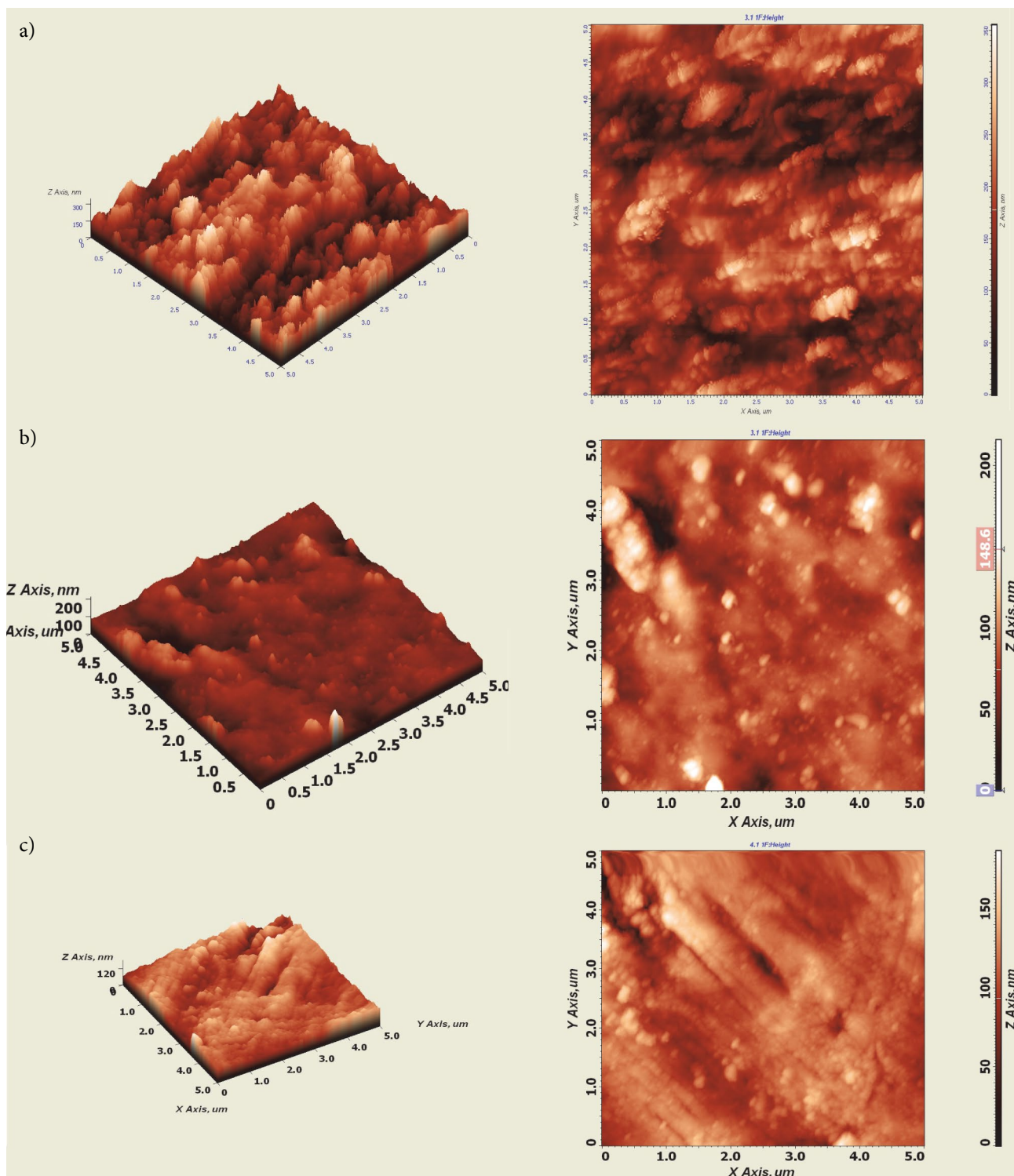


Fig. 7. AFM images of the uncrosslinked and cross linked PVA-PES membranes used in the present study (a: PVA-PES uncrosslinked; b: PVA-PES-0.2% borax; c: PVA-PES-0.5% borax)

percent elongation of the membrane increased significantly after cross linking with borax. Maximum tensile strength of the uncrosslinked PVA-PES composite membrane was  $2.15 \text{ N/mm}^2$  which rose to  $2.29$  and  $2.54 \text{ N/mm}^2$  for PVA-

PES, composite membranes with 0.5% and 0.2% Borax respectively. Modulus of elasticity of the borax cross-linked composite membranes was marginally higher than their uncross-linked counterpart. Similar observation for ten-



sile properties were reported in case of Ethylene 1-Octene Copolymer film on addition of Metallocene in the blend of Metallocene and Ziegler–Natta catalysts.<sup>35,36</sup> In another study, the elongation at break was found to increase linearly to about 50 wt% of metallocene polyethylene content in the blend of high-density polyethylene (HDPE)-metallocene polyethylene (MCPE) and polypropylene (PP)-metallocene polyethylene (MCPE).<sup>37</sup> It is noteworthy to mention that there is a small decrease in the tensile strength of 0.5% borax cross-linked composite membrane as compared to 0.2% borax cross-linked one. This was plausibly due to sub-microscopic cracks developed from internal stresses as a result of shrinkage or thermal changes after cross-linking.<sup>38</sup> However, further investigations need to be carried out to ascertain the observation. Cross-linking results in the increase of strength and reduced mobility of the molecular segments. Theoretically it is expected that tensile strength increases with cross-linking density as weak van der Waals' bonds being replaced by strong covalent bonds. It is noteworthy to mention that a little cross-linking may increase the tensile strength, but high degrees of cross-linking could drastically decrease tensile strength and make the polymer very brittle. Therefore, an optimum dose of the cross linker should be care-

fully chosen to obtain a suitable composite membrane for pervaporation.

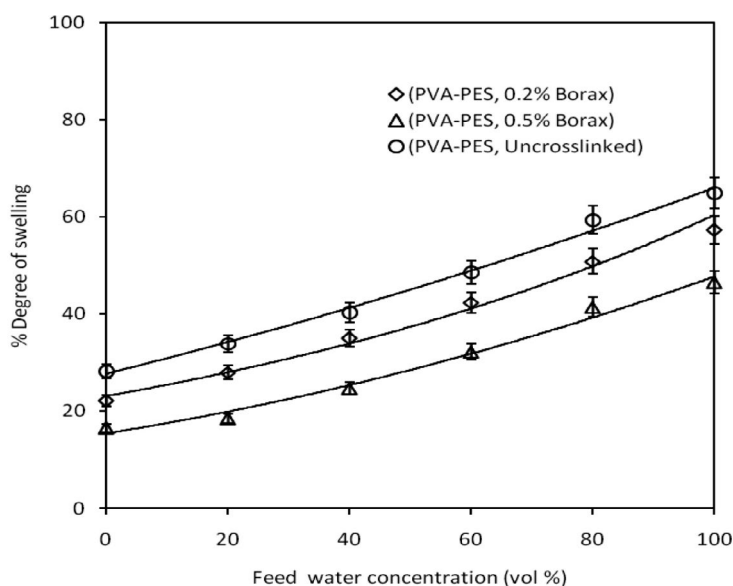
### 3. 8 Swelling Study

Swelling of dense polymeric membrane plays a key role in the transport of molecules during pervaporation by increasing the free volume. The greater the affinity between solvent and polymer, the higher is the swelling. As a result, the membrane becomes more open and facilitates more liquid to move through, which in turn influences both permeability and selectivity.

Hence it is worth analyzing the swelling behavior of the composite membranes in feed solutions to study its chemical characteristics. Fig. 8 represents the degree of swelling of both cross linked and uncrosslinked composite membranes used in the present work as a function of feed water concentration (by volume%) at a fixed temperature of 30 °C. The figure indicates that the degree of swelling increased almost linearly with increasing water content in the feed mixture. Uncross linked PVA-PES membrane exhibited as high as 59.4% degree of swelling at 80% feed water concentration. But the water uptake propensity substantially reduced in the borax crosslinked

**Table 3.** Mechanical Property of PVA-PES composite membranes cross linked with borax. (The figures in the bracket in column 5 indicate standard deviation.)

Membrane Name	Max Tensile strength (N/mm <sup>2</sup> )	Max Strain (%)	% Elongation at Max	Modulus of Elasticity (N/mm <sup>2</sup> )
(PVA-PES)	2.15	9.46	8.84	17.565 (± 0.54)
(PVA-PES-Borax 0.5%)	2.2916	10.678	10.678	21.4616 (± 0.37)
(PVA-PES-Borax 0.2%)	2.5416	12.438	12.438	20.4347 (± 0.39)



**Fig. 8.** Percentage degree of swelling as a function of feed water concentration at a constant temperature.

membranes. At 80% feed water concentration the degree of swelling was found out to be 58.2% and 48.7% for PVA-PES -0.2% borax and PVA-PES-0.5% borax membranes respectively.

During swelling the polymer structure expands as the trapped solution occupies the free volume in the matrix and penetrates into the network of the polymer chains to swell them. The effect of swelling may give rise to two situations. Firstly, expansion of membrane free volume presumably facilitates the larger molecules to pass, thereby increasing permeability and reducing selectivity. Additionally compaction of membrane pores could also occur leading to an increase in selectivity and reduction in permeability. However, our subsequent studies of flux and permeability with the borax cross-linked composite membranes corroborate the former assumption as pervaporation membranes are mostly dense in nature. Degree of swelling of 0.2% borax cross linked composite was less than that of 0.5% borax cross linked counterpart. This was probably due to the fact that addition of more cross-linker might have reduced membrane free volume resulting in restricted segmental motion.<sup>39</sup>

### 3. 9. Flux and Separation Factor

Flux and separation factors are the two important performance indices of pervaporation membranes. In addition to the membrane structure and morphology, these indices are influenced by the physico-chemical parameters of the process such as temperature, feed concentration and feed flow rate. However, in the following section we report the effect of only feed flow rate on total flux and separation factor at a constant temperature and feed concentration. Fig. 9 represents total pervaporation flux and separation factor as a function of feed flow rate.

For all the membranes, cross linked or otherwise, total pervaporation flux was found to increase with feed flow rate whereas the separation factor decreased. At a flow rate of 0.06 m<sup>3</sup>/h total pervaporation flux was estimated to be 8.81 m<sup>3</sup>(STP)/m<sup>2</sup>h and 7.21 m<sup>3</sup>(STP)/m<sup>2</sup>h for 0.2% and 0.5% borax cross linked PVA-PES composite membranes respectively, while for the uncrosslinked PVA-PES composite the flux was 7.85 m<sup>3</sup>(STP)/m<sup>2</sup>h. Separation factor was found to be 3.50 at a flow rate of 0.02 m<sup>3</sup>/h for 0.2% borax crosslinked membrane, which reduced to 2.45 at 0.06 m<sup>3</sup>/h flow rate. For 0.5% borax cross-linked membrane the highest separation factor was only 1.54 at a flow rate of 0.02 m<sup>3</sup>/h and it dropped to 1.05 when flow rate was increased to 0.06 m<sup>3</sup>/h. Both in terms of flux and separation factor PVA-PES-0.2% borax composite membrane was found superior to PVA-PES-0.5% borax crosslinked and its uncrosslinked counterpart. Doping of excess cross linkers led to the reduction in the membrane free volume as discussed in the earlier section. A drop of the separation factor with increased borax loading could also be reasoned from the poor interfacial adhesion between the borax particles and the polymer matrix. Increase of feed flow rate results in the increase in turbulence at the membrane surface facilitating augmentation of pervaporation flux. As the turbulence increases, the boundary layer thickness decreases and the likelihood of concentration polarization on the upstream side of membrane diminishes as well. This implies that the water concentration near membrane surface approaches to that in the bulk phase<sup>9</sup> with swellable hydrophilic channels of PVA matrix providing available paths leading to facile permeation flux as feed water content increases.<sup>6</sup> Moreover, Jafari et al. (2012) demonstrated by a computational fluid dynamics (CFD) study that increasing feed flow rate can enhance feed kinetic energy substantially which in turn increases the extent of turbu-

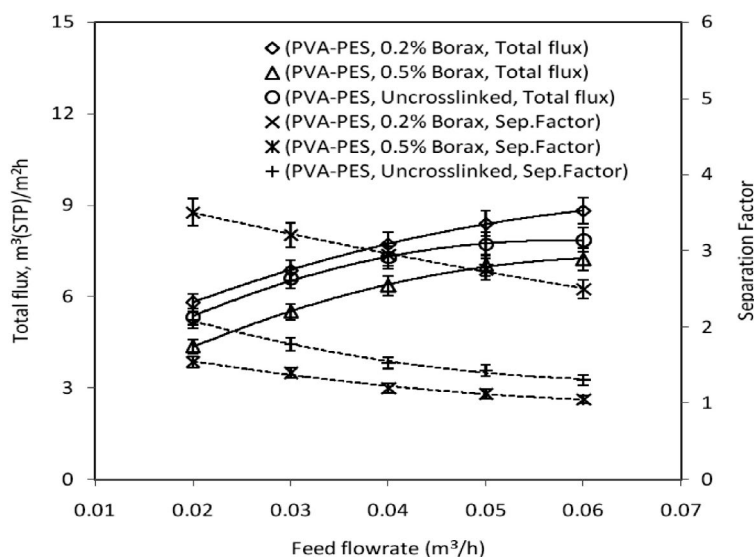


Fig. 9 Total pervaporation flux and separation factor as a function of feed flow rate in the pervaporation of EG-water system (Temperature: 45 °C, Feed concentration: 80% Ethylene glycol by volume)

lence.<sup>7</sup> But at the same time a reverse trend was observed in case of separation factor plausibly due to the less pronounced coupling effect between EG and water molecules at the prevailing feed concentration of the present study. Further this could be due to the weaker EG-water hydrogen bonding interactions leading to low mutual drag between water and EG molecules and decelerating transport of EG molecules.<sup>3,11</sup> However, literature reports contradictory observations of separation factor behavior with changing feed flow rate in the pervaporation. While a host of studies observed the decreasing trend of separation factor with increasing feed flow rate,<sup>6,9</sup> a few other reported the reverse trend.<sup>7,11</sup> Therefore, it is imperative to carry out further rigorous experiment in this direction to ascertain the effect of flow rate on the flux and separation factor using a wide concentration of feed mixture.

### 3. 10. Permeability, Selectivity and Diffusion Coefficient

Water permeability and selectivity of the membranes used in the present study as a function of feed flow rate are

presented in Table 4. Water permeabilities of all the membranes were found to increase with the increasing feed flow rate while the membrane selectivities decreased. Highest water permeability of 14.56 barrer was exhibited by PVA-PES-0.2% borax membrane at a flow rate of 0.6 m<sup>3</sup>/h, whereas at the same flow rate the water permeabilities of PVA-PES-0.5% and PVA-PES uncrosslinked membranes were 10.02 and 11.12 barrer respectively. Selectivity of PVA-PES-0.2% borax composite membrane was found out to be 3.65 at 0.02 m<sup>3</sup>/h feed flow rate.

The reason for the increasing water permeability with increasing flow rate can be attributed to the promotion of turbulence at the membrane surface and which was most effective in 0.2% borax cross linked membrane compared to 0.5% borax cross-linked and the uncrosslinked ones. The increase in turbulence of feed solution resulted in the decrease of boundary layer thickness. Therefore, mass transfer resistance of boundary layer on the upstream of membrane decreased as well, leading to increased water permeability. Transport of solute during pervaporation is predominantly governed by solution diffusion mechanism and therefore estimation of diffusion coefficients of both

**Table 4.** Water permeability and selectivity of the membranes used in the present study as a function of feed flow rate. (Each experimental data point is the average of three readings; the figures in the bracket from column 2 to column 7 indicate standard deviation.)

Feed flow rate (m <sup>3</sup> /h)	(PVA-PES-0.2% Borax)		(PVA-PES-0.5% Borax)		(PVA-PES, Uncrosslinked)	
	Water Permeability (Barrer)	Membrane selectivity	Water Permeability (Barrer)	Membrane selectivity	Water Permeability (Barrer)	Membrane selectivity
0.02	9.97 (± 0.35)	3.65 (± 0.19)	5.36 (± 0.21)	1.61 (± 0.32)	8.66 (± 0.27)	2.15 (± 0.42)
0.03	11.73 (± 0.41)	3.34 (± 0.24)	7.29 (± 0.17)	1.42 (± 0.30)	10.29 (± 0.22)	1.82 (± 0.30)
0.04	13.06 (± 0.29)	3.06 (± 0.35)	8.61 (± 0.40)	1.26 (± 0.28)	10.91 (± 0.34)	1.56 (± 0.28)
0.05	14.09 (± 0.32)	2.86 (± 0.14)	9.32 (± 0.31)	1.18 (± 0.13)	11.32 (± 0.18)	1.45 (± 0.23)
0.06	14.56 (± 0.27)	2.58 (± 0.22)	10.02 (± 0.25)	1.10 (± 0.26)	11.12 (± 0.15)	1.32 (± 0.14)



**Fig. 10.** Water and ethylene glycol diffusion coefficient as a function of feed flow rate in the pervaporation of EG-water mixture (Temperature: 45 °C, Feed concentration: 80% Ethylene glycol by volume)

EG and water assumes importance. Water and EG diffusion coefficients as a function of feed flow rate are presented in Fig. 10. As shown in the figure both the EG and water diffusion coefficients increased with increasing feed flow rate. However the magnitude of water diffusion coefficients was higher than EG diffusion coefficients under all experimental conditions. At a feed flow rate of 0.06 m<sup>3</sup>/h diffusion coefficients of water were estimated to be  $1.51 \times 10^{-10}$  m<sup>2</sup>/s and  $1.19 \times 10^{-10}$  m<sup>2</sup>/s in the PVA-PES-0.2% and PVA-PES-0.5% composite membranes respectively. But diffusion coefficients of EG at the same flow rate were  $0.61 \times 10^{-10}$  m<sup>2</sup>/s and  $1.12 \times 10^{-10}$  m<sup>2</sup>/s for PVA-PES-0.2% and PVA-PES-0.5% membranes respectively. The higher diffusion coefficient of water compared to EG may be ascribed to the smaller size (kinetic diameter) of water molecules than EG.<sup>27</sup> It was also observed that the diffusion coefficients of water decreased as borax content in the PVA-PES composite increased from 0.2 to 0.5%. This was probably due to the reduction of membrane free volume resulting in restricted segmental motion of the diffusing water molecules through the composite membrane network.<sup>39</sup> In addition the mutual interaction between EG-water molecules presumably reduced plasticization effect, which in turn suppressed the sorption as well as diffusion.

### 3. 11. Effect of Feed Temperature

Intrinsic membrane permeability of ethylene glycol and water as a function of feed temperature and with a fixed feed concentration of 80% (vol) ethylene glycol for all three prepared membrane is presented in Fig. 11.

A perusal of Fig. 11 indicates that permeability of both water and ethylene glycol increase with increase in temperature, although the magnitude of permeability of water was higher than that of ethylene glycol. It was also

observed (data not shown) that the membrane selectivity decreased with increase in temperature. The PVA-PES-0.2% borax cross linked membrane shows highest water permeability and lowest ethylene glycol permeability than other two membranes at any feed temperature. The processes involved in permeation, sorption and diffusion are activated processes and the temperature effect can be described by Arrhenius type relationship.<sup>12</sup> The relationship of flux or permeance of a penetrant across a membrane with operating temperature can be described by the Arrhenius equations as follows:

$$X = X_0 \exp\left(\frac{-E_X}{RT}\right) \quad (8)$$

where  $X$  is the pervaporation flux ( $J$ ),  $X_0$  is the pre-exponential factor (permeation rate constant)  $R$  is the universal gas constant ( $J/mol K$ ),  $T$  is the operation temperature ( $K$ ), and  $E_X$  is the apparent activation energies of permeance ( $kJ/mol$ ). The apparent activation energy of water permeation ( $E_{PW}$ ) and ethylene glycol permeation ( $E_{EG}$ ) for all three membranes are presented in Table 5. The results indicate that the activation energy of water permeation through PVA-PES-0.2% borax cross linked membrane was significantly lower than those of ethylene glycol permeation, suggesting a higher separation efficiency of the membranes. If the activation energy is positive, the permeation flux increases with an increase in temperature, which has also been reported in most pervaporation experiments in the literature.<sup>40,41</sup> The present study also corroborates the same observation. Due to its molecular size and shape, the activation energy of diffusion for ethylene glycol will be greater than that for water. As the water content in the feed decreases the polymeric membrane become less swollen and the mobility of chain segments decreases, thus increasing

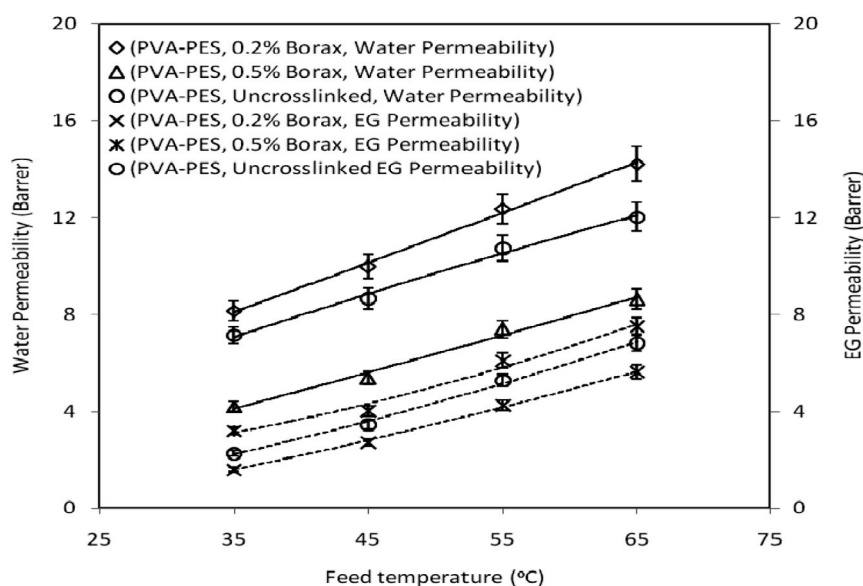


Fig. 11. Water and ethylene glycol permeability as a function of feed temperature

the energy required for the diffusive jump of ethylene glycol molecules. The interaction between permeants is thought to have an enhancing effect on the permeation activation energy because associated molecules require more energy for permeation than isolated molecules. In contrast, the plasticization action diminishes the activation energy by making the polymeric chain segments more flexible.

**Table 5.** Apparent activation energy of water and ethylene glycol permeation through PVA-PES composite membranes cross linked with borax.

Membrane Name	Water activation energy (kJ/mol)	Ethylene glycol activation energy (kJ/mol)
(PVA-PES)	15.40	32.38
(PVA-PES-Borax 0.5%)	21.57	25.80
(PVA-PES-Borax 0.2%)	16.32	36.69

## 4. Conclusions

Borax cross linked PVA-PES composite membranes were prepared for the pervaporation dehydration of EG-water mixtures. The PVA layers were successfully cross linked with two different concentrations e.g. 0.2% and 0.5% (by weight) borax as cross linking agents although 0.2% borax crosslinked PVA-PES composite was found better in terms of flux, permeability and separation factor. The as-prepared composite membranes were characterized by FTIR, XRD, TGA, DSC, FESEM, AFM, swelling degree and mechanical property analyses. The salient findings from the above tests indicate that borax could be effectively cross linked in the PVA network imparting adequate thermal and mechanical stability, over a wide temperature range. Crosslinking could reduce crystallinity and hydrophilicity of membrane thereby affecting swelling and permeation behavior. The resulting 0.2% borax cross linked PVA-PES composite membrane exhibited a separation factor of 3.50 with a pervaporation flux of 8.81 m<sup>3</sup> (STP)/m<sup>2</sup>h for 80% EG in the feed at 70 °C. Although pervaporation flux and diffusion coefficients of both EG and water increased with increasing feed flow rate, separation factor and selectivity decreased. The diffusion coefficient of water was higher than that of EG at a fixed temperature and feed concentration. The long-term investigation of process conditions showed that the composite membranes displayed the desirable operating and structural stability. In essence the findings of the present study indicate that the borax crosslinked PVA-PES composite membrane proves suitable for the dehydration of EG-water mixture in a wide range of concentrations.

## 5. Acknowledgements

The authors are grateful to the Sophisticated Instrumentation Centre for Advanced Research and Testing (SI-

CART) for their valuable help to carry out certain analyses. Suggestions by the anonymous reviewers to improve the manuscript are also gratefully acknowledged.

## 5. 1. Nomenclature

EG	ethylene glycol
TG	thermogravimetry
FTIR	Fourier transformed infrared
AFM	Atomic force microscopy
FE-SEM	Field Emission Scanning electron microscopy
PVA	Polyvinyl alcohol
PES	Polyether sulfone
$W_{wet}$	weight of swallow membrane (g)
$W_{dry}$	weight of dry membrane (g)
$P_{m,i}$	membrane permeability (cm <sup>3</sup> (STP)cm/cm <sup>2</sup> s cm Hg)
$J_i$	mass flux (kg/m <sup>2</sup> h)
$x$	mole fraction of feed
$y$	mole fraction of permeate
$P_p$	permeate pressure
$P_s$	saturated vapor pressure
$j_i$	molar flux (cm <sup>3</sup> (STP)/cm <sup>2</sup> s) of component 'i'
$v_i^G$	molar volume of gas i (22.4 l(STP)/mol)
$D_i$	diffusion coefficient (m <sup>2</sup> /s)

### Greek letters

$\beta$	Ideal separation factor
$\alpha$	Membrane selectivity
$\gamma$	Activity coefficient
$\delta$	membrane thickness (mm)

## 7. References

- J. Xi, D. Ding, Y. Shao, X. Liu, G. Lu, Y. Wang, *ACS sustainable Chem Eng.* **2014**, *10*, 2355. DOI:10.1021/sc500380c
- D. Sun, P. Yang, Sun, H-L., Li, B-B. *Euro. Polymer J.* **2015**, *62*,155. DOI:10.1016/j.eurpolymj.2014.11.027
- M. Shahverdi, T. Mohammadi, A. Pak, *J. Appl. Polym. Sci.* **2011**, *119*, 1704. DOI:10.1002/app.32862
- D. Wu, J. Martin, J. Du, Y. Zhang, D. Lawless, X. Feng, *J Membr. Sci.* **2015**, *493*, 622. DOI:10.1016/j.memsci.2015.07.016
- Y. Wang, T. S. Chung, B.W. Neo, M. Gruender *J Membr. Sci.* **2011**, *378*, 339. DOI:10.1016/j.memsci.2011.05.020
- B. Baheri, M. Shahverdi, M. Rezakazemi, E. Motaei, T. Mohammadi *Chem. Eng. Commu.* **2015**, *202*, 316. DOI:10.1080/00986445.2013.841149
- M. Jafari, A. Bayat, T. Mohammadi, M. Kazemimoghadam, *Chem Engg Res Design*, **2012**, *91*, 2412. DOI:10.1016/j.cherd.2013.04.016
- C. Yu, C. Zhong, Y. Liu, X. Gu, G. Yang, W. Xing, N. Xu, *Chem Engg Res Design.* **2012**, *90*, 1372. DOI:10.1016/j.cherd.2011.12.003
- S. Y. Hu, Y. Zhang, D. Lawless, X. Feng, *J Membr. Sci.* **2012**, *418*, 34. DOI:10.1016/j.memsci.2012.06.010

10. P. S. Rao, S. Sridhar, M. Y. Wey, A. Krishnaiah, *Ind. Eng. Chem. Res.* **2007**, *46*, 2155. DOI:10.1021/ie061268n
11. R. Guo, X. Fang, H. Wu, Z. Jiang, *J Membr. Sci.* **2008**, *322*, 32. DOI:10.1016/j.memsci.2008.05.015
12. D. Rana, T. Matsuura, *Chem. Rev.* **2010**, *110*, 2448. DOI:10.1021/cr800208y
13. R. Y. M. Huang, R. Pal, F. G. Y. Moon, *J. Membr. Sci.* **2000**, *167*, 275. DOI:10.1016/S0376-7388(99)00293-8
14. A. Jonsson, B. Jonsson, *J. Membr. Sci.* **1991**, *56*, 49. DOI:10.1016/0376-7388(91)85015-W
15. W. U. Hong, L. I. Xianshi, N. I. E. Mingchen, L. I. Ben, J. Zhongyi, *Chinese J. Chem. Eng.* **2011**, *19*, 855. DOI:10.1016/S1004-9541(11)60088-8
16. H. K. Dave, K. Nath, *J Water Proc. Eng.* **2016**, *14*, 124.
17. R. W. Baker, J. G. Wijmans, Y. Huang, *J. Membr. Sci.* **2010**, *348*, 346. DOI:10.1016/j.memsci.2009.11.022
18. O. Koysuren, M. Karaman, M. Dinc, *J Appl. Polym. Sci.* **2012**, *124*, 2736. DOI:10.1002/app.35035
19. M. Kobayashi, Y. Kitaoka, *Macromol Symp.* **1997**, *114*, 303. DOI:10.1002/masy.19971140141
20. G. Ramadevudu, L., S.Rao, S., M. Shareeffuddin, C. Narasimha, M., Lakshminpathi, Rao M. *Global J Sci Frontier Res Phys Space Sci.* **2012**, *12*, 41.
21. P. Das, S. K. Ray, S. B. Kuila, H.S. Samanta, N.R. Singha, *Sep. Purif. Technol.* **2011**, *81*, 159. DOI:10.1016/j.seppur.2011.07.020
22. P. S. Rachipudi, M. Y. Kariduraganavar, A. A. Kittur, A. M. Sajjan, *J membr. Sci.* **2011**, *383*, 224.
23. D. Rana, B. M. Mandal, S. N. Bhattacharyya, *Macromolecules.* **1996**, *29*, 1579.
24. D. Rana, K. Bag, S. N. Bhattacharyya, B. M. Mandal, *J. Polym. Sci. Part B: Polym. Phys.* **2000**, *38*, 369. DOI:10.1002/(SICI)1099-0488(20000201)38:3<369::AID-POLB3>3.0.CO;2-W
25. D. Rana, B. M. Mandal, S. N. Bhattacharyya, *Polymer.* **1996**, *37*, 2439. DOI:10.1016/0032-3861(96)85356-0
26. D. Rana, B. M. Mandal, S. N. Bhattacharyya, *Polymer.* **1993**, *34*, 1454. DOI:10.1016/0032-3861(93)90861-4
27. S. B. Kuila, S. K. Ray, P. Das, N. R. Singha, *Chem. Eng Processing.* **2011**, *30*, 391. DOI:10.1016/j.cep.2011.02.011
28. Y. Nishino, John, Manley R. S. *Macromolecules.* **1988**, *21*, 1270.
29. S. S. Kulkarni, A. A. Kittur, M.I. Aralaguppi, M.Y. Kariduraganavar, *J Appl. Polymer Sci.* **2004**, *94*, 1304. DOI:10.1002/app.21088
30. Z. Chen, D. Rana, T. Matsuura, Y. Yang, C. Q. Lan, *Sep. Purif. Technol.* **2014**, *133*, 303. DOI:10.1016/j.seppur.2014.07.015
31. D. Rana, T. Matsuura, R. M. Narbaitz, K. C. Khulbe, *J Appl. Polymer Sci.* **2006**, *101*, 2292. DOI:10.1002/app.23723
32. Y. Yang, D. Rana, T. Matsuura, C. Q. Lan, *Sep. Purif. Technol.* **2016**, *164*, 56. DOI:10.1016/j.seppur.2016.03.023
33. Z. Chen, D. Rana, T. Matsuura, D. Meng, C. Q. Lan, *Chem. Engg. J.* **2015**, *276*, 174. DOI:10.1016/j.cej.2015.04.030
34. D. Rana, B. Scheier, R. M. Narbaitz, T. Matsuura, S. Tabe, S. Y. Jasim, K. C. Khulbe, *J Membr. Sci.* **2012**, *409*, 346. DOI:10.1016/j.memsci.2012.04.005
35. D. Rana, K. Cho, T. Woo, B. H. Lee, S. Choe, *J Appl. Polymer Sci.* **1999**, *74*, 1169. DOI:10.1002/(SICI)1097-4628(19991031)74:5<1169::AID-APP13>3.0.CO;2-W
36. D. Rana, H. L. Kim, H. Kwang, J. Rhee, K. Cho, T. Woo, B. H. Lee, S. Choe, *J Appl. Polymer Sci.* **2000**, *76*, 1950.
37. D. Rana, C. H. Lee, K. Cho, B. H. Lee, S. Choe, *J Appl. Polymer Sci.* **1998**, *69*, 2441. DOI:10.1002/(SICI)1097-4628(19980919)69:12<2441::AID-APP15>3.0.CO;2-#
38. K. S. Anseth, C. N. Bowman, L. Brannon-Peppas, *Biomaterials.* **1996**, *17*, 1647. DOI:10.1016/0142-9612(96)87644-7
39. H. Qu, Y. Kong, H. Lv, Y. Zhang, J. Yang, D. Shi, *Chem. Eng. J.* **2010**, *157*, 60. DOI:10.1016/j.cej.2009.09.044
40. Guo, R., Changlai, H., Ben, L., Zhongyi, J. *J. Membr. Sci.* **2007**, *289*, 191. DOI:10.1016/j.memsci.2006.11.055
41. Hu C, Ben L, Guo R, Hong W, Zhongyi, J. *Sep. Purif. Technol.* **2007**, *55*, 327. DOI:10.1016/j.seppur.2007.01.005

## Povzetek

Preučevano je bilo odstranjevanje vode iz etilen glikol (EG) – vodne mešanice na laboratorijskem preduparjalniku z uporabo različnih ravnih membran. Polivinil alkohol-polieter sulfonska (PVA-PES) kompozitna membrana je bila sintetizirana in premerežena z uporabo dveh različnih koncentracij dinatrijevega tetraborata (0.2 in 0.5 %). Pripravljenim membranam so okarakterizirali morfologijo, medmolekularne interakcije, termo-mehansko stabilnost ter fizikalno kemijske lastnosti z uporabo vrstične elektronske mikroskopije (FESEM), mikroskopije na atomsko silo (AFM), fourierjeve transformacijske infrardeče spektroskopije (FT-IR), rentgenske difrakcije (XRD), termogravimetrične analize (TGA), diferenčne dinamične kalorimetrije (DSC) in sposobnosti adsorpcije vode. Poleg tega so bile lastnosti membran ovrednotene s faktorjem ločbe, selektivnostjo, propustnostjo in difuzijskim koeficientom topljenca v EG-vodni mešanici pri različnih pretokih napajanja. Tako glede fluksa kot selektivnosti se je PVA-PES membrana zamrežena z 0.2 % borata izkazala boljše od membrane zamrežene z 0.5 % borata oziroma nezamrežene membrane. Zamreženje kompozitne membrane z boratom se je odrazilo v nižji kristaliničnosti in manjšem nabrekanju, a z izboljšano termično stabilnostjo in mehanskimi lastnostmi.

Scientific paper

# Magnetically Separable Ag/CuFe<sub>2</sub>O<sub>4</sub>/Reduced Graphene Oxide Ternary Nanocomposite with High Performance for the Removal of Nitrophenols and Dye Pollutants from Aqueous Media

Ladan Nirumand, Saeed Farhadi\* and Abedin Zabardasti

Department of Chemistry, Lorestan University, Khorramabad 68135-465, Iran

\* Corresponding author: E-mail: sfarhadi1348@yahoo.com (S. Farhadi)  
Tel.: +986633120611; Fax: +986633120618

Received: 05-07-2018

## Abstract

In this work, a novel ternary magnetic nanocomposite namely Ag/CuFe<sub>2</sub>O<sub>4</sub>/rGO was produced by a facile solvothermal route. The reduction of graphene oxide (GO) to reduced form (rGO) and the in-situ deposition of CuFe<sub>2</sub>O<sub>4</sub> and Ag nanoparticles on rGO occurred simultaneously in a one-pot reaction. The structure, composition and morphology of the as-prepared nanocomposite were characterized by FT-IR, XRD, VSM, FESEM, EDX, TEM, and BET analyses. The results indicated that the Ag and CuFe<sub>2</sub>O<sub>4</sub> nanoparticles were successfully loaded on the surface of rGO. The catalytic performance of the Ag/CuFe<sub>2</sub>O<sub>4</sub>/rGO nanocomposite was evaluated for the reduction of nitroarenes to corresponding amines in the presence of sodium borohydride (NaBH<sub>4</sub>) as a reducing agent. The nanocomposite exhibited the high performance in the reduction of the reduction of nitroarenes with 100% conversion within 10–30 min. The catalytic activity of the Ag/CuFe<sub>2</sub>O<sub>4</sub>/rGO was enhanced compared with Ag/CuFe<sub>2</sub>O<sub>4</sub>, Ag/rGO and CuFe<sub>2</sub>O<sub>4</sub>/rGO samples due to easier electron transfer process. Furthermore, the adsorption data revealed that cationic methylene blue (MB) dye could be removed almost completely on the Ag/CuFe<sub>2</sub>O<sub>4</sub>/rGO composite within 2 min and the composite could also selectively adsorb MB from the mixed solution with anionic methyl orange (MO). Due to the existence of magnetic CuFe<sub>2</sub>O<sub>4</sub> nanoparticles, the Ag/CuFe<sub>2</sub>O<sub>4</sub>/rGO nanocomposite can be magnetically separated and reused without any change in structure and performance.

**Keywords:** Graphene oxide nanosheets; Silver nanoparticles; Ternary magnetic nanocomposite; Nitrophenols reduction; Dyes adsorption

## 1. Introduction

Nitroarenes are one of the most common pollutants that often exist in industrial wastewaters, while aromatic amines are of various commercial importance as an intermediate for the production of pharmaceutical ingredients, various polymers and dyes.<sup>1–3</sup> In fact, synthesis of aminoarenes from the corresponding nitro compounds is an important process in the chemical industries and several methods for preparation of them were found, such as stoichiometric reducing agents and catalytic hydrogenation.<sup>4–7</sup> A large amount of industrial wastewaters also contain organic dye pollutants. Organic dyes are one of the main causes of the pollution of industrial wastewater that removal of them through different technologies such as adsorption is of great importance in environmental process-

es.<sup>8–15</sup> Hence, there is a need to find a new desirable material, which not only has the capacity of reducing the nitroarenes but also can achieve adsorption and selective separation of organic pollutants. To date, many researches have been carried out in the area of metal nanoparticles-based heterogeneous catalysts as they possess a high surface to volume ratio and reusability, ease of separation and enhanced catalytic properties.<sup>16–18</sup> Among them, gold and silver nanoparticles are particularly attractive due to their high electrical, optical, and catalytic properties,<sup>19–21</sup> but they require suitable supports such as metal oxides, zeolites or graphene derivatives to immobilize them and prevent aggregation during the reaction.<sup>22–25</sup>

Graphene, single-layer carbon atoms densely packed into a two-dimensional (2D) lattice, has high surface area, excellent electrical conductivity and high mechanical

strength.<sup>26</sup> It can be used as a promising catalyst support on which the metal nanocatalysts can be stabilized and result in the further enhanced catalytic performance.<sup>27,28</sup> One of the applications of graphene-based materials is also the removal of organic dye pollutants from water.<sup>29,30</sup> Many polymeric and inorganic adsorbents such as carbon-based materials,<sup>31</sup> porous metal oxides,<sup>32</sup> clays,<sup>33</sup> chitosan,<sup>34</sup> zeolites,<sup>35</sup> and metal–organic frameworks (MOFs)<sup>36</sup> have developed for adsorption removal of pollutants from aqueous solutions. Among them, carbonous materials such as graphene have shown excellent performance in adsorption of organic contaminants from water. However, such adsorbents are usually separated by tedious filtrating from water after the adsorption/catalytic process. To overcome this weakness, coupling with magnetic materials is highly desirable. Spinel ferrites with general formula  $MFe_2O_4$  ( $M = Mn, Fe, Co, Ni, Cu, \text{etc.}$ ) have been of great interest in many magnetic applications.<sup>37</sup>

Considering the above, in this work, we have synthesized the novel magnetic Ag/CuFe<sub>2</sub>O<sub>4</sub>/rGO ternary nanocomposite via solvothermal method which fully characterized by various spectroscopic techniques. During the formation of the composite, the reduction of graphene oxide (GO) to rGO and the in-situ deposition of CuFe<sub>2</sub>O<sub>4</sub> and Ag nanoparticles on rGO occurred simultaneously in a one-pot reaction. Due to high catalytic activity of Ag, the nanocomposite displayed excellent performance for catalytic reduction of nitroarenes by using NaBH<sub>4</sub> in aqueous solutions. Also, owing to the existence of graphene with high surface area and adsorption capacity, the Ag/CuFe<sub>2</sub>O<sub>4</sub>/rGO nanocomposite exhibited high performance on the removal of dye pollutants from wastewater. Moreover, the magnetic properties of CuFe<sub>2</sub>O<sub>4</sub> make the separation of the nanocomposite easier, avoiding environmental contamination from processing.

## 2. Experimental

### 2.1. Materials

All reagents including solvents and all materials used for the synthesis of nanocomposite, 2-nitrophenol (2-NP), 4-nitrophenol (4-NP), 2-nitroaniline (2-NA), 4-nitroaniline (4-NA), sodium borohydride (NaBH<sub>4</sub>), methylene blue (MB) and methyl orange (MO) were purchased from Merck or Sigma-Aldrich company with high purity ( $\geq 98\%$ ) and used without further purification.

### 2.2. Preparation of Ag/CuFe<sub>2</sub>O<sub>4</sub>/rGO Nanocomposite

Graphene oxide (GO) nanosheets were prepared from natural graphite powder by a modified Hummer's method.<sup>38</sup> The graphite oxide layers were separated from each other through ultrasonication to acquire graphene oxide sheets. For synthesis of the Ag/CuFe<sub>2</sub>O<sub>4</sub>/rGO nano-

composite, the as-prepared GO (0.1 g), Fe(NO<sub>3</sub>)<sub>3</sub>·9H<sub>2</sub>O (2 mmol, 0.40 g) and Cu(NO<sub>3</sub>)<sub>2</sub>·3H<sub>2</sub>O (1 mmol, 0.12 g) were dispersed in 30 mL of ethylene glycol (EG) to form a clear solution, followed by the addition of sodium acetate (45 mmol, 3.10 g) and AgNO<sub>3</sub> (1.2 mmol, 0.20 g). The mixture was ultrasonicated for 120 min. Subsequently, the obtained suspension was transferred into a Teflon-lined stainless-steel autoclave. The autoclave was sealed and put into the oven, which was heated and maintained at 200 °C for 9 h, then taken out and allowed to cool naturally at room temperature. Finally, the black product was magnetically collected and washed thoroughly with water and ethanol, followed by drying at 50 °C for a few hours. It was denoted as Ag/CuFe<sub>2</sub>O<sub>4</sub>/rGO nanocomposite with 23 wt% Ag as confirmed by ICP-AES analysis. For comparison, Ag/CuFe<sub>2</sub>O<sub>4</sub>, Ag/rGO and CuFe<sub>2</sub>O<sub>4</sub>/rGO samples were synthesized under the same conditions in the absence of rGO, CuFe<sub>2</sub>O<sub>4</sub> and Ag, respectively. Also, the samples of rGO and Ag nanoparticles were prepared via the reduction of GO (0.1 g) and AgNO<sub>3</sub> (0.2 g), respectively, in 30 mL of ethylene glycol (EG) as solvent and reducing agent under hydrothermal conditions at 200 °C for 9 h.

### 2.3. Characterization Techniques

X-ray diffraction (XRD) measurements were carried out on a Rigaku D-max X-Ray diffractometer using Cu K $\alpha$  radiation ( $\lambda = 1.540 \text{ \AA}$ ). Fourier transform infrared (FT-IR) spectra were recorded using Shimadzu FT-IR 160 spectrometer over the wavenumber range from 4000 to 400 cm<sup>-1</sup>. Raman spectra were obtained using a Raman microscope with laser wavelength of 785 nm. The morphology and size of the nanocomposite particles were characterized by Mira3 Tescan, scanning electron microscope (FESEM) outfitted with energy field dispersive X-ray analyzer (EDX) for the elemental analysis of the sample. TEM images were obtained on the electron microscope (Philips CM120) at the accelerating voltage of 100 kV. The magnetic properties were measured using a vibrating sample magnetometer (Model: MDKFD, Magnetic Daneshpajoh Kashan Co., Iran) with a maximum magnetic field of 10 kOe. The Brunauer-Emmett-Teller (BET) surface area was measured by N<sub>2</sub> adsorption measurements at 77 K using Belsorp mini apparatus. UV-visible spectra were obtained from a Cary 100 Varian spectrophotometer in a wavelength range of 200–800 nm. The concentration of metals in the filtrate was determined by inductively coupled plasma atomic emission spectroscopy (Perkin Elmer ICP-AES).

### 2.4. Catalytic Reduction Tests

In order to study the catalytic performance of as-synthesized Ag/CuFe<sub>2</sub>O<sub>4</sub>/rGO nanocomposite in reductive processes, the reduction of some nitroaromatic compounds to corresponding amino derivatives by excess



$\text{NaBH}_4$  in aqueous solution was investigated. For this work, freshly prepared aqueous solution of  $\text{NaBH}_4$  (0.5 mL, 20 mM) was mixed with as-prepared aqueous solution (3 mL, 0.2 mM) of the nitroaromatic compounds, in the quartz cell (1.0 cm path length and 4 mL volume). Then, 3 mg of the  $\text{Ag}/\text{CuFe}_2\text{O}_4/\text{rGO}$  nanocatalyst was added into the solution and the progress of reduction was monitored by UV-Vis spectrophotometer in the range of 200–800 nm, with cycling over definite time intervals at room temperature.

## 2. 5. Dye Adsorption Tests

The adsorption experiments were performed as follows: 50 mg of the  $\text{Ag}/\text{CuFe}_2\text{O}_4/\text{rGO}$  nanomaterial was added into 50 mL of dye solution (25 mg/L) under stirring. At predetermined time intervals, the concentrations of dye solutions, from which the adsorbent was removed by magnetic separation, were determined by measuring the absorbance of dye solution (MB,MO) using a Cary 100 Varian UV-Vis spectrophotometer. A similar experiment was also done with 50 mL of MB solutions with different concentrations (25, 50, 75 and 100 mg/L). Moreover, the UV-Vis spectroscopy was performed to determine the selective adsorption ability of  $\text{Ag}/\text{CuFe}_2\text{O}_4/\text{rGO}$  nanocomposite at given time intervals. The amount of dye removal efficiency was calculated by the following equation:

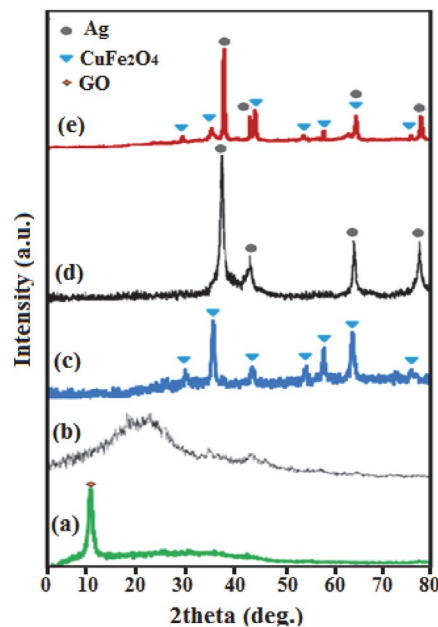
Removal efficiency (%) =  $(C_0 - C_t)/C_0 \times 100$ , where  $C_0$  and  $C_t$  are the dye concentrations (mg/L) at the initial and  $t$  time, respectively. In all aqueous solutions containing dye and  $\text{Ag}/\text{CuFe}_2\text{O}_4/\text{rGO}$  nanocomposite, the residual concentrations of Ag and Cu after removing the adsorbent were detected to be less than 0.1 wt% by ICP-AES analysis.

## 3. Results and Discussion

### 3. 1. Characterization of the $\text{Ag}/\text{CuFe}_2\text{O}_4/\text{rGO}$ Nanocomposite

The XRD analysis was used to investigate the composition and structure of the products. Figure 1 shows the XRD patterns of GO, rGO,  $\text{CuFe}_2\text{O}_4$ , Ag and  $\text{Ag}/\text{CuFe}_2\text{O}_4/\text{rGO}$  samples. Figure 1(a) and (b) shows the XRD patterns of pure GO and GO after it was reduced in EG solvent under hydrothermal conditions. Figure 1(a) shows that GO exhibited a sharp and high-intensity diffraction peak at about  $2\theta = 11.5^\circ$ . This result shows that a highly organized layer structure with an interlayer distance ( $d$  spacing) of 0.80 nm along the (002) orientation was produced. The (002) peak shifted to  $2\theta = 21.5$  with  $d$ -spacing of 0.35 nm after reduction; thus, the  $d$ -spacing decreased from 0.80 nm to 0.35 nm. This decrease in  $d$ -spacing was caused by the elimination of oxygen-containing functional groups and  $\text{H}_2\text{O}$  molecules from the graphite interlayers during the reduction process. As seen in Figure 1(c), the diffrac-

tion peaks indexed at  $2\theta = 30.2^\circ, 35.6^\circ, 43.2^\circ, 53.6^\circ, 57.1^\circ, 62.7^\circ$  and  $74.2^\circ$  are attributed to (220), (311), (400), (107), (511), (440) and (533) planes of cubic spinel structure of  $\text{CuFe}_2\text{O}_4$  (JCPDS-34-0425).<sup>39</sup> The XRD pattern of Ag nanoparticles in Figure 1(d) shows peaks at  $2\theta$  values of  $38.3^\circ, 43.5^\circ, 64.6^\circ$  and  $77.5^\circ$  which could be assigned to the (111), (200), (220) and (311) planes of metallic silver (JCPDS-04-0783).<sup>40</sup> From the XRD pattern of the  $\text{Ag}/\text{CuFe}_2\text{O}_4/\text{rGO}$  nanocomposite (Figure 1(e)), it is clear that all appeared peaks can be attributed to  $\text{CuFe}_2\text{O}_4$  and Ag phases. No characteristic diffraction peaks for rGO appeared in the pattern indicating that rGO nanosheets are not stacked during the nanocomposite formation process. The reason can be attributed to the fact that Ag and  $\text{CuFe}_2\text{O}_4$  nanoparticles anchored on the surface of rGO nanosheets prevented the exfoliated rGO nanosheets from restacking.<sup>41</sup> The average particle size of nanocomposite was calculated to be about 27 nm using the classical Scherrer equation:  $D_{\text{XRD}} = 0.9\lambda/(\beta\cos\theta)$ , where  $D_{\text{XRD}}$  represents the crystallite size,  $\lambda$  is the wavelength of Cu  $K\alpha$  (0.154 nm),  $\beta$  is the full width at half maximum of the diffraction peak, and  $\theta$  is the Bragg angle.



**Figure 1.** XRD patterns of (a) GO, (b) rGO, (c)  $\text{CuFe}_2\text{O}_4$ , (d) Ag and (e)  $\text{Ag}/\text{CuFe}_2\text{O}_4/\text{rGO}$  samples.

FT-IR spectra of GO, rGO,  $\text{CuFe}_2\text{O}_4$  and  $\text{Ag}/\text{CuFe}_2\text{O}_4/\text{rGO}$  samples are shown in Figure 2. In FT-IR spectrum of GO (Figure 2(a)) obvious characteristic bands of GO could be seen, including C=O stretching vibrations of COOH groups ( $1727\text{ cm}^{-1}$ ), graphitic C=C stretching vibrations ( $1618\text{ cm}^{-1}$ ), O-H deformation vibrations of tertiary C-OH ( $1398\text{ cm}^{-1}$ ), and C-O stretching vibrations of epoxy/alkoxy groups ( $1027\text{ cm}^{-1}$ ).<sup>42</sup> After hydrothermal treatment of the pure GO in EG solvent, the band of C=O

was eliminated and the intensity of O-H and C-O bands were considerably decreased, which indicated the removal of oxygen-containing functional groups and reduction of GO (Figure 2(b)). In the case of pure  $\text{CuFe}_2\text{O}_4$  (Figure 2(c)), the two characteristic bands appeared at 565 and

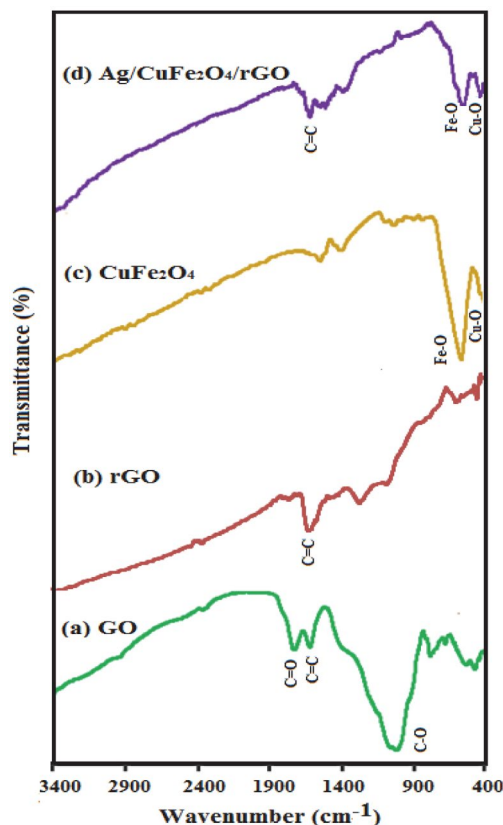


Figure 2. FT-IR spectra of (a) GO, (b) rGO, (c)  $\text{CuFe}_2\text{O}_4$ , and (d)  $\text{Ag/CuFe}_2\text{O}_4/\text{rGO}$  nanocomposite.

445  $\text{cm}^{-1}$  are related to the stretching vibrations of M–O (M = Fe and Cu) bonds in the tetrahedral and octahedral sites of spinel-type oxide, respectively.<sup>43,44</sup> As can be seen in Figure 2(d), the characteristic band of rGO at 1615  $\text{cm}^{-1}$  related to the graphitic C=C bond and the vibrational bands of  $\text{CuFe}_2\text{O}_4$  in the range of 600–400  $\text{cm}^{-1}$  were all observed in the IR spectrum of the nanocomposite sample which demonstrate the coexistence of rGO and  $\text{CuFe}_2\text{O}_4$  in this hybrid nanomaterial. Moreover, the disappearance of the characteristic bands of GO confirms the formation of rGO in the nanocomposite and the restoration of a graphitic structure in graphene.<sup>42</sup>

The morphology and microstructure of pure GO and  $\text{Ag/CuFe}_2\text{O}_4/\text{rGO}$  nanocomposite were investigated by SEM analysis. The SEM micrograph of pure GO in Figure 3(a) shows the highly porous and layered structure of GO having large stacks, possibly consisting of hundreds of GO nanosheets. It should also be noted that the surfaces of the GO sheets are quite flat and smooth. Figure 3(a) shows the SEM of GO nanosheets which stacked together due to the dispersive forces between them.<sup>45</sup> As can be seen in Figure 3(b), the surfaces of graphene nanosheets were covered with the agglomerated Ag and  $\text{CuFe}_2\text{O}_4$  nanoparticles. It should also be noted that the pores between the graphene sheets were evenly filled up with the Ag and  $\text{CuFe}_2\text{O}_4$  nanoparticles. In addition, the image of the nanocomposite clearly indicated that the surface properties of the modified GO product were strongly affected. Compared to pure GO, the surfaces of rGO nanosheets in the nanocomposite are rough, and the edges are highly crumpled.

Further investigation was carried out by energy dispersive X-ray spectroscopy (EDX) to characterize the composition of as-prepared  $\text{Ag/CuFe}_2\text{O}_4/\text{rGO}$  nanocomposite. The existence of Ag, Cu, Fe, C and O elements in the nanocomposite could be proved by the EDX elemental

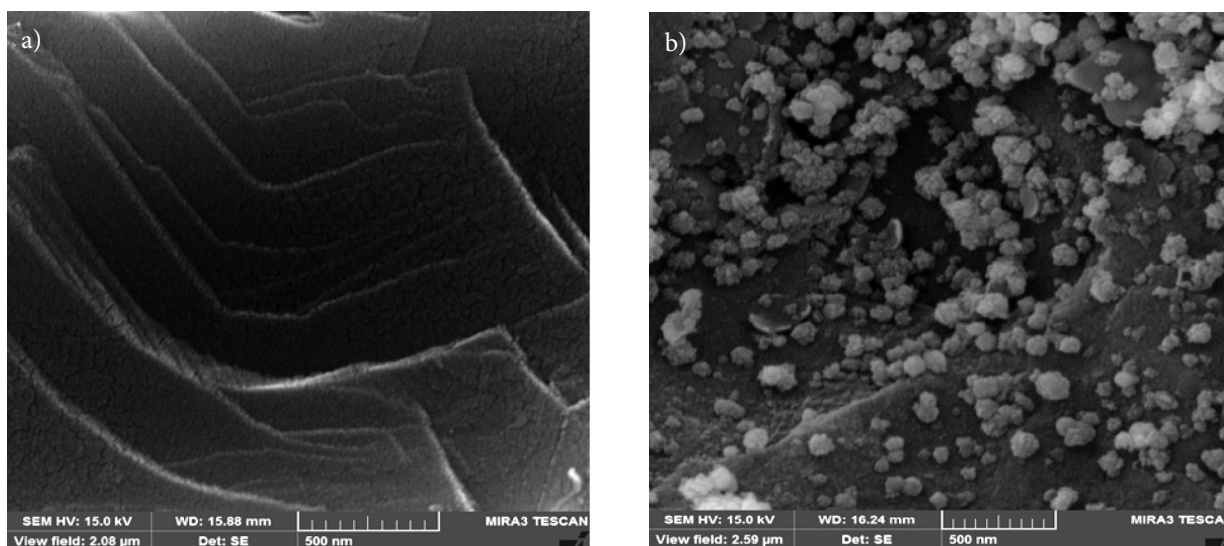
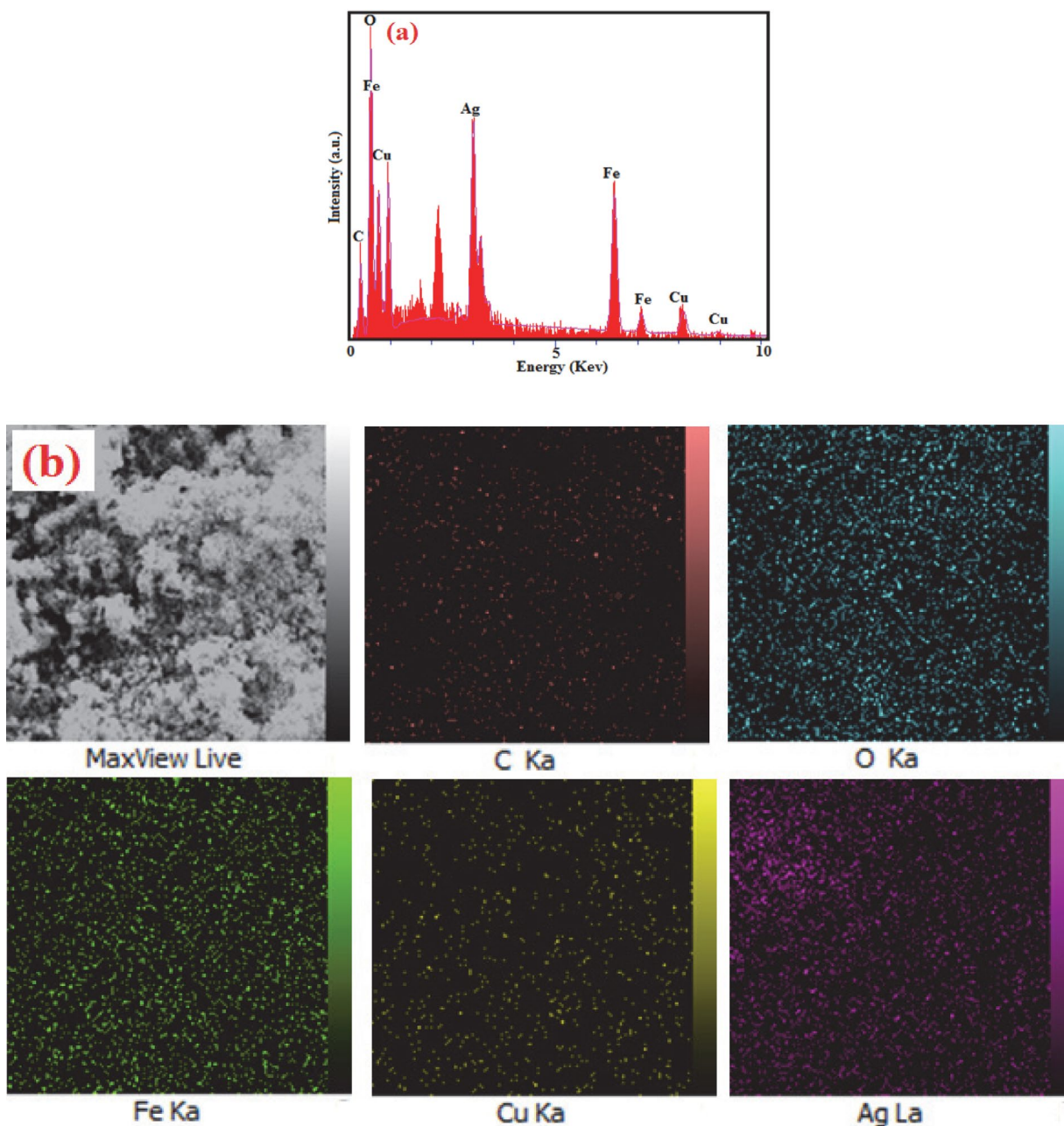


Figure 3. SEM images of (a) pure GO and (b)  $\text{Ag/CuFe}_2\text{O}_4/\text{rGO}$  nanocomposite.



**Figure 4.** (a) EDX spectrum and (b) a representative SEM image with corresponding EDX elemental mappings of the Ag/CuFe<sub>2</sub>O<sub>4</sub>/rGO nanocomposite.

spectrum as shown in Figure 4(a). Figure 4(b) shows a representative SEM image of the nanocomposite with corresponding EDX elemental mappings. The distribution of corresponding elemental mappings confirmed that the elements were uniformly distributed over the nanocomposite, confirming the homogeneity of the sample. The EDX results further indicated that the Ag and CuFe<sub>2</sub>O<sub>4</sub> nanoparticles were successfully loaded on the surface of rGO.

Figure 5 shows the TEM images of Ag/CuFe<sub>2</sub>O<sub>4</sub> and Ag/CuFe<sub>2</sub>O<sub>4</sub>/rGO samples. Figure 5(a) shows the typical TEM image of the Ag/CuFe<sub>2</sub>O<sub>4</sub>, displaying that the sample consists of a large quantity of nearly uniform spheres

nanoparticles which loosely aggregated. As can be seen in Figure 5(b), the almost transparent graphene sheets are fully exfoliated and decorated homogeneously with Ag and CuFe<sub>2</sub>O<sub>4</sub> nanoparticles having an average diameter of 30 nm in consistent with the average particle size calculated from Debye-Scherrer formula. No obvious aggregation was seen in Figure 5(b). The rGO sheets could not only prevent agglomeration of the Co<sub>3</sub>O<sub>4</sub> nanoparticles and enable a good dispersion of these spherical particles, but also substantially enhance the specific surface area of the composite.

Raman analysis is a powerful technique to monitor significant structural changes of GO nanostructures

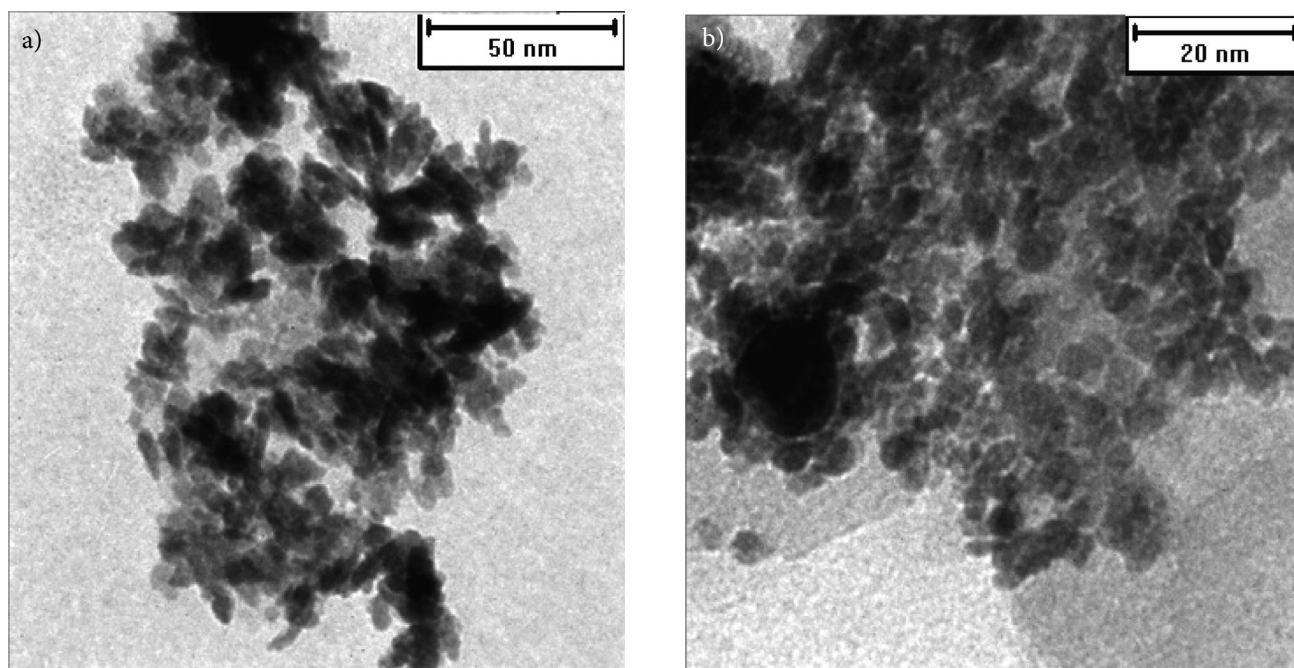


Figure 5. TEM images of (a) Ag/CuFe<sub>2</sub>O<sub>4</sub> and (b) Ag/CuFe<sub>2</sub>O<sub>4</sub>/rGO nanocomposite.

during the reduction and composite formation. Figure 6 presents the Raman spectra of GO, rGO and Ag/CuFe<sub>2</sub>O<sub>4</sub>/rGO nanocomposite samples. Figure 6(a) and (b) shows the Raman spectra of the pure GO and GO sample after its reduction in EG solvent under hydrothermal conditions.

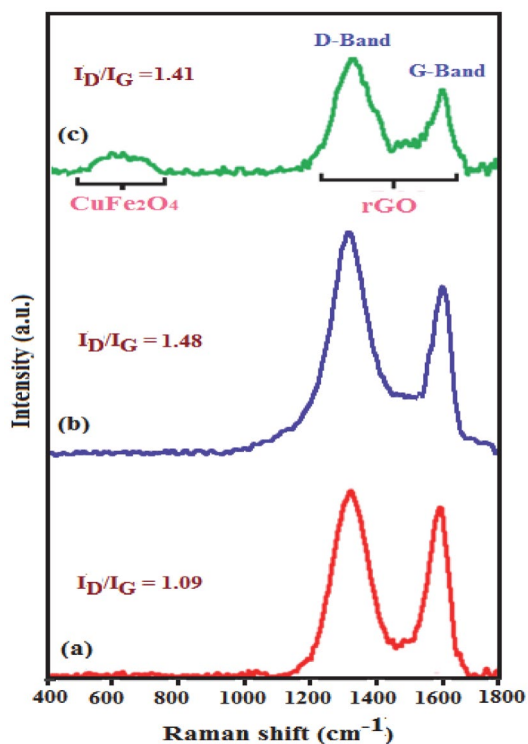
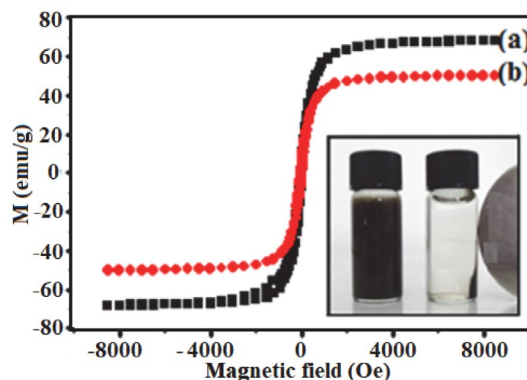


Figure 6. Raman spectra of (a) GO, (b) rGO and (c) Ag/CuFe<sub>2</sub>O<sub>4</sub>/rGO.

According to the Raman spectra of GO and rGO, the two characteristic bands at about 1318 and 1589 cm<sup>-1</sup> can be attributed to the disordered structure (D band, sp<sup>3</sup> carbon atoms of disorders and defects) and graphitic structure (G band, sp<sup>2</sup> carbon atoms in graphitic sheets) of GO nanosheets, respectively.<sup>46</sup> As can be seen in Figure 6(c), the D and G bands still exist in the Raman spectrum of Ag/CuFe<sub>2</sub>O<sub>4</sub>/rGO composite, besides a broad band around 600 cm<sup>-1</sup> related to the A<sub>1g</sub> stretching vibration of Fe-O bond in the FeO<sub>6</sub> groups of CuFe<sub>2</sub>O<sub>4</sub> nanoparticles.<sup>47</sup> Then, this finding demonstrates the coexistence of CuFe<sub>2</sub>O<sub>4</sub> and rGO in the nanocomposite. Compared to pure GO and rGO samples, the position of D and G bands slightly shifted likely due to the strong interaction of the Ag and CuFe<sub>2</sub>O<sub>4</sub> nanoparticles with the rGO nanosheets. Furthermore, the D band to G band intensity ratios for rGO ( $I_D/I_G = 1.48$ ) and Ag/CuFe<sub>2</sub>O<sub>4</sub>/rGO ( $I_D/I_G = 1.41$ ) are larger compared with that of pure GO ( $I_D/I_G = 1.09$ ), which can be attributed to the increase in the degree of disorder and defects, and also the decrease in the average size of sp<sup>2</sup> domains.<sup>48</sup> The increase in the  $I_D/I_G$  ratio also confirms that the GO has been deoxygenated and reduced to rGO.

The magnetic properties of CuFe<sub>2</sub>O<sub>4</sub> and Ag/CuFe<sub>2</sub>O<sub>4</sub>/rGO samples were examined using a vibrating sample magnetometer (VSM) at ambient temperature. From Figure 7(a) and (b), the saturation magnetizations ( $M_s$ ) of the CuFe<sub>2</sub>O<sub>4</sub> and Ag/CuFe<sub>2</sub>O<sub>4</sub>/rGO were found to be 68 emu/g and 48.2 emu g<sup>-1</sup>, respectively. The slope defined as S-like shape of the magnetic hysteresis loops as well as the fact that both materials exhibit zero coercivity ( $H_c$ ) and very low remanence ( $M_r$ ) at ambient tempera-

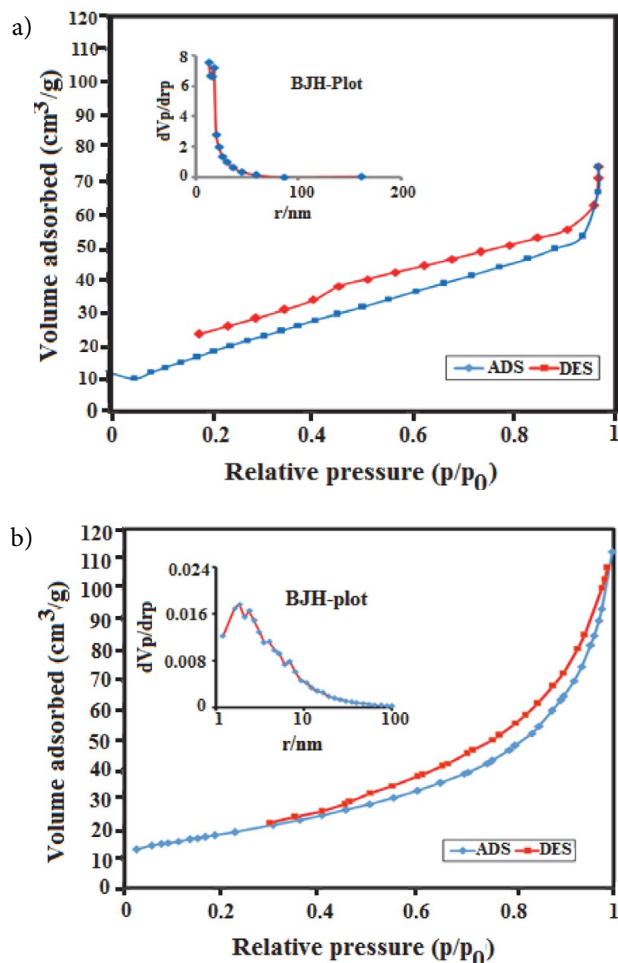


**Figure 7.** Magnetic hysteresis loops of (a) pure  $\text{CuFe}_2\text{O}_4$  and (b)  $\text{Ag}/\text{CuFe}_2\text{O}_4/\text{rGO}$  at room temperature. The inset image shows the  $\text{Ag}/\text{CuFe}_2\text{O}_4/\text{rGO}$  suspension in the absence and presence of an external magnetic field.

ture allowed ranking them as superparamagnetic.<sup>49</sup> The lower range of magnetization ( $\text{emu g}^{-1}$ ) for the  $\text{Ag}/\text{CuFe}_2\text{O}_4/\text{rGO}$  can be related to the decrease of  $\text{CuFe}_2\text{O}_4$  content due to the presence of non-magnetic components

(silver and graphene) in the nanocomposite. From the inset Figure 7, it is evident that homogeneous black  $\text{Ag}/\text{CuFe}_2\text{O}_4/\text{rGO}$  suspension can be easily separated from solution under an external magnet influence.

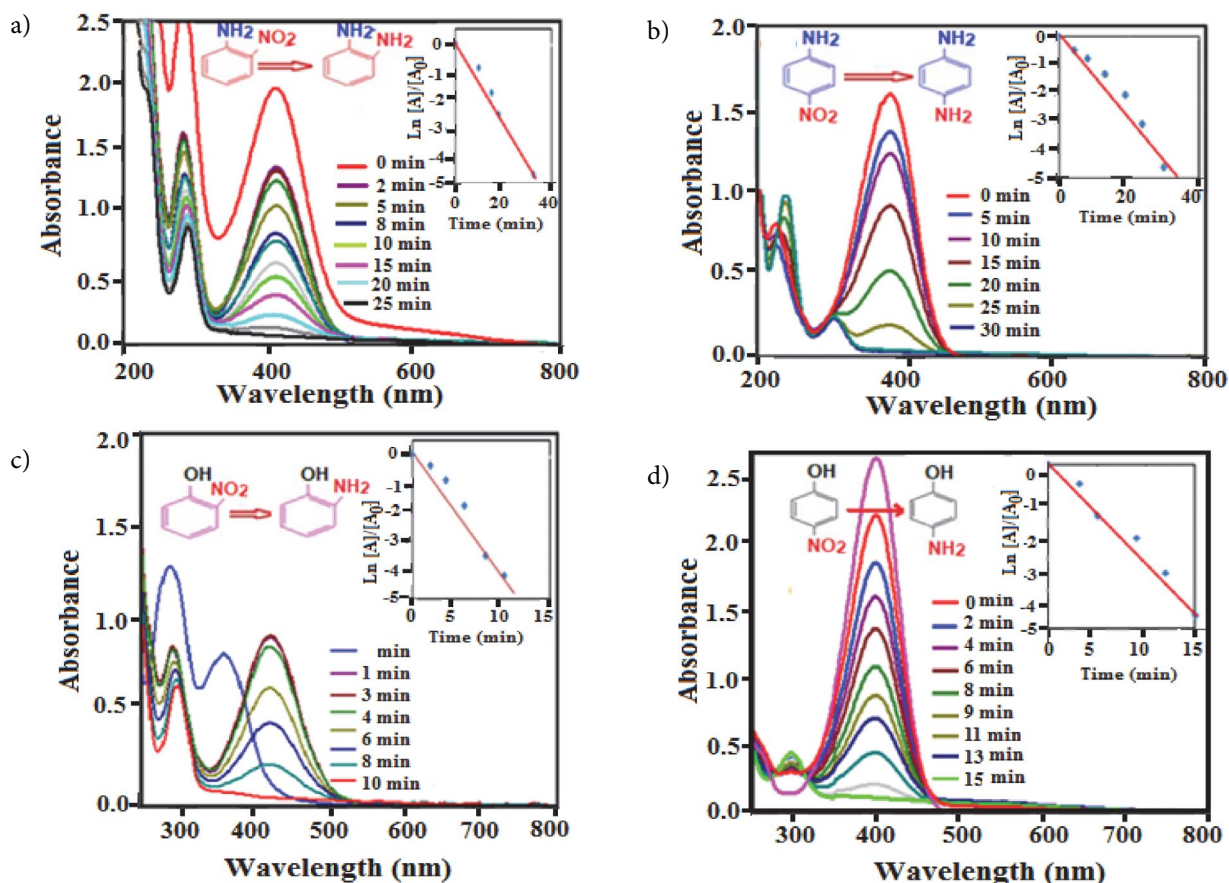
Figure 8 shows the nitrogen adsorption–desorption isotherms and corresponding pore size distributions curves (the inset) of  $\text{rGO}$  and  $\text{Ag}/\text{CuFe}_2\text{O}_4/\text{rGO}$  samples. As seen in Figure 8(a) and (b), the isotherms of  $\text{GO}$  and  $\text{Ag}/\text{CuFe}_2\text{O}_4/\text{rGO}$  nanocomposite can be classified to type-IV with  $\text{H}_4$ -type hysteresis loop for  $\text{rGO}$  and  $\text{H}_3$ -type hysteresis loop for the nanocomposite at high relative pressures according to the IUPAC classification, which indicate the presence of mesopores.<sup>50</sup> The BET surface area ( $S_{\text{BET}}$ ) of the  $\text{Ag}/\text{CuFe}_2\text{O}_4/\text{rGO}$  nanocomposite is  $90.20 \text{ m}^2/\text{g}$  with the total pore volume of  $0.261 \text{ cm}^3/\text{g}$ , which are greater than the values of  $\text{rGO}$  ( $S_{\text{BET}} = 79.15 \text{ m}^2/\text{g}$  and total pore volume =  $0.123 \text{ cm}^3/\text{g}$ ). It can be concluded that immobilizing  $\text{Ag}$  and  $\text{CuFe}_2\text{O}_4$  nanoparticles on the surface of graphene nanosheets increases the surface area and porosity which are favorable factors for improving the catalytic and adsorption performances.



**Figure 8.**  $\text{N}_2$  adsorption-desorption isotherms and pore-size distribution curves (the insets) of (a)  $\text{rGO}$  and (b) the  $\text{Ag}/\text{CuFe}_2\text{O}_4/\text{rGO}$  nanocomposite.

### 3. 2. Catalytic Reduction of Nitroarenes over the $\text{Ag}/\text{CuFe}_2\text{O}_4/\text{rGO}$ Nanocomposite

The catalytic activity of the  $\text{Ag}/\text{CuFe}_2\text{O}_4/\text{rGO}$  nanocomposite was evaluated for the reduction of 2-nitroaniline (2-NA), 4-nitroaniline (4-NA), 2-nitrophenol (2-NP) and 4-nitrophenol (4-NP) in the presence of sodium borohydride ( $\text{NaBH}_4$ ). In the reduction process, the initial concentrations of  $\text{NaBH}_4$  and nitroaromatics were  $20 \text{ mM}$  and  $0.2 \text{ mM}$ , respectively. Figure 9(a)-(d) shows the typical UV-visible spectra and concentration changes of nitroaromatic compounds in the presence of  $\text{Ag}/\text{CuFe}_2\text{O}_4/\text{rGO}$  nanocomposite and  $\text{NaBH}_4$ . All compounds have an absorbance peak at about  $400 \text{ nm}$  under alkaline conditions.<sup>51–56</sup> The intensity of this peak decreases when the reduction proceeds in the presence of  $\text{Ag}/\text{CuFe}_2\text{O}_4/\text{rGO}$  nanocatalyst. The characteristic absorption peaks of 2-NA, 4-NA, 2-NP and 4-NP were disappeared in 25, 30, 10 and 15 min, respectively. Since the reductive reactions were carried out under the same experimental conditions, the different rates can be related to the structures of organic compounds. The pseudo first-order kinetics can be applied to evaluate the rate constants in the reduction process, because the concentration of  $\text{NaBH}_4$  is higher compared to that of nitroarenes and it can be considered as a constant during the reaction time. The concentration of mentioned compounds at time  $t$  is defined as  $C_t$  and the initial concentration of them at  $t = 0$  is regarded as  $C_0$ . The  $C_t/C_0$  is measured from the relative intensity of absorbance ( $A_t/A_0$ ). As shown in the insets of Figure 9(a)-(d), the linear relationship of  $\ln[A_t]/[A_0]$  versus time ( $t$ ) indicates that the reduction of nitrophenols and nitroanilines over  $\text{Ag}/\text{CuFe}_2\text{O}_4/\text{rGO}$  nanocomposite follows the pseudo first-order kinetics.



**Figure 9.** UV–visible absorption spectra of reaction solutions containing (a) 2-nitroaniline (b) 4-nitroaniline (c) 2-nitrophenol (d) 4-nitrophenol. The insets show plots of  $\ln[A]/[A_0]$  against time.

As shown in Figure S1 (Supporting Information (SI)) Ag/CuFe<sub>2</sub>O<sub>4</sub>, Ag/rGO and CuFe<sub>2</sub>O<sub>4</sub>/rGO samples showed lower activity for the reduction of 4-NP com-

pared to the ternary Ag/CuFe<sub>2</sub>O<sub>4</sub>/rGO nanocomposite, and they could not be regarded as effective catalysts for this reaction. Moreover, no considerable change in the ab-

**Table 1.** Comparison of the results obtained for the reduction of 4-NP in the present work with those obtained by some reported catalysts.

Entry	Catalyst	Conditions	Time	Ref.
1	Ni-PVA/SBA-15	H <sub>2</sub> O, NaBH <sub>4</sub> , r.t.	85 min	[57]
2	Hierarchical Au/CuO NPs	H <sub>2</sub> O, NaBH <sub>4</sub> , r.t.	80 min	[58]
3	Cu NPs	THF/H <sub>2</sub> O, NaBH <sub>4</sub> , 50 °C	2 h	[59]
4	PdCu/graphene	EtOH/H <sub>2</sub> O, NaBH <sub>4</sub> , 50 °C	1.5 h	[60]
5	Au-GO	H <sub>2</sub> O, NaBH <sub>4</sub> , r.t.	30 min	[61]
6	CoFe <sub>2</sub> O <sub>4</sub> NPs	H <sub>2</sub> O, NaBH <sub>4</sub> , r.t.	50 min	[62]
7	FeNi <sub>2</sub> nano-alloy	H <sub>2</sub> O, NaBH <sub>4</sub> , r.t.	60 min	[63]
8	NiCo <sub>2</sub> nano-alloy	H <sub>2</sub> O, NaBH <sub>4</sub> , r.t.	30 min	[64]
9	CdS/GO	H <sub>2</sub> O, NaBH <sub>4</sub> , r.t.	30 min	[65]
10	dumbbell-like CuO NPs	H <sub>2</sub> O, NaBH <sub>4</sub> , r.t.	12 min	[66]
11	Ni NPs	H <sub>2</sub> O, NaBH <sub>4</sub> , r.t.	16 min	[67]
12	CuFe <sub>2</sub> O <sub>4</sub> NPs	H <sub>2</sub> O, NaBH <sub>4</sub> , r.t.	14 min	[68]
13	Au NPs	H <sub>2</sub> O, NaBH <sub>4</sub> , r.t.	4 min	[69]
14	Pd/RGO/Fe <sub>3</sub> O <sub>4</sub> NPs	H <sub>2</sub> O, NaBH <sub>4</sub> , r.t.	1 min	[70]
15	Cu/Fe <sub>3</sub> O <sub>4</sub> NPs	H <sub>2</sub> O, NaBH <sub>4</sub> , r.t.	55 sec	[71]
16	Cu NPs/Perlite	H <sub>2</sub> O, NaBH <sub>4</sub> , r.t.	2.5 min	[72]
17	Ag/CuFe <sub>2</sub> O <sub>4</sub> /GO	H <sub>2</sub> O, NaBH <sub>4</sub> , r.t.	15 min	This work

sorbance band of 4-NP at 400 nm was observed in the absence of Ag/CuFe<sub>2</sub>O<sub>4</sub>/rGO, confirming that the reduction is mostly catalyzed by the Ag/CuFe<sub>2</sub>O<sub>4</sub>/rGO nanocomposite. In the presence of Ag/CuFe<sub>2</sub>O<sub>4</sub>/rGO nanocomposite and NaBH<sub>4</sub>, the nitroarenes are easily reduced in aqueous solutions.

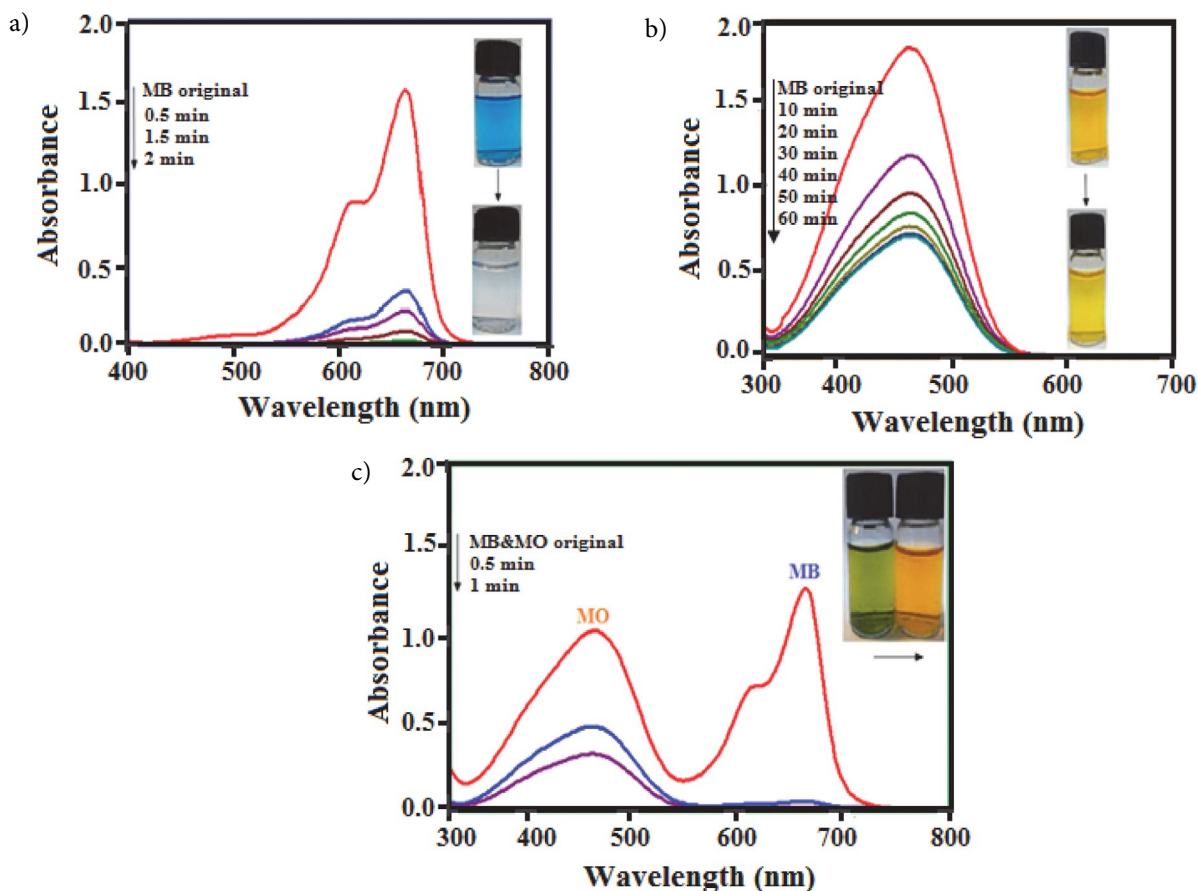
The study of the reaction mechanism helps to design a catalyst with better output. Figure S2 shows the catalytic mechanism of 4-NP reduction by the Ag/CuFe<sub>2</sub>O<sub>4</sub>/rGO nanocomposite in the presence of NaBH<sub>4</sub>. During the hydrogenation reduction process, BH<sub>4</sub><sup>-</sup> and 4-NP are first adsorbed on the surface of the catalyst, and then the Ag nanoparticles transfer electrons from BH<sub>4</sub><sup>-</sup> to 4-NP, leading to the production of 4-aminophenol (4-AP).<sup>21</sup> After the reaction is completed, the Ag/CuFe<sub>2</sub>O<sub>4</sub>/rGO nanocatalyst can be separated easily from the solution by a magnet and applied for next reaction.

The obtained results in the reduction of 4-NP with NaBH<sub>4</sub> over the Ag/CuFe<sub>2</sub>O<sub>4</sub>/rGO nanocatalyst were compared with some reported catalysts in the literature (Table 1).<sup>57–72</sup> It is clear that with respect to the reaction conditions and/or reaction times, the present method is more suitable and/or superior (Table 1, entries 1–9). The reaction in the presence of most reported catalysts required

longer reaction times. However, compared with some these reports, the Ag/CuFe<sub>2</sub>O<sub>4</sub>/rGO catalyst also presented close or lower catalytic activity for the reduction of 4-NP (Table 1, entries 10–16). Nevertheless, the Ag/CuFe<sub>2</sub>O<sub>4</sub>/rGO can be easily prepared and reused without the use of harsh, toxic and expensive chemicals which is very important in practical applications.

### 3. 3. Adsorption Performance of the Ag/CuFe<sub>2</sub>O<sub>4</sub>/rGO Nanocomposite

There are some methods on the effective elimination of hazardous substances from aqueous solutions, such as photo and sonocatalytic degradation, oxidation and adsorption that among them, adsorption is a good choice due to its higher efficiency and simpler operation.<sup>73</sup> In this context, considering the structure of the packed sp<sup>2</sup>-bonded carbon atoms of rGO and magnetic property of CuFe<sub>2</sub>O<sub>4</sub>, it is expected that the Ag/CuFe<sub>2</sub>O<sub>4</sub>/rGO can be used as a novel and effective adsorbent for the removal of organic aromatic pollutants from wastewaters. The adsorption capacity was evaluated using two dyes: positively charged methylene blue (MB) and negatively charged methyl orange (MO). As indicated in Figure 10(a), the



**Figure 10.** The adsorption capacity of Ag/CuFe<sub>2</sub>O<sub>4</sub>/rGO toward different organic dyes: (a) MB, (b) MO and (c) mixed dyes (MB + MO). Experimental conditions: dosage of adsorbent = 50 mg, [dye] = 25 mg/L, temperature = 25 °C and pH=7.

characteristic UV-vis absorption band of MB at 664 nm, decreased and disappeared within only 2 min. The extraordinary removal of MB could be largely ascribed to the  $\pi$ - $\pi$  stacking between dyes and rGO nanosheets.<sup>40</sup> The electrostatic interactions between the positively charged dye and negatively charged residual oxygen-containing functional groups of rGO, were also effective in the adsorption process. The Ag/CuFe<sub>2</sub>O<sub>4</sub> nanoparticles could be acted as spacers to minimize the agglomeration of the rGO nanosheets. The adsorption ability of Ag/CuFe<sub>2</sub>O<sub>4</sub>/rGO nanocomposite towards MO dye was also investigated (Figure 10(b)). From the figure, the absorbance of MO at 463 nm decreased slightly after 60 min and the removal efficiency of MO was about 61%. Moreover, to confirm the ability of the Ag/CuFe<sub>2</sub>O<sub>4</sub>/rGO nanocomposite to separate MB and MO dye molecules, a mixed dye solution was selected to determine the selective adsorption capacity of the solid composite. From Figure 10(c), the absorption peak of MB disappeared quickly; just leaving the absorption peak of MO, indicating that Ag/CuFe<sub>2</sub>O<sub>4</sub>/rGO composite could selectively adsorb the cationic MB dye when exposed to the mixed solutions of MB+MO. The finding indicates that the Ag/CuFe<sub>2</sub>O<sub>4</sub>/rGO nanocomposite also possesses selective adsorption ability towards the cationic dyes in wastewater.

### 3. 3. 1. Effect of the Initial Concentration of MB

As shown in Figure 11(a), the effect of the initial concentration of MB solution on adsorption efficiency was studied. Accordingly to the obtained results, the adsorption percentage of the nanocomposite towards MB can reach up to about 100% at lower initial concentrations (15 and 25 and 75 mg/L). However, for MB with concentration of 100 mg/L, adsorption percentage decreased to 70% within 30 minutes and the Ag/CuFe<sub>2</sub>O<sub>4</sub>/rGO nanocomposite could not adsorb more dye molecules due to saturation of adsorption capacity.

### 3. 3. 2. Effect of Type of Adsorbent

Figure 11(b) represents the adsorption capacities of Ag/CuFe<sub>2</sub>O<sub>4</sub>, rGO and Ag/CuFe<sub>2</sub>O<sub>4</sub>/rGO samples toward MB dye. As seen, the removal efficiency of MB by rGO and Ag/CuFe<sub>2</sub>O<sub>4</sub> nanoparticles are 78% and 25% respectively. The high adsorption performance of graphene sheets mainly is due to the large surface area and graphitized basal plane structure of it, which could provide excellent conditions for adsorption of dyes.<sup>31</sup> However, in the presence of Ag/CuFe<sub>2</sub>O<sub>4</sub>/rGO nanocomposite, the removal efficiency of MB is increased to 100% indicating the as-prepared nanocomposite is more suitable and superior. The Ag and CuFe<sub>2</sub>O<sub>4</sub> nanoparticles on the surface of graphene prohibit the restacking of its layers and thus increase the surface area and adsorption capacity of the composite. This result is consistent with BET analyses.

### 3. 3. 3. Effect of Adsorbent Dosage

The influence of the adsorbent dosage on MB adsorption in Figure 11(c) indicates that with the increase of the adsorbent dosage from 25 to 35 mg, the removal efficiency of MB is enhanced to 78%, and when the dosage is 50 mg, it reaches 100% within 2 min. The finding indicates that 50 mg is the suitable dosage for the adsorption of 25mg/L MB solution.

### 3. 3. 4. Effect of pH

As shown in Figure 11(d), the initial solution pH plays an important role in the adsorption of MB on the surface of Ag/CuFe<sub>2</sub>O<sub>4</sub>/rGO nanocomposite. The adsorption of MB increases gradually as pH value increases from 2 to 7 and finally maintains the high level with increasing pH. In acidic pHs, the surface of Ag/CuFe<sub>2</sub>O<sub>4</sub>/rGO nanocomposite is positively charged due to protonation reaction. Thus, the electrostatic repulsion between positively charged MB dye and Ag/CuFe<sub>2</sub>O<sub>4</sub>/rGO nanocomposite leads to the low adsorption of MB in this pH range. However, at pH  $\geq$  7, the surface of the adsorbent is negatively charged and more available to retain the cationic MB dye, resulting in the increase of MB adsorption. In the pH range of 7-11, the removal of MB reaches maximum and remains approximately constant.

### 3. 3. 5. Recyclability of the Ag/CuFe<sub>2</sub>O<sub>4</sub>/rGO Nanocomposite

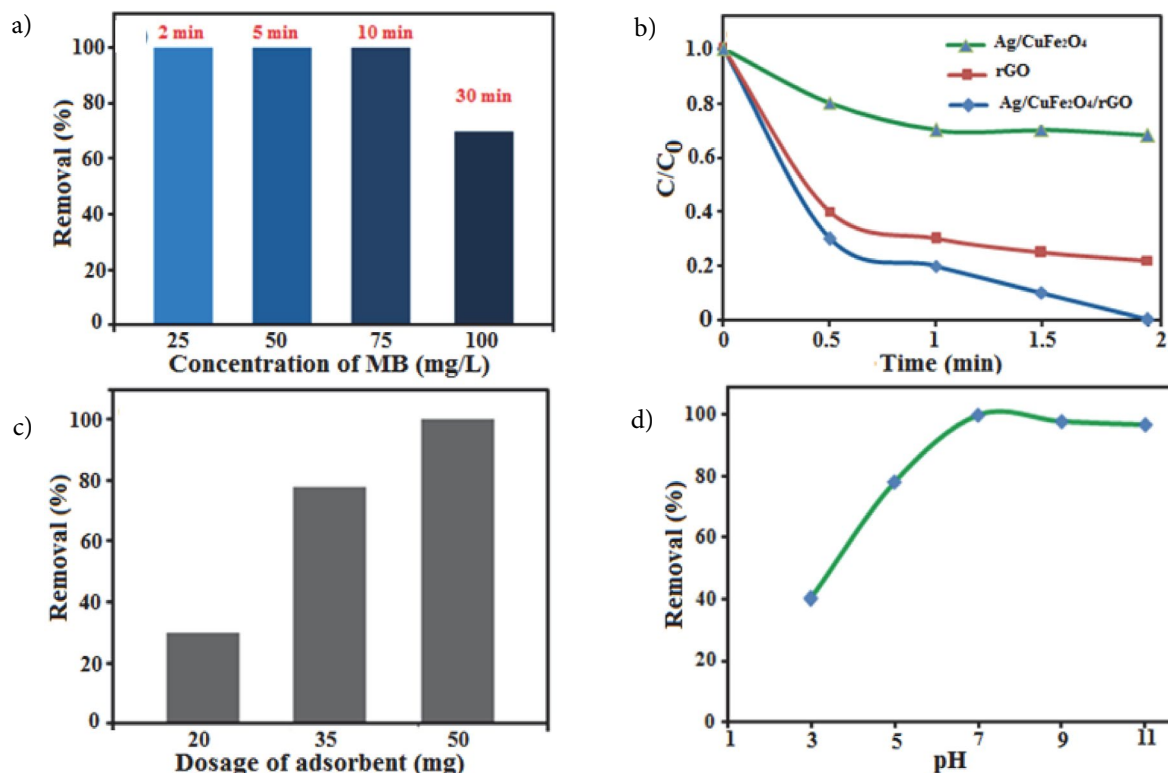
To evaluate the stability and reusability of the Ag/CuFe<sub>2</sub>O<sub>4</sub>/rGO nanocomposite which are important factors for practical applications, recycling experiments were performed. The composite was separated from the reaction mixture by an external magnet after the first use in the adsorption of MB and washed thoroughly with ethanol. The recovered nanocomposite was found to be reusable for at least five runs without significant loss in activity. As shown in Figure S3, the slight decrease of performance could be observed after five runs.

The amounts of Ag and Cu metals in aqueous solution after each run were analyzed by ICP-AES. It was shown that the leaching of these metals from the catalyst is negligible, confirming the stability of the composite. Furthermore, the structural stability was investigated by XRD, FT-IR, EDX and SEM analyses after five runs. As shown in Figure S4, these results did not show significant change after the fifth run in comparison with those of the fresh sample.

## 4. Conclusions

In summary, the Ag/CuFe<sub>2</sub>O<sub>4</sub>/rGO nanocomposite was prepared through a facile one-top solvothermal route. The Ag/CuFe<sub>2</sub>O<sub>4</sub> nanoparticles were loaded on the surface





**Figure 11.** The adsorption capacity of the Ag/CuFe<sub>2</sub>O<sub>4</sub>/rGO nanocomposite toward MB solutions with different values of (a) concentration of dye, (b) type of adsorbent, (c) dosage of adsorbent and (d) pH.

of GO and the nanocomposite displayed magnetic property. The catalytic performance of this composite was excellent for reduction of nitroarenes in the presence of NaBH<sub>4</sub>. The adsorption capacity of MB and MO dyes was also investigated and indicated that the removal efficiency of MB was 100% within only 2 min. Interestingly, due to the fast adsorption of MB molecules, the Ag/CuFe<sub>2</sub>O<sub>4</sub>/rGO nanocomposite could be used as effective and selective adsorbent for the removal of MB molecules from the mixed MB+MO dye solution. The Ag/CuFe<sub>2</sub>O<sub>4</sub>/rGO was separated from solution for reusing by simply applying an external magnetic field. Results obtained in this work open a way to the fabrication of effective nanomaterials for serving as an ideal platform to study the various heterogeneous catalytic processes and wastewater purification.

## 5. Acknowledgements

The authors gratefully acknowledge the Lorestan University Research Council and Iran Nanotechnology Initiative Council (INIC) for their financial supports.

## 6. References

1. Y. Wu, M. Wen, Q. Wu and H. Fang, *J. Phys. Chem. C*, **2014**, *118*, 6307–6313. DOI:10.1021/jp412711b
2. Y. Lu, Y. Mei, M. Ballauff and M. Drechsler, *J. Phys. Chem. B*, **2006**, *110*, 3930–3937. DOI:10.1021/jp412711b
3. Z. Jiang, J. Xie, D. Jiang, J. Jing and H. Qin, *CrystEngComm*, **2012**, *14*, 4601. DOI:10.1039/c2ce25205h
4. A. Saha and B. Ranu, *J. Org. Chem.*, **2008**, *73*, 6867–6870. DOI:10.1021/jo800863m
5. S. Gosh, *Appl. Catal. A: Gen.*, **2004**, *268*, 61–66. DOI:10.1016/j.apcata.2004.03.017
6. S. Zhou, M. Wen, N. Wang, Q. Wu, Q. Wu and L. Cheng, *J. Mater. Chem.*, **2012**, *22*, 16858–16864. DOI:10.1039/c2jm32397d
7. G. Wienhöfer, I. Sorribes, A. Boddien, F. Westerhaus, K. Junge, H. Junge, R. Llusar and M. Beller, *J. Am. Chem. Soc.*, **2011**, *133*, 12875–12879.
8. S. Farhadi and F. Siadatnasab, *Chin. J. Catal.*, **2016**, *37*, 1487–1495. DOI:10.1016/S1872-2067(16)62473-7
9. S. Karthikeyan, V. K. Gupta, R. Boopathy, A. Titus and G. Sekaran, *J. Mol. Liq.*, **2012**, *173*, 153–163. DOI:10.1016/j.molliq.2012.06.022
10. Y. Liu, C. Luo, J. Sun, H. Li, Z. Sun and S. Yan, *J. Mater. Chem. A*, **2015**, *3*, 5674–5682. DOI:10.1039/C4TA07112C
11. L. Zhang, B. Shan, H. Yang, D. Wu, R. Zhu, J. Nie and R. Cao, *RSC Adv.*, **2015**, *5*, 23556–23562.
12. P. Chowdhury and T. Viraraghavan, *Sci. Total Environ.*, **2009**, *407*, 2474–2492. DOI:10.1016/j.scitotenv.2008.12.031
13. F.-J. Ma, S.-X. Liu, C.-Y. Sun, D.-D. Liang, G.-J. Ren, F. Wei, Y.-G. Chen and Z.-M. Su, *J. Am. Chem. Soc.*, **2011**, *133*, 4178–4181. DOI:10.1021/ja109659k

14. M. Y. Zhu, D. H. Meng, C. J. Wang, J. Di and G. W. Diao, *Chin. J. Catal.*, **2013**, *34*, 2125–2129. DOI:10.1016/S1872-2067(12)60717-7
15. J. J. Yan, K. Wang, H. Xu, J. Qian, W. Liu, X. W. Yang and H. M. Li, *Chin. J. Catal.*, **2013**, *34*, 1876–1882. DOI:10.1016/S1872-2067(12)60677-9
16. R. K. Narayanan and S. J. Devaki, *Ind. Eng. Chem. Res.*, **2015**, *54*, 1197–1203. DOI:10.1021/ie5038352
17. K. R. Gopidas, J. K. Whitesell and M. A. Fox, *Nano Lett.*, **2003**, *3*, 1757–1760. DOI:10.1021/nl0348490
18. R. Narayanan and M. A. El-Sayed, *J. Am. Chem. Soc.*, **2003**, *125*, 8340–8347. DOI:10.1021/ja035044x
19. T. T. Nge, M. Nogi and K. Suganuma, *J. Mater. Chem. C*, **2013**, *1*, 5235–5243. DOI:10.1039/c3tc31220h
20. S. J. Devaki, R. K. Narayanan and S. Sarojam, *Mater. Lett.*, **2014**, *116*, 135–138. DOI:10.1016/j.matlet.2013.10.110
21. F. Lin and R. Doong, *J. Phys. Chem. C*, **2011**, *115*, 6591–6598. DOI:10.1021/jp110956k
22. C. Xu, J. Xie, D. Ho, C. Wang, N. Kohler, E. G. Walsh, J. R. Morgan, Y. E. Chin and S. Sun, *Angew. Chem. Int. Ed.*, **2008**, *47*, 173–176. DOI:10.1002/anie.200704392
23. M. S. Chen, *Science*, **2004**, *306*, 252–255. DOI:10.1126/science.1102420
24. M. Comotti, W.-C. Li, B. Spliethoff and F. Schüth, *J. Am. Chem. Soc.*, **2006**, *128*, 917–924. DOI:10.1021/ja0561441
25. S. Tang, S. Vongehr and X. Meng, *J. Mater. Chem.*, **2010**, *20*, 5436. DOI:10.1039/c0jm00456a
26. A. K. Geim and K. S. Novoselov, *Nat. Mater.*, **2007**, *6*, 183–191. DOI:10.1038/nmat1849
27. S. Zhang, Y. Y. Shao, H. G. Liao, I. A. Aksay, G. P. Yin and Y. H. Lin, *Chem. Mater.*, **2011**, *23*, 1079–1081. DOI:10.1021/cm101568z
28. R. S. Weatherup, C. Baecht, B. Dlubak, B. C. Bayer, P. R. Kidambi, R. Blume, R. Schloegl and S. Hofmann, *Nano Lett.*, **2013**, *13*, 4624–4631. DOI:10.1021/nl401601x
29. Y. Wenzhu and C. Huaqiang, *RSC Adv.*, **2016**, *6*, 100636–100642.
30. H. M. Sun, L. Y. Cao and L. H. Lu, *Nano Res.*, **2011**, *4*, 550–62. DOI:10.1007/s12274-011-0111-3
31. S. Wang, J. Wei, S. Lv, Z. Guo and F. Jiang, *Clean – Soil, Air, Water*, **2013**, *41*, 992–1001. DOI:10.1002/clen.201200093
32. Y. J. Xu, G. Weinberg, X. Liu, O. Timpe, R. Schlogl and D. S. Su, *Adv. Funct. Mater.*, **2008**, *18*, 3613–3619. DOI:10.1002/adfm.200800726
33. T. Zhu, J. S. Chen and X. W. Lou, *J. Phys. Chem. C*, **2012**, *116*, 6873–6878. DOI:10.1021/jp300224s
34. M. Valix, W. H. Cheung and G. McKay, *Langmuir*, **2006**, *22*, 4574–4582. DOI:10.1021/la051711j
35. N. K. Lazaridis, G. Z. Kyzas, A. A. Vassiliou and D. N. Bikiaris, *Langmuir*, **2007**, *23*, 7634–7643. DOI:10.1021/la700423j
36. Z. Hasan and S. H. Jhung, *J. Hazard. Mater.*, **2015**, *283*, 329–339. DOI:10.1016/j.jhazmat.2014.09.046
37. W. Lv, D.-M. Tang, Y.-B. He, C.-H. You, Z.-Q. Shi, X.-C. Chen, C.-M. Chen, P.-X. Hou, C. Liu and Q.-H. Yang, *ACS Nano*, **2009**, *3*, 3730–3736. DOI:10.1021/nn900933u
38. Y. Fu, J. Wang, Q. Liu and H. Zeng, *Carbon*, **2014**, *77*, 710–721. DOI:10.1016/j.carbon.2014.05.076
39. H. Yanga, J. Yana, Z. Lua, X. Chenga and Y. Tang, *J. Alloys Compd.*, **2009**, *476*, 715–719. DOI:10.1016/j.jallcom.2008.09.104
40. G. Liu, W. Jiang, Y. Wang, S. Zhong, D. Sun, J. Liu and F. Li, *Ceram. Inter.*, **2015**, *41*, 4982–4988. DOI:10.1016/j.ceramint.2014.12.063
41. J. Wang, T. Tsuzuki, B. Tang, X. Hou, L. Sun and X. Wang, *ACS Appl. Mater. Interfaces*, **2012**, *4*, 3084–3090. DOI:10.1021/am300445f
42. C. Zhu, S. Guo, P. Wang, L. Xing, Y. Fang, Y. Zhai and S. Dong, *Chem. Commun.*, **2010**, *46*, 7148–7150. DOI:10.1039/c0cc01459a
43. J. E. Tasca, A. Ponzinibbio, G. Diaz, R. D. Bravo and A. Lavat and M. G. González, *Top. Catal.*, **2010**, *53*, 1087–1090. DOI:10.1007/s11244-010-9538-0
44. S. Hashemian, M. Rahimi and A. A. Kerdegari, *Desalin. Water Treat.*, **2015**, *57*, 14696–14707. DOI:10.1080/19443994.2015.1065766
45. Z.-H. Huang, G. Liu and F. Kang, *ACS Appl. Mater. Interfaces*, **2012**, *4*, 4942–4947. DOI:10.1021/am3013104
46. Y. Sun, D. Shao, C. Chen, S. Yang and X. Wang, *Environ. Sci. Technol.*, **2013**, *47*, 9904–9910. DOI:10.1021/es401174n
47. Y. Fu, Q. Chen, M. He, Y. Wan, X. Sun, H. Xia and X. Wang, *Ind. Eng. Chem. Res.*, **2012**, *51*, 11700–11709. DOI:10.1021/ie301347j
48. S. Bai, X. Shen, X. Zhong, Y. Liu, G. Zhu, X. Xu and K. Chen, *Carbon*, **2012**, *50*, 2337–2346. DOI:10.1016/j.carbon.2012.01.057
49. A. S. K. Kumar and S. J. Jiang, *J. Mol. Liq.* **2017**, *237*, 387–401. DOI:10.1016/j.molliq.2017.04.093
50. K. Pourzare, S. Farhadi and Y. Mansourpanah, *Acta Chim. Slov.*, **2017**, *64*, 945–958. DOI:10.17344/acsi.2017.3642
51. Y. Deng, Y. Cai, Z. Sun, J. Liu, C. Liu, J. Wei, W. Li, C. Liu, Y. Wang and D. Zhao, *J. Am. Chem. Soc.*, **2010**, *132*, 8466–8473. DOI:10.1021/ja1025744
52. N. Pradhan, A. Pal and T. Pal, *Eng. Asp.*, **2002**, *196*, 247–257. DOI:10.1016/S0927-7757(01)01040-8
53. S. Jana, S. Ghosh, S. Nath, S. Pande, S. Praharaj, S. Panigrahi, S. Basu, T. Endo and T. Pal, *Appl. Catal. A: Gen.*, **2006**, *313*, 41–48. DOI:10.1016/j.apcata.2006.07.007
54. Y. Zhu, J. Shen, K. Zhou, C. Chen, X. Yang and C. Li, *J. Phys. Chem. C*, **2011**, *115*, 1614–1619. DOI:10.1021/jp109276q
55. M. Wang, Y. Ni and A. Liu, *ACS Omega*, **2017**, *2*, 1505–1512.
56. Y. Zhong, Y. Ni, S. Li and M. Wang, *RSC Adv.*, **2016**, *6*, 15831–15837.
57. R. J. Kalbasi, A. A. Nourbakhsh and F. Babaknezhad, *Catal. Commun.*, **2011**, *12*, 955–960. DOI:10.1016/j.catcom.2011.02.019
58. S. Y. Gao, X. X. Jia, Z. D. Li and Y. L. Chen, *J. Nanopart. Res.*, **2012**, *14*, 1–11.
59. Z. Duan, G. Ma and W. Zhang, *Bull. Korean Chem. Soc.*, **2012**, *33*, 4003–4006. DOI:10.5012/bkcs.2012.33.12.4003
60. A. K. Shil, D. Sharma, N. R. Guha and P. Das, *Tetrahedron Lett.*, **2012**, *53*, 4858–4861. DOI:10.1016/j.tetlet.2012.06.132

61. Y. Choi, H. S. Bae, E. Seo, S. Jang, K. H. Park and B. S. Kim, *J. Mater. Chem.* **2011**, *21*, 15431–15436. DOI:10.1039/c1jm12477c
62. M. Nasrollahzadeh, M. Bagherzadeh and H. Karimi, *J. Colloid Interface Sci.*, **2016**, *465*, 271–278. DOI:10.1016/j.jcis.2015.11.074
63. K. L. Wu, R. Yu and X. W. Wei, *Cryst. Eng. Commun.*, **2012**, *14*, 7626–7632. DOI:10.1039/c2ce25457c
64. K. L. Wu, X. W. Wei, X. M. Zhou, D. H. Wu, X. W. Liu, Y. Ye and Q. Wang, *J. Phys. Chem. C*, **2011**, *115*, 16268–16274. DOI:10.1021/jp201660w
65. S. Liu, Z. Chen, N. Zhang, Z. R. Tang and Y. J. Xu, *J. Phys. Chem. C*, **2013**, *117*, 8251–8261. DOI:10.1021/jp400550t
66. W. Che, Y. Ni, Y. Zhang and Y. Ma, *J. Phys. Chem. Solids*, **2015**, *77*, 1–7. DOI:10.1016/j.jpcs.2014.09.006
67. D. Z. Jiang, J. Xie, D. Jiang, X. Wei and M. Chen, *Cryst. Eng. Comm.*, **2013**, *15*, 560–569. DOI:10.1039/C2CE26398J
68. J. Feng, L. Su, Y. Ma, C. Ren, Q. Guo and X. Chen, *Chem. Eng. J.* **2013**, *221*, 16–24. DOI:10.1016/j.cej.2013.02.009
69. Q. Cui, B. Xia, S. Mitzscherling, A. Masic, L. Li, M. Bargheer and H. Möhwald, *Colloids Surf. A: Physicochem. Eng. Aspects*, **2015**, *465*, 20–25. DOI:10.1016/j.colsurfa.2014.10.028
70. M. Atarod, M. Nasrollahzadeh and S. M. Sajadi, *J. Colloid Interface Sci.*, **2016**, *465*, 249–258. DOI:10.1016/j.jcis.2015.11.060
71. M. Nasrollahzadeh, M. Atarod and S. M. Sajadi, *Appl. Surf. Sci.*, **2016**, *364*, 636–644. DOI:10.1016/j.apsusc.2015.12.209
72. M. Nasrollahzadeh and S. M. Sajadi, *Ceram. Inter.*, **2015**, *41*, 14435–14439. DOI:10.1016/j.ceramint.2015.07.079
73. A. Mahdizadeh, S. Farhadi and A. Zabardasti, *RSC Adv.*, **2017**, *7*, 53984–53995.

## Povzetek

Z razmeroma enostavno solvotermalno sintezo smo pripravili ternarni magnetni nanokompozit Ag/CuFe<sub>2</sub>O<sub>4</sub>/rGO. Redukcija grafen oksida (GO) do reducirane zvrsti (rGO) in "in-situ" depozicija CuFe<sub>2</sub>O<sub>4</sub> in nanodelcev Ag na rGO je potekala hkrati. Za določanje strukture, sestave in morfologije pripravljenega nanokompozita smo uporabili naslednje tehnike: infrardečo spektroskopijo (FT-IR), rentgensko praškovo difrakcijo (XRD), merilnik namagnetnosti s tresočim se vzorcem (VSM), vrstično elektronsko mikroskopijo s poljsko emisijo (FESEM), energijsko disperzijsko spektroskopijo rentgenskih žarkov (EDXS), presevno elektronsko mikroskopijo (TEM) in meritve površine (BET). Rezultati so pokazali, da so se nanodelci Ag in CuFe<sub>2</sub>O<sub>4</sub> uspešno vezali na površino rGO. Katalitsko učinkovitost nanokompozita Ag/CuFe<sub>2</sub>O<sub>4</sub>/rGO smo določali z reakcijo redukcije nitroarenov do ustreznih aminov v prisotnosti natrijevega borohidrida (NaBH<sub>4</sub>) kot reducenta. Nanokompozit je pokazal visoko učinkovitost pri redukciji nitroarenov s 100% konverzijo v 10-30 minutah. Katalitska aktivnost Ag/CuFe<sub>2</sub>O<sub>4</sub>/rGO je bila izboljšana v primerjavi z vzorci Ag/CuFe<sub>2</sub>O<sub>4</sub>, Ag/rGO in CuFe<sub>2</sub>O<sub>4</sub>/rGO zaradi lažjega prenosa elektronov. Poleg tega so podatki o adsorpciji pokazali, da lahko kationsko barvilo metilensko modro (MB) skoraj v celoti odstranimo z uporabo kompozita Ag/CuFe<sub>2</sub>O<sub>4</sub>/rGO v 2 minutah. Postopek je selektiven, kar smo preverili z uporabo kompozita za adsorpcijo barvila MB iz mešane raztopine z anionskim barvilom metil oranž (MO). Sestava nanokompozita, v katerem so tudi magnetni nanodelci CuFe<sub>2</sub>O<sub>4</sub>, nam omogoča, da lahko po uporabi kompozit enostavno ločimo in ponovno uporabimo.

Scientific paper

# Study on Synthesis and Biological Activity of Some Pyridopyridazine Derivatives

Sevilay Akçay,<sup>1</sup> Mahmut Ülger,<sup>2</sup> Fatma Kaynak Onurdağ<sup>3</sup> and Yasemin Dündar<sup>1,\*</sup>

<sup>1</sup> Department of Pharmaceutical Chemistry, Faculty of Pharmacy, Gazi University, Ankara, Turkey.

<sup>2</sup> Department of Pharmaceutical Microbiology, Faculty of Pharmacy, Mersin University, Mersin, Turkey.

<sup>3</sup> Department of Pharmaceutical Microbiology, Faculty of Pharmacy, Trakya University, Edirne, Turkey.

\* Corresponding author: E-mail: yasemina@gazi.edu.tr, akkocysmn@gmail.com  
Phone: +90-312-2023237; Fax: +90-312-2235018

Received: 06-07-2018

## Abstract

In this study, new pyrido[3,4-*d*]pyridazine derivatives were synthesized and evaluated for their *in vitro* antibacterial, antifungal and antimycobacterial activities. Among the synthesized compounds, compound **10** (1-(4-benzylpiperazin-1-yl)pyrido[3,4-*d*]pyridazin-4(3*H*)-one) and compound **12** (1-(4-benzylpiperidin-1-yl)pyrido[3,4-*d*]pyridazin-4(3*H*)-one) were found to have the highest antimycobacterial activity. However, all compounds were found ineffective against tested Gram-positive, Gram-negative bacteria and fungus.

**Keywords:** Pyrido[3,4-*d*]pyridazine derivatives; pyrido[3,4-*d*]pyridazin-4(3*H*)-one; pyrido[3,4-*d*]pyridazin-1(2*H*)-one; antimycobacterial activity.

## 1. Introduction

Tuberculosis (TB) is a chronic and often deadly infectious disease caused by the *Mycobacterium tuberculosis*.<sup>1</sup> According to the World Health Organization (WHO) Global Tuberculosis Report 2017, in 2016, there were an estimated 1.3 million TB deaths among HIV-negative people and an additional 374.000 deaths among HIV-positive people.<sup>1</sup> Standard TB therapy involves taking isoniazid (INH), rifampicin (RIF), pyrazinamide (PZA) and ethambutol (EMB) for two months (intensive phase), prolong treatment with INH and RIF for four months (continuation phase).<sup>2</sup> In patients with RIF-resistant TB or multidrug-resistant TB, treatment regimens with at least five effective antituberculosis agents during the intensive phase is recommended, including PZA and four group second-line antituberculosis drugs. The regimen may be further strengthened with high dose INH and/or EMB.<sup>3</sup>

INH, the first-line drug, is a key component in all TB therapy regimens recommended by the WHO.<sup>1–3</sup> PZA is also an important first-line drug which has sterilizing activity against semi-dormant tuberculin bacilli.<sup>4</sup> Hence, re-

searchers have modified the INH and PZA scaffolds to develop novel compounds to obtain better antitubercular activity. Additionally, many researchers have worked on hybrid molecules of INH and other antitubercular drugs.<sup>5–12</sup> Therefore, our group decided to study pyrido[3,4-*d*]pyridazine ring system which has INH and PZA like scaffold (Figure 1).

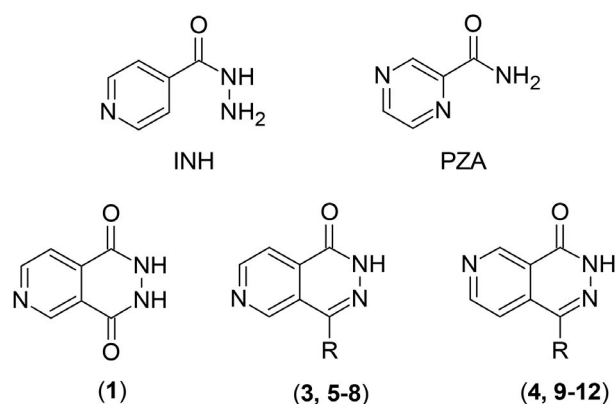


Figure 1. INH, PZA and the general structure of the synthesized compounds.

2,3-Dihydropyrido[3,4-*d*]pyridazin-1,4-dione (1) and its derivatives are generally synthesized by the reaction of hydrazine hydrate with 3,4-pyridinedicarboxylic acid derivatives, such as 3,4-pyridinedicarboxylic anhydride, 3,4-pyridinedicarbonitriles, dimethyl or diethyl pyridine-3,4-dicarboxylate, 1*H*-pyrrolo[3,4-*c*]pyridine-1,3 (2*H*)-dione.<sup>13–17</sup> In this study, 3,4-pyridinedicarboxylic acid was used as the starting material and then converted to 3,4-pyridinedicarboxylic anhydride *via* acetic acid anhydride, followed by the cyclization with hydrazine hydrate. Subsequent to chlorination of pyridazinone ring with phosphorus oxychloride and hydrolysis to monochloro derivatives, the final compounds were obtained *via* nucleophilic aromatic substitution reaction. Synthesized novel 4-substituted pyrido[3,4-*d*]pyridazin-1(2*H*)-one derivatives and 1-substituted pyrido[3,4-*d*]pyridazin-4(3*H*)-one derivatives were evaluated for their antimycobacterial, antibacterial, and antifungal properties.

## 2. Experimental

### 2.1. Chemistry

All chemicals and solvents were purchased locally from Merck AG and Aldrich Chemicals. The microwave reaction was carried out in a MicroSYNTH Microwave Lab station (Milestone S.r.l.). Flash chromatography was performed with a Combi-flashRf automated flash chromatography system with RediSep columns (Teledyne-Isco, Lincoln, NE, USA). Melting points were determined with an Electrothermal-9200 Digital Melting Point Apparatus and are uncorrected. Fourier-transform infrared attenuated total reflectance (FTIR-ATR) spectra were recorded on Perkin Elmer Spectrum 400 FT-IR and FT-NIR spectrometers with a Universal ATR sampler. <sup>1</sup>H NMR spectra were recorded in DMSO-*d*<sub>6</sub> on a Varian Mercury 400, 400 MHz High Performance Digital FT-NMR spectrometer at the NMR facility of the Faculty of Pharmacy, Ankara University. All chemical shifts were recorded as δ (ppm). Microanalyses for C, H, and N were performed on a Leco-932 at the Faculty of Pharmacy, Ankara University, Ankara, Turkey, and they were within the range of ±0.4% of the theoretical value. HRMS spectra were taken on a Waters LCT Premier XE orthogonal acceleration time-of-flight (oa-TOF) mass spectrometer using ESI (+) or ESI (–) methods (Waters Corporation, Milford, MA, USA). The syntheses of 2,3-dihydropyrido[3,4-*d*]pyridazin-1,4-dione (compound 1),<sup>13</sup> 1,4-dichloropyrido[3,4-*d*]pyridazine (compound 2),<sup>13</sup> 4-chloropyrido[3,4-*d*]pyridazin-1(2*H*)-one (compound 3),<sup>13,14</sup> 1-chloropyrido[3,4-*d*]pyridazin-4(3*H*)-one (compound 4)<sup>13,14</sup> were previously reported.

#### 2,3-Dihydropyrido[3,4-*d*]pyridazin-1,4-dione (1)

8.61 g (0.05 mol) 3,4-pyridinedicarboxylic acid was added to 30 mL (0.31 mol) acetic acid anhydride, and the mixture was heated to reflux and stirred for 1 h. After cool-

ing to room temperature, 30 mL hydrazine hydrate was added and the mixture was refluxed and stirred for 4 h. The product was collected by suction filtration, washed with water and dried. Crystallized from ethanol/water to yield 98.6%; mp >300 °C; FTIR-ATR: 3404 (O–H), 3300–2200 (N–H), 1668 (C=O) cm<sup>–1</sup>; <sup>1</sup>H NMR (DMSO-*d*<sub>6</sub>): δ 9.34 (1H, s, H5), 9.03 (1H, d, *J*<sub>7–8</sub> = 5.6 Hz, H7), 7.90 (1H, d, *J*<sub>8–7</sub> = 5.6 Hz, H8); HRMS calcd. for C<sub>7</sub>H<sub>6</sub>N<sub>3</sub>O<sub>2</sub> [M–H]<sup>+</sup>: 164.0460. Found: 164.0455. Anal. Calcd. for C<sub>7</sub>H<sub>5</sub>N<sub>3</sub>O<sub>2</sub>·1/3H<sub>2</sub>O: C, 49.71; H, 3.38; N, 24.84. Found: C, 49.78; H, 3.27; N, 25.06%.

#### 1,4-Dichloropyrido[3,4-*d*]pyridazine (2)

A mixture of 6.52 g (0.04 mol) 2,3-dihydropyrido[3,4-*d*]pyridazin-1,4-dione and 18.6 mL (0.19 mol) phosphorus oxychloride in 6.46 mL (0.08 mol) pyridine was heated to reflux and stirred for 5 h. The mixture then was poured into a slush of 200 g of ice and then neutralized with NaHCO<sub>3</sub> and then extracted with 3 × 100 mL ethyl acetate. Organic phase was separated, washed with water, dried with Na<sub>2</sub>SO<sub>4</sub> and evaporated to dryness (yield 45%). 1,4-Dichloropyrido[3,4-*d*]pyridazine was subsequently used without further purification.

#### 4-Chloropyrido[3,4-*d*]pyridazin-1(2*H*)-one (3) and 1-Chloropyrido[3,4-*d*]pyridazin-4(3*H*)-one (4)

1,4-Dichloropyrido[3,4-*d*]pyridazine (5 g, 0.025 mol) was heated up to reflux temperature in 150 mL diluted HCl (1%) for 2 h. After cooling, the precipitate formed was filtered off, dried and crystallized from acetic acid to obtain 4-chloropyrido[3,4-*d*]pyridazin-1(2*H*)-one with yield of 52%. The remaining reaction medium was neutralized with ammonium hydroxide to precipitate the 1-chloropyrido[3,4-*d*]pyridazin-4(3*H*)-one, which was isolated by filtration, washed with water, dried and crystallized from water (yield 34%).

#### 4-Chloropyrido[3,4-*d*]pyridazin-1(2*H*)-one (3)

Crystallized from acetic acid to yield 52%; mp 236 °C; FTIR-ATR: 3220–2400 (N–H), 1678 (C=O) cm<sup>–1</sup>; <sup>1</sup>H NMR (DMSO-*d*<sub>6</sub>): δ 13.14 (1H, s, NH), 9.32 (1H, d, *J*<sub>5–8</sub> = 0.8 Hz, H5), 9.10 (1H, d, *J*<sub>7–8</sub> = 4.8 Hz, H7), 8.11 (1H, dd, *J*<sub>8–7</sub> = 5.2 Hz, *J*<sub>8–5</sub> = 0.8 Hz, H8); HRMS calcd. for C<sub>7</sub>H<sub>5</sub>ClN<sub>3</sub>O [M–H]<sup>+</sup>: 182.0121. Found 182.0116. Anal. calcd. for C<sub>7</sub>H<sub>4</sub>ClN<sub>3</sub>O: C, 46.30; H, 2.22; N, 23.14. Found: C, 46.11; H, 2.22; N, 23.04%.

#### 1-Chloropyrido[3,4-*d*]pyridazin-4(3*H*)-one (4)

Crystallized from water to yield 34%; mp 172 °C; FTIR-ATR: 3400–2400 (N–H), 1682 (C=O) cm<sup>–1</sup>; <sup>1</sup>H NMR (DMSO-*d*<sub>6</sub>): δ 13.13 (1H, s, NH), 9.45 (1H, s, H5), 9.13 (1H, d, *J*<sub>7–8</sub> = 5.2 Hz, H7), 7.84 (1H, dd, *J*<sub>8–7</sub> = 5.6 Hz, *J*<sub>8–5</sub> = 0.8 Hz, H8); HRMS calcd. for C<sub>7</sub>H<sub>5</sub>ClN<sub>3</sub>O [M–H]<sup>+</sup>: 182.0121. Found 182.0114. Anal. calcd. for C<sub>7</sub>H<sub>4</sub>ClN<sub>3</sub>O: C, 46.30; H, 2.22; N, 23.14. Found: C, 46.12; H, 2.28; N, 23.23%.

### General Procedure for the Synthesis of 4-Substituted Pyrido[3,4-*d*]pyridazin-1(2*H*)-one Derivatives or 1-Substituted Pyrido[3,4-*d*]pyridazin-4(3*H*)-one Derivatives

0.003 mol 4-chloropyrido[3,4-*d*]pyridazin-1(2*H*)-one or 1-chloropyrido[3,4-*d*]pyridazin-4(3*H*)-one in 5 mL diethylene glycol was treated with 0.015 mol piperazine or piperidine derivatives. The reaction mixture was heated to 140 °C (only exception compound **11**: 125 °C) for appropriate time under microwave irradiation. Reaction mixture was poured into ice-water mixture and then extracted with CH<sub>2</sub>Cl<sub>2</sub>. Organic phase was separated, washed with water, dried with Na<sub>2</sub>SO<sub>4</sub>, and evaporated to dryness and the crude product thus obtained was purified by flash chromatography.

#### 4-(4-Methylpiperazin-1-yl)pyrido[3,4-*d*]pyridazin-1(2*H*)-one (**5**)

Reaction time: 120 min. The crude product was purified by column chromatography using dichloromethane-methanol gradient system. Yield: 17.94%; mp 199 °C; FTIR-ATR: 3330–2400 (N–H), 1678 (C=O) cm<sup>-1</sup>; <sup>1</sup>H-NMR (DMSO-*d*<sub>6</sub>): δ 12.43 (1H, s, NH), 9.22 (1H, s, H5), 8.97 (1H, d, *J*<sub>7-8</sub> = 4.8 Hz, H7), 8.06 (1H, d, *J*<sub>8-7</sub> = 4.8 Hz, H8), 3.14 (4H, m, piperazine H2, H6), 2.58 (4H, m, piperazine H3, H5), 2.27 (3H, s, CH<sub>3</sub>); HRMS calcd. for C<sub>12</sub>H<sub>16</sub>N<sub>5</sub>O [M–H]<sup>+</sup>: 246.1355. Found 246.1351. Anal. calcd. for C<sub>12</sub>H<sub>15</sub>N<sub>5</sub>O·1/3H<sub>2</sub>O: C, 57.36; H, 6.28; N, 27.87. Found: C, 57.69; H, 5.93; N, 27.53%.

#### 4-(4-Benzylpiperazin-1-yl)pyrido[3,4-*d*]pyridazin-1(2*H*)-one (**6**)

Reaction time: 60 min. The crude product was purified by column chromatography using dichloromethane-methanol gradient system. The collected product was crystallized from ethanol to yield 23.75%; mp 245 °C; FTIR-ATR: 3200–2700 (N–H), 1656 (C=O) cm<sup>-1</sup>; <sup>1</sup>H NMR (DMSO-*d*<sub>6</sub>): δ 12.42 (1H, s, NH), 9.22 (1H, s, H5), 8.97 (1H, d, *J*<sub>7-8</sub> = 5.2 Hz, H7), 8.06 (1H, dd, *J*<sub>8-7</sub> = 4.8 Hz, *J*<sub>8-5</sub> = 0.8 Hz, H8), 7.35–7.27 (5H, m, C<sub>6</sub>H<sub>5</sub>), 3.58 (2H, s, CH<sub>2</sub>), 3.15 (4H, m, piperazine H2, H6), 2.62 (4H, m, piperazine H3, H5); HRMS calcd. for C<sub>18</sub>H<sub>20</sub>N<sub>5</sub>O [M–H]<sup>+</sup>: 322.1668. Found 322.1667. Anal. calcd. for C<sub>18</sub>H<sub>19</sub>N<sub>5</sub>O·1/5H<sub>2</sub>O: C, 66.53; H, 6.02; N, 21.55. Found: C, 66.82; H, 5.96; N, 21.53%.

#### 4-(4-Methylpiperidin-1-yl)pyrido[3,4-*d*]pyridazin-1(2*H*)-one (**7**)

Reaction time: 60 min. The crude product was purified by column chromatography using ethyl acetate. The collected product was crystallized from ethanol to yield 40.93%; mp 218 °C; FTIR-ATR: 3300–2700 (N–H), 1669 (C=O) cm<sup>-1</sup>; <sup>1</sup>H NMR (DMSO-*d*<sub>6</sub>): δ 12.37 (1H, s, NH), 9.19 (1H, s, H5), 8.96 (1H, d, *J*<sub>7-8</sub> = 5.2 Hz, H7), 8.05 (1H, dd, *J*<sub>8-7</sub> = 5.2 Hz, *J*<sub>8-5</sub> = 0.8 Hz, H8), 3.47–3.44 (2H, m, piperidine H2, H6), 2.76 (2H, td, piperidine H2, H6), 1.76–1.72 (2H, m, piperidine H3, H5), 1.57–1.54 (1H, m, piperi-

dine H4), 1.45 (2H, m, piperidine H3, H5), 0.99 (3H, d, CH<sub>3</sub>); HRMS calcd. for C<sub>13</sub>H<sub>17</sub>N<sub>4</sub>O [M–H]<sup>+</sup>: 245.1402. Found 245.1407. Anal. calcd. for C<sub>13</sub>H<sub>16</sub>N<sub>4</sub>O·1/5H<sub>2</sub>O: C, 62.99; H, 6.67; N, 22.60. Found: C, 63.26; H, 6.49; N, 22.53%.

#### 4-(4-Benzylpiperidin-1-yl)pyrido[3,4-*d*]pyridazin-1(2*H*)-one (**8**)

Reaction time: 30 min. The crude product was purified by column chromatography using *n*-hexane-ethyl acetate gradient system. The collected product was crystallized from ethanol to yield 18.42%; mp 225 °C; FTIR-ATR: 3300–2700 (N–H), 1685 (C=O) cm<sup>-1</sup>; <sup>1</sup>H NMR (DMSO-*d*<sub>6</sub>): δ 12.37 (1H, s, NH), 9.18 (1H, s, H5), 8.96 (1H, d, *J*<sub>7-8</sub> = 5.6 Hz, H7), 8.05 (1H, d, *J*<sub>8-7</sub> = 5.2 Hz, H8), 7.32–7.19 (5H, m, C<sub>6</sub>H<sub>5</sub>), 3.49–3.46 (2H, m, piperidine H2, H6), 2.74–2.68 (2H, m, piperidine H2, H6), 2.61 (2H, d, CH<sub>2</sub>), 1.72–1.69 (3H, m, piperidine H3, H5, H4), 1.51–1.49 (2H, m, piperidine H3, H5); HRMS calcd. for C<sub>19</sub>H<sub>21</sub>N<sub>4</sub>O [M–H]<sup>+</sup>: 321.1715. Found 321.1708. Anal. calcd. for C<sub>19</sub>H<sub>20</sub>N<sub>4</sub>O·1/2C<sub>2</sub>H<sub>5</sub>OH: C, 69.95; H, 6.75; N, 16.31. Found: C, 69.78; H, 6.54; N, 16.53%.

#### 1-(4-Methylpiperazin-1-yl)pyrido[3,4-*d*]pyridazin-4(3*H*)-one (**9**)

Reaction time: 60 min. The crude product was purified by column chromatography using dichloromethane-methanol gradient system. The collected product was crystallized from ethanol to yield 20.38%; mp 206 °C; FTIR-ATR: 3300–2600 (N–H), 1670 (C=O) cm<sup>-1</sup>; <sup>1</sup>H NMR (DMSO-*d*<sub>6</sub>): δ 12.41 (1H, s, NH), 9.42 (1H, s, H5), 9.01 (1H, d, *J*<sub>7-8</sub> = 5.2 Hz, H7), 7.75 (1H, d, *J*<sub>8-7</sub> = 5.6 Hz, H8), 3.09 (4H, m, piperazine H2, H6), 2.55 (4H, m, piperazine H3, H5), 2.26 (3H, s, CH<sub>3</sub>); HRMS calcd. for C<sub>12</sub>H<sub>16</sub>N<sub>5</sub>O [M–H]<sup>+</sup>: 246.1355. Found 246.1360. Anal. calcd. for C<sub>12</sub>H<sub>15</sub>N<sub>5</sub>O·1/6H<sub>2</sub>O: C, 58.05; H, 6.22; N, 28.21. Found: C, 58.36; H, 6.16; N, 27.95%.

#### 1-(4-Benzylpiperazin-1-yl)pyrido[3,4-*d*]pyridazin-4(3*H*)-one (**10**)

Reaction time: 30 min. The crude product was purified by column chromatography using *n*-hexane-ethyl acetate gradient system. The collected product was crystallized from ethanol to yield 45.13%; mp 230 °C; FTIR-ATR: 3200–2300 (N–H), 1672 (C=O) cm<sup>-1</sup>; <sup>1</sup>H NMR (DMSO-*d*<sub>6</sub>): δ 12.37 (1H, s, NH), 9.38 (1H, s, H5), 8.98 (1H, d, *J*<sub>7-8</sub> = 5.6 Hz, H7), 7.71 (1H, dd, *J*<sub>8-7</sub> = 5.4 Hz, *J*<sub>8-5</sub> = 0.4 Hz, H8), 7.32–7.23 (5H, m, C<sub>6</sub>H<sub>5</sub>), 3.54 (2H, s, CH<sub>2</sub>), 3.07 (4H, m, piperazine H2, H6), 2.58 (4H, m, piperazine H3, H5); HRMS calcd. for C<sub>18</sub>H<sub>20</sub>N<sub>5</sub>O [M–H]<sup>+</sup>: 322.1668. Found 322.1666. Anal. calcd. for C<sub>18</sub>H<sub>19</sub>N<sub>5</sub>O: C, 67.27; H, 5.96; N, 21.79. Found: C, 67.31; H, 6.14; N, 21.77%.

#### 1-(4-Methylpiperidin-1-yl)pyrido[3,4-*d*]pyridazin-4(3*H*)-one (**11**)

Reaction time: 45 min. The crude product was purified by column chromatography using *n*-hexane-ethyl ac-

etate gradient system. Yield: 14%; mp 186 °C; FTIR-ATR: 3300–2700 (N–H), 1673 (C=O)  $\text{cm}^{-1}$ ;  $^1\text{H}$  NMR (DMSO- $d_6$ ):  $\delta$  12.36 (1H, s, NH), 9.41 (1H, s, H5), 9.01 (1H, d,  $J_{7-8} = 5.2$  Hz, H7), 7.71 (1H, d,  $J_{8-7} = 5.2$  Hz, H8), 3.42–3.39 (2H, m, piperidine H2, H6), 2.74–2.69 (2H, m, piperidine H2, H6), 1.75–1.72 (2H, m, piperidine H3, H5), 1.56–1.54 (1H, m, piperidine H4), 1.45–1.36 (2H, m, piperidine H3, H5), 0.99 (3H, d,  $\text{CH}_3$ ); HRMS calcd. for  $\text{C}_{13}\text{H}_{17}\text{N}_4\text{O}$  [M–H] $^+$ : 245.1402. Found 245.1406. Anal. calcd. for  $\text{C}_{13}\text{H}_{16}\text{N}_4\text{O}\cdot 1/6\text{H}_2\text{O}$ : C, 63.14; H, 6.66; N, 22.66. Found: C, 63.44; H, 6.61; N, 22.25%.

### 1-(4-Benzylpiperidin-1-yl)pyrido[3,4-d]pyridazin-4(3H)-one (12)

Reaction time: 30 min. The crude product was purified by column chromatography using *n*-hexane-ethyl acetate gradient system. The collected product was crystallized from methanol-water to yield 23.51%; mp 147 °C; FTIR-ATR: 3200–2700 (N–H), 1660 (C=O)  $\text{cm}^{-1}$ ;  $^1\text{H}$  NMR (DMSO- $d_6$ ):  $\delta$  12.35 (1H, s, NH), 9.41 (1H, s, H5), 9.01 (1H, d,  $J_{7-8} = 5.2$  Hz, H7), 7.71 (1H, d,  $J_{8-7} = 5.6$  Hz, H8), 7.32–7.19 (5H, m,  $\text{C}_6\text{H}_5$ ), 3.44–3.39 (2H, m, piperidine H2, H6), 2.69–2.64 (2H, m, piperidine H2, H6), 2.60 (2H, d,  $\text{CH}_2$ ), 1.71–1.68 (3H, m, piperidine H3, H5, H4), 1.51–1.46 (2H, m, piperidine H3, H5); HRMS calcd. for  $\text{C}_{19}\text{H}_{21}\text{N}_4\text{O}$  [M–H] $^+$ : 321.1715. Found 321.1719. Anal. calcd. for  $\text{C}_{19}\text{H}_{20}\text{N}_4\text{O}\cdot 1/5\text{H}_2\text{O}$ : C, 70.43; H, 6.35; N, 17.29. Found: C, 70.66; H, 6.25; N, 17.09%.

## 2. 2. Biological Activity

### 2. 2. 1. Antibacterial and Antifungal Activity<sup>18,19</sup> Microorganisms

Standard strains of *Escherichia coli* ATCC 35218, *Pseudomonas aeruginosa* ATCC 10145, *Staphylococcus aureus* ATCC 6538, *Enterococcus faecalis* ATCC 29212, *Candida albicans* ATCC 10231 and clinical isolates from Trakya University Health Center for Medical Research and Practice Microbiology Laboratory were included in the study.

### Microdilution Method

Mueller Hinton Agar (MHA), Mueller Hinton Broth (MHB), Sabouraud Dextrose Agar (SDA), Sabouraud Liquid Medium (SLM) and RPMI-1640 medium with L-glutamine (Sigma) buffered with MOPS (Sigma) (pH 7) were used in the study. MHA, MHB, SDA and SLM were sterilized with autoclave at 121 °C for 15–20 minutes and RPMI-1640 was sterilized by filtration. Susceptibility testing was performed according to the guidelines of Clinical and Laboratory Standards Institute (CLSI) M100-S18 and M27-A3. 100  $\mu\text{L}$  of MHB and RPMI-1640 medium with L-glutamine (Sigma) buffered with MOPS (pH 7) were added to each well of the microplates for bacteria and fungi, respectively. The bacterial suspensions used for inoculation were prepared at  $10^5$  CFU/mL by diluting fresh cultures at McFarland 0.5 density. Suspensions of the yeast at McFarland den-

sity was diluted 1:100 and 1:20 respectively and  $2.5\cdot 10^3$  CFU/mL were inoculated to the two fold-diluted solutions of the compounds. Stock solutions of the tested compounds were dissolved in DMSO. Standard antibiotic solutions were dissolved in appropriate solvents recommended by CLSI guidelines. Stock solutions of the tested compounds and standard drugs were diluted two-fold in the wells of the microplates so the solution of the synthesized compounds and standard drugs were prepared at 1024, 512, 256, 128, 64, 32, 16, 8, 4, 2, 1, 0.5  $\mu\text{g}/\text{mL}$  and standard drugs were prepared at 64, 32, 16, 8, 4, 2, 1, 0.5, 0.25, 0.125, 0.0625, 0.03125  $\mu\text{g}/\text{mL}$  concentrations. All solvents and diluents, pure microorganisms and pure media were used in control wells. A 10  $\mu\text{L}$  microorganisms inoculum was added to each well of the microplates. Microplates including bacteria were incubated at 37 °C for 16–20 hours and microplates including fungi were incubated at 35 °C for 24–48 hours. After incubation, the lowest concentration of the compounds that completely inhibits macroscopic growth was determined and reported as minimum inhibitory concentrations (MICs).

### 2. 2. 2. Antimycobacterial Activity<sup>20,21</sup>

#### Agar Proportion Method

The minimum inhibitory concentration (MIC) values of each synthesized compound were tested by agar dilution in duplicate as recommended by the Clinical Laboratory Standards Institute (CLSI).<sup>20,21</sup> Positive and negative growth controls were run in each assay. Isoniazid (INH) (Sigma I3377) and rifampicin (RIF) (Sigma R3501) were used as control agents. *M. tuberculosis* H37Rv was used as the standard strain and was provided by Refik Saydam National Public Health Agency, National Tuberculosis Reference Laboratory, Ankara, Turkey. Stock solutions of synthesized compounds and reference compounds were prepared in DMSO/H<sub>2</sub>O (50%) at a concentration of 1000  $\mu\text{g}/\text{mL}$ . These solutions were then filtered through a 0.22  $\mu\text{m}$  membrane filter (Millipore, USA). Middlebrook 7H10 agar medium (BBL, Becton Dickinson and Company, Sparks, MD, USA) was supplemented with oleic acid-albumin-dextrose-catalase (OADC, BBL, Becton Dickinson and Company, Sparks, MD, USA). Synthesized compounds and control agents were added to obtain an appropriate final concentration in the medium. The final concentrations of INH and RIF were 0.2–1  $\mu\text{g}/\text{mL}$  and 1  $\mu\text{g}/\text{mL}$ , respectively. Synthesized compounds were prepared at final concentrations of 5, 10, 20, 40 and 80  $\mu\text{g}/\text{mL}$ . Agar without any references and synthesized compounds were used as a positive growth control, and 3 mL of prepared medium was dispensed into sterile tubes. The DMSO concentration in the final solutions was not above 1% for antimycobacterial activity.

#### Inoculum Preparation

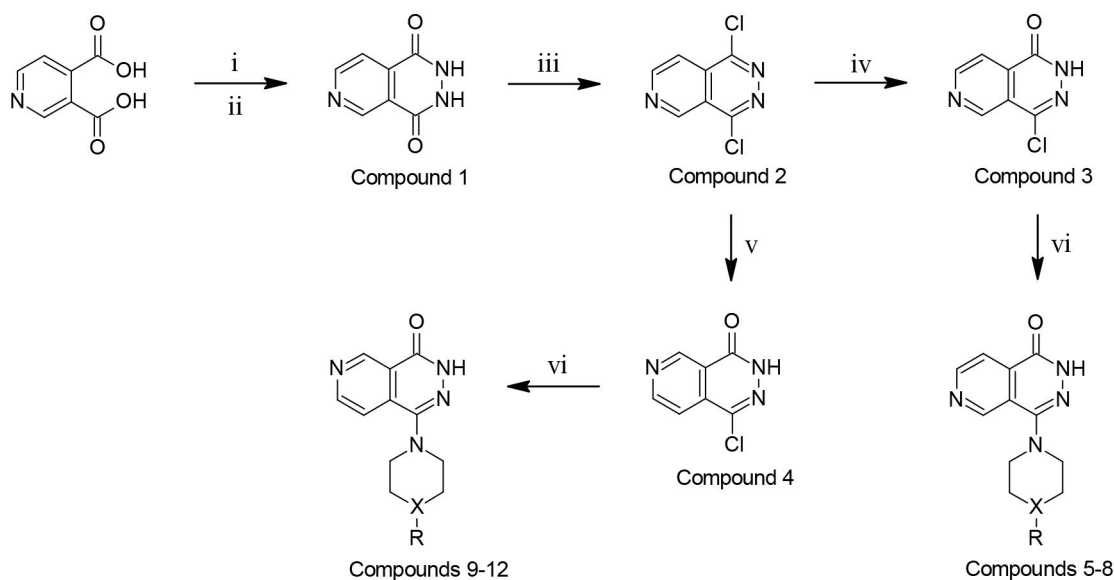
H37Rv was maintained in Lowenstein-Jensen medium. A culture suspension was prepared by subculturing in Middlebrook 7H9 broth (BBL, Becton Dickinson and

Company, Sparks, MD, USA) supplemented with 10% OADC at 37 °C for 7–10 days, until a density corresponding to  $10^{-2}$  to  $10^{-4}$  dilutions were obtained from McFarland standard No. 1. Then 0.1 mL of the diluted suspension was inoculated onto the control and the other tubes with compounds in different concentrations. The tubes were incubated at 37 °C in an atmosphere of 5% CO<sub>2</sub> for 3 weeks. The MIC values were defined as the lowest concentration that inhibited more than 90% of the bacterial growth and the results of INH and RIF were interpreted according to

the CLSI. The MIC was considered the lowest concentration that showed no visible colonies in all dilutions.

### 3. Result and Discussion

The synthetic routes for the synthesized compounds are outlined in Scheme 1. The starting compound 2,3-dihydropyrido[3,4-*d*]pyridazin-1,4-dione (1) was readily prepared by the reaction of 3,4-pyridinedicarboxylic acid



**Scheme 1.** Reagents and conditions: (i) acetic acid anhydride, reflux, 1 h; (ii) hydrazine hydrate, reflux, 4 h; (iii) phosphorus oxychloride, pyridine, reflux, 5 h; (iv) dil. HCl, reflux, 2 h; (v) dil. HCl, reflux, 2 h, neutralized with NH<sub>4</sub>OH; (vi) appropriate piperazine or piperidine derivatives, diethylene glycol, and heat under MW. X = N, C; R: methyl, benzyl.

**Table 1.** Antibacterial, antifungal and antimycobacterial activity of the synthesized compounds

Comp.	A	B	C	D	E	F	G	H	I	J	K	L
1	256	128	256	128	256	512	256	256	128	128	80	40
3	256	128	256	128	256	512	256	256	128	128	80	80
4	256	128	256	128	256	512	256	256	128	128	80	40
5	256	256	256	128	256	512	256	256	128	128	80	40
6	256	256	256	128	256	512	256	256	128	128	80	40
7	256	256	256	128	256	512	256	256	128	128	80	40
8	256	128	256	128	256	512	256	256	64	128	80	80
9	256	128	256	128	256	256	256	256	128	128	80	40
10	256	128	256	128	256	256	256	256	128	128	40	40
11	256	256	256	128	256	512	256	256	128	128	80	80
12	256	256	256	128	256	512	256	256	128	128	40	40
St1	2	<0.0078	1	2	1	0.03125	1	1	–	–	–	–
St2	0.5	4	–	–	0.5	0.5	0.5	0.5	–	–	–	–
St3	>32	4	–	–	8	1	–	–	–	–	–	–
St4	–	–	–	–	–	–	–	–	1	1	–	–
St5	–	–	–	–	–	–	–	–	–	–	0.2	0.2
St6	–	–	–	–	–	–	–	–	–	–	1	1

A: *Escherichia coli* ATCC 35218, B: *E. coli* isolate, C: *Pseudomonas aeruginosa* ATCC 10145, D: *P. aeruginosa* isolate, E: *Staphylococcus aureus* ATCC 6538, F: *S. aureus* isolate, G: *Enterococcus faecalis* ATCC 29212, H: *E. faecalis* isolate, I: *Candida albicans* ATCC 10231, J: *C. albicans* isolate, K:  $10^{-2}$  Dilution of *M. tuberculosis* H37Rv L:  $10^{-4}$  Dilution of *M. tuberculosis* H37Rv. St1: Meropenem, St2: Amoxicillin clavulanic acid, St3: Cefuroxime, St4: Fluconazole, St5: Isoniazid, St6: Rifampicin.



and acetic acid anhydride and subsequent treatment with hydrazine hydrate. Compound **1** was then reacted with phosphorus oxychloride in the presence of pyridine to obtain 1,4-dichloropyrido[3,4-*d*]pyridazine (**2**). Subsequent hydrolysis under acid conditions afforded 4-chloropyrido[3,4-*d*]pyridazin-1(2*H*)-one (**3**). The remaining reaction medium was neutralized with ammonium hydroxide to precipitate the 1-chloropyrido[3,4-*d*]pyridazin-4(3*H*)-one (**4**). 4-Substituted pyrido[3,4-*d*]pyridazin-1(2*H*)-one derivatives or 1-substituted pyrido[3,4-*d*]pyridazin-4(3*H*)-one derivatives was readily prepared by the reaction of 4-chloropyrido[3,4-*d*]pyridazin-1(2*H*)-one or 1-chloropyrido[3,4-*d*]pyridazin-4(3*H*)-one and appropriate piperazine/piperidine derivatives in diethylene glycol under microwave irradiation (MW). The structures of the compounds were elucidated by FT-IR, <sup>1</sup>H NMR spectral data, HRMS and elemental analysis.

All the synthesized compounds were screened for their antimycobacterial activities against *Mycobacterium tuberculosis* H37Rv; for their antibacterial activities against for *Escherichia coli* ATCC 35218, *Pseudomonas aeruginosa* ATCC 10145, *Staphylococcus aureus* ATCC 6538, *Enterococcus faecalis* ATCC 29212 and their clinical isolates; for their antifungal activities against *Candida albicans* ATCC 10231 and their clinical isolates. The preliminary screening results of the prepared compounds are shown in Table 1. Results are expressed as minimal inhibitory concentration (MIC, µg/mL).

Among the synthesized compounds, compounds **10** and **12** displayed moderate inhibition activity against *Mycobacterium tuberculosis* with 40 µg/mL MIC value (10<sup>-2</sup> dilution). In 10<sup>-4</sup> dilution, all tested compounds, except compounds **3**, **8** and **11** showed moderate antitubercular activity with a MIC value of 40 µg/mL. Besides, all compounds were found ineffective against tested Gram-positive, Gram-negative bacteria and fungus. Only compound **8** showed poor activity (MIC 64 µg/mL) against *Candida albicans* ATCC 10231.

## 4. Conclusion

In conclusion, a series of novel pyrido[3,4-*d*]pyridazine derivatives were designed, synthesized, and evaluated for their *in vitro* antimycobacterial activities against *Mycobacterium tuberculosis* H37Rv. Among the synthesized compounds, compounds **10** and **12** exhibited promising antimycobacterial activity with MIC value of 40 µg/mL.

**Conflict of Interest.** The authors declare that they have no conflict of interest.

## 5. References

- Global Tuberculosis Report 2017, Geneva, World Health Organization (WHO), 2017.
- Guidelines for Treatment of Drug-susceptible Tuberculosis and Patient Care, 2017 Update. Geneva, World Health Organization (WHO), 2017.
- WHO Treatment Guidelines for Drug-Resistant Tuberculosis, 2016 Update. Geneva, World Health Organization (WHO), 2016.
- M. Stehr, A. A. Elamin, M. Singh, *Expert Rev. Anti Infect. Ther.* **2015**, *13*, 593–603. DOI:10.1586/14787210.2015.1021784
- L. A. Dutra, T. R. F. de Melo, C. M. J. L. Chin dos Santos, *Int. Res. J. Pharm. Pharmacol.* **2012**, *2*, 1–9.
- H. H. Jardosh, M. P. Patel, *Eur. J. Med. Chem.* **2013**, *65*, 348–359. DOI:10.1016/j.ejmech.2013.05.003
- N. Anand, K. Upadhyaya, R. P. Tripathi, *Chemistry and Biology Interface*, **2015**, *5*, 84–127.
- G. F. dos Santos Fernandes, P. C. de Souza, E. Moreno-Viguri, M. Santivañez-Veliz, R. Paucar, S. Pérez-Silanes, K. Chegaev, S. Guglielmo, L. Lazzarato, R. Fruttero, C. Man Chin, P. B. da Silva, M. Chorilli, M. C. Solcia, C. M. Ribeiro, C. S. P. Silva, L. B. Marino, P. L. Bosquesi, D. M. Hunt, L. P. S. de Carvalho, C. A. de Souza Costa, S. H. Cho, Y. Wang, S. G. Franzblau, F. R. Pavan, J. L. dos Santos, *J. Med. Chem.* **2017**, *60*, 8647–8660. DOI:10.1021/acs.jmedchem.7b01332
- F. S. Castelo-Branco, E. C. de Lima, J. L. de Oliveira Domingos, A. C. Pinto, M. C. S. Lourenço, K. M. Gomes, M. M. Costa-Lima, C. F. Araujo-Lima, C. A. F. Aiub, I. Felzenszwalb, T. E. M. M. Costa, C. Penido, M. G. Henriques, N. Boechat, *Eur. J. Med. Chem.* **2018**, *146*, 529–540. DOI:10.1016/j.ejmech.2018.01.071
- J. Zitko, P. Paterová, V. Kubíček, J. Mandíková, F. Trejtnar, J. Kuneš, M. Doležal, *Bioorg. Med. Chem. Lett.* **2013**, *23*, 476–479. DOI:10.1016/j.bmcl.2012.11.052
- B. Servusová, P. Paterová, J. Mandíková, V. Kubíček, R. Kučear, J. Kuneš, M. Doležal, J. Zitko, *Bioorg. Med. Chem. Lett.* **2014**, *24*, 450–453. DOI:10.1016/j.bmcl.2013.12.054
- Y.-Q. Hu, S. Zhang, F. Zhao, C. Gao, L.-S. Feng, Z.-S. Lv, Z. Xu, X. Wu, *Eur. J. Med. Chem.* **2017**, *133*, 255–267. DOI:10.1016/j.ejmech.2017.04.002
- I. Matsuura, K. Okui, *Chem. Pharm. Bull.* **1969**, *17*, 2266–2272. DOI:10.1248/cpb.17.2266
- K. Körmendy, T. Kovács, F. Ruff, I. Kövesdi, *Acta Chim. Hung.* **1983**, *112*, 487–499.
- J. A. Kaizerman, W. Aaron, S. An, R. Austin, M. Brown, A. Chong, T. Huang, R. Hungate, B. Jiang, M. G. Johnson, G. Lee, B. S. Lucas, J. Orf, M. Rong, M. M. Toteva, D. Wickramasinghe, G. Xu, Q. Ye, W. Zhong, D. L. McMinn, *Bioorg. Med. Chem. Lett.*, **2010**, *20*, 4607–4610. DOI:10.1016/j.bmcl.2010.06.006
- J. R. Greenwood: Pyridazinediones and Amino Acid Receptors: Theoretical Studies, Design, Synthesis, and Evaluation of Novel Analogues, PhD Thesis, The Department of Pharmacology, The University of Sydney. **1999**, pp. 1–262.
- B. Prek, B. Stanovnik, *Acta Chim. Slov.* **2017**, *64*, 798–803. DOI:10.17344/acsi.2017.3695
- Clinical and Laboratory Standards Institute (CLSI) (formerly NCCLS). Performance Standards for Antimicrobial

- Susceptibility Testing 18<sup>th</sup> Informational Supplement. CLSI M100-S18, Clinical and Laboratory Standards Institute, 940 West Valley Road, Wayne, Pennsylvania, USA, 2008.
19. Clinical and Laboratory Standards Institute (CLSI) (formerly NCCLS). Reference Method for Broth Dilution Antifungal Susceptibility Testing of Yeast Approved Standard, M27-A3, Clinical and Laboratory Standards Institute, 940 West Valley Road, Wayne, Pennsylvania, USA, 2006.
20. National Committee for Clinical Laboratory Standards. Susceptibility Testing of Mycobacteria, Nocardia, and Other Aerobic Actinomycetes: Approved Standard NCCLS Document M24-A. Wayne, Pennsylvania, 2003.
21. Clinical and Laboratory Standards Institute (CLSI) (formerly NCCLS). Antimycobacterial Susceptibility Testing for *M. tuberculosis*: Tentative Standard NCCLS Document M24-T. Villanova, Pennsylvania, 2002.

## Povzetek

V tej študiji smo sintetizirali nekaj novih pirido[3,4-*d*]piridazinskih derivatov in ovrednotili njihove *in vitro* protibakterijske, protiglivične in antimikobakterijske aktivnosti. Med sintetiziranimi spojinami sta spojini **10** (1-(4-benzilpiperazin-1-il)pirido[3,4-*d*]piridazin-4(3*H*)-on) in **12** (1-(4-benzilpiperidin-1-il)pirido[3,4-*d*]piridazin-4(3*H*)-on) izkazali največjo antimikobakterijsko aktivnost. Vendar so se vse spojine izkazale kot neučinkovite proti testiranim Gram-pozitivnim in Gram-negativnim bakterijam ter glivam.

Scientific paper

# Synthesis, Crystal Structures and Catalytic Property of Dioxomolybdenum(VI) Complexes Derived from Tridentate Schiff Bases

Xue-Wen Zhu

Key Laboratory of Surface & Interface Science of Henan, School of Material & Chemical Engineering, Zhengzhou University of Light Industry, Zhengzhou 450002, P.R. China

\* Corresponding author: E-mail: zhuxuewen2017@126.com

Received: 10-07-2018

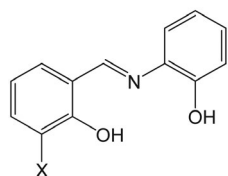
## Abstract

A pair of structurally similar new dioxomolybdenum(VI) complexes,  $[\text{MoO}_2\text{L}^1(\text{EtOH})] \cdot \text{EtOH}$  (**1**) and  $[\text{MoO}_2\text{L}^2(\text{MeOH})]$  (**2**), where  $\text{L}^1$  and  $\text{L}^2$  are the dianionic form of 2-[(2-hydroxyphenylimino)methyl]-6-methoxyphenol ( $\text{H}_2\text{L}^1$ ) and 2-ethoxy-6-[(2-hydroxyphenylimino)methyl]phenol ( $\text{H}_2\text{L}^2$ ), respectively, were prepared and characterized by IR and UV-Vis spectroscopy, as well as single crystal X-ray diffraction. X-ray analyses indicate that the complexes are dioxomolybdenum(VI) species. Complex **1** contains ethanol as co-ligand, and complex **2** contains methanol as co-ligand. The coordination geometry around the Mo atoms can be described as distorted octahedron, with one imino-N and two phenolate-O of the Schiff base ligand, and one oxo group defining the equatorial plane, and with the other oxo group and one solvent-O occupying the axial positions. The catalytic oxidation property of the complexes with *tert*-butylhydroperoxide in  $\text{CH}_2\text{Cl}_2$  was studied. Both complexes have excellent catalytic properties on cyclooctene and cyclohexene, and good properties on 1-hexene and 1-octene.

**Keywords:** Schiff base; Dioxomolybdenum complex; Crystal structure; Catalytic property

## 1. Introduction

Schiff base complexes have various catalytic properties, such as ring opening polymerization of cycloalkenes,<sup>1</sup> oxidation of hydrocarbons,<sup>2</sup> ring opening of large cycloalkanes,<sup>3</sup> reduction of ketones to alcohols,<sup>4</sup> alkylation of allylic substrates,<sup>5</sup> improve enantioselectivity in the cyclopropanation reactions.<sup>6</sup> The capability of molybdenum to formation of complexes with oxygen-, nitrogen-, and sulfur-containing ligands led to development of molybdenum Schiff base complexes which are efficient catalysts both in homogeneous and heterogeneous reactions.<sup>7</sup> The properties of the complexes vary obviously with the different types of ligands and coordination sites. Recently, we



Scheme 1.  $\text{H}_2\text{L}^1$ : X = OMe;  $\text{H}_2\text{L}^2$ : X = OEt

have reported a molybdenum complex with hydrazone ligand and its catalytic property.<sup>8</sup> In the present work, two new dioxomolybdenum(VI) complexes with Schiff base ligands 2-[(2-hydroxyphenylimino)methyl]-6-methoxyphenol ( $\text{H}_2\text{L}^1$ ) and 2-ethoxy-6-[(2-hydroxyphenylimino)methyl]phenol ( $\text{H}_2\text{L}^2$ ; Scheme 1),  $[\text{MoO}_2\text{L}^1(\text{EtOH})] \cdot \text{EtOH}$  (**1**) and  $[\text{MoO}_2\text{L}^2(\text{MeOH})]$  (**2**), are presented.

## 2. Experimental

### 2.1. Materials and Methods

3-Methoxysalicylaldehyde, 3-ethoxysalicylaldehyde, 2-aminophenol and  $\text{MoO}_2(\text{acac})_2$  were purchased from Sigma-Aldrich and used as received. All other reagents were of analytical reagent grade. The ligands  $\text{H}_2\text{L}^1$  and  $\text{H}_2\text{L}^2$  were synthesized according to the literature method with modification.<sup>9</sup> Elemental analyses of C, H and N were carried out in a Perkin-Elmer automated model 2400 Series II CHNS/O analyzer. FT-IR spectra were obtained on a Perkin-Elmer 377 FT-IR spectrometer with samples prepared as KBr pellets. UV-Vis spectra were obtained on a

Lambda 900 spectrometer. X-ray diffraction was carried out on a Bruker APEX II CCD diffractometer.  $^1\text{H}$  and  $^{13}\text{C}$  NMR spectra were recorded on a Bruker 300 MHz instrument.

## 2. 2. Synthesis of 2-[(2-hydroxyphenylimino)methyl]-6-methoxyphenol ( $\text{H}_2\text{L}^1$ )

3-Methoxysalicylaldehyde (0.010 mol, 1.52 g) and 2-aminophenol (0.010 mol, 1.10 g) were dissolved in ethanol (50 mL). The mixture was stirred for 30 min to give red solution. Then, the solvent was removed by distillation. The red solid was recrystallized from ethanol to give the Schiff base  $\text{H}_2\text{L}^1$ . Yield: 2.12 g (87%). IR data ( $\text{cm}^{-1}$ ): 3432 (O–H), 1628 (C=N), 1277 (Ar–O). UV-Vis data ( $\text{CH}_3\text{OH}$ ,  $\lambda_{\text{max}}$ , nm): 267, 346, 451.  $^1\text{H}$  NMR (500 MHz, DMSO)  $\delta$  14.02 (s, 1H, OH), 9.74 (s, 1H, OH), 8.95 (s, 1H, CH=N), 7.37 (d, 1H, ArH), 7.20–7.07 (m, 3H, ArH), 6.98–6.84 (m, 3H, ArH), 3.81 (s, 3H,  $\text{CH}_3$ ).  $^{13}\text{C}$  NMR (126 MHz, DMSO)  $\delta$  161.54, 151.80, 150.95, 148.15, 134.47, 127.98, 123.78, 119.57, 119.48, 119.22, 117.89, 116.49, 115.22, 55.85. Anal. calcd. for  $\text{C}_{14}\text{H}_{13}\text{NO}_3$  (%): C, 69.12; H, 5.39; N, 5.76. Found (%): C, 68.95; H, 5.50; N, 5.83.

## 2. 3. Synthesis of 2-ethoxy-6-[(2-hydroxyphenylimino)methyl]phenol ( $\text{H}_2\text{L}^2$ )

3-Ethoxysalicylaldehyde (0.010 mol, 1.66 g) and 2-aminophenol (0.010 mol, 1.10 g) were dissolved in ethanol (50 mL). The mixture was stirred for 30 min to give red solution. Then, the solvent was removed by distillation. The red solid was recrystallized from ethanol to give the Schiff base  $\text{H}_2\text{L}^2$ . Yield: 2.33 g (91%). IR data ( $\text{cm}^{-1}$ ): 3435 (O–H), 1628 (C=N), 1275 (Ar–O). UV-Vis data ( $\text{CH}_3\text{OH}$ ,  $\lambda_{\text{max}}$ , nm): 270, 345, 450.  $^1\text{H}$  NMR (500 MHz, DMSO)  $\delta$  13.89 (s, 1H, OH), 9.76 (s, 1H, OH), 8.95 (s, 1H, CH=N), 7.37 (d, 1H, ArH), 7.20–7.03 (m, 3H, ArH), 6.98–6.84 (m, 3H, ArH), 4.07 (q, 2H,  $\text{CH}_2$ ), 1.33 (t, 3H,  $\text{CH}_3$ ).  $^{13}\text{C}$  NMR (126 MHz, DMSO)  $\delta$  161.53, 151.80, 151.02, 147.50, 134.47, 127.96, 123.81, 118.86, 119.48, 118.83, 117.45, 116.49, 118.16, 64.87, 14.75. Anal. calcd. for  $\text{C}_{15}\text{H}_{15}\text{NO}_3$  (%): C, 70.02; H, 5.88; N, 5.44. Found (%): C, 70.15; H, 5.96; N, 5.37.

## 2. 4. Synthesis of Complex 1

$\text{H}_2\text{L}^1$  (0.010 mol, 2.43 g) and  $\text{MoO}_2(\text{acac})_2$  (0.010 mol, 2.65 g) were mixed and dissolved in ethanol (50 mL). The mixture was stirred for 1 h to give yellow solution. Single crystals of the complex, suitable for X-ray diffraction, were grown from the solution upon slowly evaporation for a few days. Yield: 1.87 g (41%). IR data ( $\text{cm}^{-1}$ ): 3357 (O–H), 1612 (C=N), 1263 (Ar–O), 929 and 910 (Mo=O). UV-Vis data ( $\text{CH}_3\text{OH}$ ,  $\lambda_{\text{max}}$ , nm): 273, 330. Anal. calcd. for  $\text{C}_{18}\text{H}_{23}\text{MoNO}_7$  (%): C, 46.86; H, 5.03; N, 3.04. Found (%): C, 46.67; H, 4.89; N, 3.13.

## 2. 5. Synthesis of Complex 2

$\text{H}_2\text{L}^2$  (0.01 mol, 2.57 g) and  $\text{MoO}_2(\text{acac})_2$  (0.01 mol, 2.65 g) were mixed and dissolved in methanol (50 mL). The mixture was stirred for 1 h to give yellow solution. Single crystals of the complex, suitable for X-ray diffraction, were grown from the solution upon slowly evaporation for a few days. Yield: 2.12 g (51%). IR data ( $\text{cm}^{-1}$ ): 3382 (O–H), 1611 (C=N), 1267 (Ar–O), 930 and 912 (Mo=O). UV-Vis data ( $\text{CH}_3\text{OH}$ ,  $\lambda_{\text{max}}$ , nm): 275, 330. Anal. calcd. for  $\text{C}_{16}\text{H}_{17}\text{MoNO}_6$  (%): C, 46.28; H, 4.13; N, 3.37. Found (%): C, 46.10; H, 4.07; N, 3.51.

## 2. 6. X-ray Crystallography

X-ray diffraction was carried out at a Bruker APEX II CCD area diffractometer equipped with MoK $\alpha$  radiation ( $\lambda = 0.71073 \text{ \AA}$ ). The collected data were reduced with SAINT,<sup>10</sup> and multi-scan absorption correction was performed using SADABS.<sup>11</sup> The structures of the complexes were solved by direct method, and refined against  $F^2$  by full-matrix least-squares method using SHELXTL.<sup>12</sup> All of the non-hydrogen atoms were refined anisotropically. The hydrogen atoms were placed in calculated positions and constrained to ride on their parent atoms. The crystallographic data and refinement parameters for the complexes

Table 1. Crystallographic and refinement data for the complexes

	1	2
Formula	$\text{C}_{18}\text{H}_{23}\text{MoNO}_7$	$\text{C}_{16}\text{H}_{17}\text{MoNO}_6$
Formula weight	461.31	415.25
Crystal shape/color	Block/yellow	Block/yellow
$T$ (K)	298(2)	298(2)
Crystal dimensions ( $\text{mm}^3$ )	$0.23 \times 0.22 \times 0.18$	$0.27 \times 0.27 \times 0.22$
Crystal system	Monoclinic	Monoclinic
Space group	$P2_1/c$	$P2_1/c$
$a$ ( $\text{\AA}$ )	8.3857(11)	10.0718(10)
$b$ ( $\text{\AA}$ )	6.9208(12)	18.1333(12)
$c$ ( $\text{\AA}$ )	34.0235(15)	19.234(2)
$\beta$ ( $^\circ$ )	91.317(2)	97.354(2)
$V$ ( $\text{\AA}^3$ )	1967.7(4)	3483.9(6)
$Z$	4	8
$D_{\text{calc}}$ ( $\text{g cm}^{-3}$ )	1.557	1.583
$\mu$ (Mo K $\alpha$ ) ( $\text{mm}^{-1}$ )	0.705	0.783
$F(000)$	944	1680
Measured reflections	9054	20401
Unique reflections	3611	6469
Observed reflections ( $I \geq 2\sigma(I)$ )	2385	5125
Parameters	251	443
Restraints	1	5
Goodness of fit on $F^2$	1.135	1.093
$R_1, wR_2$ [ $I \geq 2\sigma(I)$ ] <sup>a</sup>	0.0896, 0.1551	0.0395, 0.1001
$R_1, wR_2$ (all data) <sup>a</sup>	0.1393, 0.1742	0.0549, 0.1096

$$^a R_1 = F_o - F_c/F_o, wR_2 = [\sum w(F_o^2 - F_c^2)/\sum w(F_o^2)]^{1/2}$$

**Table 2.** Selected bond distances (Å) and angles (°) for the complexes.

1			
Mo(1)–O(1)	1.919(6)	Mo(1)–O(2)	1.950(6)
Mo(1)–O(4)	2.315(7)	Mo(1)–O(5)	1.683(6)
Mo(1)–O(6)	1.708(6)	Mo(1)–N(1)	2.255(7)
O(5)–Mo(1)–O(6)	103.8(3)	O(5)–Mo(1)–O(1)	98.6(3)
O(6)–Mo(1)–O(1)	100.7(3)	O(5)–Mo(1)–O(2)	97.8(3)
O(6)–Mo(1)–O(2)	97.6(3)	O(1)–Mo(1)–O(2)	151.7(3)
O(5)–Mo(1)–N(1)	92.7(3)	O(6)–Mo(1)–N(1)	162.7(3)
O(1)–Mo(1)–N(1)	81.6(3)	O(2)–Mo(1)–N(1)	74.7(3)
O(5)–Mo(1)–O(4)	170.1(3)	O(6)–Mo(1)–O(4)	86.0(3)
O(1)–Mo(1)–O(4)	80.8(3)	O(2)–Mo(1)–O(4)	79.1(3)
N(1)–Mo(1)–O(4)	77.4(2)		
2			
Mo(1)–O(1)	1.975(3)	Mo(1)–O(2)	1.951(3)
Mo(1)–O(4)	1.685(3)	Mo(1)–O(5)	1.690(3)
Mo(1)–O(6)	2.301(3)	Mo(1)–N(1)	2.286(3)
Mo(2)–O(10)	1.684(3)	Mo(2)–O(11)	1.691(3)
Mo(2)–O(8)	1.958(3)	Mo(2)–O(7)	1.968(3)
Mo(2)–N(2)	2.273(3)	Mo(2)–O(12)	2.329(3)
O(4)–Mo(1)–O(5)	104.70(16)	O(4)–Mo(1)–O(2)	102.31(14)
O(5)–Mo(1)–O(2)	95.90(14)	O(4)–Mo(1)–O(1)	95.52(14)
O(5)–Mo(1)–O(1)	104.44(14)	O(2)–Mo(1)–O(1)	148.54(12)
O(4)–Mo(1)–N(1)	90.80(14)	O(5)–Mo(1)–N(1)	163.45(14)
O(2)–Mo(1)–N(1)	74.77(12)	O(1)–Mo(1)–N(1)	79.32(12)
O(4)–Mo(1)–O(6)	169.69(13)	O(5)–Mo(1)–O(6)	84.85(14)
O(2)–Mo(1)–O(6)	80.18(12)	O(1)–Mo(1)–O(6)	78.07(11)
N(1)–Mo(1)–O(6)	80.14(12)	O(10)–Mo(2)–O(11)	105.69(18)
O(10)–Mo(2)–O(8)	96.57(15)	O(11)–Mo(2)–O(8)	100.16(15)
O(10)–Mo(2)–O(7)	102.51(15)	O(11)–Mo(2)–O(7)	98.82(14)
O(8)–Mo(2)–O(7)	148.24(12)	O(10)–Mo(2)–N(2)	163.87(15)
O(11)–Mo(2)–N(2)	89.44(14)	O(8)–Mo(2)–N(2)	74.83(12)
O(7)–Mo(2)–N(2)	80.14(11)	O(10)–Mo(2)–O(12)	84.58(15)
O(11)–Mo(2)–O(12)	169.73(14)	O(8)–Mo(2)–O(12)	78.56(13)
O(7)–Mo(2)–O(12)	78.24(11)	N(2)–Mo(2)–O(12)	80.38(12)

are listed in Table 1. Selected bond lengths and angles are listed in Table 2.

## 2. 7. Catalytic Epoxidation of Olefins

Epoxidation of cyclooctene, cyclohexene, 1-octene and 1-hexene catalyzed by the complexes with *tert*-butylhydroperoxide (TBHP) in CH<sub>2</sub>Cl<sub>2</sub> was carried out according to the following general procedure. To a 25 mL round bottomed flask equipped with a magnetic stirring bar and immersed into water thermo-stated bath, was added 10 mL CH<sub>2</sub>Cl<sub>2</sub>, 1.0 mmol TBHP, 0.01 mmol catalyst and 1.0 mmol olefin. The mixture was refluxed with vigorous stirring for 2 h at an appropriately chosen temperature. The progress of the reaction was monitored by carefully withdrawing aliquots of the sample at different time intervals to determine concentrations of the products by GC analysis, using *n*-hexane as an internal standard and was left to proceed until near complete conversion of TBHP. The con-

centration of the TBHP was determined by iodometric titration method.<sup>13</sup> The yield of epoxide (%) was calculated according to the starting amount of olefin. Assignments of the products were made by comparison with authentic samples. All the reactions were run in triplicates. Control experiments showed that no epoxide was formed in a measurable extent in the absence of catalyst.

## 3. Results and Discussion

### 3. 1. General

The Schiff base ligands H<sub>2</sub>L<sup>1</sup> and H<sub>2</sub>L<sup>2</sup> were readily prepared by the condensation reaction of 2-aminophenol with 3-methoxysalicylaldehyde and 3-ethoxysalicylaldehyde, respectively. The molybdenum(VI) complexes **1** and **2** were synthesized by stirring equimolar quantities of the Schiff bases with MoO<sub>2</sub>(acac)<sub>2</sub> in ethanol or methanol at room temperature. Single crystals of the complexes are sta-

ble in air at ambient condition. The complexes are soluble in methanol, ethanol, acetonitrile, DMSO, DMF, but insoluble in water. The chemical formulae of the complexes have been confirmed by elemental analyses, IR spectra, and single crystal X-ray diffraction.

### 3. 2. Spectral Characterization

The bands at  $1628\text{ cm}^{-1}$  characteristic of the azomethine groups present in the free Schiff bases, were shifted to lower wave numbers at  $1612\text{ cm}^{-1}$  for **1** and  $1611\text{ cm}^{-1}$  for **2**, indicating that the involvement the azomethine nitrogen atoms in coordination. The bands at  $1275\text{--}1277\text{ cm}^{-1}$  in the spectra of the Schiff bases are ascribed to the phenolic C–O stretching vibration. These bands are found at  $1263$  and  $1267\text{ cm}^{-1}$  in the spectra of the complexes. These changes suggest that the hydroxyl groups of the Schiff bases took part in the complex formation. The Schiff bases and the complexes exhibit broad bands at  $3300\text{--}3400\text{ cm}^{-1}$ , which may be assigned to the  $\nu(\text{O-H})$ . Further evidence of the bonding is also shown by the observation that new bands in the IR spectra of the metal complexes appear at  $450\text{--}650\text{ cm}^{-1}$  assigned to Mo–N and Mo–O stretching vibrations. The Mo=O stretching mode occur as double bands at  $930$  and  $910\text{ cm}^{-1}$ , assigned to the symmetric and asymmetric stretching modes of the  $\text{MoO}_2$  moieties.<sup>14</sup>

Electronic absorption spectra of the Schiff base and the complexes were obtained in methanol solutions. The electronic absorption spectra of the free Schiff bases displayed three bands at  $270$ ,  $345$  and  $450\text{ nm}$ , which are assigned for the  $\pi\rightarrow\pi^*$  and  $n\rightarrow\pi^*$  transitions, respectively. In the electronic spectra of the complexes, the strong bands centered at  $273\text{ nm}$  are attributed to the intra-ligand  $\pi\rightarrow\pi^*$  absorption peak of the Schiff base ligand. The LMCT and to some extent  $\pi\rightarrow\pi^*$  bands appear at about  $330\text{ nm}$ .

### 3. 3. Structural Description of Complex 1

The molecular structure of complex **1** is shown in Figure 1. It contains a dioxomolybdenum complex molecule and an ethanol molecule of crystallization. The coordination geometry around the Mo atom can be described as distorted octahedron, with one imino-N and two phenolate-O of the Schiff base ligand, and one oxo group defining the equatorial plane, and with the other oxo group and one ethanol-O occupying the axial positions. The Schiff base ligand coordinates to the Mo atom in a meridional fashion forming five- and six-membered chelate rings with bite angles of  $74.7(3)$  and  $81.6(3)^\circ$ . The dihedral angle between the two benzene rings of the Schiff base ligand is  $6.5(3)^\circ$ . The O=Mo=O angle ( $103.8(3)^\circ$ ) and the Mo=O distances ( $1.683(3)\text{--}1.708(3)\text{ \AA}$ ) are typical for *cis*-dioxomolybdenum(VI) complexes.<sup>7</sup> The imino nitrogen and ethanol oxygen atoms, which are *trans* to the terminal oxo groups, bond to the Mo(VI) atom with distances of  $2.255(7)\text{ \AA}$  for nitrogen and  $2.315(7)\text{ \AA}$  for oxygen, respectively. The Mo–O distances vary from  $1.919(6)$  to  $1.950(6)\text{ \AA}$  for the phenolate oxygen, which are in accord with these types of bonds in hexa-coordinated dioxomolybdenum(VI) complexes.<sup>7</sup>

In the crystal structure of the complex, the  $[\text{MoO}_2\text{L}^1(\text{EtOH})]$  complex molecules are linked by ethanol molecules through two intermolecular O–H...O hydrogen bonds [ $\text{O}(7)\text{--H}(7\text{A}) = 0.82\text{ \AA}$ ,  $\text{H}(7\text{A})\cdots\text{O}(6)^i = 1.91\text{ \AA}$ ,  $\text{O}(7)\cdots\text{O}(6)^i = 2.725(9)\text{ \AA}$ ,  $\text{O}(7)\text{--H}(7\text{A})\cdots\text{O}(6)^i = 174(5)^\circ$ ; symmetry code for *i*:  $x, 1 + y, z$ ], to form one dimensional chains along the *b* axis (Figure 2).

### 3. 4. Structural Description of Complex 2

The molecular structure of complex **2** is shown in Figure 3. It contains two dioxomolybdenum complex mol-

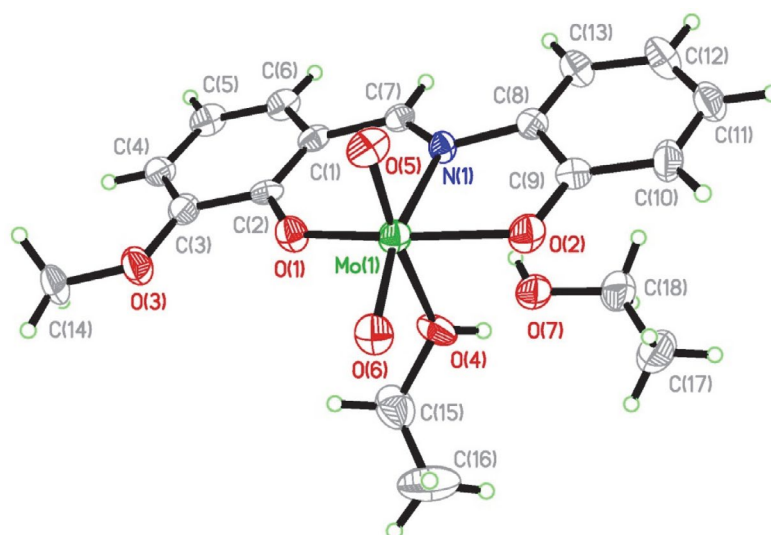


Figure 1. A perspective view of complex **1** with the atom labeling scheme. Thermal ellipsoids are drawn at the 30% probability level.

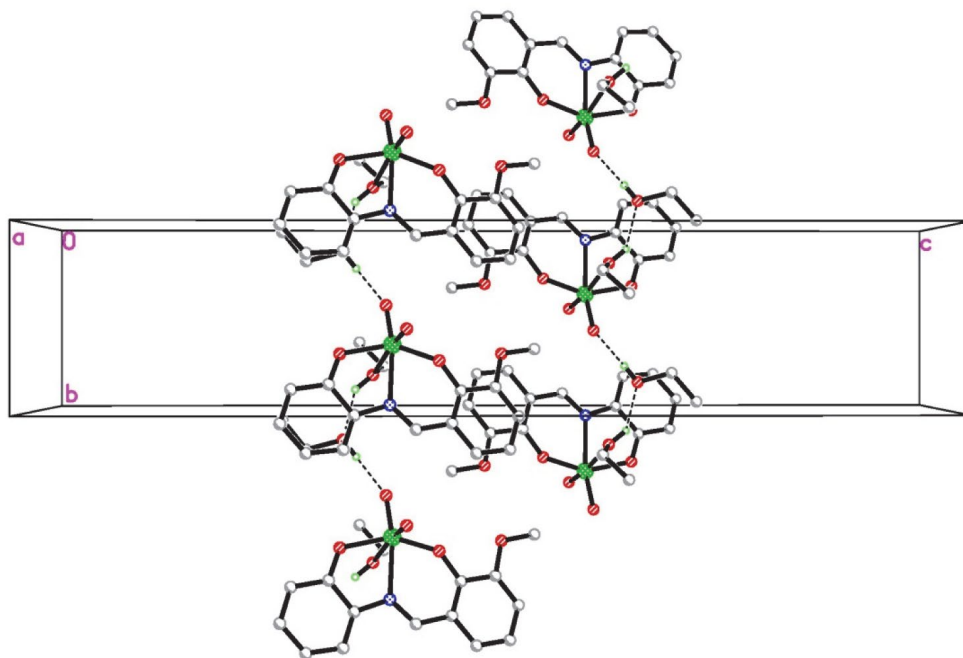


Figure 2. The hydrogen bonds (dashed lines) linked molecules into one dimensional chains of complex 1, viewed along the *a* axis.

ecules in the asymmetric unit. The two complex molecules are linked through O–H...O hydrogen bonds [O(12)–H(12A) = 0.85(1) Å, H(12A)...O(1) = 1.96(2) Å, O(12)...O(1) = 2.792(4) Å, O(12)–H(12A)...O(1) = 169(4)°; O(6)–H(6) = 0.85(1) Å, H(6)...O(7) = 1.92(1) Å, O(6)...O(7) = 2.776(4) Å, O(6)–H(6)...O(7) = 175(2)°]. The coordination geometry around the Mo atom can be described as distorted octahedron, with one imino-N and two phenolate-O of the Schiff base ligand, and one oxo group defining the equatorial plane, and with the other oxo group and one metha-

mol-O occupying the axial positions. The Schiff base ligand coordinates to the Mo atom in a meridional fashion forming five- and six-membered chelate rings with bite angles of 74.68(12) and 81.67(12)° for Mo(1) moiety, and 74.83(12) and 80.14(11)° for Mo(2) moiety. The dihedral angles between the two benzene rings of the Schiff base ligands are 10.8(5)° and 6.7(5)°. The O=Mo=O angles (104.70(16) and 105.69(18)°) and the Mo=O distances (1.684(3)–1.691(3) Å) are typical for *cis*-dioxomolybdenum(VI) complexes.<sup>7</sup> The imino nitrogen and ethanol oxygen atoms, which are *trans* to the terminal oxo groups, bond to the Mo(VI) atom with distances of 2.273(3)–2.286(7) Å for nitrogen and 2.301(3)–2.329(3) Å for oxygen, respectively. The Mo–O distances vary from 1.951(3) to 1.975(3) Å for the phenolate oxygen, which are in accord with these types of bonds in hexa-coordinated dioxomolybdenum(VI) complexes.<sup>7</sup> In the crystal structure of the complex, molecules are stack along the *a* axis (Figure 4).

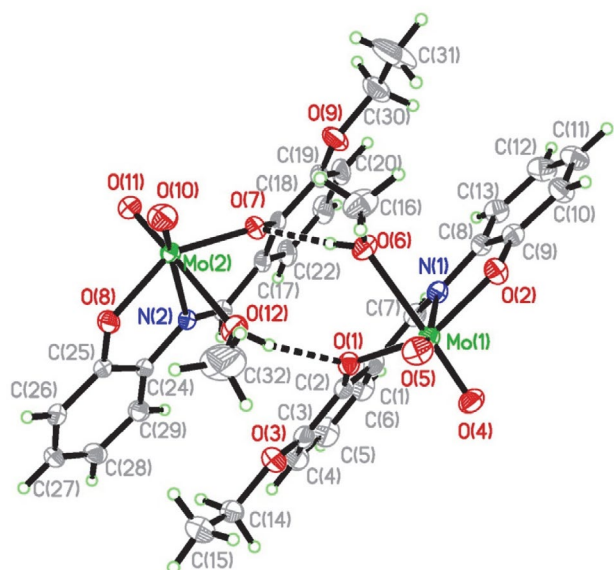


Figure 3. A perspective view of complex 2 with the atom labeling scheme. Thermal ellipsoids are drawn at the 30% probability level. Hydrogen bonds are shown as dashed lines.

### 3. 5. Catalytic property of the Complexes

Catalytic property of the complexes was investigated in the epoxidation of cyclooctene, cyclohexene, 1-octene and 1-hexene with TBHP and CH<sub>2</sub>Cl<sub>2</sub> as a solvent at different temperatures 25, 45 and 65 °C. The catalytic reactions were initially performed in order to test the performance of the system under the easiest possible reaction conditions. A substrate, oxidant, and catalyst ratio of 100:100:1 was used. In general, the epoxide yields are higher for cyclic olefins than those for terminal olefins. As seen in Table 3, the order of increasing reactivity based on yield% are as cyclooctene > cyclohexene > 1-hexene > 1-octene. In addition, the ep-

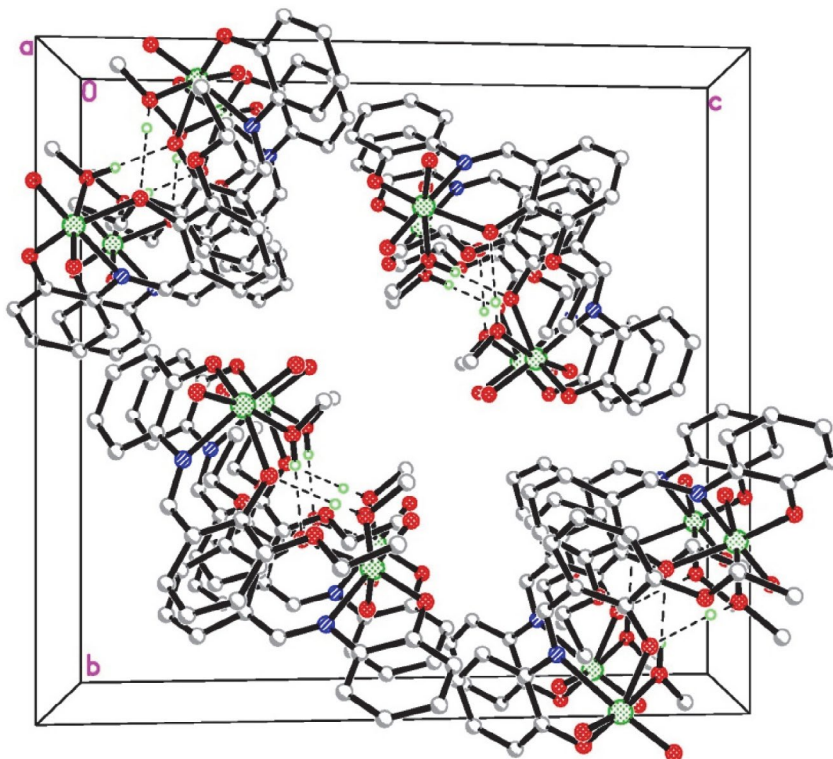


Figure 4. The hydrogen bonds (dashed lines) linked dimeric structure of complex 2, viewed along the *a* axis.

Table 3. Epoxide yields (%) for the catalytic processes at different temperatures

Substrate	25 °C		45 °C		65 °C	
	1	2	1	2	1	2
Cyclooctene	87	85	93	93	98	97
Cyclohexene	81	81	89	90	94	94
1-Hexene	70	73	78	80	85	84
1-Octene	62	61	70	70	77	75

oxide yields increase with the rise in temperature. Both complexes have similar catalytic properties, because of their similar structures. As a comparison, the catalytic property of the complexes on cyclohexene is similar to the molybdenum complex with tris(hydroxymethyl)amino methane as ligand.<sup>15</sup> The complexes have in general higher catalytic property on the substrates than the molybdenum complex derived from the Schiff base ligand *N,N'*-bis(salicylidene)4,5-dichloro-1,2-phenylenediamine.<sup>7d</sup>

#### 4. Conclusion

Two new dioxomolybdenum(VI) complexes derived from the Schiff base ligands 2-[(2-hydroxyphenylimino)methyl]-6-methoxyphenol and 2-ethoxy-6-[(2-hydroxyphenylimino)methyl]phenol have been prepared and structurally characterized. The Mo atoms in the complexes are in octahedral coordination. Both complexes have ef-

fective catalytic properties on cyclooctene and cyclohexene.

#### 5. Supplementary Material

CCDC-1849701 and 1849702 contain the supplementary crystallographic data for this paper. These data can be obtained free of charge at <http://www.ccdc.cam.ac.uk/const/retrieving.html> or from the Cambridge Crystallographic Data Centre (CCDC), 12 Union Road, Cambridge CB2 1EZ, UK; fax: +44(0)1223-336033 or e-mail: [deposit@ccdc.cam.ac.uk](mailto:deposit@ccdc.cam.ac.uk).

#### 6. References

1. D. Huang, C. Wang, Y. Song, *Russ. J. Gene. Chem.* **2013**, *83*, 2361–2369. DOI:10.1134/S1070363213120281



2. (a) S. Biswas, A. Dutta, M. Dolai, M. Debnath, A. D. Jana, M. Ali, *RSC Advances* **2014**, *4*, 34248–34256; DOI:10.1039/C4RA06078D  
(b) B. Bahramian, F. D. Ardejani, V. Mirkhani, K. Badii, *Appl. Catal. A General* **2008**, *345*, 97–103. DOI:10.1016/j.apcata.2008.04.028
3. (a) A. Schriesheim, R. J. Muller, C. A. Rowe, *J. Am. Chem. Soc.* **1962**, *84*, 3164–3172; DOI:10.1021/ja00875a026  
(b) F. Farzaneh, M. Ghiasi, M. Ghandi, M. Ghandi, V. Daadmehr, *Porous Mater.* **2013**, *20*, 267–275; DOI:10.1007/s10934-012-9596-8  
(c) K. Pamin, G. Pozzi, E. Tabor, W. Bukowski, J. Poltowicz, *Catal. Commun.* **2013**, *39*, 102–105.
4. G. Ventakachalam, R. Ramesh, *Inorg. Chem. Commun.* **2005**, *8*, 1009–1013. DOI:10.1016/j.inoche.2005.08.004
5. D. Pou, A. E. Platero-Prats, S. Perez, C. Lopez, X. Solans, M. Font-Bardia, P. W. N. M. van Leeuwen, G. P. F. van Strijdonck, Z. Freixa, *J. Organomet. Chem.* **2007**, *692*, 5017–5025. DOI:10.1016/j.jorganchem.2007.07.027
6. (a) G. Koz, D. Astley, S. T. Astley, *Turk. J. Chem.* **2011**, *35*, 553–560;  
(b) D. S. Masterson, T. L. Hobbs, D. T. Glatzhofer, *J. Mol. Catal. A Chem.* **1999**, *145*, 75–81. DOI:10.1016/S1381-1169(99)00041-2
7. (a) M. Bagherzadeh, R. Latifi, L. Tahsini, V. Amani, A. Ellern, L. K. Woo, *Polyhedron* **2009**, *28*, 2517–2521; DOI:10.1016/j.poly.2009.05.036  
(b) Z. Moradi-Shoeili, M. Zare, M. Bagherzadeh, M. Kubicki, D. M. Boghaei, *J. Coord. Chem.* **2015**, *68*, 548–559; DOI:10.1080/00958972.2014.993321  
(c) M. Bagherzadeh, M. Amini, H. Parastar, *Inorg. Chem. Commun.* **2012**, *20*, 86–89; DOI:10.1016/j.inoche.2012.02.023  
(d) A. A. A. Aziz, *J. Mol. Struct.* **2010**, *979*, 77–85; DOI:10.1016/j.molstruc.2010.06.004
- (e) R. D. Chakravarthy, K. Suresh, V. Ramkumar, D. K. Chand, *Inorg. Chim. Acta* **2011**, *376*, 57–63; DOI:10.1016/j.ica.2011.05.033  
(f) S. Rayati, N. Rafiee, A. Wojtczak, *Inorg. Chim. Acta* **2012**, *386*, 27–35. DOI:10.1016/j.ica.2012.02.005
8. X. W. Zhu, *Russ. J. Coord. Chem.* **2018**, *44*, 421–424. DOI:10.1134/S1070328418070084
9. (a) H. Petek, C. Albayrak, M. Odabasoglu, I. Senel, O. Buyukgungor, *Struct. Chem.* **2010**, *21*, 681–690; DOI:10.1007/s11224-010-9598-6  
(b) B. Chattopadhyay, S. Basu, P. Chakraborty, S. K. Choudhuri, A. K. Mukherjee, M. Mukherjee, *J. Mol. Struct.* **2009**, *932*, 90–96. DOI:10.1016/j.molstruc.2009.05.047
10. Bruker, SMART (Version 5.625) and SAINT (Version 6.01). Bruker AXS Inc., Madison, Wisconsin, USA, 2007.
11. G. M. Sheldrick, SADABS. Program for Empirical Absorption Correction of Area Detector, University of Göttingen, Germany, 1996.
12. G. M. Sheldrick, SHELXTL V5.1 Software Reference Manual, Bruker AXS, Inc., Madison, Wisconsin, USA, 1997.
13. W. F. Brill, *J. Am. Chem. Soc.* **1963**, *85*, 141–145. DOI:10.1021/ja00885a006
14. (a) S. N. Rao, K. N. Munshi, N. N. Rao, M. M. Bhadbhade, E. Suresh, *Polyhedron* **1999**, *18*, 2491–2497; DOI:10.1016/S0277-5387(99)00139-4  
(b) S. M. El-Medani, M. M. Aboaly, H. H. Abdalla, R. M. Ramadan, *Spectrosc. Lett.* **2004**, *37*, 619–632. DOI:10.1081/SL-200037610
15. (a) Q. Liu, J. Lin, J. Liu, W. Chen, Y. Cui, *Acta Chim. Slov.* **2016**, *63*, 279–286;  
(b) M. Liang, D.-H. Zou, *Acta Chim. Slov.* **2016**, *63*, 180–185; DOI:10.17344/acsi.2015.2169  
(c) Y. Sui, X. Zeng, X. Fang, X. Fu, Y. Xiao, L. Chen, M. Li, S. Cheng, *J. Mol. Struct. A* **2007**, *270*, 61–67.

## Povzetek

Sintetizirali smo dva strukturno sorodna nova dioksomolibdenova(VI) kompleksa,  $[\text{MoO}_2\text{L}^1(\text{EtOH})] \cdot \text{EtOH}$  (**1**) in  $[\text{MoO}_2\text{L}^2(\text{MeOH})]$  (**2**), kjer sta  $\text{L}^1$  in  $\text{L}^2$  dianionski obliki 2-[(2-hidroksifenilimino)metil]-6-metoksifenola ( $\text{H}_2\text{L}^1$ ) in 2-etoksi-6-[(2-hidroksifenilimino)metil]fenola ( $\text{H}_2\text{L}^2$ ), ter ju okarakterizirali z IR in UV-Vis spektroskopijo, kakor tudi z monokristalno rentgensko difrakcijo. Strukturna analiza je razkrila, da sta oba kompleksa dioksomolibdenovi(VI) zvrsti. Kompleks **1** vsebuje kot ligand tudi molekulo etanola, kompleks **2** pa molekulo metanola. Koordinacijsko geometrijo okoli Mo atomov lahko opišemo kot popačen oktaeder z enim imino N-atomom, dvema fenolatnima O-atomoma in eno okso skupino, ki skupaj definirajo ekvatorialno ravnino, ter drugo okso skupino in molekulo topila, ki zasedata aksialni legi. Proučili smo tudi katalitične lastnosti kompleksov pri reakcijah oksidacije s *tert*-butilhidroperoksidom v  $\text{CH}_2\text{Cl}_2$ . Oba kompleksa izkazujeta odlične katalitične lastnosti v primeru ciklooktena in cikloheksena ter dobre lastnosti v primeru 1-heksena in 1-oktena.

Scientific paper

# A Nano-Sepiolite Clay Electrochemical Sensor for the Rapid Electro-Catalytic Detection of Hydroquinone in Cosmetic Products

Sevda Aydar,<sup>1</sup> Dilek Eskiköy Bayraktepe<sup>2</sup> Hayati Filik<sup>2</sup> and Zehra Yazan<sup>2,\*</sup><sup>1</sup> Faculty of Engineering, Department of Chemistry, Istanbul University, 34320 Avcılar, Istanbul, Turkey<sup>2</sup> Ankara University, Faculty of Science, Chemistry Department, 06560 Ankara, Turkey

\* Corresponding author: E-mail: zehrayazan67@gmail.com

Phone: +903122126720/1284 fax: +903122232395

Received: 13-07-2018

## Abstract

In this paper, a simple and sensitive electrochemical nano-sensor was developed for the analysis of hydroquinone based on sepiolite clay modified carbon paste sensor by using differential pulse adsorptive stripping voltammetry and square wave adsorptive stripping voltammetry. Surface morphology of sensors was characterized by using scanning electron microscopic technique, electrochemical impedance spectroscopy, and cyclic voltammetry. Electrochemical redox properties of hydroquinone were investigated by cyclic voltammetry. The oxidation peak current of hydroquinone in differential pulse and square wave adsorptive stripping voltammetry changes linearly in the concentration range of 0.01–700  $\mu\text{molL}^{-1}$  and 0.01–700  $\mu\text{molL}^{-1}$ , respectively. Excellent limit of detection (LOD) and limit of quantification (LOQ) values were found as 0.01096  $\mu\text{molL}^{-1}$  and 0.03654  $\mu\text{molL}^{-1}$  for differential pulse, and 0.01031  $\mu\text{molL}^{-1}$  and 0.03438  $\mu\text{molL}^{-1}$  for square wave adsorptive stripping voltammetry, respectively. Additionally, the newly proposed sensor was applied to the analysis of hydroquinone in cosmetic cream with satisfying results.

**Keywords:** Hydroquinone; sepiolite clay; carbon paste electrode; cosmetic cream; voltammetry

## 1. Introduction

Hydroquinone (HQ) is a phenol derivative with antioxidant properties that can cause toxicity in several organs, such as the kidneys. It is used as a topical treatment for skin hyperpigmentation in various cosmetic products.<sup>1</sup> It is metabolized mainly to glutathione conjugates and forms mutagenic DNA adducts in *in-vitro* systems. Due to its high toxicity, several methods have been established for the determination, such as high performance liquid chromatography,<sup>2</sup> fluorescence,<sup>3</sup> chemiluminescence,<sup>4</sup> spectrophotometry,<sup>5–6</sup> gas chromatography-mass spectrometry,<sup>7</sup> capillary electro-chromatography,<sup>8</sup> and electrochemical methods.<sup>9–13</sup>

Most of the methods, in particular chromatographic methods, are both time consuming and based on the use of organic liquids in excess volumes. Electrochemical techniques for hydroquinone assay are cost effective, fast and highly sensitive. The non-destructive nature and extremely low sample consumption makes them one of the preferred techniques.<sup>11</sup>

Electrochemical devices for use in clinical, cosmetic and environmental monitoring are developing rapidly.<sup>14,15</sup> Many researchers focused on the design of the electrochemical sensors using nano electrode materials to modify the electrode so as to improve the quality of signal. Among many electrode improvement components, carbon nanotubes,<sup>16</sup> graphene,<sup>17</sup> nano-sized metal oxides,<sup>18</sup> and clay minerals<sup>19</sup> proved to be promising.

Nanomaterials provide a conductive sensing interface and have catalytic effects on the electrochemical process. On the other hand, the clay electrode contributes to the electrical conductivity and catalytic effect to electron-transfer rates. We chose sepiolite (natural clay mineral) for our sensor composition because of its high surface area and surface activity.<sup>19</sup>

Here, we extend the investigations on the use of sepiolite clay for the analysis of HQ in cosmetic products. We developed a sensitive, selective, and reliable adsorptive stripping anodic voltammetric methods for the determination of HQ with a high precision and accuracy together with a wide linear range and low limit of detection.

## 2. Experimental

### 2.1. Reagents and Apparatus

Sepiolite clay, graphite powder, mineral oil and all solvents were supplied from Sigma. HQ was also supplied from Merck and other used chemicals were analytical grade. The stock solution of HQ ( $1.0 \times 10^{-3} \text{ molL}^{-1}$ ) was prepared by dissolving solid HQ in water and kept at  $+4^\circ\text{C}$  until experiment.  $0.04 \text{ molL}^{-1}$  Britton-Robinson buffer was used as the supporting electrolyte.

All electrochemical measurements were performed by using CHI 660C (from USA) and C3 cell stand (BASi) with a solid electrode system. Ag/AgCl ( $3.0 \text{ molL}^{-1}$  NaCl, BAS MF-2052) was used as reference electrode, NSC/CPE and BCPE sensors as working electrodes, and platinum wire electrode (BAS MW-1032) as auxiliary electrode.

Before all assays, pH was measured with a HANNA Instruments HI2211 pH/ORP meter with an accuracy of  $\text{pH} \pm 0.01$ . Double-distilled water was supplied mpMINI-pure system. All assays were carried out at  $25^\circ\text{C}$ .

Scanning electron microscopic (SEM) images were recorded on Carl Zeiss AG, EVO<sup>®</sup> 50 Series.

### 2.2. Sensor Preparation Procedure

Bare carbon paste (BCPE) and modified carbon paste (NSC/CPE) electrodes were prepared for comparative purposes. For the preparation of modified carbon paste electrodes, the varying proportions of sepiolite 3.3% (1.0/30); 5% (1.5/30); 6.7% (2.0/30); 8.3% (2.5/30) with proper masses of graphite powder and mineral oil ( $10 \mu\text{L}$ ), making the final weight to 30 mg, were mixed in a mortar and ground for 5 min with a pestle. Both the bare containing 30 mg graphite powder and modified paste were filled into the hole of the electrode body and the electric contact was made with a copper wire in the center of the cylindrical body. The outward surface of the electrode was polished with a piece of polishing paper until it had a shiny surface. Before all assays, the surface cleaning of carbon paste sensors was carried out by washing with water-ethanol mixture (1:1) before all experiments.

### 2.3. Analytical Procedure

The cyclic, differential pulse and square wave voltammetric experiments were carried out at room temperature in an electrochemical cell containing BR buffer solution and the required volume of hydroquinone standard solution. CV measurements were recorded by cycling the potential between  $-0.2$  and  $+1.0 \text{ V}$  at a scan rate of  $0.10 \text{ Vs}^{-1}$ . The adsorptive stripping square wave voltammetry (AdsSWV) measurements were performed by scanning the potential from  $0.2$  to  $+0.8 \text{ V}$  at a frequency of  $20 \text{ Hz}$ , pulse amplitude of  $0.025 \text{ V}$ , and with scan increments of  $0.008 \text{ V}$ . The adsorptive stripping differential pulse voltammetry (AdsDPV) conditions were given as follows: ampli-

tude:  $0.05 \text{ V}$ , pulse width:  $0.05 \text{ s}$ , sample width:  $0.0167 \text{ s}$ , pulse period:  $0.5 \text{ s}$ ; HQ solutions of  $8.0 \times 10^{-8} \text{ molL}^{-1}$  in the potential range of  $0.2$  to  $+0.8 \text{ V}$ .

The solution was stirred at  $400 \text{ rpm}$  at optimum stripping conditions. After the pre-concentration period, the stirring was stopped and voltammograms were recorded.

### 2.4. Cream Sample Preparation

Pharmaceutical and cosmetic cream samples (Expigment Cream 4% HQ) were taken from pharmacy. The cream was kept at room temperature until assay. Known amounts of cream ( $15 \text{ mg}$ ) were dissolved in  $50 \text{ mL}$  distilled water. The solution was shaken for  $30 \text{ min}$  in an ultrasonic bath to facilitate the complete dissolution of hydroquinone. This solution has served as the stock solution for the preparation of the samples for analysis. Appropriate volume of aliquot was taken from the clear part of solution and transferred into the working cells. The volume of the working solution was completed to  $10 \text{ mL}$  by BR buffer ( $\text{pH } 2.0$ ).

## 3. Results and Discussion

### 3.1. Optimum Composition of Sepiolite clay

The composition of modified electrodes has a significant effect on electrochemical signal of modified electrodes by means of changing the sensitivity and selectivity of electrodes and redox potential shift.<sup>20</sup> For this purpose, sepiolite clay electrodes were prepared with the different combinations in the range between 3.3% and 8.3% (*w/w*). Then the voltammetric responses of the modified electrodes were studied by CV technique in the presence of  $1.0 \times 10^{-4} \text{ molL}^{-1}$  HQ in BR buffer solution  $\text{pH } 2.0$  (Fig. 1).

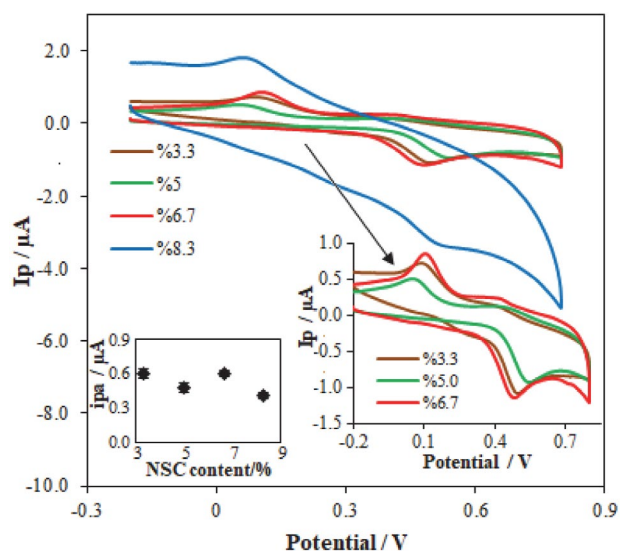


Fig. 1. Cyclic voltammograms of  $1.0 \times 10^{-4} \text{ molL}^{-1}$  HQ in different compositions of NSC/CPE zoomed to specific composition range indicated with arrow in  $\text{pH } 2.0$  BR buffer at scan rate:  $0.10 \text{ Vs}^{-1}$ .

As seen in Fig. 1, both obtained anodic and cathodic peak currents of HQ on sepiolite clay modified carbon paste electrode containing 6.7% sepiolite clay are higher than those obtained on sepiolite clay carbon paste electrodes with other percentages of clay. Also, the lowest potential difference between anodic and cathodic peak potential ( $\Delta E_p$ ) value was obtained from sepiolite clay modified carbon paste electrode containing 6.7% sepiolite clay. Herein, the optimal modified electrode composition for the sepiolite sensor electrode was found as 6.7% sepiolite clay (2.0 mg sepiolite/30 mg paste, 93% graphite powder, and 10  $\mu\text{L}$  mineral oil).

### 3. 2. Characterization of Sensors

Cyclic voltammetry (CV), electrochemical impedance spectroscopy (EIS) and scanning electron microscopic (SEM) techniques were used for the surface characterization of the sensors (BCPE, NSC/CPE). Firstly, CV voltammograms of  $5.0 \times 10^{-3} \text{ molL}^{-1} \text{ Fe(CN)}_6^{3-/4-}$  in KCl ( $0.1 \text{ molL}^{-1}$ ) solution were used to compare the electrochemical properties of sensors (Fig. 2a). The trial experiments were carried out at a scan rate of  $0.10 \text{ Vs}^{-1}$ .

Clearly, the modified sensor gives rise to the best CV signal with the smaller  $\Delta E_p$  difference and the best peak current signal compared to the bare sensor in the standard

solution. Then, at different scan rates, CV measurements were taken for the comparison of the specific areas of two sensors in  $5.0 \times 10^{-3} \text{ molL}^{-1} \text{ Fe(CN)}_6^{3-/4-}$  standard solution medium. Randles-Sevcik equations were evaluated by CV measurements at different scan rates ( $i_p$  vs  $v^{1/2}$ ). The active surface areas of NSC/CPE and BCPE were calculated by the means of  $i_p^a$  versus  $v^{1/2}$  plot's slope and a known diffusion coefficient of  $\text{Fe(CN)}_6^{3-/4-}$   $7.6 \times 10^{-6} \text{ cm}^2\text{s}^{-1}$ .<sup>21</sup> The surface area of BCPE was evaluated to be  $0.081 \pm 0.0017 \text{ cm}^2$  and that of the NSC/CPE was  $0.089 \pm 0.0013 \text{ cm}^2$ . These results show 1.1 times increase in the surface areas of sensors.

The electrochemical impedance measurements were also used to compare the surface areas of modified electrode and bare electrode. The same redox couple was used as the standard analyte. Fig. 2b displays the Nyquist plots obtained with the two electrodes. The diagrams in Fig. 2b clearly show that NSC/CPE electrode displays the smallest electrical resistance which is indicative of the relatively higher surface area. The radius of semicircles is  $\sim 4000 \Omega$  for NSC/CPE and  $\sim 7000 \Omega$  for BCPE. It was attributed to accelerate electron-transfer rate of sepiolite clay as stated in the literature.<sup>19</sup>

SEM images of the BCPE and NSC/CPE surfaces exhibit their own characteristics. The BCPE sensor has nearly featureless, smooth surface (Fig. 2c), whereas the sur-

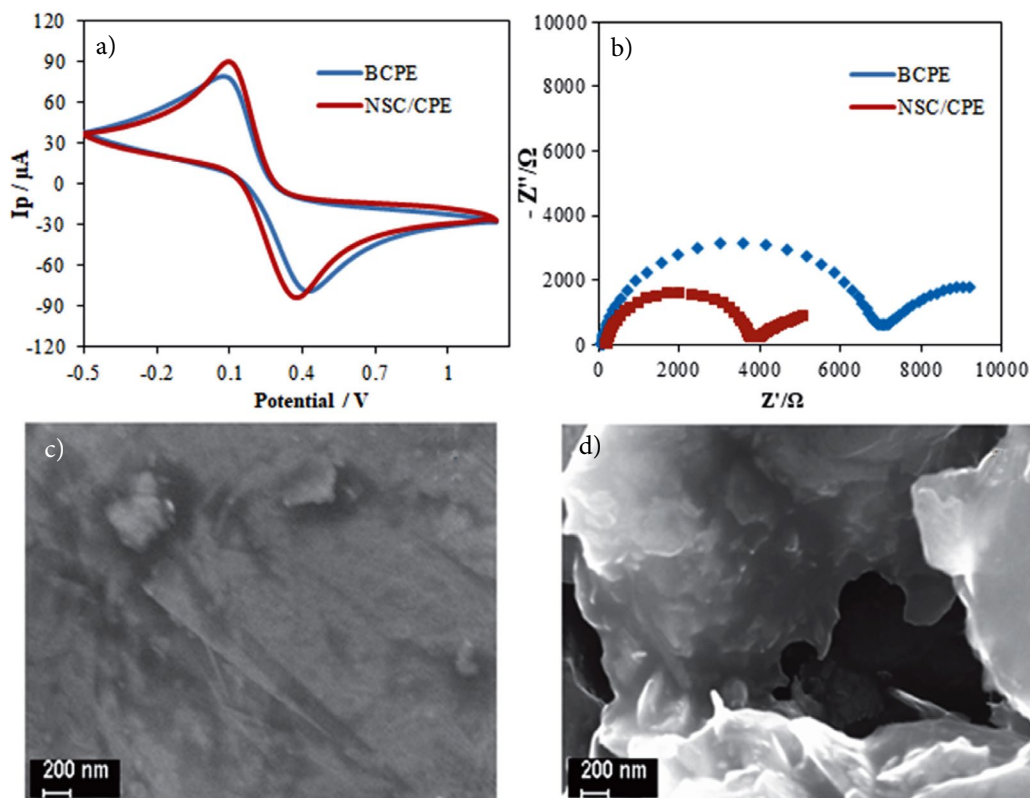


Fig. 2 a. Cyclic voltammograms of  $5.0 \text{ mmolL}^{-1} \text{ Fe(CN)}_6^{3-/4-}$  in  $0.1 \text{ molL}^{-1} \text{ KCl}$  solution on BCPE and NSC/CPE ( $v$ :  $0.1 \text{ Vs}^{-1}$ ). b. Nyquist diagrams of BCPE and NSC/CPE in the same conditions (amplitude:  $0.005 \text{ V}$ , frequency range of  $0.05$ – $100000 \text{ Hz}$ ). SEM images of (c) BCPE, (d) NSC/CPE electrodes.

face morphology of the NSC/CPE sensor exhibit typical holes indicating a larger specific surface area (Fig. 2d).

### 3.3. Electrochemical Behavior of HQ

Cyclic voltammetry is one of the most suitable methods to investigate the electrochemical behavior of the analyte in different modified electrodes. The comparison of current and potential responses of HQ on the two electrodes was studied by cyclic voltammetry in 0.04 M Britton-Robinson buffer (pH 2.0) solution at the scan rate value of  $0.10 \text{ V s}^{-1}$  (Fig. 3). As can be seen in Fig. 3, using nano sepiolite clay modified electrode, the well-defined oxidation peak for HQ was obtained. NSC/CPE electrode produces almost 1.4 times higher oxidation current signal compared to bare electrode. Also, the electrochemical oxidation peak of HQ was obtained at about 0.139 V negative potential compared to the bare electrode (Table 1). The potential differences between the anodic and cathodic peaks ( $\Delta E_p$ ) at NSC/CPE are lower than with the BCPE sensor. These results indicate that the nano-clay has electro-catalytic effect on redox signals of HQ.

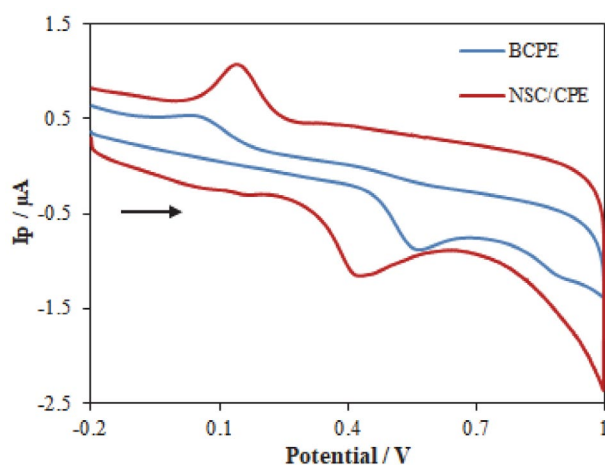


Fig. 3. Cyclic voltammograms of  $1.0 \times 10^{-4} \text{ mol L}^{-1}$  HQ at BCPE (blue line) and NSC/CPE (red line) in 0.04 M BR buffer, pH 2.0, scan rate:  $0.1 \text{ V s}^{-1}$ .

Table 1. Comparison of peak potential and peak current of  $1.0 \times 10^{-4} \text{ mol L}^{-1}$  HQ on BCPE and NSC/CPE by using CV method, pH: 2.0 BR buffer, scan rate:  $0.10 \text{ V s}^{-1}$ .

Electrode	$E_p^a / \text{V}$	$E_p^k / \text{V}$	$\Delta E_p / \text{V}$	$i_p^a / \mu\text{A}$	$i_p^k / \mu\text{A}$	$i_p^k / i_p^a$
BCPE	0.561	0.050	0.511	0.42	0.25	0.59
NSC/CPE	0.422	0.140	0.282	0.60	0.62	1.03

### 3.4. Influence of pH

The effect of pH on the peak current and peak potential responses of HQ ( $1.0 \times 10^{-4} \text{ mol L}^{-1}$ ) at NSC/CPE sensor was investigated by DPV method in  $0.04 \text{ mol L}^{-1}$  BR buffer solution (Fig. 4). The number of protons involved in

the electrochemical process were sought for using oxidation peak potentials of HQ in the pH range of 2.0–5.0 with 1.0 pH unit increments.

The relation between the anodic peak potential,  $E_p^a$  and pH was found to be as:  $E_p^a = -0.0509 \text{ pH} + 0.4989$  ( $R^2 = 0.9977$ ). The slope of  $-0.0509$  for oxidation peak is close to theoretical Nernstian value of  $-0.059$ .<sup>22</sup> This result shows that the transferred numbers of electrons and protons are equal in the oxidation mechanism of HQ.

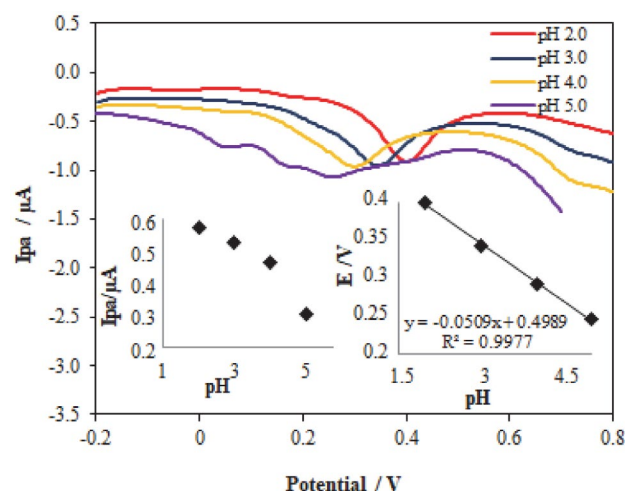


Fig. 4. CVs of  $1.0 \times 10^{-4} \text{ mol L}^{-1}$  HQ at different pH values at NSC modified electrode (Insets are the plots of pH vs  $E_p$  and pH vs  $i_p$ ).

### 3.5. Influence of Scan Rate

The relationship between the peak currents / potentials and the scan rate gives some important information about whether electrochemical process is adsorption or diffusion controlled. We investigated the effect of scan rate in between  $0.005 \text{ V s}^{-1}$  and  $0.5 \text{ V s}^{-1}$  on peak current of  $1.0 \times 10^{-4} \text{ mol L}^{-1}$  HQ at pH 2.0 by CV (Fig. 5). The linear rela-

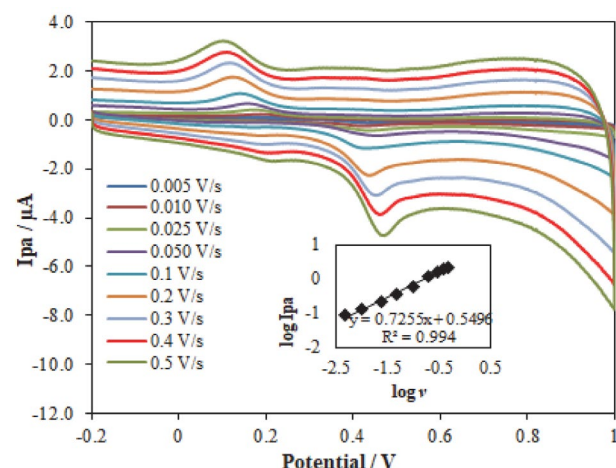


Fig. 5. CVs of  $1.0 \times 10^{-4} \text{ mol L}^{-1}$  HQ at different scan rates at NSC modified electrode in  $0.04 \text{ M BR}$  buffer at pH 2.0 (inset is the plot of  $\log i_p$  vs  $\log v$ ).

tionship between anodic oxidation peak current of HQ and scan rate was found according to the following equation:

$$\log i_p = 0.7255 \log v + 0.5496$$

The slope of the function correlation  $\log i_p$ - $\log v$  is 0.72 (between 0.5 and 1.0). This results showed adsorption-controlled process of electrochemical reaction.<sup>11</sup> Also, the oxidation peak potential values were changing with the increasing of scan rate (Fig. 5). This behavior indicates that the electrochemical oxidation of HQ on NSC/CPE sensor was of a quasi-reversible nature.<sup>26</sup>

Taking into account pH and scan rate studies, it can be said that the hydroquinone was oxidized by  $2e^-/2H^+$  to give quinone. Our obtained results are in a good accordance with previous literature data.<sup>27</sup>

### 3. 6. Electrochemical Detection of HQ on Modified Electrode

AdsDPV and AdsSWV methods were used for the determination of HQ on NSC/CPE surface at optimum deposition potential and time. In adsorption studies, it is important to optimize the deposition potential and time. Fig. 6a shows the changes in the range between  $-0.2$  and  $+1.0$  V of deposition potential versus peak current for  $3.0$

$\times 10^{-5} \text{ molL}^{-1}$  HQ in AdsDPV method. Deposition times were changed in the range  $0.0$ – $150$  s (Fig. 6b). Similarly, the same parameters were changed for AdsSWV method (Fig. 6c and d). The graphs obtained from AdsDPV method show that the deposition potential and deposition time are  $-0.2$  V and  $40$  s, respectively. The optimum deposition potential and time were chosen as  $0.7$  V and  $45$  s, respectively, by AdsSWV.

### 3. 7. Calibration Studies and Validation of Optimized Methods

The linear relationship between the HQ concentrations and peak currents was studied by using AdsDPV and AdsSWV methods under optimized method and optimum medium conditions. HQ concentration changed in the range between  $0.01$  and  $700 \mu\text{molL}^{-1}$ . Fig. 7a and b show a perfect linear relationship among  $i_p^a$  and  $C_{\text{HQ}}$ . The linear equations for AdsDPV and AdsSWV are given below:

$$i_p^a (\mu\text{A}) = 0.0346 C_{\text{HQ}} - 0.0448, R^2 = 0.9993 \text{ (Inset of Fig. 7a)}$$

$$i_p^a (\mu\text{A}) = 0.0459 C_{\text{HQ}} - 0.0222, R^2 = 0.9984 \text{ (Inset of Fig. 7b)}$$

As can be seen in Fig. 7a and b, linear calibration curves were obtained for hydroquinone in the range of  $0.01$  –  $700 \mu\text{molL}^{-1}$ .

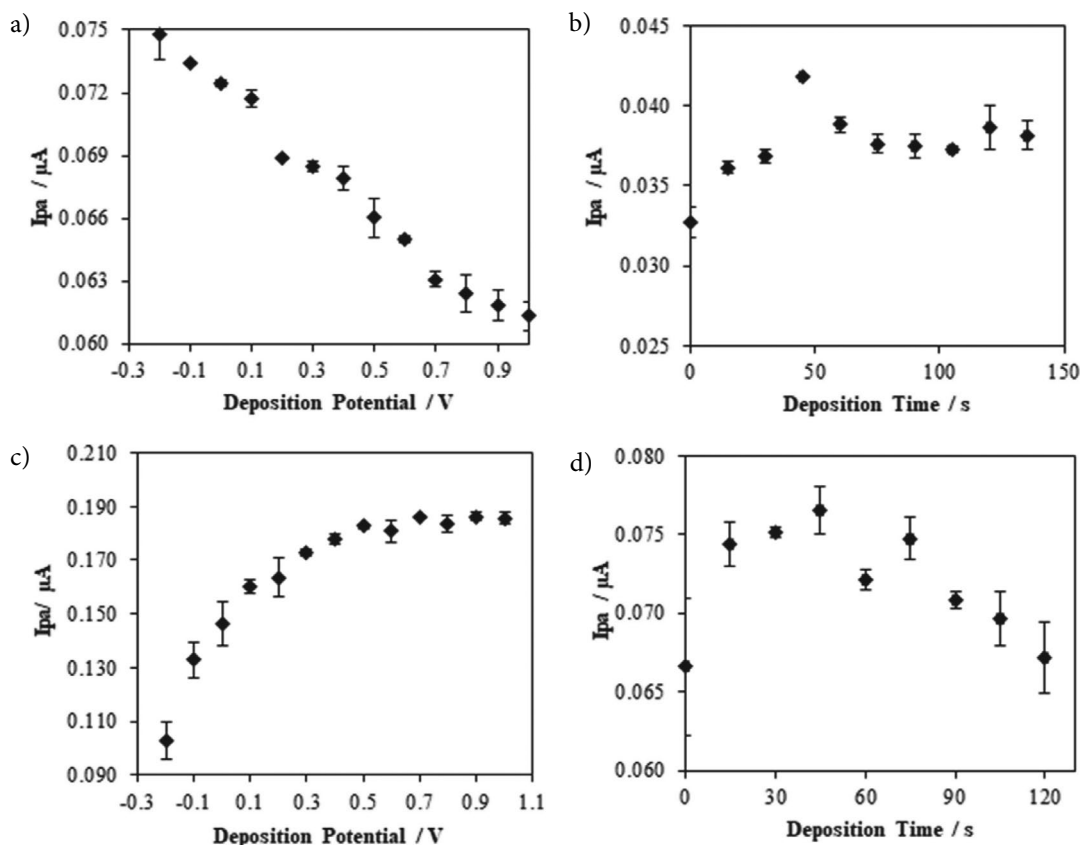
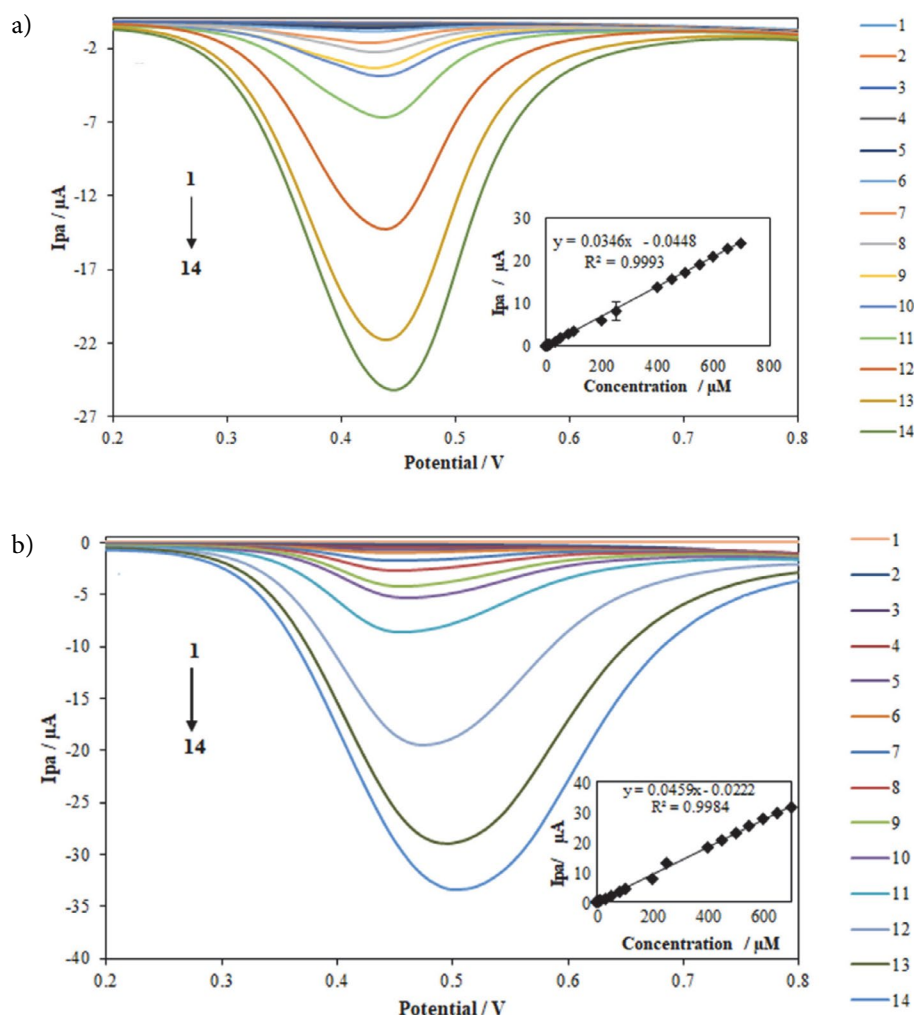


Fig. 6 a. The effect of the deposition potential on the peak current. b. the effect of deposition time on peak current using AdsDPV. c. and d. the graphs obtained using AdsSWV ( $3.0 \times 10^{-5} \text{ molL}^{-1}$  HQ in  $0.04 \text{ molL}^{-1}$  BR buffer pH 2.0).



**Fig. 7** a. AdsDPV voltammograms of the different concentrations of HQ on NSC modified electrode in pH 2.0 Britton Robinson buffer (1) blank, (2–14):  $1.0 \times 10^{-8}$ ,  $1.0 \times 10^{-7}$ ,  $1.0 \times 10^{-6}$ ,  $5.0 \times 10^{-6}$ ,  $1.0 \times 10^{-5}$ ,  $3.0 \times 10^{-5}$ ,  $5.0 \times 10^{-5}$ ,  $8.0 \times 10^{-5}$ ,  $1.0 \times 10^{-4}$ ,  $2.0 \times 10^{-4}$ ,  $4.0 \times 10^{-4}$ ,  $6.0 \times 10^{-4}$ ,  $7.0 \times 10^{-4}$  molL<sup>-1</sup>; b. AdsSW voltammograms of HQ at different concentrations. (1) blank, (2–14):  $1.0 \times 10^{-8}$ ,  $1.0 \times 10^{-7}$ ,  $1.0 \times 10^{-6}$ ,  $5.0 \times 10^{-6}$ ,  $1.0 \times 10^{-5}$ ,  $3.0 \times 10^{-5}$ ,  $5.0 \times 10^{-5}$ ,  $8.0 \times 10^{-5}$ ,  $1.0 \times 10^{-4}$ ,  $2.0 \times 10^{-4}$ ,  $4.0 \times 10^{-4}$ ,  $6.0 \times 10^{-4}$ ,  $7.0 \times 10^{-4}$  molL<sup>-1</sup>.

To calculate LOD and LOQ values, the following equations were used:

$$\text{LOD} = \frac{3s}{m}, \quad \text{LOQ} = \frac{10s}{m} \quad (1)$$

Here,  $s$  is the standard deviation for the HQ concentration studied ( $8.0 \times 10^{-8}$  molL<sup>-1</sup>), and  $m$  is the slope of the calibration graph. According to these equations, LOD and LOQ values were found as  $0.01031 \mu\text{molL}^{-1}$  and  $0.03438 \mu\text{molL}^{-1}$  for AdsDPV;  $0.01096 \mu\text{molL}^{-1}$  and  $0.03654 \mu\text{molL}^{-1}$  for AdsSWV, respectively (Table 2). According to our literature knowledge, these LOD and LOQ values are the lowest results found up to now.

A comparison table of other literature reports about HQ (Table 3) with our new voltammetric sensor (NSC/CPE) and validation parameters of the proposed new methods (Table 2) are given below:

It is important to investigate the precision of proposed methods and modified electrode by determining the repeatability, reproducibility, and stability of modified electrode. The percent relative standard deviation (RSD%) values of repeatability of peak current and potential values (intra-day and inter-day) were found by using AdsSWV and AdsDPV methods and it can be seen in Table 2 that the %RSD values are not higher than 5.0%. These results show a high repeatability. Furthermore, the reproducibility of NSC/CPE sensor was tested by using five electrodes prepared in the same day. The %RSD values of reproducibility were calculated to be 3.7% and 4.8% of the mean value for AdsSWV and AdsDPV, respectively.

To investigate the ageing of NSC/CPE sensor, the signals of HQ were recorded in different days. After ten days, the sensor signal was found to have retained 99.3% and 99.5% of its initial value. The electrode gave a response of 98.1% of the initial response after thirty days.

**Table 2.** The statistical results of regression analysis for the determination of HQ

Regression parameters	NSC/CPE	
	AdsSWV	AdsDPV
Potential, V	0.504	0.448
Linear working range, $\mu\text{M}$	0.01–700	0.01–700
Slope of calibration graph, $\mu\text{A}/\mu\text{M}$	0.045	0.034
Intercept of calibration graph, $\mu\text{A}$	0.022	0.044
Limit of detection (LOD), $\mu\text{M}$	0.01096	0.01031
Limit of quantification (LOQ), $\mu\text{M}$	0.03654	0.03438
Regression coefficient ( $R^2$ )	0.998	0.999
Repeatability of peak potential, RSD*% (intra-day)	0.9	2.6
Repeatability of peak potential, RSD*% (inter-day)	2.8	4.6
Repeatability of peak current, RSD*% (intra-day)	4.7	0.5
Repeatability of peak current, RSD*% (inter-day)	1.8	3.4
Reproducibility of peak current, RSD*%	3.7	4.8
Reproducibility of peak potential, RSD*%	1.7	0.5

\*RSD is the relative standard deviation of 5 replications.

**Table 3.** The comparison of the performances of various electrochemical sensors for HQ analysis.

Sensor	Technique	Linearity range $\mu\text{molL}^{-1}$	LOD $\mu\text{molL}^{-1}$	Application	Reference
NiO/NPs	SWV	0.1–500	0.05	tap and wastewater	18
eosin Y film GCE	DPV	1–130	0.14	local tap water	22
GR–TiO <sub>2</sub> /GCE	DPV	0.5–100	0.082	tap and lake water	23
single-walled carbon nanohorn/GCE	LSV	0.5–100	0.1	tap water	24
Au-G nanocomposite	DPV	1–100	0.2	tap water	25
NSC/CPE	AdsDPV	0.01–700	0.01031	Cream	This paper
	AdsSWV	0.01–700	0.01096		

(NiO: Nickel oxide nanoparticles; TiO<sub>2</sub>: Titanium dioxide nanoparticles; NPs: nanoparticle, GCE: glassy carbon electrode, GR: graphene, Au-G: gold-graphene)

After all experiments, the newly proposed sensor was kept at +4 °C.

### 3. 8. Interferences

In order to confirm the selectivity of the NSC/CP electrode, the influence of possible impurities was investigated for proposed methods with NSC/CP electrode. To this end, synthetical solutions of 0.1  $\mu\text{molL}^{-1}$  HQ were mixed with proper amounts of Na<sup>+</sup>, Co<sup>2+</sup>, K<sup>+</sup>, Mg<sup>2+</sup>, Cl<sup>-</sup>, NO<sub>3</sub><sup>-</sup>, Cu<sup>2+</sup>, Fe<sup>3+</sup>, with the intent of adjusting their concentrations to 10  $\mu\text{molL}^{-1}$  (100 times higher than HQ); Ni<sup>2+</sup> 5  $\mu\text{molL}^{-1}$  (50 times higher than HQ); uric acid (UA) and ascorbic acid (AA) 1  $\mu\text{molL}^{-1}$  (10 times higher than HQ).

Peak currents obtained for pure HQ and samples mixed with other contaminants were compared. NaCl, Mg(-NO<sub>3</sub>)<sub>2</sub>, KCl, Co(NO<sub>3</sub>)<sub>2</sub>, Ni(NO<sub>3</sub>)<sub>2</sub>, Fe(NO<sub>3</sub>)<sub>3</sub>, Cu(NO<sub>3</sub>)<sub>2</sub>, AA and UA caused less than 5% interference effect for both AdsSWV and AdsDPV methods. The results show that both methods with NSC/CP electrode exhibited good selectivity. Interference effect was at an acceptable level from analytical point of view.

### 3. 9. Real Sample Analysis and Recovery

Using the developed electrode, the cosmetic sample (Expigment cream) was analyzed for hydroquinone content. The accuracy of developed methods was tested by re-

**Table 4.** Main recovery results and the relative standard deviations for the determination of HQ in pharmaceutical cream

Method	Added ( $\mu\text{g}$ )	Found ( $\mu\text{g}$ )	Average	Recovery %	RSD %
AdsSWV	0.54	0.56; 0.52; 0.51; 0.55; 0.50	0.53 ± 0.03	98.6	5.58
	3.36	3.52; 3.54; 3.46; 3.50; 3.57	3.52 ± 0.04	104.6	1.21
	12	10.13; 9.86; 9.94; 10.12; 10.27	10.08 ± 0.17	100.8	1.71
AdsDPV	0.54	0.55; 0.55; 0.57; 0.56; 0.57	0.56 ± 0.01	104.6	1.72
	3.36	3.64; 3.65; 3.62; 3.64; 3.66	3.64 ± 0.01	108.6	0.47
	12	12.15; 11.83; 11.93; 12.24; 12.33	12.09 ± 0.21	105.5	6.56



covery studies. Recovery studies were performed by analyzing the cosmetic sample enriched with known amounts of HQ using proposed methods (Table 4). The recovery data indicate that the proposed methods can be used safely in cosmetic samples with presented excipients. According to these results, the proposed methods have definite precision and accuracy.

### 3. Conclusion

A simple electrochemical sensor made up of nano-clay modified carbon paste electrode was developed for analysis of hydroquinone in cosmetic sample. The sensor has the advantages of high sensitivity, electrocatalytic effect, ease of preparation, good stability, practical surface renewal, high precision, low cost, large linear range, and low limit of detection. The electrode proved to be applicable to HQ assay in real sample. The developed methods and NSC modified electrode were compared to previously reported results.

### 4. References

1. Y. Zhang, J. Huang, G. Jiang, Z. Song, Z. Xie, *Sensors & Transducers*, **2014**, 174 (7), 261–267. DOI:10.1111/ics.12228
2. J. S. Jeon, B. H. Kim, S. H. Lee, H. J. Kwon, H. J. Bae, S. K. Kim, J. A. Park, J. H. Shim, A. M. Abd El-Aty, H. C. Shin, *Int. J. Cosmet. Sci.*, **2015**, 37, 567–573.
3. M. F. Pistonesi, M. S. Di Nezio, M. E. Centurion, M. E. Palomeque, A. G. Lista, B. S. Fernandez Band, *Talanta*, **2006**, 69, 1265–1268. DOI:10.1016/j.talanta.2005.12.050
4. Y. Chao, X. Zhang, L. Liu, L. Tian, M. Pei, W. Cao, *Microchim Acta*, **2015**, 182, 943. DOI:10.1007/s00604-014-1415-2
5. R. Khoshneviszadeh, B. S. Fazly Bazzaz, M. R. Housaindokht, A. Ebrahim-Habibi, O. Rajabi, *Iran. J. Pharm. Res.*, **2015**, 14 (2), 473–478.
6. M. R. Elghobashy, L. I. Bebawy, R. F. Shokryb, S. S. Abbas, *Spectrochim. Acta Part A: Molecular and Biomolecular Spectroscopy*, **2016**, 157, 116–123. DOI:10.1016/j.saa.2015.12.019
7. K. Jurica, I. B. Karačonji, S. Šegan, D. M. Opsenica, D. Kremer, *Arh Hig Rada Toksikol*, **2015**, 66, 197–202. DOI:10.1515/aiht-2015-66-2696
8. C. Desiderio, L. Ossicini, S. Fanali, *J. Chromatogr. A*, **2000**, 887, 489–496. DOI:10.1016/S0021-9673(99)01197-8
9. A. Kumara, B.E. Kumara Swamy, *J. Electroanal. Chem.* **2017**, 799, 505. DOI:10.1016/j.jelechem.2017.06.026
10. P. S. Ganesh, B. Eshwaraswamy, K. Swamy, *Anal. Bioanal. Electrochem.*, **2016**, 8, 615–628.
11. P. S. Ganesh, B.E. Kumara Swamy, *J. Electroanal. Chem.*, **2015**, 756, 193–200. DOI:10.1016/j.jelechem.2015.08.027
12. L. A. Alshahrani, X. Li, H. Luo, L. Yang, M. Wang, S. Yan, P. Liu, Y. Yang, Q. Li, *Sensors*, **2014**, 14(12), 22274–22284. DOI:10.3390/s14122274
13. L. Zheng, L. Xiong, Y. Li, J. Xu, X. Kang, Z. Zou, S. Yang, J. Xia, *Sens. Actuators B*, **2013**, 177, 344. DOI:10.1016/j.snb.2012.11.006
14. Y. Zhang, J. B. Zheng, *Electrochim. Acta*, **2007**, 52, 7210–7216. DOI:10.1016/j.electacta.2007.05.039
15. J. Tashkhouriana, M. Daneshi, F. Nami-Anaa, M. Behbahani, A. Bagheri, *J. Hazard. Mater.*, **2016**, 318, 117–124. DOI:10.1016/j.jhazmat.2016.06.049
16. H. Filik, A. A. Avan, S. Aydar, *Food Anal. Methods*, **2016**, 9, 2251–2260. DOI:10.1007/s12161-016-0420-y
17. J. Huang, Z. Xie, Z. Xie, S. Luo, L. Xie, L. Huang, Q. Fan, *Anal. Chim. Acta*, **2016**, 913, 121–127. DOI:10.1016/j.aca.2016.01.050
18. H. Soltani, A. Pardakhty, S. Ahmadzadeh, *J. Mol. Liq.*, **2016**, 219, 63–67. DOI:10.1016/j.molliq.2016.03.014
19. M. Pekin, D. E. Bayraktepe, Z. Yazan, *Ionics*, **2017**, 23, 3487–3495. DOI:10.1007/s11581-017-2132-8
20. D. E. Bayraktepe, T. Yanardağ, Z. Yazan, A. Aksüt, *Rev. Roum. Chim.*, **2015**, 60(4), 287–295.
21. H. Beitollah, M. Goodarzi, *J. Mol. Liq.*, **2012**, 173, 137–143. DOI:10.1016/j.molliq.2012.06.026
22. J. He, *Anal. Methods*, **2014**, 6, 6494–6503. DOI:10.1039/C4AY00575A
23. Y. Zhang, *Sens. Actuators B*, **2014**, 204, 102–108. DOI:10.1016/j.snb.2014.07.078
24. S. Zhu, W. Gao, L. Zhang, J. Zhao, G. Xu, *Sens. Actuators B*, **2014**, 198, 388–394. DOI:10.1016/j.snb.2014.03.082
25. X. Ma, Z. Liu, C. Qiu, T. Chen, H. Ma, *Microchim. Acta*, **2013**, 180, 461–468. DOI:10.1007/s00604-013-0949-z
26. A. J. Bard and L.R. Faulkner, *Electrochemical Methods*, Wiley, New York, **1980**.
27. Z. Guohua, L. Mingfang, H. Zhonghua, L. Hongxu, C. Tongcheng, *J. Mol. Catal. A: Chem.*, **2006**, 255, 86–91. DOI:10.1016/j.molcata.2006.03.039

## Povzetek

V tej raziskavi smo razvili preprost in občutljiv elektrokemijski nanosenzor za analizo hidrokinona, osnovan na s sepiolitno glino modificiranem senzorju z ogljikovo pasto, za uporabo pri diferencialni pulzni adsorpcijski inverzni voltametriji in pri adsorpcijski inverzni voltametriji s pravokotnimi pulzi. Površinsko morfologijo senzorjev smo okarakterizirali z vrstično elektronsko mikroskopijo, elektrokemijsko impedančno spektroskopijo in ciklično voltametrijo. Elektrokemijske redoks lastnosti hidrokinona smo raziskali s ciklično voltametrijo. Oksidacijski maksimalni tok za hidrokinon se pri diferencialni pulzni adsorpcijski inverzni voltametriji in pri adsorpcijski inverzni voltametriji s pravokotnimi pulzi linearno spreminja v koncentracijskem območju  $0,01\text{--}700\ \mu\text{molL}^{-1}$  za prvo in  $0,01\text{--}700\ \mu\text{molL}^{-1}$  za drugo metodo. Določili smo odlične meje zaznave (LOD) in meje določitve (LOQ), in sicer  $0,01096\ \mu\text{molL}^{-1}$  ter  $0,03654\ \mu\text{molL}^{-1}$  za diferencialno pulzno adsorpcijsko inverzno voltametrijo in  $0,01031\ \mu\text{molL}^{-1}$  ter  $0,03438\ \mu\text{molL}^{-1}$  za adsorpcijsko inverzno voltametrijo s pravokotnimi pulzi. Dodatno smo razviti senzor uporabili za določitev hidrokinona v kozmetični kremi z zadovoljivimi rezultati.

Scientific paper

# Alumazene Reactivity with Quinolinols – Addition and Substitution Reactions on the $\text{Al}_3\text{N}_3$ Ring

Iva Kollhammerova,<sup>1</sup> Michal Babiak,<sup>2</sup> Marek Necas,<sup>1,2</sup> Petr Taborsky,<sup>1</sup>  
Josef Kucera<sup>1</sup> and Jiri Pinkas<sup>1,2,\*</sup>

<sup>1</sup> Masaryk University, Faculty of Science, Department of Chemistry, Kotlarska 2, CZ-61137 Brno, Czech Republic.

<sup>2</sup> Masaryk University, Central European Institute of Technology (CEITEC MU), Kamenice 5, CZ-62500 Brno, Czech Republic.

\* Corresponding author: E-mail: jpinkas@chemi.muni.cz

Received: 22-07-2018

## Abstract

Molecular structures of two compounds obtained in reactions of alumazene  $[\text{DippNAlMe}]_3$  (**1**, Dipp = 2,6-*i*-Pr<sub>2</sub>C<sub>6</sub>H<sub>3</sub>) with substituted quinolinols have been elucidated by the single-crystal X-ray diffraction analysis. Quinolin-8-ol (Hq) provides a dinuclear complex  $[(\text{DippNH})_2\text{Al}_2\text{Me}_2(\text{q})_2]$  (**2**) with a central  $\text{Al}_2\text{O}_2$  ring and five-coordinate Al atoms. The compound **2** · THF crystallizes in the orthorhombic *Pbca* space group. The molecular structure of a mononuclear complex  $[(\text{DippNH})\text{Al}(\text{Meq})_2]$  (**3**) obtained in the reaction of **1** with 2-methylquinolin-8-ol (HMeq) possesses a five-coordinate Al center. The structure was solved in a triclinic cell *P*–1. The dinuclear complex **2** can be considered as a model product of alcohol addition on the formal Al–N double bond, while the mononuclear complex **3** represents subsequent reaction of remaining Al–Me moiety with proton. Both complexes **2** and **3** are highly luminescent showing emission around 500 nm in solid state.

**Keywords:** Alumazene; crystal structure; quinolin-8-ol; 2-methylquinolin-8-ol; luminescence

## 1. Introduction

So far only two examples of synthetic procedures leading to cyclic trimeric iminoalane (alumazene-type) molecules were published. The first one is a two-step synthesis from trimethylaluminium and diisopropylaniline in toluene. Dimeric aminoalane formed in the initial step is transformed in the second step by heating to trimeric iminoalane  $[\text{DippNAlMe}]_3$  (**1**, Dipp = 2,6-*i*-Pr<sub>2</sub>C<sub>6</sub>H<sub>3</sub>).<sup>1–3</sup> The second route to an alumazene derivative is a one-pot reaction of  $(\text{Me}_3\text{Si})_3\text{Al} \cdot \text{OEt}_2$  with 2,6-diisopropylaniline. An adduct  $[(\text{Me}_3\text{Si})_3\text{Al} \cdot \text{N}(\text{H})_2(\text{Dipp})]$  is formed by coordination of the nitrogen lone pair to the Al center. Refluxing in toluene leads to the formation of  $[\text{DippNAlSiMe}_3]_3$  (**4**).<sup>4</sup> Alumazene in comparison with its isoelectronic analogue benzene is not aromatic, its  $\pi$  electrons are not delocalized, and the Al–N bonds are highly polar.<sup>5,6</sup> Chemical reactivity of alumazene reflects this bonding situation. The Al atoms are Lewis acidic and are capable of accepting lone pairs of Lewis O- and N-bases. Several types of mono-, bis-, and trisadducts were reported in the literature.<sup>7–11</sup> Stepwise fluorination of alumazene **1** by  $\text{Me}_3\text{SnF}$  or by  $\text{BF}_3$  represents

metathesis reactivity leading to the substitution of the methyl groups on aluminium.<sup>12</sup> Dealkylsilylation reactions of **1** with trimethylsilyl esters of sulfonic, phosphoric, and phosphonic acids are another type of alumazene reactivity.<sup>13,14</sup> These reactions are driven by the formation of strong Al–O–P/S bonds and elimination of small molecules, such as  $\text{SiMe}_4$ . Although all bonds in the planar  $\text{Al}_3\text{N}_3$  core of **1** are of the same length, the ring can undergo reactions that can be classified as an addition on a formal double bond. This type of transformations can be exemplified by reactions of **1** with silanetriols and isoelectronic triaminosilanes. Adamantane-like structures are formed in these reactions by triple proton transfer to the alumazene nitrogen atoms and connecting the three Al atoms to oxygens or nitrogens of the particular reagent. In the resulting molecules, alumazene ring lost its planarity and both Al and N atoms are four-coordinate.<sup>15</sup> Cyclopentadienyl Ti(IV) and Zr(IV) trifluorides react with **1** under fluorine-nitrogen exchange creating adamantane-like cage molecules.<sup>16,17</sup>

Quinolin-8-olate complexes of aluminium are widely investigated because they are suitable materials for use in organic light-emitting diodes (OLED). Metal complexes

bearing quinolin-8-olato derivatives are applied as the emissive and electron transporting materials in electroluminescent devices.<sup>18–20</sup> The most frequently used material is Al(quinolin-8-olate)<sub>3</sub> (Alq<sub>3</sub>)<sup>18</sup> which has been carefully studied and its physico-chemical properties, such as refractive index<sup>21,22</sup> and absorption coefficient<sup>23,24</sup> have been measured.

Besides the tris(quinolin-8-olato) complexes, other types of ligand arrangement are sought as they provide a way to control emission wavelength. Bis(2,4-dimethyl-quinolin-8-olato)(triphenylsilanolato)aluminum was synthesized from aluminium iso-propoxide and two ligands, 2,4-dimethyl-quinolin-8-ol and triphenylsilanol. This complex with five-coordinate Al showed no glass temperature and no phase transition before the melting point and the thermally stable thin films could be easily formed.<sup>25</sup> The photoluminescence (PL) spectrum of the complex shows the largest hypsochromic shift among the blue-emitting [q<sub>2</sub>AlOR]-type complexes. Some complexes of Al with polymerizable quinolin-8-olato ligands were used in a copolymerization reactions leading to products with good PL properties.<sup>26</sup> Two new complexes were prepared by the reactions between AlCl<sub>3</sub>·6H<sub>2</sub>O and 5,7-dichloro- or 5,7-dibromo-quinolin-8-ol providing homoleptic Al(ligand)<sub>3</sub> complexes.<sup>27</sup> Authors studied their electroluminescent properties. A series of 3-, 4-, and 5-methylquinolin-8-olate complexes of Al and Ga was prepared and the photo- and electroluminescence properties were examined.<sup>28</sup> Although methylation improved PL quantum efficiency, it also reduced intermolecular interactions and decreased charge transport through the film. Complexes of aluminium with 4-(2-arylvinyl)-quinolin-8-olates prepared by anhydrous Heck coupling with judicious choice of substituents display enhanced PL intensity and quantum yield.<sup>29</sup>

Quinolin-8-olate complexes of Al are also used as catalysts in the ring-opening polymerization (ROP). Mononuclear and dinuclear complexes with bulky 2-(arylimino)quinolin-8-ols were prepared. The dimeric complexes were obtained by the stoichiometric reaction of AlMe<sub>3</sub> with the corresponding ligands in *n*-heptane. These compounds are insoluble in *n*-heptane and only slightly soluble in toluene, THF, CH<sub>2</sub>Cl<sub>2</sub>, and CHCl<sub>3</sub>. The stoichiometric reactions of appropriate ligands with AlMe<sub>3</sub> in toluene produce molecular compounds Me<sub>2</sub>AlL and by-products Me<sub>2</sub>AlL·AlMe<sub>3</sub>. The mononuclear complexes exhibit high activity towards the ROP reaction of  $\epsilon$ -caprolactone in the presence of benzyl alcohol, while the dinuclear complexes exhibit no activity in this polymerization reaction.<sup>30,31</sup> The complexes of aluminium with quinoline-based N,N,O-tridentate and N,N,N-chelate ligands were used for ring-opening polymerization of  $\epsilon$ -caprolactone. Complexes were prepared by simple mixing of ligand and AlMe<sub>3</sub> at room temperature in toluene.<sup>32,33</sup>

The aim of this research was to investigate the reactivity of alumazene **1** towards quinolinols as chelating li-

gands bearing an active proton and a nitrogen donor atom. The two ligands used in this study differ in their steric hindrance and we expected different products from their reactions. We present here the synthesis and characterization by single-crystal X-ray diffraction analysis of two complexes **2** and **3** displaying a different nuclearity and metal-to-ligand ratio.

## 2. Experimental

### 2.1. General Procedures and Characterization

All manipulations were performed under a dry nitrogen atmosphere by Schlenk techniques or in MBraun Unilab dry box maintained under 1 ppm of both O<sub>2</sub> and H<sub>2</sub>O. Solvents were stored and handled under nitrogen atmosphere in a glovebox or in Schlenk flasks. Melting points were measured on a Buchi B540 apparatus in glass capillaries sealed in glovebox. The IR spectra (4000–400 cm<sup>-1</sup>) were recorded on a Bruker Tensor T27 spectrometer. Samples were prepared as KBr pellets. EI-MS measurements were performed on a TSQ Quantum XLS mass spectrometer. Solid samples of **2** and **3** were introduced into the spectrometer via direct insertion probe (DIP) in open quartz capillaries and heated from r. t. to 450 °C. The source temperature was set to 200 °C and ionization energy to 22 eV. Aluminium contents were determined on an ICP optical emission spectrometer iCAP 6500 Duo (Thermo, UK) equipped with a solid-state generator with a frequency of 27.12 MHz and a maximum power input 1350 W. The measurements of Al were performed at 308.2, 394.4 and 396.1 nm with RF power of 1150 W; analysis pump rate 1 cm<sup>3</sup> min<sup>-1</sup>; nebulizer gas flow 0.65 dm<sup>3</sup> min<sup>-1</sup>; coolant gas flow 12 dm<sup>3</sup> min<sup>-1</sup>; auxiliary gas flow 0.6 dm<sup>3</sup> min<sup>-1</sup>; flush time 30 s; flush pump rate 2 cm<sup>3</sup> min<sup>-1</sup>; pump stabilization time 5 s; integration time (high WL range) 5 s; the number of repeats 3; plasma view radial.

### 2.2. Reagents

Quinolin-8-ol (Hq, Aldrich, 99 %) and 2-methylquinolin-8-ol (HMeq, Aldrich, 98 %) were dried under dynamic vacuum for 2 d prior to use. Solvents were dried over and distilled from Na/benzophenone under nitrogen. Solvents were degassed prior to use. Alumazene **1** was prepared by a modified procedure from AlMe<sub>3</sub> and 2,6-diisopropylaniline.<sup>3</sup>

### 2.3. Synthesis of **2**

Quinolin-8-ol (0.023 g, 0.16 mmol) was added to the solution of **1** (0.1045 g, 0.1603 mmol) in dry deoxygenated heptane (1 mL). THF (5 mL) was added and the reaction mixture was stirred for 2 h. The reacting mixture was concentrated to ¼ of its starting volume and stored at –25 °C.

After six months, colorless crystals were obtained. The crystals for the X-ray diffraction analysis were used directly from the mother liquor. Yield: Crystals 0.013 g, 5.5 %, polycrystalline powder 0.140 g, 73 %. Melting point: 247 °C.

EI DIP MS (22 eV):  $m/z$  (int. %) 651.84 (10) [M – *i*-Pr – 2CH<sub>3</sub>]<sup>+</sup>; 460.74 (40) [M – Dipp – *i*-Pr – 4CH<sub>3</sub>]<sup>+</sup>; 333.73 (30) [M – Dipp – *i*-Pr – 4CH<sub>3</sub> – C<sub>9</sub>H<sub>6</sub>N]<sup>+</sup>; 314.90 (90) [M – Dipp – *i*-Pr – 4CH<sub>3</sub> – C<sub>9</sub>H<sub>6</sub>NO]<sup>+</sup>; 282.49 (70); 184.03 (100); 144.95 (100) [C<sub>9</sub>H<sub>7</sub>NO]<sup>+</sup>.

Elemental analysis: Al% Calcd. for C<sub>48</sub>H<sub>62</sub>N<sub>4</sub>O<sub>3</sub>Al<sub>2</sub> 6.77. Exp. 6.44 ± 0.03.

IR (cm<sup>-1</sup>): ν 3046 w, 2961 w, 2928 w, 2865 w, 1065 m, 1058 m, 1499 vs, 1470 s, 1385 vs, 1330 m, 1283 w, 1230 w, 1115 m, 1033 w, 825 m, 805 m, 789 m, 749 s, 649 m, 549 m, 457 w, 419 m.

## 2. 4. Synthesis of 3

2-methylquinolin-8-ol (0.024 g, 0.15 mmol) was added to the solution of **1** (0.119 g, 0.183 mmol) in dry deoxygenated THF (5 mL). The reaction mixture was concentrated to ¼ of its starting volume and stored at –25 °C. The colorless crystals for the X-ray diffraction analysis were used directly from the mother liquor. Yield: Crystals 0.028 g, 10 %, polycrystalline powder 0.194 g, 68 %. Melting point: 214 °C.

EI DIP MS (22 eV):  $m/z$  (int. %) 343.01 (77) [M – HNDipp]<sup>+</sup>; 176.92 (55) [HNDipp]<sup>+</sup>; 161.86 (100) [Dipp]<sup>+</sup>.

Elemental analysis: Al% Calcd. for C<sub>32</sub>H<sub>34</sub>N<sub>3</sub>O<sub>2</sub>Al 5.19. Exp. 5.15 ± 0.05.

IR (cm<sup>-1</sup>): ν 3053 m, 2962 s, 2926 m, 2867 w, 1613 m, 1578 vs, 1508 vs, 1465 vs, 1432 vs, 1432 vs, 1394 m, 1341 m, 1332 w, 1274 vs, 1262 s, 1243 w, 1171 w, 1114 vs, 1018 s, 869 w, 829 s, 795 s, 772 vs, 741 s, 688 m, 675 s, 530 m, 435 w.

## 2. 5. X-Ray Structure Determination

Diffraction data were collected using a Rigaku X-ray diffraction system, equipped with a MicroMax007HF double wavelength rotating anode X-ray source ( $\lambda = 0.71075$  Å, Mo radiation), VariMax DW optics, a partial  $\chi$  axis geometry goniometer, a Saturn 724+ HG CCD detector and a Cryostream cooling device. *CrystalClear*<sup>34</sup> software was used for data collection.

Processing of diffraction images was carried out using *CrysAlisPro*.<sup>35</sup> *SHELXT* and *SHELXL* programs<sup>36</sup> were used to solve and refine models (full matrix least-squares refinement on  $F^2$ ). All non-hydrogen atoms were refined anisotropically. ADPs of nitrogen bonded hydrogen atoms were set to 1.2  $U_{eq}$  of carrier atoms, and respective N–H distances were restrained to 0.88 Å. All other hydrogen atoms were placed to the calculated positions and refined as riding (CH<sub>3</sub> hydrogens also rotating), with their  $U_{iso}$  val-

Table 1. Crystal data and structure refinement summary

Compound	2 · THF	3
Empirical formula	C <sub>48</sub> H <sub>62</sub> Al <sub>2</sub> N <sub>4</sub> O <sub>3</sub>	C <sub>32</sub> H <sub>34</sub> AlN <sub>3</sub> O <sub>2</sub>
Formula weight	796.97	519.60
Temperature (K)	120(2)	120(2)
Crystal system	orthorhombic	triclinic
Space group	<i>Pbca</i>	<i>P</i> –1
<i>a</i> (Å)	18.4340(2)	9.25960(10)
<i>b</i> (Å)	19.5025(2)	12.05340(10)
<i>c</i> (Å)	24.8159(3)	13.09420(10)
$\alpha$ (°)	90	97.9350(10)
$\beta$ (°)	90	97.0130(10)
$\gamma$ (°)	90	109.2860(10)
Volume (Å <sup>3</sup> )	8921.54(17)	1344.06(2)
<i>Z</i>	8	2
$\rho_{calc}$ (g/cm <sup>3</sup> )	1.187	1.284
$\mu$ (mm <sup>-1</sup> )	0.110	0.110
<i>F</i> (000)	3424.0	552.0
Reflections collected	52737	16096
Independent reflections ( $R_{int}$ , $R_{sigma}$ )	8470	5048
	(0.0201, 0.0102)	(0.0136, 0.0123)
Data / restraints / parameters	8470 / 244 / 576	5048 / 1 / 352
Goodness-of-fit on $F^2$	1.017	1.037
Final <i>R</i> indices	$R_1 = 0.0442$	$R_1 = 0.0358$
[ $I \geq 2\sigma(I)$ ]	$wR_2 = 0.1171$	$wR_2 = 0.0940$
Final <i>R</i> indices	$R_1 = 0.0477$	$R_1 = 0.0385$
[all data]	$wR_2 = 0.1205$	$wR_2 = 0.0962$
Largest diff. peak / hole (e Å <sup>-3</sup> )	0.47/–0.31	0.32/–0.27

ues set to 1.2  $U_{eq}$  (1.5  $U_{eq}$  for methyl hydrogens) of respective carrier atoms. Positionally disordered fragments were treated by geometric restraints, ADP similarity restraints and rigid bond restraints. In these cases, the sum of site occupancy factors was fixed to be equal to 100 %. Relevant crystallographic data are shown in Table 1.

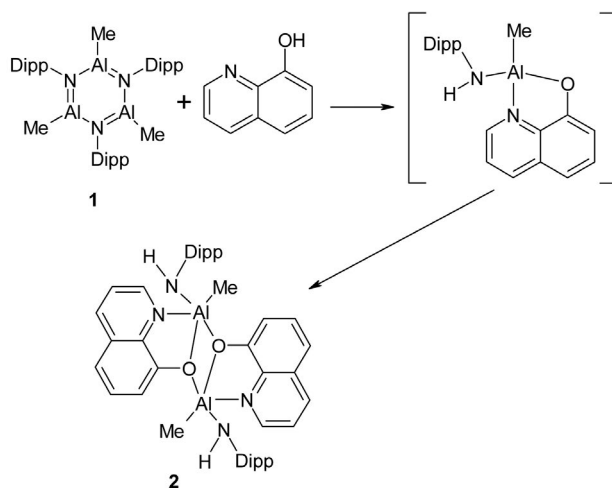
## 2. 6. Luminescence Measurements

Samples of **2** and **3** were prepared as powders in quartz capillaries (4 mm diam.) and as dilute solutions (0.719 mol l<sup>-1</sup> for **2** and 0.718 mol l<sup>-1</sup> for **3**) in CH<sub>2</sub>Cl<sub>2</sub>. Emission and excitation spectra were measured by steady-state fluorescence spectroscopy on the Aminco Bowman Series 2 spectrofluorometer equipped with 150 W Xe lamp. Excitation monochromator was set at 370 nm for both samples. Emission monochromator was set at 502 nm for sample **2** and 497 nm for sample **3**. Quantum yields were estimated using secondary method with quinine bisulphate in H<sub>2</sub>SO<sub>4</sub> as a luminescence standard. Luminescence lifetimes were measured by time correlated single photon counting instrument SPC130EM (Becker and Hickl GmbH) equipped with 408 nm laser diode (picosecond resolution, repeating frequency 150 MHz). All luminescence measurements were recorded at 25 °C.

## 3. Results and Discussion

### 3. 1. Synthesis

The compound **2** was prepared as yellow air- and moisture-sensitive crystals, by the reaction of alumazene **1** with quinolin-8-ol in the 1:1 molar ratio (Scheme 1). In the first step quinoline adds at a formal Al-N double bond in **1**. Trimeric iminoalane ring structure is destabilized and intermediate substituted aminoalane is probably formed. This intermediate dimerizes and aluminium atoms are connected by oxygen bridges to form the central



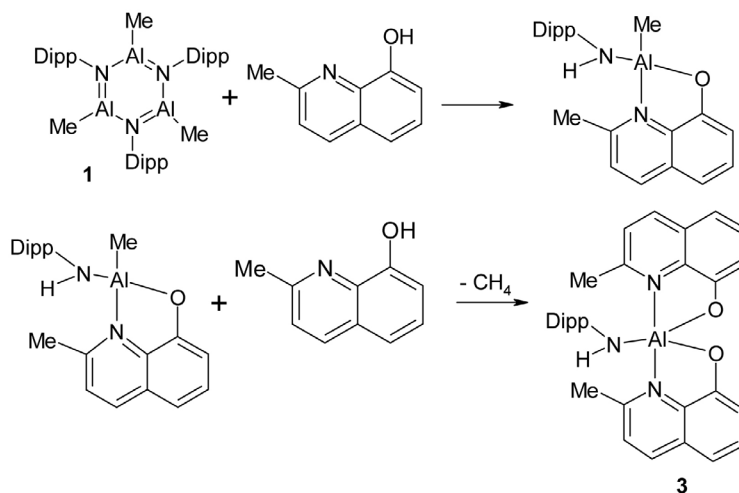
Scheme 1

Al<sub>2</sub>O<sub>2</sub> ring. Aluminium coordination number increases to five by bonding to quinoline nitrogen.

The compound **3** was prepared as air- and moisture-sensitive colorless crystals, by the reaction of **1** with 2-methylquinolin-8-ol in the 1:1 molar ratio (Scheme 2). The first step of the reaction proceeds as in the previous case and 2-methylquinolin-8-ol adds at the formal Al-N double bond in alumazene **1**. However, in the second step the intermediate aminoalane reacts with the second molecule of 2-methylquinolin-8-ol by the proton transfer to the methyl group and CH<sub>4</sub> is eliminated. The resulting molecule is monomeric and the coordination number of aluminium atom is increased to five by coordination of two quinolinol nitrogens.

### 3. 2. Crystal Structures

Single crystals of **2** suitable for the X-ray diffraction analysis were grown from the mother liquor. The molecular structure is displayed in Figure 1, selected interatomic



Scheme 2

distances and angles are listed in Table 2. Molecules of **2** crystallize in the orthorhombic space group *Pbca*. Bonds between aluminium and oxygen atom are longer in comparison with oxoaminoalumosilicates [NH(Dipp)MeAl]<sub>3</sub>O<sub>3</sub>SiR<sub>1</sub> with adamantane-like structure, where the Al–O bond distance is 1.74–1.75 Å. Also the bond between aluminum and nitrogen is in comparison with **1** (1.78 Å) elongated to 1.84 Å. The Al–N bond to quinolinol is 2.09 Å long and it is comparable with other donor-acceptor bonds in alumazene–nitrile adducts and in alumazene–pyridine adducts. The Al–C bond as well N–C bond are similar to starting alumazene **1**.<sup>8,15,37</sup> The aluminium atom is five-coordinate and its coordination environment lies between trigonal bipyramidal and tetragonal pyramidal shape ( $\tau = 0.53$ ). All nitrogen atoms have coordination number three, as is the case for bridging oxygen atoms. One molecule of solvent tetrahydrofuran (THF) cocrys-

tallizes within the structure. Packing in the unit cell of **2** is shown in Figure 2.

Suitable single crystals of **3** for the X-ray diffraction analysis were grown from the mother liquor. The molecular structure is displayed in Figure 3, selected interatomic distances and angles are listed in Table 3. Molecules crystallize in the triclinic space group *P*-1. The Al–O bonds are shorter than in **2**, but longer than Al–O bonds in oxoaminoalumosilicates [NH(Dipp)MeAl]<sub>3</sub>O<sub>3</sub>SiR<sub>1</sub> (1.74–1.75 Å). The Al1–N41 bond is comparable to **2** but it is longer in comparison with **1** (1.78 Å). The other Al–N bonds are 2.08 Å long and they are comparable with Al–N in other alumazene–nitrile and alumazene–pyridine adducts. The coordination number of aluminium is five and its environment is close to trigonal bipyramidal ( $\tau = 0.76$ ).<sup>8,15,37</sup> Packing in the unit cell of **3** is shown in Figure 4.

Table 2. Selected interatomic distances and angles of **2** · THF

Distances (Å)					
Al1–N3	1.8368(13)	O1–C10	1.3512(17)	Al2–N2	2.1195(13)
Al1–O1	1.8921(11)	N3–C21	1.4112(18)	Al2–C2	1.9647(18)
Al1–O2	1.9516(11)	Al2–N4	1.8283(13)	O2–C19	1.3572(18)
Al1–C1	1.9653(17)	Al2–O1	1.9769(10)	N4–C33	1.4196(18)
Al1–N1	2.0864(13)	Al2–O2	1.8778(12)		
Angles (°)					
O1–Al1–N3	113.80(6)	O2–Al2–N4	116.87(6)		
O1–Al1–O2	73.85(5)	O2–Al2–O1	73.57(4)		
O1–Al1–N1	80.01(5)	O2–Al2–N2	79.41(5)		
O1–Al1–C1	118.68(6)	O2–Al2–C2	117.54(7)		

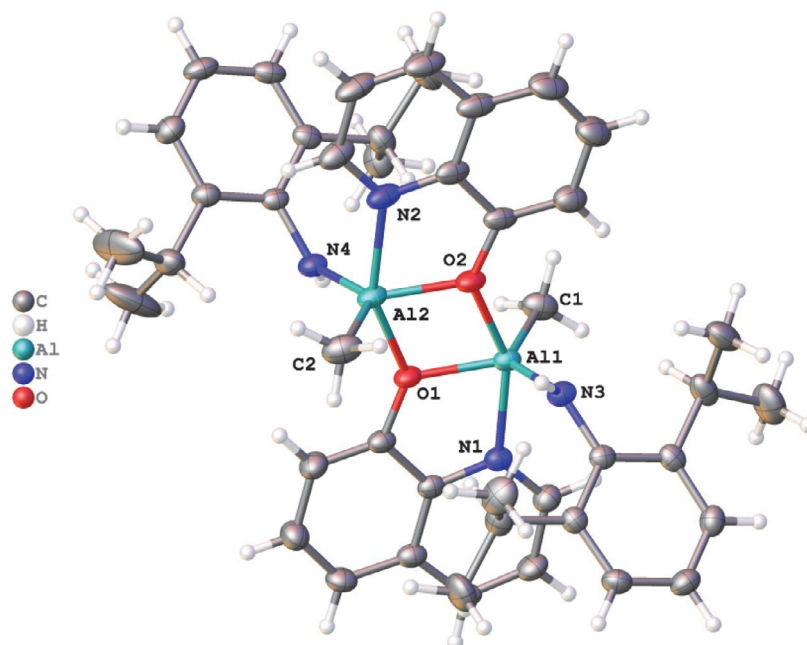
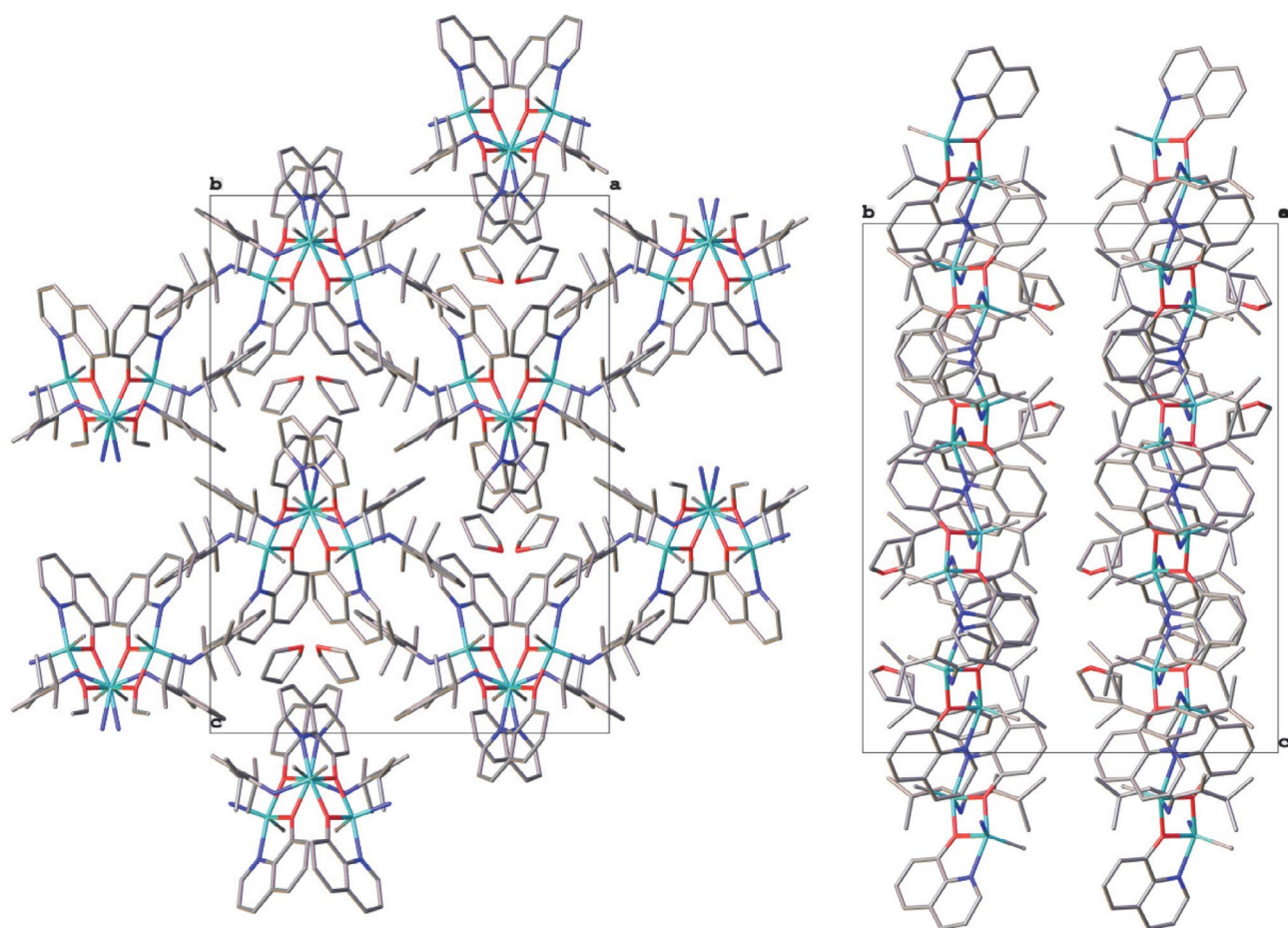
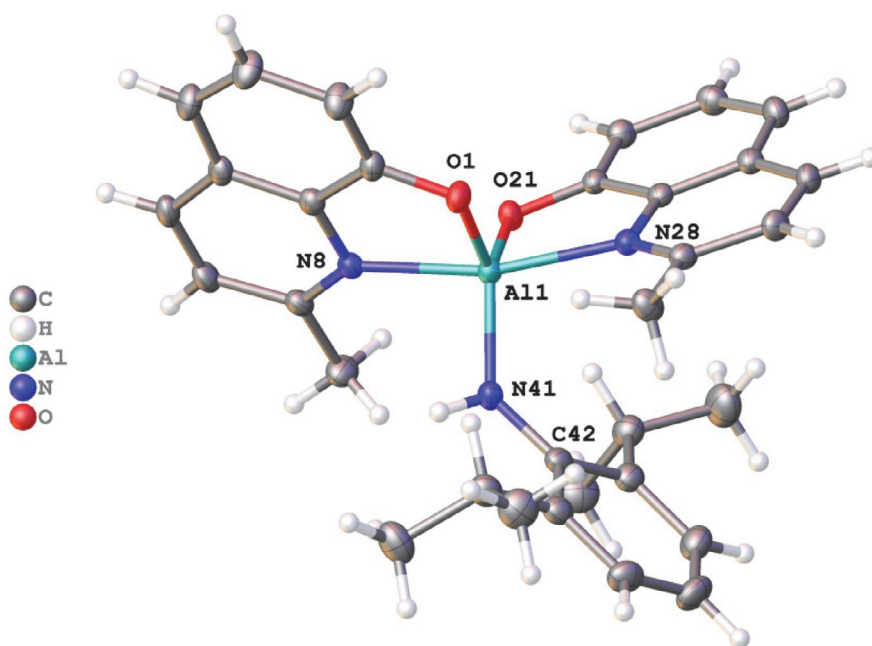


Figure 1. Thermal ellipsoid plot of **2** (disordered solvent molecule was omitted for clarity)



**Figure 2.** Packing in the unit cell of **2**, viewed along *b*-crystallographic axis (left) and *a*-crystallographic axis (right), hydrogen atoms were omitted for clarity

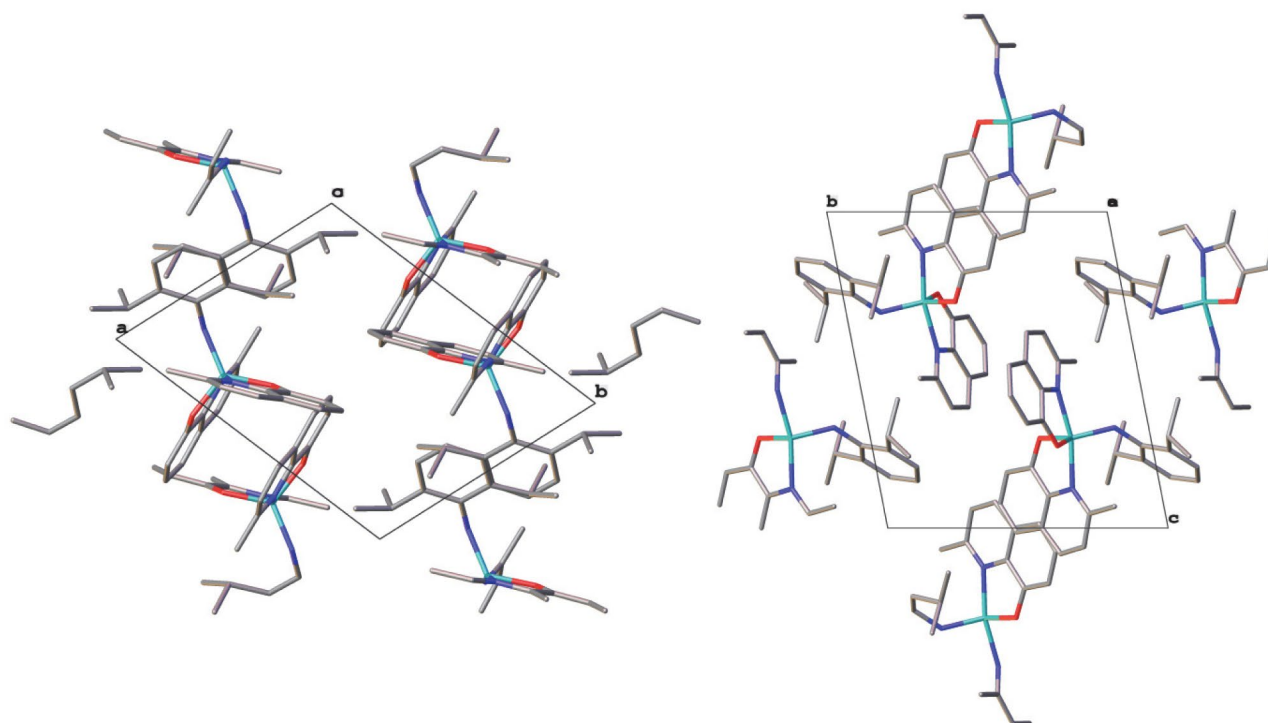


**Figure 3.** Thermal ellipsoid plot of **3**



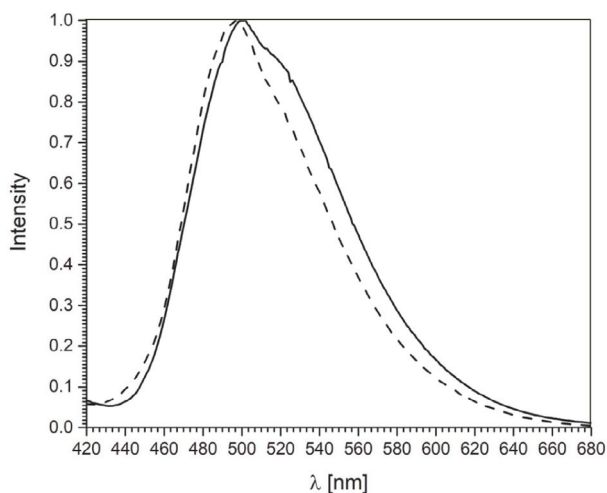
**Table 3.** Selected interatomic distances and angles of **3**

Distances (Å)					
Al1–N8	2.0784(11)	Al1–O21	1.8039(9)	Al1–O1	1.8034(9)
Al1–N28	2.0782(11)	Al1–N41	1.8301(11)	N41–C42	1.4057(16)
Angles (°)					
O1–Al1–N8	83.78(4)	O1–Al1–N28	89.93(4)		
O1–Al1–O21	116.08(4)	O1–Al1–N41	119.44(5)		

**Figure 4.** Packing in the unit cell of **3**, viewed along *c*-crystallographic axis (left) and *a*-crystallographic axis (right), hydrogen atoms were omitted for clarity

### 3. 3. Luminescence Properties

Emission spectra display maxima at 502 nm for **2** and at 497 nm for **3** in solid state (Figure 5). The excitation spectrum of **2** in solid state has shown a wide absorption region (300–450 nm) with maximum around 370 nm while the spectrum of diluted solution of **2** (in CH<sub>2</sub>Cl<sub>2</sub>) is shifted to higher wavelengths showing several maxima (375, 450, 465 nm). The excitation spectrum of **3** in solid state has maximum also around 370 nm whereas diluted solution of **3** shows at least two distinct peaks (372 and 446 nm). Emission maxima of complexes diluted in CH<sub>2</sub>Cl<sub>2</sub> were slightly shifted to shorter wavelengths (500 nm for complex **2**, respectively 481 nm for complex **3**). Luminescence quantum yields were estimated using secondary method. We have used quinine bisulphate as a standard. Quantum yield of complex **2** was found to be 0.29 whereas **3** displays a yield of only 0.12. Luminescence lifetime of diluted complex **2** was found to be about 17 ns (Figure 6).

**Figure 5.** Normalized corrected emission spectra of **2** (solid) and **3** (dashed) complexes in solid state

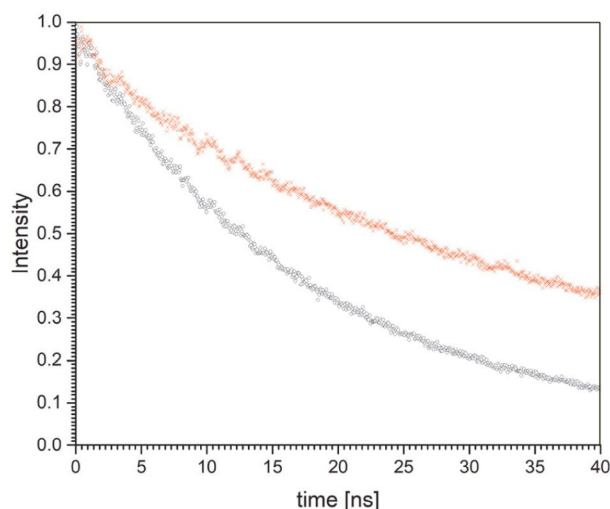


Figure 6. Lifetime measurement of **2** (bottom trace) and **3** (upper trace)

Lifetime of complex **3** was measured to be significantly longer (27 ns).

#### 4. Conclusions

New crystalline complexes **2** and **3** were prepared and structurally characterized. The alumazen ring **1** behaves in these reactions as a structure with alternating double and single Al–N bonds, although the calculations predict that the free electron pair is localized at the nitrogen atom and delocalization energy is minimal in comparison to benzene.<sup>5,6,38</sup> Previous reactions of alumazene (**1**) were designed as reactions with N- or O-bases.<sup>7–10</sup> In the present case we use the ligands with the N-donor site and the acidic OH group. The proton is transferred to alumazene imidic nitrogen. In both **2** and **3**, the oxygen and nitrogen ligand atoms are coordinated to the aluminium in chelating fashion. Although the used quinolinols differ only in one Me substituent, the final products are quite different. It is well known that the Me group in position 2- on the pyridine ring hinders the formation of tris complexes.<sup>19</sup> The first step of both reactions is identical, addition to a formal Al–N double bond and deoligomerization of the trimeric Al<sub>3</sub>N<sub>3</sub> ring. In the second step in the case of complex **2**, dimerization of an intermediate occurs, while in the case of **3**, an intermediate undergoes substitution reaction of the remaining Me group at aluminium atom and the monomeric product is formed. Both **2** and **3** are interesting precursors for the synthesis of a series of derivatives as they still possess reactive moieties, Al–CH<sub>3</sub> and Al–NH–Dipp, capable of further reactions with protic reagents, such as alcohols, silanols, and carboxylic acids. Both complexes (**2** and **3**) have relatively high luminescence quantum yields and show greenish-blue (cyan) emission in the solid state. The described complexes may open routes to the development of cyan-light-emitting

OLEDs using subtractive colour systems (or subtractive CMYK systems).

#### 5. Acknowledgements

The results of this research have been acquired within CEITEC 2020 (LQ1601) project with financial contribution made by the MEYS CR within special support paid from the National Program for Sustainability II funds. CIISB research infrastructure project LM2015043 funded by MEYS CR is gratefully acknowledged for the financial support of the measurements at the CF X-ray Diffraction and Bio-SAXS and the Josef Dadok National NMR Centre. The authors thank P. Machac for MS measurements and L. Simonikova for ICP-OES analyses.

#### 6. Supplementary Material

The crystallographic data of the structures described in this paper were deposited with the Cambridge Crystallographic Data Centre as supplementary publication no. CCDC-1850453 (**2**) and 1850454 (**3**). Copies of these data are available free of charge from <http://www.ccdc.ac.uk/contents/retrieving.html>, or from the Cambridge Crystallographic Data Centre, 12 Union Road, Cambridge CB2 1EZ, UK; fax: (+44)1223-336-033; or email: [deposit@ccdc.cam.ac.uk](mailto:deposit@ccdc.cam.ac.uk).

#### 7. References

1. K. M. Waggoner, H. Hope, P. P. Power, *Angew. Chem. Int. Ed. Engl.* **1988**, *27*, 1699–1700. DOI:10.1002/anie.198816991
2. K. M. Waggoner, P. P. Power, *J. Am. Chem. Soc.* **1991**, *113*, 3385–3393. DOI:10.1021/ja00009a025
3. J. Pinkas, *Inorganic Experiments*, Woollins J. D., Ed., VCH Weinheim, 3rd Edition, **2010**, 402–404, ISBN-10: 3-527-32472-0, ISBN-13: 978-3-527-32472-9.
4. M. Fan, E. N. Duesler, H. Hoth, R. T. Paine, *Main Group Chem.* **2011**, *10*, 37–50. DOI:10.3233/MGC-2010-0033
5. W. H. Fink, J. C. Richards, *J. Am. Chem. Soc.* **1991**, *113*, 3393–3398. DOI:10.1021/ja00009a026
6. J. J. Engelberts, R. W. A. Havenith, J. H. van Lenthe, L. W. Jenneskens, P. W. Foyer, *Inorg. Chem.* **2005**, *44*, 5266–5272. DOI:10.1021/ic050017o
7. J. Löbl, M. Necas, J. Pinkas, *Main Group Chem.* **2006**, *5*, 79–88. DOI:10.1080/10241220600923850
8. J. Löbl, A. Y. Timoshkin, T. Cong, M. Necas, H. W. Roesky, J. Pinkas, *Inorg. Chem.* **2007**, *46*, 5678–5685. DOI:10.1021/ic700488p
9. D. A. Doinikov, I. Kollhammerova, J. Löbl, M. Necas, A. Y. Timoshkin, J. Pinkas, *J. Organometal. Chem.* **2016**, *809*, 38–44. DOI:10.1016/j.jorganchem.2016.02.039
10. K. Maheswari, N. M. Rajendran, J. Meyer, N. D. Reddy, *Organometallics* **2010**, *29*, 3799–3807.

- DOI:10.1021/om100406y
11. J. Pinkas, H. Wessel, Y. Yang, M. L. Montéro, M. Noltemeyer, M. Fröba, H. W. Roesky, *Inorg. Chem.* **1998**, *37*, 2450–2457. DOI:10.1021/ic9713036
  12. H. Hohmeister, H. Wessel, P. Lobinger, H. W. Roesky, P. Muller, I. Uson, H. G. Schmidt, M. Noltemeyer, J. Magull, *J. Fluorine Chem.* **2003**, *120*, 59–64. DOI:10.1016/S0022-1139(02)00285-3
  13. J. Pinkas, J. Löbl, D. Dastych, M. Necas, H. W. Roesky, *Inorg. Chem.* **2002**, *41*, 6914–6918. DOI:10.1021/ic0257625
  14. J. Löbl, J. Pinkas, H. W. Roesky, W. Plass, H. Görls, *Inorg. Chem.* **2006**, *45*, 6571–6573. DOI:10.1021/ic060490h
  15. H. Wessel, C. Rennekamp, S.-D. Waezsada, H. W. Roesky, M. L. Montero, I. Usón, *Organometallics* **1997**, *16*, 3243–3245. DOI:10.1021/om970273b
  16. H. Wessel, M. L. Montéro, C. Rennekamp, H. W. Roesky, P. H. Yu, I. Uson, *Angew. Chem.-Internat. Ed.* **1998**, *37*, 843–845. DOI:10.1002/(SICI)1521-3773(19980403)37:6<843::AID-ANIE843>3.0.CO;2-2
  17. H. Wessel, C. Rennekamp, H. W. Roesky, M. L. Montero, P. Muller, I. Uson, *Organometallics* **1998**, *17*, 1919–1921. DOI:10.1021/om9800748
  18. C. W. Tang, S. A. Vanslyke, *Appl. Phys. Lett.* **1987**, *51*, 913–915. DOI:10.1063/1.98799
  19. C. H. Chen, J. Shi, *Coord. Chem. Rev.* **1998**, *171*, 161–174. DOI:10.1016/S0010-8545(98)90027-3
  20. L. S. Hung, C. H. Chen, *Mater. Sci. Eng. R* **2002**, *39*, 143–222. DOI:10.1016/S0927-796X(02)00093-1
  21. A. Niko, C. Hochfilzer, T. Jost, W. Graupner, G. Leising, *Mater. Res. Soc. Symp. Proc.* **1998**, *488*, 713–718. DOI:10.1557/PROC-488-713
  22. D. Z. Garbuzov, S. R. Forrest, A. G. Tsekoun, P. E. Burrows, V. Bulovic, M. E. Thomson, *J. Appl. Phys.* **1996**, *80*, 4644–4648. DOI:10.1063/1.363447
  23. A. Aziz, K. L. Narasihman, *Synth. Metals* **2000**, *114*, 133–137. DOI:10.1016/S0379-6779(00)00232-0
  24. D. Z. Garbuzov, V. Bulovic, P. E. Burrows, S. R. Forrest, *Chem. Phys. Lett.* **1996**, *249*, 433–437. DOI:10.1016/0009-2614(95)01424-1
  25. J. T. Lim, C. H. Jeong, J. H. Lee, G. Y. Yeom, H. K. Jeong, S. Y. Chai, I. M. Lee, W. I. Lee, *J. Organometal. Chem.* **2006**, *691*, 2701–2707.
  26. J. Luo, Ch. Yang, J. Zheng, J. Ma, L. Liang, M. Lu, *Eur. Polymer J.* **2011**, *47*, 385–393. DOI:10.1016/j.eurpolymj.2010.12.013
  27. H. Jang, L.-M. Do, Y. Kim, T. Zyung, Y. Do, *Synth. Metals* **2001**, *121*, 1667–1668. DOI:10.1016/S0379-6779(00)00941-3
  28. L. S. Sapochak, A. Padmaperuma, N. Washton, F. Endrino, G. T. Schmett, J. Marshall, D. Fogarty, P. E. Burrows, S. R. Forrest, *J. Am. Chem. Soc.* **2001**, *123*, 6300–6307. DOI:10.1021/ja010120m
  29. W. A. E. Omar, O. E. O. Hormi, *Tetrahedron* **2009**, *65*, 4422–4428. DOI:10.1016/j.tet.2009.03.028
  30. W.-H. Sun, M. Shen, W. Zhang, W. Huang, S. Liu, C. Redshaw, *Dalton Trans.* **2011**, *40*, 2645–2653. DOI:10.1039/c0dt01207f
  31. M. Shen, W. Zhang, K. Nomura, W.-H. Sun, *Dalton Trans.* **2009**, *41*, 9000–9009. DOI:10.1039/b910155a
  32. M. Wen-An, W. Zhong-Xia, *Dalton Trans.* **2011**, *40*, 1778–1786. DOI:10.1039/c0dt01001d
  33. M. Wen-An, W. Zhong-Xia, *Organometallics* **2011**, *30*, 4364–4373. DOI:10.1021/om200423g
  34. Rigaku, **2014**. CrystalClear-SM Expert 2.1 b32.
  35. Rigaku Oxford Diffraction, **2016**, CrysAlisPro Software system, vision 1.171.38.43, Rigaku Corporation, Oxford, UK.
  36. G. M. Sheldrick, *Acta Cryst. A* **2008**, *64*, 112–122. DOI:10.1107/S0108767307043930
  37. J. Löbl, Ph. D. Thesis, MU Brno, **2007**.
  38. A. S. Lisovenko, A. Y. Timoshkin, *Russ. J. General Chem.* **2011**, *81*, 831–839. DOI:10.1134/S1070363211050069

## Povzetek

S pomočjo monokristalne rentgenske difrakcije smo določili strukturi dveh spojin dobljenih z reakcijo alumazena [(Dipp)NAlMe]<sub>3</sub> (**1**, Dipp = 2,6-*i*-Pr<sub>2</sub>C<sub>6</sub>H<sub>3</sub>) z dvema kinolinoloma. Kinolin-8-ol (Hq) tvori dvojedrni kompleks [(DippNH)<sub>2</sub>Al<sub>2</sub>Me<sub>2</sub>(q)<sub>2</sub>] (**2**) z osrednjim Al<sub>2</sub>O<sub>2</sub> obročem in petkoordiniranima Al atomoma. Spojina **2** · THF kristalizira v ortorombni *Pbca* prostorski skupini. Molekulska struktura enojedrnega kompleksa [(DippNH)Al(Meq)<sub>2</sub>] (**3**) izoliranega pri reakciji **1** z 2-metilkinolin-8-olom (HMeq) ima petkoordiniran Al center. Struktura je bila rešena v triklini celici *P*-1. Dvojedrni kompleks **2** lahko obravnavamo kot modelni produkt adicije alkohola na formalno Al–N dvojno vez, medtem ko enojedrni kompleks **3** predstavlja primer nadaljnje pretvorbe preostale Al–Me skupine s protonom. Oba kompleksa **2** in **3** imata močno luminiscenco z emisijo okoli 500 nm v trdnem stanju.

Scientific paper

# Synthesis, Crystal Structures and Catalytic Property of Oxidovanadium(V) Complexes with Similar Aroylhydrazones

Min Liang,<sup>1,\*</sup> Nan Sun<sup>2</sup> and Dong-Hui Zou<sup>3</sup>

<sup>1</sup> School of Chemistry and Chemical Engineering, Qiqihar University, Qiqihar 161006, P. R. China.

<sup>2</sup> College of Chemistry, Chemical Engineering and Material Science, Shandong Normal University, Jinan 250014, P.R. China

<sup>3</sup> College of Food and Bio-Engineering, Qiqihar University, Qiqihar 161006, P. R. China

\* Corresponding author: E-mail: liangmin09@163.com

Received: 23-07-2018

## Abstract

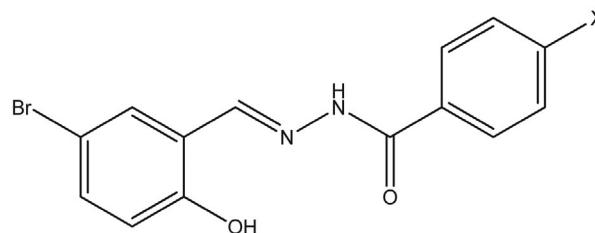
A pair of new oxidovanadium(V) complexes, [VOL<sup>1</sup>L]·EtOH (1) and [VOL<sup>2</sup>L]·EtOH (2) (L = acetohydroxamate), derived from the aroylhydrazones *N*'-(5-bromo-2-hydroxybenzylidene)-4-methoxybenzohydrazide (H<sub>2</sub>L<sup>1</sup>) and *N*'-(5-bromo-2-hydroxybenzylidene)-4-methylbenzohydrazide (H<sub>2</sub>L<sup>2</sup>), have been prepared and characterized by elemental analyses, FT-IR, <sup>1</sup>H and <sup>13</sup>C NMR spectroscopy and single-crystal structural X-ray diffraction. The complexes have octahedral structures in which the aroylhydrazone ligands behave as binegative donors. Single-crystal structure analyses reveal that the V centers are coordinated by the donor atoms of the aroylhydrazone ligands, the acetohydroxamate ligands and the oxido groups. Crystal structures of the complexes are stabilized by hydrogen bonds. The complexes function as effective olefin epoxidation catalysts.

**Keywords:** Aroylhydrazone; oxidovanadium complex; catalytic activity; crystal structure

## 1. Introduction

In recent years, remarkable attention has focused on vanadium compounds because of their biochemical significance<sup>1</sup> and industrial catalytic processes.<sup>2</sup> For instance, the use of oxovanadium complexes in asymmetric synthesis,<sup>3</sup> in C–C bond formation as well as in C–C, C–O and C–H bond cleavages,<sup>4</sup> catalytic oxidation of various olefins,<sup>5</sup> oxidative halogenation and selective epoxidation of unsaturated hydrocarbons and allyl alcohols.<sup>6</sup> Aroylhydrazones bearing typical –CO–NH–N=CH– group are interesting ligands in the preparation of various metal complexes which have considerable biological and catalytic properties.<sup>7</sup> A number of vanadium complexes with various types of ligands have been prepared, yet, those derived from hydrazones only few have been reported with catalytic oxidation on olefins. In this paper we are concerned about the structural investigation and catalytic activity of two vanadium complexes with hydrazone ligands, which have similar structures except for the terminal substituted groups, Me and OMe. In the present work, a pair of new vanadium(V) complexes [VOL<sup>1</sup>L]·EtOH (1) and [VOL<sup>2</sup>L]·EtOH (2) (L = acetohydroxamate),

derived from the aroylhydrazones *N*'-(5-bromo-2-hydroxybenzylidene)-4-methoxybenzohydrazide (H<sub>2</sub>L<sup>1</sup>) and *N*'-(5-bromo-2-hydroxybenzylidene)-4-methylbenzohydrazide (H<sub>2</sub>L<sup>2</sup>; Scheme 1), are presented.



Scheme 1. H<sub>2</sub>L<sup>1</sup> (X = OMe) and H<sub>2</sub>L<sup>2</sup> (X = Me)

## 2. Experimental

### 2.1. Materials and Methods

All chemicals and solvents used were of analytical reagent grade and used as received. Micro analyses for C, H, N were carried out using a Perkin Elmer 2400 CHNS/O

elemental analyzer. FT-IR spectra were recorded on a FT-IR 8400-Shimadzu as KBr discs in the range of 400–4000  $\text{cm}^{-1}$ .  $^1\text{H}$  and  $^{13}\text{C}$  NMR spectra were recorded at 25 °C on the Bruker AVANCE 300 MHz spectrometer. X-ray diffraction data were collected using a Bruker Smart Apex II diffractometer.

## 2. 2. Synthesis of the Aroylhydrazones

An ethanolic solution (20 mL) containing 5-bromo-2-hydroxybenzaldehyde (1.0 mmol, 0.201 g) was added dropwise to the ethanolic solution of 4-methoxybenzohydrazide (1.0 mmol, 0.166 g) for  $\text{H}_2\text{L}^1$ , and 4-methylbenzohydrazide (1.0 mmol, 0.150 g) for  $\text{H}_2\text{L}^2$ , respectively, with constant stirring. The mixtures were refluxed for 30 min, and the resulting precipitate was filtered off, washed with cold ethanol and dried in desiccator over silica gel.

$\text{H}_2\text{L}^1$ : Yield: 0.29 g, 83%. For  $\text{C}_{15}\text{H}_{13}\text{BrN}_2\text{O}_3$ : anal. calcd., %: C, 51.60; H, 3.75; N, 8.02. Found, %: C, 51.75; H, 3.83; N, 7.94. FT-IR (KBr),  $\text{cm}^{-1}$ :  $\nu(\text{OH})$  3455,  $\nu(\text{NH})$  3237,  $\nu(\text{CH})$  2810–3120,  $\nu(\text{C}=\text{O})$  1647,  $\nu(\text{C}=\text{N})$  1609,  $\nu(\text{C}-\text{O})$  1255.  $^1\text{H}$  NMR (300 MHz,  $\text{DMSO}-d_6$ , ppm):  $\delta$  = 12.08 (s, 1H; OH), 11.38 (s, 1H; NH), 8.59 (s, 1H; CH=N), 7.94 (d, 2H; ArH), 7.78 (s, 1H; ArH), 7.43 (d, 1H, ArH), 7.08 (d, 2H; ArH), 6.90 (d, 1H, ArH), 3.86 (s, 3H,  $\text{CH}_3$ ).  $^{13}\text{C}$  NMR (75 MHz,  $\text{DMSO}-d_6$ , ppm)  $\delta$  = 162.24, 156.40, 145.26, 133.38, 130.58, 129.63, 124.72, 121.32, 118.66, 113.80, 110.37, 55.46.

$\text{H}_2\text{L}^2$ : Yield: 0.30 g, 90%. For  $\text{C}_{15}\text{H}_{13}\text{BrN}_2\text{O}_2$ : anal. calcd., %: C, 54.07; H, 3.93; N, 8.41. Found, %: C, 54.23; H, 4.02; N, 8.35. FT-IR (KBr),  $\text{cm}^{-1}$ :  $\nu(\text{OH})$  3445,  $\nu(\text{NH})$  3229,  $\nu(\text{CH})$  2815–3120,  $\nu(\text{C}=\text{O})$  1647,  $\nu(\text{C}=\text{N})$  1617,  $\nu(\text{C}-\text{O})$  1280.  $^1\text{H}$  NMR (300 MHz,  $\text{DMSO}-d_6$ , ppm):  $\delta$  = 12.14 (s, 1H; OH), 11.35 (s, 1H; NH), 8.63 (s, 1H; CH=N), 7.89–7.80 (m, 3H; ArH), 7.47–7.35 (m, 3H, ArH), 6.93 (d, 1H; ArH), 2.41 (s, 3H,  $\text{CH}_3$ ).  $^{13}\text{C}$  NMR (75 MHz,  $\text{DMSO}-d_6$ , ppm)  $\delta$  = 162.20, 156.38, 145.31, 142.27, 133.35, 130.22, 129.54, 126.89, 121.32, 118.66, 113.80, 110.37, 21.12.

## 2. 3. Synthesis of the Complexes

An ethanolic solution (10 mL) of  $\text{VO}(\text{acac})_2$  (0.1 mmol, 0.026 g) was added to the ethanolic solution of acetohydroxamic acid (0.1 mmol, 0.0075 g) and  $\text{H}_2\text{L}^1$  (0.1 mmol, 0.035 g) for **1** and  $\text{H}_2\text{L}^2$  (0.1 mmol, 0.033 g) for **2**, respectively, and the resulting orange mixture was refluxed for 30 min. After cooling, the solution was filtered and left to stand overnight. Orange single crystals suitable for crystallographic analysis separated after a week and dried in a vacuum desiccator over silica gel.

**[VOL<sup>1</sup>L] · EtOH (1)**: Yield: 0.027 g, 51%. For  $\text{C}_{19}\text{H}_{21}\text{BrN}_3\text{O}_7\text{V}$ : anal. calcd., %: C, 42.72; H, 4.00; N, 7.87. Found, %: C, 42.61; H, 3.89; N, 7.78. IR (KBr)  $\text{cm}^{-1}$ :  $\nu(\text{OH})$  3427,  $\nu(\text{NH})$  3217,  $\nu(\text{CH})$  2820–3100,  $\nu(\text{C}=\text{N})$  1610,

$\nu(\text{C}-\text{O})$  1176,  $\nu(\text{VO})$  968.  $^1\text{H}$  NMR (300 MHz,  $\text{DMSO}-d_6$ , ppm):  $\delta$  = 14.05 (s, 1H; NH), 9.05 (s, 1H; CH=N), 7.99 (d, 1H; ArH), 7.85 (m, 2H; ArH), 7.65 (q, 1H, ArH), 7.03 (d, 2H; ArH), 6.86 (d, 1H, ArH), 3.80 (s, 3H,  $\text{OCH}_3$ ), 2.10 (t, 3H,  $\text{CH}_3$ ).

**[VOL<sup>2</sup>L] · EtOH (2)**: Yield: 0.022 g, 43%. For  $\text{C}_{19}\text{H}_{21}\text{BrN}_3\text{O}_6\text{V}$ : anal. calcd., %: C, 44.04; H, 4.08; N, 8.11. Found, %: C, 43.87; H, 4.22; N, 8.27. IR (KBr)  $\text{cm}^{-1}$ :  $\nu(\text{OH})$  3434,  $\nu(\text{NH})$  3231,  $\nu(\text{CH})$  2820–3130,  $\nu(\text{C}=\text{N})$  1608,  $\nu(\text{C}-\text{O})$  1192,  $\nu(\text{VO})$  968.  $^1\text{H}$  NMR (300 MHz,  $\text{DMSO}-d_6$ , ppm):  $\delta$  = 14.06 (s, 1H; NH), 9.08 (s, 1H; CH=N), 7.99 (d, 1H; ArH), 7.81 (m, 2H; ArH), 7.65 (q, 1H, ArH), 7.30 (d, 2H; ArH), 6.86 (d, 1H, ArH), 2.38 (s, 3H,  $\text{CH}_3$ ), 2.11 (t, 3H,  $\text{CH}_3$ ).

## 2. 6. X-Ray structure Determination

The crystal structures of the complexes were measured on a Bruker SMART Apex II CCD diffractometer using Mo-K $\alpha$  radiation ( $\lambda$  = 0.71073 Å) and a graphite monochromator at 25 °C. Unit cell and reflection data were obtained by standard methods<sup>8</sup> and are summarized in Table 1. The structures were solved, refined, and prepared for publication using the SHELXTL package (structure solution refinements and molecular graphics),<sup>9</sup> and using full-matrix least-squares techniques by using  $F^2$  with anisotropic displacement factors for all non-hydrogen atoms. The amino H atoms were located from difference Fourier maps and refined isotropically, with N–H distanc-

Table 1. Crystal data and structure refinement for the complexes

Parameters	1	2
Molecular formula	$\text{C}_{19}\text{H}_{21}\text{BrN}_3\text{O}_7\text{V}$	$\text{C}_{19}\text{H}_{21}\text{BrN}_3\text{O}_6\text{V}$
Formula weight	534.24	518.24
Temperature (K)	298(2)	298(2)
Crystal system	Monoclinic	Monoclinic
Space group	$P2_1/n$	$P2_1/n$
<i>a</i> (Å)	8.3528(5)	8.4310(8)
<i>b</i> (Å)	16.0871(10)	15.1788(14)
<i>c</i> (Å)	16.5986(10)	16.8336(16)
$\beta$ (°)	95.496(2)	93.271(2)
<i>V</i> (Å <sup>3</sup> )	2220.1(2)	2150.7(4)
<i>Z</i>	4	4
<i>D</i> <sub>calc</sub> (g/cm <sup>3</sup> )	1.598	1.600
$\mu$ (mm <sup>-1</sup> )	2.291	2.359
<i>F</i> (000)	1080	1048
Reflections collected	20456	10964
Independent reflection ( <i>R</i> <sub>int</sub> )	4269 (0.0554)	3996 (0.0242)
Reflections observed ( <i>I</i> > 2 $\sigma$ ( <i>I</i> ))	3054	3278
Data/restraints/parameters	4269/1/287	3996/1/276
Goodness-of-fit on <i>F</i> <sup>2</sup>	1.028	1.029
Final <i>R</i> indices ( <i>I</i> > 2 $\sigma$ ( <i>I</i> ))	0.0485, 0.1020	0.0342, 0.0805
<i>R</i> indices (all data)	0.0833, 0.1184	0.0470, 0.0867
Highest peak and deepest hole (e Å <sup>-3</sup> )	0.447, -0.425	0.428, -0.365

es restrained to 0.90(1) Å. Positions of the remaining hydrogen atoms were calculated from the geometry of the molecular skeleton and their thermal displacement parameters were refined isotropically on a groupwise basis. Selected bond lengths and angles are reported in Table 2. H-bonding distances and angles are shown in Table 3.

**Table 2.** Selected bond lengths (Å) and angles (°) for the complexes

<b>1</b>			
Bond lengths (Å)			
V(1)–O(1)	1.861(3)	V(1)–O(2)	1.942(3)
V(1)–O(4)	2.216(3)	V(1)–O(5)	1.850(3)
V(1)–O(6)	1.581(3)	V(1)–N(1)	2.080(3)
Bond angles (°)			
O(6)–V(1)–O(5)	96.64(14)	O(6)–V(1)–O(1)	99.49(15)
O(5)–V(1)–O(1)	105.02(12)	O(6)–V(1)–O(2)	97.41(14)
O(5)–V(1)–O(2)	90.35(11)	O(1)–V(1)–O(2)	155.56(12)
O(6)–V(1)–N(1)	100.73(14)	O(5)–V(1)–N(1)	158.40(12)
O(1)–V(1)–N(1)	84.74(11)	O(2)–V(1)–N(1)	74.84(11)
O(6)–V(1)–O(4)	172.74(14)	O(5)–V(1)–O(4)	76.12(11)
O(1)–V(1)–O(4)	82.16(12)	O(2)–V(1)–O(4)	83.30(11)
N(1)–V(1)–O(4)	86.43(11)		
<b>2</b>			
Bond lengths (Å)			
V(1)–O(1)	1.8570(19)	V(1)–O(2)	1.9468(19)
V(1)–O(3)	2.2276(19)	V(1)–O(4)	1.8444(18)
V(1)–O(5)	1.580(2)		
V(1)–N(1)	2.080(2)		
Bond angles (°)			
O(5)–V(1)–O(4)	96.43(10)	O(5)–V(1)–O(1)	99.41(11)
O(4)–V(1)–O(1)	105.00(8)	O(5)–V(1)–O(2)	97.60(10)
O(4)–V(1)–O(2)	90.28(8)	O(1)–V(1)–O(2)	155.59(9)
O(5)–V(1)–N(1)	100.43(10)	O(4)–V(1)–N(1)	158.73(8)
O(1)–V(1)–N(1)	84.99(8)	O(2)–V(1)–N(1)	74.79(8)
O(5)–V(1)–O(3)	172.15(10)	O(4)–V(1)–O(3)	75.72(7)
O(1)–V(1)–O(3)	82.97(8)	O(2)–V(1)–O(3)	82.53(8)
N(1)–V(1)–O(3)	87.20(7)		

**Table 3.** Hydrogen bonding interactions (Å, °)

<i>D</i> – <i>H</i> ... <i>A</i>	<i>d</i> ( <i>D</i> – <i>H</i> )	<i>d</i> ( <i>H</i> ... <i>A</i> )	<i>d</i> ( <i>D</i> ... <i>A</i> )	Angle ( <i>D</i> – <i>H</i> ... <i>A</i> )
<b>1</b>				
N(3)–H(3)···O(7)	0.90(1)	1.85(3)	2.697(5)	156(6)
O(7)–H(7)···N(2) <sup>i</sup>	0.82	2.00(3)	2.814(5)	176(5)
<b>2</b>				
O(6)–H(6)···N(2) <sup>ii</sup>	0.82	2.02	2.839(3)	172(5)
N(3)–H(3)···O(6)	0.90(1)	1.82(2)	2.697(3)	163(4)

Symmetry codes: i)  $x + \frac{1}{2}, -y + \frac{3}{2}, z - \frac{1}{2}$ ; ii)  $\frac{1}{2} + x, \frac{3}{2} - y, -\frac{1}{2} + z$ .

## 2. 7. Catalytic Epoxidation of Olefins

To a solution of olefins (0.28 mmol), NaHCO<sub>3</sub> (0.11 mmol, 9.24 mg) and catalyst ( $9.4 \times 10^{-4}$  mmol) in the mixture of CH<sub>3</sub>OH/CH<sub>2</sub>Cl<sub>2</sub> (1.2 mL; V:V = 7:3) was added

H<sub>2</sub>O<sub>2</sub> (1.1 mmol, 30% H<sub>2</sub>O<sub>2</sub> in water) as oxidant. After the reaction was over at 74.5 min, for the products analysis, the solution was subjected to multiple ether extraction, and the extract was also concentrated down to 0.5 mL by distillation in a rotary evaporator at room temperature and then a sample (2 μL) was taken from the solution and analyzed by GC. The retention times of the peaks were compared with those of commercial standards, and chlorobenzene was used as an internal standard for GC yield calculation.

## 3. Results and Discussion

### 3. 1. Synthesis and Characterization

The reaction of VO(acac)<sub>2</sub> and acetohydroxamic acid with the tridentate aroylhydrazone ligands H<sub>2</sub>L<sup>1</sup> and H<sub>2</sub>L<sup>2</sup> in ethanol led to the formation of the complexes. Crystals of the complexes are stable at room temperature and soluble in DMSO, DMF, ethanol, acetonitrile and less soluble in other common solvents like dichloromethane, chloroform, and insoluble in benzene, *n*-hexane and CCl<sub>4</sub>.

### 3. 2. <sup>1</sup>H NMR Spectra

<sup>1</sup>H NMR data of the aroylhydrazone ligands when compared with the complexes reveal that the ligands serve as tridentate binategative ONO donor. The azomethine C–H signal in the complexes is shifted up-field from its original position in the free ligands upon coordination of the –CH=N– groups, on account of reduction of electron density at the azomethine C–H. The aromatic protons also show some deviation in the complexes as compared to the free ligand since in the complexes they are in direct conjugation to the coordinated O and N of the hydrazone ligands.

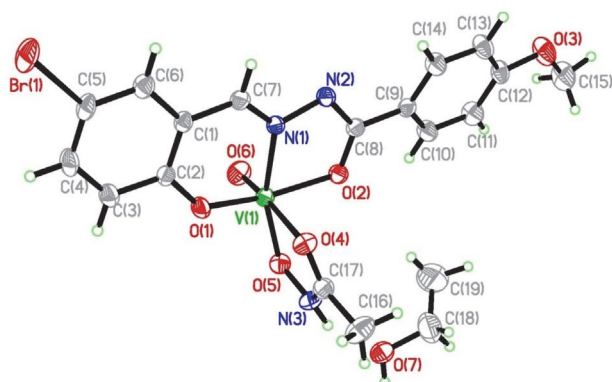
### 3. 3. IR Spectra

IR spectra of the free aroylhydrazone ligands show bands at 3220–3240 cm<sup>-1</sup> for ν(N–H), 1647 cm<sup>-1</sup> for ν(C=O) and 3445–3455 cm<sup>-1</sup> for ν(O–H).<sup>10</sup> The ν(C=O) bands are absent in the spectra of the complexes as the ligands bind in binategative mode losing protons from the carbohydrazone groups. The strong peak at about 1610 cm<sup>-1</sup> can be assigned to ν(C=N).<sup>11</sup> The complexes exhibit characteristic bands at 968 cm<sup>-1</sup> for the stretching of V=O groups.<sup>12</sup>

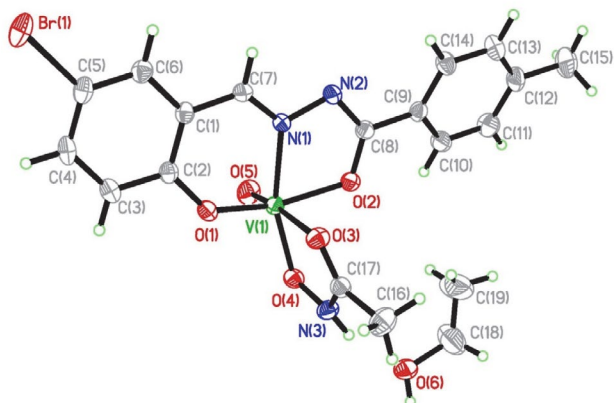
### 3. 4. Structure Description

The perspective views of the complexes together with the atom numbering schemes are shown in Figs. 1 and 2. The asymmetric units of the complexes contain one complex molecule and one ethanol molecule. The coordination geometry around each V atom reveals a distorted

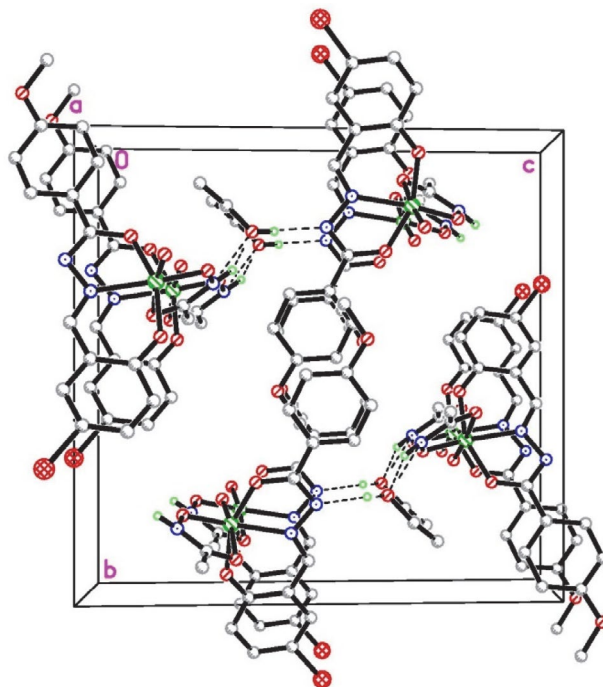
octahedral environment with an  $\text{NO}_3$  chromophore. The ligand molecule behaves as binategative tridentate one binding through the phenolate oxygen, the enolate oxygen and the imine nitrogen and occupies three positions in the basal plane. The fourth donor of the basal plane is furnished by the hydroxyl O atom of the acetohydroxamate ligand. The oxo group and the carbonyl O atom of the acetohydroxamate ligand are located at the axial positions. The V atoms are found to be deviated from the corresponding mean basal planes by 0.283(2) Å for 1 and 0.279(2) Å for 2. The C(8)–O(2) bond lengths are closer to single bond length rather than C–O double bond length. However, the shorter length compared to C–O single bond may be attributed to extended electron delocalization in the ligand. Similarly shortening of C(8)–N(2) bond lengths together with the elongation of N(1)–N(2) lengths also supports the electron cloud delocalization in the ligand system. The ligand molecules form five-membered and six-membered chelate rings with the V centers. The bond lengths related to the V atoms are similar to those observed in other vanadium complexes.<sup>13</sup> In the crystal structures of the complexes, the vanadium complex molecules are linked by ethanol molecules through hydrogen bonds (Figs. 3 and 4).



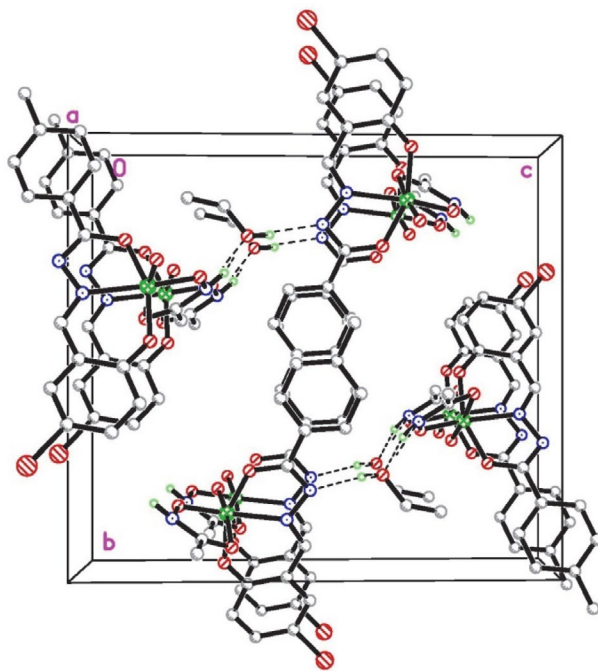
**Figure 1.** An ORTEP diagram of complex 1 with atom labeling scheme and 30% probability thermal ellipsoids for all non-hydrogen atoms. Hydrogen bonds are shown as dashed lines.



**Figure 2.** An ORTEP diagram of complex 2 with atom labeling scheme and 30% probability thermal ellipsoids for all non-hydrogen atoms. Hydrogen bonds are shown as dashed lines.



**Figure 3.** Hydrogen bonds linked structures of complex 1.



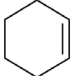
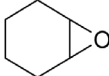
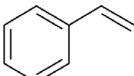
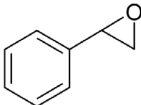

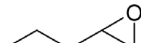
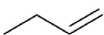
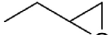
**Figure 4.** Hydrogen bonds linked structures of complex 2.

### 3. 5. Catalytic Property

The reactions were performed in (70:30) mixture of  $\text{CH}_3\text{OH}/\text{CH}_2\text{Cl}_2$  (1.2 mL) under air at room temperature. The molar ratios for catalyst:substrate: $\text{NaHCO}_3$ : $\text{H}_2\text{O}_2$  are 1:298:117:1170. The GC conversion (%) is measured relative to the starting olefin after 74.5 min. The complexes show effective catalytic property in the oxidation of various olefins to their corresponding epoxides. The details of cata-

lytic properties with respect to epoxidation of olefins with the complexes as catalysts are given in Table 4. Excellent epoxide yields and selectivity (> 99%) were observed for all aliphatic and aromatic substrates. The results of catalytic studies using the catalysts reveal that the efficiency of catalyst toward all the substrates is similar with maximum conversion, TON, and selectivity. When H<sub>2</sub>O<sub>2</sub> (1.1 mmol, 30% H<sub>2</sub>O<sub>2</sub> in water) was used as a sole oxidant the catalytic efficiency is not high, but when NaHCO<sub>3</sub> (0.11 mmol, 9.24 mg) was added as a co-catalyst the efficiency of the system increases many times. The key aspect of such a reaction is that H<sub>2</sub>O<sub>2</sub> and hydrogen carbonate react in an equilibrium process to produce peroxydicarbonate, HCO<sub>4</sub><sup>-</sup>, which is a more reactive nucleophile than H<sub>2</sub>O<sub>2</sub> and speeds up the epoxidation reaction. The catalytic properties of the presented complexes are comparable to the molybdenum and vanadium complexes reported in literature.<sup>14</sup>

Table 4. The catalytic oxidation results

Substrate	Product		Conversion (%) (TON) <sup>a</sup>
		1	100 (337)
		2	100 (331)
		1	100 (325)
		2	100 (320)
		1	95 (295)
		2	93 (303)
		1	94 (292)
		2	95 (288)

<sup>a</sup> TON = (mmol of product)/mmol of catalyst.

## 4. Conclusion

A pair of new oxidovanadium(V) complexes with aroylhydrazone ligands have been prepared and structurally characterized using X-ray structure analysis, FT-IR and <sup>1</sup>H NMR spectra. The complexes have octahedral geometry with positions around the central atom being occupied with donor atoms of the aroylhydrazone ligand, the acetohydroxamate ligand and one oxo group. The complexes show effective catalytic property in the oxidation of various olefins to their corresponding epoxides.

## 5. Supplementary Material

CCDC reference numbers 1845890 and 1845891 contain the supplementary crystallographic data for this

article. These data can be obtained free of charge at <http://www.ccdc.cam.ac.uk>, or from Cambridge Crystallographic Data Center, 12 Union Road, Cambridge CB2 1EZ, UK; Fax: +44 1223 336 033; Email: [deposit@ccdc.cam.ac.uk](mailto:deposit@ccdc.cam.ac.uk).

## 6. References

- (a) C. Rozzo, D. Sanna, E. Garribba, M. Serra, A. Cantara, G. Palmieri, M. Pisano, *J. Inorg. Biochem.* **2017**, *174*, 14–24; DOI:10.1016/j.jinorgbio.2017.05.010  
(b) T. Jakusch, T. Kiss, *Coord. Chem. Rev.* **2017**, *351*, 118–126; DOI:10.1016/j.ccr.2017.04.007  
(c) S. Sultan, U. Ashiq, R. A. Jamal, M. Mahroof-Tahir, Z. Shaikh, B. Shamshad, M. Lateef, L. Iqbal, *Biometals* **2017**, *30*, 873–891; DOI:10.1007/s10534-017-0054-6  
(d) S. Kumar, A. Syed, S. Andotra, R. Kaur, Vikas, S. K. Pandey, *J. Mol. Struct.* **2018**, *1154*, 165–178. DOI:10.1016/j.molstruc.2017.10.009
- (a) V. K. Singh, A. Maurya, N. Kesharvani, P. Kachhap, S. Kumari, A. K. Mahato, V. K. Mishra, C. Haldar, *J. Coord. Chem.* **2018**, *71*, 520–541; DOI:10.1080/00958972.2018.1434516  
(b) I. Gryca, K. Czerwinska, B. Machura, A. Chrobok, L. S. Shulpina, M. L. Kuznetsov, D. S. Nesterov, Y. N. Kozlov, A. J. L. Pombeiro, I. A. Varyan, G. B. Shulpin, *Inorg. Chem.* **2018**, *57*, 1824–1839; DOI:10.1021/acs.inorgchem.7b02684  
(c) J. C. Pessoa, M. R. Maurya, *Inorg. Chim. Acta* **2017**, *455*, 415–428; DOI:10.1016/j.ica.2016.04.012  
(d) R. N. Senapati, P. Dutta, S. Rana, K. M. Parida, S. Sahu, A. Sarkar, *Inorg. Nano-Met. Chem.* **2017**, *47*, 1429–1435;  
(e) R. C. Dey, M. M. Islam, M. Halder, A. S. Roy, S. M. Islam, *Chemistryselect* **2016**, *1*, 6797–6804. DOI:10.1002/slct.201601369
- (a) P. Kelly, S. E. Lawrence, A. R. Maguire, *Eur. J. Org. Chem.* **2006**, *19*, 4500–4509; DOI:10.1002/ejoc.200600320  
(b) Y. N. Belokon, W. Clegg, R. W. Harrington, C. Young, M. North, *Tetrahedron* **2007**, *63*, 5287–5299; DOI:10.1016/j.tet.2007.03.140  
(c) N. U. H. Khan, S. Agrawal, R. I. Kureshy, S. H. R. Abdi, V. J. Mayani, R. V. Jasra, *Eur. J. Org. Chem.* **2006**, *14*, 3175–3180; DOI:10.1002/ejoc.200600208  
(d) Y. N. Belokon, M. North, T. Parsons, *Org. Lett.* **2000**, *2*, 1617–1619. DOI:10.1021/ol005893e
- (a) Y. Kataoka, I. Makihira, T. Yamagata, K. Tani, *Organometallics* **1997**, *16*, 4788–4795; DOI:10.1021/om970545a  
(b) S. Ghorai, C. Mukherjee, *Chem. Commun.* **2012**, *48*, 10180–10182; DOI:10.1039/c2cc35963d  
(c) C. Milsmann, S. P. Semproni, P. J. Chirik, *J. Am. Chem. Soc.* **2014**, *136*, 12099–12107; DOI:10.1021/ja5062196  
(d) D. R. Wang, A. Behrens, M. Farahbakhsh, J. Gatzjens, D. Rehder, *Chem. Eur. J.* **2003**, *9*, 1805–1813; DOI:10.1002/chem.200390207  
(e) F. Franceschi, E. Solari, C. Floriani, M. Rosi, A. Chiesi-Villa, C. Rizzoli, *Chem. Eur. J.* **1999**, *5*, 708–721. DOI:10.1002/(SICI)1521-3765(19990201)5:2<708::AID-CHEM708>3.0.CO;2-I



5. (a) M. L. Kuznetsov, J. C. Pessoa, *Dalton Trans.* **2009**, 28, 5460–5468; DOI:10.1039/b902424g  
 (b) R. Hajian, S. Tangestaninejad, M. Moghadam, V. Mirkhani, I. Mohammadpoor-Baltork, A. R. Khosropour, *J. Coord. Chem.* **2011**, 64, 4134–4144; DOI:10.1080/00958972.2011.636038  
 (c) K. Nomura, S. Zhang, *Chem. Rev.* **2011**, 111, 2342–2362; DOI:10.1021/cr100207h  
 (d) G. Romanowski, J. Kira, M. Wera, *Polyhedron* **2014**, 67, 529–539. DOI:10.1016/j.poly.2013.10.008
6. (a) S. Rana, B. Pandey, A. Dey, R. Haque, G. Rajaraman, D. Maiti, *ChemCatChem* **2016**, 8, 3367–3374; DOI:10.1002/cctc.201600843  
 (b) M. Zhao, J. T. Mohr, *Tetrahedron* **2017**, 73, 4115–4124; DOI:10.1016/j.tet.2016.12.055  
 (c) S. Rana, R. Haque, G. Santosh, D. Maiti, *Inorg. Chem.* **2013**, 52, 2927–2932; DOI:10.1021/ic302611a  
 (d) N. Mizuno, Y. Nakagawa, K. Yamaguchi, *J. Mol. Catal. A* **2006**, 251, 286–290. DOI:10.1016/j.molcata.2006.02.012
7. (a) S. Parveen, S. Govindarajan, H. Puschmann, R. Revathi, *Inorg. Chim. Acta* **2018**, 477, 66–74; DOI:10.1016/j.ica.2018.02.022  
 (b) M. Sennappan, P. M. Krishna, A. A. Hosamani, R. H. Krishna, *J. Mol. Struct.* **2018**, 1164, 271–279; DOI:10.1016/j.molstruc.2018.03.054  
 (c) J. E. Philip, S. A. Antony, S. J. Eettinilkunnathil, M. R. P. Kurup, M. P. Velayudhan, *Inorg. Chim. Acta* **2018**, 469, 87–97; DOI:10.1016/j.ica.2017.09.006  
 (d) Z. L. You, H. Y. Yu, B. Y. Zheng, C. L. Zhang, C. W. Lv, K. Li, L. Pan, *Inorg. Chim. Acta* **2018**, 469, 44–50; DOI:10.1016/j.ica.2017.09.011  
 (e) M. A. Naziri, E. Sahin, N. Seferoglu, B. Shaabani, *J. Coord. Chem.* **2018**, 71, 89–103. DOI:10.1080/00958972.2018.1432857
8. (a) Brukewwwwr, SMART (Version 5. 624) and SAINT (Version 6. 04) Programs Using the Windows NT System, Bruker AXS Inc., Madison, WI, USA, 2001;  
 (b) G. M. Sheldrick, *Acta Crystallogr.* **2008**, A64, 112–122. DOI:10.1107/S0108767307043930
9. G. M. Sheldrick, SHELXTL, Version 5.10, Bruker AXS Inc., Madison, WI, USA, 1997.
10. (a) E. Kwiatkowski, G. Romanowski, W. Nowicki, M. Kwiatkowski, K. Suwinska, *Polyhedron* **2003**, 22, 1009–1018; DOI:10.1016/S0277-5387(03)00041-X  
 (b) A. R. Yaul, G. B. Pethe, A. S. Aswar, *Russ. J. Coord. Chem.* **2010**, 36, 254–258. DOI:10.1134/S1070328410040032
11. D. Sadhukhan, M. Maiti, E. Zangrando, S. Pathan, S. Mitra, A. Patel, *Polyhedron* **2014**, 69, 1–9. DOI:10.1016/j.poly.2013.11.007
12. A. Sarkar, S. Pal, *Polyhedron* **2006**, 25, 1689–1694. DOI:10.1016/j.poly.2005.11.009
13. (a) J.-X. Lei, J. Wang, Y. Huo, Z. You, *Acta Chim. Slov.* **2016**, 63, 670–677; DOI:10.17344/acsi.2016.2589  
 (b) Q. Liu, J. Lin, J. Liu, W. Chen, Y. Cui, *Acta Chim. Slov.* **2016**, 63, 279–286;  
 (c) Z.-Q. Han, S. Han, Y. Wang, *Acta Chim. Slov.* **2016**, 63, 200–203; DOI:10.17344/acsi.2016.2266  
 (d) S. Guo, N. Sun, Y. Ding, A. Li, Y. Jiang, W. Zhai, Z. Li, D. Qu, Z. You, *Z. Anorg. Allg. Chem.* **2018**, 644, 1172–1176; DOI:10.1002/zaac.201800060  
 (e) L. Li, K.-W. Lv, Y.-T. Li, G.-F. Jiang, Y. Xin, L. Ye, Y. Zhang, H. Liu, C.-H. Shang, Z.-L. You, *Chinese J. Inorg. Chem.* **2017**, 33, 905–912.
14. (a) M. Liang, D.-H. Zou, *Acta Chim. Slov.* **2016**, 63, 180–185; DOI:10.17344/acsi.2015.2169  
 (b) L. Wang, Y.-J. Han, Q.-B. Li, L.-W. Xue, *Acta Chim. Slov.* **2016**, 63, 822–826; DOI:10.17344/acsi.2016.2699  
 (c) T. Jakusch, K. Kozma, E. A. Enyedy, N. V. May, A. Roller, C. R. Kowol, B. K. Keppler, T. Kiss, *Inorg. Chim. Acta* **2018**, 472, 243–253; DOI:10.1016/j.ica.2017.08.018  
 (d) E. Kober, Z. Janas, J. Jezierska, *Inorg. Chem.* **2016**, 55, 10888–10898; DOI:10.1021/acs.inorgchem.6b01283  
 (e) A.-M. Li, *J. Coord. Chem.* **2014**, 67, 2076–2085. DOI:10.1080/00958972.2014.931577

## Povzetek

Sintetizirali smo dva nova oksidovanadijeva(V) kompleksa, [VOL<sup>1</sup>L] · EtOH (1) in [VOL<sup>2</sup>L] · EtOH (2) (L = acetohidroksamat), pripravljenega iz aroilhidrazona N<sup>7</sup>-(5-bromo-2-hidroksibenziliden)-4-metoksibenzohidrazida (H<sub>2</sub>L<sup>1</sup>) in N<sup>7</sup>-(5-bromo-2-hidroksibenziliden)-4-metilbenzohidrazida (H<sub>2</sub>L<sup>2</sup>) ter ju okarakterizirali z elementno analizo, FT-IR, <sup>1</sup>H in <sup>13</sup>C NMR spektroskopijo in monokristalno rentgensko strukturno difrakcijo. Kompleksa imata oktaedrično strukturo, v kateri je aroilhidrazonski ligand dianion. Monokristalna strukturna analiza razkrije, da je V center koordiniran z donorskimi atomi aroilhidrazonskega liganda, acetohidroksamatnega liganda in oksido skupino. Kristalna struktura kompleksov je stabilizirana z vodikovimi vezmi. Kompleksa sta učinkovita katalizatorja za epoksidacijo olefinov.

Scientific paper

# An Electrochemical Sensing Platform Based on Iridium Oxide for Highly Sensitive and Selective Detection of Nitrite and Ascorbic Acid

Totka Dodevska,\* Ivan Shterev and Yanna Lazarova

Department of Organic Chemistry and Inorganic Chemistry, University of Food Technologies, 26, Maritsa Boulevard, Plovdiv 4002, Bulgaria

\* Corresponding author: E-mail: dodevska@mail.bg  
Tel.: +359 32 603 679; Fax: +359 32 644 102

Received: 10-08-2018

## Abstract

Iridium oxide ( $\text{IrO}_x$ ) was electrodeposited onto glassy carbon electrode applying two-step potential cycling procedure. The electrocatalytic properties of the modified electrode  $\text{IrO}_x/\text{GC}$  were evaluated with regards to electrochemical oxidation of nitrite and ascorbic acid (AA). The developed electrode-catalyst have been extensively studied by various electrochemical techniques. Differential pulse voltammetry (DPV) experiments indicated that the modified electrode possesses excellent electrocatalytic activity towards the oxidation of both nitrite and AA in neutral medium and offers simultaneous quantification of these substances. Constant potential amperometry studies also were performed – the  $\text{IrO}_x/\text{GC}$  showed sensitive response to nitrite ( $159.7 \mu\text{A mM}^{-1} \text{cm}^{-2}$ ) with a wide linear range from 0.002 to 10 mM at 0.77 V (vs.  $\text{Ag}/\text{AgCl}$ , 3 M KCl), and to AA ( $96.2 \mu\text{A mM}^{-1} \text{cm}^{-2}$ ) with a linear range from 0.01 to 3 mM at 0.025 V. The detection limit was  $0.63 \mu\text{M}$  nitrite and  $4 \mu\text{M}$  AA, respectively, and both of them had fast response within 5 s. Considering the simple and rapid electrodeposition procedure for preparation,  $\text{IrO}_x/\text{GC}$  is a new electrode-catalyst for sensitive and selective quantitative detection of nitrite and AA. The wide linear range, good selectivity, reproducibility of the amperometric response and long-time stability of the  $\text{IrO}_x/\text{GC}$  make it a promising sensing material for practical nonenzymatic quantitative detection of nitrite and AA.

**Keywords:** Electrochemistry; electrocatalytic oxidation; sensor; nitrite; ascorbic acid

## 1. Introduction

Nitrite ( $\text{NO}_2^-$ ) is widely used food additive in meat products as an antimicrobial agent (prevents bacterial growth), a preservative (retards lipid peroxidation) and a color fixative.<sup>1</sup> Nitrate also has been found in beverages, commercially available vegetables and drinking water. The concentration of  $\text{NO}_2^-$  is one of the most important parameters in water quality – the World Health Organization (WHO) recommends a guideline value of  $3 \text{ mg L}^{-1}$  ( $65 \mu\text{M}$ ) and a provisional guideline value of  $0.2 \text{ mg L}^{-1}$  ( $4.3 \mu\text{M}$ ) for short-term and long-term exposures, respectively;<sup>2,3</sup> according to the regulation of the European Community the maximum permissible nitrite content in drinking water is  $0.1 \text{ mg L}^{-1}$  ( $2.2 \mu\text{M}$ ).<sup>4,5</sup> A serious threat to human health is the overweight content of nitrite in food products, as the excessive ingestion of nitrites via the dietary intake has potential toxic and mutagenic effects. Nitrite consumption has been linked with chronic obstructive pulmonary disease,<sup>6</sup> methemoglo-

binemia<sup>7</sup> – nitrite interacts with the hemoglobin ( $\text{Fe}^{2+}$ ) to form methemoglobin ( $\text{Fe}^{3+}$ ) which has no oxygen carrying ability, gastric and oesophageal cancer<sup>8</sup> – nitrite ion is an essential precursor in the formation of highly carcinogenic nitrosamines in the stomach. The acceptable daily intake of nitrite is  $0\text{--}0.07 \text{ mg kg}^{-1}$  (body weight) per day.<sup>9</sup>

Classical analytical techniques have been employed for quantitative detection of nitrite such as coulometric titration,<sup>10</sup> spectrophotometry,<sup>11</sup> chemiluminescence,<sup>12</sup> capillary electroforesis,<sup>13</sup> high-performance liquid chromatography.<sup>14</sup> Most of these analytical methods, however, require complex painstaking procedures for sample pre-treatment, as well as involve fairly expensive and sophisticated instruments. Therefore, the importance of improved analytical methods for determination of nitrite has received considerable attention.

Nitrite ion is an electroactive and can be quantified electrochemically. In comparison with the aforementioned techniques, electrochemical analysis has been considered

as a low-cost and effective way due to its intrinsic simplicity and high sensitivity. The electrochemical sensor devices provide the opportunity for an accurate, sensitive, selective, interference-free, fast, cost-effective and susceptible to automation analysis, and are a promising alternative of the traditional analytical techniques.

The electrochemical determination of nitrite can be realized based on oxidation or reduction, as oxidation is usually preferred because cathodic measurement is prone to interference from other easily reducible species such as nitrate ion (product of nitrite reduction) and molecular oxygen. At the same time detection based on the oxidation of nitrite offers some advantages, such as no interference from nitrate ion, sulfate ion, and molecular oxygen. Nitrite can be oxidised at conventional electrode – bare glassy carbon (GC), platinum or gold electrodes, but the direct electrooxidation of nitrite ions requires high overpotential at the surface of the unmodified electrode and quantification suffers from interference from other compounds. The process is accompanied by co-oxidation of interfering species that present in the real samples. As a result, the registered signal is higher and does not correspond to the real concentration of the analyte.

In order to improve the oxidation response of  $\text{NO}_2^-$  (resp., the selectivity of detection), the applied potential should be efficiently lowered. This can be achieved by modifying the surface of the bare electrode with suitable electrocatalytic active phase, that facilitates electron-transfer process – conducting polymer films,<sup>15–22</sup> metal particles decorated polymers,<sup>3,23,24</sup> metal complexes,<sup>25–27</sup> metal-organic frameworks,<sup>28</sup> metal or metal oxide particles,<sup>29–35</sup> bimetallic nanomaterials,<sup>36</sup> ionic liquid,<sup>29,37</sup> methylene blue,<sup>38</sup> chemically reduced graphene oxide.<sup>39</sup>

One of the main interfering substances in the quantitative detection of nitrite in food samples is ascorbic acid. Ascorbic acid (AA), also known as vitamin C, is one of the most important vitamins that takes part in some important biological reactions such as free radical scavenging and cancer preventing. This compound exists in plant, especially fresh fruits and leafy vegetables, and animal tissues. The strong antioxidant activity of AA and its ability to protect oxidizable constituents, including phenolic and flavor compounds, is the main factor AA to be frequently used in food industry to prevent unwanted changes in color or flavor. Additives, based on AA, are widely used in production of several foods and drinks such as beer, jam, sweets, fruit juices, fish products and meats. AA is used as well as in cosmetics (as a skin conditioning agent) and in pharmaceutical industry (as a diet supplement in various forms). Side effects are not observed at normal AA intake (about 70–90 mg for adults),<sup>40</sup> due to the fact that it is water soluble and quickly excreted. After single oral doses of vitamin C greater than 2 g daily, gastrointestinal distress and diarrhea are the most common side effects. However, in individuals with renal dysfunction, production of kidney stones is observed as a serious side effect with vitamin C overdose. Due to the crucial

role of AA in biochemistry and in industrial applications, recently there is a considerable research interest to develop electrochemical sensors for detection of AA content in various samples including foods, drugs and biological fluids.<sup>40–51</sup>

Among the above-mentioned modified electrodes-catalysts applied for nitrite detection, metal oxide-modified electrodes possess some unique electrochemical properties and advantages compared to the other – high stability, enhancement of reaction rate due to the redox couples of oxide species of two different states, as well as weak adsorption or exclusion of hydrogen species on an oxide surface.<sup>31</sup> Because of the high electron transfer rate constant of Ir(IV)/Ir(III) redox couple,  $\text{IrO}_x$  were used as an electron transfer mediator and successfully applied in electrocatalysis.<sup>52–55</sup> The present research reports an amperometric sensor for nitrite and AA detection, based on modified with iridium oxide GC electrode. As an electrode material, GC is distinguished by its chemical inertness, low background currents, wide potential window and low price. Cyclic voltammetry (CV) was applied to form iridium oxide layers at the surface of the bare GC electrode as the fastest and simplest electrodeposition technique, that not requires expensive equipment or special experimental conditions (high temperature and pressure). The developed electrode exhibits remarkable electrocatalytic activity in two independent electrocatalytic processes – oxidation of nitrite (at an applied potential of 0.77 V vs. Ag/AgCl, 3 M KCl) and oxidation of AA (at 0.025 V) and offers simultaneous quantification of both substances. The modified electrode has advantages such as high sensitivity in a relatively wide range of substrate concentrations, selectivity, excellent reproducibility of the current signal and long-term stability.

## 2. Experimental

### 2.1. Materials

$\text{Na}_2\text{IrCl}_6$ , HCl,  $\text{H}_2\text{SO}_4$ , NaOH,  $\text{NaNO}_2$ ,  $\text{NaNO}_3$ ,  $\text{NaOOCCH}_3$ , NaCl,  $\text{Na}_2\text{CO}_3$ , KCl, KBr,  $\text{KBrO}_3$ , KI,  $\text{MgCl}_2$ ,  $\text{CuSO}_4$  were purchased from Fluka;  $\text{Na}_2\text{HPO}_4 \cdot 12\text{H}_2\text{O}$ ,  $\text{NaH}_2\text{PO}_4 \cdot 2\text{H}_2\text{O}$ ,  $\text{K}_3[\text{Fe}(\text{CN})_6]$ , sodium citrate ( $\text{Na}_3\text{C}_6\text{H}_5\text{O}_7$ ), ascorbic acid ( $\text{C}_6\text{H}_8\text{O}_6$ ) and glucose ( $\text{C}_6\text{H}_{12}\text{O}_6$ ) were purchased from Sigma-Aldrich. All chemicals used were of analytical grade and double distilled water was used to prepare aqueous solutions. Buffer solution, 0.1 M, was made of monobasic and dibasic sodium phosphates dissolved in double distilled water with pH 7.0 adjusted with NaOH. The working electrode was a disc (3 mm diameter) from glassy carbon rod (Metrohm) in Teflon holder.

### 2.2. Apparatus and Measurements

All the electrochemical measurements were performed using potentiostat EmStat2 (PalmSens BV, The

Netherlands) interfaced with a computer and controlled by 'PSTrace 2.5.2' software. A conventional thermostated three-electrode cell including a working electrode, an Ag/AgCl (3 M KCl) as a reference electrode, and a platinum wire as a counter electrode was used. Before the measurement the background electrolyte was purged with pure argon for at least 15 min to remove dissolved oxygen. The modified electrode was investigated using cyclic voltammetry (CV), differential pulse voltammetry (DPV) and amperometry at a constant potential. Cyclic voltammograms (CVs) were recorded at scan rates from 10 to 150  $\text{mV s}^{-1}$ . The DPV parameters were chosen as follows: scan rate 9  $\text{mV s}^{-1}$ , pulse amplitude 50 mV, pulse interval 70 ms. Amperometric ( $i-t$ ) curves were monitored at a constant applied potential under hydrodynamic condition. The experimental data analysis was performed using software package 'OriginPro 8.0'.

### 2. 3. Electrodeposition of Iridium Oxide onto Glassy Carbon Electrode

Prior to the modification, the glassy carbon electrode surface was polished mechanically using 0.05  $\mu\text{m}$  alumina slurry, rinsed, sonicated in double distilled water for 5 min and allowed to dry at room temperature. The electrodeposition of  $\text{IrO}_x$  onto the GC electrode was carried out in two-step procedure as follows: deposition of iridium from 2.0 %  $\text{Na}_2\text{IrCl}_6$  in 0.1 M HCl solution using CV from  $-0.3$  to  $0.3$  V applying 100 cycles at scan rate of  $100 \text{ mV s}^{-1}$  and subsequent oxidation of iridium applying 100 cycles from  $-0.3$  to  $1.4$  V in electrolyte  $0.5 \text{ M H}_2\text{SO}_4$ .<sup>55</sup>

## 3. Results and Discussion

### 3. 1. Electrochemical Behavior of $\text{IrO}_x/\text{GC}$ Modified Electrode

The electrochemical behavior of the  $\text{IrO}_x/\text{GC}$  modified electrode was investigated by cyclic voltammetry. The

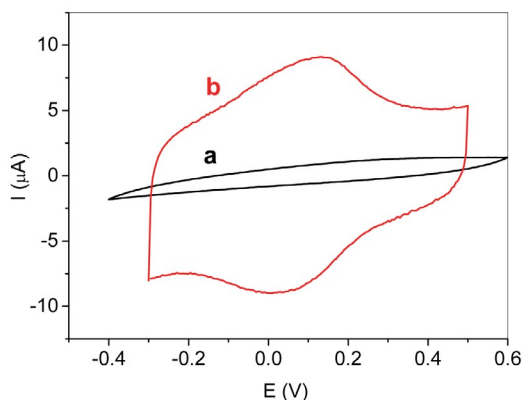


Fig. 1. CVs of the bare GC electrode (curve a) and  $\text{IrO}_x/\text{GC}$  modified electrode (curve b) in PBS, pH 7.0, recorded at scan rate of  $50 \text{ mV s}^{-1}$ .

cyclic voltammograms of the bare GC electrode and  $\text{IrO}_x/\text{GC}$  modified electrode registered in PBS pH 7.0 are shown in Fig. 1. Compared with the bare GC electrode (curve a), the background current of the modified electrode is apparently larger, which indicates that the effective electrode surface area is significantly enhanced (curve b). The pair of well-defined redox peaks at  $0.13 \text{ V}$  and  $0.02 \text{ V}$ , respectively, assigned to the redox couple  $\text{Ir(III)/Ir(IV)}$ , proves the successful modification of the electrode surface.

For the evaluation of the electrochemically active surface area of the modified electrode, cyclic voltammograms were registered at different scan rates using  $[\text{Fe}(\text{CN})_6]^{3-/4-}$  in 0.1 M KCl as a redox probe. The data confirm that the  $\text{IrO}_x$ -deposit favors the electron transfer rate of the redox probe. A noticeable enhancement in the peak magnitude accompanied with decreased peak potential separation ( $\Delta E_p$ ) were observed after the modification of bare GC, which indicated that the  $\text{IrO}_x$ -deposit could enhance the effective surface area and the conductivity of the electrode.

For the single electron transfer of  $\text{Fe}^{3+}/\text{Fe}^{4+}$  redox reaction at a scan rate of  $50 \text{ mV s}^{-1}$  for  $\text{IrO}_x/\text{GC}$  modified electrode was determined peak potential separation  $\Delta E_p = 0.09 \text{ V}$ , which is  $0.07 \text{ V}$  lower than that of the bare GC electrode ( $\Delta E_p = 0.16 \text{ V}$ ). A linear dependence was obtained between the peak currents and the square root of the scan rate, demonstrating that the redox process of ferri/ferrocyanide at the modified electrode surface is diffusion controlled (Fig. 2). The electro-active surface area was estimated according to Randles–Ševčík equation:

$$I_p = 0.4463 \left( F^3 / RT \right)^{1/2} n^{3/2} A_0 D_0^{1/2} C_0 v^{1/2} \quad (1)$$

where  $I_p$  is the peak current (A),  $v$  is the applied scan rate ( $\text{V s}^{-1}$ ),  $n = 1$  (number of electrons involved in the redox reaction),  $A_0$  is the electrode surface area ( $\text{cm}^2$ ),  $D_0$  is diffusion coefficient ( $D_0 = 7.6 \times 10^{-6} \text{ cm}^2 \text{ s}^{-1}$ ),  $C_0$  is the bulk concentration of the substrate ( $C_0 = 5 \times 10^{-3} \text{ M}$ ). In this system, the slope is 243.94, taking temperature  $T = 298 \text{ K}$ , molar gas constant  $R = 8.314 \text{ J K}^{-1} \text{ mol}^{-1}$ , and Faraday's

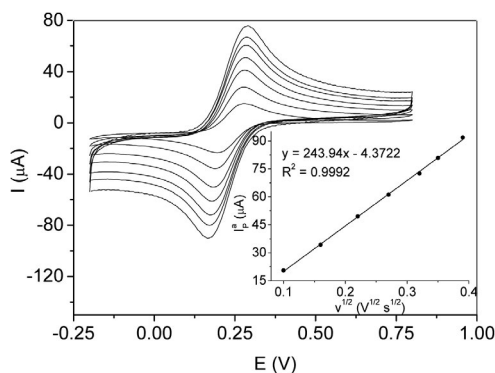


Fig. 2. CVs of modified electrode  $\text{IrO}_x/\text{GC}$  in presence of 5 mM of  $\text{K}_3[\text{Fe}(\text{CN})_6]$  in 0.1 M KCl solution registered at different scan rates ( $10\text{--}150 \text{ mV s}^{-1}$ ). Inset: plot of anodic peak current vs.  $v^{1/2}$ .

constant  $F = 96480 \text{ C mol}^{-1}$ , the effective surface area was calculated to be  $0.065 \text{ cm}^2$ . Compared with the bare GC electrode ( $0.036 \text{ cm}^2$ , calculated analogously), the electroactive surface area of the  $\text{IrO}_x/\text{GC}$  modified electrode was increased by approximately 80 %.

### 3. 2. Electrocatalytic Oxidation of Nitrite and Ascorbic Acid

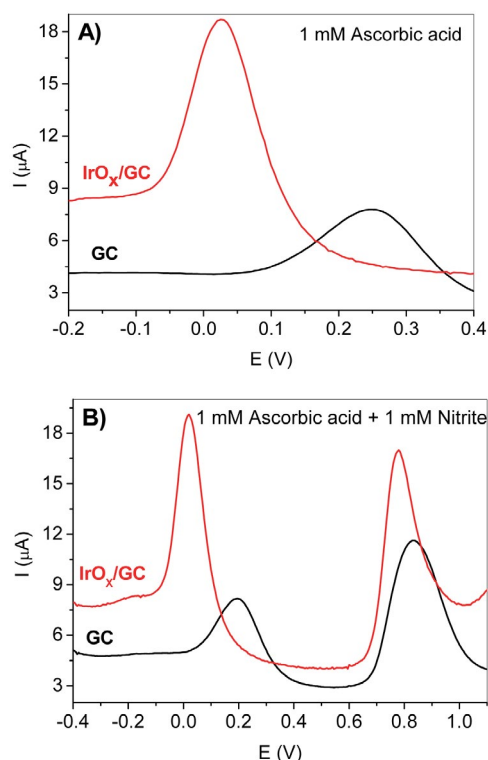
To study the application of the modified electrode  $\text{IrO}_x/\text{GC}$  in electrochemical sensing of nitrite and AA, electrooxidation and quantitative detection of these substances in neutral medium were investigated. The performance of the modified electrode regarding the sensing of each of the substances was evaluated using two electrochemical techniques – DPV and constant potential amperometry, according to the sensitivity, linear range, detection limit, and stability.

DPV technique was first employed to study the electrochemical oxidation of AA on  $\text{IrO}_x/\text{GC}$  and bare GC electrode in PBS, pH 7.0 (Fig. 3A). The electrooxidation of AA was shown in the form of peak shaped differential pulse voltammogram with maximum current intensity at 0.25 V on bare GC (black curve) and at 0.025 V (red curve) on modified  $\text{IrO}_x/\text{GC}$  electrode, respectively. The modified electrode possesses a better sensitivity and selectivity in comparison to the bare GC – the oxidation peak potential

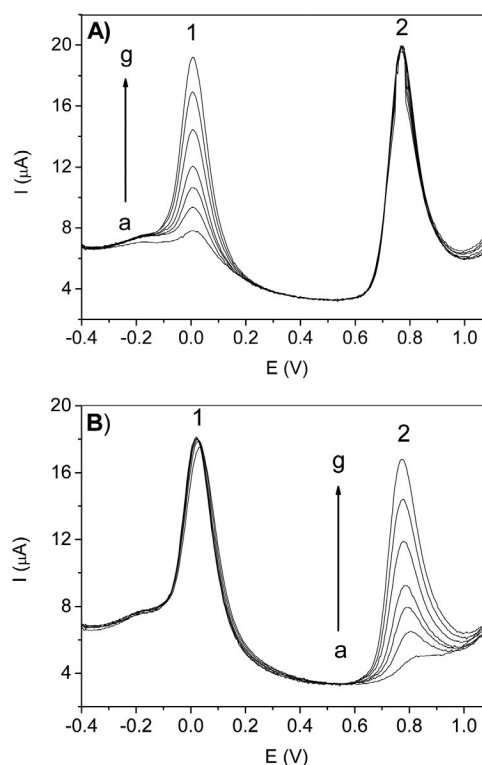
of ascorbic acid at the modified electrode is significantly shifted (by  $\sim 0.225 \text{ V}$ ) in the negative direction compared with the bare GC, and 2.5-fold increase in the peak current at the modified  $\text{IrO}_x/\text{GC}$  was observed. The oxidation potential value ( $0.025 \text{ V}$ ) is significantly lower than the AA oxidation potential reported in previous research articles.<sup>40,45–51</sup> The results indicate that the presented modified electrode is distinguished by a higher efficiency in the selective detection of ascorbic acid compared to other electrocatalysts.

The possibility of the modified electrode for simultaneous detection of AA and nitrite was next examined. In buffer solution, that contains 1 mM AA and 1 mM nitrite, DPV response of the modified electrode  $\text{IrO}_x/\text{GC}$  shows two well-defined and well-separated oxidation peak current responses as presented in Fig. 3B. It is obvious that the oxidation potential of AA is much more negative than those of nitrite ( $0.77 \text{ V}$ ). The peak separation is about  $0.745 \text{ V}$  between AA and nitrite, implying it is feasible to detect nitrite in the presence of AA by DPV with the  $\text{IrO}_x/\text{GC}$  electrode.

Fig. 4A shows the DPV curves obtained at the  $\text{IrO}_x/\text{GC}$  when the concentration of AA is changed (peak 1) while the concentration of nitrite kept constant (peak 2). The peak current associated with the oxidation of AA is increased linearly with the increase in AA concentration,



**Fig. 3.** A) DPV response of modified electrode  $\text{IrO}_x/\text{GC}$  for 1 mM ascorbic acid in PBS (pH 7.0); B) Simultaneous DPV response of  $\text{IrO}_x/\text{GC}$  for a mixture of ascorbic acid (1 mM) and nitrite (1 mM) in PBS (pH 7.0).



**Fig. 4.** DPVs response of  $\text{IrO}_x/\text{GC}$  in PBS (pH 7.0) containing: A) 1 mM nitrite (peak 2) in the presence of different concentrations of AA (peak 1); B) 1 mM AA (peak 1) in the presence of different concentrations of nitrite (peak 2). Concentrations (in mM) as follows: (a) 0.1, (b) 0.2, (c) 0.3, (d) 0.4, (e) 0.6, (f) 0.8 and (g) 1.0.

while the peak height of nitrite remains stable. The observed phenomenon clearly shows that it is possible to detect selectively AA concentration in the presence of nitrite ions. An analogous analytical test was also carried out at a constant concentration of AA and varying concentration of nitrite (Fig 4B). The obtained results prove that the modified electrode possesses the ability to detect single species separately or to determine the specific concentrations of mixtures of the two species.

### 3. 2. 1. Voltammetric and Amperometric Detection of Nitrite

The DPV curves of the bare GC and of the IrO<sub>x</sub>/GC electrode (Fig. 3B) clearly show that the modified electrode exhibits higher electrocatalytic activity towards nitrite oxidation. In the presence of nitrite the higher peak current and shift towards lower potential indicate better catalytic behaviour of the modified electrode.

Fig. 5 presents the DPV curves of nitrite with different concentrations (0.2–3.1 mM). The peak current was proportional to the nitrite concentration and it can be expressed in a model such as:  $y = ax + b$ , where  $a$  is the slope of the calibration curve in terms of sensitivity. The linear regression equation was as follows:  $I_p (\mu\text{A}) = 9.419 C (\text{mM}) + 0.397$  and was accomplished with a correlation coefficient of 0.998 (Fig. 4, inset). The proposed electrode shows good electrochemical sensitivity of  $133.2 \mu\text{A mM}^{-1} \text{cm}^{-2}$  (normalized to the electrode geometric surface area) up to 3.1 mM nitrite.

The reproducibility of the current response of the modified electrode is essential for its successful application as a sensing element in construction of electrochemical sensor systems. In this connection, the reproducibility of the DPV current of IrO<sub>x</sub>/GC to 0.6 mM and 1.2 mM nitrite was examined. For 10 successive independent measurements in presence of 0.6 mM nitrite the electrode response was  $6.099 \pm 0.064 \mu\text{A}$  and the relative standard deviation (RSD) was calculated to be 1.05 %. Analogous studies car-

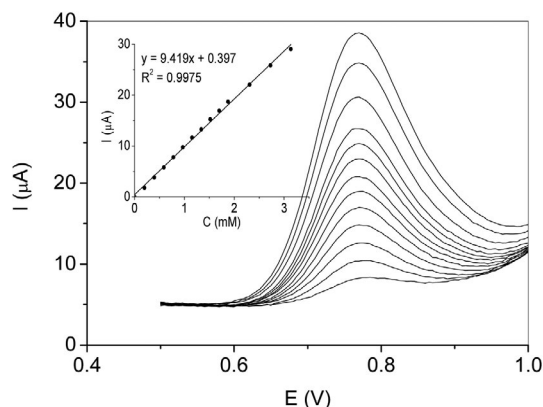


Fig. 5. DPVs of modified electrode IrO<sub>x</sub>/GC in the presence of various concentrations of nitrite in PBS (pH 7.0). Inset: linear relationship between the peak current and the concentration.

ried out in presence of 1.2 mM nitrite show electrode response of  $11.659 \pm 0.114 \mu\text{A}$  and RSD of 0.98 %. The results prove that the modified electrode possesses excellent reproducibility of the current signal.

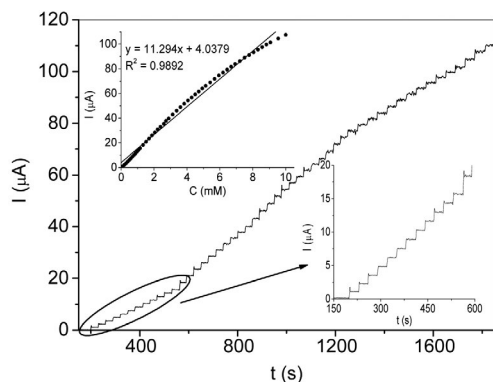
Selectivity plays a vital role in practical use of sensors. In order to study the selectivity of the modified electrode, the interference effect of various species (in concentrations 10 times that of nitrite): Cl<sup>-</sup>, Br<sup>-</sup>, CO<sub>3</sub><sup>2-</sup>, NO<sub>3</sub><sup>-</sup>, SO<sub>4</sub><sup>2-</sup>, BrO<sub>3</sub><sup>-</sup>, CH<sub>3</sub>COO<sup>-</sup>, Mg<sup>2+</sup>, Cu<sup>2+</sup>, glucose and sodium citrate, was examined during DPV current response for NO<sub>2</sub><sup>-</sup>, performing an independent DPV measurement for each substance, respectively. The response current increased about 6.8 % when Br<sup>-</sup> was injected into the buffer solution, suggesting this anion might have a moderate interference in the detection of nitrite. In the other experiments, no obvious interference was observed – the changes in current response on the modified electrode keep within 5 % in the presence of 10 mM Cl<sup>-</sup>, CO<sub>3</sub><sup>2-</sup>, NO<sub>3</sub><sup>-</sup>, SO<sub>4</sub><sup>2-</sup>, BrO<sub>3</sub><sup>-</sup>, CH<sub>3</sub>COO<sup>-</sup>, Mg<sup>2+</sup>, Cu<sup>2+</sup>, glucose and sodium citrate in 1 mM nitrite solution, indicating that they have negligible interference for nitrite detection (Table 1).

Table 1. Changes in DPV current response on the modified electrode in the presence of several inorganic and organic compounds (10 mM of each interferent) in 1 mM nitrite solution.

Interferent	Signal change (%)	Interference
NaCl	-2.6	Negligible
KBr	+6.8	Moderate
MgCl <sub>2</sub>	-3.6	Negligible
Na <sub>2</sub> CO <sub>3</sub>	-0.96	Negligible
NaNO <sub>3</sub>	-1.2	Negligible
CuSO <sub>4</sub>	-0.66	Negligible
KBrO <sub>3</sub>	+4.4	Negligible
NaOOCCH <sub>3</sub>	-0.55	Negligible
C <sub>6</sub> H <sub>12</sub> O <sub>6</sub>	-0.32	Negligible
Na <sub>3</sub> C <sub>6</sub> H <sub>5</sub> O <sub>7</sub>	-1.3	Negligible

The amperometric response was evaluated for the modified electrode with the successive additions of nitrite at a fixed potential. Fig. 6 displays the authentic record of the amperometric response of IrO<sub>x</sub>/GC to successive additions (in 30 s intervals) of NO<sub>2</sub><sup>-</sup> stock solution at a constant applied potential of 0.77 V under constant stirring. A remarkable increase and a fast response of the amperometric current were observed. Upon addition of nitrite the modified electrode shows increasing staircase current response, corresponding to the electrochemical oxidation of the analyte, which evidences that IrO<sub>x</sub>/GC efficiently promoted the electrooxidation of nitrite. Steady-state current value was reached within 5 s.

The background subtracted steady-state response of the electrode (Fig. 6, inset) was proportional to the nitrite concentration up to 10 mM (correlation coefficient of 0.989) with a sensitivity of  $11.294 \mu\text{A mM}^{-1}$  (or  $159.7 \mu\text{A mM}^{-1} \text{cm}^{-2}$ ), calculated on the basis of 49 points. The lim-



**Fig. 6.** Amperometric response of modified electrode  $\text{IrO}_x/\text{GC}$  in PBS (pH 7.0) for successive additions of nitrite at potential of 0.77 V. Inset: the enlarged initial section of the amperometric curve (12 injections of 0.1 mM  $\text{NO}_2^-$  and 1 injection of 0.2 mM  $\text{NO}_2^-$  were added) and the corresponding calibration plot.

it of detection is 0.63  $\mu\text{M}$  (defined at a signal-to-noise ratio of 3), which is lower than the drinking water limit quantity postulated by the WHO (4.3  $\mu\text{M}$ ).<sup>2</sup>

The selectivity of the modified electrode for nitrite was also confirmed by amperometric measurements. For interference test, we used the same common interfering

ions and organic substances as reported for our DPV experiments. Amperometric response of  $\text{IrO}_x/\text{GC}$  towards the additions of these substances, followed by nitrite addition, were examined at a constant potential of 0.77 V. Fig. 7 shows the authentic response of electrode  $\text{IrO}_x/\text{GC}$  for the interval (in 25 s) additions of 0.35 mM nitrite and a 10-fold concentration of the above mentioned interfering substances. The amperometric record clearly shows that the tested species had no effect on the quantitative nitrite detection. No response was observed for modified electrode in the presence of interfering substances and the electrode response for nitrite after adding interfering substances was not changed. The results reveal the application potential of the modified electrode  $\text{IrO}_x/\text{GC}$  for precise sensing of nitrite in real samples.

The comparison of sensing performance based on different electrochemical methods and modified materials for the detection of nitrite in previous reports was shown in Table 2. We have summarized various nitrite sensors with respect to the working potential, sensitivity, linearity, detection limit and the reproducibility of the signal. From the data presented it can be seen that the proposed  $\text{IrO}_x$ -modified glassy carbon electrode possesses superior reproducibility of the current response. It is found that the

**Table 2.** Comparison of the proposed  $\text{IrO}_x/\text{GC}$  with other reported sensors for determination of nitrite.

Sensing electrode <sup>a</sup>	Technique <sup>b</sup>	E, V	Sensitivity, $\mu\text{A mM}^{-1} \text{cm}^{-2}$	Linear range, $\mu\text{M}$	Detection limit, $\mu\text{M}$	RSD, %
p-NiTAPc/GC <sup>56</sup>	DPA	0.82 <sup>c</sup>	–	0.5–8000	0.1	2.8 (n = 12)
CDP/GS/MWCNTs/GC <sup>19</sup>	CV	0.7 <sup>c</sup>	12.68 <sup>e</sup>	5–6750	1.65	3.7(n = 5)
Hb/PLE <sup>57</sup>	DPV	–0.8 <sup>c</sup>	2.164 <sup>g</sup>	10–220	5.0	2.0(n = 3)
Nano-Pt/P3MT/GC <sup>24</sup>	DPV	0.78 <sup>d</sup>	222.82	8–1700	1.5	3.4(n = 10)
Thionine/ACNTs/GC <sup>58</sup>	DPV	0.8 <sup>d</sup>	–	3–500	1.12	2.75(n = 5)
AgPs-IL-CPE <sup>29</sup>	SWV	–	–	50–1000	3.0	0.3(n = 7)
EAG/SPCE <sup>59</sup>	Amp	0.8 <sup>d</sup>	126	0.1–16400	0.038	1.4(n = 5)
GR/PPy/CS/GC <sup>20</sup>	Amp	0.9 <sup>c</sup>	40.0 <sup>e</sup>	0.5–722	0.1	1.8(n = 10)
Poly-TBO-SWCNT/GC <sup>21</sup>	Amp	0.92 <sup>d</sup>	84.3 <sup>e</sup>	1–4000	0.37	–
Nano-Au/P3MT/GC <sup>60</sup>	Amp	0.78 <sup>c</sup>	–	10–1000	2.3	3.0(n = 10)
PAOA/GC <sup>61</sup>	Amp	1.0 <sup>c</sup>	64.3	5–2000	2.0	1.2(n = 6)
CoHCF/CPE <sup>27</sup>	Amp	0.92 <sup>d</sup>	11.11 <sup>e</sup>	100–2150	1.19	3.27
CR-GO/GC <sup>39</sup>	Amp	0.8 <sup>d</sup>	0.0267 <sup>f</sup>	8.9–167	1.0	2.29(n = 4)
MWCNTs/MB paper <sup>38</sup>	Amp	0.83 <sup>d</sup>	400	12–2500	3.6	–
PANI-MoS <sub>2</sub> /GC <sup>22</sup>	Amp	0.9 <sup>c</sup>	28.68	4–4834	1.5	–
Fe-HNPs/GC <sup>33</sup>	Amp	0.73 <sup>c</sup>	19.83 <sup>e</sup>	9–3000	2.6	0.7
AgNPs/GC <sup>34</sup>	Amp	0.82 <sup>c</sup>	–	10–1000	1.2	–
ZnO@rFGO/GC <sup>35</sup>	Amp	0.9 <sup>d</sup>	–	10–5000	41	–
AuNPs/SG/GC <sup>62</sup>	Amp	0.73 <sup>c</sup>	45.44 <sup>e</sup>	10–3960	0.2	1.92(n = 8)
$\text{IrO}_x/\text{GC}$ <sup>This work</sup>	DPV	0.77 <sup>d</sup>	133.2	10–3100	0.63	2.6(n = 5)
	Amp		159.7	2–10000	5	1.05(n = 10)

<sup>a</sup>GC – glassy carbon; SPCE – screen printed carbon electrode; CPE – carbon paste electrode; NPs – nanoparticles; MWCNTs – multiwall carbon nanotubes, SWCNTs – singlewall carbon nanotubes; p-NiTAPc – polymeric nickel tetraaminothiophalocyanine; CDP/GS – poly-cyclodextrin/graphene; Hb – hemoglobin; PLE – pencil lead electrode; EAG – electrochemically activated graphite; ACNTs – aligned carbon nanotubes; GR/PPy/CS – graphene/polypyrrole/chitosan; TBO – Toluidine Blue O; P3MT – poly(3-methylthiophene); PAOA – poly(aniline-co-o-aminophenol); CoHCF – cobalt hexacyanoferrate; CR-GO – chemically reduced graphene oxide; MB – methylene blue; PANI – polyaniline; IL – ionic liquid; Fe-HNPs – hollow hematite nano-polyhedrons; rFGO – reduced functionalized graphene oxide; <sup>b</sup>DPA – differential pulse amperometry; CV – cyclic voltammetry; DPV – differential pulse voltammetry; SWV – square wave voltammetry; Amp – amperometry; <sup>c</sup> Reference electrode: saturated calomel electrode; <sup>d</sup> Reference electrode: Ag/AgCl, 3 M KCl; <sup>e</sup> in:  $\mu\text{A mM}^{-1}$ ; <sup>f</sup> in:  $\text{A M}^{-1}$ ; <sup>g</sup> in:  $\text{nA } \mu\text{M}^{-1}$ .

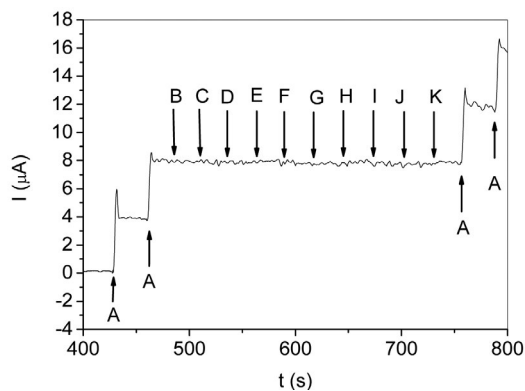


Fig. 7. Amperometric *i-t* curve of modified electrode IrO<sub>x</sub>/GC for the determination of 0.35 mM NO<sub>2</sub><sup>-</sup> (A) in the presence of 3.5 mM of different interfering species (B) CH<sub>3</sub>COO<sup>-</sup>, (C) Cl<sup>-</sup>, (D) Br<sup>-</sup>, (E) CO<sub>3</sub><sup>2-</sup>, (F) citrate, (G) BrO<sub>3</sub><sup>-</sup>, (H) NO<sub>3</sub><sup>-</sup>, (I) SO<sub>4</sub><sup>2-</sup>, (J) glucose and (K) Mg<sup>2+</sup>, added one by one with an interval of 25 s to 0.1 M PBS (pH 7.0) at an applied potential of 0.77 V.

developed electrocatalyst is more preferable than a number of other electrode-catalysts, employed as nitrite sensors, in one or more categories, particularly because of the lower working potential, higher sensitivity and wider linear range.

### 3. 2. 2. Voltammetric and Amperometric Detection of Ascorbic Acid

The analytical parameters of the modified electrode IrO<sub>x</sub>/GC for AA quantitative detection also were studied in detail. A clear increase in DPV peak current was observed upon increasing the concentration of AA and the peak current was found to increase linearly as a function of the concentration up to 1.9 mM with a correlation coefficient of 0.999 (Fig. 8, Inset). The sensitivity calculated from the slope of the regression line was 9.55 μA mM<sup>-1</sup> (135 μA mM<sup>-1</sup> cm<sup>-2</sup>). Measurements (n = 10) done with the presented modified electrode in presence of 1 mM AA showed current signal of 9.256 ± 0.084 μA

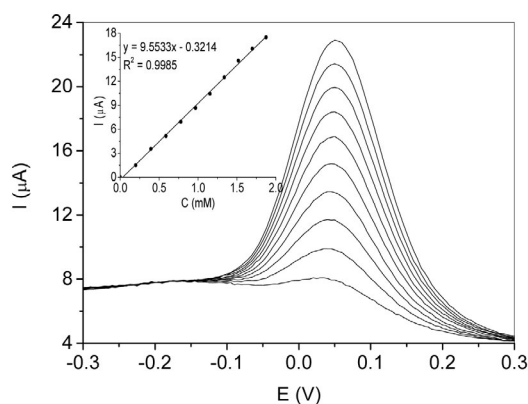


Fig. 8. DPVs of modified electrode IrO<sub>x</sub>/GC in the presence of various concentrations of AA in PBS (pH 7.0). Inset: linear relationship between the peak current and the concentration.

featuring extremely high reproducibility (RSD equal to 0.91 %).

Fig. 9 displays the current-time response of the modified electrode recorded after successive additions of 0.1 and 0.2 mM AA into magnetically stirred PBS (pH 7.0) at an applied potential of 0.025 V. The electrode reaction is fast in reaching a dynamic equilibrium upon each addition of AA and the response time was 5 s. The calibration plot corresponding to the amperometric current response is illustrated as an Inset of the same figure. The sensitivity was 96.2 μA mM<sup>-1</sup> cm<sup>-2</sup> and the linear response was proportional to the AA concentration in the range from 0.01 to 3 mM (0.994), being wider than those reported for other modified electrodes.<sup>44,46,48–51</sup> The merits of the presented modified electrode IrO<sub>x</sub>/GC can be evaluated by the comparative review presented in Table 3. As can be seen, the IrO<sub>x</sub>/GC exhibits comparable or better analytical performance than other published electrochemical sensors for AA detection.

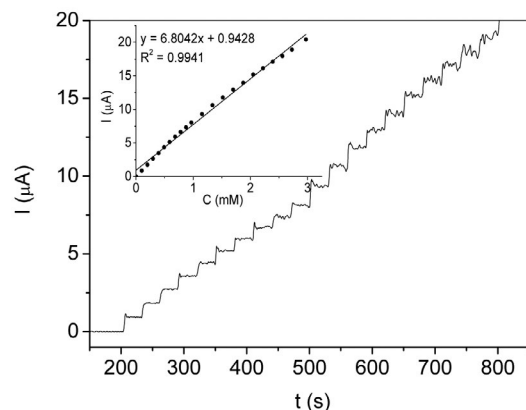


Fig. 9. Amperometric response of modified electrode IrO<sub>x</sub>/GC in PBS (pH 7.0) for successive additions of AA at an applied potential of 0.025 V. Inset: calibration plot of chronoamperometric currents vs. AA concentration.

Several forms of inorganic and organic interference were tested to determine whether they could affect the detection of AA with the modified electrode. These interferences were investigated in 0.1 M PBS (pH 7.0) containing 0.5 mM AA at constant potential of 0.025 V. The results showed that concentrations of 3 mM NaCl, KI, KBr, Na<sub>2</sub>CO<sub>3</sub>, MgCl<sub>2</sub>, NaOOCCH<sub>3</sub>, sodium citrate and glucose did not influence the current signal, confirming the high selectivity of IrO<sub>x</sub>/GC in AA quantitative determination.

Since long-term stability is crucial factor when the modified material is used in sensor system, the developed electrode IrO<sub>x</sub>/GC was stored at room temperature and measured every 4 days. After 20 days storage the current response to 1 mM nitrite (measured by constant potential amperometry at 0.77 V) retained 94% of the initial value, demonstrating the good stability of the electrodeposited catalytic active phase.



**Table 3.** Comparison of the proposed IrO<sub>x</sub>/GC with other reported sensors for determination of ascorbic acid.

Sensing electrode <sup>a</sup>	Technique	E, V	Sensitivity, $\mu\text{A mM}^{-1} \text{cm}^{-2}$	Linear range, $\mu\text{M}$	Detection limit, $\mu\text{M}$	RSD, %
pdon/CNTs/GC <sup>44</sup>	Amp	-0.1 <sup>c</sup>	2.1 <sup>e</sup>	2–1000	0.8	4.8(n = 5)
GDSP/CPE <sup>45</sup>	Amp	0.4 <sup>c</sup>	21.879 <sup>e</sup>	150–8000	3.375	–
EMGON/CPE <sup>46</sup>	Amp	0.38 <sup>c</sup>	78.63 <sup>e</sup>	up to 1000	1.54	1.15(n = 15)
Q-chitosan/C <sup>40</sup>	Amp	0.1 <sup>d</sup>	76	10–5000	3	–
Au-PANI/GC <sup>47</sup>	Amp	-0.2 <sup>h</sup>	25.69	10–12000	8.2	5.9(n = 3)
Au/EPA/CPE <sup>48</sup>	Amp	0.3 <sup>d</sup>	21.7 <sup>e</sup>	50–750	2.75	2.23(n = 3)
CoTNPPcMWCNTs/GC <sup>49</sup>	Amp	0.215 <sup>c</sup>	–	10–1600	5	–
AuNPs/GO/GC <sup>50</sup>	Amp	0.15 <sup>d</sup>	101.86	0.11–600	0.11	–
PEDOT/CPE <sup>51</sup>	CV	0.29 <sup>d</sup>	12.3 <sup>e</sup>	50–3000	–	–
IrO <sub>x</sub> /GC <sup>This work</sup>	DPV		135	50–1900	10	0.91(n = 10)
	Amp	0.025 <sup>d</sup>	96.2	10–3000	4	3.2(n=5)

<sup>a</sup> pdon – 1,10-phenanthroline-5,6-dione; GDSP – gold decorated SiO<sub>2</sub>@polyaniline (PANI) core-shell microspheres; EMGON – electroactive mesoporous gold-organosilica nanocomposite; Q-chitosan – hydroquinone modified chitosan; Au/EPA – gold/aniline-pentamer-based electroactive polyaniline; CoTNPPc – cobalt(II) tetra-neopentylphthalocyanine; <sup>h</sup> Reference electrode: saturated mercurous sulfate electrode (SMSE). Other abbreviations are the same as Table 2.

## 4. Conclusion

In summary, applying simple and rapid two-step procedure for electrodeposition of iridium oxide onto glassy carbon, a new type modified electrode IrO<sub>x</sub>/GC was developed. DPV experiments indicated that the IrO<sub>x</sub>/GC possesses excellent electrocatalytic activity towards the oxidation of both nitrite and AA. The proposed modified electrode-catalyst, studied by DPV and constant potential amperometry, exhibits remarkable analytical characteristics for its use in nitrite and AA sensing applications – wide linear range, high sensitivity, good selectivity, fast and stable amperometric response with excellent reproducibility and long-term stability. The sensor performances were unaffected by the presence of variety of inorganic and organic interferences make it a promising sensing material for sensitive and selective nonenzymatic quantitative detection of nitrite and AA.

## 5. References

- R. Pegg, F. Shahidi: Nitrite Curing of Meat. Food & Nutrition Press Inc., Trumbull, CT, USA, **2008**, pp. 1–268. <https://onlinelibrary.wiley.com/doi/abs/10.1002/9780470385081.ch1>
- World Health Organization, Guidelines for Drinking-Water Quality: Fourth Edition Incorporating the First Addendum, WHO, Geneva, **2017**, ISBN-13: 978-92-4-154995-0 <https://www.ncbi.nlm.nih.gov/books/NBK442376/>
- P. Rastogi, V. Ganesan, S. Krishnamoorthi, *J. Mater. Chem. A* **2014**, *2*, 933–943. DOI:10.1039/C3TA13794E
- E. Beamonte, J. Bermudez, A. Casino, *J. Environ. Manag.* **2007**, *83*, 307–314. DOI:10.1016/j.jenvman.2006.03.010
- D. Zhang, H. Ma, Y. Chen, H. Pang, Y. Yu, *Anal. Chim. Acta* **2013**, *792*, 35–44. DOI:10.1016/j.aca.2013.07.010
- R. Jiang, D. Paik, J. Hankinson, R. Barr, *Am. J. Respir. Crit. Care Med.* **2007**, *175*, 798–804. DOI:10.1164/rccm.200607-969OC
- T. Chan, *Toxicol. Lett.* **2011**, *200*, 107–108. DOI:10.1016/j.toxlet.2010.11.002
- P. Jakszyn, C. Gonzalez, *World J. Gastroenterol.* **2006**, *12*, 4296–4303. <https://www.ncbi.nlm.nih.gov/pubmed/16865769>
- P. Erkekoglu, H. Sipahi, T. Baydar, *Food Anal. Meth.* **2009**, *2*, 61–65. DOI:10.1007/s12161-008-9045-0
- K. Lenghartova, L. Lauko, F. Cacho, E. Beinrohr, *Acta Chim. Slov.* **2015**, *62*, 152–158. DOI:10.17344/acsi.2014.838
- H. Filik, D. Giray, B. Ceylan, R. Apak, *Talanta* **2011**, *85*, 1818–1824. DOI:10.1016/j.talanta.2011.07.052
- Z. Lin, X. Dou, H. Li, Y. Ma, J. Lin, *Talanta* **2015**, *132*, 457–462. DOI:10.1016/j.talanta.2014.09.046
- X. Wang, E. Adams, A. Van Schepdael, *Talanta* **2012**, *97*, 142–144. DOI:10.1016/j.talanta.2012.04.008
- W. Jobgen, S. Jobgen, H. Li, C. Meininger, G. Wu, *J. Chromatogr. B* **2007**, *851*, 71–82. DOI:10.1016/j.jchromb.2006.07.018
- G. Xu, G. Xu, M. Xu, Z. Zhang, Y. Tian, H. Choi, W. Lee, *Bull. Korean Chem. Soc.* **2012**, *33*, 415–419. DOI:10.5012/bkcs.2012.33.2.415
- L. Chen, X. Liu, C. Wang, S. Lv, C. Chen, *Microchim. Acta* **2017**, *184*, 2073–2079. DOI:10.1007/s00604-017-2189-0
- J. Dai, D. Deng, Y. Yuan, J. Zhang, F. Deng, S. He, *Microchim. Acta* **2016**, *183*, 1553–1561. DOI:10.1007/s00604-016-1773-z
- C. Yang, Q. Lu, S. Hu, *Electroanalysis* **2006**, *18*, 2188–2193. DOI:10.1002/elan.200603646
- Y. Zhang, R. Yuan, Y. Chai, W. Li, X. Zhong, H. Zhong, *Biosens. Bioelectron.* **2011**, *26*, 3977–3980. DOI:10.1016/j.bios.2011.03.017
- D. Ye, L. Luo, Y. Ding, Q. Chen, X. Liu, *Analyst* **2011**, *136*, 4563–4569. DOI:10.1039/C1AN15486A
- D. Gligor, A. Walcarius, *J. Solid State Electrochem.* **2014**, *18*, 1519–1528. DOI:10.1007/s10008-013-2365-z

22. Y. Zhang, P. Chen, F. Wen, C. Huang, H. Wang, *Ionics* **2016**, 22, 1095–1102. DOI:10.1007/s11581-015-1634-5
23. K. Promsuwan, P. Thavarungkul, P. Kanatharana, W. Limbut, *Electrochim. Acta* **2017**, 232, 357–369. DOI:10.1016/j.electacta.2017.02.138
24. Y. Zhou, H. Xian, F. Li, S. Wu, Q. Lu, Y. Li, L. Wang, *Electrochim. Acta* **2010**, 55, 5905–5910. <http://dx.doi.org/10.1016/j.electacta.2010.05.043>
25. D. Zhang, H. Ma, Y. Chen, H. Pang, Y. Yu, *Anal. Chim. Acta* **2013**, 792, 35–44. DOI:10.1016/j.aca.2013.07.010
26. R. Hallaj, A. Salimi, B. Kavosi, G. Mansouri, *Sens. Actuat. B* **2016**, 233, 107–119. DOI:10.1016/j.snb.2016.04.028
27. H. Heli, I. Eskandari, N. Sattarahmady, A. Moosavi-Movaheidi, *Electrochim. Acta* **2012**, 77, 294–301. DOI:10.1016/j.electacta.2012.06.014
28. C. Kung, T. Chang, L. Chou, J. Hupp, O. Farha, K. Ho, *Electrochim. Commun.* **2015**, 51, 2414–2417. DOI:10.1039/C4CC09272D
29. E. Menart, V. Jovanovski, S. B. Hočvar, *Electrochim. Commun.* **2015**, 52, 45–48. DOI:10.1016/j.elecom.2015.01.017
30. P. K. Sonkar, V. Ganesan, *J. Solid State Electrochem.* **2015**, 19, 2107–2115. DOI:10.1007/s10008-014-2725-3
31. L. Zhang, F. Yuan, X. Zhang, L. Yang, *Chem. Centr. J.* **2011**, 5, 75–84. DOI:10.1186/1752-153X-5-75
32. Y. Liu, J. Zhou, J. Gong, W. Wu, N. Bao, Z. Pan, H. Gu, *Electrochim. Acta* **2013**, 111, 876–887. DOI:10.1016/j.electacta.2013.08.077
33. C. Xia, X. Yanjun, W. Ning, *Electrochim. Acta* **2012**, 59, 81–85. DOI:10.1016/j.electacta.2011.10.039
34. Z. Wang, F. Liao, T. Guo, S. Yang, C. Zeng, *J. Electroanal. Chem.* **2012**, 664, 135–138. DOI:10.1016/j.jelechem.2011.11.006
35. A. Marlinda, A. Pandikumar, N. Yusoff, N. Huang, H. Lim, *Microchim. Acta* **2014**, 182, 1113–1122. DOI:10.1007/s00604-014-1436-x
36. Q. Xie, W. He, S. Yu, X. Chen, X. Zhang, Y. Shen, *Anal. Meth.* **2014**, 6, 7716–7721. DOI:10.1039/C4AY01461H
37. L. Zhou, J. Wang, L. Gai, D. Li, Y. Li, *Sens. Actuat. B* **2013**, 181, 65–70. DOI:10.1016/j.snb.2013.02.041
38. T. Ömür, M. Alanyahoğlu, *Ionics* **2017**, 23, 3507–3516. DOI:10.1007/s11581-017-2142-6
39. V. Mani, A. Periasamy, S. Chen, *Electrochim. Commun.* **2012**, 17, 75–78. DOI:10.1016/j.elecom.2012.02.009
40. H. Jirimali, R. Nagarale, D. Saravanakumar, J. Lee, W. Shin, *Carbohydr. Pol.* **2013**, 92, 641–644. DOI:10.1016/j.carbpol.2012.09.024
41. A. Pisoschi, A. Pop, A. Serban, C. Fafaneata, *Electrochim. Acta* **2014**, 121, 443–460. DOI:10.1016/j.electacta.2013.12.127
42. T. Dodevska, E. Horozova, N. Dimcheva, *Mat. Sci. Eng. B* **2013**, 178, 1497–1502. DOI:10.1016/j.mseb.2013.08.012
43. N. Dimcheva, T. Dodevska, E. Horozova, *J. Electrochem. Soc.* **2013**, 160, 414–419. DOI:10.1149/2.025308jes
44. M. Wu, X. Mao, X. Li, X. Yang, L. Zhu, *J. Electroanal. Chem.* **2012**, 682, 1–6. DOI:10.1016/j.jelechem.2012.06.007
45. C. Weng, Y. Chen, C. Chien, S. Hsu, Y. Jhuo, J. Yeh, C. Dai, *Electrochim. Acta* **2013**, 95, 162–169. DOI:10.1016/j.electacta.2013.01.150
46. C. Weng, P. Hsu, S. Hsu, C. Chang, W. Hung, P. Wu, J. Yeh, *J. Mater. Chem. B* **2013**, 1, 4983–4991. DOI:10.1039/C3TB20433B
47. H. Zhang, F. Huang, S. Xu, Y. Xia, W. Huang, Z. Li, *Electrochim. Commun.* **2013**, 30, 46–50. DOI:10.1016/j.elecom.2013.02.007
48. M. Tsai, S. Lu, Y. Lai, G. Lai, G. Dizon, T. Yang, Y. Lin, Y. Chou, *eXPRESS Pol. Lett.* **2018**, 12, 71–81. DOI:10.3144/expresspolymlett.2018.6
49. X. Zuo, N. Li, H. Zhang, *J. Mater. Sci.* **2012**, 47, 2731–2735. DOI:10.1007/s10853-011-6099-y
50. J. Song, L. Xu, R. Xing, Q. Li, C. Zhou, D. Liu, H. Song, *Sci. Rep.* **2014**, 4, 7515–7520. DOI:10.1038/srep07515
51. J. Sui, W. Li, Q. Pan, *Int. J. Polym. Mater.* **2016**, 66, 258–264. DOI:10.1080/00914037.2016.1201826
52. A. Salimi, R. Hallaj, B. Kavosi, B. Hagighi, *Anal. Chim. Acta* **2010**, 661, 28–34. DOI:10.1016/j.aca.2009.12.005
53. M. Roushani, M. Sarabaegi, *J. Electroanal. Chem.* **2014**, 717, 147–152. DOI:10.1016/j.jelechem.2014.01.013
54. L. Preda, T. Kondo, T. Spataru, M. Matin, M. Radu, P. Osiceanu, A. Fujishima, N. Spataru, *Chem. ElectroChem.* **2017**, 4, 1908–1915. DOI:10.1002/celec.201700155
55. Y. Lazarova, I. Shterev, T. Dodevska, *Monatsh. Chem.* **2018**, 149, 1955–1962. DOI:10.1007/s00706-018-2275-y
56. Z. Wen, T. Kang, *Talanta* **2004**, 62, 351–355. DOI:10.1016/j.talanta.2003.08.003
57. M. Majidi, A. Saadatirad, E. Alipour, *Electroanalysis* **2013**, 25, 1–9. DOI:10.1002/elan.201300082
58. K. Zhao, H. Song, S. Zhuang, L. Dai, P. He, Y. Fang, *Electrochim. Commun.* **2007**, 9, 65–70. DOI:10.1016/j.elecom.2006.07.001
59. S. Palanisamy, C. Karuppiyah, S. Chen, P. Periakaruppan, *J. Electroanal. Chem.* **2014**, 727, 34–38. DOI:10.1016/j.jelechem.2014.05.025
60. X. Huang, Y. Li, Y. Chen, L. Wang, *Sens. Actuat. B* **2008**, 134, 780–786. DOI:10.1016/j.snb.2008.06.028
61. L. Liu, H. Cui, H. An, J. Zhai, Y. Pan, *Ionics* **2017**, 23, 1517–1523. DOI:10.1007/s11581-017-1972-6
62. S. Li, G. Zhao, R. Zhang, Y. Hou, L. Liu, H. Pang, *Microchim. Acta* **2013**, 180, 821–827. DOI:10.1007/s00604-013-0999-2

## Povzetek

Iridijev oksid ( $\text{IrO}_x$ ) smo z dvostopenjskim postopkom elektrodepozicije nanegli na elektrodo iz steklastega ogljika. Elektrokatalitične lastnosti modificirane elektrode iz steklastega ogljika  $\text{IrO}_x/\text{GC}$  so bile ovrednotene v primerih elektrokemijske oksidacije nitrita in askorbinske kisline. Razviti elektrodni katalizator smo preučevali z različnimi elektrokemijskimi metodami. Poskusi diferencialne pulzne voltametrije (DPV) so pokazali, da ima modificirana elektroda odlično elektrokatalitsko aktivnost pri oksidaciji nitrita in askorbinske kisline v nevtralnem mediju in omogoča tudi kvantitativno določevanje teh snovi. Izvedli smo tudi amperometrične meritve s konstantnim potencialom. Modificirana elektroda iz steklastega ogljika  $\text{IrO}_x/\text{GC}$  je pokazala občutljivost na nitrit ( $159,7 \mu\text{A mM}^{-1} \text{cm}^{-2}$ ) v širokem linearnem območju od 0,002 do 10 mM pri 0,77 V (glede na Ag/AgCl, 3 M KCl) in na askorbinsko kislino ( $96,2 \mu\text{A mM}^{-1} \text{cm}^{-2}$ ) v linearnem območju od 0,01 do 3 mM pri 0,025 V. Meja zaznavnosti je bila v primeru določevanja nitrita 0,63  $\mu\text{M}$  v primeru askorbinske kisline pa 4  $\mu\text{M}$ ; v obeh primerih je bil odziv elektrode hiter (5 s). Glede na preprost in hiter postopek elektrodepozicije za pripravo modificirane elektrode  $\text{IrO}_x/\text{GC}$  predstavlja le-ta nov elektrodni katalizator za občutljivo in selektivno kvantitativno detekcijo nitritov in askorbinske kisline. Širok linearni razpon, dobra selektivnost, ponovljivost amperometričnega odziva in dolgotrajna stabilnost modificirane elektrode  $\text{IrO}_x/\text{GC}$  so obetavne lastnosti novega materiala za senzorje, ki je primeren za kvantitativno detekcijo nitrita in askorbinske kisline.

Scientific paper

# Oscillations During Flow Boiling in Single Microchannels

Anže Sitar,<sup>1,\*</sup> Andrej Lebar,<sup>1,2</sup> Michele Crivellari,<sup>3</sup> Alvis Bagolini<sup>3</sup>  
and Iztok Golobič<sup>1</sup>

<sup>1</sup> University of Ljubljana, Faculty of Mechanical Engineering, Aškerčeva 6, 1000 Ljubljana, Slovenia.

<sup>2</sup> University of Ljubljana, Faculty of Health Sciences, Zdravstvena pot 5, 1000 Ljubljana, Slovenia.

<sup>3</sup> Fondazione Bruno Kessler, Center for Materials and Microsystems, Via Sommarive 18, I - 38123 Povo, Trento, Italy.

\* Corresponding author: E-mail: anze.sitar@fs.uni-lj.si  
phone: +386 1 4771 309

Received: 14-08-2018

## Abstract

Flow boiling of degassed double-distilled water in a single  $50 \times 50 \mu\text{m}$  and  $100 \times 50 \mu\text{m}$  microchannel was investigated on the basis of experimental measurements and high-speed visualization. The visualized events during boiling were analyzed in terms of the bubble frequencies and boiling front oscillations in microchannels. A digital image sequence analysis algorithm was composed to determine the time dependence of bubble and meniscus locations. The results show (i) the dynamic characteristics of boiling in microchannels, (ii) the increase of fundamental oscillation frequencies with increasing heat flux and temperature of the microchannel bottom, (iii) the amplitudes of the flow boiling oscillations are inversely proportional to the fundamental frequencies. The outcomes of the study are important as the oscillations during boiling in single microchannels are experimentally confirmed to be predictable in terms of oscillation frequencies and amplitudes trends and dependencies. This knowledge is especially significant at constructing efficient two-phase micro heat exchangers, micro mixers or micro reactors, as the cross section and the length of the channel become exceedingly important design parameters in micro devices with boiling.

**Keywords:** Microchannels; flow boiling; oscillations; visualization; fundamental frequencies.

## 1. Introduction

Flow boiling in microchannels has the potential for achieving higher heat transfer coefficients compared to the single-phase liquid flow. However, boiling in microchannels is hindered by instabilities and early dryouts, which prevent wide implementation and overall heat transfer enhancement as presented by Kandlikar et al.<sup>1</sup> Moreover, the incipience of boiling in microchannels requires high excess temperature difference between the channel wall and the bulk fluid as shown by Ghiaasiaan and Chedester<sup>2</sup> and also Kandlikar.<sup>3</sup> Accordingly, at the onset of nucleate boiling (ONB) the emerging bubble grows very rapidly due to the highly superheated liquid which was confirmed by Edel and Mukherjee.<sup>4</sup> As the vapor bubble fills up the cross section of the microchannel it encounters all the heated walls, which occurs shortly after nucleation due to the small hydraulic diameters. The additional heated surface

accelerates the bubble growth, which results in a highly unstable flow with oscillations. The fluctuations of the working fluid during boiling present a severe challenge, especially when the vapor backflow becomes distinctive and hinders the forward flow of fresh liquid as shown by Barber et al.<sup>5</sup> If the vapor backflow reaches the inlet manifold, it obstructs the liquid flow to all the channels connected to the manifold. It is therefore crucial to prevent pronounced vapor backflows in microchannels during flow boiling.

One of the possible solutions for flow stabilization during boiling is the incorporation of inlet restrictors between the inlet manifold and the microchannels (Kandlikar et al.,<sup>6</sup> Kuo and Peles,<sup>7</sup> Wang et al.,<sup>8</sup> Sitar et al.<sup>9</sup> and Szczukiewicz et al.),<sup>10</sup> which provide higher upstream pressure drop, promote the downstream flow of the vapor bubble and suppress the vapor backflow.

Another approach to reduce flow instabilities is to fabricate potential nucleation sites. This precaution mea-

sure lowers the fluid superheat required for ONB and therefore also slows down the vapor bubble growth, which induces less explicit vapor backflows. Nucleation sites can be easily etched in silicon, though recent advances in micro-engineering allow similar feature geometries to be machined in a wider range of materials as it was demonstrated by Kandlikar,<sup>11</sup> Liu et al.,<sup>12</sup> Sabotin et al.<sup>13</sup> and Balasubramanian et al.<sup>14</sup> The dimensioning of the potential nucleation cavities should consider the nucleation criteria, which were initially modeled by Hsu<sup>15</sup> and afterwards also by Kandlikar et al.<sup>16</sup>

Several authors have analyzed fluctuations during boiling from pressure or temperature measurements (Muwanga et al.,<sup>17</sup> Zhang et al.,<sup>18</sup> Tuo and Hrnjak,<sup>19</sup> Liu et al.).<sup>20</sup> In a single microchannel experiments the boiling instabilities could be distinctly manifested in the pressure measurements, if the pressure sensor is located close enough to the boiling process. However, pressure and temperature measurements in a single microchannel unambiguously indicate only the oscillation frequencies, whereas the amplitudes of the oscillating meniscus during boiling are more difficult to interpret from the measurements. Consequently, the boiling front oscillations in the manufactured microchannels were analyzed from the results of visualization, as the pressure/temperature measurements are insufficient.

The published experimental results regarding heat flux and/or temperature effect on the bubble frequency during pool and flow boiling are ambiguous. On one hand, Gerardi et al.<sup>21</sup> investigated pool boiling of water and nanofluids with an infrared camera and found a strong dependence of the bubble departure frequency on the wall superheat. Additional confirmation of the heat flux strong effect on the departure frequency in pool boiling is seen from the experimental results conducted by Dong et al.<sup>22</sup> On the other hand, Kim et al.<sup>23</sup> incorporated nanowires to the boiling surface and their results show a small to no significant effect of heat flux on the bubble detaching frequency on the plain or enhanced silicon surface. Similar results of the bubble nucleation frequency with small dependence on the wall superheat in pool boiling was presented in Hutter et al.<sup>24</sup> A small effect of the heat flux on the nucleation frequency during vertical subcooled flow boiling was encountered by Chu et al.<sup>25</sup>

The employment of numerical analysis to flow boiling in microchannels is being studied by various research groups, however a fully functional numerical model is still far from being reached due to the complexity of the boiling phenomena. Numerical modelling of pressures, temperatures and velocities is commonly associated with two-phase non-boiling flows Cioncolini and Thome,<sup>26</sup> specific flow patterns in predominantly larger circular microchannels Magnini and Thome,<sup>27</sup> single bubble growth and bubble merger in larger square microchannels Mukherjee et al.<sup>28</sup> and Ling et al.,<sup>29</sup> single bubble analysis Ferrari et al.,<sup>30</sup> and is therefore not entirely relatable to the solely annular flow observed during boiling in our experimental work.

Another approach is a mechanistic model presented by Patel et al.,<sup>31</sup> which covers a two-phase flow of air and water and would need some tailoring to model the bubble shapes and heat transfer coefficients during flow boiling.

The current study was focused on detecting the instabilities with high speed imaging, which were afterwards analyzed in order to evaluate the amplitudes and the fundamental frequencies of the oscillations and the effect of the working conditions on flow boiling. Similar research of boiling dynamics in microchannels was not found in the reviewed literature, moreover some of the published work have contradictory conclusions. The presented experimental work and analysis aim at determining the flow boiling characteristics in microchannels to allow an improved construction of the future two-phase micro devices.

## 2. Experimental Setup and Test Section

A simplified schematic diagram of the experimental setup employed for visualization and measurements is presented in Figure 1, whereas the complete wiring with the details of the measurement equipment is available in Sitar et al.<sup>9</sup> The visualization system is comprised of a microscope, a powerful light source and a high-speed camera.

Temperature, pressure, and heat transfer rate were measured simultaneously while the visualization system acquired dynamics of the bubble nucleation, growth, and oscillations during boiling in microchannels. Heat flux  $q$  was determined from the heater surface  $A_h$  and the heat transfer rate  $Q_h$ , which was calculated according to the equation

$$Q_h = U_h \frac{U_{sh}}{R_{sh}}, \quad (1)$$

where  $R_{sh}$  is the electrical resistance of the incorporated reference shunt,  $U_h$  and  $U_{sh}$  are the voltage drops across the heater and shunt, respectively. The shunt included had an electrical resistance of  $0.05 \Omega \pm 0.25 \%$ . The measured voltage signal passed through the amplification module and the data acquisition board, both of which introduce a measurement uncertainty in linear dependence of the measured voltage signal. The combined expanded relative temperature measurement uncertainty  $W(T)$  with a 95 % level of confidence was determined to be 1.5 % in the range from 50 °C to 200 °C, whereas  $W(Q_h)$  was calculated to be from 6.6 % to 4.6 % for the heat rates ranging in between 6.9 W and 16 W. These heat rates correspond to heat fluxes from 150 kW/m<sup>2</sup> to 350 kW/m<sup>2</sup>, respectively. The combined expanded absolute measurement uncertainty of the pressure measurements  $U(p)$  was 65 mbar up to the measured gauge pressure of 4 bar in the test section. The details of the measurement uncertainty analysis was presented in Sitar and Golobič.<sup>32</sup>

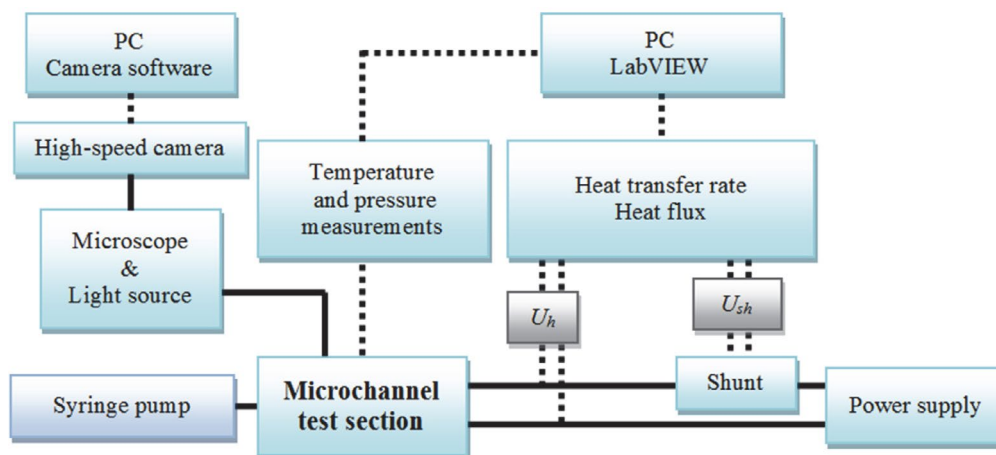


Figure 1. Experimental setup.

Degassed double-distilled water was the working fluid in all experiments which were conducted in single  $50 \times 50 \mu\text{m}$  and  $100 \times 50 \mu\text{m}$  (width  $\times$  depth) microchannels, which is presented schematically in Figure 2. In the microchannel test sections the inlet/outlet channel with the width of 1 mm was gradually narrowed to the final width of  $50 \mu\text{m}$  or  $100 \mu\text{m}$ . Water was pumped through the microchannels at a constant volumetric flow from the left to the right hand side of the microchannel test section.

The used microchannels had smooth walls and bottom without any tailored potential nucleation sites. The only additional feature in the single microchannels was the inlet restrictor with a cross section of  $20 \times 50 \mu\text{m}$ .

The high-speed visualizations and measurements were performed simultaneously at a steady-state, which

was defined as a state with the measured temperatures change of less than 2 K during a 10 min period. The temperature measurements were done at the bottom side of the silicon wafer in the middle of the microchannel, 9.7 mm upstream (inlet temperature) and 9.7 mm downstream (outlet temperature) of the middle of the test section. The gauge pressure was measured at the inlet of the microchannels, whereas the outlet of the test section is presumed to be at atmospheric pressure.

### 3. Digital Image Sequence Analysis

In each experiment sets of up to 100,000 images were acquired and stored. In order to determine time depen-



Figure 2. Design of a single microchannel with an inlet flow restrictor.

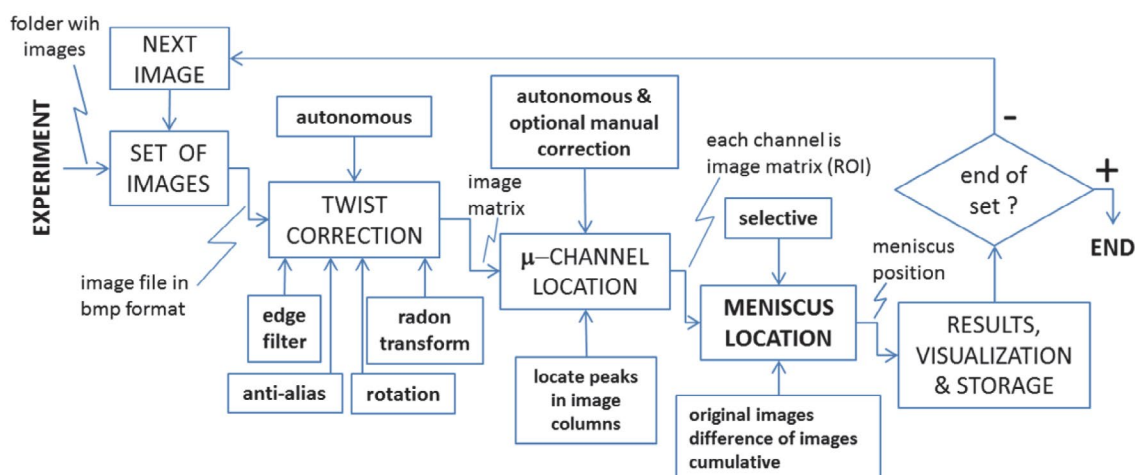


Figure 3. Functional diagram of the digital image sequence analysis.

dence of the meniscus location, a digital image procedure was applied to each set. In Figure 3 the analysis workflow is given in the form of a functional diagram, which is to be explained in the following. Image analysis was performed completely in the Matlab environment.

Due to manipulation of the test section and the camera during experiments a small undesired twist of the microchannel array coordinate system towards the coordinate system of the camera occurred, which was evaluated by using Radon transform and consequently corrected by image rotation.

Next task in the workflow diagram (Figure 3) was to find the locations of microchannels, which are marked with green dots in the Figure 4. Locations were determined by locating the darkest points in a single column of the image matrix.

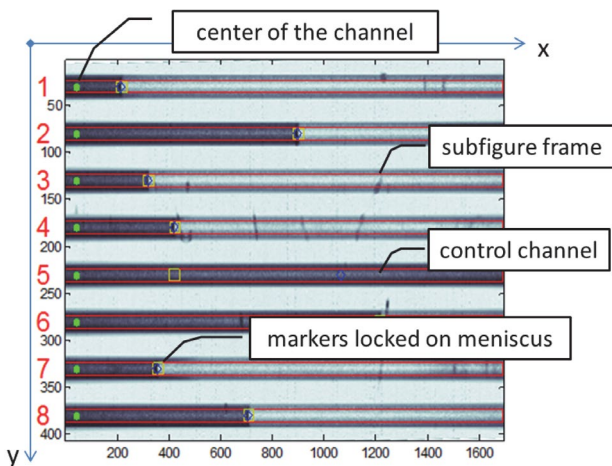


Figure 4. Labeled microchannels and automatically determined centers of the channels (green dots).

After the microchannel centers were known, each channel was identified as a region of interest (ROI) determined by the boundary indexes in the image matrix, which were calculated from the microchannel centers and channel width.

Determination of the meniscus location is the core function of image sequence analysis workflow (Figure 5).

Initially it was based on the straightforward fact that the image brightness changes significantly at the border between the liquid and vapor phase, as it is seen in Figure 5 (a). In order to decrease brightness variations (noise) along the microchannel, a cumulative sum of columns in ROI was calculated, which is given in Figure 5 (b). Location of the meniscus is then determined by applying a threshold and the first point which exceeds the threshold is the location of the meniscus.

An improvement of the discussed method is to compute the derivative of the brightness variation, as it can be observed in Figure 5 (c). The highest peak is expected to correspond to the meniscus location. Several partially unavoidable challenges have been found in locating the meniscus location: bubbles nucleating upstream of meniscus, microchannel surface features, potential dust and stains etc. In order to overcome this challenge, an analysis was performed on the differences of the consecutive images instead of on just one single image. Brightness variation and derivative of image brightness variation was observed. The difference of consecutive images from the example presented in Figure 5 is shown in Figure 6.

Analysis of the meniscus location on the differences of images yielded more reliable results. Despite the significant improvement, analysis failed to track the meniscus properly in cases with many bubbles emerging upstream.

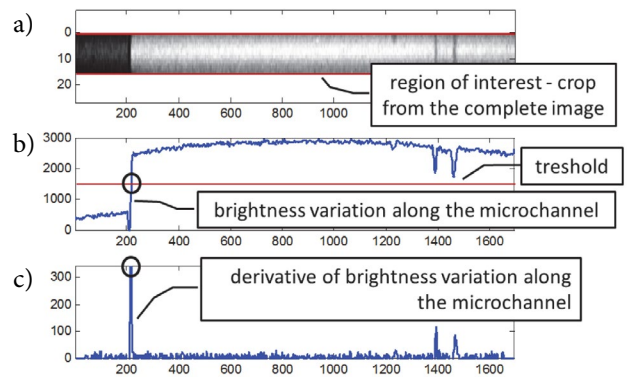


Figure 5. Identification of the meniscus location – a) ROI of channel #1 cropped from the complete image (Figure 5); b) brightness variation; c) derivative of the brightness variation.

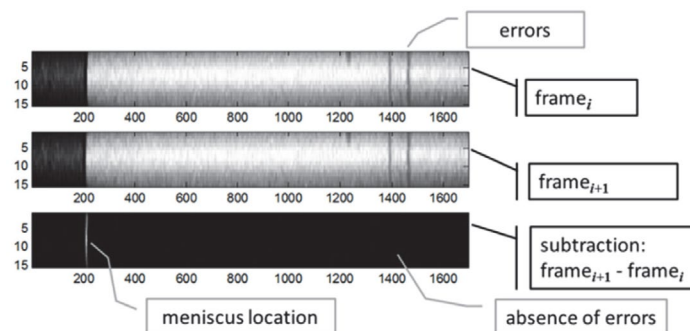


Figure 6. Subtraction of consecutive images.

In those cases all of the image pixel values in ROI were summed. If the channel was full of water it was overall dark and the sum of all the pixel values was smaller. Inversely the sum of pixel values was higher if the channel was filled with vapor. Consecutive summation values were stored in an array for further analysis. This method yielded very smooth and reliable results, which can be used for fundamental frequency analysis.

The developed digital sequence analysis is capable of tracking meniscus location in an array of microchannels, while the operation of the algorithm is simplified during image analysis of the single channel experiments. Due to better positioning of the experimental setup, rotation correction was omitted and due to the improved illumination, meniscus location was determined based on brightness variation detection similar as in Figure 5 (b).

## 4. Results and Discussion

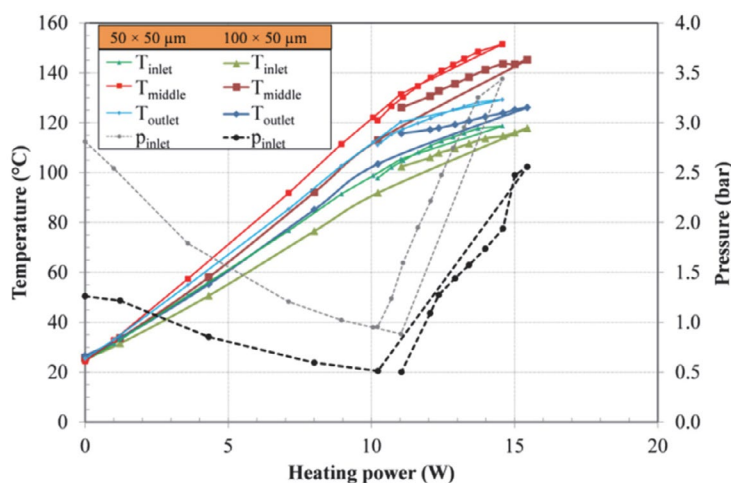
The primary goal of any two-phase heat transfer device is an efficient heat transfer as well as a stable and predictable behavior during operation. Flow boiling in microchannels is often accompanied by instabilities and vapor backflows, which inhibit constant flow of the working fluid and reduce the heat transfer.

The ONB was achieved at higher temperatures compared to our previous experimental work in an array of microchannels, due to the smooth walls and bottom of the single microchannels. Consequentially, the temperature and heat flux were increased until ONB was reached at temperatures from 140 °C to 160 °C in the middle of the microchannel. Afterwards, the heat flux was stepwise lowered and the data was acquired at a steady-state point along with the high-speed image acquisition. The comparison of the measured temperatures and pressures for the same volumetric flow of 0.2 ml/min in a microchannel with a

cross-section of  $50 \times 50 \mu\text{m}$  and  $100 \times 50 \mu\text{m}$  is presented in Figure 7. The results are undoubtedly showing lower inlet gauge pressure and also temperatures at all three measured location in the microchannel with the larger cross-section. The inlet gauge pressure was lowered from 2.81 bar to 0.88 bar during the single-phase flow in the  $50 \times 50 \mu\text{m}$  microchannel, and was raised up to 3.44 bar at the ONB at 14.6 W of heating power. The measured gauge pressure in the larger  $100 \times 50 \mu\text{m}$  microchannel was initially 1.26 bar and lowered down to 0.51 bar prior to the ONB, which then caused the elevation of the gauge pressure up to 2.56 bar.

The results of high-speed visualizations were analyzed to establish the characteristics of oscillations, especially the peak to peak amplitude and the frequency of the meniscus during boiling. The location of the liquid-vapor boundary was determined according to the presented digital image sequence analysis. Afterwards, the amplitude of the oscillations and FFT was derived from the acquired data to determine the fundamental frequencies. Figure 8 depicts a small portion of the performed FFT analysis in a  $50 \times 50 \mu\text{m}$  microchannel at volumetric flow of 0.2 ml/min. The presented data confirms that the oscillations in the single microchannel were periodic at all the presented temperatures, as the fundamental frequencies could be undoubtedly and accurately determined from the FFT.

The fundamental frequencies and the corresponding peak to peak amplitudes of all the observed oscillations in single microchannels with a cross section of  $50 \times 50 \mu\text{m}$  and  $100 \times 50 \mu\text{m}$  are presented in Figure 9. The framerate of the high-speed visualizations varied from 10,000 to 100,000 fps and were adapted to allow proper observation of the boiling process. The experimental results were approximated with a first order inverse polynomial function and the approximation curve is similar in both microchannels. However, a detailed comparison of the experimental results showed a maximum oscillation frequency in the  $50 \times 50 \mu\text{m}$  microchannel to be above 20 kHz,



**Figure 7.** Comparison of temperatures and pressures in a single  $50 \times 50 \mu\text{m}$  and  $100 \times 50 \mu\text{m}$  microchannel at the same volumetric flow of 0.2 ml/min.



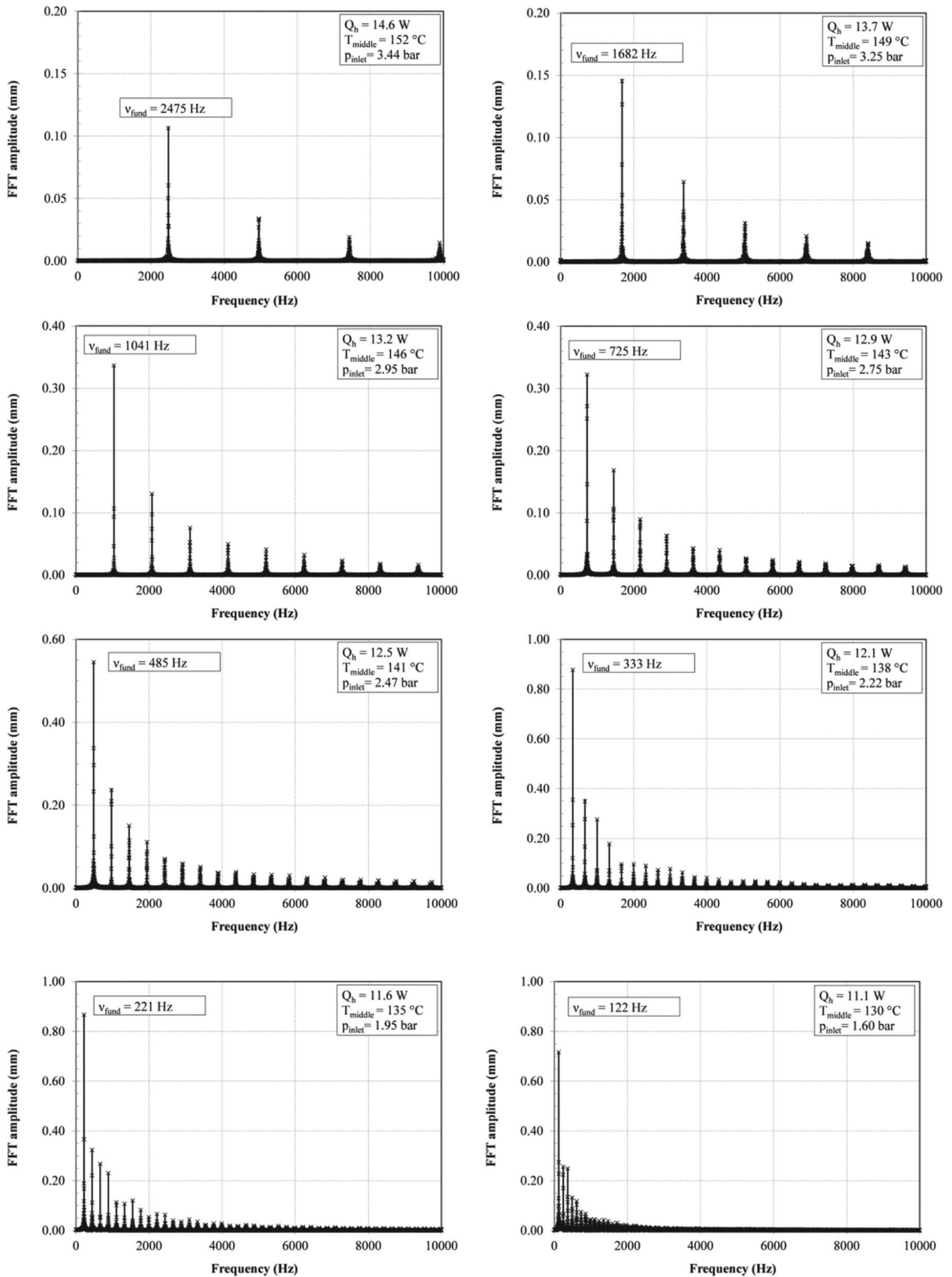


Figure 8. FFT analysis of meniscus oscillations during boiling in a single  $50 \times 50 \mu\text{m}$  microchannel at temperatures ranging from  $152^{\circ}\text{C}$  to  $130^{\circ}\text{C}$  in the middle of the microchannel.

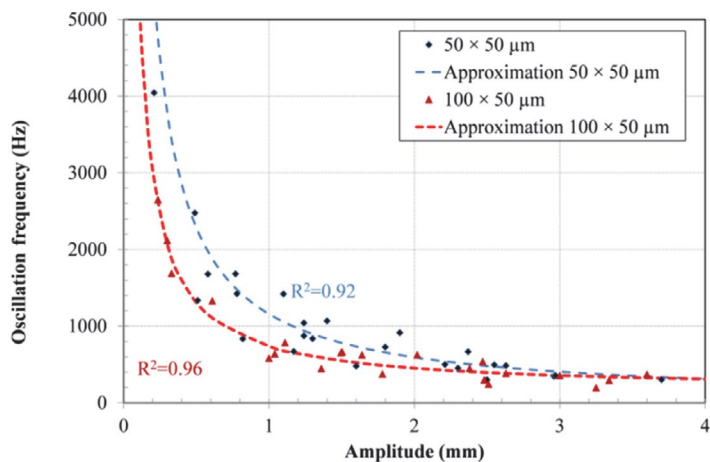


Figure 9. Oscillation frequency dependence on oscillation amplitude in a single  $50 \times 50 \mu\text{m}$  and  $100 \times 50 \mu\text{m}$  microchannel.

whereas the maximum frequency recorded in the  $100 \times 50 \mu\text{m}$  was 2.65 kHz.

Despite the difference between the highest fundamental frequencies observed at the ONB in single microchannels, there is an undeniable similarity in the frequen-

cy-amplitude dependency. The basis of the similar behavior of the boiling water originates from the reciprocal nature of the frequency-amplitude relationship. The fundamental frequencies of oscillations during boiling was found to be inversely dependent on the amplitudes by Ivey,<sup>33</sup> which is

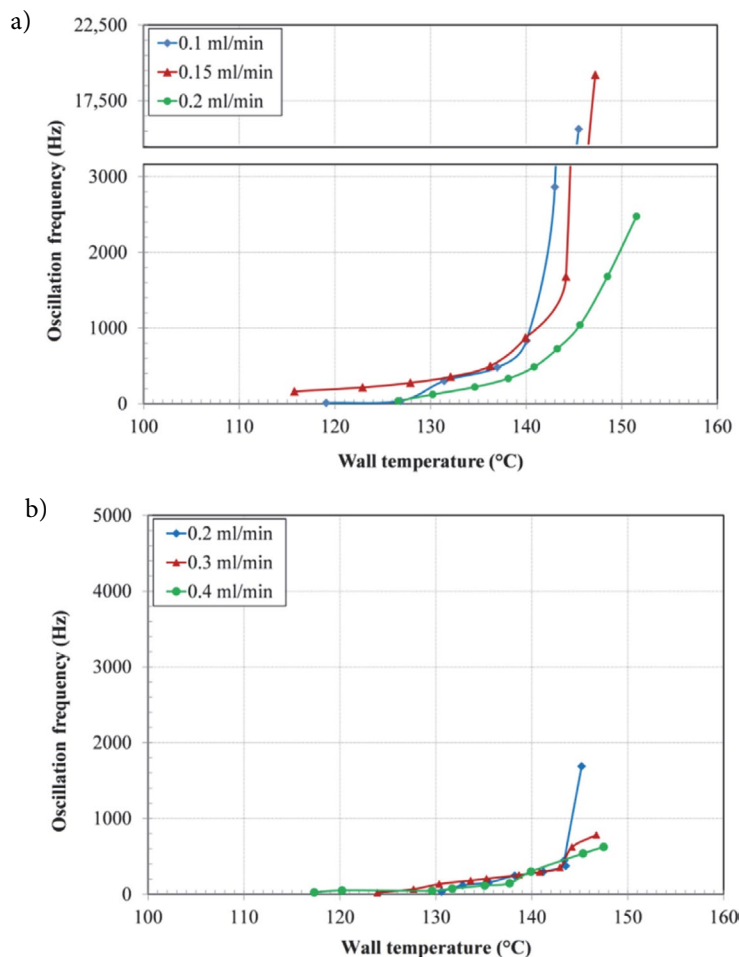


Figure 10. Oscillation frequency dependence on wall temperature at various volumetric flows in a single (a)  $50 \times 50 \mu\text{m}$  and (b)  $100 \times 50 \mu\text{m}$  microchannel.

experimentally validated also for flow boiling in microchannels in Figure 9. The largest amplitudes were recorded at the lowest frequencies as the meniscus shifts further downstream if there is more time available before another bubble nucleates.

The effect of the wall temperature in the middle of the microchannels on the fundamental frequencies is presented in Figure 10. The experiments performed in the  $50 \times 50 \mu\text{m}$  microchannel are given in Figure 10 (a) at three volumetric flows. The highest fundamental frequency was almost 21 kHz at the ONB at  $147^\circ\text{C}$  with the water volumetric flow set to 0.15 ml/min. The wall temperature had similar effect on the oscillation frequencies also in the  $100 \times 50 \mu\text{m}$  microchannel, as it is seen in Figure 10 (b).

However, the maximum achieved fundamental frequencies of the boiling oscillations were significantly lower in the microchannel with the larger cross-section, which implicates that the characteristics of oscillations are fairly well connected to the size of the microchannel. Generally, the frequencies were lowering with decreasing heat transfer rate and temperature for all of the performed experiments. In addition, the effect of the various mass fluxes on the fundamental frequencies is not seen from the experimental results in Figure 10.

## 5. Conclusions

Flow boiling of degassed water was visualized in single  $50 \times 50 \mu\text{m}$  and  $100 \times 50 \mu\text{m}$  microchannels. The results confirm periodical oscillations at all the measured steady state points. The analysis of the experimental results of temperature, pressure and heat transfer rate consistently shows that (i) higher volumetric flow; (ii) smaller microchannel cross-section and (iii) the presence of boiling are followed by a significant increase of the pressure drop in the microchannel. The fundamental frequency and peak to peak amplitude of oscillations were found to be inversely proportional in both single microchannels included in the research. The onset of boiling was achieved at relatively high wall temperatures from  $140^\circ\text{C}$  to  $160^\circ\text{C}$  due to the absence of properly sized nucleation sites. The recorded oscillation frequencies reached above 20 kHz in the  $50 \times 50 \mu\text{m}$  microchannel and were the highest at the ONB as the heat transfer rate and temperature was afterwards gradually decreased. The highest fundamental frequency in the larger  $100 \times 50 \mu\text{m}$  microchannel at a steady-state was approximately 2 kHz, which demonstrates the effect of the microchannel size on the boiling characteristics. In the presented literature for pool boiling the nucleation frequencies are several orders lower compared to our experimental results in microchannels. The fundamental frequency of boiling was consistently and significantly lowering and the amplitude was increasing with decreasing temperature and heat transfer rate for both analyzed single microchannels.

The boiling regime observed in the microchannels was for the most part limited to annular flow, as the cross-section of the channels was too small for the formation of a bubbly, slug or churn flow. Additionally, the meniscus between the liquid and vapor phase was oscillating with a frequency related to the bubble nucleation frequency, which further depends on the working fluid, the available sizes of the nucleation sites, the temperature, etc.

The effect of the wall superheat and heat flux on the characteristics of flow boiling in microchannels is evident from the results presented, which is crucial for developing and designing future two-phase heat transfer devices. Namely, the wall temperature and microchannel size along with other working conditions are determining the length of the microchannel in which liquid and vapor phase are periodically altered. Heat is transferred substantially more efficient over this length compared to all the other surfaces of the microchannel, as the latent heat of the working fluid is exploited solely in this section of the microchannels. Therefore, the amplitudes and frequencies of the oscillating meniscus are important parameters of the performance of two-phase micro devices. Higher heat fluxes demand shorter lengths of microchannels for efficient heat transfer, which could be achieved with a larger number of inlets and outlets. Future work should broaden the controlled working conditions to analyze their effect on oscillations during boiling and consequentially on heat transfer. Researchers in the field of micro two-phase devices such as micro heat exchangers or micro reactors should consider the effect of the working conditions on flow boiling in microchannels and adapt their designs accordingly.

## 6. References

1. S. G. Kandlikar, S. Colin, Y. Peles, S. Garimella, R. F. Pease, J. J. Brandner, D. B. Tuckerman, *J. Heat Transfer* **2013**, *135*, 091001-091018. DOI:10.1115/1.4024354
2. S. M. Ghiaasiaan, R. C. Chedester, *Int. J. Heat Mass Transfer* **2002**, *45*, 4599–4606. DOI:10.1016/S0017-9310(02)00167-9
3. S. G. Kandlikar, *Heat Transfer Engineering* **2010**, *31*, 159–167. DOI:10.1080/01457630903304335
4. Z. J. Edel, A. Mukherjee, *Int. J. Multiphase Flow* **2011**, *37*, 1257–1265. DOI:10.1016/j.ijmultiphaseflow.2011.07.007
5. J. Barber, D. Brutin, K. Sefiane, J. L. Gardarein, L. Tadrist, *Int. J. Heat Mass Transfer* **2011**, *54*, 4784–4795. DOI:10.1016/j.ijheatmasstransfer.2011.06.026
6. S. G. Kandlikar, D. A. Willistein, J. Borrelli, **2005**, pp. 115–124.
7. C. J. Kuo, Y. Peles, *Int. J. Heat Mass Transfer* **2007**, *50*, 4513–4526. DOI:10.1016/j.ijheatmasstransfer.2007.03.047
8. G. Wang, P. Cheng, A. E. Bergles, *Int. J. Heat Mass Transfer* **2008**, *51*, 2267–2281. DOI:10.1016/j.ijheatmasstransfer.2007.08.027
9. A. Sitar, I. Sedmak, I. Golobic, *Int. J. Heat Mass Transfer* **2012**, *55*, 6446–6457. DOI:10.1016/j.ijheatmasstransfer.2012.06.040

10. S. Szczukiewicz, N. Borhani, J. R. Thome, *Int. J. Heat Fluid Fl.* **2013**, *42*, 176–189. DOI:10.1016/j.ijheatfluidflow.2013.03.006
11. S. G. Kandlikar, *Applied Physics Letters* **2013**, *102*, 051611–051611–051611–051615.
12. K. Liu, B. Lauwers, D. Reynaerts, *Int J Adv Manuf Technol* **2010**, *47*, 11–19. DOI:10.1007/s00170-009-2056-1
13. I. Sabotin, G. Tristo, M. Junkar, J. Valentinčič, *Chemical Engineering Research and Design* **2013**, *91*, 778–788. DOI:10.1016/j.cherd.2012.09.013
14. K. Balasubramanian, P. S. Lee, C. J. Teo, S. K. Chou, *Int. J. Heat Mass Transfer* **2013**, *67*, 234–252. DOI:10.1016/j.ijheatmasstransfer.2013.08.023
15. Y. Y. Hsu, *J. Heat Transfer* **1962**, *84*, 207–216. DOI:10.1115/1.3684339
16. S. G. Kandlikar, V. R. Mizo, M. D. Cartwright, E. Ikenze, Proc. HTD-Vol. 342, ASME Proceedings of the 32nd National Heat Transfer Conference, **1997**, pp. 11–18.
17. R. Muwanga, I. Hassan, R. MacDonald, *J. Heat Transfer* **2007**, *129*, 1341–1351. DOI:10.1115/1.2754946
18. T. Zhang, Y. Peles, J. T. Wen, T. Tong, J.-Y. Chang, R. Prasher, M. K. Jensen, *Int. J. Heat Mass Transfer* **2010**, *53*, 2347–2360. DOI:10.1016/j.ijheatmasstransfer.2010.02.005
19. H. Tuo, P. Hrnjak, *Int. J. Heat Mass Transfer* **2014**, *71*, 639–652. DOI:10.1016/j.ijheatmasstransfer.2013.10.024
20. Y. Liu, D. F. Fletcher, B. S. Haynes, *Int. J. Heat Mass Transfer* **2013**, *58*, 503–512. DOI:10.1016/j.ijheatmasstransfer.2012.11.068
21. C. Gerardi, J. Buongiorno, L.-w. Hu, T. McKrell, *Nanoscale Research Letters* **2011**, *6*, 232. DOI:10.1186/1556-276X-6-232
22. L. Dong, X. Quan, P. Cheng, *Int. J. Heat Mass Transfer* **2014**, *71*, 189–196. DOI:10.1016/j.ijheatmasstransfer.2013.11.068
23. B. S. Kim, S. Shin, D. Lee, G. Choi, H. Lee, K. M. Kim, H. H. Cho, *Int. J. Heat Mass Transfer* **2014**, *70*, 23–32. DOI:10.1016/j.ijheatmasstransfer.2013.10.061
24. C. Hutter, A. Sanna, T. G. Karayiannis, D. B. R. Kenning, R. A. Nelson, K. Sefiane, A. J. Walton, *Exp. Therm. Fluid Sci.* **2013**, *51*, 94–102. DOI:10.1016/j.expthermflusci.2013.07.005
25. I.-C. Chu, H. C. No, C.-H. Song, *Journal of Nuclear Science and Technology* **2011**, *48*, 936–949. DOI:10.1080/18811248.2011.9711780
26. A. Cioncolini, J. R. Thome, *Int. J. Multiphase Flow* **2017**, *89*, 321–330. DOI:10.1016/j.ijmultiphaseflow.2016.11.003
27. M. Magnini, J. R. Thome, *Int. J. Multiphase Flow* **2017**, *91*, 296–314. DOI:10.1016/j.ijmultiphaseflow.2017.01.015
28. A. Mukherjee, S. G. Kandlikar, Z. J. Edel, *Int. J. Heat Mass Transfer* **2011**, *54*, 3702–3718. DOI:10.1016/j.ijheatmasstransfer.2011.01.030
29. K. Ling, G. Son, D.-L. Sun, W.-Q. Tao, *Int. J. Therm. Sci.* **2015**, *98*, 135–147. DOI:10.1016/j.ijthermalsci.2015.06.019
30. A. Ferrari, M. Magnini, J. R. Thome, *Int. J. Heat Mass Transfer* **2018**, *123*, 928–944. DOI:10.1016/j.ijheatmasstransfer.2018.03.012
31. R. S. Patel, J. A. Weibel, S. V. Garimella, *Int. J. Heat Mass Transfer* **2017**, *114*, 841–851. DOI:10.1016/j.ijheatmasstransfer.2017.06.121
32. A. Sitar, I. Golobic, *Int. J. Heat Mass Transfer* **2015**, *81*, 198–206. DOI:10.1016/j.ijheatmasstransfer.2014.10.034
33. H. J. Ivey, *Int. J. Heat Mass Transfer* **1967**, *10*, 1023–1040. DOI:10.1016/0017-9310(67)90118-4

## Povzetek

Na osnovi eksperimentalnih rezultatov in vizualizacije s hitrotekočo kamero smo analizirali konvektivno vrenje razplinjene redestilirane vode v enojnih  $50 \times 50 \mu\text{m}$  in  $100 \times 50 \mu\text{m}$  mikrokanalih. Vrenje smo parametrizirali glede na vizualizirane frekvence pojavljanja mehurčkov oz. oscilacije vrelnne fronte. Izdelali smo računalniški algoritem za zaznavanje lokacije mehurčkov in meniskusa med parno in kapljevito fazo. Rezultati kažejo, da (i) je vrenje v mikrokanalih dinamičen proces, (ii) se lastne frekvence nihanja povečujejo s povečevanjem gostote toplotnega toka in temperature na dnu mikrokanala, (iii) so amplitude nihanja med vrenjem inverzno sorazmerne lastnim frekvencam nihanja. Z raziskavo smo eksperimentalno potrdili, da so nihanja med vrenjem v enojnih mikrokanalih predvidljiva z vidika trendov in odvisnosti lastne frekvence ter amplitude nihanja. Poznavanje procesa vrenja je še posebej pomembno pri konstruiranju učinkovitih dvofaznih mikro prenosnikov toplote, mikro mešalnikov ali mikro reaktorjev. Namreč, v mikro napravah, ki vključujejo vrenje, postaneta presek in dolžina kanala izjemno pomembna parametra za uspešno načrtovanje učinkovite naprave.

Scientific paper

# Dinuclear Ternary Copper(II) Complex: Synthesis, Characterization, Structure and DNA-Binding Studies

Muhammad Iqbal,<sup>1,\*</sup> Afifa Mushtaq,<sup>2</sup> Saqib Ali,<sup>2,\*</sup> Manzar Sohail<sup>3</sup> and Paul A. Anderson<sup>4</sup>

<sup>1</sup> Department of Chemistry, Bacha Khan University, Charsadda 24420, KPK, Pakistan

<sup>2</sup> Department of Chemistry, Quaid-i-Azam University, Islamabad 45320, Pakistan

<sup>3</sup> Department of Chemistry, School of Natural Sciences, National University of Science and Technology, H-12, Islamabad 44000, Pakistan.

<sup>4</sup> School of Chemistry, The University of Birmingham, Edgbaston, Birmingham, B15 2TT, U.K.

\* Corresponding authors: E-mail: iqbalmo@yahoo.com, iqbal@bkuc.edu.pk (M. Iqbal)

Tel.: +92 91 6002934; fax: +92 91 6540060.

drsa54@hotmail.com, saqibali@qau.edu.pk (S. Ali)

Tel.: +92 51 90642130; fax: +92 51 90642241.

Received: 30-08-2018

## Abstract

A dinuclear centrosymmetric copper(II) complex has been prepared and characterized *via* FT-IR, UV-Visible and electron spin resonance spectroscopy, electrochemical method, and powder and single crystal XRD techniques. The two copper(II) ions are connected by two  $\mu$ -1,1-O atoms belonging to *para*-fluorophenyl acetate ligands. Each copper(II) ion is coordinated by two other carboxylate ligands in monodentate and a 2,2'-bipyridine molecule in bidentate manner. Thus the geometry around each penta-coordinated copper(II) ion is square pyramidal with distortion factor  $\tau = 0.04$ . Purity and uniform crystalline nature of the complex was assessed from powder XRD spectrum. ESR signal consisted of partially resolved hyperfine splitting pattern while electrochemical studies revealed diffusion controlled electron transfer processes with diffusion coefficient of  $1.628 \times 10^{-7} \text{ cm}^2 \text{ s}^{-1}$ . The results of all spectroscopic experiments support each other. The complex afforded mixed binding mode with DNA yielding DNA-binding constant values of  $3.667 \times 10^4$  and  $1.438 \times 10^4 \text{ M}^{-1}$  using cyclic voltammetry and absorption spectroscopy, respectively. The preliminary studies heralded good structural and biological importance of the synthesized complex.

**Keywords:** Oxygen-bridged copper complex; structure; electrochemistry; DNA-binding study.

## 1. Introduction

Binuclear copper(II) carboxylates with 2,2'-bipyridine adopt diverse bridging groups which affect their properties. There can be single bridging group such as a trans-bidentate ligand like 1,4-dibenzoate ion.<sup>1</sup> Such relatively longer spacer ligand precludes the possibility of electronic interaction between two copper(II) ions of the binuclear molecule. In such binuclear copper(II) complexes the observed EPR signal is typical of monomeric complexes with  $g \sim 2$ .<sup>2</sup> Another common bridging group in binuclear copper(II) complexes is chlorine<sup>3</sup> where the di-

chloro-bridged dinuclear complexes with 2,2'-bipyridine were found catalytically more active than their mononuclear analogue.<sup>3</sup> Some complexes contain water molecules bridging the two copper(II) centers<sup>4</sup> where the weaker super-exchange interactions in analogues containing 1,10-phenanthroline and 2,2'-bipyridine have been attributed to the diaqua bridges.

Carboxylate ligand is known for its versatile binding as well as bridging mode. Although the 1,2-bridging mode of carboxylate<sup>5</sup> as well as thio-carboxylate ligand<sup>6</sup> is common, it is also able to bridge two metal centers of dinuclear complexes in 1,1-O-bridging fashion as in phenyl acetate

and maleate derivatives of copper(II) with 2,2'-bipyridine.<sup>7,8</sup> The latter type of bridging can be alone<sup>7</sup> or in combination with other 1,1-bridging groups. The other 1,1-bridging groups can be hydroxyl, aquo<sup>9</sup> and Cl<sup>10</sup> along with a variety of 1,2-bridging groups. These groups have been found to alter the properties of the resulting complexes considerably. This paper reports the synthesis, characterization and DNA-binding properties of a double 1,1-O-bridging copper(II) carboxylate containing biologically important ligand 2,2'-bipyridine.

## 2. Experimental

### 2. 1. Materials and Methods

Anhydrous CuSO<sub>4</sub>, 4-fluorophenyl acetic acid, 2,2'-bipyridine, KCl, NaHCO<sub>3</sub> and sodium salt of the salmon sperm DNA were purchased from Fluka, Switzerland. Solvents like chloroform, methanol and dimethyl sulfoxide were obtained from Merck, Germany. Melting point was measured using an electro-thermal melting point apparatus Gallenkamp, serial number C040281, U.K. FT-IR spectrum was recorded in the range from 4000 to 400 cm<sup>-1</sup> on a Nicolet-6700 FT-IR spectrophotometer, Thermo Scientific, USA, equipped with attenuated total reflectance (ATR) sampling technique. Powder XRD spectrum was obtained at 298 K with a PANalytical, XPert PRO diffractometer employing Cu-K $\alpha$  radiation ( $\lambda = 1.540598 \text{ \AA}$ ). Bruker ESP-300 spectrometer operating at X-band frequencies (-9.5 GHz) was used to obtain the solid state EPR spectrum of the finely powdered single crystalline sample of the complex.

### 2. 2. Single crystal X-ray Crystallography

Diffraction data for the complex were collected at the Australian Synchrotron ( $\lambda = 0.708457 \text{ \AA}$ ) at 100(2) K on beamline MX1.<sup>11</sup> XDS software was used for the data reduction and indexing of diffraction pattern.<sup>12</sup> Direct method was used to solve the crystal structure while using the program SHELXL-97, it was refined against F<sup>2</sup> with full-matrix least-squares method.<sup>13</sup> Refinement of all non-hydrogen atoms was performed with anisotropic displacement parameters.

### 2. 3. Electrochemical Study

Voltammetric study was conducted using an SP-300 potentiostat, serial number 0134, BioLogic Scientific Instruments, France. Complex was dissolved in aqueous DMSO (1:4) solution containing 0.01 M KCl, under an N<sub>2</sub> saturated environment. Measurements were made in a conventional three-electrode cell with a thin platinum wire as counter electrode, a bare glassy carbon electrode (GCE) with a surface area of 0.196 cm<sup>2</sup> as the working electrode and saturated silver/silver chloride electrode (Ag/AgCl) as reference electrode. Prior to each experi-

ment, the GCE was cleaned properly such as polishing with alumina (Al<sub>2</sub>O<sub>3</sub>) and washing with organic solvent and distilled water. All the measurements were performed at room temperature (25  $\pm$  0.5  $^{\circ}$ C).

### 2. 4. DNA-Binding Study by Cyclic Voltammetry

The salmon sperm DNA (SSDNA) solution was prepared by overnight stirring of the solution after adding small amount of its sodium salt to it. Then its absorption spectrum was taken and concentration of DNA was calculated using Beer-Lambert's law putting molar absorptivity = 6600 M<sup>-1</sup> cm<sup>-1</sup>.<sup>14</sup> Complex solution was prepared at 3 mM in aqueous DMSO (1:4) and its voltammograms were recorded in pure form as well as with 10, 20, 30, 40, 50 and 60  $\mu$ M DNA.

### 2. 5. DNA-Binding Study by UV-Visible Spectroscopy

The complex was prepared at 6 mM in aqueous DMSO (1:4) and its absorption spectra were taken in pure form as well as in the presence of 10–90  $\mu$ M DNA. Successive additions of SSDNA were made to the reference as well as sample cells (1 cm path length) and the spectra recorded at room temperature (25  $\pm$  1  $^{\circ}$ C).

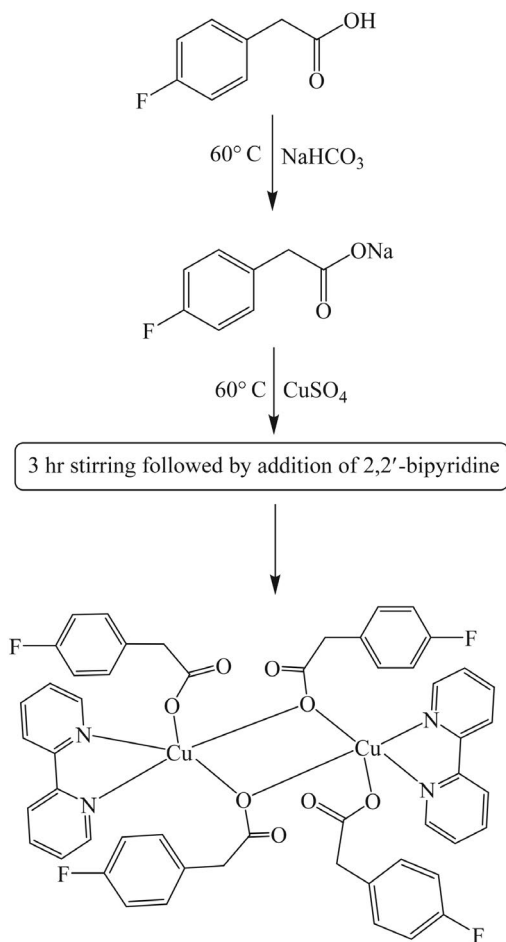
### 2. 6. Synthetic Procedure of the Complex

4-Fluorophenyl acetic acid (6 mmol, 0.925 g) was neutralized via reacting with an equimolar quantity of sodium bicarbonate (0.504 g, 6 mmol) in distilled water. After neutralization, copper sulphate (0.240 g, 3 mmol) was added to the reaction mixture and was stirred for 3 h at 60  $^{\circ}$ C as depicted in Scheme 1. This was followed by the addition of solid 2,2'-bipyridine (0.468 g, 3 mmol) and stirring was continued for further 3 h. The final product was washed with distilled water and dried in air. A mixture of chloroform and methanol (1:1) was used for crystallization.

Light blue crystals; m.p. 150–152  $^{\circ}$ C; yield (70%). FT-IR (cm<sup>-1</sup>): 1614  $\nu$ (OCO)<sub>asym</sub>, 1421  $\nu$ (OCO)<sub>sym</sub>,  $\Delta\nu = 193, 2955 \nu$ CH<sub>2</sub>, 3084  $\nu$ (Ar-H), 1590, 1473  $\nu$ Ar(C=C), 1217  $\nu$ (Ar-F), 421  $\nu$ (Cu-O), 506  $\nu$ (Cu-N).

## 3. Results and Discussion

Copper(II) complex with 4-fluorophenyl acetic acid and 2,2'-bipyridine has been isolated in quantitative yield by following Scheme 1. The complex has been characterized by various analytical techniques such as infra-red, UV-Visible and electron spin resonance spectroscopy as well as powder and single crystal X-ray diffraction while the purity level of the complex was confirmed by powder



Scheme 1. Synthetic procedure of the complex

XRD pattern. DNA binding constant for the complex were evaluated, using cyclic voltammetry and UV-Visible spectrophotometry.

### 3. 1. FT-IR Data

FT-IR spectrum of the complex showed all the expected bands which helped to deduce its structure. The bonding mode of the carboxylate moiety was indicated by its characteristic stretching frequency observed at 1614 and 1421  $\text{cm}^{-1}$  corresponding to the asymmetric and symmetric OCO stretching vibrations, respectively. The appearance of a Cu–O absorption band at 421  $\text{cm}^{-1}$  confirmed the coordination of the carboxylate ligands through oxygen. The values of  $\Delta\nu = \{\nu_{\text{asym}}(\text{OCO}) - \nu_{\text{sym}}(\text{OCO})\} = 193$  calculated for the complex indicated bridging bidentate mode of coordination of the carboxylate moiety to copper(II) ion in the complex.<sup>15</sup> In addition, the appearance of C=N stretching band of the complex at 1598  $\text{cm}^{-1}$  instead of its normally observed characteristic region (1610–1625  $\text{cm}^{-1}$ )<sup>16,17</sup> indicated the involvement of the nitrogen atom of bipyridine in bonding with copper(II) ion.<sup>18</sup> The appearance of a new medium intensity band for

the complex in the region 506  $\text{cm}^{-1}$ , attributable to a Cu–N vibration further supported it.<sup>19</sup> The aromatic C=C and C–H stretching vibrations were observed at 1590, 1473 and 3084  $\text{cm}^{-1}$ , respectively. The methylene C–H stretching frequency of the complex was observed at 2955  $\text{cm}^{-1}$  which were supported by the presence of bands at 730 and 1359  $\text{cm}^{-1}$  corresponding to its rocking and bending vibrations, respectively. Methyl C–H stretching frequency gave rise to absorption band at 2985  $\text{cm}^{-1}$  supported by the band at 1443  $\text{cm}^{-1}$  assignable to the bending vibrational motion of this functionality. Aromatic C–F was indicated by well-defined peak at 1217  $\text{cm}^{-1}$ .

According to the literature, 2,2'-bipyridine and 1,10-phenanthroline give rise to absorption bands at 756, 851, 1090, 1138, 1274, 1434 and 3337  $\text{cm}^{-1}$ .<sup>20</sup> Keeping in view these absorption values, the bands appearing at 3329, 1275, 1167, 1090 and 775  $\text{cm}^{-1}$  have been assigned to the coordinated 2,2'-bipyridine molecule. The presence of lattice water molecules was indicated by a broad absorption band at 3200–3600  $\text{cm}^{-1}$ .

### 3. 2. Powder XRD Study

Powder X-ray diffraction spectrum of the synthesized complex has been obtained and compared with the respective simulated spectrum of the complex by superimposing the spectra. The experimental and simulated powder XRD spectra are in complete agreement mutually as shown in Fig. 1, indicating that the complex has been isolated and crystallized in completely pure form.

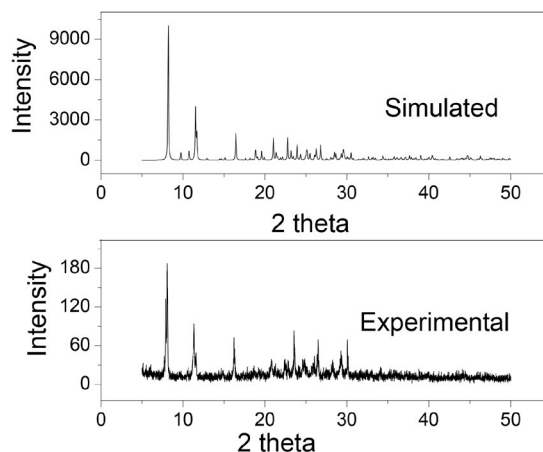
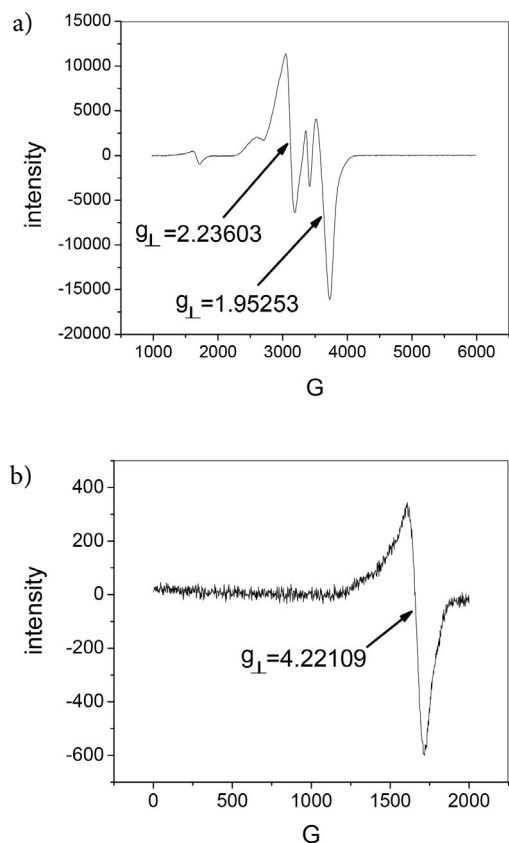


Figure 1. Experimental and simulated powder XRD spectra of the complex.

### 3. 3. ESR Spectroscopy

X-band ESR spectrum of crystalline sample of the complex in solid state is shown in Fig. 2A. The spectrum is typical of dinuclear copper(II) complexes in triplet state<sup>21</sup> showing partially resolved hyperfine splitting with  $g^{\perp}$  values 2.23603 and 1.95253 indicating dimeric structure for the



**Figure 2.** A, X-Band ESR spectrum of complex showing partially resolved hyperfine splitting. B, low field spectrum showing the 'half-filled' forbidden transition.

complex in solid state.<sup>21,22</sup> The low field spectrum shown in Fig. 2B indicates the 'half-filled' forbidden transition.<sup>21</sup> Thus the typical ESR signal confirmed the +2 oxidation state of copper in the complex and supported the nuclearity and structure of the synthesized copper(II) complex.

### 3. 4. Structural Description of the Complex

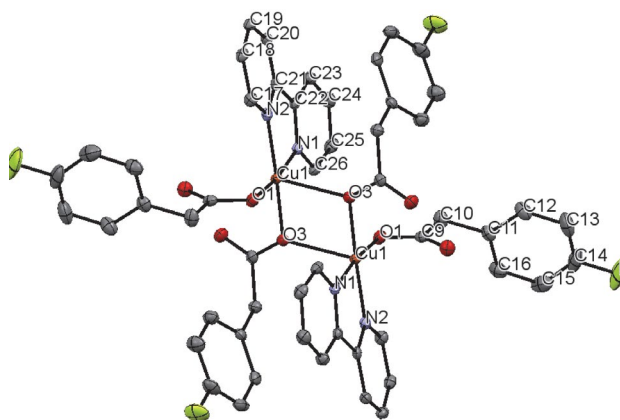
The ORTEP diagram with the atom numbering scheme of the complex is shown in Fig. 3, while the crystal data and refinement parameters are given in Tables 1 and 2. In the dinuclear complex, the two copper(II) ions are connected by two  $\mu$ -1,1-O atoms belonging to carboxylate ligands. Each copper(II) ion is coordinated by two other carboxylate ligands in monodentate and a 2,2'-bipyridine molecule in bidentate manner. This results in square pyramidal geometry for each penta-coordinated copper(II) ion. The complex is centrosymmetric in which the metal centers are bridged by  $\mu$ -1,1-O atoms and the center of symmetry is lying at the center of the  $\text{Cu}_2\text{O}_2$  parallelogram core. Constituting the axial position of one square pyramid, each of the bridging oxygen atoms is part of the square plane of the other square pyramid. Each pair of the copper atoms constitutes a four cornered planar  $\text{Cu}_2\text{O}_2$  core where the two bipyridine molecules are *trans* oriented

with respect to the  $\text{Cu}_2\text{O}_2$  core making five-membered chelate rings with Cu. The distortion factor  $\tau$  ( $= \beta - \alpha/60^\circ$ , where  $\beta$  and  $\alpha$  are the largest ( $174.48(6)^\circ$ ) and second largest ( $172.31(7)^\circ$ ) angles around the five-coordinated metal ion) calculated for the complex was 0.04, which shows a slightly distorted square pyramidal geometry for each copper(II).<sup>23</sup> The Cu–N bond distances are 1.9999(18) and 2.0189(18) Å and are similar to the corresponding distances found in previously reported dinuclear copper-bipyridine complexes.<sup>24</sup>

Cu–O distances of the complex are quite asymmetrical. The Cu–O bond distances in the equatorial plane are 1.9441(16) and 1.9800(15) Å which are typical of the Cu–O equatorial distances of the previously reported dimeric<sup>25</sup> and polymeric<sup>26,27</sup> complexes. The axial Cu–O distance is 2.3535(15) Å indicating relatively weaker bond with copper. Since copper(II) complexes with square pyramidal geometry are Jahn-Teller inactive, the elongation of the apical Cu–O bonds is owing to the filled antibonding  $a_1$  ( $d_z^2$ -orbital) leading to more electron density of the filled antibonding orbital along the apical Cu–O bond axis.<sup>28</sup> The  $b_1$  ( $d_{x^2-y^2}$ ) orbital is half filled and is not offering that much repulsion to the four ligands (two Cu–O and two Cu–N bonds) present in the basal plane. Such elongation of the apical bond has been found typical of the previously reported complexes as well.<sup>29</sup> The nearly perfect square pyramidal geometry around copper has been made possible by the asymmetric nature of the Cu–O bond distance of the bridging oxygen. This Cu–O–Cu asymmetric bonding of the bridging oxygen is also typical of other copper(II) complexes.<sup>25</sup> The smallest angle around Cu is  $\text{N–Cu–N} = 80.74(7)^\circ$  being formed by the copper ion and two nitrogen atoms of bipyridine molecule and has been found typical of other copper(II) complexes with N- and O-donor ligands.<sup>30</sup>

#### Packing arrangement:

The packing diagram of the complex is shown in Fig. 4, where the uncoordinated oxygen atoms of the carboxyl-



**Figure 3.** ORTEP drawing of the complex with atom numbering scheme. H-atoms not shown for clarity.



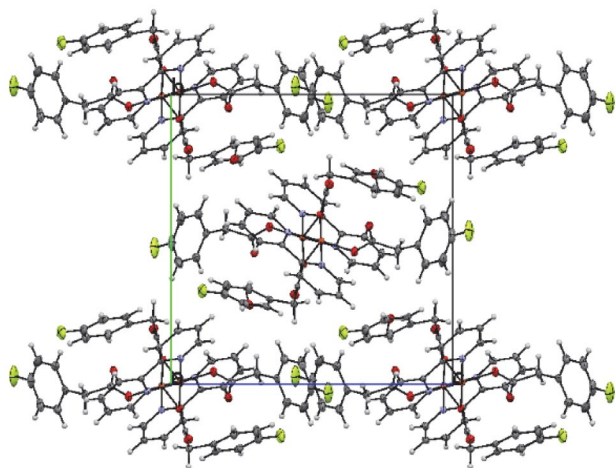


Figure 4. Packing diagram of complex

Table 1. Structure refinement parameters of the dinuclear complex

Empirical formula	C <sub>52</sub> H <sub>44</sub> F <sub>4</sub> Cu <sub>2</sub> N <sub>4</sub> O <sub>10</sub>
Formula weight (g mol <sup>-1</sup> )	1088.01
T (K)	100(2)
Crystal system	Monoclinic
Space group	P2 <sub>1</sub> /n
Unit cell dimensions	
a (Å)	9.948(2)
b (Å)	15.335(3)
c (Å)	15.460(3)
α (°)	90
β (°)	101.58(3)
γ (°)	90
V (Å <sup>3</sup> )	2310.5(8)
Z	2
ρ (calculated) (Mg/m <sup>3</sup> )	1.564
μ (mm <sup>-1</sup> )	1.004
F(000)	1116
Reflections collected	14039
Independent reflections	4035
Data / restraints / parameters	4035 / 0 / 405
Goodness-of-fit on F <sup>2</sup>	1.077
Final R indices [I > 2 σ(I)]	R <sub>1</sub> = 0.0335, wR <sub>2</sub> = 0.086
R indices (all data)	R <sub>1</sub> = 0.0375, wR <sub>2</sub> = 0.0883

ate ligand establish weaker interactions with the hydrogen atoms of the 2,2'-bipyridine ligand of the side lying dimer and those of the lattice water molecule. Additionally, the water molecule present in the crystal lattice is responsible for strong intermolecular interactions: its oxygen and hydrogen atoms are able to interact with the methylene hydrogen and the uncoordinated oxygen atoms of the carboxylate ligands of the two neighboring dinuclear complexes, respectively, thus completing the packing. Similarly, one out of two fluorine atoms of each of the two asymmetric units of the dimeric molecules of the complex is closer enough to attract methylene hydrogen atoms of a ligand in the next dimer.

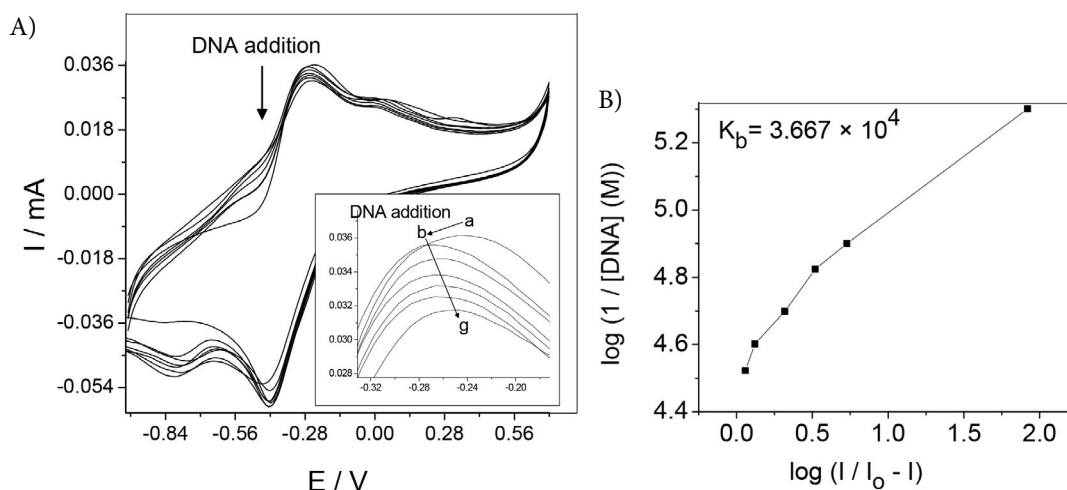
Table 2. Selected bond lengths and angles of the dinuclear complex

Distances, Å	
N1–Cu1	1.9999(18)
N2–Cu1	2.0189(18)
O1–Cu1	1.9441(16)
O3–Cu1	1.9800(15)
Cu1–O3	2.3535(15)
Angles, °	
O1–Cu1–O3	91.69(7)
O1–Cu1–N2	172.31(7)
O3–Cu1–N2	95.51(7)
O1–Cu1–N1	91.89(7)
O3–Cu1–N1	174.48(6)
N2–Cu1–N1	80.74(7)
O1–Cu1–O3	90.41(6)
O3–Cu1–O3	77.84(6)
N2–Cu1–O3	93.76(6)
N1–Cu1–O3	106.33(6)

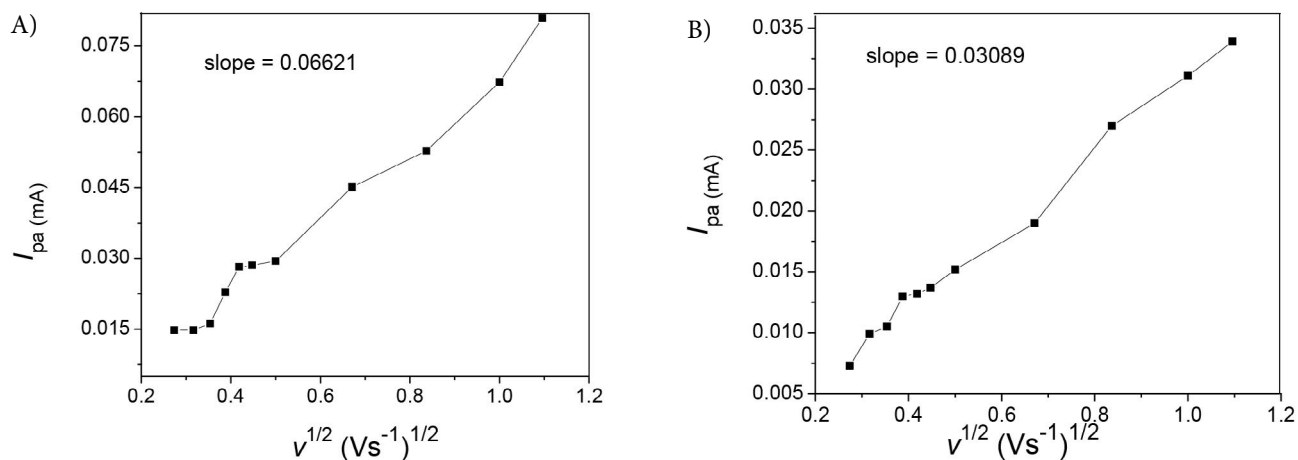
### 3. 5. DNA Binding Study Through Cyclic Voltammetry

DNA binding ability of the complex has been explored using cyclic voltammetry where the shift of peak potential was used to interpret the mode of DNA binding activity of the complex. According to literature, shifting of potential to the less positive region on addition of DNA exhibits electrostatic mode of interaction with complex,<sup>31,32</sup> while to a more positive region indicates intercalative mode. However, a mixed DNA-complex binding behavior is usually observed in practice. Based on the above criteria, a mixed binding mode has been observed for the synthesized complex. A shift of 40 mV in the potential to the less positive region was observed on addition of DNA to the complex solution as shown in Fig. 5A, exhibiting an electrostatic mode of interaction with the complex.<sup>31</sup> However, after successive addition of SSDNA, the potential kept shifting to the right side which shows a concomitant intercalative mode of binding with SSDNA as well. The intercalative ability of the complex is attributed to the homo- as well as heterocyclic aromatic rings in the molecular structure of the complex while the concomitant electrostatic mode is owing to the presence of fluorine atoms at the *para*-position of the phenyl rings which are able to establish electrostatic interaction with DNA base pairs. In short, the presence of polar as well as planar groups give rise to a mixed DNA binding mode. Since the shift in peak potential towards less positive region is far more compared to the shift towards more positive region, the major mode of binding will be electrostatic.

The diminution in the peak current as a consequence of DNA addition to the complex solution as evident from Fig. 5 (inset) is attributed to the decrease in concentration of the free complex as a result of the formation of complex-DNA adduct. The slope value of  $i_p$  vs.



**Figure 5.** A, Cyclic voltammograms of the complex in the absence and presence of 10-60  $\mu\text{M}$  DNA. The peak current decreases and the peak potential is shifted to the right hand side on successive additions of DNA as shown in inset. B, plot of  $\log(1/[DNA])$  vs.  $\log(I/(I_0 - I))$  for the calculation of binding constant of complex through cyclic voltammetry.



**Figure 6.** Plots of anodic peak current,  $i_p$  vs. square root of scan rate,  $\nu^{1/2}$  before (A) and after (B) DNA addition showing reduction in slope value with DNA addition.

$\nu^{1/2}$  plot is reduced from 0.066 to 0.030 on addition of DNA as shown in Fig. 6 indicating the binding of DNA with complex.<sup>33,34</sup> This decrease was used as basis for the calculation of binding constant of the complex with DNA making use of the straight line plot of  $\log 1/[DNA]$  vs.  $\log I/(I_0 - I)$  (Fig. 5B), using the following equation (equation 3.1):<sup>35</sup>

$$\log(1/[DNA]) = \log K_b + \log I/(I_0 - I) \quad (1)$$

where  $K_b$  is the binding constant,  $I_0$  and  $I$  are the peak currents of the complex in the absence and presence of DNA, respectively. The value of  $K_b$  was found to be  $3.667 \times 10^4 \text{ M}^{-1}$  which is comparable to other structurally related copper(II)<sup>36,37</sup> and Rh(II)<sup>38</sup> complexes.

Since the electro-active complex moves to the electrodes *via* diffusion, its diffusion coefficient  $D_0$  should suffer diminution with DNA addition.  $D_0$  was calculated

using the Randles-Sevcik equation<sup>39</sup> (equation 3.2) *via* putting various parameters in it and measuring voltammograms at different scan rates before and after DNA addition.

$$i_p = (2.99 \times 10^5) n(\alpha n)^{1/2} A C^* D_0^{1/2} \nu^{1/2} \quad (2)$$

where  $i_p$ ,  $n$ ,  $\alpha$ ,  $A$ ,  $C^*$ ,  $D_0$  and  $\nu$  denote the peak current in ampere, the number of electrons involved charge transfer coefficient, surface area of electrode, molar concentration of complex, diffusion coefficient in  $\text{cm}^2\text{s}^{-1}$  and scan rate in  $\text{V s}^{-1}$ , respectively.

The slope value was obtained making use of the respective  $i_p$  vs.  $\nu^{1/2}$  plots for oxidation and reduction while Bard and Faulkner relation<sup>40</sup> (equation 3.3) was used to calculate  $\alpha n$ .

$$\alpha n = 47.7/[E_p - E_p/2] \text{ mV} \quad (3)$$

where  $E_p$  is the peak potential and  $E_p/2$  is the peak potential at half of the maximum peak current value. The values of  $D_o$  thus calculated for the complex before and after DNA addition are  $28.255 \times 10^{-8}$  and  $8.413 \times 10^{-8} \text{ cm}^2\text{s}^{-1}$ . The higher value of  $D_o$  of the free complex shows higher mobility of the complex before DNA addition which indicates the interaction of complex and DNA.<sup>41,42</sup> Thus the voltammetric study indicated the potent DNA-binding potency of the complex.

### 3. 6. Absorption Spectroscopy

The complex showed a broad band in the visible region of the electromagnetic spectrum with  $\lambda_{\text{max}} = 680 \text{ nm}$  attributed to d-d transition of  $\text{Cu}^{2+}$ <sup>43,44</sup> which is typical of geometrically similar copper(II) complexes and helped to confirm the structure of the complex in solution. Such broad absorption band with  $\lambda_{\text{max}} = 680 \text{ nm}$  is typical of a distorted octahedral geometry in solution as shown in Fig. 7A (peak a). This indicates the attachment of a DMSO molecule to the square pyramidal copper in the complex. According to the literature, other copper(II) complexes of similar geometry have been found to show absorbance in the same wave length region.<sup>45,46</sup> Using Beer-Lambert's law,  $\epsilon$  of the complex was calculated to be  $193 \text{ L mol}^{-1} \text{ cm}^{-1}$  which is of the same magnitude as those of the structurally related copper(II) complexes.<sup>43</sup>

### 3. 7. DNA Study Through Absorption Spectroscopy

Since the absorption of the complex depends on concentration, variation of absorbance of complex is a sensitive method of DNA-binding activity. Shift in  $\lambda_{\text{max}}$  as well as reduction in absorbance are accompanied with binding of the complex with DNA. When  $\lambda_{\text{max}}$  is shifted towards shorter wavelength side, an electrostatic mode is manifested while intercalative mode is exhibited by shift towards longer wavelengths.<sup>47,48</sup> Absorbance of the synthesized complex exhibited marked decrease with addition of DNA

(10–90  $\mu\text{M}$ ) along with small red shift of 4 nm as indicated in its spectrum shown in Fig. 7A. This type of binding has been termed as 'mixed binding mode' i.e., partial intercalation with groove binding mode.

The decrease in absorbance as a result of DNA addition gave the basis for quantitative affinity of copper(II) complex for DNA by calculating its binding constant  $K_b$  using the famous Benesi-Hildebrand equation<sup>49</sup> (equation 3.4):

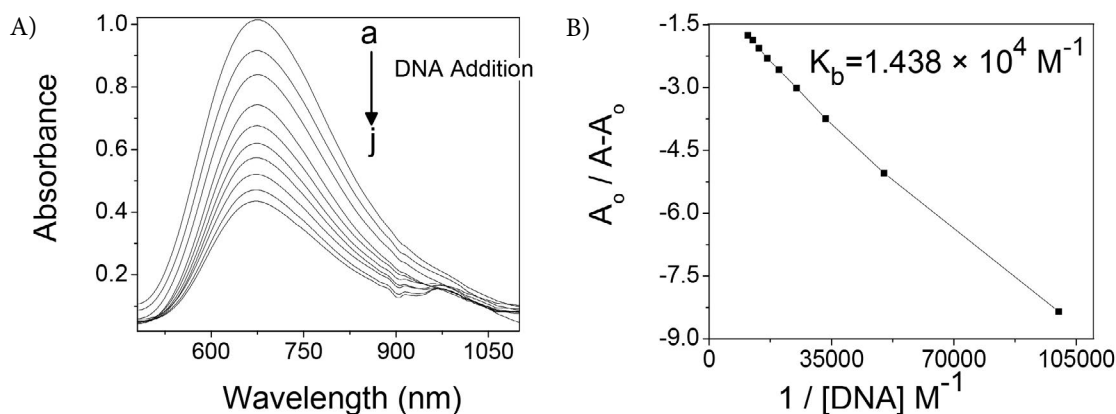
$$\frac{A_o}{A - A_o} = \frac{\epsilon_G}{\epsilon_{H-G} - \epsilon_G} + \frac{\epsilon_G}{\epsilon_{H-G} - \epsilon_G} \frac{1}{K[\text{DNA}]} \quad (4)$$

where  $A$  and  $A_o$  are the absorbance of the complex in the presence and absence of DNA while  $\epsilon_{H-G}$  and  $\epsilon_G$  are their absorption coefficients, respectively. The ratio of slope to intercept of the plot of the term on the left-hand side of equation 3.4 vs.  $1/[\text{DNA}]$  gives  $K_b$  as shown in Fig. 7B.

The binding constant value of the complex was  $1.438 \times 10^4 \text{ M}^{-1}$  which is of the same order of magnitude as that calculated using cyclic voltammetry. The *para*-fluoro group on the phenyl ring and the planar aromatic rings may be responsible for the facile DNA-binding ability of the complex. Similar binding potency has been observed for other copper(II) complexes as well.<sup>50,51</sup> Thus the results of the absorption spectroscopy and cyclic voltammetry for the DNA-binding potency are in support of each other. The DNA-binding ability of the complex explored through these two techniques heralds the biological relevance of the synthesized complex.

## 4. Conclusion

Mixed N- and O-donor ligand copper(II) carboxylate complex has been synthesized, isolated and purified in quantitative yield. Its characterization has been confirmed through single crystal XRD while the purity level was evaluated by superimposing the simulated and experimental powder XRD plots which were found in complete agreement showing that the crystalline sample was composed of



**Figure 7.** A, Absorption spectra of complex. Peak a indicates spectrum of pure complex while other peaks (b-j) are after DNA addition (10–90  $\mu\text{M}$ ). B, Plot of  $A_o/(A - A_o)$  vs.  $1/[\text{DNA}]$  for the calculation of binding constant of complex through absorption spectroscopy.

the single crystalline phase without any other impurity. Crystal structure has shown that the geometry around copper(II) ion is square pyramidal in the dinuclear complex with asymmetrically bridging oxygen atom. The DNA binding ability of the complex was judged from CV and UV-Visible spectroscopy by calculating the intrinsic binding constant of the complex with DNA from both techniques. Both techniques resulted in  $K_b$  values of the same order of magnitude such as  $3.667 \times 10^4$  and  $1.438 \times 10^4 \text{ M}^{-1}$ , respectively. Moreover, the reduction of the diffusion co-efficient of the complex on addition of DNA further supported the DNA binding ability of the complex.

**Supplementary material:** CCDC 890111 contains all the crystallographic information about the synthesized complex. The data is accessible at <http://www.ccdc.cam.ac.uk/conts/retrieving.html>, or from the Cambridge Crystallographic Data Centre, 12 Union Road, Cambridge CB2 1EZ, UK; fax: +44 1223 336 033; or e-mail: [deposit@ccdc.cam.ac.uk](mailto:deposit@ccdc.cam.ac.uk).

## 5. Acknowledgements

M.I. is thankful to Dr. Paul W. Davies and Mr. Terry Green for ESR spectra obtained at School of Chemistry, The University of Birmingham, Edgbaston, Birmingham, B15 2TT, U.K

## 6. References

- W. Huang, D. Hu, S. Gou, H. Qian, H.-K. Fun, S. S. S. Raj, Q. Meng, *J. Mol. Struct.* **2003**, *649*, 269–278. DOI:10.1016/S0022-2860(03)00080-2
- T.-D. Shfith, J.R. Pitbrow, *Coord. Chem. Rev.* **1974**, *13*, 173–278. DOI:10.1016/S0010-8545(00)80255-6
- E. Liu, Y.Z. Zhang, L. Li, C. Yang, J.C. Fettinger, G. Zhang, *Polyhedron* **2015**, *99*, 223–229. DOI:10.1016/j.poly.2015.07.080
- K. C. Thatipamula, G. Bhargavi, M. V. Rajasekharan, *Polyhedron* **2015**, *97*, 182–187. DOI:10.1016/j.poly.2015.05.027
- A. Mushtaq, S. Ali, M. Iqbal, M. N. Tahir, H. Ismail, *J. Chem. Soc. Pak.* **2017**, *39*, 471–477.
- G. A. van Albada, I. Mutikainen, U. Turpeinen, J. Reedijk, *Inorg. Chim. Acta* **2001**, *324*, 273–277. DOI:10.1016/S0020-1693(01)00613-2
- M. Iqbal, S. Ali, M. N. Tahir, N. Muhammad, N. A. Shah, M. Sohail, V. Pandarinathan, *J. Mol. Struct.* **2015**, *1093*, 135–143. DOI:10.1016/j.molstruc.2015.03.058
- K. N. Lazarou, V. Psycharis, S. P. Perlepes, C. P. Raptopoulou, *Polyhedron* **2009**, *28*, 1085–1096. DOI:10.1016/j.poly.2009.01.023
- S. D. Kurbah, A. Kumar, I. Syiemlieh, A. K. Dey, R. A. Lal, *J. Mol. Struct.* **2018**, *1154*, 535–542. DOI:10.1016/j.molstruc.2017.10.054
- S. Youngme, J. Phatchimkun, N. Wannarit, N. Chaichit, S. Meejoo, G. A. van Albada, J. Reedijk, *Polyhedron* **2008**, *27*, 304–318. DOI:10.1016/j.poly.2007.09.009
- T. M. McPhillips, S. E. McPhillips, H. J. Chiu, A. E. Cohen, A. M. Deacon, P. J. Ellis, E. Garman, A. Gonzale, N. K. Sauter, R. P. Hizackerley, S. M. Soltis, P. Kuhn, *J. Synchrotron. Rad.* **2002**, *9*, 401–406. DOI:10.1107/S0909049502015170
- W. Kabsch, *Acta Cryst. D* **2010**, *66*, 125–132. DOI:10.1107/S0907444909047337
- G. M. Sheldrick, *Acta Cryst. A* **2008**, *64*, 112–122. DOI:10.1107/S0108767307043930
- C. V. Sastri, D. Eswaramoorthy, L. Giribabu, B. G. Maiya, *J. Inorg. Biochem.* **2003**, *94*, 138–145. DOI:10.1016/S0162-0134(02)00622-0
- S. Leconte, R. Ruzziconi, *J. Fluorine Chem.* **2002**, *11*, 167–172. DOI:10.1016/S0022-1139(02)00161-6
- K. V. Shuvaev, S. Sproules, J. M. Rautiainen, E. J. L. McInnes, D. Collison, C. E. Anson, A. K. Powell, *Dalton Trans.* **2013**, *42*, 2371–2381. DOI:10.1039/C2DT31946B
- C. Jayabalakrishnan, K. Natarajan, *Transit. Met. Chem.* **2002**, *27*, 75–79. DOI:10.1023/A:1013437203247
- Z. H. Abd El-Wahab, M. M. Mashaly, A. A. Salman, B. A. El-Shetary, A. A. Faheim, *Spectrochim. Acta A* **2004**, *60*, 2861–2873. DOI:10.1016/j.saa.2004.01.021
- M. Shakir, N. Begum, S. Parveen, P. Chingsubam, S. Tabasum, *Synth. React; Inorg; Met. Org. Chem.* **2004**, *34*, 1135–1148. DOI:10.1081/SIM-120039262
- A. Hangan, A. Bodoki, L. Oprean, G. Alzuet, M. Liu-González, J. Borrás, *Polyhedron* **2010**, *29*, 1305–1313. DOI:10.1016/j.poly.2009.12.030
- K. C. Thatipamula, G. Bhargavi, M. V. Rajasekharan, *Polyhedron* **2015**, *97*, 182–187. DOI:10.1016/j.poly.2015.05.027
- I. Banerjee, P. N. Samanta, K. K. Das, R. Ababei, M. Kalisz, A. Girard, C. Mathonière, M. Nethaji, R. Clérac, M. Ali, *Dalton Trans.* **2013**, *42*, 1879–1892. DOI:10.1039/C2DT30983A
- A.W. Addison, T. N. Rao, J. Reedijk, J. van Rijn, G. C. Verschoor, *J. Chem. Soc. Dalton Trans.* **1984**, 1349–1356. DOI:10.1039/DT9840001349
- F. Xu, T. Tao, K. Zhang, X.-X. Wang, W. Huang, X.-Z. You, *Dalton Trans.* **2013**, *42*, 3631–3645. DOI:10.1039/c2dt32281a
- A. Mushtaq, S. Ali, M. N. Tahir, H. Ismail, B. Mirza, M. Saadiq, M. A. Haleem, M. Iqbal, *Acta Chim. Slov.* **2017**, *64*, 397–408. DOI:10.17344/acsi.2017.3250
- O. Castillo, A. Luque, S. Iglisias, C. Guzman-Mirallas, P. Roman, *Inorg. Chem. Commun.* **2001**, *4*, 640–642. DOI:10.1016/S1387-7003(01)00291-X
- P. Phuengphai, S. Youngme, N. Chaichit, C. Pakawatchai, G.A. Albada, M. Quesada, J. Reedijk, *Polyhedron* **2006**, *25*, 2198–2206. DOI:10.1016/j.poly.2006.01.014
- M. A. Halcrow, *Chem. Soc. Rev.* **2013**, *42*, 1784–1795. DOI:10.1039/C2CS35253B
- M. Iqbal, S. Ali, M. N. Tahir, *Acta Chim. Slov.* **2018**, *65*, 131–137. DOI:10.17344/acsi.2017.3702
- G. S. Baghel, J.P. Chinta, A. Kaiba, P. Guionneau, C.P. Rao, *Cryst. Growth Des.* **2012**, *12*, 914–926. DOI:10.1021/cg2013683

31. M. T. Carter, M. Rodriguez, A. J. Bard, *J. Am. Chem. Soc.* **1989**, *111*, 8901–8911. DOI:10.1021/ja00206a020
32. M. S. Mohamed, A. A. Shoukry, A. G. Ali, *Spectrochim. Acta Part A* **2012**, *86*, 562–570. DOI:10.1016/j.saa.2011.11.015
33. K. Abdi, H. Hadadzadeh, M. Weil, M. Salimi, *Polyhedron* **2012**, *31*, 638–648. DOI:10.1016/j.poly.2011.10.028
34. Q. X. Wang, F. Gao, K. Jiao, *Electroanalysis* **2008**, *20*, 2096–2099. DOI:10.1002/elan.200804291
35. Q. Feng, N.Q. Li, Y. Y. Jiang, *Anal. Chim. Acta* **1997**, *344*, 97–104. DOI:10.1016/S0003-2670(97)00008-1
36. J. L. Garcia-Gimenez, J. Hernandez-Gil, A. Martinez-Ruiz, A. Castineiras, M. Liu-Gonzalez, F.V. Pallardo, J. Borrás, G.A. Pina, *J. Inorg. Biochem.* **2013**, *121*, 167–178. DOI:10.1016/j.jinorgbio.2013.01.003
37. K. Suntharalingam, D. J. Hunt, A. A. Duarte, A. J. P. White, D. J. Mann, R. Vilar, *Chem. Eur. J.* **2012**, *18*, 15133–15141. DOI:10.1002/chem.201202482
38. A. M. Angeles-Boza, P. M. Bradley, P. K.-L. Fu, S. E. Wicke, J. Bacsa, K. R. Dunbar, C. Turro, *Inorg. Chem.* **2004**, *43*, 8510–8519. DOI:10.1021/ic049091h
39. J. Wang, *Analytical Electrochemistry*, 1st ed., VCH Publishers, 1994, pp. 165–166.
40. A. J. Bard, L. R. Faulkner, *Electrochemical Methods, Fundamentals and Applications*, 2nd ed., Wiley, New York, 2004, pp. 236.
41. M. Chauhan, K. Banerjee, F. Arjmand, *Inorg. Chem.* **2007**, *46*, 3072–3082. DOI:10.1021/ic061753a  
DOI:10.1016/j.jinorgbio.2012.09.019
42. G.-Y. Li, K.-J. Du, J.-Q. Wang, J.-W. Liang, J.-F. Kou, X.-J. Hou, L.-N. Ji, H. Chao, *J. Inorg. Biochem.* **2013**, *119*, 43–53.
43. S. Majumder, M. Fleck, C. R. Lucas, S. Mohanta, *J. Mol. Struct.* **2012**, *1020*, 127–133. DOI:10.1016/j.molstruc.2012.04.003
44. V. Rajendiran, R. Karthik, M. Palaniandavar, H. Stoeckli-Evans, V. S. Periasamy, M. A. Akbarsha, B.S. Srinag, H. Krishnamurthy, *Inorg. Chem.* **2007**, *46*, 8208–8221. DOI:10.1021/ic700755p
45. M. Saif, M. M. Mashaly, M. F. Eid, R. Fouad, *Spectrochim. Acta Part A* **2012**, *92*, 347–356. DOI:10.1016/j.saa.2012.02.098
46. E. Q. Procopio, T. Fukushima, E. Barea, J. A. R. Navarro, S. Horike, S. Kitagawa, *Chem. Eur. J.* **2012**, *18*, 13117–13125. DOI:10.1002/chem.201201820
47. L. Jia, J. Shi, Z.-H. Sun, F.-F. Li, Y. Wang, W.-N. Wu, Q. Wang, *Inorg. Chim. Acta* **2012**, *391*, 121–129. DOI:10.1016/j.ica.2012.05.014
48. X. Li, Y.-T. Li, Z.-Y. Wu, Y.-J. Zheng, C.-W. Yan, *Inorg. Chim. Acta* **2012**, *385*, 150–157. DOI:10.1016/j.ica.2012.01.047
49. M.Y. Ni, Y. Wang, H.L. Li, *Pol. J. Chem.* **1997**, *71*, 816–822.
50. P. Zivec, F. Perdih, I. Turel, G. Giester, G. Psomas, *J. Inorg. Biochem.* **2012**, *117*, 35–47. DOI:10.1016/j.jinorgbio.2012.08.008
51. A. Kellett, O. Howe, M. O'Connor, M. McCann, B. S. Creaven, S. McClean, A. F.-A. Kia, A. Casey, M. Devereux, *Free Radical Biol. Med.* **2012**, *53*, 564–576. DOI:10.1016/j.freeradbiomed.2012.05.034

## Povzetek

Sintetizirali smo dvojedrni centrosimetrični bakrov(II) kompleksi in ga okarakterizirali z FT-IR, UV-vidno in EPR spektroskopijo, praškovno in monokristalno XRD analizo ter elektrokemijsko metodo. Dva bakrova(II) iona sta povezana preko dveh  $\mu$ -1,1-O atomov *p*-fluorofenilacetatnega liganda. Vsak bakrov(II) ion je koordiniran z dvema monodentatnima karboksilatnima ligandoma in bidentatno z molekulo 2,2'-bipiridina. Geometrija okoli pentakoordiniranega bakrovega(II) iona je kvadratno piramidalna s faktorjem popačenja  $\tau = 0.04$ . Čistost in uniformnost kristaliničnega produkta je bila ugotovljena z praškovnim XRD posnetkom. EPR signal ima delno razrešljivo hiperfino strukturo, medtem ko elektrokemijske študije kažejo na difuzijsko kontroliran prenos elektrona z difuznim koeficientom  $1.628 \times 10^{-7} \text{ cm}^2 \text{ s}^{-1}$ . Rezultati spektroskopskih eksperimentov so si v soglasju. Kompleks se veže na DNA z veznima konstantama  $3.667 \times 10^4$  in  $1.438 \times 10^4 \text{ M}^{-1}$ , kot je določeno s ciklično voltometrijo oziroma absorpcijsko spektroskopijo. Preliminarni rezultati kažejo na strukturno in biološko pomembnost pripravljene kompleksa.

Scientific paper

# A Study on the Properties of Poly (Styrene-co-Methyl Methacrylate)/Silica Aerogel Nanocomposites Prepared via *in situ* SR&NI ATRP

Khezrollah Khezri<sup>1</sup> and Yousef Fazli<sup>2,\*</sup><sup>1</sup> Young Researchers and Elite Club, Central Tehran Branch, Islamic Azad University, Tehran, Iran<sup>2</sup> Department of Chemistry, Faculty of Science, Arak Branch, Islamic Azad University, Arak, Iran, P.O. Box 14155-6455, Tel: +988633412603

\* Corresponding author: E-mail: yousef.fazli75@gmail.com; y-fazli@iau-arak.ac.ir

Received: 30-08-2018

## Abstract

Simultaneous reverse and normal initiation technique for atom transfer radical copolymerization (SR&NI ATRP) of styrene and methyl methacrylate in the presence of hexamethyldisilazane (HMDS)-modified silica aerogel nanoparticles (H-SAN) and investigating the effect of addition of H-SAN on the copolymerization and thermal properties of the products are discussed. Some unique features of the H-SAN are evaluated using nitrogen adsorption/desorption isotherm, SEM and TEM. Conversion and molecular weight determinations were carried out using GC and SEC respectively. Adding of H-SAN by 3 wt% results in decrement of conversion from 94 to 73%. In addition, molecular weight of copolymer chains decreases from 19500 to 16000 g.mol<sup>-1</sup>. However, polydispersity index values increases from 1.29 to 1.65. Linear increase of  $\ln(M_0/M)$  with time for all the samples shows that copolymerization proceeds in a living manner. Increasing thermal stability of the nanocomposites is demonstrated by TGA. DSC results show a decrease in glass transition temperature from 70.3 to 63.5 °C by addition of 3 wt% H-SAN.

**Keywords:** Nanocomposite; kinetics study; silica aerogel nanoparticles; poly (styrene-co-methyl methacrylate); SR&NI ATRP

## 1. Introduction

Nanocomposites are new class of materials that can combine the inherent properties of the organic phase (such as dielectric, ductility and processability) and inorganic phase (such as rigidity and thermal stability).<sup>1–3</sup> Usage of nanoscale materials with small size and large interfacial area per unit volume results in nanocomposites possess unique features in which are not provided by traditional composites.<sup>4–6</sup> For example, polymer layered silicate nanocomposites present improvements in various properties (such as strength, thermal expansion coefficient, barrier, flammability resistance, environmental stability, and etc) in comparison with unmodified polymer.<sup>4,7</sup> Due to the unique features of the nanocomposites, they can be employed in diverse applications such as electronics, adhesives, and automotive fields.<sup>8</sup> In situ polymerization, solution blending and melt intercalation are three famous methods for the preparation of polymer nanocomposites.<sup>9</sup> Incorporation of tailor-made polymers (organic phase) for the preparation of nanocom-

posites is an attractive topic since the molecular features of the organic phase can be tailored and some specific properties of the resulting hybrid can be dictated.<sup>10</sup>

Aerogels are highly porous materials with surface areas between 500 and 1600 m<sup>2</sup>/g and densities between 0.002 and 0.8 g/cm<sup>3</sup>. Aerogels present unique physical properties that have made them attractive and many useful for thermal and acoustic insulation, low constant dielectric materials, and Cherenkov radiation counters.<sup>11–14</sup> Silica aerogels are consisting of about 99% air and 1% solid silica in the form of highly cross-linked network structure (three-dimensional network of nanoparticles).<sup>15–17</sup> Large surface area, high degree of porosity, very low bulk density, very low thermal conductivity, high optical transmission, low refractive index, and low sound velocity are some unique properties of the silica aerogels that make them appropriate potential candidate for many applications (e.g. thermal insulation, drug delivery system, catalysis, adsorption, and etc).<sup>11,16,18–21</sup>

Application of various initiation techniques can be considered as one the main advantages of ATRP over other

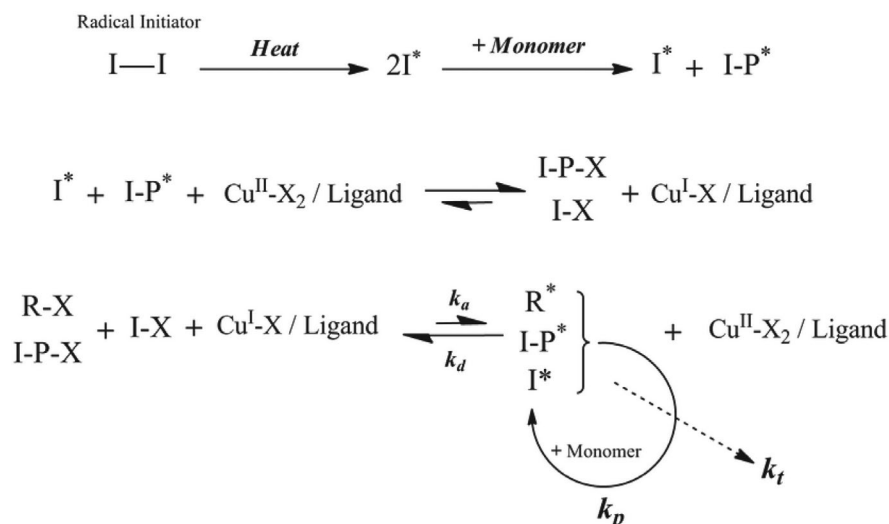


Figure 1. Schematic mechanism for SR&NI ATRP

the controlled living radical polymerization (CLRP) methods. SR&NI ATRP as an interesting initiation technique for ATRP is developed since it can provide many useful characteristics such as application low concentration of transition metal complex, application of transition metal complex in its higher oxidation state ( $\text{CuBr}_2$ ), and its ability to produce pure block copolymer.<sup>22–23</sup> Schematic mechanism of SR&NI ATRP is presented in figure 1.

Reviewing related literature indicates that some studies have been done on the synthesis and investigating properties of silica aerogel/polymer nanocomposites.<sup>24–28</sup> Application of various initiation techniques for ATRP in the presence of different nano-fillers (e.g. clay and diatomite) were also reported previously.<sup>29–31</sup> In this study, pristine silica aerogel nanoparticles were modified by HMDS as a surface modifier agent and hydrophobic silica aerogel nanoparticles were obtained. Abundant advantages of SR&NI ATRP were employed to synthesize well-defined poly (styrene-co-methyl methacrylate) nanocomposites. Investigating the effect of H-SAN addition on the polymerization parameters (conversion, molecular weight, and PDI values) are carefully performed. By these results it can be concluded that increment of H-SAN in the polymerization media how can affect the polymerization kinetics (positive effect of negative effect). In addition, thermal properties of the prepared nanocomposites are studied in detail. By these results it can be comprehended that addition of H-SAN in the polymer matrix how can improve thermal features of the nanocomposites in comparison with the neat polymer.

## 2. Experimental

### 2. 1. Materials

Styrene (St, Aldrich, 99%) and methyl methacrylate (MMA, Merck, 99%) were passed through an alumina

filled column to remove inhibitors. Copper(I) bromide ( $\text{CuBr}$ , Aldrich, 98%),  $\text{N,N,N',N'',N''}$ -pentamethyldiethylenetriamine (PMDETA, Aldrich, 99%), ethyl alpha-bromoisobutyrate (EBiB, Aldrich, 97%), 2,2'-azobisisobutyronitrile (AIBN, Acros), anisole (Aldrich, 99%), tetrahydrofuran (THF, Merck, 99%), neutral aluminum oxide (Aldrich, 99%), tetraethoxysilane (TEOS, Merck), n-hexane (Merck), Ethanol (EtOH, Merck, 99%), oxalic acid (Aldrich, >99%), ammonium hydroxide (Tabriz Petrochemical Company) and hexamethyldisilazane (HMDS, Merck) were used as received.

### 2. 2. Synthesis of Hydrophilic and HMDS-modified Silica Aerogel Nanoparticles

Pristine and H-SAN were prepared according to the procedure as reported previously.<sup>20,32</sup>

### 2. 3. SR&NI Atom Transfer Random Radical Copolymerization of Styrene and Methyl Methacrylate

Typical batch of copolymerization was run at 110 °C with the molar ratio of 200:1:0.2:0.2:0.12 for  $[\text{M}]:[\text{EBiB}]:[\text{CuBr}_2]:[\text{PMDETA}]:[\text{AIBN}]$  giving a theoretical molecular weight of 20457  $\text{g}\cdot\text{mol}^{-1}$  at final conversion. At first, styrene (0.073 mol, 8.34 ml), methyl methacrylate (0.058 mol, 6.2 ml),  $\text{CuBr}_2$  (0.17 mmol, 0.039 g), PMDETA (0.17 mmol, 0.03 ml) and anisole (10 ml) were added to the reactor. Then, it was degassed and back-filled with nitrogen three times, and then left under  $\text{N}_2$  with stirring at room temperature. After that, reaction temperature was increased to 110 °C during 5 min. Subsequently, predeoxygenated solution of AIBN (0.1 mmol, 0.017 g) in the styrene (0.043 mol, 5 ml) and predeoxygenated EBiB (0.87 mmol, 0.12 ml) were injected into the reactor to start the copolymerization reaction. At the beginning of the reac-

tion, copolymerization media was green and gradually changed to brown. Samples were taken at the end of the reaction to measure the final conversion.

## 2. 4. Preparation of Poly (Styrene-co-methyl Methacrylate)/Silica Aerogel Nanocomposites by *in Situ* SR&NI ATRP

For preparation of nanocomposites, a desired amount of H-SAN was dispersed in 7 ml of styrene and the mixture was stirred for 17 hours. Then, the remained 1.34 ml of styrene was added to the mixture. Subsequently, copolymerization procedure was applied accordingly. Designation of the samples with the percentage of modified silica aerogel nanoparticles is given in table 1.

## 2. 5. Characterization

Materials porosity was characterized by N<sub>2</sub> adsorption/desorption curves obtained with a Quntasurb QS18 (Quntachrom) apparatus. The surface area and pore size distribution values were obtained with the corrected BET equation (Brunauer-Emmett-Teller). Surface morphology of the samples was examined by Scanning Electron Microscope (SEM, Philips XL30) with acceleration voltage of 20 kV. Also, transmission electron microscope (TEM, FEG Philips CM) with an accelerating voltage of 200 kV was used. Gas chromatography (GC) is a simple and highly sensitive characterization method and does not require removal of the metal catalyst particles. GC was performed on an Agilent-6890N with a split/splitless injector and flame ionization detector, using a 60 m HP-INNOWAX capillary column for the separation. The GC temperature profile included an initial steady heating at 60 °C for 10 min and a 10 °C/min ramp from 60 to 160 °C. The samples were also diluted with acetone. The ratio of monomer to anisole was measured by GC to calculate monomer conversion throughout the reaction. Size exclusion Chromatography (SEC) was used to measure the molecular weight and molecular weight distribution. A Waters 2000 ALLIANCE with a set of three columns of pore sizes of 10000, 1000, and 500 Å was utilized to determine polymer average molecular weight and polydispersity index (PDI). Thermal gravimetric analysis (TGA) was carried out with a PL thermo-gravimetric analyzer (Polymer Laboratories, TGA 1000, UK). Thermograms were obtained from ambi-

ent temperature to 700 °C at a heating rate of 10 °C/min. Thermal analysis were carried out using a differential scanning calorimetry (DSC) instrument (NETZSCH DSC 200 F3, Netzsch Co, Selb/Bavaria, Germany). Nitrogen at a rate of 50 mL/min was used as purging gas. Aluminum pans containing 2–3 mg of the samples were sealed using DSC sample press. The samples were heated from ambient temperature to 220 °C at a heating rate of 10 °C/min.

## 3. Results and Discussion

Nitrogen adsorption/desorption isotherm of the H-SAN indicate that this material can be classified as a mesoporous type according to the IUPAC classification (figure 2).<sup>32</sup>

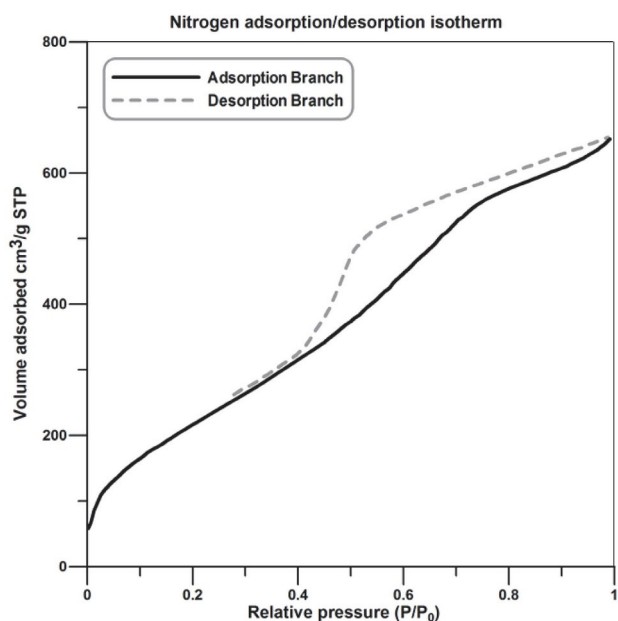


Figure 2. Nitrogen adsorption/desorption isotherm of the H-SAN

According to extracted data from nitrogen adsorption/desorption isotherm, BET surface area and average pore diameter of the synthesized aerogel (modified silica aerogel nanoparticles) are calculated 958.67 m<sup>2</sup>/g and 4.05 nm respectively.

TEM and SEM images of the H-SAN are displayed in figure 3. According to these images, H-SAN present

Table 1. Designation of the samples

Sample	Method of Preparation	Proportion of H-SAN (wt%)	Dispersion Time Prior to the Copolymerization (h)
PRSM	SR&NI ATRP	0	–
RSMAC 1	In situ SR&NI ATRP	1	17
RSMAC 2	In situ SR&NI ATRP	2	17
RSMAC 3	In situ SR&NI ATRP	3	17



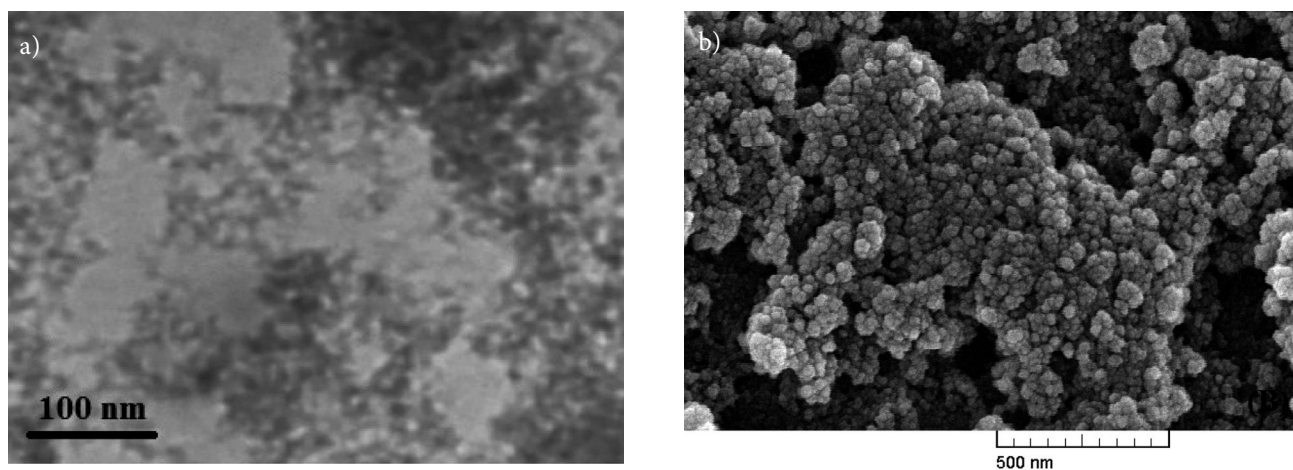


Figure 3. TEM (A) and SEM (B) images of the H-SAN

spongy structure and the particles are relatively mono-dispersed. In addition, average diameter of the particles is estimated around 25 nm.

General procedure for the synthesis of tailor-made random poly (styrene-co-methyl methacrylate) chains via SR&NI ATRP in the presence of H-SAN is shown in figure 4.

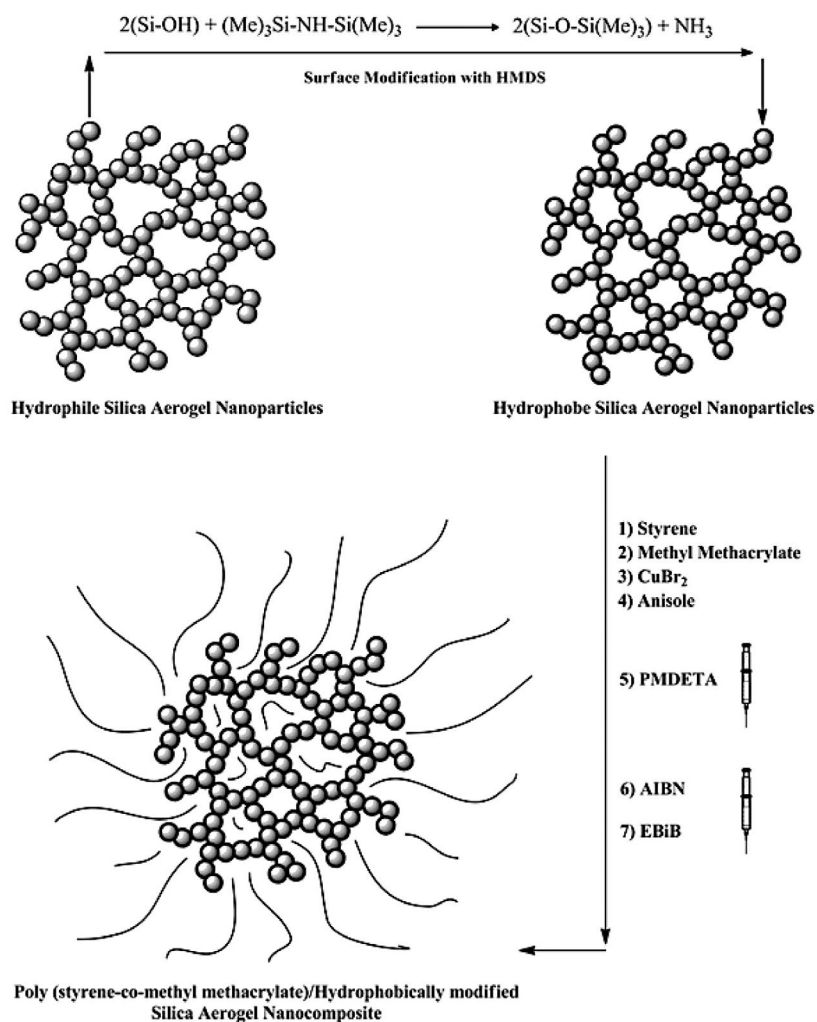


Figure 4. General procedure for preparation of poly (styrene-co -methyl methacrylate)/H-SAN nanocomposites by *in situ* SR&NI ATRP

During the copolymerization process, monomer conversion with time can present various behaviors. Thus, examining the variation of conversion with time for the copolymerization system can be considered as an important parameter. Variation of monomers (MMA and St) conversion versus time for the neat poly (styrene-co-methyl methacrylate) and its different nanocomposites are presented in figure 5. According to the results, by proceeding of the reaction, an increment in the conversion is obtained. Also, copolymerization of MMA and St without the modified silica aerogel nanoparticles results in higher conversion in various time steps. On the other hands, by increasing modified silica aerogel nanoparticles content lower monomer conversions are obtained (conversion: RSMAC 3 < RSMAC 2 < RSMAC 1 < PRSM). These results indicate that presence of H-SAN can result in negative effect on the copolymerization rate and final conversion of the monomers. Negative effect of the modified silica aerogel nanoparticles on the copolymerization may be attributed to the three main factors; *i*) Impurity role of the H-SAN: it is demonstrated that existence of some nano-fillers in the copolymerization media can disturb the ATRP equilibrium and therefore products with lower conversion, lower molecular weights, and higher PDI values can be prepared.<sup>33–35</sup> *ii*) Restriction of the mobility: due to the porous structure of the H-SAN, mobility of the radicals and growing macro-radicals in the solution can be restricted

and therefore copolymerization rate and monomers conversion can be decreased. It is clear that by increasing modified silica aerogel nanoparticles content, more restriction will be happened and therefore higher decrement in the conversion can be obtained.<sup>41–43</sup> *iii*) Irreversible reactions: It is demonstrated that growing radicals in the copolymerization media can irreversibly react with various functional moieties. Thus, growing radicals can irreversibly react with the moieties (such as un-modified hydroxyl groups) on the H-SAN and therefore can present negative effect on the copolymerization rate and conversion.<sup>33–35</sup>

Variation of number-averaged molecular weight ( $M_n$ ) with conversion during the copolymerization is represented in figure 6. Theoretical line in this figure is displayed to present theoretical  $M_n$  values for the various conversions. As it can be expected, in the neat copolymer and different nanocomposites by increasing conversion copolymer chains with higher  $M_n$  were obtained. According to the results, PRSM has higher  $M_n$  values in comparison with the different nanocomposites (RSMAC 1–3). On the other hands, addition of the H-SAN in the copolymerization media results in decrement of  $M_n$  of the products. By increasing H-SAN content, more decrement in  $M_n$  is observed ( $M_n$ : PRSM > RSMAC 1 > RSMAC 2 > RSMAC 3). This negative effect of the H-SAN on the molecular weight of the copolymer chains can be also attributed to the three above mentioned reasons (impurity role, restric-

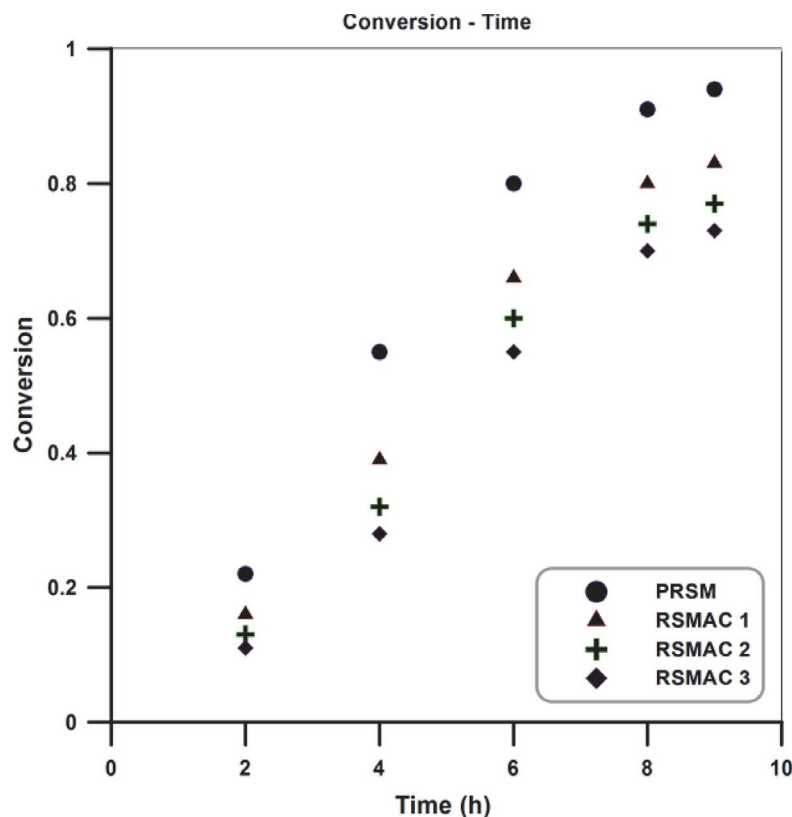


Figure 5. Variation of monomers conversion with time for the PRSM and RSMAC 1–3

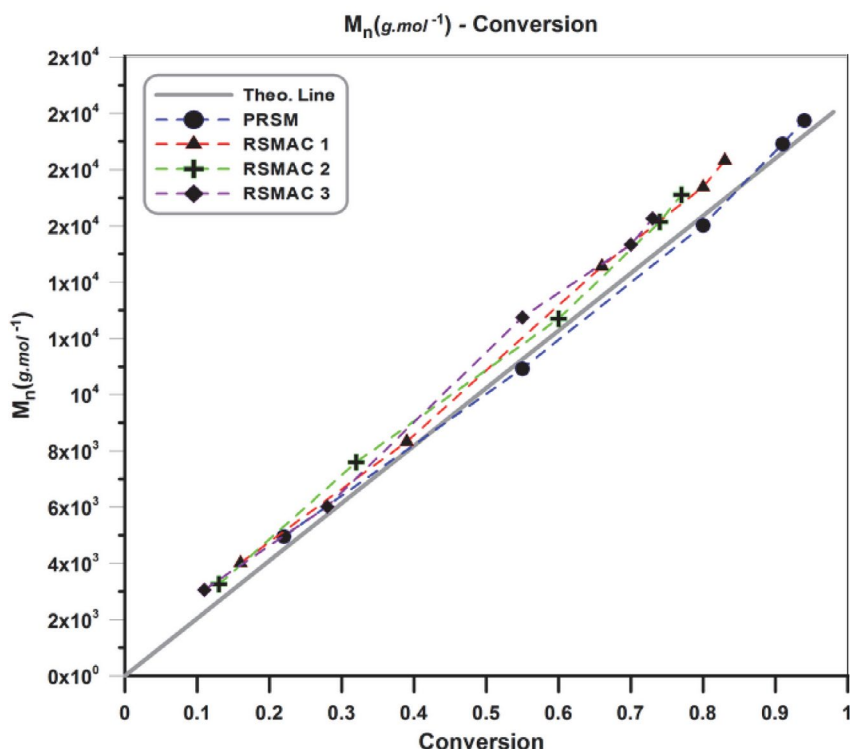


Figure 6. Variation of molecular weight versus conversion for the PRSM and RSMAC 1-3

tion of the mobility, and irreversible reactions).<sup>33–35</sup> By precise evaluation of the results an appropriate agreement between experimental and theoretical  $M_n$  values are observed that this agreement can be considered as a suitable evidence for demonstration of the living nature of the copolymerization system.

Variation of PDI values with conversion for the neat copolymer and its various nanocomposites is displayed in figure 7. Since the copolymerization system (SR&NI ATRP) is a member of CLRP family, it could be predicted that PDI values present a decrement by proceeding of the reaction (by increasing of conversion). Although addition of nano-fillers can affect CLRP equilibrium, they can not change the living nature of the system and therefore a decrement in PDI values by increasing conversion are observed in the pure copolymer (PRSM) and its different nanocomposites (RSMAC 1-3). According to the figure 7, PDI value of the PRSM is lower than RSMAC 1-3. In the nanocomposites, by increasing modified silica aerogel nanoparticles content higher PDI values are obtained (PDI: PRSM < RSMAC 1 < RSMAC 2 < RSMAC 3). Increment of PDI values by increasing H-SAN content can be attributed to the impurity role of the H-SAN. The occurrence of termination and transfer reactions between the propagating (macro)radicals and H-SAN can be considered as the main reason of emerging high PDI values in the nanocomposites samples.<sup>33–35</sup>

Figure 8 shows pseudo-first-order kinetic plots for the synthesized nanocomposites and the neat copolymer.

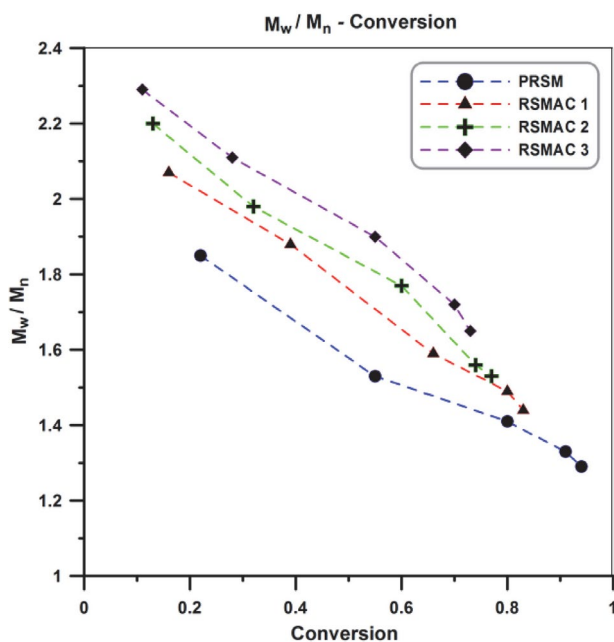


Figure 7. Variation of PDI values with conversion for the PRSM and RSMAC 1-3

Results indicate that the slope of the curves (PRSM and RSMAC 1-3) remains fairly constant in the whole of the copolymerization and therefore it can be concluded that steady-state kinetics for all of the samples is obtained. According to the figure, PRSM and RSMAC 1-3 present lin-

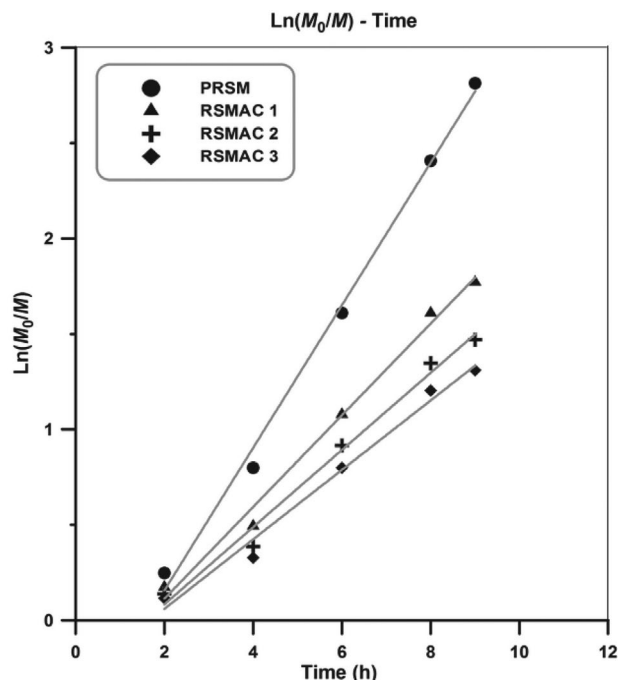


Figure 8. Kinetic plots with respect to the reaction time

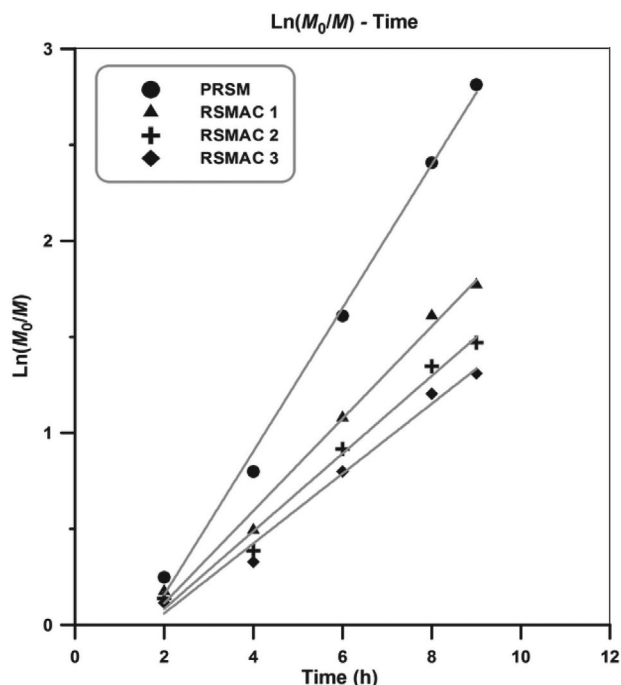


Figure 9. SEC traces of the neat random poly(styrene-co-methyl methacrylate) and its nanocomposites

early increment of  $\text{Ln}(M_0/M)$  with time in which constant radical concentration in the copolymerization media can be concluded.<sup>33–34</sup> Results also indicate that by increasing H-SAN content a considerable decrement in the copolymerization rate will be obtained.

PRSM and RSMAC 1–3 display monomodal peak in their SEC traces (figure 9). According to this figure, PRSM presents narrow distribution in comparison with the RSMAC 1–3. Also, by increasing H-SAN loading broader distribution are obtained (molecular weight distribution:  $\text{PRSM} < \text{RSMAC 1} < \text{RSMAC 2} < \text{RSMAC 3}$ ).

SEC traces demonstrate that SR&NI ATRP of MMA and St in the presence of H-SAN results in copolymer with broader molecular weight distribution. On the other hand, absence of the H-SAN in the copolymerization media leads to copolymer with lower PDI values. As it mentioned above, H-SAN can disturb the equilibrium of SR&NI ATRP due its three main roles (impurity role, restriction of the mobility, and irreversible reactions).<sup>33–35</sup> According to the extracted data in table 2, by addition of 3 wt% of the H-SAN monomer conversion decreases from

94% to 73%. Meanwhile PDI values present an increment from 1.29 to 1.65.

$$M_n^{\text{Theo}} = \frac{[M]_0}{[\text{EBiB}]_0} \times \text{Conv.} \times M_w \quad (1)$$

where,  $[M]_0$  and  $[\text{EBiB}]_0$  are initial concentration of the monomers and ATRP initiator, respectively. Conversion is denoted by *Conv.* and the symbol of the average molecular weight of the monomers is  $M_w$ .

TGA thermograms of the PRSM and RSMAC 1–3 in the temperature window of 25–700 °C in two different styles are displayed in figure 10. Char values at 700 °C are also presented in this figure. As expected, by increasing H-SAN content, char values of the prepared nanocomposites should be increased (char values:  $\text{PRSM} < \text{RSMAC 1} < \text{RSMAC 2} < \text{RSMAC 3}$ ).

Figure 10 indicates that thermal stability of the PRSM is lower than various nanocomposites. Also, it can be concluded that by increasing H-SAN content, more im-

Table 2. Molecular weights and PDI values of the extracted copolymers resulted from SEC traces

Sample	Reaction Time (h)	Conversion (%)	$M_n$ (g.mol <sup>-1</sup> )		$M_w$ (g mol <sup>-1</sup> )	PDI
			Exp.	Theo.		
PRSM	9	94	19757	19230	25487	1.29
RSMAC 1	9	83	18336	16979	26405	1.44
RSMAC 2	9	77	17104	15752	26169	1.53
RSMAC 3	9	73	16268	14934	26842	1.65

Theoretical molecular weight is calculated by using Equation 1:

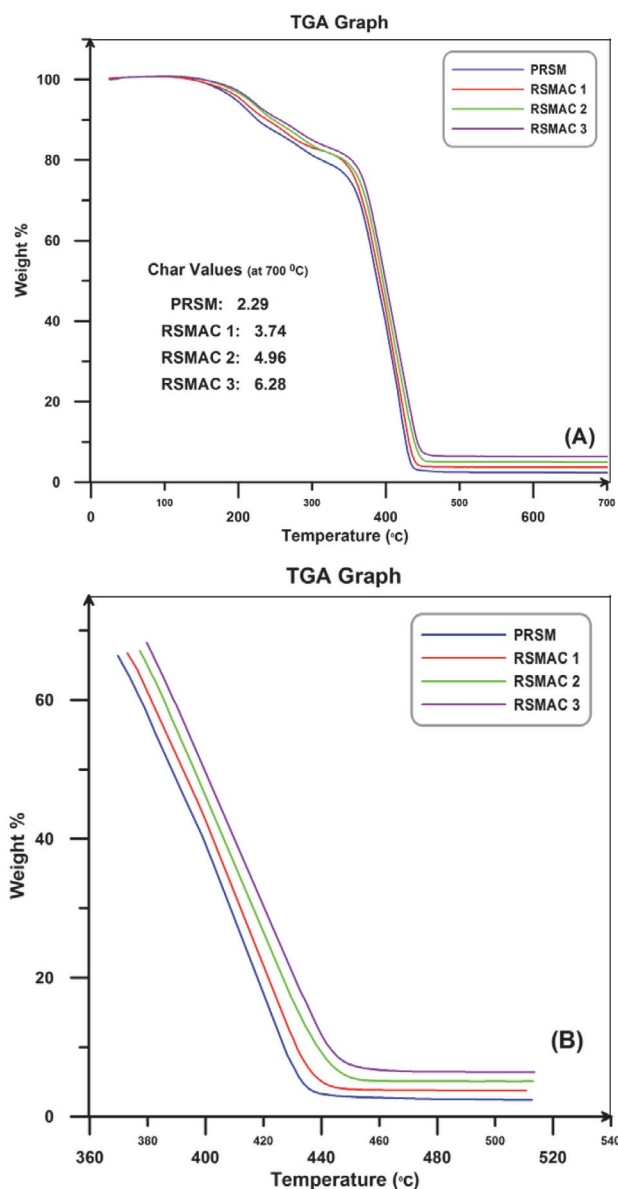


Figure 10. TGA thermograms of the PRSM and RSMAC 1-3

improvements in thermal stabilities can be obtained (thermal stability: PRSM < RSMAC 1 < RSMAC 2 < RSMAC 3). Except the main degradation step in the TGA graphs (at the temperatures above 350 °C) that is attributed to the degradation of the synthesized copolymer and its nanocomposites, some other degradation can be also recognized. This degradation in the lower temperatures is ascribed by evaporation of water molecules and volatile materials such as residual monomers and HMDS.

Extracted data from TGA are graphically illustrated in figure 11. Degradation temperature of the samples versus amount of degradation is employed to show that addition of H-SAN in the copolymer matrix, results in an improvement of thermal stabilities of the nanocomposites ( $T_x$ : temperature threshold at which X% of neat copoly-

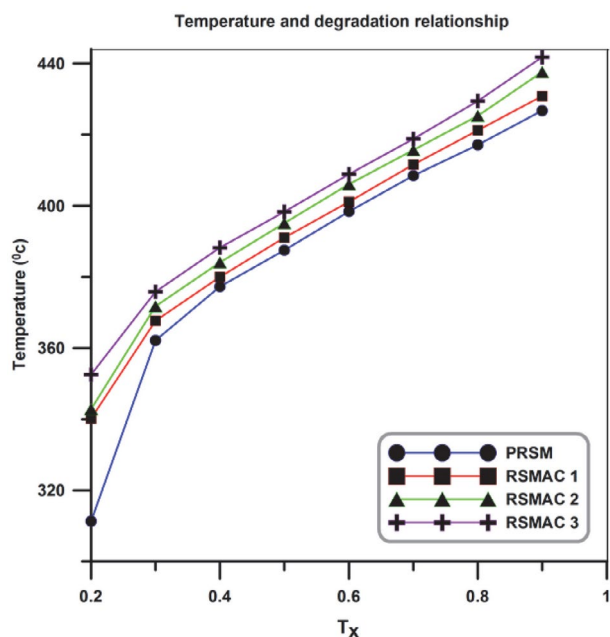


Figure 11. Graphical illustration of temperature and degradation relationship

mer and its nanocomposites is degraded). Char values at 700 °C are also reported in the figure 10.

TGA results demonstrate that incorporation of H-SAN in the copolymer matrix leads to improvements in thermal stabilities. This improvement can be ascribed by using inorganic nature of the H-SAN. Modified silica aerogel nanoparticles as inorganic nano-filler can result in higher thermal stabilities of the RSMAC 1-3 in comparison with the PRSM.<sup>36</sup> Absorption of the introduced gas (in oxygen atmosphere) in the porous structure of the incorporated nano-filler (H-SAN is classified as mesoporous materials) may be considered as another factor for increment of thermal stabilities of the nanocomposites in comparison with the PRSM.<sup>33</sup>

Improvement in thermal stability may be ascribed by inorganic nature of the incorporated nano-filler. H-SAN as inorganic nano-filler that are incorporated and dispersed within the copolymer matrices can result in improvement of thermal stability of the nanocomposites in comparison with the neat copolymer.<sup>36</sup> Moreover, since the synthesized nano-filler is a member of mesoporous materials family it can absorb introduced gas (in O<sub>2</sub> atmosphere) can also results in increment of thermal stability of the nanocomposites. Finally, because of the three-dimensional network structure of the H-SAN, these nanoparticles can not be appropriately dispersed and therefore can not significantly improve thermal stabilities of the nanocomposites.<sup>37</sup>

Evaluation the effect of the H-SAN on the chain confinement and also determination of glass transition temperature ( $T_g$ ) are performed by DSC analysis. DSC curves of the PRSM and RSMAC 1-3 are presented in figure 12.

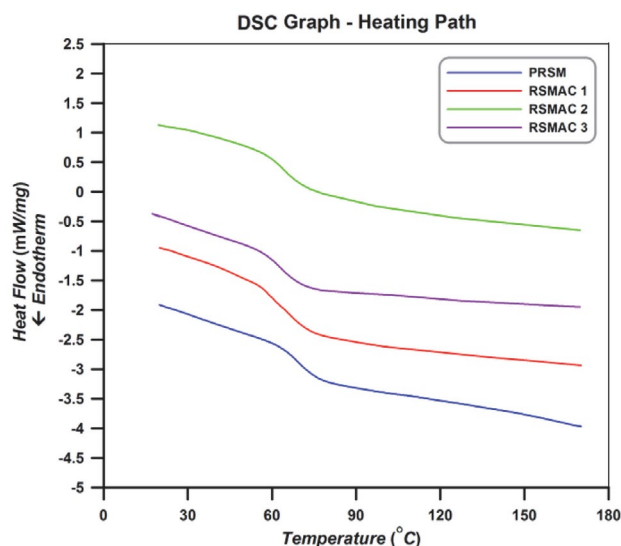


Figure 12. DSC Thermograms of the PRSM and RSMAC 1-3

Although the samples are heated from room temperature to 220 °C to remove their thermal history, cooling path of the analysis in the temperature range of 20–170 °C is displayed in this figure.

According to the figure 12, an obvious inflection in the cooling path are occurred which shows  $T_g$  values of the PRSM and RSMAC 1-3. In addition, amorphous structures of the synthesized samples can be also concluded. Extracted  $T_g$  values of the samples from DSC graphs (in the cooling path) are summarized in table 3.

Table 3.  $T_g$  values of the PRSM and RSMAC 1-3

Sample	$M_n$ (g mol <sup>-1</sup> )	PDI	$T_g$ (°C)
PRSM	19757	1.29	70.3
RSMAC 1	18336	1.44	67.4
RSMAC 2	17104	1.53	65.3
RSMAC 3	16268	1.65	63.5

According to the table 3, PRSM presents higher  $T_g$  value in comparison with the other samples (RSMAC 1-3). By incorporating of the H-SAN in the copolymer matrix a decrement in  $T_g$  value was happened ( $T_g$ : RSMAC 3 < RSMAC 2 < RSMAC 1 < PRSM). Decrement in  $T_g$  values by adding H-SAN in the copolymer matrix is related to the reduction of the packing of the copolymer chains. By dispersing H-SAN within the copolymer matrix, packing of the copolymer chains will be reduced and therefore copolymer chains can obtain more segment mobilities in which results in decrement of  $T_g$  values. In addition, due to the three-dimensional network structure of the H-SAN these nanoparticles can not appropriately dispersed within the copolymer matrix and therefore some free volume spaces for the dangling copolymer chains may be created. This is

also responsible for more segment mobilities of the copolymer chains which in turn results in  $T_g$  reduction. Moreover, according to the table 2, by increasing H-SAN in the copolymer matrix an increment in PDI value and also a decrement in  $M_n$  are observed. These parameters should be also considered since decrease in  $M_n$  and increment of PDI values may cause reduction of  $T_g$  values.<sup>38–39</sup> Previous studies indicate that  $T_g$  values can be changed by addition of low volume of different nano-fillers.<sup>40–41</sup> Reduction of  $T_g$  value by incorporating alumina nanoparticles as a nano-fillers was also reported by Schadler et al.<sup>42</sup>

## 4. Conclusions

Tailor-made random poly (styrene-co-methyl methacrylate) and its different nanocomposites in the presence of H-SAN were synthesized by *in situ* SR&NI ATRP. Porous and spongy structure, spherical shape and high surface are some unique properties of the prepared H-SAN. SR&NI ATRP of styrene and methyl methacrylate in the presence of H-SAN results in a decrease of conversion from 94 to 73%. Moreover, molecular weight of the random copolymer chains decrease from 19757 to 16268 g.mol<sup>-1</sup> and PDI values increase from 1.29 to 1.65. Improvement in thermal stability of the nanocomposites and decreasing  $T_g$  values from 70.3 to 63.5 °C was also obtained by addition of 3 wt% of the H-SAN.

## 5. References

1. F. Audouin, H. Blas, P. Pasetto, P. Beaunier, C. Boissie`re, *Macromol. Rapid Commun.* **2008**, 29, 914–921. DOI:10.1002/marc.200800179
2. M. Alexandre, P. Dubois, *Mater. Sci. Eng.* **2000**, 28, 1–63. DOI:10.1016/S0927-796X(00)00012-7
3. L. Wei, N. Hu, Y. Zhang, *Materials* **2010**, 3, 4066–4079. DOI:10.3390/ma3074066
4. H. Zou, S. Wu, J. Shen, *Chem. Rev.* **2008**, 108, 3893–3957. DOI:10.1021/cr068035q
5. S. L. Burkett, N. Ko, N. D. Stern, J. A. Caissie, D. Sengupta, *Chem. Mater.* **2006**, 18, 5137–5143. DOI:10.1021/cm0614517
6. X. Fu, S. Qutubuddin, *Polymer* **2001**, 42, 807–813. DOI:10.1016/S0032-3861(00)00385-2
7. J. M. Brown, D. Curliss, R. A. Vaia, *Chem. Mater.* **2000**, 12, 3376–3384. DOI:10.1021/cm000477+
8. F. Hussain, M. Hojjati, M. Okamoto, R. E. Gorga, *J. Compos. Mater.* **2006**, 40, 1511–1575. DOI:10.1177/0021998306067321
9. S. Varghese, J. Karger-Kocsis, *Polymer* **2003**, 44, 4921–4927. DOI:10.1016/S0032-3861(03)00480-4
10. J. Pyun, K. Matyjaszewski, *Chem. Mater.* **2001**, 13, 3436–3448. DOI:10.1021/cm011065j
11. Y. Fazli, H. Alijani, K. Khezri, *Adv. Polym. Technol.* **2016**, 35, 21549–21558. DOI:10.1002/adv.21549

12. N. Gupta, W. Ricci, *J. Mater. Proces. Technol.* **2008**, *198*, 178–182. DOI:10.1016/j.jmatprotec.2007.06.084
13. D. J. Boday, R. J. Stover, B. Muriithi, M. W. Keller, J. T. Wertz, K. A. D. Obrey, D. A. Loy, *ASC Appl. Mater. Interfaces* **2009**, *1*, 1364–1369. DOI:10.1021/am900240h
14. Y. Fazli, H. Alijani, K. Khezri, *J. Inorg. Organomet. Polym.* **2015**, *25*, 1189–1199. DOI:10.1007/s10904-015-0227-0
15. Y. Tao, M. Endo, K. Kaneko, *Rec. Pat. Chem. Eng.* **2008**, *1*, 192–200. DOI:10.2174/1874478810801030192
16. F. Shi, L. Wang, J. Liu, *Mater. Let.* **2006**, *60*, 3718–3722. DOI:10.1016/j.matlet.2006.03.095
17. K. Khezri, Y. Fazli, *High Temp. Mater. Proc.* **2016**, *36*, 955–962
18. S. Mulik, C. Sotiriou-Leventis, G. Churu, H. Lu, N. Leventis, *Chem. Mater.* **2008**, *20*, 5035–5046. DOI:10.1021/cm800963h
19. X. Zhou, L. Zhong, Y. Xu, *Inorg. Mater.* **2008**, *44*, 976–979. DOI:10.1134/S0020168508090148
20. P. B. Sarawade, J.-K. Kim, A. Hilonga, H. T. Kim, *Solid State Sci.* **2010**, *12*, 911–918. DOI:10.1016/j.solidstatesciences.2010.01.032
21. L. D. Gelb, *J. Phys. Chem. C* **2007**, *111*, 15792–15802. <https://doi.org/10.1021/jp0737505>
22. K. Min, M. Li, K. Matyjaszewski, *J. Polym. Sci. Part A: Polym. Chem.* **2005**, *43*, 3616–3622. DOI:10.1002/pola.20809
23. M. Li, K. Min, K. Matyjaszewski, *Macromolecules* **2004**, *37*, 2106–2112. DOI:10.1021/ma035284x
24. D. J. Boday, P. Y. Keng, B. Muriithi, J. Pyun, D. A. Loy, *J. Mater. Chem.* **2010**, *20*, 6863–6865. DOI:10.1039/c0jm01448f
25. M. Sarsabili, K. Kalantari, K. Khezri, *J. Therm. Anal. Calorim.* **2016**, *126*, 1261–1272. DOI:10.1007/s10973-016-5641-1
26. Y. W. Chen-Yang, Y. L. Wang, Y. T. Chen, Y. K. Li, H. C. Chen, H. Y. Chiu, *J. Power Sour.* **2008**, *182*, 340–348. DOI:10.1016/j.jpowsour.2008.04.001
27. D. J. Boday, R. J. Stover, B. Muriithi, M. W. Keller, J. T. Wertz, K. A. D. Obrey, D. A. Loy, *ASC Appl. Mater. Interfaces* **2009**, *1*, 1364–1369. DOI:10.1021/am900240h
28. A. Costela, I.G. Moreno, C. Go´mez, O. Garcı´a, R. Sastre, A. Roig, E. Molins, *J. Phys. Chem. B* **2005**, *109*, 4475–4480. DOI:10.1021/jp040714m
29. K. Khezri, M. Ghasemi, Y. Fazli, *Z. Phys. Chem.* **2018**, *232*, 471–487.
30. K. Khezri, Y. Fazli, *Polym. Sci. Ser. B* **2017**, *59*, 109–116. DOI:10.1134/S1560090417010092
31. Y. Fazli, K. Khezri, *J. Polym. Res.* **2018**, *25*, 9–19. DOI:10.1007/s10965-017-1405-2
32. M. Karimi, S. Davoudizadeh, S. Bahadorikhalili, K. Khezri, *Z. Phys. Chem.* DOI:10.1515/zpch-2018-1202. DOI:10.1515/zpch-2018-1202
33. M. Sarsabili, R. Rahmatolahzadeh, S.A. Shobeiri, M. Hamadani, A. Farazin, K. Khezri, *Polym Adv Technol.* **2018**, *29*, 424–432. DOI:10.1002/pat.4131
34. K. Khezri, Y. Fazli, *J. Thermoplast. Compos. Mater.* DOI:10.1177/0892705718805128
35. S. Davoudizadeh, M. Sarsabili, K. Khezri, *Z. Phys. Chem.* **2017**, *231*, 1543–1558. DOI:10.1515/zpch-2016-0812
36. K. Khezri, H. Alijani, Y. Fazli, *Acta Chim. Slov.* **2018**, DOI: 10.17344/acsi.2018.4331. DOI:10.17344/acsi.2018.4331
37. K. Khezri, H. Alijani, Y. Fazli, *Z. Phys. Chem.* **2016**, *230*, 111–129.
38. K. Khezri, H. Mahdavi, *Micropor. Mesopor. Mater.* **2016**, *228*, 132–140. DOI:10.1016/j.micromeso.2016.03.022
39. Y. Fazli, K. Khezri, *Colloid Polym Sci* **2017**, *295*, 247–257. DOI:10.1007/s00396-016-3997-1
40. F. Chen, A. Clough, B.M. Reinhard, M.W. Grinstaff, N. Jiang, T. Koga, O.K.C. Tsui, *Macromolecules* **2013**, *46*, 4663–4670. DOI:10.1021/ma4000368
41. B. Natarajan, Y. Li, H. Deng, L.C. Brinson, L.S. Schadler, *Macromolecules* **2013**, *46*, 2833–2841. DOI:10.1021/ma302281b
42. B. J. Ash, R. W. Siegel, L. S. Schadler, *J. Polym. Sci. Part B: Polym. Phys.* **2004**, *42*, 4371–4388. <https://doi.org/10.1002/polb.20297>

## Povzetek

Tehniko SR&NI ATRP (polimerizacija s prenosom atoma (ATRP); simultaneous reverse and normal initiation (SR&NI)) smo uporabili za kopolimerizacijo stirena in metil metakrilata v prisotnosti aerogela na osnovi nanodelcev silicijevega dioksida (H-SAN) in z dodatkom heksametildisilizana (HMDS). Preučevali smo vpliv dodatka aerogela H-SAN na samo kopolimerizacijo in termične lastnosti produktov. Produkta smo karakterizirali z vrstično elektronsko mikroskopijo (SEM) in presevno elektronsko mikroskopijo (TEM) in jim z uporabo dušika določili adsorpcijske in desorpcijske izoterme. Konverzijo in molekulska masa smo določili s plinsko kromatografijo (GC) in velikostno izključitveno kromatografijo (SEC). Dodatek 3 ut% H-SAN je vodil v zmanjšanje pretvorbe s 94 % na 73 %. Molekulska masa polimernih verig se je znižala od 19500 g mol<sup>-1</sup> na 16000 g mol<sup>-1</sup>. Indeks polidisperznosti se je povečal z 1,29 na 1,65. Linearno povečanje ln(M<sub>0</sub>/M) s časom za vse vzorce nam daje vpogled v proces kolpolimerizacije. Povečano termično stabilnost nanokompozita smo dokazali s termogravimetrično analizo (TGA). Rezultati diferenčne dinamične kalorimetrije (DSC) kažejo na znižanje temperature steklastega prehoda (T<sub>g</sub>) s 70,3 °C na 63,5 °C v primeru dodatka 3 ut% aerogela H-SAN.

Scientific paper

# Synthesis, Structure, Photoluminescence, Energy Transfer Mechanism and Band Gap of a Terbium-Mercury Complex with a 3-D Framework

Wei-Sheng Lin,<sup>1</sup> Wen-Tong Chen,<sup>2,3\*</sup> Han-Mao Kuang<sup>2</sup> and Hui Luo<sup>2</sup>

<sup>1</sup> Department of Ecological and Resources Engineering, Fujian Key laboratory of Eco-Industrial Green Technology, Wuyi University, Wuyishan, Fujian 354300, China

<sup>2</sup> Institute of Applied Chemistry, School of Chemistry and Chemical Engineering, Jinggangshan University, Ji'an, Jiangxi 343009, China

<sup>3</sup> State Key Laboratory of Structural Chemistry, Fujian Institute of Research on the Structure of Matter, Chinese Academy of Sciences, Fuzhou, Fujian 350002, China

\* Corresponding author: E-mail: wtchen\_2000@aliyun.com  
Tel.: +86(796)8100490; fax +86(796)8100490

Received: 07-11-2018

## Abstract

A novel terbium-mercury compound  $[\text{Tb}(\text{IA})_3(\text{H}_2\text{O})_2(\text{Hg}_2\text{Cl}_4)]_n \cdot n\text{HgCl}_2 \cdot n\text{H}_2\text{O}$  (**1**, HIA = isonicotinic acid) was prepared via a hydrothermal reaction and structurally characterized through single-crystal X-ray diffraction technique. This compound is characterized by a three-dimensional (3-D) framework. Photoluminescence experiments with solid-state samples uncovered that this compound can show yellow light emission with the emission peaks at 490, 545, 586 and 621 nm, respectively. These photoluminescence emission peaks are originated from the characteristic emission of the 4f electrons intrashell transition of the  $^5D_4 \rightarrow ^7F_J$  ( $J = 6, 5, 4, 3$ ) of the  $\text{Tb}^{3+}$  ions. An energy transfer mechanism is expatiated by applying the energy level figure of the terbium ions and isonicotinic acid. This compound possesses a remarkable CIE chromaticity coordinates (0.3525, 0.4032). A wide optical band gap of 2.51 eV of the title compound is determined by using the solid-state UV/Vis diffuse reflectance spectroscopy.

**Keywords:** Crystal; hydrothermal reaction; photoluminescence; semiconductor; terbium

## 1. Introduction

For many years, lanthanide materials have gained more and more attention because they can usually show interesting magnetic and photoluminescence performances.<sup>1–4</sup> Nowadays, researchers from chemistry and material region have accomplished a large number of explorations on lanthanide materials, in order to reveal their practical applications in the fields such as luminescence probes, light-emitting diodes (LEDs), magnetism, electrochemical displays, and so on.<sup>5,6</sup> Generally speaking, lanthanide materials could display fine photoluminescence emissions, if the f-f electronic transition of the lanthanide ions can occur. However, this f-f electronic transition is hard to happen because lanthanide ions usually have a low absorption coefficient. It is deemed that some organic ligands can act as an ‘antenna’ to absorb UV light and effectively transfer

the UV light energy to the lanthanide ions; this is so-called ‘antenna effect’.<sup>7,8</sup> To our knowledge, the semiconductor performances about lanthanide materials are rarely explored yet when it is compared to the studies on the magnetic and photoluminescence performances.<sup>9</sup>

Terbium ions possess abundant 4f electrons and orbitals, so, coordination compounds containing terbium ions are expected to be able to display attractive photoluminescence properties.<sup>10–12</sup> Group 12 (IIB) elements (zinc, cadmium and mercury) have also gained a lot of interest due to following reasons: different coordination numbers, interesting photoluminescence and photoelectric performances, and so forth.<sup>10–16</sup> IIB elements can also be used for semiconductor materials and, up to date, many semiconductor materials with IIB elements have been reported.<sup>17–20</sup> In recent years, our group keeps



studying the magnetism, photoluminescence and semiconductor materials. We mainly aim at terbium-IIB-VI-IA (VIA = halogen) materials, in order to explore their crystal structures, magnetism, photoluminescence and band structures. In present work, we report the preparation, crystal structure, photoluminescence, energy transfer mechanism and band structure of a novel terbium-mercury material  $[\text{Tb}(\text{IA})_3(\text{H}_2\text{O})_2(\text{Hg}_2\text{Cl}_4)]_n \cdot n\text{HgCl}_2 \cdot n\text{H}_2\text{O}$  (**1**, HIA = isonicotinic acid) with a 3-D framework.

## 2. Experimental

### 2.1 Materials and Instrumentation

The reagents  $\text{TbCl}_3 \cdot 6\text{H}_2\text{O}$ ,  $\text{HgCl}_2$ , isonicotinic acid are AR grade and purchased from commercial source. Photoluminescence measurements were performed on a F97XP photoluminescence spectrometer. UV/Vis diffuse reflectance spectrum was conducted on a TU1901 UV/Vis spectrometer equipped with an integrating sphere.

### 2.2. Synthesis of $[\text{Tb}(\text{IA})_3(\text{H}_2\text{O})_2(\text{Hg}_2\text{Cl}_4)]_n \cdot n\text{HgCl}_2 \cdot n\text{H}_2\text{O}$ (**1**, HIA = Isonicotinic Acid)

$\text{TbCl}_3 \cdot 6\text{H}_2\text{O}$  (2 mmol, 748 mg),  $\text{HgCl}_2$  (2 mmol, 542 mg), isonicotinic acid (2 mmol, 246 mg) and 10 mL distilled water were loaded into a 25 mL Teflon-lined stainless steel vessel. The vessel was heated at 433 K for one week. When the vessel was slowly cooled down to room temperature, colorless crystals were collected. The yield was 52% based on  $\text{HgCl}_2$ .

### 2.3. X-ray Structure Determination

A suitable single crystal was adhered onto the tip of a glass fiber and mounted to a SuperNova CCD diffractometer. The graphite monochromated Mo- $K\alpha$  radiation is applied for the measurement. The intensity data set was obtained in a  $\omega$  scan mode. CrystalClear software was applied to the data reduction and empirical absorption correction.<sup>21</sup> The crystal structure was solved by using the direct methods. The final structure was refined on  $F^2$  by full-matrix least-squares using the Siemens SHELXTLTM V5 crystallographic software package.<sup>22</sup> All non-hydrogen atoms were found on the difference Fourier maps and refined anisotropically (except the lattice water molecule O3W). Because the O3W was disordered, it had to be splitted into two sites, namely, O3WA and O3WB. Both O3WA and O3WB were not refined anisotropically and the site occupations were 30% and 70% for O3WA and O3WB, respectively. The crystal data and details of data collection and refinement are depicted in Table 1; selected bond lengths and bond angles are shown in Table 2.

Table 1. Crystallographic data and structural analysis

Formula	$\text{C}_{18}\text{H}_{18}\text{Cl}_6\text{Hg}_3\text{N}_3\text{O}_9\text{Tb}$
$M_r$	1393.74
Crystal system	monoclinic
Space group	$P2_1/n$
$a$ (Å)	11.9193(4)
$b$ (Å)	9.5228(3)
$c$ (Å)	32.7149(7)
$\beta$ (°)	94.100(2)
$V$ (Å <sup>3</sup> )	3703.81(19)
$Z$	4
Reflections collected	19656
Independent, observed reflections ( $R_{\text{int}}$ )	6285, 5261 (0.0479)
$d_{\text{calcd.}}$ (g/cm <sup>3</sup> )	2.499
$\mu$ (mm <sup>-1</sup> )	14.756
$F(000)$	2504
$T$ (K)	293(2)
$R_1, wR_2$	0.0880, 0.2046
$S$	1.135
Largest and Mean $\Delta/\sigma$	0.003, 0
$\Delta\rho$ (max, min) (e/Å <sup>3</sup> )	3.376, -3.576

Table 2. Selected bond lengths (Å) and bond angles (°)

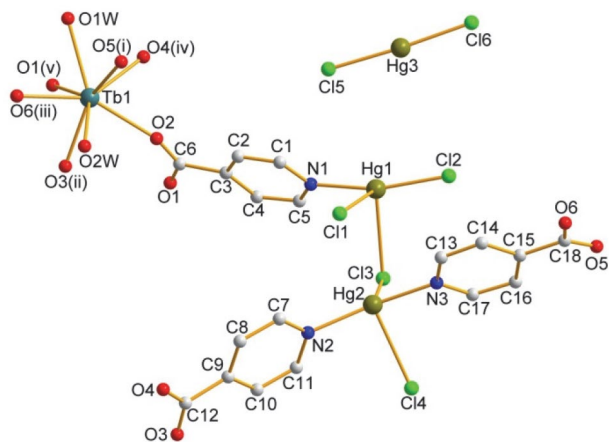
Bond Lengths (Å)		Bond Angles (°)	
Hg(1)–N(1)	2.122(5)	N(1)–Hg(1)–Cl(1)	88.44(13)
Hg(1)–Cl(1)	2.7920(19)	N(1)–Hg(1)–Cl(2)	164.51(14)
Hg(1)–Cl(2)	2.3051(15)	N(1)–Hg(1)–Cl(3)	90.83(13)
Hg(1)–Cl(3)	2.8723(16)	Cl(1)–Hg(1)–Cl(2)	101.75(6)
Hg(2)–N(2)	2.136(5)	Cl(1)–Hg(1)–Cl(3)	93.76(5)
Hg(2)–N(3)	2.127(4)	Cl(2)–Hg(1)–Cl(3)	100.00(6)
Hg(2)–Cl(3)	2.7307(16)	N(2)–Hg(2)–N(3)	160.96(18)
Hg(2)–Cl(4)	2.8477(16)	N(2)–Hg(2)–Cl(3)	104.78(14)
Hg(3)–Cl(5)	2.3140(18)	N(2)–Hg(2)–Cl(4)	91.88(14)
Hg(3)–Cl(6)	2.2943(17)	N(3)–Hg(2)–Cl(3)	94.26(12)
Tb(1)–O(5) <sup>i</sup>	2.276(5)	N(3)–Hg(2)–Cl(4)	87.98(12)
Tb(1)–O(3) <sup>ii</sup>	2.313(5)	Cl(3)–Hg(2)–Cl(4)	90.46(5)
Tb(1)–O(6) <sup>iii</sup>	2.334(5)	Cl(5)–Hg(3)–Cl(6)	176.36(7)
Tb(1)–O(4) <sup>iv</sup>	2.354(5)	O(3) <sup>ii</sup> –Tb(1)–O(1) <sup>v</sup>	73.87(17)
Tb(1)–O(1) <sup>v</sup>	2.360(5)	O(6) <sup>iii</sup> –Tb(1)–O(4) <sup>iv</sup>	143.57(19)
Tb(1)–O(2)	2.375(5)	O(4) <sup>iv</sup> –Tb(1)–O(2)	73.10(18)
Tb(1)–O(1W)	2.491(5)	O(4) <sup>iv</sup> –Tb(1)–O(1W)	69.47(18)
Tb(1)–O(2W)	2.498(6)	O(1W)–Tb(1)–O(2W)	126.28(18)

Symmetry codes: (i)  $-x - \frac{1}{2}, y + \frac{1}{2}, -z + \frac{1}{2}$ ; (ii)  $-x - 1, -y + 2, -z + 1$ ; (iii)  $x + \frac{1}{2}, -y + 2\frac{1}{2}, z - \frac{1}{2}$ ; (iv)  $x + 1, y, z$ ; (v)  $-x, -y + 2, -z + 1$ .

## 3. Results and Discussion

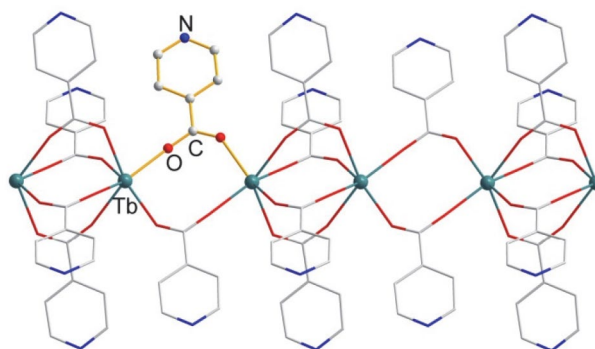
Compound **1** crystallizes in the space group  $P2_1/n$  of the monoclinic system with four formula units in each cell, as uncovered by single crystal X-ray diffraction analysis. The asymmetric unit contains three mercury(II) ions, six chloride ions, one terbium(III) ion, three isonicotinate, two coordinating water molecules and one lattice water molecule. Its molecular structure consists of one  $[\text{Tb}(\text{IA})_3(\text{H}_2\text{O})_2(\text{Hg}_2\text{Cl}_4)]_n$  moiety, one  $\text{HgCl}_2$  moiety and

one lattice water molecule, as presented in Fig. 1. All crystallographically independent atoms reside at the general positions.

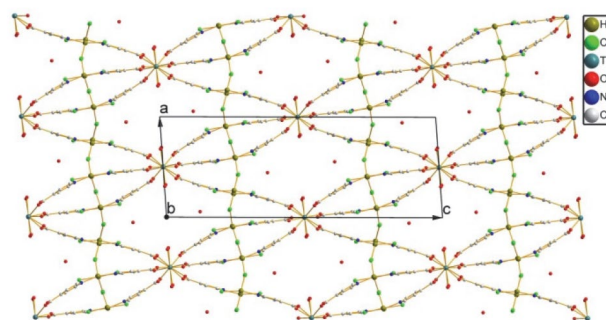


**Figure 1.** A molecular structure of compound **1** with lattice water and hydrogen atoms being omitted for clarity. Symmetry transformations used to generate equivalent atoms: (i)  $-x - \frac{1}{2}, y + \frac{1}{2}, -z + 1\frac{1}{2}$ ; (ii)  $-x - 1, -y + 2, -z + 1$ ; (iii)  $x + \frac{1}{2}, -y + 2\frac{1}{2}, z - \frac{1}{2}$ ; (iv)  $x + 1, y, z$ ; (v)  $-x, -y + 2, -z + 1$ .

There are three crystallographically independent mercury(II) ions existing in compound **1**. Hg1 ion is surrounded by one nitrogen atom of one isonicotinate and three chloride ions to yield a distorted tetrahedron with the bond angles of N–Hg–Cl and Cl–Hg–Cl being of  $88.44(13)^\circ$ – $164.51(14)^\circ$  and  $93.76(5)^\circ$ – $101.75(6)^\circ$ , respectively. Hg2 ion is coordinated by two nitrogen atoms of two isonicotinates and two chloride ions to yield a distorted tetrahedron with the bond angles of N–Hg–N, N–Hg–Cl and Cl–Hg–Cl being of  $160.96(18)^\circ$ ,  $87.98(12)^\circ$ – $104.78(14)^\circ$  and  $90.46(5)^\circ$ , respectively. Hg3 ion is bound by two chloride ions and form a nearly linear mode with the bond angle of Cl–Hg–Cl being of  $176.36(7)^\circ$ . The Hg–N and Hg–Cl bond lengths locate in the span of  $2.122(5)$ – $2.136(5)$  Å and  $2.2943(17)$ – $2.8723(16)$  Å, respectively. These bond lengths are normal and comparable with those found in the literature.<sup>23–25</sup> The terbium ion is coordinated by eight oxygen atoms, of which six are from six isonicotinates and two come from two coordinating water molecules, yielding a slightly distorted square anti-prismatic geometry. The Tb–O bond lengths are located in the range of  $2.276(5)$  Å –  $2.498(6)$  Å, which is also normal and comparable with those found in the literature.<sup>26–28</sup> The neighbouring terbium ions are interlinked by four or two isonicotinates to form a one-dimensional (1-D) Tb-(IA)<sub>4</sub>-Tb-(IA)<sub>2</sub>-Tb-(IA)<sub>4</sub> chain running along the *b*-axis, as shown in Fig. 2. The distances between every two neighbouring terbium ions are  $4.3996(4)$  Å and  $5.1233(4)$  Å. The 1-D Tb-(IA)<sub>4</sub>-Tb-(IA)<sub>2</sub>-Tb-(IA)<sub>4</sub> chains are interconnected by mercury ions to yield a 3-D framework, as shown in Fig. 3.

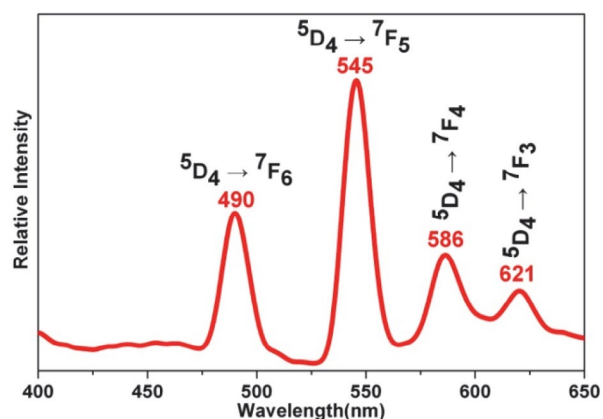


**Figure 2.** A 1-D Tb-(IA)<sub>4</sub>-Tb-(IA)<sub>2</sub>-Tb-(IA)<sub>4</sub> chain in compound **1**.



**Figure 3.** The 3-D framework of compound **1**.

In this work, we performed the photoluminescence experiments of compound **1** in the solid state and the results of the photoluminescence spectrum are shown in Fig. 4. When it was excited by using the 353 nm wavelength of UV light, it displays a characteristic photoluminescence spectrum of Tb<sup>3+</sup> ions. The photoluminescence diagram contains four sharp emission bands with the strongest one at 545 nm. These peaks reside at 490, 545, 586 and 621 nm. They can be ascribed to the characteristic emission of the 4*f* electrons intrashell transition of the <sup>5</sup>D<sub>4</sub> → <sup>7</sup>F<sub>*J*</sub> (*J* = 6, 5, 4 and 3, respectively) of the Tb<sup>3+</sup> ions.<sup>29</sup> The CIE (Com-



**Figure 4.** Solid-state photoluminescence spectra of complex **1** measured at room temperature.

mission Internationale de l'Éclairage) chromaticity coordinates of the title compound are (0.3525, 0.4032) which locates in the yellow region, as given in Fig. 5. As a result, compound **1** could be expected as a possible yellow light emitting material.

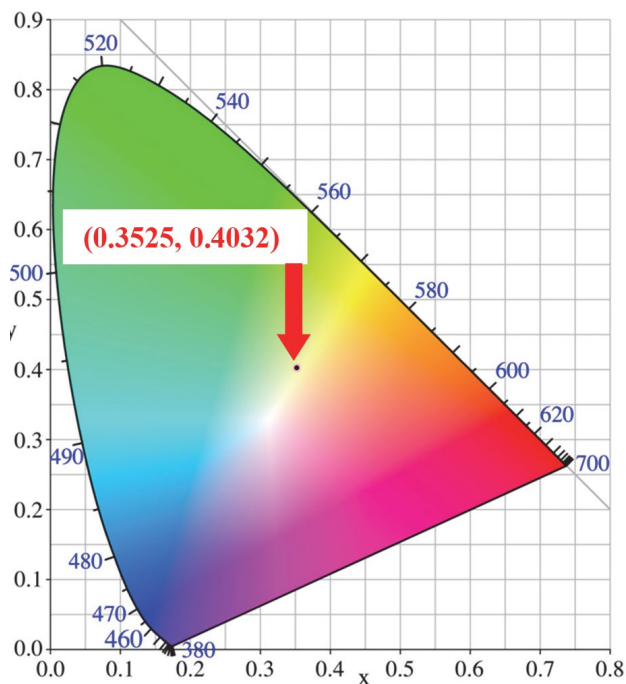


Figure 5. The CIE chromaticity diagram and chromaticity coordinate of the photoluminescence emission spectrum of **1**.

In order to reveal the energy transfer mechanism of the photoluminescence emission of **1**, we also carried out the phosphorescence emission spectrum of the isonicotinic acid at 77 K, as given in Fig. 6. The onset of the emission curve of the isonicotinic acid can be estimated to be 434 nm. Therefore, the lowest triplet state energy of isonicotinic acid is calculated to be  $23041 \text{ cm}^{-1}$ . The energy difference between the lowest triplet state of isonicotinic acid and the resonant energy level of terbium ions ( ${}^5D_4$ ,  $20500 \text{ cm}^{-1}$ ) is  $2541 \text{ cm}^{-1}$  for compound **1**, as shown in Fig. 7. Based on the intramolecular energy transfer theory revealed by Sato and Dexter,<sup>30–31</sup> the intramolecular energy transfer efficiency mainly depends on two processes. The first one is the energy transfer from the lowest triplet energy levels of the ligands to the resonant energy levels of lanthanide centers through the Dexter's resonant exchange interactions. The second one is the reverse energy transfer from the lanthanide centers to the ligands through a thermal deactivation process. The reverse energy transfer process possibly happens easier once the energy difference is small enough. These two energy transfer processes are obviously contrary, even though both of them depend on the energy gap between the lowest triplet energy levels of the

ligands and the resonant energy levels of the lanthanide centers. A best energy gap can be estimated to be around  $3000 \pm 500 \text{ cm}^{-1}$ , as found by the intramolecular energy transfer mechanism. As the above discussions, the energy gap of the terbium ions in compound **1** is  $2541 \text{ cm}^{-1}$ ; this is in the range of  $3000 \pm 500 \text{ cm}^{-1}$ . As a result, compound **1** can be expected to exhibit ideal photoluminescence properties. This prediction is in good line with the photoluminescence emission diagram of the title compound, as given in Fig. 4. From Fig. 4 it can be easily found out that the emission bands are well separated and sharp. Therefore, the above discussions uncover that isonicotinic acid is a good ligand to excite  $\text{Tb}^{3+}$  ions for the title compound; namely, it is a suitable "antenna".

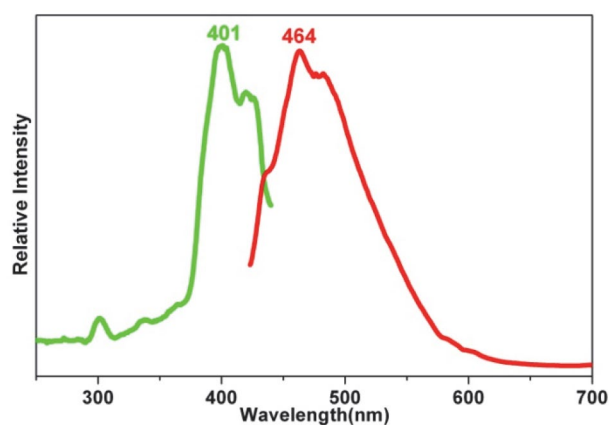


Figure 6. Phosphorescence spectrum of isonicotinic acid measured at 77 K.

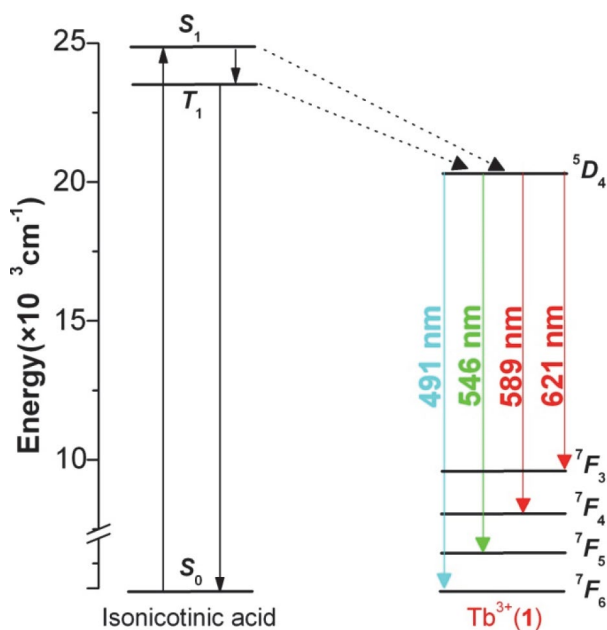


Figure 7. A schematic and partial energy level diagram of the main energy absorption transfer and phosphorescence processes in **1** and the isonicotinic acid.

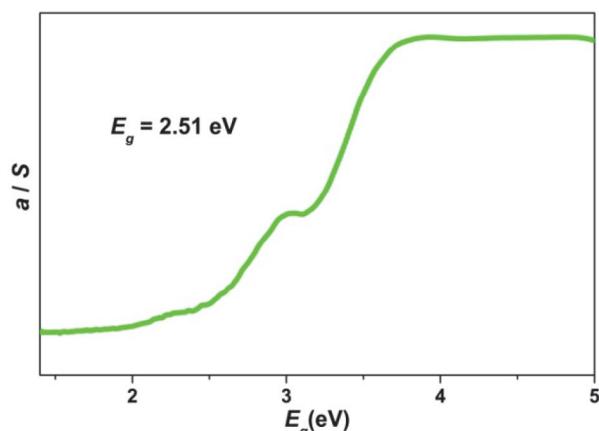


Figure 8. Solid-state UV/Vis diffuse reflectance spectrum of **1**.

Mercury is a well-known element in semiconductor materials such as  $\text{Hg}_x\text{Cd}_{1-x}\text{Te}$  (i.e. MCT) which is a very important infrared detector in military area. Compound **1** consists of mercury element and, so, it may probably display semiconductor performances. Based on this consideration, we carried out its solid-state UV/Vis diffuse reflectance spectrum under room temperature. The reflectance data set was treated by using the Kubelka-Munk function, i.e.  $\alpha/S = (1 - R)^2/2R$ . The  $R$  is the reflectance,  $\alpha$  is the absorption coefficient, while  $S$  means the scattering coefficient which is practically wavelength independent if the particle size is larger than 5  $\mu\text{m}$ . By extrapolating the linear part of the absorption edge of the curve, the optical band gap value can be determined as shown in Fig. 8. The solid-state diffuse reflectance spectrum shows that compound **1** has an optical band gap of 2.51 eV and, so, this compound can be classified as a wide band gap semiconductor material. The solid-state diffuse reflectance spectrum diagram exhibits a slow slope of the optical absorption edge, which means an indirect transition process.<sup>32</sup> This optical band gap of 2.51 eV is clearly smaller than 5.47 eV of diamond which is one of the third generation semiconductor materials; but it is obviously larger than that of  $\text{CuInS}_2$  (1.55 eV),  $\text{CdTe}$  (1.5 eV) and  $\text{GaAs}$  (1.4 eV) which are well-known highly efficient photovoltaic materials.<sup>33–34</sup>

## 4. Conclusions

In conclusion, a novel terbium-mercury compound was prepared via a hydrothermal reaction and structurally characterized by single crystal X-ray diffraction technique. It is characterized by a 3-D framework. It shows yellow light photoluminescence emission with the emission peaks at 490, 545, 586 and 621 nm which are originated from the characteristic emission of the  $4f$  electrons intrashell transition of the  $^5D_4 \rightarrow ^7F_j$  ( $J = 6, 5, 4, 3$ , respectively) of the  $\text{Tb}^{3+}$

ions. An energy transfer mechanism was expatiated by applying the energy level figure of the terbium ions and isonicotinic acid. It possesses a remarkable CIE chromaticity coordinates (0.3525, 0.4032). It also shows a wide optical band gap of 2.51 eV. So, this compound is a potential candidate for yellow light photoluminescence and wide band gap semiconductor materials.

## 5. Acknowledgements

We gratefully acknowledge the financial support of the NSF of China (21361013, 31460488), NSF of Fujian (2018J01447), Jiangxi Provincial Department of Education's Item of Science and Technology (GJJ170637), and the open foundation (20180008) of the State Key Laboratory of Structural Chemistry, Fujian Institute of Research on the Structure of Matter, Chinese Academy of Sciences.

## 6. Supplementary Material

Crystallographic data for the structural analysis have been deposited with the Cambridge Crystallographic Data Centre, CCDC 1864724. Copies of this information may be obtained free of charge from the Director, CCDC, 12 Union Road, Cambridge, CBZ 1EZ, UK (Fax: +44-1223-336033; email: deposit@ccdc.cam.ac.uk or www: <http://www.ccdc.cam.ac.uk>).

## 7. References

- S. Han, R. Deng, X. Xie, X. Liu, *Angew. Chem. Int. Edit.* **2014**, *53*, 11702–11715. DOI:10.1002/anie.201403408
- G. Huang, C. Daiguebonne, G. Calvez, Y. Suffren, O. Guilou, T. Guizouarn, B. Le Guennic, O. Cador, K. Bernot, *Inorg. Chem.* **2018**, DOI:10.1021/acs.inorgchem.8b01640.
- R. F. Mendes, D. Ananias, L. D. Carlos, J. Rocha, F. A. A. Paz, *Cryst. Growth Des.* **2017**, *17*, 5191–5199. DOI:10.1021/acs.cgd.7b00667
- X.-G. Yi, Z.-X. Zhang, W.-T. Chen, L.-Z. Lin, H.-L. Chen, *J. Solid State Chem.* **2018**, *266*, 16–22. DOI:10.1016/j.jssc.2018.07.004
- F. Pointillart, O. Cador, B. Le Guennic, L. Ouahab, *Coord. Chem. Rev.* **2017**, *346*, 150–175. DOI:10.1016/j.ccr.2016.12.017
- J. A. Kitchen, *Coord. Chem. Rev.* **2017**, *340*, 232–246. DOI:10.1016/j.ccr.2017.01.012
- H. J. Zhang, R. Q. Fan, Y. W. Dong, W. Chen, X. Du, P. Wang, Y. L. *Crystengcomm* **2016**, *18*, 3711–3724.
- M. B. Coban, A. Amjad, M. Aygun, H. Kara, *Inorg. Chim. Acta* **2017**, *455*, 25–33. DOI:10.1016/j.ica.2016.10.010
- N. Ahmed, J. Nisar, R. Kouser, A. G. Nabi, S. Mukhtar, Y. Saeed, M. H. Nasim, *Mater. Res. Express* **2017**, *4*, 065903/1–065903/8.

10. K. P. Zhuravlev, V. I. Tsaryuk, V. A. Kudryashova, *J. Fluorine Chem.* **2018**, *212*, 137–143.  
DOI:10.1016/j.jfluchem.2018.06.002
11. N. Souri, P. Tian, C. Platas-Iglesias, K. L. Wong, A. Nonat, L. J. Charbonniere, *J. Am. Chem. Soc.* **2017**, *139*, 1456–1459.  
DOI:10.1021/jacs.6b12940
12. X. Chen, L. Zhang, Z. Zhang, L. Zhu, W. Zhu, *Cryst. Eng. Comm.* **2015**, *17*, 7856–7865. DOI:10.1039/C5CE01273B
13. M. Arici, *Cryst. Growth Des.* **2017**, *17*, 5499–5505.  
DOI:10.1021/acs.cgd.7b01024
14. B. Mohapatra, S. Verma, *Cryst. Growth Des.* **2013**, *13*, 2716–2721. DOI:10.1021/cg4006168
15. L. N. Wang, L. Fu, J. W. Zhu, Y. Xu, M. Zhang, Q. You, P. Wang, J. Qin, *Acta Chim. Slov.* **2017**, *64*, 202–207.  
DOI:10.17344/acsi.2016.3109
16. P. Wang, Y. S. Wu, X. M. Han, S. S. Zhao, J. Qin, *Acta Chim. Slov.* **2017**, *64*, 431–437. DOI:10.17344/acsi.2017.3268
17. Y. Yoshida, H. Ito, Y. Nakamura, M. Ishikawa, A. Otsuka, H. Hayama, M. Maesato, H. Yamochi, H. Kishida, G. Saito, *Cryst. Growth Des.* **2016**, *16*, 6613–6630.  
DOI:10.1021/acs.cgd.6b01294
18. L. Zhang, H. Lin, Y. Wu, S. Zhuo, *Chem. Phys. Lett.* **2016**, *661*, 224–227. DOI:10.1016/j.cplett.2016.08.079
19. Y. Zeng, D. F. Kelley, *J. Phys. Chem. C* **2016**, *120*, 17853–17862.  
DOI:10.1021/acs.jpcc.6b06282
20. T. Uematsu, E. Shimomura, T. Torimoto, S. Kuwabata, *J. Phys. Chem. C* **2016**, *120*, 16012–16023.  
DOI:10.1021/acs.jpcc.5b12698
21. Rigaku, CrystalClear Version 1.35, Rigaku Corporation, Japan, Tokyo (2002).
22. Siemens, SHELXTL™ Ver. 5 Reference Manual, Siemens Energy & Automation Inc., Madison, Wisconsin, USA (1994).
23. H. R. Khavasi, N. Rahimi, *Cryst. Growth Des.* **2017**, *17*, 834–845. DOI:10.1021/acs.cgd.6b01673
24. R. J. F. Berger, J. Schoiber, U. Monkowius, *Inorg. Chem.* **2017**, *56*, 956–961. DOI:10.1021/acs.inorgchem.6b02613
25. Y.-T. Dong, B. Tu, H. Xu, Y.-L. Huang, Q.-L. Zhang, Z.-C. Hu, B.-X. Zhu, *Wuji Huaxue Xuebao (Chinese J. Inorg. Chem.)* **2017**, *33*, 651–658.
26. L.-M. Zheng, J.-X. Liu, *J. Solid State Chem.* **2017**, *245*, 45–49.  
DOI:10.1016/j.jssc.2016.10.008
27. J. Wu, X.-L. Li, L. Zhao, M. Guo, J. Tang, *Inorg. Chem.* **2017**, *56*, 4104–4111. DOI:10.1021/acs.inorgchem.7b00094
28. X. Li, T. Li, X. J. Shi, L. Tian, *Inorg. Chim. Acta* **2017**, *456*, 216–223. DOI:10.1016/j.ica.2016.11.002
29. M. A. Katkova, V. A. Ilchev, A. N. Konev, I. I. Pestova, G. K. Fukin, M. N. Bochkarev, *Org. Electron.* **2009**, *10*, 623–630.  
DOI:10.1016/j.orgel.2009.02.020
30. S. Sato, M. Wada, *Bull. Chem. Soc. Jpn.* **1970**, *43*, 1955–1962.  
DOI:10.1246/bcsj.43.1955
31. D. L. Dexter, *J. Chem. Phys.* **1953**, *21*, 836–850.  
DOI:10.1063/1.1699044
32. F. Q. Huang, K. Mitchell, J. A. Ibers, *Inorg. Chem.* **2001**, *40*, 5123–5126. DOI:10.1021/ic0104353
33. P. Dürichen, W. Bensch, *Eur. J. Solid State Inorg. Chem.* **1997**, *34*, 1187–1198.
34. R. Tillinski, C. Rumpf, C. Näther, P. Duerichen, I. Jess, S. A. Schunk, W. Bensch, *Z. Anorg. Allg. Chem.* **1998**, *624*, 1285–1290.  
DOI:10.1002/(SICI)1521-3749(199808)624:8<1285::AID-ZAAC1285>3.0.CO;2-5

## Povzetek

S hidrotermalno sintezo smo pripravili novo terbij-živosrebrovo spojino  $[\text{Tb}(\text{IA})_3(\text{H}_2\text{O})_2(\text{Hg}_2\text{Cl}_4)]_n \cdot n\text{HgCl}_2 \cdot n\text{H}_2\text{O}$  (1, HIA = izonikotinska kislina) ter jo strukturno okarakterizirali z monokristalno rentgensko difrakcijo. Spojina tvori tridimenzionalno (3-D) mrežo. Študij fotoluminiscence vzorca v trdnem razkriva, da spojina emitira rumeno svetlobo pri 490, 545, 586 in 621 nm. Ti fotoluminiscenčni emisijski vrhovi so posledica karakteristične emisije znotraj lupinskih prehodov  $4f$  elektronov  ${}^5D_4 \rightarrow {}^7F_J$  ( $J = 6, 5, 4, 3$ )  $\text{Tb}^{3+}$  ionov. Mehanizem prenosa energije smo določili z uporabo diagrama energijskih nivojev terbijevih ionov in izonikotinske kisline. Spojina ima kromatične koordinate CIE (0.3525, 0.4032). Z UV-Vis difuzno odbojno spektroskopijo na trdnem vzorcu smo za spojino določili širok optični pas pri 2.51 eV.

*Technical paper*

# Nanostructured Semiconducting Metal Oxides for Ammonia Sensors. A Novel HSAB Sensing Paradigm

Bogdan-Catalin Serban,<sup>1,\*</sup> Octavian Buiu,<sup>1</sup> Cornel Cobianu,<sup>1</sup>  
Mihai Brezeanu,<sup>2</sup> Marius Bumbac<sup>3</sup> and Cristina Mihaela Nicolescu<sup>4</sup>

<sup>1</sup>National Institute for Research and Development in Microtechnologies, IMT-Bucharest, 126 A Str Erou Iancu Nicolae, 077190, Voluntari, Ilfov, Romania

<sup>2</sup>University Politehnica of Bucharest, Romania, Faculty of Electronics, Telecommunications and IT, 313 Splaiul Independentei, Sector 6, 060042, Bucharest, Romania

<sup>3</sup>Valahia University of Targoviste, Faculty of Sciences and Arts, Sciences and Advanced Technologies Department, 2 Bd. Carol I, 130024, Targoviste, Dambovita, Romania

<sup>4</sup>Valahia University of Targoviste, Institute of Multidisciplinary Research for Science Technology, 2 Bd. Carol I, 130024, Targoviste, Dambovita Romania

\* Corresponding author: E-mail: bogdan.serban@imt.ro  
Tel: +40 724284128

Received: 25-06-2018

## Abstract

The paper demonstrates how the Hard-Soft Acid Base (HSAB) theory can be used as a valuable criterion in the selection process of semiconducting metal oxides (MOX) suitable as sensing layers for ammonia detection. Six different cases of ammonia detection performed by chemiresistive sensors employing MOX and related nanocomposites as sensing layers are identified and discussed. The role of HSAB as an efficient selection tool for appropriate sensing layer (any type of gas), is further reinforced by analyzing and discussing literature results on MOX-based trimethylamine sensing layers. By analyzing the operation of a fiber-optic ammonia sensor, we demonstrate that the HSAB principle can be also successfully applied to the selection of sensing layers for detectors employing other sensing principles, different than the chemiresistive one. Changing the sensing paradigm (i.e., the amino groups-based compounds are part of the sensing layer, rather than part of the analyte), the paper shows that these types of molecules (polymers, carbon nanotubes, ionic liquids) are appropriate constituents of a CO<sub>2</sub> sensing layer, in full accordance to the HSAB criteria.

**Keywords:** MOX; HSAB; ammonia; sensor; nanostructure; carbon dioxide.

## 1. Introduction

Ammonia (NH<sub>3</sub>), a natural gas that is present throughout the atmosphere, is a highly toxic compound, with low odor threshold (20 ppm), corrosive to the skin, eyes, throat and lungs. The most widely recognized exposure limits for ammonia are an eight-hour TWA (Time Weighted Average) of 25 ppm, with a 15-minute STEL (Short Term Exposure Limit) of 35 ppm.<sup>1</sup> Strong irritation of the nose and throat occurs at 500 ppm, while exposure to 1000 ppm or more causes lungs injury (pulmonary edema).<sup>2–3</sup> Extremely high concentrations, around 5000–10,000 ppm, are fatal to humans within the first 5–10 minutes of exposure.<sup>4</sup>

Ammonia, one of the most important industrial raw materials in the world, is widely used in many industries including chemical and petrochemical, food/beverage, pulp and paper, fertilizer and the oil industry, pharmaceuticals, etc. Its global production exceeds 100 million tons per year. Ammonia is also the key precursor in the synthesis of many chemical compounds with high economic value, such as urea (Bosch –Meiser process), hydroxylamine and ammonium carbonate (Raschig process), acrylonitrile (Sohio process), hydrazine (Olin Raschig process), ammonium nitrate, hexamethylenetetramine, to name but a few.<sup>5</sup> Anhydrous ammonia is also extensively

used as a coolant in industrial refrigeration systems, replacing environmentally unfriendly chlorofluorocarbon refrigerants. It is worth mentioning that ammonia is an ingredient in the formulation of many cleaning products.<sup>6</sup>

Given all the above, sensing of ammonia is an important process in various areas of domestic and industrial applications, such as environmental monitoring (monitoring ambient conditions, level of ammonia in stables), automotive (measure NH<sub>3</sub> emission from vehicles), chemical industry (chemical leakage alarm), medical diagnostics (breath analysis), food safety, etc.<sup>7</sup> Therefore, the design and manufacturing of an NH<sub>3</sub> gas sensor has been demanded for process control and monitoring in laboratories, factories and public places.

There are many principles and methods described in literature for measuring ammonia. Besides conducting polymer gas detectors,<sup>8</sup> catalytic sensors,<sup>9</sup> spectrophotometric and other optical devices,<sup>10–11</sup> chemiresistive-based sensors employing semiconducting metal oxides (MOX) as sensing layers were also widely used in the last decades.<sup>12</sup> These types of sensors are typically operated at elevated temperature, usually more than 400 °C. The major benefits of MOX-based sensors are their significant higher lifetime, increased robustness, ease of manufacturing, simplicity of measurement, low cost, and a wide detection range: from 1 to 1000 ppm. MOX-based sensors are by far the least expensive type of ammonia sensors and are not damaged or consumed by prolonged exposure to the analyte. However, because their output signal is non-linear, they need to be calibrated and adjusted for being reliably used in the desired detection range.<sup>13</sup> Another drawback of MOX-based sensors is the significant cross-sensitivity, particularly with relative humidity.

A plethora of sensing layers based on MOX were tested for the NH<sub>3</sub> detection, yielding different sensitivity, selectivity, and response time performance. Different mechanisms and models have been proposed to coherently explain the sensing capabilities of MOX.

In this paper, we introduce and use, for the first time to our knowledge, Pearson's Hard-Soft Acid-Base (HSAB) concept as a possible criterion to assess the sensitivity and selectivity of a number of MOX and of their nanocomposites as candidates to ammonia sensing.

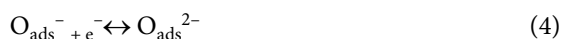
To support the conjecture that the HSAB principle can be used when selecting the appropriate gas sensing layer (in particular for NH<sub>3</sub>), we will bring into the discussion facts and conclusions related to the following three issues:

- 1) the results obtained for the MOX based – trimethylamine sensing;
- 2) evaluation of fiber-optic ammonia sensor using MOX and their nanocomposites, showing that, despite a completely different detection principle, HSAB interpretation works and explains sensing mechanism;

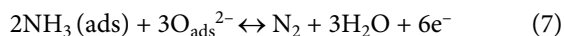
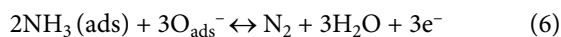
- 3) changing the sensing paradigm and showing that, using the same principle, amino group – based molecules (polymers, carbon nanotubes, ionic liquids) can be evaluated as appropriate candidates for carbon dioxide detection.

## 2. MOX-based Gas Sensing Layers Selection – General Theory

Despite the measurement simplicity required by MOX-based gas sensors, their detection mechanism is complex and not yet fully understood. Electrophysical and chemical properties, catalytic activity, thermodynamic stability, adsorption ability, the adsorption/desorption properties of the surface (highly dependent on materials used and environmental parameters) are just a few of the MOX parameters which are responsible for the sensing mechanism.<sup>14–15</sup> Beyond these aspects, it is obvious that recognition of the analyte through a gas-solid interface induces an electronic change of the metal oxide surface.<sup>16</sup> One of the most used mechanism which explains ammonia sensing can be described by the reactions 1–7:<sup>17</sup>



Once the MOX-based sensing layer is exposed to NH<sub>3</sub>, the reaction between the adsorbed oxygen ions and the NH<sub>3</sub> molecules releases electrons in the MOX, leading to a thinner space-charge layer and a lower potential barrier. Consequently, the resistance of the MOX decreases. The process can be understood by using the following set of reactions 5–7:<sup>18</sup>



Despite its reasonability (generation of electrons and decrease of MOX resistance, presence of adsorbed oxygen ions), this mechanism cannot explain the different sensing performances of different MOX-based layer. Why some MOX are more sensitive towards ammonia than others or why some MOX are selective and can discriminate between certain types of gases, but cannot discriminate between other types of gases, are some of the issues still unclear.

### 3. MOX-Based Gas Sensing Layers Selection – HSAB Theory

We consider that direct and individual interaction of MOX metal cations and ammonia can have a cardinal importance in the sensing mechanism and in answering the questions listed above. For this purpose, we introduce and use Pearson's Hard-Soft Acid-Base (HSAB) theory.

The Hard-Soft Acid Base (HSAB) theory is a qualitative concept, developed by Ralph Pearson in the early 1960s, which justifies, among others, the propensity of some chemical species to interact with other species.<sup>19</sup> The HSAB concept has proven to be a useful investigation tool in many areas of chemistry, such as: medicinal chemistry, toxicology,<sup>20</sup> quantum dot functionalization and design of quantum dot solar cells,<sup>21</sup> TiO<sub>2</sub> functionalization,<sup>22</sup> computational chemistry,<sup>23</sup> design and synthesis of sensing layers employed in nano – resonators based CO<sub>2</sub> detection,<sup>24–25</sup> design of sensing layer for sulfur dioxide detection,<sup>26</sup> ethanol gas sensing,<sup>27</sup> glucose electrochemical sensing,<sup>28</sup> NO<sub>2</sub> gas sensing,<sup>29</sup> corrosion,<sup>30</sup> adsorption phenomena.<sup>31</sup>

The HSAB principle operates with Lewis bases and acids; a molecule donating a pair of electrons is classified as a base, while a molecule accepting a pair of electrons it is classified as an acid. Pearson divides Lewis' bases and acids into hard, borderline, and soft. Hard bases tend to have low ionic radii, high HOMO energy level, while hard acids have empty orbitals in their valence shells, high positive charge and high LUMO energy level. At the same time, soft acids exhibit large ionic radii, while soft bases have large atoms with high polarizability.<sup>32</sup> Borderline species have an intermediate character between hard and soft species. It is worth pointing out that, to be classified as soft, hard or borderline, a Lewis base or acid doesn't have to possess all the above-mentioned properties.

Examples of hard, soft and borderline acids and bases are given in Table 1. The large electronegativity differences between hard acids and hard bases lead to strong

ionic interactions, while the electronegativities of soft acids and soft bases are almost the same, hence their interactions are predominantly covalent.<sup>33</sup> According to the HSAB theory, a hard base prefers to interact to a hard acid, a soft base prefers to interact to a soft acid, while a borderline base tends to bond to borderline acid.

Recently, a new concept, inverse Hard Soft Acid Bases (IHSAB), was introduced and employed for selecting and synthesizing gas sensing materials.<sup>34–35</sup> This concept, based on the reversible interaction of hard-acid surfaces with soft bases and hard-base surfaces with soft acids, relies, as dominant adsorption process, on physisorption. This is a major difference from the HSAB concept, which mainly operates with the chemisorption phenomenon. Actually, the IHSAB principle introduces the concept of electron transduction, which is defined as the transfer of electrons to or from an interface without the formation of a chemical bond.<sup>36</sup>

From the HSAB theory perspective, ammonia is classified as hard base (in bold in Table 1). Thus, according to the HSAB principle, hard acid species (with asterisk in Table 1) are feasible candidates for ammonia detection. Indeed, by investigating the literature, we found that most of the MOX exhibiting good performances (in terms of sensitivity, selectivity, recovery time, etc.) to ammonia detection are classified as hard acids according to HSAB theory. Six such cases are described and briefly analyzed below.

## 4. MOX-Based Sensing Layers for Ammonia Chemiresistive Detection

### 4. 1. The Sensing Layer is Based on One MOX with Cations Classified as Hard Acid

TiO<sub>2</sub>, In<sub>2</sub>O<sub>3</sub>, ZrO<sub>2</sub>, β-Ga<sub>2</sub>O<sub>3</sub>, α-Fe<sub>2</sub>O<sub>3</sub>, SnO<sub>2</sub>, which are MOX having hard acid cations, were used as sensing layer in chemiresistive sensors for ammonia (gas and aqueous) detection.

Table 1. Examples of hard, soft and borderline acids and bases

	Soft	Borderline	Hard
<b>Bases</b>	SCN <sup>-</sup> , C <sub>2</sub> H <sub>4</sub> , RSH, CO, R <sub>3</sub> P, R <sub>3</sub> As, (RO) <sub>3</sub> P, CN <sup>-</sup> RCN, R <sub>3</sub> P, C <sub>6</sub> H <sub>6</sub> , I <sup>-</sup>	Aniline (C <sub>6</sub> H <sub>5</sub> -NH <sub>2</sub> ) C <sub>5</sub> H <sub>5</sub> N(pyridine) N <sub>2</sub> , Br <sup>-</sup> , N <sub>3</sub> <sup>-</sup>	PO <sub>4</sub> <sup>3-</sup> , CH <sub>3</sub> OH, C <sub>2</sub> H <sub>5</sub> OH, C <sub>2</sub> H <sub>5</sub> O <sup>-</sup> , HO <sup>-</sup> , ClO <sub>4</sub> <sup>-</sup> , N <sub>2</sub> H <sub>4</sub> , CH <sub>3</sub> COO <sup>-</sup> , <b>NH<sub>3</sub><sup>+</sup></b> Me-NH <sub>2</sub> , Me <sub>2</sub> NH, Me <sub>3</sub> N, H <sub>2</sub> N- (CH <sub>2</sub> ) <sub>4</sub> -NH <sub>2</sub> , H <sub>2</sub> N-(CH <sub>2</sub> ) <sub>5</sub> -NH <sub>2</sub> , H <sub>2</sub> O, CO <sub>3</sub> <sup>2-</sup> , Cl <sup>-</sup>
<b>Acids</b>	Pt <sup>2+</sup> , Cu <sup>+</sup> , Au <sup>+</sup> , Ag <sup>+</sup> , Pd <sup>2+</sup> Metal atoms in zero oxidation state	Fe <sup>2+</sup> , Bi <sup>3+</sup> , Ni <sup>2+</sup> Zn <sup>2+</sup> , B(CH <sub>3</sub> ) <sub>3</sub> , Pb <sup>2+</sup> , NO <sup>+</sup> , Cu <sup>2+</sup>	CO <sub>2</sub> , Sm <sup>3+</sup> , Ga <sup>3+</sup> , In <sup>3+</sup> , BeMe <sub>2</sub> , Gd <sup>3+</sup> , Li <sup>+</sup> , B(OR) <sub>3</sub> , Mg <sup>2+</sup> , Al <sup>3+</sup> , BF <sub>3</sub> , Fe <sup>3+</sup> , Co <sup>3+</sup> , BCl <sub>3</sub> , Ti <sup>4+</sup> , La <sup>3+</sup> , Cr <sup>3+</sup> , Zr <sup>4+</sup> , AlMe <sub>3</sub>



Karuganaran et al. developed a  $\text{NH}_3$  planar structure sensor employing a  $\text{TiO}_2$  film deposited by a direct current (DC) reactive magnetron sputtering technique onto a silicon substrate having interdigitated comb shaped electrodes.<sup>37</sup> Appropriate annealing temperature of the film formation was found to be 873 K, while an operating temperature at 250 °C ensured highest sensitivity to the detection of the  $\text{NH}_3$  gas.

Li et al. used single-crystalline  $\text{In}_2\text{O}_3$  nanowires for  $\text{NH}_3$  detection at room temperature. Ammonia sensing layer based on  $\text{In}_2\text{O}_3$  nanowires exhibited “on/off” ratios (i.e., the ratio between the measured currents during and before the  $\text{NH}_3$  exposure) around 50 and response times around 20 s, with ambient air initialization for 1%  $\text{NH}_3$ .<sup>38</sup> It has also been found that oxygen has a relatively minor effect on the nanowire conductance. The authors explained the sensing mechanism based on the electrons transfer from the adsorbed  $\text{NH}_3$  molecules into the  $\text{In}_2\text{O}_3$  nanowire, explanation which agrees with the HSAB theory, as  $\text{In}^{3+}$  is classified as hard acid, while ammonia molecule is hard base.

Deshmukh et al. reported on the development of an ammonia sensor using  $\text{ZrO}_2$  thin film as sensing layer. The film was prepared using the spray pyrolysis technique.<sup>39</sup> The sensor showed quick response (4 s) and fast recovery (10 s).

Pandeeswari et al. used nanocrystallite  $\beta\text{-Ga}_2\text{O}_3$  thin films for ammonia sensing at 30 °C.<sup>40</sup> In this case, the lowest detection limit of ammonia was found to be 0.5 ppm. The response and recovery times were 40 s and 18 s, respectively (for a 0.5 ppm  $\text{NH}_3$  level). The authors demonstrated that the nanocrystallite  $\beta\text{-Ga}_2\text{O}_3$  thin film has a comparatively lower sensitivity for toluene, xylene, formaldehyde and acetone than for ammonia. This result agrees with the HSAB theory. None of the other measurands is a hard base, so it is reasonable to explain the preference of  $\text{Ga}^{3+}$  – a hard acid and part of the sensing layer – for ammonia (hard base).

Abaker et al. reported on the utilization of  $\alpha\text{-Fe}_2\text{O}_3$  nanoellipsoids thin films for developing a highly sensitive chemical sensor for aqueous ammonia.<sup>41</sup> The device exhibited a very high and reproducible sensitivity of  $\sim 4.678 \mu\text{A cm}^{-2} \text{mM}^{-1}$ , a detection limit of  $\sim 0.04 \text{ nM}$  and a short response time (10.0 s).

By far,  $\text{SnO}_2$  is the most widely used MOX for ammonia detection. Rout et al. investigated ammonia sensing characteristics of  $\text{SnO}_2$  nanoparticles over a wide range of concentrations (1–800 ppm) and temperatures (100–300 °C).<sup>42</sup> No interference with  $\text{NH}_3$  detection was found from  $\text{H}_2$ , CO, nitrogen oxides,  $\text{H}_2\text{S}$  and  $\text{SO}_2$ . Experimental results described in literature revealed that the  $\text{SnO}_2$ -based gas sensors exhibit linear dependence between the logarithm of the gas sensitivity and logarithm of the sample concentration when detecting both ammonia and methanol, at an operating temperature of 350 °C.<sup>43</sup>  $\text{SnO}_2$  shows high sensitivity towards both ammonia and other hard

bases (such as methanol, for instance), but cannot discriminate between. This, again, is in good agreement with the HSAB theory.

## 4. 2. The Sensing Layer Comprises 2 Types of MOXs, One of them Acting as Promoter

**Both MOX contain cations classified as hard acid.**

Wang et al. demonstrated that hybrid  $\text{Co}_3\text{O}_4/\text{SnO}_2$  core-shell nanospheres can be used as sensing layer for real-time, rapid-response, ammonia gas sensors.<sup>44</sup> The core – shell architecture enabled improved flexibility of the gas sensor surface compared to commonly used sensing layers. Cations of both metal oxides semiconducting are hard acids.

## 4. 3. The Sensing Layer Comprises 2 Types of MOXs, One of them Acting as Promoter

**Only the cations of the promoter are classified as hard acid.**

$\text{Cr}_2\text{O}_3$ -activated ZnO and zinc oxide thin film doped with  $\text{Al}_2\text{O}_3$ ,  $\text{TiO}_2$  are examples for this category.<sup>45–46</sup> Here, the promoter enhances the sensitivity of the sensing layer towards ammonia and trimethylamine molecules. It is important to emphasize that pure ZnO thick films ( $\text{Zn}^{2+}$  being a borderline acid, according to HSAB theory), prepared by screen-printing technique, is almost insensitive to  $\text{NH}_3$ . However, when pure ZnO thick films – for which the surface was activated with  $\text{Cr}^{3+}$  (a hard acid) – were measured, experimental results demonstrated that the structure is sensitive and highly selective to 300 ppm of  $\text{NH}_3$  gas, at room temperature. The changed sensitivity could be attributed to the presence of hard acid species (i. e.,  $\text{Cr}^{3+}$  cations).

## 4. 4. The Sensing Layer is a Nanostructured Composite Material, Comprising:

**a. One semiconducting metal oxide whose cations are classified as hard acid and**

**b. A carbonic material**

Examples include  $\text{SnO}_2/\text{MWCNTs}$  composite,<sup>47</sup> porous indium oxide nanotubes/carbon nanotubes,  $\text{Fe}_2\text{O}_3/\text{carbon nanotubes}$ . All these nanocomposites were used for selective ammonia gas sensing.

## 4. 5. The Sensing Layer is a Nanostructured Composite Material Consisting of:

**a. One semiconducting metal oxide whose cations are classified as hard acid and**

**b. Another semiconducting material**

Examples include *p*-toluenesulfonic acid doped polyaniline-titanium dioxide,  $\text{SnO}_2\text{-SnS}_2$  nanocomposite,

TiO<sub>2</sub>-PANI (polyaniline) / PA6 (polyamide 6) composite nanofibers. All these nanocomposites were used for highly sensitive ammonia gas sensing.<sup>48</sup>

#### 4. 6. The Sensing Layer Contains Two Types of Semiconducting Metal Oxides, but Only the Core Metal Oxide's Cations are Classified as Hard Acid

A good example in this category is the NiO-wrapped mesoporous TiO<sub>2</sub> microspheres. In comparison with pure TiO<sub>2</sub>, the sensor using 10 wt% NiO-wrapped mesoporous TiO<sub>2</sub> composite microspheres as sensing layer, exhibits no response to other volatile organic compounds (VOCs) and an excellent selectivity to detect ammonia in humid air with UV illumination at room temperature.<sup>49</sup>

All the examples presented above demonstrate that, at least in the first stage, the interaction between the analyte (ammonia and aliphatic amines) and MOX acting as sensing layer, can be analyzed and interpreted in terms of the HSAB theory.

### 5. MOX-Based Sensing Layers for Chemiresistive Detection of Other Hard Base Gases

Besides ammonia, there are several other amino groups based compounds which are categorized as hard bases, in accordance to the HSAB theory. Among these, one can mention methylamine, dimethylamine and biogenic amines, such as trimethylamine, cadaverine, and putresceine. Biogenic amines are degradation products found in spoiled meat products and are a good indicator for bacterial contamination. Trimethylamine is a suitable target for the detection of biogenic amines due to its volatility.<sup>50</sup>

A significant effort has been devoted to design suitable sensing layers for trimethylamine monitoring. A question arises: if trimethylamine is classified as hard base (like ammonia), is it possible to use the same type of reasoning when selecting MOX – based trimethylamine sensing layers as that employed for designing ammonia sensing layers? Reviewing the literature data, it can be indeed demonstrated that most of the MOXs (either simple or composite, with different thickness, morphologies and structural architectures) used with promising results in trimethylamine sensing, do contain species which can be classified as hard acids and that can be used, also, for ammonia sensing. Branch-like hierarchical heterostructure ( $\alpha$ -Fe<sub>2</sub>O<sub>3</sub>/TiO<sub>2</sub>), TiO<sub>2</sub>, ZnO – In<sub>2</sub>O<sub>3</sub> composite nanofibers, ZnO – Cr<sub>2</sub>O<sub>3</sub> hetero-nanostructures are just a few examples supporting the idea that HSAB interaction could play an important role in trimethylamine sensing mechanism.<sup>51–55</sup>

## 6. MOX-Based Sensing Layers for Ammonia Optical Detection

MOXs can be used, as sensing element, in the detection and monitoring of ammonia in devices employing fiber – optics technics. Examples of fiber optical sensors showing good ammonia detection capabilities include Gd<sub>2</sub>O<sub>3</sub> nanorods (with thickness ranging from 80 to 120 nm), thin films based on Ag/SnO<sub>2</sub> and nanocrystalline SnO<sub>2</sub>.<sup>56–58</sup> All these MOXs contain hard acid species. For fiber optic ammonia sensor, the sensing mechanism is completely different than the one specific to chemiresistive sensors. Here, the sensing principle relies on the change of the MOX refractive index upon its reaction with NH<sub>3</sub>. So, it is reasonable to consider that the interaction between MOXs cations and ammonia – following the HSAB related rules – drives the sensing.

## 7. HSAB Theory Employed as a Sensing Layer Selection Tool

Since the HSAB theory proves to be highly applicable in choosing sensing layer and has virtually general validity (i.e., not being limited to a certain sensing principle), one can anticipate that the roles of the hard acid – hard base tandem can be interchanged. It is reasonable to rationalize that, if ammonia (a hard base) can be sensed using MOXs containing hard acids cations, then amino group-based molecules, which are formally derivatives of ammonia, can be used as sensing layers for any type of gas classified as hard acid. Indeed, CO<sub>2</sub> (a hard acid) sensing can be performed with amino group – based molecules, such as polymers, carbon nanotubes, ionic liquids and their matrix nanocomposites, thus confirming the interaction predicted by the HSAB theory. Among these, one can enumerate CO<sub>2</sub> sensing layers based on polyallylamine, polyallylamine-amino carbon nanotubes (CNTs) matrix nanocomposite, polyethyleneimine-amino CNTs matrix nanocomposite.<sup>24,59–60</sup> All these types of CO<sub>2</sub> sensing layers were used on Surface Acoustic Waves (SAW) devices, employing quartz as a piezoelectric substrate, as depicted in Figure 1.

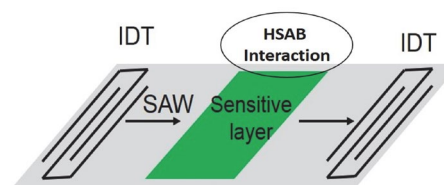
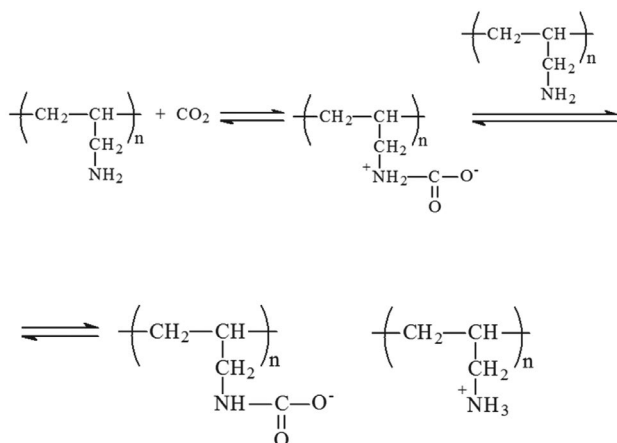


Figure 1. The structure of SAW device.

The HSAB interaction of CO<sub>2</sub> with the above-mentioned amino group-based molecules is reversible, yielding to carbamates. A well-known example is the reaction of CO<sub>2</sub> with polyallylamine (PAA), shown in Scheme 1.

Scheme 1. Reaction of PAA with CO<sub>2</sub>.

Furthermore, a convincing semiquantitative demonstration of the validity of HSAB principle in SAW CO<sub>2</sub> sensing with amino groups based compounds, comes from comparing the frequency shifts (at 2500 ppm of CO<sub>2</sub> exposure), for the three sensing layers: polyallylamine (PAA), polyallylamine – amino carbon nanotubes (aCNTs, shown in Figure 2) and polyethyleneimine (PEI) – aminocarbon nanotubes. As depicted in Figure 3, better results (in terms of sensitivity) are obtained when using as sensing layers simple polymers (PAA) rather than matrix nanocomposites (polyallylamine-amino CNTs and polyethyleneimine-amino CNTs), respectively. The most reasonable explanation for these results is related to the type of amino groups at the surface of the carbon nanotubes. According to HSAB, primary amino groups grafted on the CNT are categorized as borderline bases, and their affinity for CO<sub>2</sub> molecules is lower in comparison with that exhibited by the aliphatic amino groups which exist in PEI and PAA.

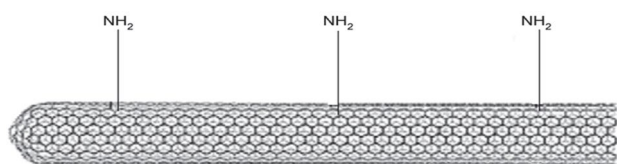
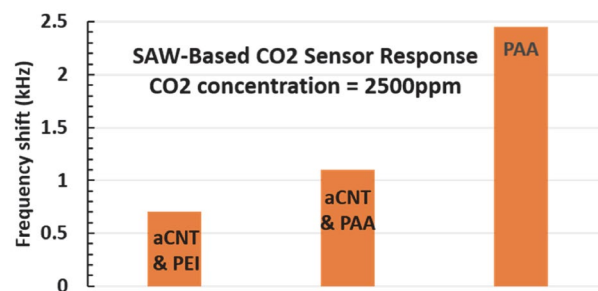
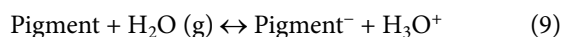
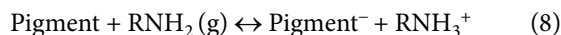


Figure 2. The structure of amino carbon nanotubes.

Figure 3. Frequency shifts at 2500 ppm CO<sub>2</sub> concentration for different sensing layers used to coat SAW devices.

For this reason, both PAA-amino CNTs and PEI-amino CNTs nanocomposites show lower sensitivity than simple polymers.<sup>61–64</sup>

The HSAB principle – based approach can work only if there is a direct interaction between ammonia (amine) and metal oxides surface. If the surface of the metal oxide semiconducting is covered with other molecules, a different type of sensing mechanism should be considered. For instance, if TiO<sub>2</sub> is sensitized with different anthocyanin pigments, the following reactions are responsible for the changing resistance of the TiO<sub>2</sub>:



In (10), R stands for H and Me. As it can be observed, there is a proton exchange (in this case we can discuss about Bronsted – Lowry acid and bases) and the presence of adsorbed water is a *sine qua non* condition for dissolving and diffusing the analyte into the interfacial region.<sup>65</sup>

## 8. Conclusions

The paper introduces the Hard-Soft Acid Base (HSAB) theory as a valuable tool for the selection of MOX – based sensing layers for ammonia and aliphatic amines detection. Six case studies of ammonia detection by means of chemiresistive sensors employing MOXs – based sensing layers were discussed in the view of this concept. To further support the suitability of the HSAB concept in selecting sensing layers, an example of a fiber-optic ammonia sensor using MOX and their nanocomposites as sensing layer was found to also fit HSAB interpretation. Within the same HSAB framework, we demonstrate that the same MOXs (hard acids) employed as sensing layer for NH<sub>3</sub> detection, can be used for trimethylamine detection, given that both NH<sub>3</sub> and trimethylamine are hard bases. By changing the sensing paradigm, the paper shows that, by applying the HSAB principle, amino groups-based molecules (formally derivatives of ammonia, thus, hard bases), such as polymers, carbon nanotubes and ionic liquids, are appropriate sensing layers for CO<sub>2</sub> (hard acid) detection.

Obviously, the NH<sub>3</sub> – MOX interaction is not the only factor influencing the overall performance of the sensor. Aspects such as morphology and thickness of the sensing layer, deposition method, presence of promoters, temperature, humidity, do influence the sensing process. At the same time, more refined calculus in terms of electronegativity, HOMO and LUMO energy levels and local hardness are necessary for better understanding key sensing properties of MOXs and their nanocomposites towards NH<sub>3</sub> and related molecules.

## 9. References

1. Good for Gas Instrumentation, <https://goodforgas.com/> (accessed: June 11, 2018).
2. National Research Council, Acute exposure guideline levels for selected airborne chemicals, The National Academies Press, USA, **2010**.
3. R. E. De la Hoz, D. P. Schuetter, W. N. Rom, *Am. J. Ind. Med.*, **1996**, 29(2), 209–214.  
DOI:10.1002/(SICI)1097-0274(199602)29:2<209: AID-AJIM12>3.0.CO;2-7
4. R. A. Michaels, *Environ. Health Perspect.*, **1999**, 107 (8), 617–627. DOI:10.1289/ehp.99107617
5. L. Pauling, General chemistry, Courier Corporation, North Chelmsford, USA, **1988**.
6. R. Chang, J. Overby, General chemistry: the essential concepts, Mc Graw Hill, New York, USA, **2000**.
7. B. Timmer, W. Olthuis, A. Van Den Berg, *Sens. Actuators B*, **2005**, 107(2), 666–677. DOI:10.1016/j.snb.2004.11.054
8. R. Blair, H. Sheperd, T. Faltens, P. C. Haussmann, R. B. Kaner, S. H. Tolbert, B. H. Weiller, *J. Chem. Educ.*, **2008**, 85(8), 1102–1104. DOI:10.1016/j.snb.2004.11.054
9. F. Winqvist, A. Spetz, I. Lundstrom, *Anal. Chim. Acta*, **1984**, 164, 127–138. DOI:10.1016/S0003-2670(00)85624-X
10. A. Elamari, N. Gisin, J. L. Munoz, S. Poitry, M. Tsacopoulos, H. Zbinden, *Sens. Actuators B*, **1997**, 38/39, 183–188.  
DOI:10.1016/S0925-4005(97)80190-6
11. G. H. Mount, B. Rumberg, J. Havig, B. Lamb, H. Westberg, D. Yonge, K. Johnson, R. Kincaid, *Atmos. Environ.*, **2002**, 36 (11), 1799–1810. DOI:10.1016/S1352-2310(02)00158-9
12. S. Jain, A. Patrike, S. S. Badadhe, M. Bhardwaj, S. Ogale, *ACS Omega*, **2018**, 3(2), 1977–1982.
13. C. N. Xu, N. Miura, Y. Ishida, K. Matuda, N. Yamazoe, *Sens. Actuators B*, **2000**, 65, 163–165.  
DOI:10.1016/S0925-4005(99)00413-X
14. D. Williams, *Sens. Actuators B*, **1999**, 57, 1–16.  
DOI:10.1016/S0925-4005(99)00133-1
15. S. R. Morrison, *Sens. Actuators B*, **1987**, 11, 283–287.  
DOI:10.1016/0250-6874(87)80007-0
16. S. M. Kanan, O. M. El-Kadri, I. A. Abu-Yousef, M. C. Kanan, *Sensors*, **2009**, 9(10), 8158–8196. DOI:10.3390/s91008158
17. X. Wang, H. Quin, Y. Chen, J. Hu, *J. Phys. Chem. C*, **2014**, 118, 28548–28561. DOI:10.1021/jp501880r
18. X. Liu, N. Chen, B. Han, X. Xiao, G. Chen, I. Djerdj, Y. Wang, *Nanoscale*, **2015**, 7(36), 14872–14880.  
DOI:10.1039/C5NR03585F
19. R. G. Pearson, *J. Am. Chem. Soc.*, **1963**, 85, 3533–3539.  
DOI:10.1021/ja00905a001
20. R. M. Lopachin, T. Gavin, A. Decaprio, D. S. Barber, *Chem. Res. Toxicol.*, **2012**, 25, 239–251. DOI:10.1021/tx2003257
21. B. C. Serban, M. N. Mihaila, V. G. Dumitru, C. Bostan, S. D. Costea, Quantum dot solar cell, US Patent Number 8,299,355 B2, date of patent October 30, **2012**.
22. B. C. Serban, M. N. Mihaila, V. G. Dumitru, C. Bostan, S. D. Costea, M. Bercu, Quantum dot solar cell, US Patent Number 8,148,632 B2, date of patent April 3, **2012**.
23. F. R. Ramos-Morales, S. Durand-Niconoff, J. Correa-Basurto, F. J. Meléndez-Bustamante, J. S. Cruz-Sánchez, *J. Mex. Chem. Soc.*, **2008**, 52(4), 241–248.
24. B. C. Serban, A. K. Sarin-Kumar, S. Costea, M. Mihaila, O. Buiu, M. Brezeanu, N. Varachiu, C. Cobianu, *Romanian Journal of Inf. Sci. & Tech.*, **2009**, 12(3), 376–384.
25. B. C. Serban, M. Mihaila, C. Cobianu, V. G. Dumitru, O. Buiu, Carbon dioxide sensor, US Patent Number 8,826,724 B2, date of patent September 9, **2014**.
26. B. C. Serban, C. Cobianu, M. N. Mihaila, V.-G. Dumitru, US Patent Number 8,230,720 B2, date of patent July 31, **2012**.
27. B. C. Serban, O. Buiu, M. Brezeanu, O. Ionescu, C. Cobianu, *Romanian Journal of Inf. Sci. & Tech.*, **2018**, 21(1), 93–96.
28. J. Nai, S. Wang, Y. Bai, L. Guo, *Small*, **2013**, 9(18), 3147–3152.  
DOI:10.1002/smll.201203076
29. B. C. Serban, C. Cobianu, M. Mihaila, V.-G. Dumitru, O. Buiu, US Patent Number 8,563,319 B2, date of patent October 22, **2013**.
30. F. H. Walters, *J. Chem. Educ.*, **1991**, 68 (1), 29–31.  
DOI:10.1021/ed068p29
31. A. Alfarrá, E. Frackowiak, F. Beguin, *Appl. Surf. Sci.*, **2004**, 228 (1–4), 84–92. DOI:10.1016/j.apsusc.2003.12.033
32. R. G. Pearson, *Inorg. Chem.*, **1988**, 27(4), 734–740.  
DOI:10.1021/ic00277a030
33. R. G. Pearson, *Inorg. Chim. Acta*, **1995**, 240(1–2), 93–98.  
DOI:10.1016/0020-1693(95)04648-8
34. J. L. Gole, S. Ozdemir, *ChemPhysChem*, **2010**, 11(12), 2573–2581. DOI:10.1002/cphc.201000245
35. J. L. Gole, Gas sensors, methods of preparation thereof, methods of selecting gas sensor materials, and methods of use of gas sensors, U.S. Patent Number 8,573,030 B2, date of patent November 5, **2013**.
36. W. I. Laminack, J. L. Gole, *Nanomaterials*, **2013**, 3(3), 469–485. DOI:10.3390/nano3030469
37. B. Karuganaran, P. Uthirakumar, S. J. Chung, S. Velumani, E. K. Suh, *Mater. Charact.*, **2007**, 58(8–9), 680–684.  
DOI:10.1016/j.matchar.2006.11.007
38. C. Li, D. Zhang, B. Lei, S. Han, X. Liu, C. Zhou, *J. Phys. Chem. B*, **2003**, 107(45), 12451–12455. DOI:10.1021/jp0361531
39. S. B. Deshmukh, R. H. Bari, *Intl. Lett. Chem., Phys. Astron.*, **2015**, 56, 144–154.
40. R. Pandeewari, B. G. Jeyaprakash, *Sens. Actuators B*, **2014**, 195, 206–214. DOI:10.1016/j.snb.2014.01.025
41. M. Abaker, A. Umar, S. Baskoutas, G. N. Dar, S. Zaidi, A. Al-Sayari, S. H. Kim, S. W. Hwang, *J. of Phys. D: Appl. Phys.*, **2011**, 44(42), 425401–425404.  
DOI:10.1088/0022-3727/44/42/425401
42. C. S. Rout, M. Hegde, A. Govindaraj, C. N. R. Rao, *Nanotechnology*, **2007**, 18(20), 205504–205508.  
DOI:10.1088/0957-4484/18/20/205504
43. A. Teeramongkonrasmee, M. Sriyudthsak, *Sens. Actuators B*, **2000**, 66(1–3), 256–259.  
DOI:10.1016/S0925-4005(00)00346-4
44. L. Wang, Z. Lou, R. Zhang, T. Zhou, J. Deng, T. Zhang, *ACS Appl. Mat. Interfaces*, **2016**, 8(10), 6539–6545.  
DOI:10.1021/acsami.6b00305

45. D. R. Patil, L. A. Patil, P. P. Patil, *Sens. Actuators B*, **2007**, *126*(2), 368–374. DOI:10.1016/j.snb.2007.03.028
46. S. H. Park, J. Y. Ryu, H. H. Choi, T. H. Kwon, *Sens. Actuators B*, **1998**, *46*(2), 75–79. DOI:10.1016/S0925-4005(97)00324-9
47. N. Va Hieu, L. T. B. Thuy, N. D. Chien, *Sens. Actuators B*, **2008**, *129*(2), 888–895. DOI:10.1016/j.snb.2007.09.088
48. M. O. Ansari, F. Mohammad, *Sens. Actuators B*, **2011**, *157*(1), 122–129. DOI:10.1016/j.snb.2011.03.036
49. X. Li, N. Chen, S. Lin, J. Wang, J. Zhang, *Sens. Actuators B*, **2015**, *209*, 729–734. DOI:10.1016/j.snb.2014.12.031
50. G. Falony, S. Vieira-Silva, J. Raes, *Annu. Rev. Microbiol.*, **2015**, *69*, 305–321. DOI:10.1146/annurev-micro-091014-104422
51. Z. Lou, F. Li, J. Deng, L. Wang, T. Zhang, *ACS Appl. Mater. Interfaces*, **2013**, *5*(23), 12310–12316. DOI:10.1021/am402532v
52. Y. Takao, Y. Iwanaga, Y. Shimizu, M. Egashira, *Sens. Actuators B*, **1993**, *10*(3), 229–234. DOI:10.1016/0925-4005(93)87011-D
53. P. M. Perillo, D. F. Rodriguez, *J. Alloys and Compd.*, **2016**, *657*, 765–769. DOI:10.1016/j.jallcom.2015.10.167
54. C. S. Lee, I. D. Kim, J. H. Lee, *Sens. Actuators B*, **2013**, *181*, 463–470. DOI:10.1016/j.snb.2013.02.008
55. H. S. Woo, C. W. Na, I. D. Kim, J. H. Lee, *Nanotechnology*, **2012**, *23*(24), 245501–245504. DOI:10.1088/0957-4484/23/24/245501
56. J. S. Kumar, B. Ranghanatawwn, D. Sastikumar, in: *AIP Conference Proceedings Vol. 1832 (1)*, **2017**, 050119.
57. A. Pathak, S. K. Mishra, B. D. Gupta, *Appl. Opt.*, **2015**, *54*(29), 8712–8721. DOI:10.1364/AO.54.008712
58. B. Renganathan, G. Gobi, D. Sastikumar, R. Srinivasan, A. C. Bose, *Sens. Lett.*, **2010**, *8*(2), 292–296. DOI:10.1166/sl.2010.1266
59. B. C. Serban, M. Brezeanu, C. Cobianu, S. Costea, O. Buiu, A. Stratulat, N. Varachiu, Materials selection for gas sensing. An HSAB perspective, in: *Proc. IEE International Semiconductor Conference (CAS)*, **2014**, pp. 21–30.
60. V. Avramescu, C. Bostan, B. C. Serban, I. Georgescu, S. Costea, N. Varachiu, C. Cobianu, in: *Proc. IEEE International Semiconductor Conference (CAS)*, **2009**, 27–36.
61. B. C. Serban, A.K. Sarin Kumar, M. Brezeanu, C. Cobianu, O. Buiu, C. Bostan, N. Varachiu, S. Costea, in: *Proc. IEEE International Semiconductor Conference (CAS)*, **2011**, 127–130.
62. B. C. Serban, A. K. Sarin Kumar, M. Brezeanu, C. Cobianu, O. Buiu, C. Bostan, N. Varachiu, S. Costea, *Romanian Journal of Inf. Sci. & Tech*, **2011**, *14*(3), 222–231.
63. B. C. Serban, C. Cobianu, M. Bercu, N. Varachiu, M. N. Mihaila, C. G. Bostan, S. I. Voicu, Matrix nanocomposite containing amino carbon nanotubes for carbon dioxide sensor detection, US Patent Number 7,913,541 B2, date of patent March 31, **2011**.
64. B. C. Serban, C. Cobianu, M.N. Mihaila, V.-G. Dumitru, Functionalized monolayers for carbon dioxide detection by a resonant nanosensor, US Patent Number 8,230,720 B2, date of patent July 31, **2012**.
65. L. Yanxiao, Z. Xiao-Bo, H. Xiao-Wei, S. Ji-Yong, Z. Jie-Wen, M. Holmes, L. Hao. *Biosens. Bioelectron.*, **2015**, *67*, 35–41. DOI:10.1016/j.bios.2014.05.040

## Povzetek

V prispevku je prikazano, kako lahko uporabimo teorijo trdih in mehkih kislin in baz (Hard-Soft Acid base (HSAB)) kot koristen kriterij pri izbiri polprevodnih kovinskih oksidov, primernih za pripravo senzorskih plasti za detekcijo amonijaka. Preučili smo šest različnih primerov detekcije amonijaka, pri katerih uporabljajo senzorje na osnovi kovinskih oksidov in sorodnih nanokompozitov. Vlogo teorije HSAB, kot učinkovitega izbirnega orodja za ustrezno senzorsko plast, primerno za kakršnokoli vrsto plina, smo dodatno raziskali z analizo literarnih podatkov trimetilaminskih senzorskih plasti na osnovi kovinskih oksidov. Z analizo delovanja senzorja iz optičnih vlaken za detekcijo amonijaka dokazujemo, da se lahko HSAB princip uspešno uporabi tudi pri izbiri senzorskih plasti za detektorje, ki uporabljajo druge načine zaznavanja. Če spremenimo paradigmo in spojine na osnovi amino skupin postanejo del senzorskega sloja in ne analizirane spojine, lahko te vrste materialov (polimeri, ogljikove nanocevke, ionske tekočine) uporabimo v senzorskih plasteh za zaznavanje CO<sub>2</sub>, kar je v celoti v skladu z merili HSAB.

Erratum for

# “A Nano-Sepiolite Clay Electrochemical Sensor for the Rapid Electro–Catalytic Detection of Hydroquinone in Cosmetic Products”

Sevda Aydar,<sup>1</sup> Dilek Eskiköy Bayraktepe<sup>2</sup> and Zehra Yazan<sup>2,\*</sup>

<sup>1</sup> Faculty of Engineering, Department of Chemistry, Istanbul University, 34320 Avcılar, Istanbul, Turkey

<sup>2</sup> Ankara University, Faculty of Science, Chemistry Department, 06560 Ankara, Turkey

\* Corresponding author: E-mail: zehrayazan67@gmail.com

Phone: +903122126720/1284 fax: +903122232395

Acta Chim Slov. 2018 Sep; 65(3): 946–954. ID 4615.

DOI: 10.17344/acsi.2018.4615

With this Erratum, we would like to change the authors of this paper as:

**Sevda Aydar,<sup>1</sup> Dilek Eskiköy Bayraktepe,<sup>2</sup> Hayati Filik<sup>1</sup> and Zehra Yazan<sup>2,\*</sup>**

<sup>1</sup> Faculty of Engineering, Department of Chemistry, Istanbul University, 34320 Avcılar, Istanbul, Turkey

<sup>2</sup> Ankara University, Faculty of Science, Chemistry Department, 06560 Ankara, Turkey

\* Corresponding Author: Email: zehrayazan67@gmail.com

Phone: +903122126720/1284 fax: +903122232395

Acta Chimica Slovenica Vol. 65 (2018)

## AUTHOR INDEX

Abbasi Zohreh .....	278	Benvidi Ali .....	278
Abdul Raman Abdul Aziz .....	166	Beyzaei Hamid .....	757
Abdullah Nor Ain Fathihah .....	231	Bhandari S. Mayuri .....	492
Abrishamifar Seyyed Milad .....	208	Bhimapaka China Raju .....	34
Abu Shawish Hazem M. ....	811	Blagojević Dragana .....	380
Afifa Mushtaq .....	989	Blazhev Gavazov Kiril .....	847
Akçay Sevilay .....	932	Böhm Stanislav .....	475
Akel, Soukaina .....	470	Bougarrani, Salma .....	470
Akmese Bediha .....	539	Bouziani, Asmae .....	470
Aksoy Erkan .....	512	Bozdoğan Abdürrezzak Emin .....	65
Alakbarzade Ganira Ilgar. ....	365	Bozhinova Kristina .....	213
Alcheikh wis Abdulmounem .....	646	Brezeanu Mihai .....	1014
Al-Hazzaa Mansour I. ....	221	Buiu Octavian .....	1014
Ali Sqib .....	131	Bumbac Marius .....	1014
Alijani Hassan .....	652	Buzuk Marijo .....	698
Amani Ali Mohammad .....	882	Canbaz Topal Gamze .....	586
Amani Mohammad Al .....	750	Carlos Zeppone Iracilda .....	547
Amiraslanov Imameddin		Carr Paul D. ....	372
Rajabali .....	365	Castro Alves de Lima e Sixelizio ...	739
Anderson Paul A. ....	989	Chang Yoon-Young .....	599
Ang Lee Sin .....	231	Charlyn Greiler Lena .....	865
Antypenko Lyudmyla .....	836	Chen Wen-Tong .....	1008
Arjmand Omid .....	882	Chen Yinran .....	271
Arjmandi Ali .....	50	Cherupally Dayakar .....	34
Aryan Reza .....	757	Chin Fun Suk .....	578
Asan Adem .....	539	Choi Jong-Soo .....	599
Asif Mohammad .....	221	Ciuffreda Pierangela .....	801
Assarian Arezoo . ....	569	Cobianu Cornel .....	1014
Ates Aytan .....	586	Crivellari Michele .....	980
Aydar Sevda .....	946	Cvitanović Tomaš Tanja .....	253
Aygün Muhittin .....	86	Čontala Alja .....	630
Babanly Mahammad Baba .....	365	D. Marković Bojan .....	59
Babapoor Aziz .....	882	Danaee Iman .....	312
Babiak Michal .....	955	Dardeer Hemat M. ....	787
Bagolini Alvise .....	980	Dave Hareh K .....	902
Bahrami Panah Niloufar .....	312	De Abreu Ribeiro Carolina Livia ...	547
Baltabayev Murat Ergalievich .....	127	De Godoy-Netto Viera Adelino .....	547
Banaei Maryam .....	278	De Souza Alves Rodrigo .....	547
Bangal Mukund N. ....	239	Debeljak Nataša .....	842
Baranipour Parviz .....	757	Dehghan Gholamreza .....	670
Barut Celepci Duygu .....	86	Dehghan Tezerjani Marzie .....	278
Baseia Basilio .....	739	Delarami Samareh Hojat .....	757
Bayraktepe Dilek Eskiköy .....	946	Delchev Borissov Vassil .....	521
Bayrami Abolfazl .....	166	Delchev Vassil B .....	462
Baytar Orhan .....	407	Denac Matjaž .....	344
Bazel' Yaroslav .....	388	Deng Yuan .....	271

Deshmukh Dattatray G. ....	239	Hazm Eddine Jamal .....	730
Divarova Vidka .....	213	Heena Khajuria .....	319
Dodevska Totka .....	970	Hegab Mohamed I. ....	401
Draganescu Dan .....	97	Heidari Negar .....	208
Dragomir Mirela .....	679	Hosten C. Eric .....	531
Dumitras Mihai .....	97	Houssat Mourad .....	730
Dündar Yasemin .....	932	Ibrahim Ahmed A. ....	221
El Azzouzi, Laila .....	470	Iftikhar Mehwish .....	611
El Azzouzi, Mohammed .....	470	Ignat Maria .....	97
El Telbani Emad M .....	401	Imamaliyeva Samira Zakir .....	365
Elçi Gökhan Şükrü .....	512	Imamović Mugdin .....	380
Elçi Latif .....	512	İnan Benan .....	160
Elif Heybet Hakli .....	266	Iqbal Jamshed .....	108
El-Sayed Elsherbiny Hamdy .....	853	Iqbal Muhammad .....	131
El-Shehry Mohamed F .....	401	Ivanović Evica .....	483
Ertürk Ali Serol .....	65	J. Sabo Tibor .....	59
Esmacili Hossein .....	750	Jadhav R. Namdeo. ....	492
Esmacili Hossein .....	882	Jagličić Zvonko .....	191
Esmaielzadeh Sheida .....	416	Jahanbani Shahriar .....	278
Fadda Ahmed Ali .....	787	Jahandideh Sara .....	882
Fadda Ahmed Ali .....	853	Jahangir Muhammad Taj .....	718
Fang Zhijie .....	611	Jamnik Polona .....	172
Farhadi Saeed .....	448	Jaramillo Andres F .....	429
Farhadi Saeed .....	919	Jasiewicz Beata .....	795
Farooq Muhammad .....	823	Jevrić Lidija. ....	483
Fateh Hamed .....	882	Jia-Bao Liu .....	296
Fateh Mohammad Ali .....	882	Jigmet Ladol .....	319
Fazli Yousef .....	652	K. Perera B. Gayani .....	150
Fazli Yousef .....	998	K. Tubić Biljana .....	59
Fecková Barbora .....	842	Kancheva Bogomilova Pavlina .....	521
Ferreira Luiz de Almeida Jorge .....	739	Kannan Arunachalam .....	621
Filik Hayati .....	946	Kanthecha Darshana N .....	333
Franchi Spinardi José Silmar .....	547	Karadžić Milica .....	483
Garbe Leif-Alexander .....	836	Kargar Hadi .....	50
Gašperšič Jernej. ....	769	Karimi Pouya .....	757
Gavaric Aleksandra .....	438	Kartal Temel Nuket .....	138
Gavazov Kiril B. ....	462	Kastelic Miha .....	769
Ghasemzadeh Mohammad Ali .....	199	Kaynak Onurdağ Fatma .....	932
Gokmen Ozay Ozgür .....	266	Kello Martin .....	875
Golobič Iztok .....	980	Keresztesi Ágnes .....	709
Gtari Wiem Felah .....	289	Kešelj Dragana .....	380
Gugała-Fekner Dorota .....	119	Khalifa Mohamed Ezzat .....	1
Gürbüz Mustafa Ulv .....	65	Khan Nazia .....	108
Gürkan Ramazan .....	138	Khezri Khezrollah .....	652
Haase Hajo .....	865	Khezri Khezrollah .....	998
Hachani Eddine Salah .....	646	Khuhawar Yar Muhammad. ....	718
Hachani Salah Eddine .....	183	Kimáková Patrícia .....	842
Halim A. Peter .....	554	Koduru Reddy Janardhan .....	599
Hamuláková Slávka .....	875	Kok Ying Kuan. ....	578
Hanif Nazlı İbrahim .....	86	Kolarević Ana .....	801
Haq Nawaz Sheikh .....	319	Kollhammerova Iva .....	955
Harrach Ahmed .....	730	Kommera, Rajkumar .....	34
Hasan Nasrollahi Seyed Mostafa ....	199	Kourosh Behradfar .....	296
Hashemi Alireza Seyyed .....	750	Kovačević Strahinja .....	483
Hashemi Alireza .....	882	Krishna K. Hari .....	621
Hassani Ameziane Chakib .....	730	Kuang Han-Mao .....	1008



Kuate Kaptso Giscard .....	823	Mousavi Mojtaba Seyyed .....	750
Kucera Josef .....	955	Mousumi Das .....	354
Kumar Suresh Muthuvel .....	621	Mraz Miha .....	253
Kupcová Elena .....	388	Muhammad Iqbal .....	989
Kvíčalová Magdalena .....	475	Murthy Thampunuri Ramalinga .....	34
Kwaw Emmanuel .....	823	Musil Vojko .....	344
Lakouraj Moslem Mansour .....	75	Nagendra Govindappa .....	354
Lalithamba Haraluru Shankraiah .....	354	Najafi Meysam .....	208
Lariche Milad Janghorban .....	208	Najafi Meysam .....	303
Latrach, Lahbib .....	470	Namazian Mansoor .....	372
Lazarević Jelena S .....	801	Naseer Muhammad Moazzam .....	108
Lazarova Yanna .....	970	Nath Kaushik .....	902
Lazić Dragica .....	380	Nebbache Nadia .....	183
Lebar Andrej .....	980	Nebbache Nadia .....	646
Lekova Vanya .....	213	Necas Marek .....	955
Leskovac Mirela .....	344	Necira Zelikha .....	183
Liang Min .....	964	Necira Zelikha .....	646
Likožar Blaž .....	769	Nicolescu Cristina Mihaela .....	1014
Lin Wei-Sheng .....	1008	Nilgün Yücel Candan .....	266
Lingamdinne Prasanna		Nirumand Ladan .....	919
Lakshmi .....	988	Novak Uroš .....	769
Lukeš Vladimír .....	23	Ochiuz Lacramioara .....	97
Luo Hui .....	1008	Odame Felix .....	328
Ma Shengmei .....	823	Odame Felix .....	531
Ma Yongkun .....	823	Osae Richard .....	823
Maček Kržmanc Marjeta .....	630	Osório A. P. Francisco .....	739
Madahi Afrooz .....	312	Ostojić Gordana .....	380
Mahltig Boris .....	865	Özçimen Didem .....	160
Mahmudova Matanat Aydin .....	365	Özkan İnci .....	586
Makrlík Emanuel .....	475	Ozkoc Guralp .....	646
Maldar Rahimeh .....	75	Patekar Mukunda R .....	239
Malhotra Shveta .....	687	Patel Mohan N. .....	333
Manesh Kumar .....	319	Patil S. Udaykumar .....	492
Manzar Sohail .....	989	Pavlic Branimir .....	438
Martinez Sanja .....	569	Payehghadr Mahmood .....	312
Mathad Vijayavithal		Peng Dong-Lai .....	895
Thippannachar .....	239	Pervez Humayun .....	108
Mauro Eduardo Antonio .....	547	Pinkas Jiri .....	955
Mazouzi Djamel Eddine .....	183	Podunavac-Kuzmanović Sanja .....	483
Medhane Vijay J. ....	239	Poklar Ulrih Nataša .....	172
Meghezzi Ahmed .....	646	Poleti Dejan .....	191
Meléndrez Manuel F. ....	429	Poliak Peter .....	23
Meyer Fatuma .....	836	Pospieszny Tomasz .....	795
Meysam Najafi .....	296	Proskurina Yu. Elena .....	662
Michalík Martin .....	23	Pustak Anđela .....	344
Milad Janghorban Lariche .....	296	Qureshi Farah .....	718
Milcheva Nikolina P. ....	847	Racheva Petya .....	213
Mirossay Ladislav .....	875	Radosavljevic Robert .....	438
Mohamed Khaled Samir .....	787	Radovanović Lidija .....	191
Mohareb M. Rafat .....	554	Raghavendra Mahadevaiah .....	354
Mojoudi Fatemeh .....	750	Rahim Pouran Shima .....	166
Mojoudi Fatemeh .....	882	Rajinder Singh .....	319
Mojtaba Mousavi .....	882	Ramic Milica .....	438
Molahosseini Hossein .....	278	Rápó Eszter .....	709
Moškon Miha .....	253	Raval Dilip B. ....	333
Moulana Zahra .....	75	Rayala Nageswara Rao .....	34

Razavi Razieh .....	208	Sýkora David .....	475
Razavi Razieh .....	303	Szentpéteriová Erika .....	842
Reiffová Katarína .....	388	Szép Robert .....	709
Rocha Vieira Fillipe .....	547	Škugor Rončević Ivana .....	698
Rodić Dušica D. ....	394	Šmelcerović Andrija .....	801
Rodić V. Marko .....	191	Šmit Ivan .....	344
Rodríguez Carlos A. ....	429	Švab Iztok .....	344
Rogan Jelena .....	191	Taborsky Petr .....	955
Rojas David. ....	429	Taherkhani Milad .....	303
Rončević Tamara N. ....	394	Tahir Muhammad Nawaz .....	131
Rong-Jun Bie .....	303	Tamous Hassan .....	811
Rozman Damjana .....	253	Tang Yijun .....	687
Ryskaliyeva Alma Kairlapovna .....	127	Tangour Bahoueddine .....	289
S. Vladimirov Sandra .....	59	Tashakkorian Hamed .....	75
Saadeh M. Salman .....	638	Tawfik Eman H. ....	787
Saadeh Salman M. ....	811	Tbaza Ahmad .....	811
Sacarescu Liviu .....	97	Tchabo William .....	823
Sadykova Zhanar .....	836	Thakkar Vasudev R. ....	333
Sanchooli Mahmood .....	757	Toncheva Galya K. ....	462
Santaniello Enzo .....	801	Toncheva Galya K. ....	847
Saqib Ali .....	989	Tonk Szende .....	709
Saravanan Dhandayutham .....	621	Topkaya Derya .....	86
Sarhandi Shahriar .....	246	Tülü Metin .....	65
Segedinac Mirjana D. ....	394	Ülger Mahmut .....	932
Semenov N. Victor .....	662	Uma Kogali .....	354
Semenova V. Galina .....	662	Vafazadeh Rasoul .....	372
Serban Bogdan-Catalin .....	1014	Valant Matjaž .....	679
Şerbetçioğlu Sert Burcu .....	160	Valdés Héctor .....	429
Sever Škapin Andrijana .....	344	Valverde Clodoaldo. ....	739
Shafeeyan Mohammad Saleh .....	166	Vañura Petr .....	475
Shaghghi Zohreh .....	670	Varshney K. Pradeep .....	687
Shahpoori-Arani Behnoosh .....	372	Vasile Aurelia .....	97
Shamhari Mohammad		Vaz Rodrigues Gabriela .....	739
Nuraqeelah .....	578	Velusamy Marappan .....	621
Shasi V. Kalivendi .....	34	Vessaly Esmaei .....	246
Shterev Ivan .....	970	Vidovic Senka .....	438
Siddiqui Muhammad Kamran .....	303	Vladic Jelena .....	438
Sierakowska Arleta .....	795	Vladislavić Nives .....	698
Singh Jiwan .....	599	Vojnović Matilda .....	483
Sitar Anže .....	980	Wafo Cheno Rosine .....	823
Siva Kumar Nadavala .....	221	Wairkar M. Sarika .....	492
Siyal N. Ali .....	512	Wan Daud Wan Mohd Ashri .....	166
Skrt Mihaela .....	172	Wee Siong Boon .....	578
Sohtun P. Winaki .....	621	Wijesirigunawardana B. Piyumi .....	150
Solár Peter .....	842	Willis Anthony C. ....	372
Solár Peter .....	875	Wu Meng .....	823
Solárová Zuzana .....	875	Xu Guiyun .....	502
Steffens Karl .....	836	Xuewu Zuo .....	296
Stojanović Gordana .....	801	Yakalı Gül .....	86
Stojnova Kirila .....	213	Yang Jae-Kyu .....	599
Stoleriu Iulian .....	97	Yaqub Muhammad .....	108
Suciu Maria .....	709	Yasseen J. Zeyad .....	638
Sun Nan .....	895	Yatish Kalanakoppal Venkatesh .....	354
Sun Nan .....	964	Yazan Zehra .....	946
Sushkova P. Tatiana .....	662	Yu Xijuan .....	502
Suvorov Danilo .....	630	Zabardasti Abedin .....	919

---

Zaib Sumera .....	108	Zhelev Zlatimir T .....	462
Zaltariov Mirela Fernanda .....	97	Zhou Xiaodong .....	271
Zare Fekri Leila .....	246	Zhu Xue-Wen .....	939
Zare Hamid Reza .....	278	Zhubatova Aigul	
Zare-Mehrjardi Hamid Reza .....	50	Moldakhmetovna .....	127
Zarenezhad Elham .....	416	Zolfaghari Mohammad Reza .....	199
Zarringhadam Parisa .....	448	Zou Dong-Hui .....	964
Zhang Mingming .....	502		



**DRUŠTVENE VESTI IN DRUGE AKTIVNOSTI**  
**SOCIETY NEWS, ANNOUNCEMENTS, ACTIVITIES**

**Vsebina**

Koledar važnejših znanstvenih srečanj s področja kemije, kemijske tehnologije in kemijskega inženirstva .....	S93
Navodila za avtorje .....	S98

**Contents**

Scientific meetings – chemistry, chemical technology and chemical engineering .....	S93
Instructions for authors .....	S98



**KOLENDAR VAŽNEJŠIH ZNANSTVENIH SREČANJ  
S PODROČJA KEMIJE IN KEMIJSKE TEHNOLOGIJE****SCIENTIFIC MEETINGS –  
CHEMISTRY AND CHEMICAL ENGINEERING****2019****January 2019**

---

- 18 – 20                    2<sup>ND</sup> INTERNATIONAL JOINT CONFERENCE ON MATERIALS SCIENCE AND  
MECHANICAL ENGINEERING (CMSME 2019)  
Phuket, Thailand  
Information:            <http://www.cmsme.net/>
- 29                        IYPT2019 OPENING CEREMONY  
Paris, France  
Information:            <http://www.iypt2019.org/>
- 29                        IYPT2019 OPENING CEREMONY  
Paris, France  
Information:            <http://www.iypt2019.org/>

**February 2019**

---

- 12                        EMPOWERING WOMEN IN CHEMISTRY: A GLOBAL NETWORKING EVENT  
Online  
Information:            <https://iupac.org/100/global-breakfast/>
- 18 – 19                    GLOBAL SUMMIT ON CHEMISTRY AND CHEMICAL ENGINEERING  
Frankfurt, Germany  
Information:            <https://scientificfederation.com/gscce-2019/>
- 21 – 22                    28<sup>TH</sup> INDUSTRIAL INORGANIC CHEMISTRY - MATERIALS AND PROCESSES  
Frankfurt am Main, Germany  
Information:            [https://dechema.de/dechema\\_eV/en/28\\_atc-p-20096142.html](https://dechema.de/dechema_eV/en/28_atc-p-20096142.html)
- 21 – 24                    3<sup>RD</sup> INTERNATIONAL CONFERENCE ON ENGINEERING PHYSICS AND  
OPTOELECTRONIC ENGINEERING (ICEPOE 2019)  
Kuala Lumpur, Malaysia  
Information:            <http://www.icepoe.org/>

**March 2019**

---

- 10 – 13                    NASCRE 4 – 4<sup>TH</sup> INTERNATIONAL SYMPOSIUM ON CHEMICAL REACTION  
ENGINEERING  
Houston, Texas  
Information:            <http://iscre.org/nascre4/>
- 11 – 13                    2<sup>ND</sup> INTERNATIONAL CONFERENCE ON MATERIALS SCIENCE AND ENGINEERING  
(ICMSE-2)  
Giza /Cairo , Egypt  
Information:            <https://icmse-egypt2019.org/>

- 11 – 15 6<sup>TH</sup> INTERNATIONAL CONFERENCE ON MULTIFUNCTIONAL, HYBRID AND NANOMATERIALS  
Sitges, Spain  
Information: <https://www.elsevier.com/events/conferences/international-conference-on-multifunctional-hybrid-and-nanomaterials>
- 13 – 14 591<sup>ST</sup> INTERNATIONAL CONFERENCE ON CHEMICAL AND BIOCHEMICAL ENGINEERING (ICCBE)  
Brussels, Belgium  
Information: <http://theiier.org/Conference2019/Belgium/1/ICCBE/>
- 14 – 15 THE INTERNATIONAL CONFERENCE ON INNOVATIVE APPLIED ENERGY  
St Cross College, University of Oxford, United Kingdom  
Information: <http://iape-conference.org/>
- 24 – 28 1<sup>ST</sup> GHI WORLD CONGRESS ON FOOD SAFETY AND SECURITY (GHI2019)  
Leiden, The Netherlands  
Information: <https://ghiworldcongress.org/>
- 28 – 29 POLYMERS AND ORGANIC CHEMISTRY 2019 (ICPOC 2019)  
Paris, France  
Information: <https://waset.org/conference/2019/03/paris/ICPOC>
- 31 – Apr. 4 AIChE SPRING MEETING 2019 AND 15<sup>TH</sup> GLOBAL CONGRESS ON PROCESS SAFETY  
New Orleans, USA  
Information: <https://www.aiche.org/conferences/aiche-spring-meeting-and-global-congress-on-process-safety/2019>

---

**April 2019**

- 9 – 12 26<sup>TH</sup> CROATIAN MEETING OF CHEMISTS AND CHEMICAL ENGINEERS (26HSKIKI)  
Šibenik, Croatia  
Information: <http://www.26hskiki.org/en/>

---

**May 2019**

- 13 – 17 THE WORLD EVENT IN SUSTAINABLE CHEMISTRY RESEARCH & INNOVATION  
La Rochelle, France  
Information: <https://www.isgc-symposium.com/>
- 15 – 16 2<sup>ND</sup> EUROPEAN CHEMISTRY CONFERENCE  
Amsterdam, Netherlands  
Information: <https://europeanchemistry.madridge.com/>
- 19 – 24 14<sup>TH</sup> IUPAC INTERNATIONAL CONGRESS OF CROP PROTECTION CHEMISTRY  
Ghent, Belgium  
Information: <https://www.iupac2019.be>
- 22 – 24 PLANT BASED SUMMIT  
Cité De Congrès Lyon, France  
Information: <http://www.plantbasedsummit.com/>
- 25 – 31 ICOSSE 2019 : 41<sup>TH</sup> INTERNATIONAL CONFERENCE ON SOFTWARE ENGINEERING  
Montréal, QC, Canada  
Information: <https://2019.icse-conferences.org/home>

---

**June 2019**

- 2 – 6 14<sup>TH</sup> INTERNATIONAL SYMPOSIUM ON MACROCYCLIC AND SUPRAMOLECULAR CHEMISTRY  
Lecce, Italy  
Information: <https://ismsc2019.eu/>



- 11 – 13 23<sup>RD</sup> GREEN CHEMISTRY & ENGINEERING CONFERENCE AND 9<sup>TH</sup> INTERNATIONAL CONFERENCE ON GREEN AND SUSTAINABLE CHEMISTRY  
Reston, Virginia, United States  
Information: <http://www.gcande.org/>
- 16 – 19 9<sup>TH</sup> INTERNATIONAL COLLOIDS CONFERENCE  
Sitges, Spain  
Information: <https://www.elsevier.com/events/conferences/international-colloids-conference>
- 16 – 19 LOSS PREVENTION 2019  
Delft, The Netherlands  
Information: <http://lossprevention2019.org/>
- 16 – 19 29<sup>TH</sup> EUROPEAN SYMPOSIUM ON COMPUTER-AIDED PROCESS ENGINEERING  
Eindhoven, The Netherlands  
Information: <https://escape29.nl/>
- 16 – 20 17<sup>TH</sup> INTERNATIONAL CONFERENCE ON CHEMISTRY AND THE ENVIRONMENT – ICCE2019  
Thessaloniki, Greece  
Information: <http://www.euchems.eu/events/17th-international-conference-chemistry-environment-icce2019/>
- 16 – 20 12<sup>TH</sup> IWA INTERNATIONAL CONFERENCE ON WATER RECLAMATION AND REUSE  
Berlin, Germany  
Information: <http://efce.info/IWA+Conference+2019.html>
- 26 – 28 THERMODYNAMICS 2019  
Huelva, Spain  
Information: <http://efce.info/Thermodynamics+2019.html>
- 26 – 30 6<sup>TH</sup> EUROPEAN CONFERENCE ON ENVIRONMENTAL APPLICATIONS OF ADVANCED OXIDATION PROCESSES (EAAOP-6)  
Portorož, Slovenia  
Information: <http://eaaop6.ki.si/>
- 26 – 30 6<sup>TH</sup> EUROPEAN CONFERENCE ON ENVIRONMENTAL APPLICATIONS OF ADVANCED OXIDATION PROCESSES – EAAOP-6  
Ljubljana, Slovenia  
Information: <http://eaaop6.ki.si/>

---

**July 2019**

- 1 – 3 CONGRESS ON NUMERICAL METHODS IN ENGINEERING  
Guimarães, Portugal  
Information: [www.cmn2019.pt](http://www.cmn2019.pt)
- 3 – 6 8<sup>TH</sup> INTERNATIONAL CONFERENCE ON EXPERIMENTS / PROCESS / SYSTEM MODELING / SIMULATION / OPTIMIZATION  
Athens, Greece  
Information: <http://www.epsmso.gr/>
- 5 – 12 IUPAC 2019 PARIS FRANCE  
Paris, France  
Information: <https://www.iupac2019.org/>
- 10 – 11 10<sup>TH</sup> WORLD CONGRESS ON GREEN CHEMISTRY AND TECHNOLOGY  
Paris, France  
Information: <https://greenchemistry.chemistryconferences.org/>
- 21 – 26 THE 18<sup>TH</sup> INTERNATIONAL SYMPOSIUM ON NOVEL AROMATIC COMPOUNDS (ISNA-18)  
Sapporo City, Japan  
Information: <https://iupac.org/event/18th-international-symposium-novel-aromatic-compounds-isna-18/>

- 26 – 28 MENDELEEV 150: 4<sup>TH</sup> INTERNATIONAL CONFERENCE ON THE PERIODIC TABLE  
ENDORSED BY IUPAC  
Saint Petersburg, Russian Federation  
Information: <http://mendelev150.ifmo.ru/>
- 30 – Aug. 1 8<sup>TH</sup> INTERNATIONAL CONFERENCE FOR NETWORK FOR INTER-ASIAN CHEMISTRY  
EDUCATORS (NICE)  
Taipei, Taiwan  
Information: <https://iupac.org/event/8th-international-conference-network-inter-asian-chemistry-educators/>

---

**August 2019**

- 4 – 8 36<sup>TH</sup> INTERNATIONAL CONFERENCE OF SOLUTION CHEMISTRY  
Xining China  
Information: <http://icsc2019.csp.escience.cn/>
- 25 – 30 6<sup>TH</sup> INTERNATIONAL CONFERENCE ON THE CHEMISTRY AND PHYSICS OF THE  
TRANSACTINIDE ELEMENTS (TAN 19)  
Wilhelmshaven, Germany  
Information: <https://www-win.gsi.de/tan19/>

---

**September 2019**

- 1 – 5 EFMC-ASMC'19 – EFMC INTERNATIONAL SYMPOSIUM ON ADVANCES IN  
SYNTHETIC AND MEDICINAL CHEMISTRY  
Athens, Greece  
Information: <https://www.efmc-asmc.org/>
- 2 – 6 1<sup>ST</sup> INTERNATIONAL CONFERENCE ON NONCOVALENT INTERACTIONS (ICNI)  
Lisbon, Portugal  
Information: <http://icni2019.eventos.chemistry.pt/>
- 8 – 13 33<sup>ND</sup> CONFERENCE OF EUROPEAN COLLOID AND INTERFACE SOCIETY (ECIS)  
Leuven, Belgium  
Information: <https://kuleuvencongres.be/ecis2019/>
- 8 – 13 INTERNATIONAL SYMPOSIUM ON IONIC POLYMERIZATION – IP '19  
Beijing, China  
Information: <https://iupac.org/event/international-symposium-on-ionic-polymerization-ip-19/>
- 9 – 13 EUROPEAN CORROSION CONGRESS  
Seville, Spain  
Information: <https://eurocorr.org/EUROCRR+2019.html>
- 15 – 19 11<sup>TH</sup> EUROPEAN CONGRESS OF CHEMICAL ENGINEERING – ECCE11 &  
4<sup>TH</sup> EUROPEAN CONGRESS OF APPLIED BIOTECHNOLOGY – ECAB5  
Florence, Italy  
Information: [http://efce.info/ECCE12\\_ECAB5-p-112545.html](http://efce.info/ECCE12_ECAB5-p-112545.html)
- 25 – 27 SLOVENIAN CHEMICAL SOCIETY ANNUAL MEETING 2019  
Portorož, Slovenia  
Information: <http://chem-soc.si/slovenian-chemical-society-annual-meeting-2019>

**2020**

---

**July 2020**

- 5 – 9 48<sup>TH</sup> WORLD POLYMER CONGRESS – MACRO2020  
Jeju Island, Korea  
Information: <http://www.macro2020.org/>

August 2020

---

- 16 – 21                    12<sup>TH</sup> TRIENNIAL CONGRESS OF THE WORLD ASSOCIATION OF THEORETICAL AND COMPUTATIONAL CHEMISTS  
Vancouver, Canada  
Information:            <http://watoc2020.ca/>
- 30 – Sept. 3            ECC8 – 8<sup>TH</sup> EuChemS CHEMISTRY CONGRESS  
Lisbon, Portugal  
Information:            <http://www.euchems.eu/events/ecc8-8th-euchems-chemistry-congress/>

# Acta Chimica Slovenica

## Author Guidelines

### Submissions

Submission to ACSi is made with the implicit understanding that neither the manuscript nor the essence of its content has been published in whole or in part and that it is not being considered for publication elsewhere. All the listed authors should have agreed on the content and the corresponding (submitting) author is responsible for having ensured that this agreement has been reached. The acceptance of an article is based entirely on its scientific merit, as judged by peer review. There are no page charges for publishing articles in ACSi. The authors are asked to read the Author Guidelines carefully to gain an overview and assess if their manuscript is suitable for ACSi.

### Additional information

- Citing spectral and analytical data
- Depositing X-ray data

### Submission material

Typical submission consists of:

- full manuscript (PDF file, with title, authors, abstract, keywords, figures and tables embedded, and references)
- supplementary files
  - **Full manuscript** (original Word file)
  - **Statement of novelty** (Word file)
  - **List of suggested reviewers** (Word file)
  - **ZIP file containing graphics** (figures, illustrations, images, photographs)
  - **Graphical abstract** (single graphics file)
  - **Proposed cover picture** (optional, single graphics file)
  - **Appendices** (optional, Word files, graphics files)

Incomplete or not properly prepared submissions will be rejected.

### Submission process

Before submission, authors should go through the checklist at the bottom of the page and prepare for submission.

Submission process consists of 5 steps.

#### Step 1: Starting the submission

- Choose one of the journal sections.
- Confirm all the requirements of the **checklist**.
- Additional plain text comments for the editor can be provided in the relevant text field.

#### Step 2: Upload submission

- Upload full manuscript in the form of a Word file (with title, authors, abstract, keywords, figures and tables embedded, and references).

#### Step 3: Enter metadata

- First name, last name, contact email and affiliation for all authors, in relevant order, must be provided. Corresponding author has to be selected. Full postal address and phone number of the corresponding author has to be provided.

- **Title and abstract** must be provided in plain text.
- Keywords must be provided (max. 6, separated by semicolons).
- Data about contributors and supporting agencies may be entered.
- **References** in plain text must be provided in the relevant text field.

#### Step 4: Upload supplementary files

- Original Word file (original of the PDF uploaded in the step 2)
- **Statement of novelty** in a Word file must be uploaded
- All **graphics** have to be uploaded in a single ZIP file. Graphics should be named Figure 1.jpg, Figure 2.eps, etc.
- **Graphical abstract image** must be uploaded separately
- **Proposed cover picture** (optional) should be uploaded separately.
- Any additional **appendices** (optional) to the paper may be uploaded. Appendices may be published as a supplementary material to the paper, if accepted.
- For each uploaded file the author is asked for additional metadata which may be provided. Depending of the type of the file please provide the relevant title (Statement of novelty, List of suggested reviewers, Figures, Graphical abstract, Proposed cover picture, Appendix).

#### Step 5: Confirmation

- Final confirmation is required.

### Article Types

**Feature Articles** are contributions that are written on editor's invitation. They should be clear and concise summaries of the most recent activity of the author and his/her research group written with the broad scope of ACSi in mind. They are intended to be general overviews of the authors' subfield of research but should be written in a way that engages and informs scientists in other areas. They should contain the following (see also general directions for article structure in ACSi below): (1) an introduction that acquaints readers with the authors' research field and outlines the important questions to which answers are being sought; (2) interesting, new, and recent contributions of the author(s) to the field; and (3) a summary that presents possible future directions. Manuscripts normally should not exceed 40 pages of one column format (letter size 12, 33 lines per page). Generally, experts in a field who have made important contribution to a specific topic in recent years will be invited by an editor to contribute such an **Invited Feature Article**. Individuals may, however, send a proposal (one-page maximum) for an Invited Feature Article to the Editor-in-Chief for consideration.

**Scientific articles** should report significant and innovative achievements in chemistry and related sciences and should exhibit a high level of originality. They

should have the following structure:

1. Title (max. 150 characters),
2. Authors and affiliations,
3. Abstract (max. 1000 characters),
4. Keywords (max. 6),
5. Introduction,
6. Experimental,
7. Results and Discussion,
8. Conclusions,
9. Acknowledgements,
10. References.

The sections should be arranged in the sequence generally accepted for publications in the respective fields and should be successively numbered.

**Short communications** generally follow the same order of sections as Scientific articles, but should be short (max. 2500 words) and report a significant aspect of research work meriting separate publication. Editors may decide that a Scientific paper is categorized as a Short Communication if its length is short.

**Technical articles** report applications of an already described innovation. Typically, technical articles are not based on new experiments.

## Preparation of Submissions

**Text** of the submitted articles must be prepared with Microsoft Word. Normal style set to single column, 1.5 line spacing, and 12 pt Times New Roman font is recommended. Line numbering (continuous, for the whole document) must be enabled to simplify the reviewing process. For any other format, please consult the editor. Articles should be written in English. Correct spelling and grammar are the sole responsibility of the author(s). Papers should be written in a concise and succinct manner. The authors shall respect the ISO 80000 standard [1], and IUPAC Green Book [2] rules on the names and symbols of quantities and units. The Système International d'Unités (SI) must be used for all dimensional quantities.

**Graphics** (figures, graphs, illustrations, digital images, photographs) should be inserted in the text where appropriate. The captions should be self-explanatory. Lettering should be readable (suggested 8 point Arial font) with equal size in all figures. Use common programs such as MS Excel or similar to prepare figures (graphs) and ChemDraw to prepare structures in their final size. Width of graphs in the manuscript should be 8 cm. Only in special cases (in case of numerous data, visibility issues) graphs can be 17 cm wide. All graphs in the manuscript should be inserted in relevant places and **aligned left**. The same graphs should be provided separately as images of appropriate resolution (see below) and submitted together in a ZIP file (Graphics ZIP). Please do not submit figures as a Word file. In **graphs**, only the graph area determined by both axes should be in the frame, while a frame around the whole graph should be omitted. The graph area should be white. The legend should be inside the graph area. The style of all graphs should be the same. **Figures and illustrations** should be of sufficient quality for the printed version, i.e. 300 dpi minimum. **Digital images and photographs** should be of high quality (minimum 250 dpi resolution). On submission, figures should be of good enough resolution to be assessed by the referees, ideally as JPEGs. High-resolution figures (in JPEG,

TIFF, or EPS format) might be required if the paper is accepted for publication.

**Tables** should be prepared in the Word file of the paper as usual Word tables. The captions should appear above the table and should be self-explanatory.

**References** should be numbered and ordered sequentially as they appear in the text, likewise methods, tables, figure captions. When cited in the text, reference numbers should be superscripted, following punctuation marks. It is the sole responsibility of authors to cite articles that have been submitted to a journal or were in print at the time of submission to ACSi. Formatting of references to published work should follow the journal style; please also consult a recent issue:

1. J. W. Smith, A. G. White, *Acta Chim. Slov.* **2008**, *55*, 1055–1059.
2. M. F. Kemmere, T. F. Keurentjes, in: S. P. Nunes, K. V. Peinemann (Ed.): *Membrane Technology in the Chemical Industry*, Wiley-VCH, Weinheim, Germany, **2008**, pp. 229–255.
3. J. Levec, Arrangement and process for oxidizing an aqueous medium, US Patent Number 5,928,521, date of patent July 27, **1999**.
4. L. A. Bursill, J. M. Thomas, in: R. Sersale, C. Collela, R. Aiello (Eds.), *Recent Progress Report and Discussions: 5th International Zeolite Conference*, Naples, Italy, 1980, Gianini, Naples, **1981**, pp. 25–30.
5. J. Szegezdi, F. Cszimadia, Prediction of dissociation using microconstants, [http://www.chemaxon.com/conf/Prediction\\_of\\_dissociation\\_constant\\_using\\_microconstants.pdf](http://www.chemaxon.com/conf/Prediction_of_dissociation_constant_using_microconstants.pdf), (assessed: March 31, 2008)

Titles of journals should be abbreviated according to Chemical Abstracts Service Source Index (CASSI).

## Special Notes

- Complete characterization, **including crystal structure**, should be given when the synthesis of new compounds in crystal form is reported.
- Numerical **data should be reported with the number of significant digits corresponding to the magnitude** of experimental uncertainty.
- **The SI system of units and IUPAC recommendations** for nomenclature, symbols and abbreviations should be followed closely. Additionally, the authors should follow the general guidelines when citing spectral and analytical data, and depositing crystallographic data.
- **Characters** should be correctly represented throughout the manuscript: for example, 1 (one) and l (ell), 0 (zero) and O (oh), x (ex), D7 (times sign), B0 (degree sign). Use Symbol font for all Greek letters and mathematical symbols.
- The rules and recommendations of the **IUBMB** and the **International Union of Pure and Applied Chemistry (IUPAC)** should be used for abbreviation of chemical names, nomenclature of chemical compounds, enzyme nomenclature, isotopic compounds, optically active isomers, and spectroscopic data.
- **A conflict of interest** occurs when an individual (author, reviewer, editor) or its organization is involved in multiple interests, one of which could possibly corrupt the motivation for an act in the

other. Financial relationships are the most easily identifiable conflicts of interest, while conflicts can occur also as personal relationships, academic competition, etc. **The Editors** will make effort to ensure that conflicts of interest will not compromise the evaluation process; potential editors and reviewers will be asked to exempt themselves from review process when such conflict of interest exists. When the manuscript is submitted for publication, **the authors** are expected to disclose any relationships that might pose potential conflict of interest with respect to results reported in that manuscript. In the Acknowledgement section the source of funding support should be mentioned. The statement of disclosure must be provided as Comments to Editor during the submission process.

- **Published statement of Informed Consent.** Research described in papers submitted to ACSi must adhere to the principles of the Declaration of Helsinki (<http://www.wma.net/e/policy/b3.htm>). These studies must be approved by an appropriate institutional review board or committee, and informed consent must be obtained from subjects. The Methods section of the paper must include: 1) a statement of protocol approval from an institutional review board or committee and 2), a statement that informed consent was obtained from the human subjects or their representatives.
- **Published Statement of Human and Animal Rights.** When reporting experiments on human subjects, authors should indicate whether the procedures followed were in accordance with the ethical standards of the responsible committee on human experimentation (institutional and national) and with the Helsinki Declaration of 1975, as revised in 2008. If doubt exists whether the research was conducted in accordance with the Helsinki Declaration, the authors must explain the rationale for their approach and demonstrate that the institutional review body explicitly approved the doubtful aspects of the study. When reporting experiments on animals, authors should indicate whether the institutional and national guide for the care and use of laboratory animals was followed.
- To avoid conflict of interest between authors and referees we expect that not more than one referee is from the same country as the corresponding author(s), however, not from the same institution.
- Contributions authored by **Slovenian scientists** are evaluated by non-Slovenian referees.
- Papers describing **microwave-assisted reactions** performed in domestic microwave ovens are not considered for publication in *Acta Chimica Slovenica*.
- *Manuscripts that are **not prepared and submitted** in accord with the instructions for authors are not considered for publication.*

## Appendices

Authors are encouraged to make use of supporting information for publication, which is supplementary material (appendices) that is submitted at the same time as the manuscript. It is made available on the Journal's web site and is linked to the article in the

Journal's Web edition. The use of supporting information is particularly appropriate for presenting additional graphs, spectra, tables and discussion and is more likely to be of interest to specialists than to general readers. When preparing supporting information, authors should keep in mind that the supporting information files will not be edited by the editorial staff. In addition, the files should be not too large (upper limit 10 MB) and should be provided in common widely known file formats to be accessible to readers without difficulty. All files of supplementary materials are loaded separately during the submission process as supplementary files.

## Proposed Cover Picture and Graphical Abstract Image

**Graphical content:** an ideally full-colour illustration of resolution 300 dpi from the manuscript must be proposed with the submission. Graphical abstract pictures are printed in size 6.5 x 4 cm (hence minimal resolution of 770 x 470 pixels). Cover picture is printed in size 11 x 9.5 cm (hence minimal resolution of 1300 x 1130 pixels)

Authors are encouraged to submit illustrations as candidates for the journal Cover Picture\*. The illustration must be related to the subject matter of the paper. Usually both proposed cover picture and graphical abstract are the same, but authors may provide different pictures as well.

\* The authors will be asked to contribute to the costs of the cover picture production.

## Statement of novelty

Statement of novelty is provided in a Word file and submitted as a supplementary file in step 4 of submission process. Authors should in no more than 100 words emphasize the scientific novelty of the presented research. Do not repeat for this purpose the content of your abstract.

## List of suggested reviewers

List of suggested reviewers is a Word file submitted as a supplementary file in step 4 of submission process. Authors should propose the names, full affiliation (department, institution, city and country) and e-mail addresses of three potential referees. Field of expertise and at least two references relevant to the scientific field of the submitted manuscript must be provided for each of the suggested reviewers. The referees should be knowledgeable about the subject but have no close connection with any of the authors. In addition, referees should be from institutions other than (and preferably countries other than) those of any of the authors.

## How to Submit

Users registered in the role of author can start submission by choosing USER HOME link on the top of the page, then choosing the role of the Author and follow the relevant link for starting the submission process. Prior to submission we strongly recommend that you familiarize yourself with the ACSi style by browsing the journal, particularly if you have not submitted to the ACSi before or recently.

## Correspondence

All correspondence with the ACSi editor regarding the paper goes through this web site and emails. Emails are sent and recorded in the web site database. In the correspondence with the editorial office please provide ID number of your manuscript. All emails you receive from the system contain relevant links. **Please do not answer the emails directly but use the embedded links in the emails for carrying out relevant actions.** Alternatively, you can carry out all the actions and correspondence through the online system by logging in and selecting relevant options.

## Proofs

Proofs will be dispatched via e-mail and corrections should be returned to the editor by e-mail as quickly as possible, normally within 48 hours of receipt. Typing errors should be corrected; other changes of contents will be treated as new submissions.

## Submission Preparation Checklist

As part of the submission process, authors are required to check off their submission's compliance with all of the following items, and submissions may be returned to authors that do not adhere to these guidelines.

1. The submission has not been previously published, nor is it under consideration for publication in any other journal (or an explanation has been provided in Comments to the Editor).
2. All the listed authors have agreed on the content and the corresponding (submitting) author is responsible for having ensured that this agreement has been reached.
3. The submission files are in the correct format: manuscript is created in MS Word but will be **submitted in PDF** (for reviewers) as well as in original MS Word format (as a supplementary file for technical editing); diagrams and graphs are created in Excel and saved in one of the file formats: TIFF, EPS or JPG; illustrations are also saved in one of these formats. The preferred position of graphic files in a document is to embed them close to the place where they are mentioned in the text (See **Author guidelines** for details).
4. The manuscript has been examined for spelling and grammar (spell checked).
5. The **title** (maximum 150 characters) briefly explains the contents of the manuscript.
6. Full names (first and last) of all authors together with the affiliation address are provided. Name of author(s) denoted as the corresponding author(s), together with their e-mail address, full postal address and telephone/fax numbers are given.
7. The **abstract** states the objective and conclusions of the research concisely in no more than 150 words.
8. Keywords (minimum three, maximum six) are provided.
9. **Statement of novelty** (maximum 100 words) clearly explaining new findings reported in the manuscript should be prepared as a separate Word file.
10. The text adheres to the stylistic and bibliographic requirements outlined in the **Author guidelines**.
11. Text in normal style is set to single column, 1.5 line spacing, and 12 pt. Times New Roman font is

recommended. All tables, figures and illustrations have appropriate captions and are placed within the text at the appropriate points.

12. Mathematical and chemical equations are provided in separate lines and numbered (Arabic numbers) consecutively in parenthesis at the end of the line. All equation numbers are (if necessary) appropriately included in the text. Corresponding numbers are checked.
13. Tables, Figures, illustrations, are prepared in correct format and resolution (see **Author guidelines**).
14. The lettering used in the figures and graphs do not vary greatly in size. The recommended lettering size is 8 point Arial.
15. Separate files for each figure and illustration are prepared. The names (numbers) of the separate files are the same as they appear in the text. All the figure files are packed for uploading in a single ZIP file.
16. Authors have read **special notes** and have accordingly prepared their manuscript (if necessary).
17. References in the text and in the References are correctly cited. (see **Author guidelines**). All references mentioned in the Reference list are cited in the text, and vice versa.
18. Permission has been obtained for use of copyrighted material from other sources (including the Web).
19. The names, full affiliation (department, institution, city and country), e-mail addresses and references of three potential referees from institutions other than (and preferably countries other than) those of any of the authors are prepared in the word file. At least two relevant references (important papers with high impact factor, head positions of departments, labs, research groups, etc.) for each suggested reviewer must be provided.
20. Full-colour illustration or graph from the manuscript is proposed for graphical abstract.
21. **Appendices** (if appropriate) as supplementary material are prepared and will be submitted at the same time as the manuscript.

## Privacy Statement

The names and email addresses entered in this journal site will be used exclusively for the stated purposes of this journal and will not be made available for any other purpose or to any other party.

ISSN: 1580-3155

---

## Koristni naslovi

---

Slovensko kemijsko društvo  
Slovenian Chemical Society



**Slovensko kemijsko društvo**

[www.chem-soc.si](http://www.chem-soc.si)

e-mail: [chem.soc@ki.si](mailto:chem.soc@ki.si)

---



**Wessex Institute of Technology**

[www.wessex.ac.uk](http://www.wessex.ac.uk)

---



**SETAC**

[www.setac.org](http://www.setac.org)

---



**European Water Association**

<http://www.ewa-online.eu/>

---



**European Science Foundation**

[www.esf.org](http://www.esf.org)

---



**European Federation of Chemical Engineering**

<https://efce.info/>

---



**I U P A C**

INTERNATIONAL UNION OF  
PURE AND APPLIED CHEMISTRY

**International Union of Pure and Applied Chemistry**

<https://iupac.org/>

---

---

## Novice evropske zveze kemijskih društev (EuCheMS) najdete na:

---



**EuCheMS: Brussels News Updates**

<http://www.euchems.eu/newsletters/>

---





Donau Lab d.o.o., Ljubljana  
Tbilisjska 85  
SI-1000 Ljubljana  
[www.donaulab.si](http://www.donaulab.si)  
[office-si@donaulab.com](mailto:office-si@donaulab.com)



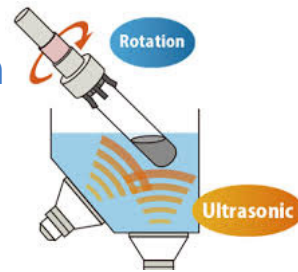
# THINKY

## Nano PREMIXER PR-1

Uniformna disperzija in deaglomeracija  
nanomaterialov (CNT, Graphene, drugi)

Dual-Sonic ultrazvočni sistem

Aktivno hlajenje kopeli



# BODITE NEUSTAVLJIVI

## MAGNEZIJ Krka 300



Granulat za pripravo napitka vsebuje magnezijev citrat in vitamin B<sub>2</sub>.



Magnezij in vitamin B<sub>2</sub> prispevata k zmanjšanju utrujenosti in izčrpanosti ter normalnemu delovanju živčnega sistema.



Magnezij prispeva tudi k delovanju mišic.



[www.magnezijkrka.si](http://www.magnezijkrka.si)

- ✔ Okus po pomaranči in limeti. ✔ Brez konzervansov.
- ✔ Brez umetnih barvil, arom in sladil. ✔ Ena vrečka na dan.

Prehransko dopolnilo ni nadomestilo za uravnoteženo in raznovrstno prehrano. Skrbite tudi za zdrav življenjski slog.

NOVO

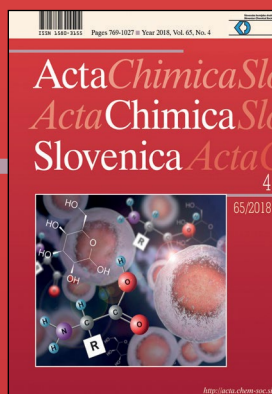
 KRKA



# ActaChimicaSlovenica

## ActaChimicaSlovenica

Metabolic network approaches from unstructured models to detailed mechanistic models foresee the major fluxes of nutrients, byproducts and final products as well as facilitate development of bioreactor operation performance. (see page 769)



Year 2018, Vol. 65, No. 4

